COASTAL RISK: SHORES AND DELTAS IN PERIL

EDITED BY: Clara Armaroli, Derek W. T. Jackson, Denise Reed and Christophe Viavattene

PUBLISHED IN: Frontiers in Earth Science and Frontiers in Marine Science

frontiers Research Topics

frontiers

ISSN 1664-8714
ISBN 978-2-88963-398-2
DOI 10.3389/978-2-88963-398-2

About Frontiers

Frontiers is more than just an open-access publisher of scholarly articles: it is a pioneering approach to the world of academia, radically improving the way scholarly research is managed. The grand vision of Frontiers is a world where all people have an equal opportunity to seek, share and generate knowledge. Frontiers provides immediate and permanent online open access to all its publications, but this alone is not enough to realize our grand goals.

Frontiers Journal Series

The Frontiers Journal Series is a multi-tier and interdisciplinary set of open-access, online journals, promising a paradigm shift from the current review, selection and dissemination processes in academic publishing. All Frontiers journals are driven by researchers for researchers; therefore, they constitute a service to the scholarly community. At the same time, the Frontiers Journal Series operates on a revolutionary invention, the tiered publishing system, initially addressing specific communities of scholars, and gradually climbing up to broader public understanding, thus serving the interests of the lay society, too.

Dedication to Quality

Each Frontiers article is a landmark of the highest quality, thanks to genuinely collaborative interactions between authors and review editors, who include some of the world's best academicians. Research must be certified by peers before entering a stream of knowledge that may eventually reach the public - and shape society; therefore, Frontiers only applies the most rigorous and unbiased reviews.
Frontiers revolutionizes research publishing by freely delivering the most outstanding research, evaluated with no bias from both the academic and social point of view. By applying the most advanced information technologies, Frontiers is catapulting scholarly publishing into a new generation.

What are Frontiers Research Topics?

Frontiers Research Topics are very popular trademarks of the Frontiers Journals Series: they are collections of at least ten articles, all centered on a particular subject. With their unique mix of varied contributions from Original Research to Review Articles, Frontiers Research Topics unify the most influential researchers, the latest key findings and historical advances in a hot research area! Find out more on how to host your own Frontiers Research Topic or contribute to one as an author by contacting the Frontiers Editorial Office: researchtopics@frontiersin.org

COASTAL RISK: SHORES AND DELTAS IN PERIL

Topic Editors:
Clara Armaroli, University of Ferrara, Italy
Derek W. T. Jackson, Ulster University, United Kingdom
Denise Reed, University of New Orleans, United States
Christophe Viavattene, Middlesex University, United Kingdom

The interaction between land and sea is controlled by a number of processes that are in general driven by the equilibrium between environmental forcing components (e.g. hydrodynamic - waves, currents, surges), atmospheric (e.g. winds) and terrestrial (e.g. catchment land cover) and sediment dynamics. In the context of the Anthropocene epoch, the equilibrium in many coastal regions is now often altered by the influence of human activities. Successive human activities globally influence (indirectly) these forcing components, helping magnify the negative impact of extreme meteorological events and sea level rise. Directly, human activity can also influence a number of processes at a local scale within and between the catchment, the sea and the coast. For example, misplaced engineered infrastructure inside these naturally dynamic environments can accentuate disequilibrium, destabilizing shores and deltas. Development in catchments can promote rapid runoff, inducing sometimes-dramatic effects on downstream urbanized areas, the socio-economy as well as on coastal resources and ecosystems.

This Research Topic aims to assemble research and review papers that focus on the dynamics of shores and deltas in peril under present conditions as well as in the future context of sea-level rise, climate change and adaptation strategies under various scenarios.

Citation: Armaroli, C., Jackson, D. W. T., Reed, D., Viavattene, C., eds. (2020). Coastal Risk: Shores and Deltas in Peril. Lausanne: Frontiers Media SA.
doi: 10.3389/978-2-88963-398-2

Table of Contents

04 ***Editorial: Coastal Risk: Shores and Deltas in Peril***
Clara Armaroli, Derek W. T. Jackson, Denise J. Reed and Christophe Viavattene

06 ***Chenier Morphodynamics on the Amazon-Influenced Coast of Suriname, South America: Implications for Beach Ecosystem Services***
Edward J. Anthony, Guillaume Brunier, Antoine Gardel and Michael Hiwat

26 ***Assessing Morphologic Controls on Atoll Island Alongshore Sediment Transport Gradients Due to Future Sea-Level Rise***
James B. Shope and Curt D. Storlazzi

39 ***Shoreline Dynamics Along a Developed River Mouth Barrier Island: Multi-Decadal Cycles of Erosion and Event-Driven Mitigation***
Christopher J. Hein, Andrew R. Fallon, Peter Rosen, Porter Hoagland, Ioannis Y. Georgiou, Duncan M. FitzGerald, Michael Morris, Sarah Baker, George B. Marino and Gregory Fitzsimons

62 ***The Risk Reduction Benefits of the Mesoamerican Reef in Mexico***
Borja G. Reguero, Fernando Secaira, Alexandra Toimil, Mireille Escudero, Pedro Díaz-Simal, Michael W. Beck, Rodolfo Silva, Curt Storlazzi and Iñigo J. Losada

83 ***Multi-Decadal to Short-Term Beach and Shoreline Mobility in a Complex River-Mouth Environment Affected by Mud From the Amazon***
Morgane Jolivet, Edward J. Anthony, Antoine Gardel and Guillaume Brunier

100 ***Coastal Impact From High-Energy Events and the Importance of Concurrent Forcing Parameters: The Cases of Storm Ophelia (2017) and Storm Hector (2018) in NW Ireland***
Emilia Guisado-Pintado and Derek W. T. Jackson

118 ***Seasonal Variability of Forces Controlling Sedimentation in the Sundarbans National Forest, Bangladesh***
R. P. Hale, C. A. Wilson and E. J. Bomer

131 ***From Hazard to Consequences: Evaluation of Direct and Indirect Impacts of Flooding Along the Emilia-Romagna Coastline, Italy***
Clara Armaroli, Enrico Duo and Christophe Viavattene

151 ***The Role of Detailed Geomorphic Variability in the Vulnerability Assessment of Potential Oil Spill Events on Mixed Sand and Gravel Beaches: The Cases of Two Adriatic Sites***
Edoardo Grottoli and Paolo Ciavola

166 ***Morphological Evolution of an Intertidal Area Following a Set-Back Scheme: A Case Study From the Perkpolder Basin (Netherlands)***
Riccardo Brunetta, João Salvador de Paiva and Paolo Ciavola

184 ***Coasts in Peril? A Shoreline Health Perspective***
J. A. G. Cooper and Derek W. T. Jackson

frontiers in Earth Science

EDITORIAL
published: 04 December 2019
doi: 10.3389/feart.2019.00323

Editorial: Coastal Risk: Shores and Deltas in Peril

Clara Armaroli[1]*, *Derek W. T. Jackson*[2], *Denise J. Reed*[3] and *Christophe Viavattene*[4]

[1] Department of Physics and Earth Sciences, University of Ferrara, Ferrara, Italy, [2] School of Geography and Environmental Sciences, Ulster University, Coleraine, United Kingdom, [3] Pontchartrain Institute for Environmental Sciences, University of New Orleans, New Orleans, LA, United States, [4] Flood Hazard Research Center, Middlesex University of London, London, United Kingdom

Keywords: coastal, erosion, flooding, storms, restoration, sea-level rise, morphodynamics, ecosystem services

Editorial on the Research Topic

Coastal Risk: Shores and Deltas in Peril

Coastal systems are the result of a natural equilibrium between hydrodynamic, atmospheric, and terrestrial parameters and sediment dynamics. In the Anthropocene, this equilibrium in many coastal regions can be altered by human activities. These activities may globally magnify the effects of extreme meteorological events and sea level rise and directly influence coastal processes down to a local scale within and between river catchments, the sea, and the coast. While most interventions, such as urban development, seawalls, and jetties are placed for specific human benefits, their indirect effects on coastal economies, societies and ecosystems can be significant.

This Research Topic brings together research from across the world to illustrate the dramatic and diverse nature of the peril that coasts and deltas face. Scientific understanding of the dynamics of these systems is essential to their current management and for the development of adaptation strategies to reduce future risk in the face of climate change.

The dynamics of beach environments and the role of storms is the focus of several papers. Guisado-Pintado and Jackson note that more frequent and more intense Atlantic storms over the last 40 years have heightened the potential risk to coastal environments, population, and infrastructure. They examined the effects of two storms on a beach system in NW Ireland and conclude that that storm energy is not always a direct indicator of coastal impact. Local forcing factors and antecedent beach conditions can be more important drivers of coastal response on sandy beaches. Storm waves from "nor'easters" which impact the New England (USA) coast during winter and early spring are a key influence on the Plum Island system studied by Hein et al. using beach surveys, sediment sampling, numerical modeling, and historical analysis. They found a migrating "hot spot" of erosion which presents challenges for local communities.

The interaction of local beach dynamics and sediment supply with larger scale, longer time scale changes imposed by migrating Amazon mudbanks is the focus of two papers. Jolivet et al. found that multi-decadal beach mobility reflects influences on the wave regime from alongshore-migrating banks (strong wave dissipation and limited beach mobility) and inter-bank areas (limited wave dissipation and larger beach mobility). Periods of erosion from these multi-scale interactions impact local communities by reducing beach space available for recreation and turtle-nesting. The beach has also been influenced by commercial sand mining (Anthony et al.), exacerbating the effect of natural sand "sinks" on downdrift areas. The importance of these beaches for turtle nesting is noted in both papers, highlighting important ecosystem effects from human impacts.

OPEN ACCESS

Edited and reviewed by:
Gordon Woo,
Risk Management Solutions,
United Kingdom

***Correspondence:**
Clara Armaroli
clara.armaroli@unife.it

Specialty section:
This article was submitted to Geohazards and Georisks, a section of the journal Frontiers in Earth Science

Received: *03 October 2019*
Accepted: *19 November 2019*
Published: *04 December 2019*

Citation:
Armaroli C, Jackson DWT, Reed DJ and Viavattene C (2019) Editorial: Coastal Risk: Shores and Deltas in Peril. Front. Earth Sci. 7:323. doi: 10.3389/feart.2019.00323

Pressures of human activity extend into estuaries where the interaction of riverine and tidal forcing on sediment dynamics governs the ability of wetlands to keep pace with sea-level rise. In the Sundarbans (Bangladesh), extensive mangroves forests are fed by a complex system of tidal channels that distribute river sediments. Hale et al. found that while increased sea levels, and associated increased in flooding frequency within the mangroves, could bring more opportunity for sediment deposition, sediment supply to the system is threatened by a proposed upstream project that could decrease the sediment loads of the Ganges and Brahmaputra Rivers by as much as 75 and 25%, respectively. Maintaining systems like the Sundarbans is important for a storm protection role, and the same issue drives restoration of estuarine wetlands elsewhere. In NW Europe, many tidal wetlands have been drained for agricultural use, often leading to land subsidence. Efforts are underway to re-introduce the tide in some "set-back" schemes to regain ecosystems and provide storm buffers to coastal protection works. Brunetta et al. examined the morphological evolution and sediment distribution on one such scheme in SW Netherlands, projecting a 8–10 years period for marsh vegetation to establish and perhaps 50 years before a mature marsh forms.

Such time scales for restoration make it important to retain coastal features that provide vital services, such as storm protection for coastal communities. Coral reefs are a good example. Shope and Storlazzi used numerical modeling to show how the morphology of atolls influences sediment transport. With SLR, all shorelines exhibited an intensification of pre-existing erosion/accretion patterns. Atoll islands most susceptible to shoreline instability with SLR are narrow, located on small atolls, with narrow and deep reef flats. Loss of reefs can have important implications, especially in tourism areas subject to coastal storms. The Mesoamerican Reef provides risk reduction benefits in Quintana Roo for human infrastructure. The annual risk reduction benefits are estimated at 4,600 people, USD 42 million damage prevention for buildings, and 20.8 million USD for hotel infrastructure (Reguero et al.). Such valuation reiterates the need to protect and maintain natural infrastructure.

The interaction between people and the coast is multifaceted and understanding dynamic feedbacks is important at a number of scales. Such complexity, however, is challenging to simply summarize so that it can be used at times of need. Response to oil spills is one example where, under emergency situations, knowledge of coastal dynamics is needed to guide clean up activities. The Adriatic Sea is a highly trafficked area for oil tankers and mixed sand and gravel beaches need to be understood to inform response planning. Grottoli and Ciavola noted that the dynamics of storm berms on these beaches lead to the potential for rapid oil burial, and discuss how such information could be better incorporated into oil spill response planning. Geomorphic complexity is further complicated by social and economic activities. Armaroli et al. use hazard modeling combined with an impact assessment model to quantify direct and indirect impacts of storm events on two villages in northern Italy. By considering the effects on people, property, and businesses the combined modeling approach was able to identify which village was subject to greater overall risk, enabling improved planning of coastal defense measures.

Several of these papers illustrate the current focus on the potential impact of coastal hazards on property and infrastructure. Cooper and Jackson argue that this has distorted approaches to assessing and managing physical coastal systems. They propose a five-category simple assessment of "coastal health" that could be used to assess the potential for returning to a naturally functioning physical coastal system.

Whether the realization that coasts and deltas are in peril is primarily driven by risk to human activities likely varies from system to system. The value of natural coastal systems is clear, however, and collectively these papers illustrate the process complexity and interacting scales of morphodynamics, across a variety of coastal settings, that must be considered for that "peril" to be managed and, if possible, mitigated.

AUTHOR CONTRIBUTIONS

DR wrote the main text with editing and additional contributions from DJ, CA, and CV.

Conflict of Interest: The authors declare that the research was conducted in the absence of any commercial or financial relationships that could be construed as a potential conflict of interest.

frontiers in Earth Science

ORIGINAL RESEARCH
published: 07 March 2019
doi: 10.3389/feart.2019.00035

Chenier Morphodynamics on the Amazon-Influenced Coast of Suriname, South America: Implications for Beach Ecosystem Services

Edward J. Anthony[1,2], Guillaume Brunier[3], Antoine Gardel[2] and Michael Hiwat[4]*

[1] UM 34 CEREGE, Aix Marseille University, CNRS, IRD, INRA, Collège de France, Aix-en-Provence, France, [2] USR LEEISA, CNRS, Cayenne, French Guiana, [3] UMR 6539 LEMAR, UBO, CNRS, IRD, Ifremer, Institut Universitaire Européen de la Mer, Plouzané, France, [4] WWF Guianas, Regional Office, Paramaribo, Suriname

OPEN ACCESS

Edited by:
Derek W. T. Jackson, Ulster University, United Kingdom

Reviewed by:
Andrew Cooper, Ulster University, United Kingdom
Duncan FitzGerald, Boston University, United States

****Correspondence:***
Edward J. Anthony
anthony@cerege.fr

Specialty section:
This article was submitted to Geohazards and Georisks, a section of the journal Frontiers in Earth Science

Received: *28 November 2018*
Accepted: *14 February 2019*
Published: *07 March 2019*

Citation:
Anthony EJ, Brunier G, Gardel A and Hiwat M (2019) Chenier Morphodynamics on the Amazon-Influenced Coast of Suriname, South America: Implications for Beach Ecosystem Services. Front. Earth Sci. 7:35. doi: 10.3389/feart.2019.00035

The 350-km long coast of Suriname, South America, is part of a unique system in the world characterized by large-scale mud supply from the Amazon and exposed to Atlantic waves. Large banks migrate alongshore from the Amazon to the Orinoco delta, separated by 'inter-bank' zones. Banks dissipate waves, partially weld onshore, and are colonized by mangroves, whereas waves in inter-bank areas cause shoreline erosion, mitigated where rare cheniers develop. Cheniers assure coastal protection and recreational and ecosystem services, notably providing nesting sites for marine turtles. Cheniers are also under pressure from sand mining. In order to gain a better understanding of how these cheniers form and evolve, a study was conducted on Braamspunt beach, a major turtle-nesting chenier in Suriname constructed from sand supplied by the Maroni River. Satellite images between 1987 and 2018 show a reduction of the alongshore extent of the chenier, following sand supply cut-off from the Maroni by a mud bank migrating westward towards the mouth of the Suriname River, exacerbated by mud-blanketing of sand. Commercial sand mining has further affected the beach, but mined volumes are not known. Field surveys (high-resolution topography, drone photogrammetry, wave measurements) conducted in February, 2016 highlight two chenier types depending on sand availability, transport and wave reworking: a high-tide reflective/low-tide dissipative and longshore transport-dominated type 1 exhibiting berm scarping, and a low, overwash-dominated type 2. As the mud-bank's leading edge impinges on the inter-bank trailing edge, sand sequestering by mud and storage in type 2 washovers entail less available sand downdrift. Type 1 lost over 4200 m^3 of sand in just 3–4 days. An increasingly deficient budget induces progressive change to type 2, morphodynamically better adapted to diminution of available sand, and epitomizing chenier fragmentation and isolation within the muddy Guianas coastal plain. By affecting the morphology and sand budget of Braamspunt, these changes lower opportunities for

turtle-nesting. Further reduction of the length of exposed chenier is apparently halted near the Suriname River mouth where mud is liquefied by the outflowing river and tidal jet, but the continued existence of this preserved beach could be endangered by sand mining.

Keywords: chenier, Amazon-Orinoco coast, mud bank, muddy Guianas coast, beach morphodynamics

INTRODUCTION

The term "chenier" designates a body of wave-reworked coarse-grained sediment resting stratigraphically on a muddy substrate (Otvos and Price, 1979; Otvos, 2018). Unlike beach ridges (Scheffers et al., 2012; Tamura, 2012), cheniers are not common because their genesis depends on a specific balance between sediment availability and wave action, and, thus, they will only develop where cohesive sediments are available in large volumes with enough sand, shelly deposits, or gravel that can be reworked by waves (Nardin and Fagherazzi, 2018). Cheniers are similar to any other wave-formed beach, except that their dynamics and preservation in coastal plains are conditioned by the supply of bedload-sized sediment in a context of ambient mud abundance, such as in river deltas (e.g., Saito et al., 2000; Hori et al., 2001; van Maren, 2005; McBride et al., 2007), and adjacent to estuaries (e.g., Anthony, 1989; Hein et al., 2016); but they also develop where sand, or gravel and shells, are reworked and segregated from mud (e.g., Woodroffe and Grime, 1999) which also serves as a substrate over which the chenier develops.

Cheniers are subjected to cross-shore wave processes acting over the beach face and eventually over the back-beach area, and to longshore transport. Once formed, cheniers can build up *in situ* through vertical and seaward growth of the beach face where the appropriate sediment is available. More commonly, limitations in the supply of appropriate sediment result in cheniers generally undergoing more or less active landward migration over their mud substrate. This occurs by overwash as waves top the low-elevation beach and transfer sediment from the active beach face to the back-beach. As waves rich in temporarily suspended sediments overwash the beach, water rapidly infiltrates into the beach, depositing lobes of sand or shells that form washovers. Since such sand remains segregated throughout from the ambient mud (i.e., mud on the foreshore, mud underlying the beach sand, and mud on the backshore in such situations of limited sand supply) as a result of wave action, the landward-migrating chenier tends to maintain its integrity and shape across-shore and alongshore. Cheniers may occur as multiple individual ridges in muddy plains, commonly referred to as chenier plains, and are sometimes organized into bands or bundles (Otvos, 2018). Cheniers can provide various ecosystem services in their ambient mud setting. They dissipate wave energy and, thus, can protect backshore areas. In their muddy settings, cheniers also serve as settlement areas, while abandoned inland cheniers are commonly sites for coast-parallel routes, and provide aggregate for building materials in situations where this is not pernicious to their role in coastal protection.

The coast of Suriname forms the present seaward fringe of the mud-dominated Guianas coastal plain on the Atlantic coast of northern South America between Amapá, in Brazil, and the Paria Peninsula in Venezuela (**Figure 1**). This also represents the world's longest muddy shoreline studded with cheniers occurring individually or in bundles between Amapá and the Orinoco River delta (Augustinus, 1978; Augustinus et al., 1989; Daniel, 1989; Prost, 1989; Wong et al., 2009; Anthony et al., 2010, 2011, 2014). This coast is exposed to trade-wind waves throughout the year, and is wave-dominated (Gratiot et al., 2007). It is the terminus of numerous rivers draining the Andes, the Andean foreland, the Llanos, and the Brazil and Guiana Shields (**Figure 1**). By far the most important of these rivers is the Amazon, which dominates the muddy fine-grained sediment dispersal and geological development of this coast (Anthony et al., 2010, 2014). The mud supplied by the Amazon is organized into a series of banks that migrate along the coast under the influence of waves and currents. The Guianas coastal mud-bank system is unique in the world in terms of the magnitude of alongshore mud migration. The mud is a product of the extremely high and pervasive supply by the Amazon, estimated as ranging from 754 to 1000 million tons a year (Martinez et al., 2009; Wittmann et al., 2011). Each mud bank can be up to 5 m thick, 10 to 60 km long and 20 to 30 km wide, and contain several times the annual mud supply of the Amazon (Anthony et al., 2014). A bank migrating alongshore efficiently dissipates wave energy (Wells and Coleman, 1981; Gratiot et al., 2007; Winterwerp et al., 2007), and is separated from its neighbors along the coast by inter-bank areas where, in the absence of mud-bank-induced dissipation, incident wave energy can be high and coastal erosion prevail. Since the banks migrate alongshore, the shoreline at any point will swing over time between bank (accretion) and inter-bank (erosion) phases. Cheniers develop in inter-bank areas of relatively high wave energy, and can become isolated and preserved inland through partial onshore welding of mud banks and growth of the muddy coastal plain. Each inter-bank phase results in the partial, or rarely, total removal, of the coastal stratigraphic package built during accretionary bank phases (Allison and Lee, 2004). Total removal of the stratigraphic package deposited during a bank phase can occur during a subsequent inter-bank phase characterized by particularly high wave-energy seasons such as during El Niño years (Gratiot et al., 2007). More commonly, removal is partial, signifying that there is a net growth of the coastal plain (Allison and Lee, 2004), potentially leading to chenier isolation with each growth cycle. Cheniers have played an important geological role in the building of the Guianas coastal plain over the last 5–6000 years (Augustinus, 1978; Augustinus et al., 1989).

The development of cheniers is conditioned by the availability of sufficient sand and shelly sand that are sorted out and concentrated by waves to form coherent sand bodies in

FIGURE 1 | Map of Suriname and the Amazon-Orinoco coast and the drainage basins of the Amazon and Orinoco Rivers and, collectively, the smaller Guiana Shield rivers between Amapá, in Brazil, and Guyana.

this overwhelmingly muddy environment. Pujos et al. (1990, 2000) concluded from heavy-mineral analyses that the quartz-dominated beach sands were derived exclusively from local sources and not winnowed out from the migrating Amazon mud banks. The most important sources of sand are the numerous smaller Guiana Shield rivers between the Amazon and the Orinoco (**Figure 1**). The hydrology and sediment fluxes of many of these rivers, which drain crystalline rocks, are still largely unknown. Even the catchment size of many of these rivers is not known with certainty. Cheniers are especially common in the vicinity, and downdrift, of the mouths of these rivers, developing in locally sand-rich settings but that are very largely dominated by mud from the distant Amazon. In addition to fluvial sand, marine carbonate debris (whole and comminuted shells), derived from the abundant skeletal remains of organisms that thrive in the rich ecosystems associated with the Amazon-Orinoco mangrove system, is also reworked onshore by waves. Finally, older cheniers inland can also be reworked to form new cheniers where coastal erosion has removed mud deposited during a previous bank phase. Coherent sand bodies can, thus, be formed in spite of the overwhelmingly muddy environment of the Guianas coast, through the local concentration of sand near, and downdrift of, river mouths, and through local efficient segregation of sand and shells from mud. The formation of such coherent sand bodies is also important as it represents an efficient way of further dissipating high incident wave energy during inter-bank phases.

Cheniers are actively exploited in the Guianas for aggregate to cater for the needs of urban and infrastructure development in the face of the rapid demographic growth characterizing this region. When practiced on active open-coast cheniers, this mining activity can have a deleterious effect on these deposits and the ecosystem services they provide. Although many rivers debouch through the Guianas coastal plain, there is a relative paucity of available sand in the coastal zone. Fluvial sand discharged to the coast is commonly buried by the abundant and pervasive Amazon mud, including in deeper inter-bank areas (Anthony et al., 2010), while estuarine sandy bedload is commonly draped with mud (Sottolichio et al., 2018). The rare and currently active cheniers of the Guianas coast also provide beach recreation outlets for the coastal populations, and, as nesting sites, are especially fundamental to the ecology of the protected marine turtles: *Lepidochelys olivacea*, *Chelonia mydas*, *Eretmochelys imbricata, Dermochelys coriacea* (Girondot et al., 2002; Péron et al., 2013).

In order to contribute to a better understanding of how cheniers develop in response to the large-scale regional mud-bank dynamics, a study was conducted on Braamspunt beach (**Figure 2A**), a remnant of a sandy chenier in Suriname that has been strongly modified by natural mud-bank activity over the last three decades. Braamspunt beach is close to the city of Paramaribo and provides a recreation outlet for the urban population. It is also an important turtle-nesting site on the 350 km-long Suriname shoreline, especially for leatherback turtles (*Dermochelys coriacea*). Over 80% of the Suriname coast is currently muddy (Gensac, 2012; Anthony, 2016), thus restricting considerably the availability of sandy beaches for turtles. The backshore wetlands behind Braamspunt beach are also an important habitat for shorebirds and other wildlife. The proximity of Braamspunt beach to the growing city of Paramaribo has also exposed the beach over the last two decades to commercial sand mining. Unfortunately, there has been no stock-taking of the volumes of sand extracted from Braamspunt beach over this period. In conjunction with changes induced by mud-bank activity, sand mining leads to a reduction of beach sediment budgets and impacts beach space available for recreation and for turtle-nesting. Here, we analyze the recent multi-decadal evolution of the Braamspunt chenier in response to mud banks and the morphodynamic changes in the remnant beach associated with this evolution. We expose the nefarious effects of sand mining in generating vulnerability of the beach, impairing its role in coastal protection and as a major site for marine turtle-nesting.

Setting of Braamspunt Beach

The migrating mud banks in the Guianas tend to cause a westward deflection of the mouths of the small rivers. The deflection commonly results in more or less prominent mud capes colonized by mangroves, reflecting the overarching influence of mud accumulation in transit from the Amazon. Braamspunt beach lines the mud cape between the mouths of the Maroni and the Suriname Rivers (**Figure 2A**). Mud capes and their associated cheniers generally provide shelter for parts of the coast to the west (downdrift direction on the Guianas coast) from direct attack by ocean waves coming from the northeast (see below). Paramaribo is niched on the west bank of the cape deflecting the mouth of the Suriname River. It is important to note that this deflection is less expressed where large rivers debouch on the coast. Fine examples are provided by the two large rivers at the borders of Suriname, the Maroni and the Corantijn Rivers (**Figure 2A**). Braamspunt beach, in what may be considered as its ancestral version (i.e., prior to the ongoing changes engendered by a mud bank, and described in this paper), is a fine example of an open-coast chenier in the Guianas. The proximity of large reservoirs of sand in the middle-ground bars at the mouth of the Maroni River suggest that the sand on Braamspunt beach has come from this river, supplemented by a small fraction of shelly debris winnowed out from the nearshore zone. The source function of the Maroni River is clearly expressed by the numerous cheniers that run west from the mouth of this river (**Figure 2B**). Braamspunt beach ends in spit recurves that reflect wave refraction at the mouth of the Suriname River.

The Suriname coast is affected by trade winds from the northeast that are mainly active from January to May. These winds generate rains on the coast from December to July, with an intervening relatively dry month in March. The annual rainfall in the coastal zone varies from 2 to 3 m. Trade winds are also the main generators of waves from the North and Central Atlantic Ocean (**Figure 2C**). These waves come from an east to northeast direction (Gratiot et al., 2007). Waves have significant periods (T_s) of 6 to 10 s, and significant offshore heights (H_s) of 1 to 2 m, the longer periods (>8 s) being associated with short spates of large swell waves generated by North Atlantic storms in autumn and winter and by Central Atlantic cyclones in summer and autumn. These longer waves have a directional range from north to north-northwest. The Suriname coast is, thus, essentially a wave-dominated coast, characterized by a clear seasonal regime. The most energetic trade-wind waves occur from December to April whereas swell waves appear to be most frequent in autumn and winter, reinforcing the relatively energetic winter to early spring wave regime induced by the trade winds. The wave climate shows variations in wave height at timescales ranging from multi-annual, hinged on El Nino phases, to multi-decadal, in association with large-scale atmosphere-ocean interactions in the North Atlantic (Walcker et al., 2015). Tides are semi-diurnal and the spring tidal range in Suriname is low-mesotidal, ca. 2 to 3 m.

MATERIALS AND METHODS

Mesoscale (Multi-Decadal Changes)

In order to track the recent multi-decadal shoreline changes along the coast of Suriname between the mouths of the Maroni and Suriname Rivers, and hence determine the changing status of the ancestral and current forms of Braamspunt beach, 10 Landsat 5 to 8 images covering the interval from July, 1987 to January, 2016, acquired from the United States Geological Survey (USGS), and two Sentinel 2A MSI (October, 2018), acquired from the European Space Agency (ESA), were used. The image resolution is 30 m for the earliest Landsat 5 TM (1987) images and 15 or 30 m for the most recent Landsat 8

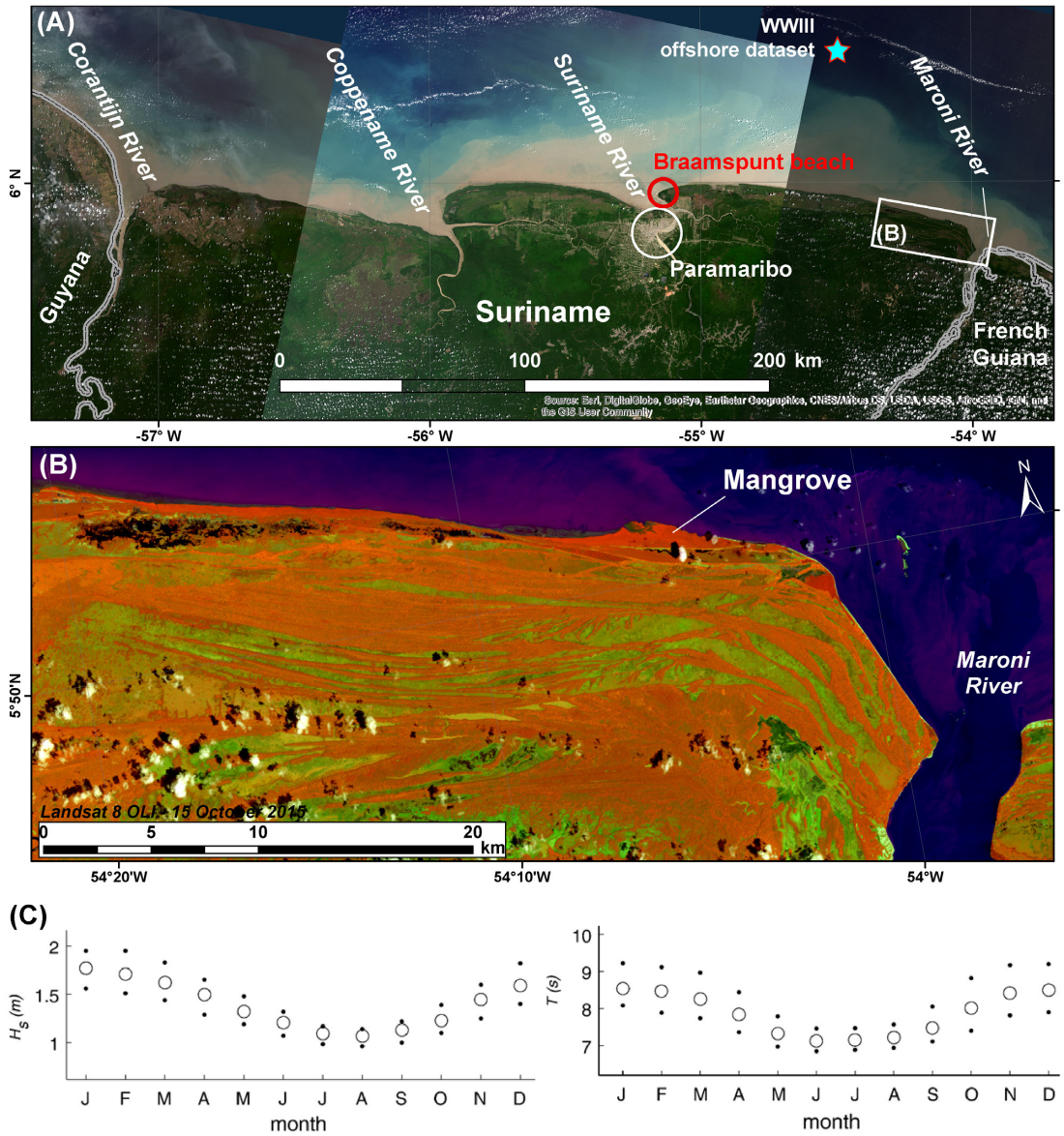

FIGURE 2 | Landsat image (2015) of the Suriname coast, location of Braamspunt chenier near the mouth of the Suriname River, and offshore WWIII data collection point for the field study **(A)**; Landsat image (2015) showing cheniers (vegetation in dark orange) separated by linear swamp depressions (light green) and running west from the mouth of the Maroni River between Suriname and French Guiana **(B)**. The diversity in orientation, length, width, and grouping of these cheniers reflect space- and time-varying bank and inter-bank dynamics. The dark red hue along the coast represents seafront mangrove swamps; **(C)** daily averages of wave-climate parameters, significant wave height H_S and wave period T, derived from a 44-year record of the ERA-40 (European ReAnalysis) wave dataset generated by the European Centre for Medium-Range Weather Forecasts (ECMWF) for the location 5° N, 52° W (modified after Gratiot et al., 2007). Dots correspond to the first and third inter-quartiles, and circles to the median values.

OLI-TIRS (2016) images. The selected Sentinel images have a 10 m-resolution in the visible and near-infrared bands. Images corresponding to the dry season were selected in order to avoid as much as possible cloud cover. The coordinate reference used for this study is the Universal Transverse Mercator (UTM) zone 21N, which comprises Suriname, associated with the Global Geodesic system WGS 1984 datum. In addition to the shoreline and its changes, the outlines of mud banks were also identified.

Regarding shoreline discrimination and change, only the 10 Landsat images were used. All the images have good overlap, and default USGS georeferencing. The shoreline was digitized for each image, using, as a reference, the external limit of vegetation. Long experience with the Guianas and other tropical coasts shows that the seaward mangrove fringe constitutes a good shoreline marker except where sandy beach deposits occur, colonized by grass vegetation with a clear seaward limit. Shoreline mobility was statistically analyzed using the ArcMap extension module

Digital Shoreline Analysis System (DSAS), version 4.3, coupled with ArcGIS® v10.2.2 (Thieler et al., 2009). The shore-normal distance of the vegetation line relative to a base line for each two sets of dates was calculated every 250 m alongshore. This distance was then divided by the time in years between two dates to generate a shoreline change rate, the End Point Rate (EPR) in DSAS 4.3, expressed in m a year.

The total annual error (E) of shoreline change rate was then defined from the following equation (Hapke et al., 2006):

$$E = \frac{\sqrt{d1^2 + d2^2}}{T} \quad (1)$$

where d_1 and d_2 are the uncertainty estimates of shoreline position for the successive sets of images and T is the time in years between image sets. The uncertainty of the shoreline position is defined by twice the pixel resolution. The obtained error E ranged from 3.4 to 8.5 m a year between 1987 and 2015.

Field Surveys of the Morphology and Dynamics of Braamspunt Beach

Two ground surveys were conducted on Braamspunt beach on February 9–10 and February 13–14, 2016, in order to map the morphology and grain-size properties of the beach, and characterize the wave conditions (**Figure 3A**). The experiments were aimed specifically at highlighting the morphodynamics and sand transport patterns that drive change on Braamspunt beach, and the beach sediment budget. They covered a spring-to-neap tidal cycle. Fortuitously, the experiments also coincided with marked variation in wave conditions between the two surveys. High-resolution topographic surveys were conducted in the course of the two field experiments using a Trimble R8 differential global positioning system (DGPS) in Real-Time Kinetics (RTK) mode. The system consists of a fixed station and a mobile station used to record the geographical coordinates and elevations of ground points. The two stations were linked by radio, which introduced a constraint since the radio signal could be lost over a distance of a couple of kilometers. The mobile unit comprised a GPS antenna and a computer that enabled acquisition and storage of data collected at 1 s-intervals over the beach. The mobile station was transported in a backpack most of the time by an operator carrying out the survey, but constraints imposed by time and tide also led us to use an all-terrain vehicle (**Figure 3B**). A total of 56,900 points were surveyed (23,050 on February 10 and 33,850 on February 13–14), giving an

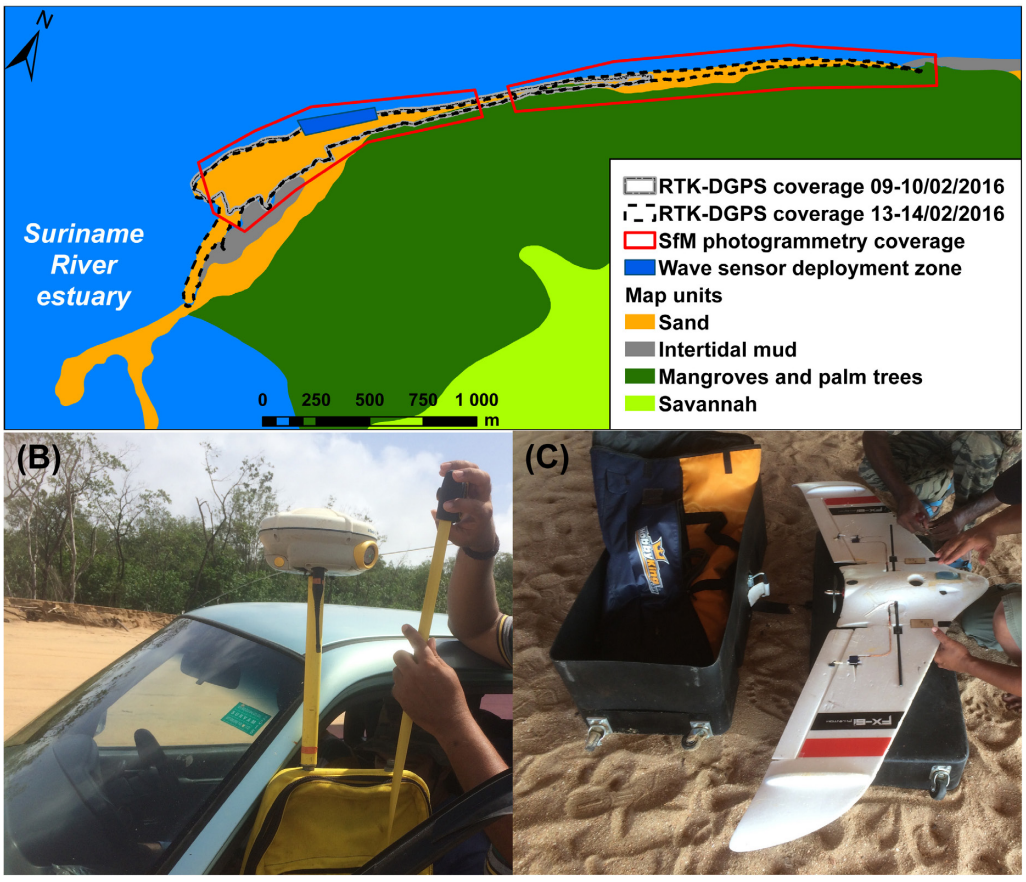

FIGURE 3 | (A) Experiments conducted on Braamspunt beach in February, 2016 and their ground coverage; **(B)** mobile GPS station on an all-terrain vehicle; **(C)** drone with custom-built wings used for photogrammetric survey.

overall density of 1 point for every 50 cm of beach. The base station deduced corrections that were relayed to the mobile antenna which then applied these corrections and computed x, y, z coordinates. In the absence of a topographic reference system and benchmarks at Braamspunt beach, we resorted to the Universal Transverse Mercator (UTM) zone 21N, which comprises Suriname, associated with the Global Geodesic system WGS 1984 datum. Elevation data were referenced to the world geoid EGM96 (Earth Gravitational Model) representing mean sea level. The constructor's (Trimble, Ltd.) error margin is ±1 to 2 cm for the x and y coordinates and ±2 to 3 cm for the z coordinate. 2.5-m cell digital elevation models (DEMs) of the gridded images were computed from the data using the Delaunay triangulation method. The comparison of the DEMs of the two surveys, named Differences of DEMs (DoDs), highlighted short-term variations in the subaerial beach volume that coincided with the shift from spring to neap tides and a significant drop in incident wave energy observed over the week of the surveys.

In addition to high-resolution ground surveying, topographic details of the beach were also obtained from aerial photogrammetry using a drone with custom-built wings (**Figure 3C**) and a camera provided and operated by the Nature Conservation Division of Suriname. Photogrammetry has, over the last decade, undergone significant new developments related notably to the workflow technique called *Surface-from-Motion* (SfM) (Westoby et al., 2012). SfM photogrammetry enables the production of high-resolution morphometric models and derived products such as digital surface models (DSMs) and orthophotographs. The technique has been applied in the mapping of a beach under the influence of mud banks drifting alongshore from the mouth of the Amazon near Cayenne, in neighboring French Guiana (Brunier et al., 2016). Several flights were operated over two sectors (west and east) of Braamspunt beach separated by the launching area near our field base (**Figure 3C**). A pocket-sized CANON Powershot S100 camera with a 12.1 MP 'high sensitivity' CMOS sensor was used to obtain photographs. The drone flew close to the ground (<100 m) in order to obtain a picture resolution less than or equal to 3.5 cm ground size pixel (GSD), and a scene size corresponding to a 120 m × 80 m picture footprint. We calibrated the parallax parameters using an overlap between pictures of about 85% end-lap in the lengthwise flight direction and about 50% side-lap between paths. Considering the scene size and the parallax parameters, the drone was flown at a speed of 70 km/h in order to keep an end-lap ratio with a shooting range of one picture per second. Moreover, we defined numerous parallel flight axes spaced 10s of meters. The stereopair alignment using SfM-photogrammetry was based on targets (Ground Control Points or GCPs) of 40 cm × 40 cm deployed on the beach and accurately georeferenced in RTK-DGPS. Furthermore, we sampled, randomly over much of the beach, and more selectively where features of interest occurred, numerous points named Ground Truth Points (GTPs), in order to assess the quality of our DSM. GTPs consisted of identified landmarks and deployed 05 m × 0.5 m plywood boards with an easily discernible black-and-white checker-board pattern. The SfM-photogrammetry workflow was operated using Agisoft Photoscan Professional software[1]. Successive DSMs can be used to establish temporal changes in beach sediment budget in the same way as DEMs can be used for this from high-resolution ground topographic survey data. In the case of Braamspunt beach, a photogrammetry-based succession of changing beach budgets was not carried out because only one DSM of the beach was obtained in the course of the experiment.

Tidal curves of the semi-fortnightly variation in water level in the course of the survey were constructed from theoretical tidal data provided by the French Service Hydrographique et Océanographique de la Marine (SHOM). The water levels do not, therefore, include oceanographic forcing effects such as ocean level setup by air pressure changes, and wind and wave forcing. In the course of both experiments, up to three NKE®-SP2T pressure sensors, equipped with turbidity sensors, were deployed on the beach in its distal part near the tip of Braamspunt (**Figure 3A**), and sampled continuously at 2 Hz. Sensor accuracy is 0.02 m. Wave heights and water levels under these values were neglected. Wave spectra were calculated over bursts of 20 min using fast Fourier transforms with a Hanning window of 600 s and 75% overlap (Sénéchal et al., 2001). A correction factor with a cutoff at 0.5 Hz was applied to account for the non-hydrostatic pressure field, as proposed by Horikawa (1988). For each burst, significant wave height (H_s) and peak period (T_p) were calculated in the spectral window [0.11; 0.5] Hz. Unfortunately, only one turbidity record could be exploited. We set a limit of 0.05 Hz between the gravity and infra-gravity wave domains. Offshore wave data (see **Figure 2A**) during the study period were derived from the third-generation *Wave Watch III (WWIII)* database of the *National Oceanic and Atmospheric Administration* (*NOAA*) of the United States[2]. *WWIII* is a spectral wave model that describes complex sea surface states based on wind data. *WWIII* calculates sea surface states every hour for regular spatial grids of half a degree of longitude and latitude. The model produces wave heights in meters (m), periods in seconds (s) and directions in degrees (°) for each grid cell.

Finally, 20 sediment samples were collected from the beach (**Figure 3A**) in order to determine grain-size characteristics and the carbonate (shell) content of the beach sand relative to the dominant quartz fraction. The samples were analyzed using a Beckman Coulter laser grain-size type LS 13 320. Samples were analyzed in the aqueous phase and particles ranging in size from 40 to 2000 μm were determined. A single grain-size curve was used to describe the entire spectrum of each sample. The percentage of carbonates in each sand sample was determined after passing it through hydrochloric acid to eliminate the organic fraction, leaving the residue of minerogenic sand.

[1]https://www.agisoft.com

[2]https://polar.ncep.noaa.gov/waves/download.shtml?

RESULTS

Mud Banks and Braamspunt Beach (1987–2016)

We identified at least two mud banks over the 29-year period of analysis (1987–2016) from the Landsat images. The alongshore continuity of the Braamspunt chenier, the beach sediment transport cell between the mouths of the Maroni and the Suriname Rivers, and the shoreline morphodynamics, have been controlled by bank attachment episodes between July, 1987 and October, 2015 (**Figure 4**). In 1987, this alongshore continuity of the beach from the Maroni River source to the Suriname River sink was masked by the attachment of mud bank 1 along much of the coast between the two river mouths (**Figure 4A**).

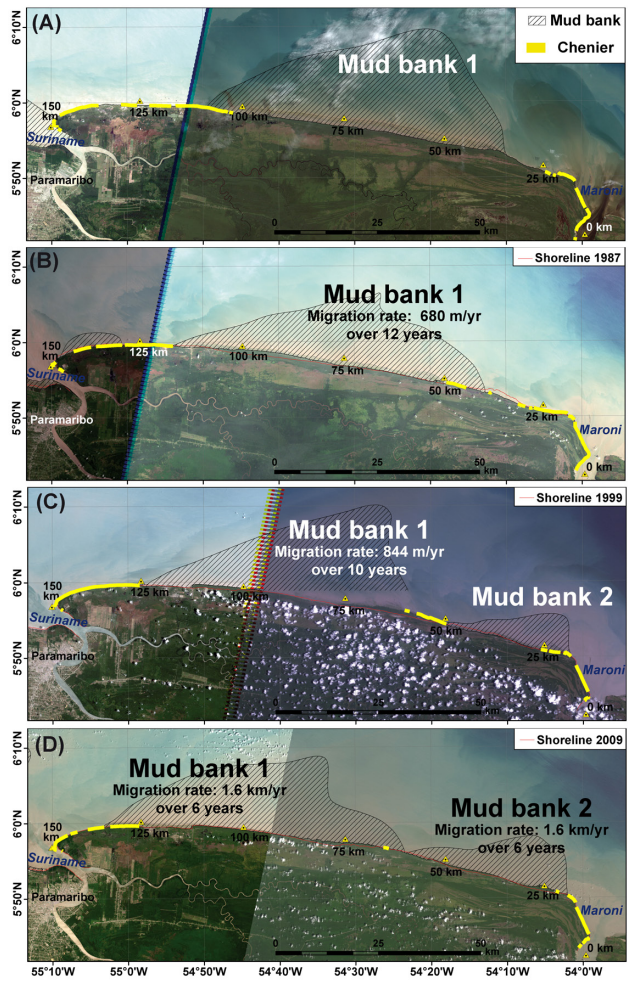

FIGURE 4 | Landsat images of analyzed shoreline changes between the Maroni and the Suriname Rivers (October 1987 to October 2015) showing the impact alongshore of migrating mud banks (muddy shoreline accretion) and inter-bank areas (shoreline erosion characterized by the landward-migrating Braamspunt chenier): **(A)** situation in 1987; **(B)** situation in 1999 with the 1987 shoreline; **(C)** situation in 2009 with the 1999 shoreline; **(D)** situation in 2015 with the 2009 shoreline.

This limited the functional Braamspunt chenier to a stretch of about 50 km east of the mouth of the Suriname River, the rest of the updrift chenier isolated by the mud bank, the inner, shore-welded, part of which was mangrove-colonized. East of the trailing edge of the mud bank, sandy beaches in the Maroni source area can be identified (**Figure 4A**). The 1999 image shows a chenier system fragmented by shore-attached mud (**Figure 4B**). In 2009, the active Braamspunt beach had been reduced in length to about 25 km, as a result of the persistence of mud-bank activity between the two river mouths, marked by the presence of a smaller bank (mud bank 2) near the mouth of the Maroni (**Figure 4C**). A further reduction of the length of the beach down to 8 km is observed in the 2015 image (**Figure 4D**). A date-to-date comparison of the satellite images shows successions of shoreline advance (mud bank) and retreat (inter-bank) at inordinately large rates exceeding 120 m a year in places (**Figures 5A–C**).

The satellite images between October, 1987 and January, 2016 (Landsat) and an additional image (Sentinel 2AMSI) in October, 2018 show the progressive reduction in the length of the active (functional) chenier and its fragmentation by mangrove-colonized sectors of shoreline (**Figure 6**). Local reworking and concentration of sand resulted in a coherent but narrow chenier in places separated by mangrove-colonized mud (**Figure 7**). By 12 January, 2016, the beach length had been reduced to 4 km as a result of the westward advance of the leading edge of mud bank 1. The October, 2018 image shows a fragmented chenier ending in a 1.6 km-long spit with recurves at the downdrift terminus formed by the estuary (**Figure 6**). The length of beach obtained from *in situ* field measurements was 7 km in January, 2015 and 5.6 km in August, 2015. By the end of January, 2016, just prior to this study, the measured beach length had been reduced to 2.6 km.

Morphodynamics of Braamspunt Beach

Offshore and Nearshore Hydrodynamic Conditions

The tidal and wave conditions that prevailed during the February, 2016 survey are depicted in **Figure 8**. The semi-diurnal tide had a mesotidal range of about 2.2 to 3 m, and the tidal cycle showed a spring-neap variation between 09/02/16 and 16/02/16. *WWIII* deep-water significant heights ranged from about 2.2 m at the start of the experiment (09/02) to about 2 m at the end of the field experiment (14/02), with a maximum of 2.9 m on 10/02. These are relatively energetic wave conditions, reflecting a typical El Nino year of rougher waves than usual. The wave heights measured by the pressure sensors on the beach (**Figure 8**) were, however, much lower, and ranged from 0.5 to 0.8 m, thus reflecting a significant amount of dissipation by mud over the shoreface, as has been documented by Gratiot et al. (2007) and Winterwerp et al. (2007), and dispersal of wave energy by refraction. About 60–80% of the deep-water energy was lost by the time the waves broke on the beach. This left a still non-negligible amount of energy that led to important beach morphological changes, as shown below. *WWIII* wave periods were relatively uniform at about 9–10 s, reflecting the trade-wind regime. Beach measurements showed a wider spread of periods ranging from about 5 to 20 s, a clear mix of both trade-wind waves (5–10 s) and longer swell waves from the

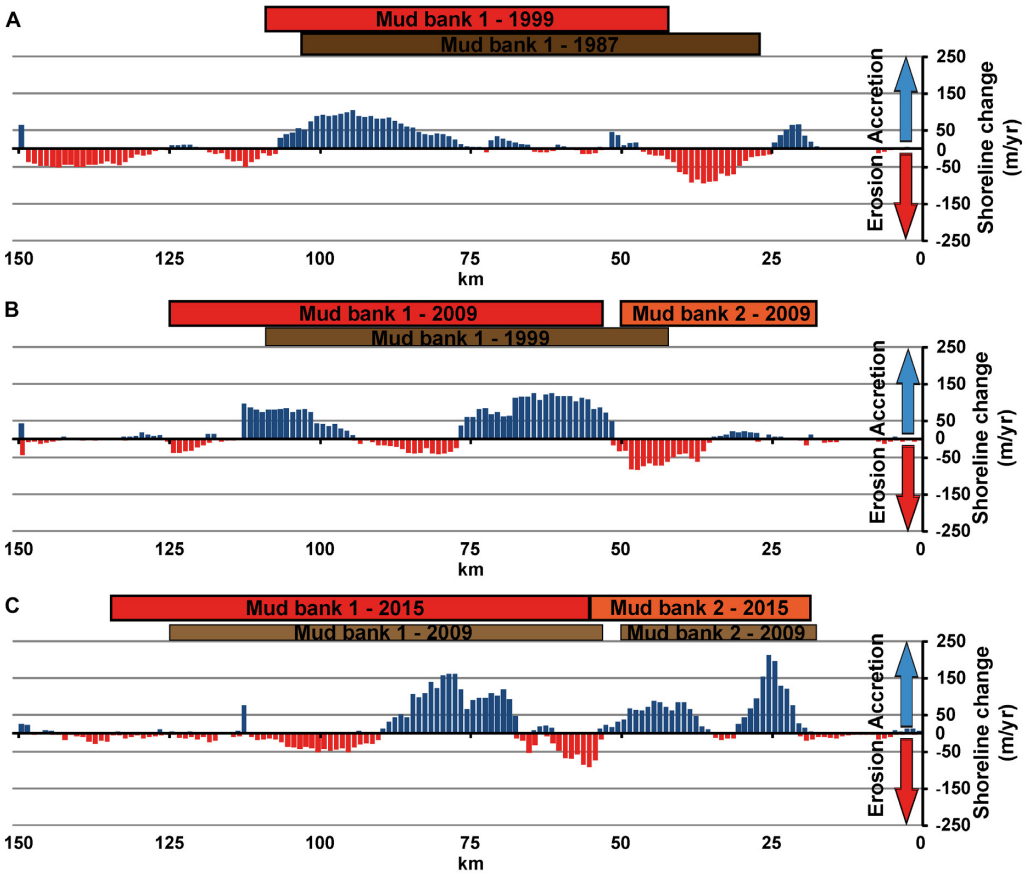

FIGURE 5 | Graphs of analyzed shoreline changes between the Maroni and the Suriname Rivers (October 1987 to October 2015) depicting the inordinately large erosion and accretion rates affecting the Guianas coast: **(A)** between 1987 and 1999; **(B)** between 1999 and 2009; **(C)** between 2009 and 2015.

Central Atlantic (12–16 s), and also possible infragravity waves (18–22 s) resulting from *in situ* wave breaking conditions in the surf zone and beach. Deep-water *WWIII* wave directions were from the northeast window, typical of the Guianas coast, and ranged from N 47 to 58°, indicating relatively high angles of 32–43° relative to the beach. Beach observations showed much lower, but still relatively high, angles of about 15–25°, following nearshore refraction. The turbidity values (NTU) and significant wave heights (Hs) showed, in the case of sensor Cpt 4 PT, the only sensor that recorded turbidity data, a clear relationship depicting temporary suspension of sand in the course of wave breaking.

Beach Grain-Size, and Morphology From Field Topographic Surveying

Braamspunt beach is characterized by well-sorted medium sand with median grain-size values of 300 to 600 μm, except in one washover sample with much coarser sand (**Figure 9**). The percentage of carbonates is highly variable, but locally significant, ranging from 4 to over 40%, reflecting preferential density sorting and concentration within the dominant quartz sand matrix. The high-resolution topography of the beach is depicted in three segments from north to the south (**Figures 10A–C**). Each segment comprises two DEMs (left: 10 February, Center: 14 February) and a DoD (right) that shows the differential between DEMs. The survey was incomplete for the northern part of the beach (**Figure 10A**) due to poor radio signal transmission on 10 February between the fixed and mobile GPS stations. The northern sector shows a narrow beach subject to erosion involving nearly 5 m of retreat of a steep reflective beach face characterized by a well-developed berm. The central sector (**Figure 10B**) exhibited a less steep profile and a beach that rapidly became wider from profile 2 southward. The beach topography also showed better contrast with this widening. Erosion was dominant on the beach face, but the berm and back-beach showed little change where the beach widened. The wide southern sector (**Figure 10C**) corresponds to the most recent spit recurve toward the Suriname River estuary. The back-beach topography in this sector showed significant variations caused by: (1) overwash processes, (2) overall beach surface lowering, and (3) inherited sand mining pits dug just prior to a State moratorium on beach sand mining in December, 2015. Much of the topographic change derived from the DoDs concerned the active beach face. Change was much less intense over the top and back of the beach. The spit sector showed alongshore alternations of beach face erosion and accretion that represent mobilized sand

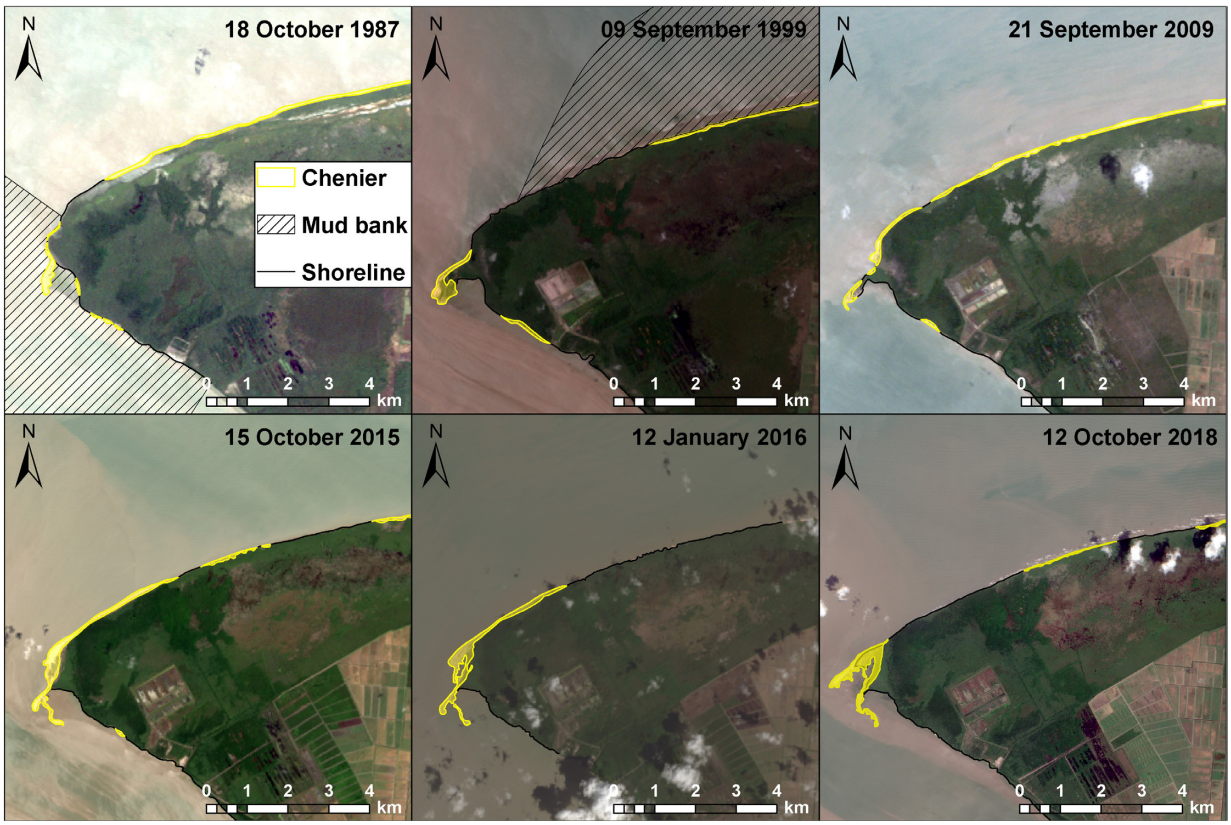

FIGURE 6 | Synthesis of analyzed changes in the Braamspunt chenier between October, 1987 and October, 2018. The latest development phase (October, 2018) of the chenier monitored in 2016, in the course of this study, has been marked by fragmentation and shortening of its downdrift sector near the distal tip of the mud cape impinging on the Suriname estuary.

'waves' migrating under the strong longshore drift that prevailed on this beach in the course of the surveys.

Beach Morphology From Photogrammetric Surveying

The orthophotographs and DSMs yielded by the photogrammetric survey, and obtained using the analytical procedure based on the SfM protocol, are shown in **Figure 11**. Both the orthophotographs and the DSMs are used to infer long- and cross-shore sediment transfer mechanisms and the resulting morphodynamics of the beach (discussed below). Various large-scale morphological features such as the spit recurves at the approaches to the Suriname River mouth, but also smaller-scale features such as beach scarps, log jams, and overwash fans, are clearly identified. It is interesting to note the strong similarity of the products of SfM photograph and the lower-resolution topographic data generated by the GPS surveys. Unfortunately, no DoDs were drawn up because only one photogrammetric survey was possible in the course of the week of the field surveys.

Sediment Budget of Braamspunt Beach and Budget Change Over the Survey Period

Braamspunt beach experienced net erosion between the two surveys, as shown by the RTK DGPS-generated DEMs and cross-shore profiles. The overall estimated sand volume of the surveyed beach, using an absolute beach base at −0.5 m, is about 570,000 m^3 of sand. This is a conservative estimate since the true absolute sandy base of the beach above ambient mud is probably lower than this value as a result of consolidation and lowering of the mud substrate and, especially, as the spit impinges on deep waters at the approach to the Suriname estuary. The net budget differentials bring out an overall loss of 4200 m^3 of sand for what corresponds to a very short (3–4 days) period of time (**Figure 10**), and a short stretch of beach (2.5 km). This highlights the fragile sediment budget of this beach. The important loss of sand could reflect updrift sequestering under mud, but, more likely, infill of holes dug out in the subtidal beach in the course of sand mining operations from boats moored near the beach, this subtidal zone not having been covered by the surveys. The differentials also show the clear propensity for downdrift transport of sand, dominantly as propagating sand waves, as we saw earlier (**Figure 10C**), and its final deposition in the large spit sector which forms an accreting sink from which sand is probably progressively transferred toward the estuarine depths. However, it was also clear in the course of the week that the spate of erosion observed and measured between the two GPS surveys was essentially driven by large waves that coincided with spring tides. These are the conditions most favorable to beach

FIGURE 7 | Narrow and fragmented chenier fronting retreating mangrove-colonized mud (February, 2016) in the trailing edge of the inter-bank area. Local reworking and concentration of the sand can lead to the appearance of a coherent chenier visible on satellite images. These narrow fragmented cheniers can migrate landward as coherent sand bodies, asphyxiating seafront mangroves.

scarping, overwashing by waves, strong longshore transport, and, overall, rapid erosion of the beach.

DISCUSSION

Morphodynamics and Recent Evolution of Braamspunt Chenier

Bank phases lead to covering, by the large amount of ambient mud, and thus, sequestering, of sand bodies present on the shore. This can result in: (1) inland isolation, within the prograded part of the muddy plain, of once active cheniers, well-identified on aerial photographs and satellite images as linear strings of sand separated by marshes (**Figure 2B**), and, (2) the cutting off of any actively functional cheniers from potential supply of sand from updrift (commonly a river source, a reworked chenier or reworked nearshore deposits). These conditions are well-illustrated by the recent evolution and current morphodynamics of Braamspunt.

Two types of cheniers were identified on the Guianas coast (Anthony et al., 2014), but their morphodynamics have never been documented before. Depending on the size and width of the sand body, and on the proximity of an approaching mud bank, cheniers can range alongshore from sectors exhibiting large beach faces and well-developed berms to sectors with low, narrow beaches dominated by frequent overwash. The former (called type 1 cheniers here) develop where sand and shells available in sufficient quantities lead to a significant gain in chenier volume, resulting in a 'normal' (or nearly so) ocean beach morphodynamic regime with a well-developed surf zone (albeit with permanent inner shoreface mud in the Guianas). These cheniers are characterized by 'typical' beach foreshore behavior dominated by swash processes and berm scarping, often with little or no overwash. These processes are best expressed at high tide when waves are higher and break further up the beach, undergoing less dissipation over the muddy shoreface (Anthony et al., 2010). Such large sandy beaches preferentially occur well-downdrift of an approaching mud bank in an inter-bank zone and where sand supply is adequate. These beaches are most typical of the vicinity of river mouths (active source zones), or, in the case of Braamspunt beach, of the sector corresponding to Profile 1 (**Figure 10**). Under a prolonged inter-bank phase, and providing there is a sufficient or continuous supply of sand, a type 1 chenier can develop alongshore for several 10s of kilometers. This is achieved through: (a) thorough winnowing of fluvial sand supplied by a river updrift (and sometimes shells from the nearshore zone) that may have been temporarily fossilized or cut off from the chenier downdrift by a bank phase, (b) but more commonly by continuous downdrift supply of sediment from an updrift river mouth acting as a significant sand source. A second type of chenier (called type 2 here) is subject to more or less active landward migration through overwash by waves at high tide. An approaching mud bank generally leads to enhancement of this chenier overwash regime by curtailing the through-drift of sand from source zones, leading to chenier fragmentation. Overwash commonly leads to sand migrating over mangroves (**Figure 7**) the seaward stands of which are progressively first asphyxiated, and then sometimes uprooted, leading to the accumulation of more or less significant amounts of drift wood (log jams). These accumulate notably on the upper beach. As the coarser beach sediment migrates over the generally poorly consolidated organic-rich muddy substrate, the increasing weight of the chenier body leads to muddy substrate consolidation and lowering in elevation of the chenier, thereby enhancing overwash processes in a feedback loop (e.g., Rosati et al., 2010). On the lower beach and in some back-beach areas, this process is clearly manifested by the appearance of sandy beach deformation structures generated by dewatering and progressive consolidation of the mud substrate underlying the cheniers (Anthony and Dolique, 2006). This process generates accommodation space into which the overlying sand above the water-exfiltration zone responds by forming subsiding packages of non-saturated sand delimited by cracks alongshore (Anthony and Dolique, 2006). These collapse features are generally ephemeral, as the sand on the lower beach is transported along the beach by longshore currents, and onshore through overwashing. As the chenier migrates inland, the subsisting consolidated muddy foreshore is exposed, commonly with remnant dead and dying mangroves undergoing uprooting by waves.

The two types of chenier development and corresponding beach morphodynamics described above have been characteristic of the recent (multi-decadal) history of Braamspunt beach. Braamspunt persisted notably as a type 1 chenier west of the leading edge of mud bank 1 near the mouth of the Suriname River, where the river's fluvial jet has resulted in mud liquefaction favorable to a clearly expressed beach with spit recurves (**Figure 6**). As mud bank 1 migrated westward, much of Braamspunt chenier underwent fragmentation and shortening,

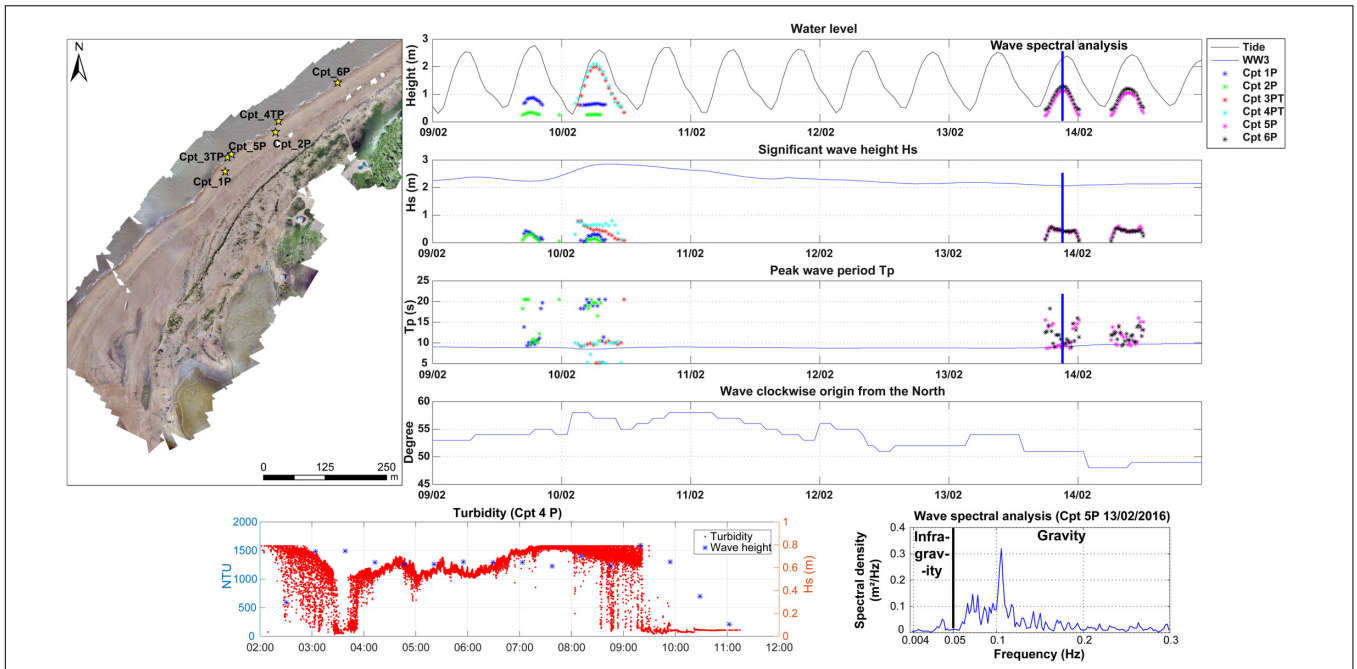

FIGURE 8 | Hydrodynamic conditions affecting Braamspunt beach from 9 to 14 February, 2016. From top to bottom: tidal variations depicted as water level, significant wave height (Hs), peak wave period (T), deep-water wave directions derived from the *WAVEWATCH III* model; (Hs) and turbidity values (NTU), showing, in the case of sensor Cpt 4 PT, a clear relationship between wave height and sediment put into suspension in the course of wave breaking. Drone-derived orthophotograph on the left shows the locations of the wave and turbidity sensors deployed in the course of the two surveys.

and evolved from an open type 1 chenier toward a more classical landward-migrating type 2 chenier.

The beach 'shortening' obtained from field measurements suggests that the high mud-bank migration rate of 1.6 km a year deduced from the 2009 to 2015 satellite images (**Figure 4D**) is significantly outstripped by the real 'ground' migration rate at the very leading edge of the bank. Here the mud bank is also smaller, and subject to refracted, but still energetic incident waves, leading to a form of bank stretching and elongation typical of the Suriname coast that has been attributed by Augustinus (2004) to the west–east shoreline orientation relative to the trade-wind waves.

During the field survey in February, 2016, Braamspunt beach showed a clear updrift–downdrift differentiation in morphology, dynamics, and sediment budgets (**Figures 10**, **11**) that reflected the aforementioned alongshore wave-energy and longshore drift variations. Once the Maroni primary source was cut off by bank welding (**Figures 4**–**6**), the northeastern part of the beach became the source zone for the beach downdrift, with a 'sink' zone in its southwestern extremity of spit recurves. This gradient is related to downdrift wave modification at the approaches to the Suriname estuary. These differences are depicted in the 12 January, 2016 Landsat 8 image (**Figure 12A**) and in a conceptual model of the two chenier types (**Figure 12B**). For simplicity, three sectors are distinguished in **Figure 12A**:

(1) The northern sector, which comprises two segments: the leading edge of the mud bank where the existing chenier (former type 1 open-beach chenier) has been isolated from the sea by mud and fossilized inland, and the 'terrestrial' shoreline junction with the leading edge of the mud bank. The former has been rapidly migrating westward, resulting in the shortening of the beach, which is now a narrow 150 m-long sandy type 2 chenier migrating landward (**Figure 12**). As the chenier migrates inland over back-beach stands of *Avicennia germinans* mangroves, it leaves in its wake a muddy foreshore with subsisting mangroves that were part of the muddy mangrove-colonized shoreline (**Figure 13A**).

(2) The southern sector, also with two segments (**Figure 12A**): a narrow 1.7 km-long reflective beach in February, 2016, and a relatively large 0.6 km-long downdrift beach segment. The former segment is a strongly eroding one, the process being materialized by beach scarping and the constitution of log jams on the beach from uprooted mangroves (**Figure 13B**). Scarping by waves occurs at high tide, and is particularly favored by spring tides which occurred at the start of the 2016 field study. Such scarping led to the truncation of older spit recurves on the lower beach (**Figures 11C,D**). Large washover lobes of sand were also being transferred toward the back-beach, the typical signature of (type 2) chenier migration (**Figure 13C**). Some of the sand removed by scarping was transported downdrift by the strong longshore drift, thus accounting for the considerable narrowing of the beach and the net budget deficit over the survey period (**Figure 10**). In addition to the role of these processes, beach narrowing and the budget deficit may also result from partial fossilization of sand under the stretched and

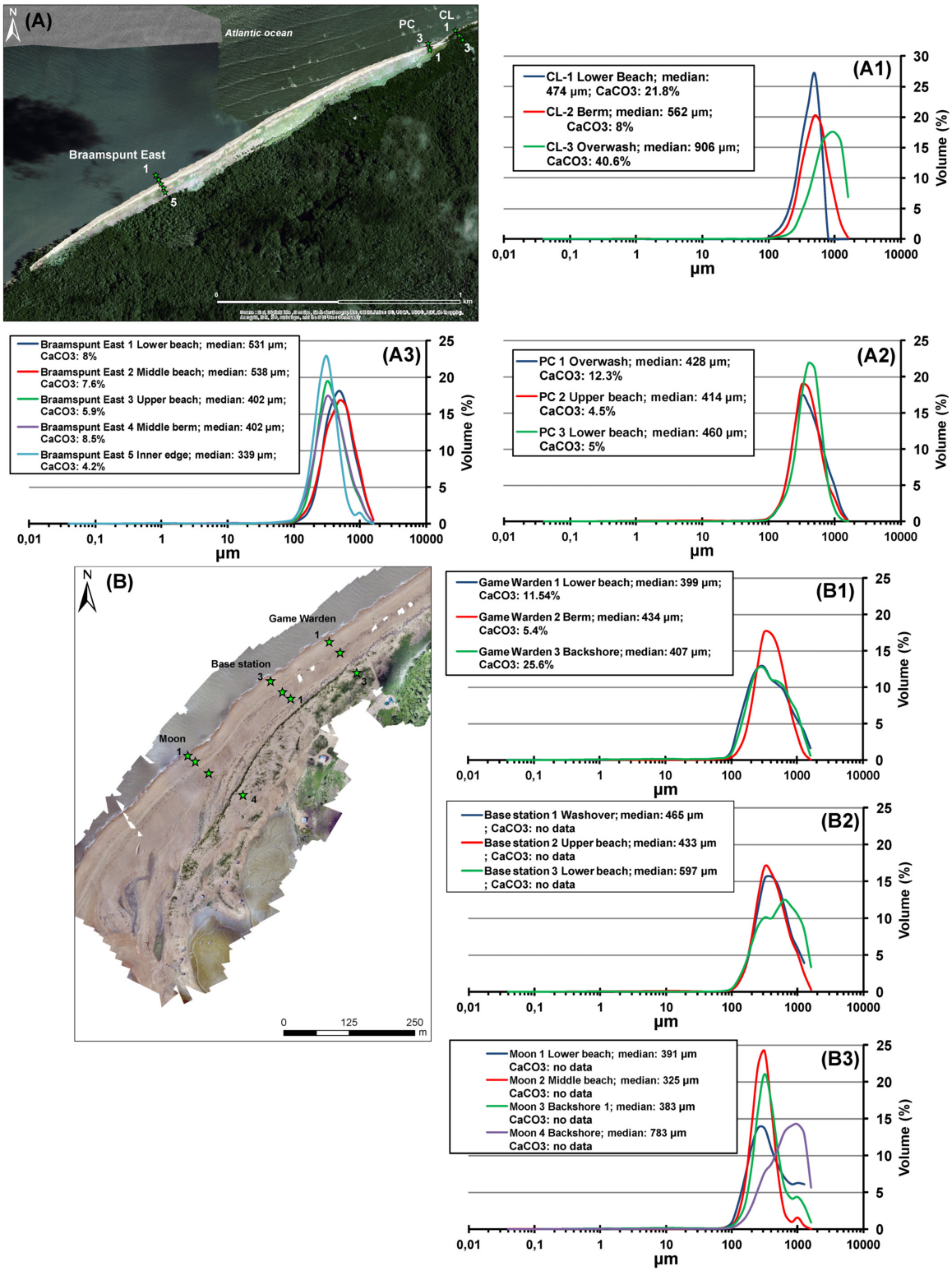

FIGURE 9 | Grain-size characteristics of Braamspunt beach determined by laser analysis, and percentage of carbonates. Satellite image **(A)** and drone-derived orthophoto **(B)** show sample locations. The grain-size curves **(A1–A3,B1–B3)** show a clear concentration around median values of 400 to 560 µm, indicating well-sorted medium sand dominated by quartz.

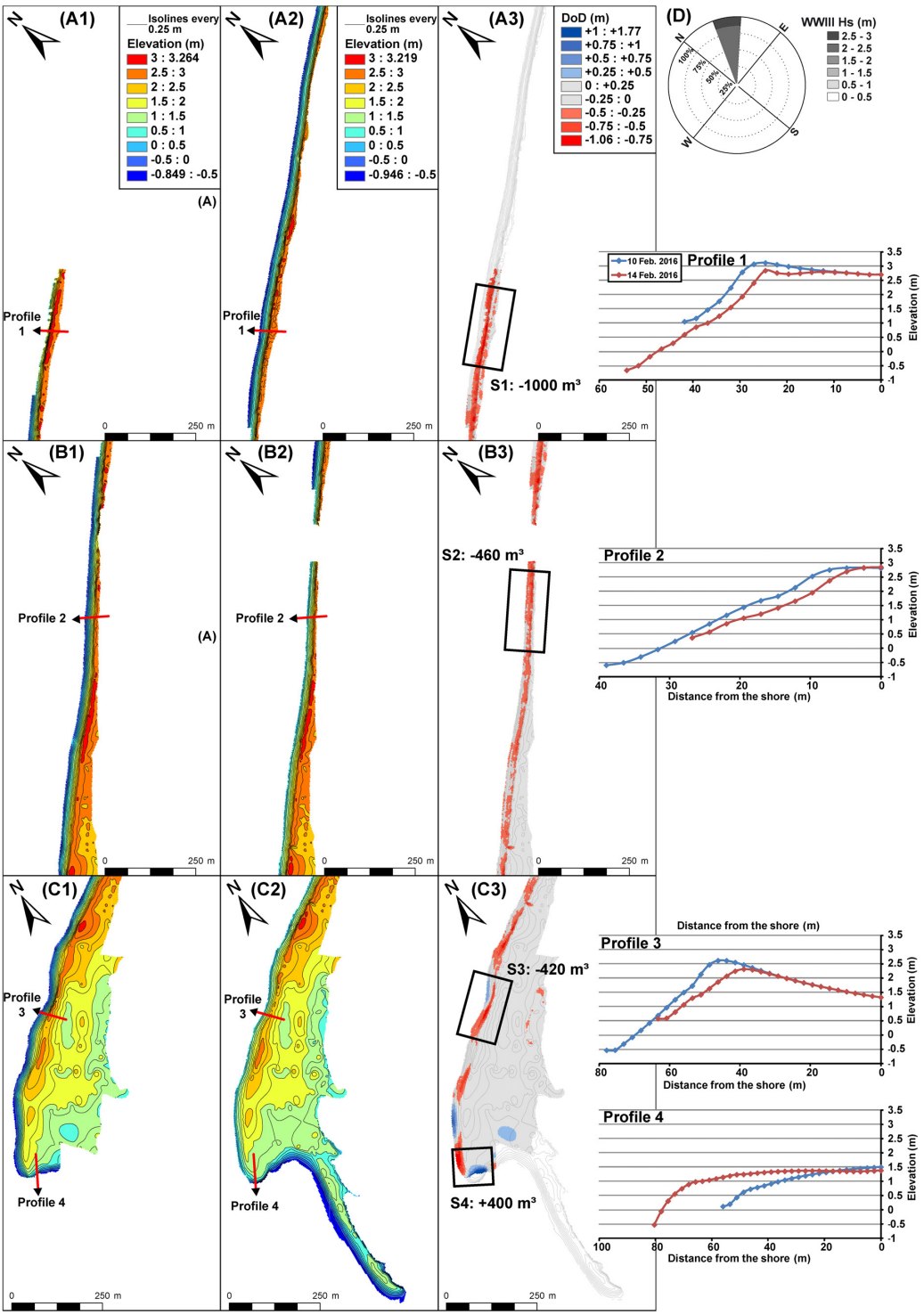

FIGURE 10 | High-resolution GPS-derived topography of Braamspunt beach depicted in three segments from the north to the south of the beach **(A–C)**, and beach sediment budget based on a beach base of –0.5 m relative to absolute datum. In the absence of local topographic benchmarks, elevation data were referenced to the world geoid EGM96 (Earth Gravitational Model) representing mean sea level. Each segment of beach comprised two digital elevation models (DEMs) (left: 10 February, center: 14 February), a DoD (right) that shows the differential between DEMs, and representative profiles. The DEMs, DoDs and profiles show a steep, narrow and eroding reflective beach in the north with a well-defined berm (profile 1), a wider but eroding and less steep beach (profile 2), a lower, retreating berm (profile 3), and a much lower (profile 4) ending steeply in the latest of the spit recurves of Braamspunt beach. The partial budgets highlight the contrast between a dominantly eroding beach along much of its length and a short spit recurve that serves as a sink for some of the sand eroded further updrift and transported by longshore currents.

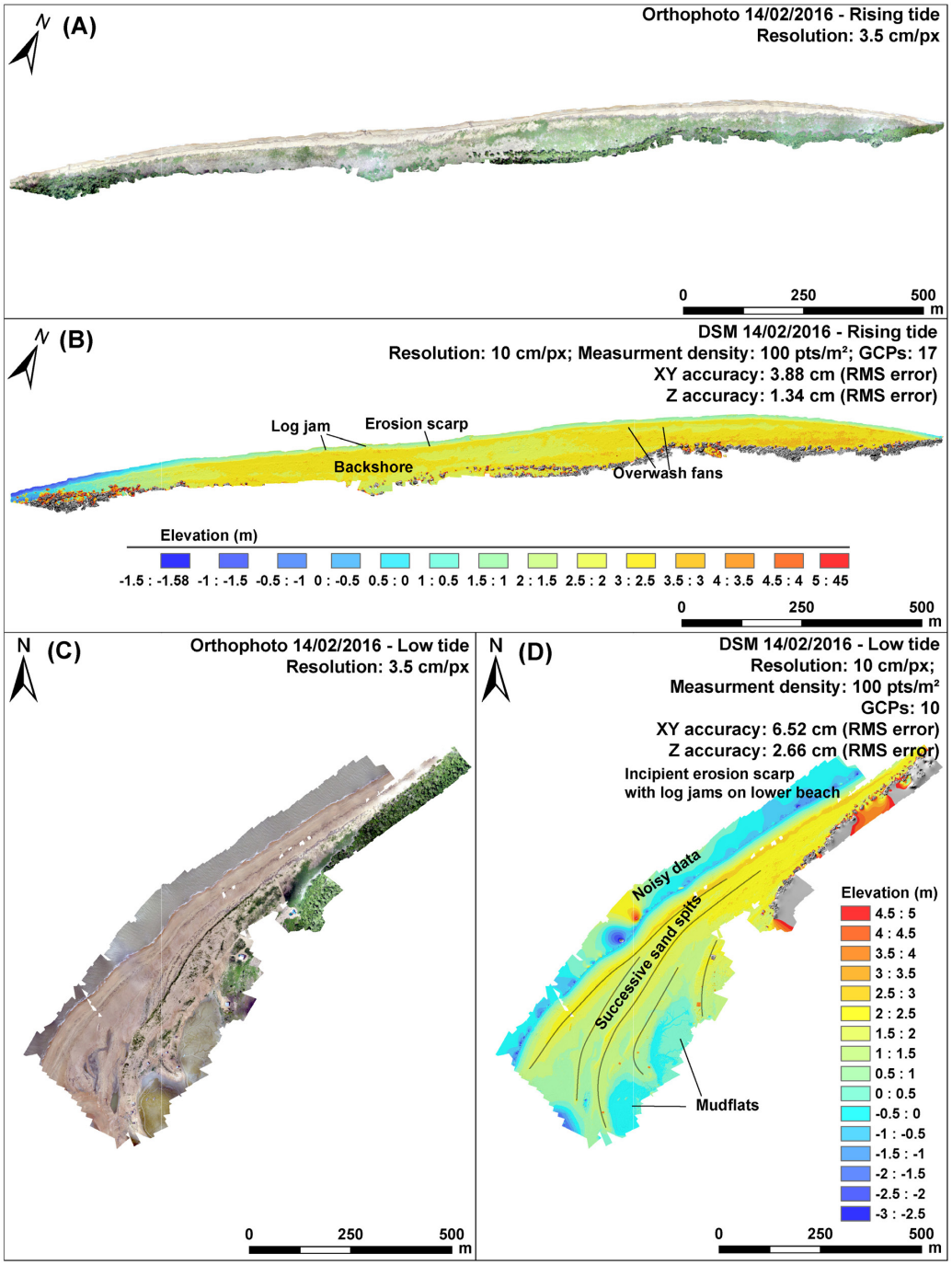

FIGURE 11 | Two high-resolution and high-density orthophotograph assemblages **(A,C)** and digital surface models (DSMs) **(B,D)** of Braamspunt beach obtained from SfM photogrammetry in February, 2016. Both the orthophotos and the DSMs depict variations in beach topography, and especially various large-scale morphological features such as spit recurves at the approaches to the Suriname River mouth, and smaller-scale features such as beach scarps and high-tide truncation of lower spit recurves, washovers, and log jams.

advancing leading edge of the mud bank. The large waves and strong longshore drift cannot be balanced (dissipated) by the sand volume of the beach to maintain stability. The narrow reflective portion of Braamspunt beach also shows small-scale alongshore morphological variability related to numerous zones of driftwood debris. The second segment forms the transition zone toward the present Braamspunt beach recurve zone into the Suriname River estuary (**Figure 12**). This sector also shows some scarping and rarer washover lobes (**Figure 13D**) associated with

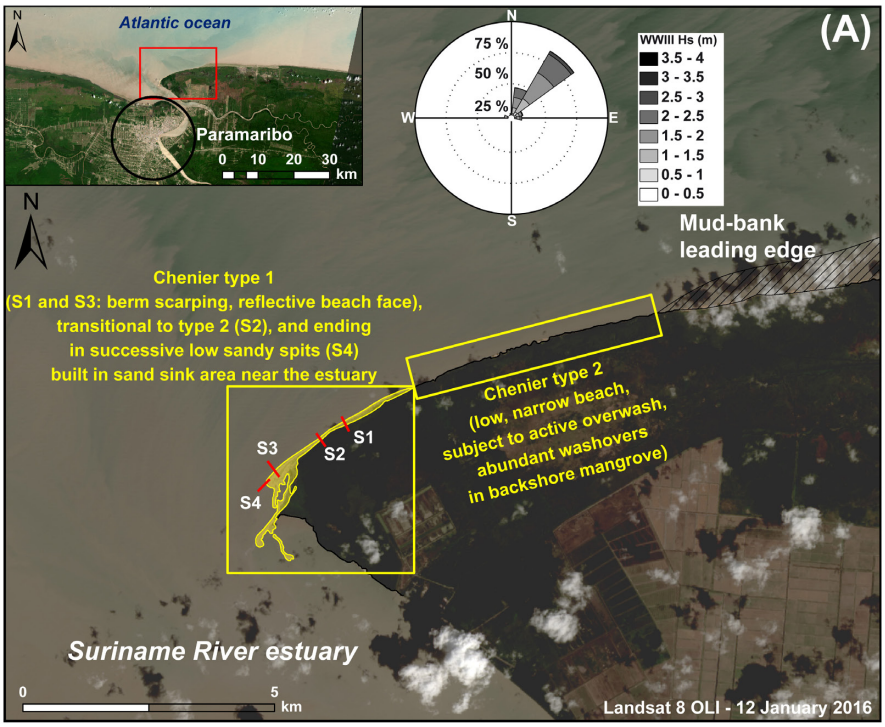

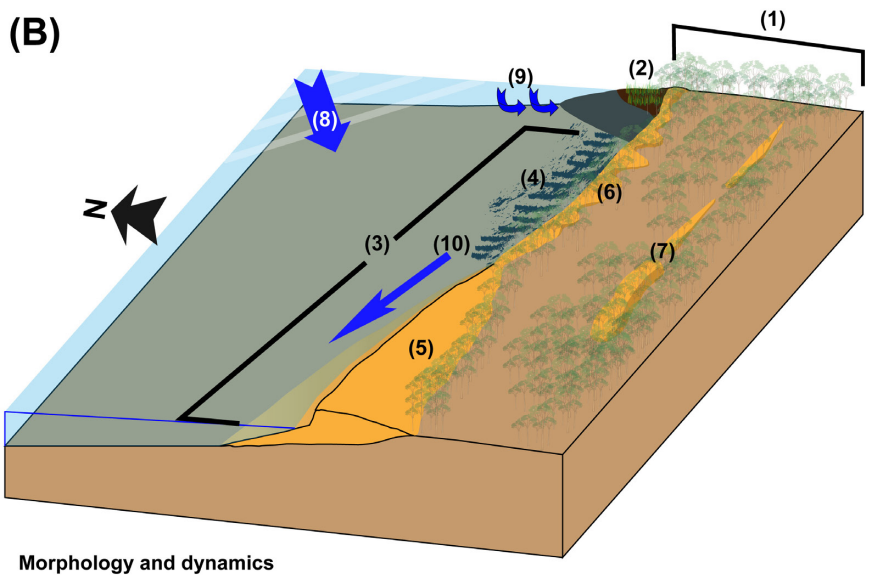

Morphology and dynamics

(1) Muddy prograding Guianas coastal plain with old mangroves and cheniers
(2) Mud-bank leading edge with young mangroves
(3) Inter-bank trailing edge
(4) Eroding muddy foreshore
(5) Chenier type 1
(6) Chenier type 2
(7) Inland cheniers
(8) Deepwater wave approach (mainly NE)
(9) Refracted waves
(10) Longshore transport

FIGURE 12 | A synthesis superimposed on a 2016 Landsat image **(A)**, and a conceptual model **(B)** of the morphodynamics and sediment transfer conditions at Braamspunt beach. S1 to S4 are representative of profiles 1 to 4 (**Figure 10**). The type 1 chenier regime is characterized by a well-developed, albeit eroding berm with overwash processes less well-expressed, and conforms to a beach dominated by dissipative-to-reflective processes. The type 2 chenier regime is dominated by overwash processes and eventual partial break up where local variations in incident wave energy occur. Mangrove colonization accompanying bank phases commonly mask cheniers, a preliminary phase to their isolation inland **(B)**.

the alongshore alternations of depositional sand waves migrating downdrift and erosional zones between these sand waves. Overall, this sector [type 1 chenier but breaking down into a type 2 washover chenier under the high-energy conditions of the experiment (**Figure 12**)] constitutes a transit zone for sand transported to the downdrift sink near the Suriname estuary, hence the net positive sediment budget here (**Figure 10**).

(3) The estuarine sector with older truncated spit recurves, where waves are nearly completely refracted.

Linking Chenier Vulnerability With Beach Morphodynamics: Impacts on Ecosystem Services

The multi-decadal to recent evolution of Braamspunt is that of a classical chenier that depends essentially on sand supply from updrift. This is a first factor of beach fragility. This sand comes from the Maroni, but transport is not direct and continuous as one would expect on a classical open-ocean beach because the sand from the Maroni source transported alongshore by wave-induced drift is partially sequestered over more or less long periods of time (up to multi-decadal) by mud banks migrating westward toward Guyana, and partially recycled onshore into landward-migrating type 2 cheniers. Sand availability is, thus, neither constant nor perennial on Braamspunt. In other words, Braamspunt does not function as a classical through-put source-to-sink (Maroni-Suriname) sediment cell, but as a potentially fragmented temporally and alongshore-variable cell.

As a result of Braamspunt's fragmented sediment cell strucure, the morphology of its dominantly reflective beach hinges on sand reworked alongshore, and only during inter-bank phases. Such reworking is common in beach systems where sand-supply stress conditions prevail. It also enables the concentration of shelly material from offshore that supplements the beach sand budget. In the case of Braamspunt, this reworking is generated by updrift sand sequestering in the advancing leading edge of mud banks during bank phases, a process that, in turn, generates a chain reaction involving a switch in beach behavior in the immediate vicinity of the bank's leading edge to an increasingly more landward-migrating type 2 chenier mode associated with beach overwash that further deprives the downdrift beach of sand (**Figure 12**). As this occurs, beach scarping and lowering occur further downdrift to balance an under-saturated wave and longshore transport system, engendering a downdrift migrating wave of erosion as the system translates downdrift. The subsisting beach (type 1 chenier) is presently preserved in its most downdrift sector (a few 100 m at most) at the mouth of the Suriname where mud is liquefied by the river's outflow jet. This preservation outcome may be considered as a form of coastal self-organization involving a morphodynamic negative feedback adjustment effect between beach and river mouth, and without which Braamspunt beach would cease to exist. The jet-flow effect of the Suriname River assures the permanence of the beach in this sector. Here, preservation of the beach is essential in turn in dissipating waves impinging on the east bank of the river mouth, thus protecting the back-beach mangrove wetlands and maintaining the mild cape morphology on this bank.

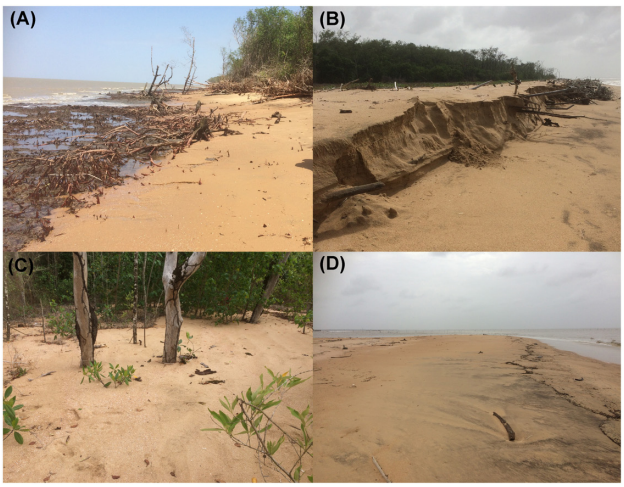

FIGURE 13 | Ground photographs showing: **(A)** landward-migrating (type 2) chenier forming the present updrift sector of Braamspunt beach. Westward migration of the eroding trailing edge of the inter-bank zone (uprooted mangroves) in response to impingement of the leading edge of the incoming mud bank (not visible here) is leading to shortening of the exposed length of beach. Landward chenier migration leads to the exposure, on the beach foreshore, of more or less consolidated former back-beach mud rich in mangrove remains; **(B)** pronounced beach scarp resulting from erosion of a steep, reflective type 1 chenier beach face (S1 and S3 in **Figure 12A**) with accumulation of mangrove debris (logjams) in the background); **(C)** view toward the back-beach (S2 in **Figure 12A**) showing washovers encroaching on *Avicennia g.* mangroves and burying their pneumatophores (breathing root network), leading to asphyxia and death of the plants; **(D)** downdrift sand transport terminus and partial sink where Braamspunt beach forms a spit in response to wave refraction caused by the Suriname River mouth re-entrant. The refracting wave front is visible in the right background. Darker shades of sand on the beach correspond to heavy minerals (black sands) deposited in this area of relatively lower wave energy as a result of refraction, and further concentrated by mild wind sorting of the beach sand. Washover lobes inherited from the higher spring tides at the start of the survey are present in the left background.

These effects have, thus, a bearing on the role of Braamspunt beach in coastal protection. They also affect the availability of the beach, or sectors thereof, for recreation, and as pristine grounds for sustained turtle nesting. The large type 1 chenier beaches are the most suitable ecotope on the Guianas coast for nesting marine turtles, and are most typical of the vicinity of river mouths (active source zones), but this ecotope has become progressively shorter with beach shortening, fragmentation, and conversion of much of Braamspunt into a type 2 chenier (**Figure 12**). This condition is not ideal for successful nesting by marine turtles, which require stable sandy beaches, beaches not subject to overwash and strong infiltration, and beaches free of mud and organic matter (Kelle et al., 2007; Caut et al., 2010). Overwash processes are hazardous to turtle nests as they involve water infiltration and sand loading on the upper beach (Caut et al., 2010; Péron et al., 2013). Scarping and beach narrowing lower the available space for turtle nesting while

generating a vertical beach face that may hinder turtle access to the beach. The important driftwood accumulation associated with the chain of processes and the beach morphodynamic effects described above also generates obstacles to turtle landing, while decomposing organic material from abundant driftwood can be nefarious to turtle eggs by altering temperatures (Girondot et al., 2002).

Sand mining is harmful to turtles due to the destruction of available beach nesting space, and, by decreasing the beach's sediment budget, it lowers the wave-buffering capacity. Even allowing for a comfortable error margin of +20–30%, the overall estimated volume of the surveyed beach (ca. 570,000 m^3) represents a moderate amount that can be depleted in the next few years, if sand mining were to continue unabated. Braamspunt beach and its ancestral forms between the Maroni and the Suriname have always played an important role in protecting the coastal plain of Suriname from exacerbated retreat during inter-bank phases by dissipating wave energy. Together with mangroves, they play this role in inter-bank areas, but although mangroves are important energy-buffering agents on the Guianas coast, they are less efficient than sandy beaches in accomplishing this role. Beaches also evince 'threshold functioning.' This implies that large-scale sand removal by mining can lead to a threshold point wherein an already strongly depleted beach can, in the face of repeated spates of high wave episodes (such as would be expected in El Nino years), completely collapse through massive washover and wave recycling of sand into the Suriname River estuarine sink. The total collapse of Braamspunt beach could have very damaging feedback effects (irreversible change, with no possibility for resilience), wherein the east bank cape at the mouth of the Suriname River can be severely eroded several kilometers back during inter-bank phases, thus exposing the estuary and the water-front of Paramaribo to incident Atlantic waves. Between 1955 and 2017, large-scale erosion, involving a total of nearly 42 km^2 of coast, resulted in the demise of the 2–3 km-wide muddy cape of Pointe Isère which hitherto diverted the mouth of the Mana River in western French Guiana (Jolivet et al., unpublished), and the catchment of which lies next to that of the Maroni River. The causes of this persistent multi-decadal erosion are still not clear.

General Implications for the Understanding of Chenier Morphodynamics in the Guianas

The range of morphodynamic conditions and processes exhibited by Braamspunt chenier have varied both alongshore and in time, depending on the influence of bank and inter-bank migration in isolating beach sediment sources and in generating alongshore-changing wave-energy dissipation and refraction. These variations can also be related to changes in local bathymetry, such as at the entrance to the Suriname River estuary, and elsewhere, as in Guyana, to coastal defense structures such as sluice gates and groynes. Part of the beach evinces the type 1 chenier regime characterized by the presence of a well-developed, albeit eroding berm where overwash processes are less well-expressed. This type conforms to that of beaches dominated by dissipative-to-reflective processes acting in the surf and swash zones and over the well-developed beach face. These processes are also modulated by tide, being best expressed at high tide when waves are higher and break further up the beach, undergoing less dissipation over the muddy shoreface. In contrast, the type 2 chenier morphodynamic regime is dominated by overwash processes. Differences alongshore in overwash can lead to spatial disorganization of the chenier and its eventual partial break up where local variations in incident wave energy occur. Mangrove trees and trunks in overwashed areas of beach also further dissipate wave energy, potentially diminishing the longshore component of such energy. In essence, therefore, sand sequestering through the overwash regime typical of active cheniers such as sector 1 in Braamspunt can deprive the beach longshore transport system of sand, thus further strengthening the downdrift propagation of the overwash type 2 chenier regime associated with increasingly more limited sand supply. This morphodynamic feedback effect signifies, in fact, that the overwash chenier regime is important in locally dissipating incident wave energy because it leads to local beach sand-trapping through the formation of more or less coalescing lobes of washovers, the regime propagating downdrift. While this sand-trapping mechanism locally enhances the coastal-protection role played by chenier development, it deprives downdrift sectors of sand, rendering the beach downdrift more vulnerable.

Two final points concern: (1) aeolian dune development, insignificant on the Guianas cheniers and beaches as a result of this common overwash regime and the mild wind speeds, and, (2) the large variability in chenier plan shapes and orientations. Cheniers appear in all sizes on the Guianas coastal plain, are commonly discontinuous alongshore, and can be variably wide (see **Figure 2B**, for instance). Their orientations also vary. Type 1 cheniers formed in the vicinity of river mouths can, for instance, vary in orientation, from orthogonal relative to the regional shoreline where they line river banks, as on the west bank of the Maroni (**Figure 2B**), to the more normal alongshore orientation as in the case of Braamspunt chenier. In addition to the specific morphodynamic process variability imposed by the bank-inter-bank context, this diversity reflects various other factors, such as the availability of sand in inter-bank areas, the impact of previous bank phases in muting down sand-winnowing processes, local to regional sand availability, and winnowing from the nearshore zone, but also the potential reworking of older inland cheniers by mobile river channels and their creek networks that recycle this sand into channel-bed deposits. Such sand may eventually be re-injected on the shore where such creeks debouch. Over the decadal to multi-decadal timescales involved in bank-inter-bank cycles, changes in channel-mouth location can also occur as the mud capes diverting the smaller river mouths during bank phases are eroded. This leads to changes, in injection points on the coast, of sand brought down by rivers, or reworked from older sand bodies inland.

CONCLUSION

The formation of cheniers on the Guianas coast is not primarily related to simple temporal alternations between low wave energy conditions (muddy sedimentation) and high wave energy conditions (sand/shell/gravel winnowing) observed in many of the world's chenier coasts. Rather, it is dependent on the unique situation of the Guianas coast, at the world-scale, wherein alongshore alternations of banks and inter-bank zones occur, engendering marked spatial and temporal variations in wave energy and sand/shell supplies. Further variability is induced by the proximity of river mouths that provide much of the sand for chenier formation. The beaches of Suriname essentially function as cheniers supplied with sediment by local rivers and with shells reworked by waves in the nearshore zone. These cheniers have not only played an important geological role in the building of the Guianas coastal plain, but are also the most important natural source of coastal protection. This protection role needs to be understood and highlighted as an important part of any future coastal zone management initiative in Suriname and the other Guianas countries. The work conducted on Braamspunt beach shows the drastic changes that have accompanied significant shortening of the beach over the last few years, in response to migration of a mud bank between the Maroni and Suriname Rivers. Sand mining has essentially affected the downdrift (west) end of the wider beach (type 1 chenier) which comprises successive spit recurves ending at the mouth of the Suriname River. These conditions, and the rarity of currently active cheniers, signify a relatively fragile beach system that has been strongly impacted by sand mining. This activity impairs the coastal protective role played by the rare subsisting beaches in Suriname, while also contributing to depriving Suriname of its already relatively rare, and therefore valuable, beach-nesting sites for marine turtles.

DATA AVAILABILITY

All datasets generated for this study are included in the manuscript and/or the supplementary files.

AUTHOR CONTRIBUTIONS

EA and MH designed the project. GB, EA, MH, and AG conducted the field work and the analyses.

FUNDING

We acknowledge WWF-Guianas, the CNRS Pépinière Interdisciplinaire de Guyane project GUIACHENIER, and the European Research and Development Fund project OYAMAR for funding.

ACKNOWLEDGMENTS

This work benefited from the help and support of many people. We would especially like to thank Karin Bilo (formerly of *WWF-Guianas*) for logistical help in the field. The game wardens of the *Nature Conservation Division of Suriname*, Roy Ho Tsoi, Romeo Ramjiawan (drone operator), and Rudi Wongsoikromo (drone operator), and Support IT specialist Quinten Notopawiro provided and operated the drone and camera used to obtain the photogrammetric data. Our sincere thanks to them, as well as to August Randwijk of the *Geological Mining Service of Suriname*. The discussions with Roy Ho Tsoi, who provided us with field measurements of beach shortening in 2015 and 2016, were particularly instructive. Our thanks also to the students of the *Anton de Kom University* for their help during the field surveys.

REFERENCES

Allison, M. A., and Lee, M. T. (2004). Sediment exchange between amazon mudbanks and fringing mangroves in French Guiana. *Mar. Geol.* 208, 169–190. doi: 10.1016/j.margeo.2004.04.026

Anthony, E. J. (1989). Chenier plain development in northern Sierra Leone, West Africa. *Mar. Geol.* 90, 297–309. doi: 10.1016/0025-3227(89)90132-1

Anthony, E. J. (2016). *Impacts of Sand Mining on Beaches in Suriname*. Georgetown: WWF Guianas.

Anthony, E. J., and Dolique, F. (2006). Intertidal subsidence and collapse features on wave-exposed, drift-aligned sandy beaches subject to Amazon mud: Cayenne, French Guiana. *Earth Surf. Process. Landf.* 31, 1051–1057. doi: 10.1002/esp.1361

Anthony, E. J., Gardel, A., Dolique, F., and Marin, D. (2011). The Amazon-influenced mud-bank coast of South America: an overview of short- to long-term morphodynamics of 'inter-bank' areas and chenier development. *J. Coast. Res.* 64, 25–29.

Anthony, E. J., Gardel, A., and Gratiot, N. (2014). Fluvial sediment supply, mud banks, cheniers and the morphodynamics of the coast of South America between the Amazon and Orinoco river mouths. *Geol. Soc. Spec. Publ.* 388, 533–560. doi: 10.1144/SP388.8

Anthony, E. J., Gardel, A., Gratiot, N., Proisy, C., Allison, M. A., Dolique, F., et al. (2010). The Amazon-influenced muddy coast of South America: a review of mud bank-shoreline interactions. *Earth Sci. Rev.* 103, 99–121. doi: 10.1016/j.earscirev.2010.09.008

Augustinus, P. G. (1978). *The Changing Shoreline of Surinam (South America)*. Doctoral dissertation, University of Utrecht, Utrecht.

Augustinus, P. G. (2004). The influence of the trade winds on the coastal development of the Guianas at various scale levels: a synthesis. *Mar. Geol.* 208, 141–151. doi: 10.1016/j.margeo.2004.04.007

Augustinus, P. G., Hazelhoff, L., and Kroon, A. (1989). The chenier coast of Suriname: modern and geological development. *Mar. Geol.* 90, 269–281. doi: 10.1016/0025-3227(89)90129-1

Brunier, G., Fleury, J., Anthony, E. J., Gardel, A., and Dussouillez, P. (2016). Close-range airborne structure-from-motion photogrammetry for high-resolution beach morphometric surveys: examples from an embayed rotating beach. *Geomorphology* 261, 76–88. doi: 10.1016/j.geomorph.2016.02.025

Caut, S., Guirlet, E., and Girondot, M. (2010). Effect of tidal overwash on the embryonic development of leatherback turtles in French Guiana. *Mar. Environ. Res.* 69, 254–261. doi: 10.1016/j.marenvres.2009.11.004

Daniel, J. R. K. (1989). The chenier plain coastal system of Guyana. *Mar. Geol.* 90, 283–287. doi: 10.1016/0025-3227(89)90130-8

Gensac, E. (2012). *Dynamique Morpho-Sédimentaire du Littoral Sous Influence Amazonienne - Influence des Forçages Hydrométéorologiques sur la Migration des Bancs de Vase et la Mangrove Côtière*. Ph. D thesis. Dunkerque: Université du Littoral Côte d'Opale.

Girondot, M., Tucker, A. D., Rivalan, P., Godfrey, M. H., and Chevalier, J. (2002). Density-dependent nest destruction and population fluctuation of Guianan leatherback turtles. *Anim. Conserv.* 5, 75–84.

Gratiot, N., Gardel, A., and Anthony, E. J. (2007). Trade-wind waves and mud dynamics on the French Guiana coast, South America: input from ERA-40 wave data and field investigations. *Mar. Geol.* 236, 15–26. doi: 10.1016/j.margeo.2006.09.013

Hapke, C. J., Reid, D., Richmond, B. M., Ruggiero, P., and List, J. (2006). *National Assessment of Shoreline Change, Part 3: Historical Shoreline Change and Associated Coastal Land Loss Along Sandy Shorelines of the California Coast*. Reston, VA: USGS, 13–14. doi: 10.3133/ofr20061219

Hein, C. J., Fitzgerald, D. M., de Souza, L. H. P., Georgious, J. Y., Buynevich, I. V., Klein, A. D. F., et al. (2016). Complex coastal change in response to autogenic basin infilling: an example from a sub-tropical Holocene strandplain. *Sedimentology* 63, 1362–1395. doi: 10.1111/sed.12265

Hori, K., Saito, Y., Zhao, Q., Cheng, X., Wang, P., Sato, Y., et al. (2001). Sedimentary facies and Holocene progradation rates of the Changjiang (Yangtze) delta, China. *Geomorphology* 41, 233–248. doi: 10.1016/S0169-555X(01)00119-2

Horikawa, K. (1988). *Nearshore Dynamics and Coastal Processes: Theory, Measurement and Predictive Models*. Tokyo: University of Tokyo Press.

Kelle, L., Gratiot, N., Nobilos, I., Thérèse, J., Wongsopawiro, R., and De Thoisy, B. (2007). Monitoring of the nesting leatherback turtle (Dermochelys coriacea): contribution of remote-sensing for real-time assessment of beach coverage in French Guiana. *Chelonian Conserv. Biol.* 6, 142–147. doi: 10.2744/1071-8443(2007)6[142:MONLTD]2.0.CO;2

Martinez, J. M., Guyot, J. L., Filizola, N., and Sondag, F. (2009). Increase in sediment discharge of the Amazon River assessed by monitoring network and satellite data. *Catena* 79, 257–264. doi: 10.1016/j.catena.2009.05.011

McBride, R. A., Taylor, M. J., and Byrnes, M. R. (2007). Coastal morphodynamics and chenier-plain evolution in southwestern Louisiana, USA: a geomorphic model. *Geomorphology* 88, 367–442. doi: 10.1016/j.geomorph.2006.11.013

Nardin, W., and Fagherazzi, S. (2018). The role of waves, shelf slope, and sediment characteristics on the development of erosional chenier plains. *Geophys. Res. Lett.* 45, 8435–8444. doi: 10.1029/2018GL078694

Otvos, E. G. (2018). "Cheniers," in *Encyclopaedia of Coastal Science*, eds C. Finkl and C. Makowski (Berlin: Springer), doi: 10.1007/978-3-319-48657-4_67-5

Otvos, E. G., and Price, W. A. (1979). Problems of Chenier genesis and terminology: an overview. *Mar. Geol.* 31, 251–263. doi: 10.1016/0025-3227(79)90036-7

Péron, C., Chevallier, D., Galpin, M., Chatelet, A., Anthony, E. J., and Gardel, A. (2013). Beach morphological changes in response to marine turtles nesting: a preliminary study of Awala-Yalimapo beach, French Guiana (South America). *J. Coastal Res. Spec. Issue* 65, 99–104. doi: 10.2112/SI65-018.1

Prost, M. T. (1989). Coastal dynamics and chenier sands in French Guiana. *Mar. Geol.* 90, 259–267. doi: 10.1016/0025-3227(89)90128-X

Pujos, M., Bouysse, P., and Pons, J. C. (1990). Sources and distribution of heavy minerals in Late Quaternary sediments of the French Guiana continental shelf. *Cont. Shelf Res.* 10, 59–79. doi: 10.1016/0278-4343(90)90035-K

Pujos, M., Pons, J. C., and Parra, M. (2000). Les minéraux lourds des sables du littoral de la Guyane française : bilan sur l'origine des dépôts de la plate-forme des Guyanes. *Oceanol. Acta* 24(Suppl.), S27–S35. doi: 10.1016/S0399-1784(01)00093-7

Rosati, J. D., Dean, R. G., and Stone, G. W. (2010). A cross-shore model of barrier island migration over a compressible substrate. *Mar. Geol.* 271, 1–16. doi: 10.1016/j.margeo.2010.01.005

Saito, Y., Wei, H., Zhou, Y., Nishimura, A., Sato, Y., and Yokota, S. (2000). Delta progradation and chenier formation in the Huanghe (Yellow River) delta, China. *J. Asian Earth Sci.* 18, 489–497. doi: 10.1016/S1367-9120(99)00080-2

Scheffers, A., Engel, M., Scheffers, S., Squire, P., and Kelletat, D. (2012). Beach ridge systems - archives for Holocene coastal events? *Prog. Phys. Geogr.* 36, 5–37. doi: 10.1177/0309133311419549

Sénéchal, N., Dupuis, H., Bonneton, P., Howa, H., and Pedreros, R. (2001). Observation of irregular wave transformation in the surf zone over a gently sloping sandy beach on the French Atlantic coastline. *Oceanolog. Acta* 24, 545–556. doi: 10.1016/S0399-1784(01)01171-9

Sottolichio, A., Gardel, A., Huybrechts, N., Maury, T., Morvan, S., and Lesourd, S. (2018). *Premières Observations de la Dynamique Hydro-Sédimentaire de L'estuaire du Maroni (Guyane française)*. Available at: http://www.paralia.fr/jngcgc/15_33_sottolichio.pdf

Tamura, T. (2012). Beach ridges and prograded beach deposits as palaeoenvironment records. *Earth Sci. Rev.* 114, 279–297. doi: 10.1016/j.earscirev.2012.06.004

Thieler, E. R., Himmelstoss, E. A., Zichichi, J. L., and Ergul, A. (2009). *Digital Shoreline Analysis System (DSAS) Version 4.0 - An ArcGIS Extension for Calculating Shoreline Change*. Reston, VA: U.S. Geological Survey.

van Maren, D. S. (2005). Barrier formation on an actively prograding delta system: the red river delta. *Vietnam. Mar. Geol.* 224, 123–143. doi: 10.1016/j.margeo.2005.07.008

Walcker, R., Anthony, E. J., Cassou, C., Aller, R. C., Gardel, A., Proisy, C., et al. (2015). Fluctuations in the extent of mangroves driven by multi-decadal changes in north atlantic waves. *J. Biogeogr.* 42, 2209–2219. doi: 10.1111/jbi.12580

Wells, J. T., and Coleman, J. M. (1981). Physical processes and fine-grained sediment dynamics, coast of Surinam, South America. *J. Sed. Petrol.* 51, 1053–1068.

Westoby, M. J., Brasington, J., Glasser, N. F., Hambrey, M. J., and Reynolds, J. M. (2012). 'Structure-from-Motion' photogrammetry: a low-cost, effective tool for geoscience applications. *Geomorphology* 179, 300–314. doi: 10.1016/j.geomorph.2012.08.021

Winterwerp, J. C., de Graaff, R. F., Groeneweg, J., and Luijendijk, A. P. (2007). Modelling of wave damping at Guyana mud coast. *Coast. Eng.* 54, 249–261. doi: 10.1016/j.coastaleng.2006.08.012

Wittmann, H., von Blackenberg, F., Maurice, L., Guyot, J. L., Filizola, N., and Kubik, P. W. (2011). Sediment production and delivery in the Amazon River basin quantified by in-situ-produced cosmogenic nuclides and recent river loads. *Geol. Soc. Am. Bull.* 123, 934–950. doi: 10.1130/B30317.1

Wong, Th. E, De Kramer, R., De Boer, P. L., Langereis, C., and Sew-A-Tion, J. (2009). The influence of sea level changes on tropical coastal wetlands: the pleistocene coropina formation, Suriname. *Sediment. Geol.* 216, 127–137. doi: 10.1016/j.sedgeo.2009.02.003

Woodroffe, C. D., and Grime, D. (1999). Storm impact and evolution of a mangrove-fringed chenier plain, Shoal Bay, Darwin, Australia. *Mar. Geol.* 159, 303–321. doi: 10.1016/S0025-3227(99)00006-7

Conflict of Interest Statement: The authors declare that the research was conducted in the absence of any commercial or financial relationships that could be construed as a potential conflict of interest.

frontiers in Marine Science

ORIGINAL RESEARCH
published: 14 May 2019
doi: 10.3389/fmars.2019.00245

Assessing Morphologic Controls on Atoll Island Alongshore Sediment Transport Gradients Due to Future Sea-Level Rise

James B. Shope[1]* *and Curt D. Storlazzi*[2]

[1] *Institute of Marine Sciences, University of California, Santa Cruz, Santa Cruz, CA, United States,* [2] *Pacific Coastal and Marine Science Center, US Geological Survey, Santa Cruz, CA, United States*

Atoll islands' alongshore sediment transport gradients depend on how island and reef morphology affect incident wave energy. It is unclear, though, how potential atoll morphologic configurations influence shoreline erosion and/or accretion patterns, and how these relationships will respond to future sea-level rise (SLR). Schematic atoll models with varying morphologies were used to evaluate the relative control of individual morphological parameters on alongshore transport gradients. Incident wave transformations were simulated using a physics-based numerical model and alongshore erosion and accretion was calculated using empirical formulae. The magnitude of the transport gradients increased with SLR: initial erosion or accretion patterns intensified. Modeled morphologic parameters that significantly influenced alongshore transport were the atoll diameter, reef flat width, reef flat depth, and island width. Modeled atolls with comparably small diameters, narrow and deep reef flats with narrow islands displayed greater magnitudes of erosion and/or accretion, especially with SLR. Windward island shorelines are projected to accrete toward the island's longitudinal ends and lagoon due to SLR, whereas leeward islands erode along lagoon shorelines and extend toward the island ends. Oblique island, oriented parallel to the incident deepwater wave direction, shorelines are forecast to build out leeward along the reef rim and toward the lagoon while eroding along regions exposed to direct wave attack. These findings make it possible to evaluate the relative risk of alongshore erosion/accretion on atolls due to SLR in a rapid, first-order analysis.

Keywords: atoll, islands, waves, sea-level rise, reef, morphology, erosion, shoreline

OPEN ACCESS

Edited by:
Clara Armaroli,
University of Ferrara, Italy

Reviewed by:
Eduardo Siegle,
University of São Paulo, Brazil
Giovanni Coco,
The University of Auckland, New Zealand

***Correspondence:**
James B. Shope
jshope@ucsc.edu

Specialty section:
This article was submitted to Coastal Ocean Processes, a section of the journal Frontiers in Marine Science

Received: *30 December 2018*
Accepted: *24 April 2019*
Published: *14 May 2019*

Citation:
Shope JB and Storlazzi CD (2019) Assessing Morphologic Controls on Atoll Island Alongshore Sediment Transport Gradients Due to Future Sea-Level Rise. Front. Mar. Sci. 6:245. doi: 10.3389/fmars.2019.00245

INTRODUCTION

Atolls are shallow, ring-shaped, coral platforms upon which small, low-elevation carbonate islands are often perched. Communities living on atoll islands are vulnerable to large wave events and changing climates (Storlazzi et al., 2015). As global climate warms, sea levels are projected to potentially increase by more than 2.0 m by 2100 due to seawater thermal expansion and glacial/ice cap melt (Church et al., 2013; Kopp et al., 2014; Slangen et al., 2014); the rate of sea-level rise (SLR) is projected to exceed the rate of coral reef platform vertical accretion (Montaggioni, 2005), leaving the future stability of these low-lying islands and their associated infrastructure, agriculture, and

habitats uncertain. Global SLR and reef degradation (bleaching, ocean acidification, etc.) will reduce the reef platform's ability to attenuate wave energy and protect shorelines from wave-driven erosion and flooding hazards (Sheppard et al., 2005; Storlazzi et al., 2011; Grady et al., 2013; Ferrario et al., 2014; Shope et al., 2017). Incident wave dynamics, atoll morphology, and sediment composition (size, induration, etc.) influence shoreline erosional and accretional patterns; therefore, changes in atoll island alongshore erosion and/or accretion with SLR are location dependent and findings for one island may not necessarily apply to another.

Many studies have explored atoll island response to SLR (Roy and Connell, 1991; Woodroffe, 2008; Webb and Kench, 2010; Rankey, 2011; Ford, 2012; Yates et al., 2013; Purkis et al., 2016) and extreme wave events (Hoeke et al., 2013; Smithers and Hoeke, 2014), as well as reef controls on shoreline sediment mobilization and erosion (Sheppard et al., 2005; Storlazzi et al., 2011; Grady et al., 2013). Although these approaches elucidate large-scale trends, most of the analyses involve a few atoll islands (excepting Webb and Kench, 2010; Rankey, 2011), and/or have only considered the effects of recent SLR. Studies of island response to recent SLR may not accurately portray how islands will respond in the future when sea levels are predicted rise more rapidly and attain, if not exceed (Church et al., 2013; Kopp et al., 2014; Slangen et al., 2014) elevations when these islands formed during the mid-Holocene highstand (Dickinson, 2009; Kench et al., 2009). An atoll island's wave-driven, alongshore erosion and/or accretion patterns can differ from another's due to a number of factors, including variable morphology such as varying reef flat width, reef depth, and island shape. There has been limited exploration modeling of the erosional and accretional effect of changing wave conditions along atoll islands (Shope et al., 2017), however, it is currently unclear how alongshore erosion and/or accretion along different atoll islands' shorelines will respond to future SLR. Shope et al. (2017) and other studies have provided rationale as to how observed or projected erosion patterns may be influenced by atoll morphology, but there has not been a rigorous evaluation of how much influence morphologic variability affects alongshore processes on atolls.

To address morphologic controls on wave-driven erosion and accretion, Grady et al. (2013) and Quataert et al. (2015) modeled the effects of varying reef dimensions on wave parameters along reef-protected shorelines using a schematic or generalized bathymetry. Both of those studies, however, utilized one-dimensional (cross-shore) transect models. To capture alongshore variability, this approach requires multiple cross-shore transects. Alongshore variability is more easily captured in a two-dimensional (2D) model, however, there has been limited two-dimensionally modeled analysis of wave-driven sediment transport along atoll island shorelines (Shope et al., 2017). Furthermore, these studies have remained site-specific, making it difficult to extrapolate finding to atoll islands as a whole and how differing atoll and island morphologies may affect the alongshore sediment transport process.

This study starts to fill this gap in understanding by proving an exploratory framework to assess the effect of differing morphologies and SLR on alongshore sediment transport gradients of atoll islands using 2D wave modeling which may be extrapolated to most atoll islands, expanding upon the methods of Shope et al. (2017). A physics-based 2D numerical wave model with varying schematized atoll bathymetries and island topographies with empirical sediment transport formulae were used to explore potential morphologic controls on wave-driven atoll island shoreline change patterns with SLR. A schematic model offers the benefit of allowing morphological parameters to be isolated and systematically varied to discern their relative controls on atoll island shoreline stability. A single morphological parameter (e.g., reef flat depth) can be altered while keeping the remainder of the morphology of the atoll constant, a condition that cannot be replicated from observational data of real atolls. Additionally, this approach allows for a large number of potential morphologies to be investigated in regards to their influence on shoreline change along an individual island. A brief overview of atoll and island morphology, characteristic ranges of morphologic parameters, and information about oceanographic forcing and wave transformation over atoll reefs is presented. The model set-up and run conditions are then discussed, including formulation and descriptions of implementation, and then alongshore change calculations and data analyses. Finally, the results of changes in shoreline erosion with varying morphology and SLR are presented, followed by a discussion of these trends in relation to previous studies.

ATOLL MORPHOLOGY AND INTERACTION WITH WAVES

Atolls are shallow carbonate platforms that exhibit a wide range of morphologies created by successive vertical accretion of coral reefs as relative sea level increases with a central lagoon (Dickinson, 2004). The platform steeply rises from depths of a few kilometers to a shallow (often < 3 m water depth) annular reef flat. Atoll reefs have steep fore-reef slopes (**Figure 1** and **Table 1**; Quataert et al., 2015), whereas the slope from the reef flat into the lagoon is usually relatively gentle ($\leq$1/20). Atoll diameters can vary widely (**Table 1**). Atolls are subject to a variety of wave conditions, ranging from small locally-generated wind waves to large swell waves generated far afield by storms and trade winds (Hoeke et al., 2013; Shope et al., 2016). Historical simulations indicate that the mean of the largest 5% of deepwater waves at many tropical Pacific atolls ranges from 4 to 8 m during the Northern Hemisphere winter and 2–4 m during its summer (Shope et al., 2016).

These waves and resulting wave-driven currents rework reef-derived sediment into islands that sit atop the reef flat (Ohde et al., 2002). These islands are small, often with widths less than 1 km (**Table 1**), low in elevation, on average 2–3 m above sea level (Woodroffe, 2008), and have fronting reef flats of various widths (**Table 1**). Island lengths vary greatly, from 100 s of m to several km.

The shallow reef crest dissipates most incident wave energy through depth-limited breaking (Ferrario et al., 2014). Wave energy that bypasses the reef crest is further dissipated by

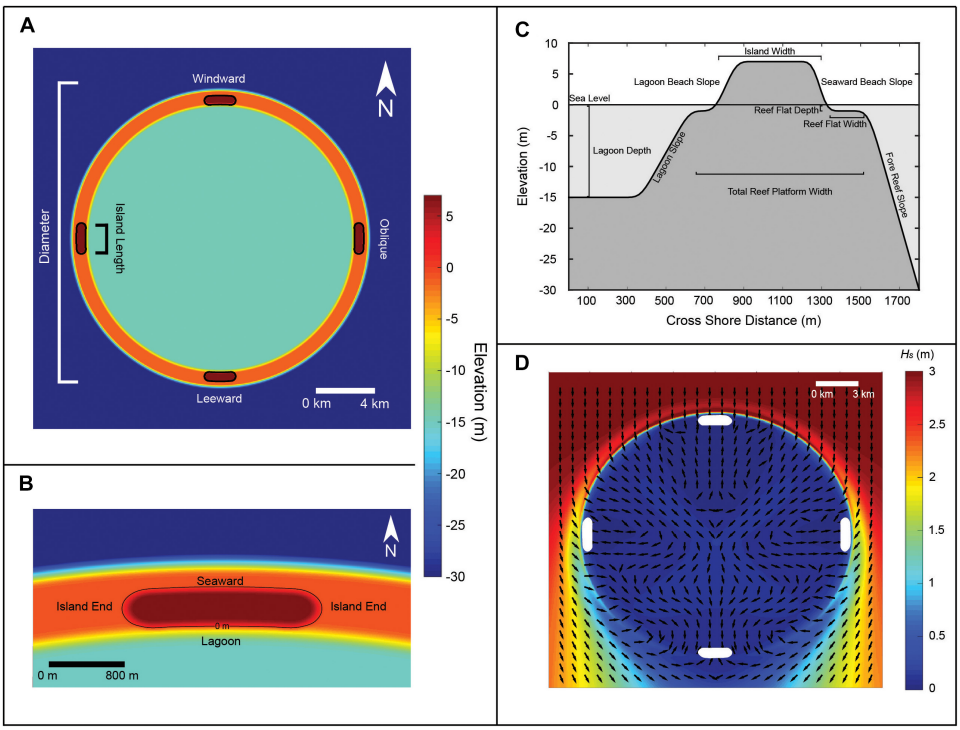

FIGURE 1 | Schematic model topography and bathymetry at the initial model configuration with example wave model output. **(A)** Topography and bathymetry at the atoll scale with labeled morphological parameters and island location in reference to incident waves coming from the top of the diagram. **(B)** A zoomed in image of the northern island indicating the shoreline divisions. Black lines indicate the 0 m contour. **(C)** Cross-section of schematized atoll island with labeled morphologic parameters. **(D)** Example wave height output for a 20 km atoll. White areas represent islands; black arrows represent wave direction. Waves approach from the top boundary of the model domain and refract around the atoll.

TABLE 1 | Morphological parameters varied within this study with a characteristic range of values determined from literature references, bathymetric data, and ESRI satellite imagery, along with values for the initial bathymetry configuration.

Parameter	Range used	Initial	References
Island width	200–1000 m	500 m	Woodroffe, 2008; Webb and Kench, 2010*
Island length	1000–5000 m	2000 m	Webb and Kench, 2010*
Ocean-facing slope	1/3–1/12	1/6	Grothe et al., 2010a,b; Rankey, 2011; Quataert et al., 2015; Beetham et al., 2016
Lagoon-facing slope	1/12–1/20	1/15	Grothe et al., 2010a,b
Fore reef slope	1/5–1/20	1/10	Hoeke et al., 2011; Quataert et al., 2015; Beetham et al., 2016
Reef flat width	50–950 m	250 m	Woodroffe, 2008; Kench et al., 2009; Quataert et al., 2015*
Reef flat depth	25–200 cm	1.0 m	Woodroffe, 2008; Yates et al., 2013; Quataert et al., 2015
Atoll diameter	5–80 km	20 km	Ford et al., 2013; Yates et al., 2013*
Sea-level rise	0–2.0 m	0 m	Church et al., 2013; Kopp et al., 2014; Slangen et al., 2014

*Presented references were not the only literary basis to determine the ranges, but provide examples of morphologies within the modeled ranges. *Denotes that ranges are supplemented by measurements using ESRI Satellite Imagery.*

frictional interactions with the rough reef flat (Lowe et al., 2005; Quataert et al., 2015), with wider reef flats providing greater energy dissipation (Grady et al., 2013; Ferrario et al., 2014; Quataert et al., 2015). With SLR or reef degradation, reef flats become deeper, reducing wave interaction with the underlying reef and thus increasing wave energy delivered to shorelines (Gourlay, 1996; Pequignet et al., 2011; Taebi and Pattiaratchi, 2014; Hoeke et al., 2015), and deeper reef flats are associated with greater alongshore sediment transport (Storlazzi et al., 2011; Grady et al., 2013).

Atoll islands are dynamic features whose shorelines respond to changing wave conditions on seasonal (Kench and Brander, 2006) and decadal (Rankey, 2011) timescales. As a result, with past SLR, atoll islands have had complex responses: many have been found to reorganize on the reef flat and even increase in total area (Webb and Kench, 2010; Yates et al., 2013). However, these trends may not persist when sea level approaches or exceeds the mid-Holocene highstand levels under which the islands formed, or as SLR rates accelerate beyond recently observed rates (Dickinson, 2009).

MATERIALS AND METHODS

Model Schematization and Bathymetry

The dimensions of many atolls and atoll islands from peer-reviewed studies and satellite imagery were analyzed to determine characteristic ranges of dimensions to inform a schematized bathymetry/topography (**Table 1**). Using this compilation, idealized atolls were created using characteristic values within the described range for each dimension.

This schematized bathymetry/topography was a circular atoll ring with four islands situated at 0, 90, 180, and 270° from north along the rim to investigate the relative influence of island position on the atoll (**Figure 1A**). The lagoon depth was 15 m, as it is assumed that there is negligible interaction between the low amplitude, high-frequency waves in the lagoon and the lagoon bottom. Beaches were created by scaling the edges of the islands using the beach slopes listed in **Table 1**. The beach slopes at the island ends were assumed to change linearly between the ocean-facing and lagoon beach slopes. Islands were elongate with rounded ends and positioned a consistent distance from the reef rim and the lagoon rim (**Figure 1B**). An "initial" atoll configuration was selected based on the ranges summarized in **Table 1**. This initial schematization was a base from which individual morphological parameters were varied within a given range, while keeping the others constant.

Model and Setup

Incident wave simulations were modeled the spectral Simulating Waves Nearshore (SWAN) model (Booij et al., 1999; Ris et al., 1999), which solves the spectral action balance equation for boundary conditions, within the DELFT3D–WAVE module. Each simulation computed wave transformations for one set of boundary conditions, with no temporal evolution of the model boundary forcings. Most default model settings were used, but the bottom friction of the reef was formulated using a Madsen coefficient of 0.1 m following Hoeke (2010) and wind-wave growth was not enabled. The wave direction bins were set to be 95 resolve the wave transformations and diffractions across the reef. To adapt SWAN for the rapid and dramatic changes in slope and depth that are found in an atoll environment, each bathymetry was smoothed to the same extent by an iterative Gaussian filter. This methodology is intended to determine the relativistic effects of individual parameters (e.g., a wider versus a narrower reef flat) between model runs. These smoothed bathymetries retained the same structure and scale of the pre-smoothed schematic, not significantly impacting the final results.

For atoll diameters of 5–20 km, the model was composed of two grids, a 60 m coarse resolution grid representing the entire atoll and a 20 m fine-resolution grid focused on the northern island of the atoll. A 20 m resolution grid was the finest grid that could be modeled coupled with 95 directional bins. Higher resolutions would result in SWAN out of memory computation errors. This resolution is comparable to available bathymetry/topography data for remote atolls (e.g., Shope et al., 2017). For larger atolls, these grids were further nested in a 180 m grid for 40 km diameter, and in a 320 m grid for 60 and 80 km diameters. The boundary deep-water wave conditions of the model were a significant wave height (H_s) of 3 m with a peak wave period (T_p) of 15 s, and a wave direction (θ_w) of 0° from north to represent large swell conditions (**Figure 1D**). Boundary conditions did not change, thus only one calculation of nearshore wave transformation was needed per morphological configuration. Simulating one wave condition allowed for a clearer analysis of differing atoll morphologies. Also, SWAN does not simulate the infragravity waves needed to fully explore how changing wave periods may affect alongshore sediment transport gradients. Sea level within the model was considered to be mean sea level relative to the atoll island shorelines. Reef and beach slope variations were too small to be well represented at the model resolutions; therefore, analysis of the alongshore transport gradient influence of these slopes was outside the capability of this study. Finally, SLR was modeled as a suite of static water elevations from +0.0 m to +2.0 m at 0.5 m increments to represent potential water level conditions by 2100 (Church et al., 2013; Kopp et al., 2014; Slangen et al., 2014). As SWAN was not coupled to a hydrodynamic flow or numerical morphology component, SLR was not represented as a continuous change to mimic the morphological evolution over the next century. Instead, each simulation represents how that exact morphology would react to higher water level conditions. Similarly, the alongshore flow generated by wave setup (and its sediment transport) was not simulated within this study as coupling to a flow model would be necessary to fully resolve the alongshore water level gradient due to wave radiation stresses. An empirical methodology to determine water level-driven alongshore transport was explored, but the transport values were found to be negligible compared to the wave-driven magnitudes. Wave simulations were modeled for each combination of morphologic variation and sea level. Short term water level fluctuations due to tidal forcing were not modeled, but their instantaneous influence can be inferred by referring to the smaller increments of SLR that were modeled. The depth of the reef flat was assumed to be static with respect to SLR. The reef flat is the primary filter for incident wave energy that drives sediment transport (Ferrario et al., 2014), and the vertical accretion of an atoll reef flat in a high energy area is 1–4 mm/y (Montaggioni, 2005) which is much smaller than projected SLR rates over the next century (Church et al., 2013; Kopp et al., 2014; Slangen et al., 2014). For this reason, reef flat growth was assumed to be negligible compared to sea level changes.

Alongshore Sediment Transport and Shoreline Change Modeling

The instantaneous alongshore sediment flux was calculated via the empirical Coastal Research Engineering Center (CERC) equation as formulated by Komar (1971) and Rosati et al. (2002), which has been used in previous shoreline change studies (e.g., Ashton and Murray, 2006; Adams et al., 2011). The formula was adapted for use along atoll island shorelines using the

methodology described by Shope et al. (2017). The CERC formula is given as:

$$Q_l = \frac{I_l}{(p_s - p_w)gN_o} \tag{1a}$$

$$I_l = K\frac{1}{8}p_w g H_b^2 Cn \sin(\alpha)\cos(\alpha) \tag{1b}$$

$$C = \frac{gT}{2\pi}\tanh\left(\frac{2\pi h}{L_o}\right) \tag{1c}$$

where Q_l is the alongshore sediment transport rate (m^3/s), p_s is the density of carbonate sand (the bulk density of coral, 1400 kg/m^3, was used; Grigg, 1982; Harney and Fletcher, 2003), p_w is the density of seawater (1024 kg/m^3), N_o is the volumetric concentration of solid grains (∼0.6), I_l is the immersed weight transport rate, H_b is the breaking wave height, C is nearshore wave celerity (m/s, a function of H_s, T_p, and h; e.g., Komar, 1998), n is the shallow water assumption for wave group velocity (0.5), α is the angle of incidence between θ_w and shoreline direction, h is water depth (m), g is the acceleration due to gravity (∼9.81 m/s^2), and L_o is wave length (m, a function of T_p and h (e.g., Komar, 1998). The tuning parameter (K) in Equation (1b) was varied at each model cell following Smith et al. (2009) to generate a better approximation of transport magnitudes. K was calculated as:

$$K = 0.7\xi_b = 0.7\frac{m}{\sqrt{\frac{H_b}{L_o}}} \tag{2}$$

where m is the beach slope. CERC calculates alongshore transport potential based on wave energy gradients assuming homogenous sized material.

Traditionally, when utilizing the CERC equation, H_b and θ_w are computed at a water depth of approximately 5 m (Adams et al., 2011). Along atoll reefs, there are two breaker zones: the first at the reef crest and the second at the island shoreline. The rapidly shoaling bathymetry causes the incident wave energy to decay such that breaking conditions at the reef crest do not represent the nearshore conditions driving alongshore transport. Therefore, H_s and θ_w output by SWAN along the shoreline were used in CERC calculations (Shope et al., 2017), as these conditions dominate the island's alongshore wave energy gradient.

The CERC formula was developed for long, linear, siliciclastic coastlines (e.g., Adams et al., 2011). Along more non-linear atoll island morphologies, it was necessary to remove highly local patterns to discern shoreline-scale (**Figure 1B**) trends. SWAN outputs in the very nearshore demonstrated a great deal of alongshore variability between neighboring points due to the nearshore model resolution (20 m) and the rectilinear grid. At this resolution, wave energy varies slightly and non-linearly from point to point alongshore, resulting in highly variable transport rates. Wave inputs and transport magnitudes were smoothed using a low-pass filter to remove rectilinear model-generated local variations smaller than approximately 1 km (20% of the initial island alongshore circumference) along the curvilinear island shorelines. This threshold was determined to give the general alongshore drift patterns of the island as a whole, while removing most sub-shoreline scale variation. As the purpose of this study was to determine shoreline-scale changes in transport gradients under idealized morphologies and conditions, smoothing these alongshore values created a clearer picture of general shoreline-scale alongshore transport.

Limitations and Assumptions

It is important to note that the CERC formula only calculates sediment transport in the alongshore direction, discounting the effects of transport onto the island and into the lagoon (Woodroffe et al., 1999; Kench et al., 2008; Smithers and Hoeke, 2014; McLean and Kench, 2015). Recent studies have investigated cross-shore sediment transport (Hoeke et al., 2013; Smithers and Hoeke, 2014; Cheriton et al., 2016), but do not compare cross-shore and alongshore transport processes. Also, these studies highlight very large events, and the average sediment transport they discuss is skewed toward these large events. Finally, there are no atoll island-wide measurements of alongshore sediment flux with which to compare in the literature. Kench and Brander (2006) concluded that due to the circular nature of sediment transport around reef islands at shorter time scales, alongshore transport processes control island morphological change with little influence from cross-shore processes. As the wave simulations and transport calculations were instantaneous and this research is specifically focused on alongshore processes, no cross-shore processes were simulated. However, processes such as infragravity wave overwash will increase with SLR (e.g., Quataert et al., 2015; Cheriton et al., 2016), and must be considered to fully project atoll island morphological evolution. It was assumed that island shorelines were composed of unlimited, unconsolidated sand-sized material despite atoll shorelines often including beach rock and shingle that inhibit wave-driven sediment transport (Vousdoukas et al., 2009). Additionally, the calculated slope utilized in Equation (2) were muted as the resolution of the model (20 m) resulted in smaller slope calculations, a smaller K tuning parameter, and smaller transport magnitues. However, the calculated transport magnitudes were only used to derive the relative effects of different atoll and island morphologies on transport gradients and were not analyzed as exact replications of real-world processes, of which there is little-to-no observational data available with which to compare. This simplified approach reduces location dependence of the analysis due to heterogeneity in island sedimentologies (e.g., Kench et al., 2005; Rankey, 2011). Additionally, these instantaneous calculations of transport gradients were rapid, allowing a larger number of morphological scenarios to be investigated (order of 1000s) compared to computationally expensive numerical morphodynamic models. Finally, the finest model grid resolution of 20 m was somewhat too coarse to represent exact alongshore transport magnitudes. The quantitative results are therefore discussed relativistically in the results section. Different morphology configurations produced relatively different transport magnitudes in response differing nearshore wave energy. These trends in transport magnitudes between modeled scenarios hold true despite the fact that the calculated magnitudes may be unrealistic.

Coastal Change Analysis

For the purposes of analysis and comparison with observational studies, alongshore sediment transport gradients were represented as potential erosion and accretion values. Potential erosion and accretion were calculated as the divergence of the calculated alongshore transport: $\partial Q_l/\partial x$, where x is the distance alongshore (e.g., Pelnard-Considere, 1956). Positive divergence values were defined as erosion and negative values as accretion. These magnitudes of shoreline change were then divided by the local grid resolution (20 m) to represent the erosion or accretion magnitude per m of shoreline. These processes are also influenced by local sediment size, which must be considered in any site-specific analysis. But in an idealized model, the size is not critical to elucidate transport trends due to varying morphologies and SLR. It is important to note that these gradients were calculated from the single swell wave condition and represent an instantaneous estimation of alongshore transport. As such, the morphology of the islands was not altered within the model in response to the calculated erosion and accretion values. Instead, each simulation should be viewed as how an atoll's configuration affects these instantaneous transport gradients. For analysis, each island was divided into four shorelines: one seaward, one lagoon, and two island ends (**Figure 1B**). Seaward shorelines face the ocean, lagoon shorelines face the central lagoon, and island end shorelines are the longitudinal ends of the islands. For oblique islands, a windward island end faces the direction of incident wave energy and a leeward island end faces away from the direction of incident wave energy. The erosion/accretion values along each shoreline were summed to discern net shoreline erosion/accretion for each scenario. These values were then compared relative to the net shoreline change for the same shoreline under different sea levels and/or morphologies. The absolute output magnitudes were not discussed within the coastal change analysis, as this idealized model aimed to explore the relative impact of different morphological parameters on shoreline erosion/accretion. This approach has been useful to explore regions where there are little-to-no calibration data for a shoreline change model (e.g., Shope et al., 2017). The purpose and strength of this numerical model to empirical erosion approach is not to simulate historic observations exactly, but rather gain confidence that physical processes are represented. This allows for determining the relative contribution of the variations in geometries (e.g., different widths, depths, and scales) to alongshore transport patterns.

RESULTS

The influence of varying island width, reef flat width, reef flat depth, and atoll diameter on erosion and/or accretion magnitudes are described here. Although explored, variations in island length are not presented, as erosion and accretion were found to be comparably insensitive to changes in this parameter via this methodology. For windward and leeward islands, results for both island ends were similar. Therefore, results of one representative island end shoreline are presented. For oblique islands, the seaward and leeward island end shorelines behaved differently, and results are presented for each shoreline. Throughout, the magnitude of the transport patterns increased with SLR; shorelines that were initially erosive or accretive with lower sea level generally displayed greater erosion or accretion magnitudes with SLR. The following describes the shoreline change trends by island, with each major shoreline of that island being described in each section. Data used in this study can be found and downloaded at: Shope and Storlazzi, 2019, http://doi.org/10.5066/P9U28JFO.

Windward Islands

Seaward shorelines were projected to be erosive under all morphology ranges. Smaller island widths (<1 km, **Figure 2A1**), narrower reef flats (<500 m, **Figure 2B1**), deeper reef flats (>1 m, **Figure 4C1**) and smaller atoll diameters (<20 km, **Figure 2D1**) resulted in greater erosion. Very narrow reef flats (<150 m) had intense erosion, even at low values of SLR. Medium-sized atolls (20–40 km) generally had lower erosion than larger and smaller diameters. The greatest magnitude of erosion with SLR occurred with deep (>1.5 m) and narrow reef flats. Lagoon shorelines were accretive under all morphologies. Smaller island widths (**Figure 3A2**), narrower reef flats (**Figure 2B2**), deeper reef flats (**Figure 2C2**), and smaller atoll diameters (**Figure 2D2**) resulted in enhanced accretion. Medium-sized atolls generally had smaller accretion magnitudes than other atoll diameters. The greatest magnitude of accretion with SLR occurred with deep reef flats and narrow island widths (<300 m). Island end shorelines were accretive under most morphology ranges, however, the magnitudes were the smallest for all islands and shorelines in this study (**Figures 2A3–4D3**). Narrow reef flats were associated with more accretion (**Figure 2B3**). Otherwise, the changes with morphologic parameters were small and did not follow a consistent pattern.

Leeward Islands

Seaward shorelines were projected to be slightly erosive at 0 m SLR and become more accretive with SLR. The magnitudes overall were generally small (**Figures 3A1–3D1**). Small island widths (<1 km), deeper reef flats (>1 m), and narrow reef flats (<500 m) were characterized by more accretion. The increase in accretion was greatest for small island widths. Lagoon shorelines were erosive under almost all morphologies. Smaller island widths (**Figure 3A2**), narrower reef flats (**Figure 3B2**), and deeper reef flats (**Figure 3C2**) were characterized by more erosion. The greatest magnitude of erosion occurred with deep reef flats and narrow island widths. At atoll diameters smaller than 10 km the lagoon shoreline was erosive (**Figure 3D2**). Island end shorelines were accretive under almost all morphologies. Smaller island widths (**Figure 3A3**), narrower reef flats (**Figure 3B3**), and deeper reef flats (**Figure 3C3**) had greater accretion magnitudes. The greatest accretion magnitudes occurred with deep reef flats and narrow island widths. At an atoll diameter of 5 km this shoreline was erosive, but at atoll diameters greater than 5 km it was accretive (**Figure 3D3**).

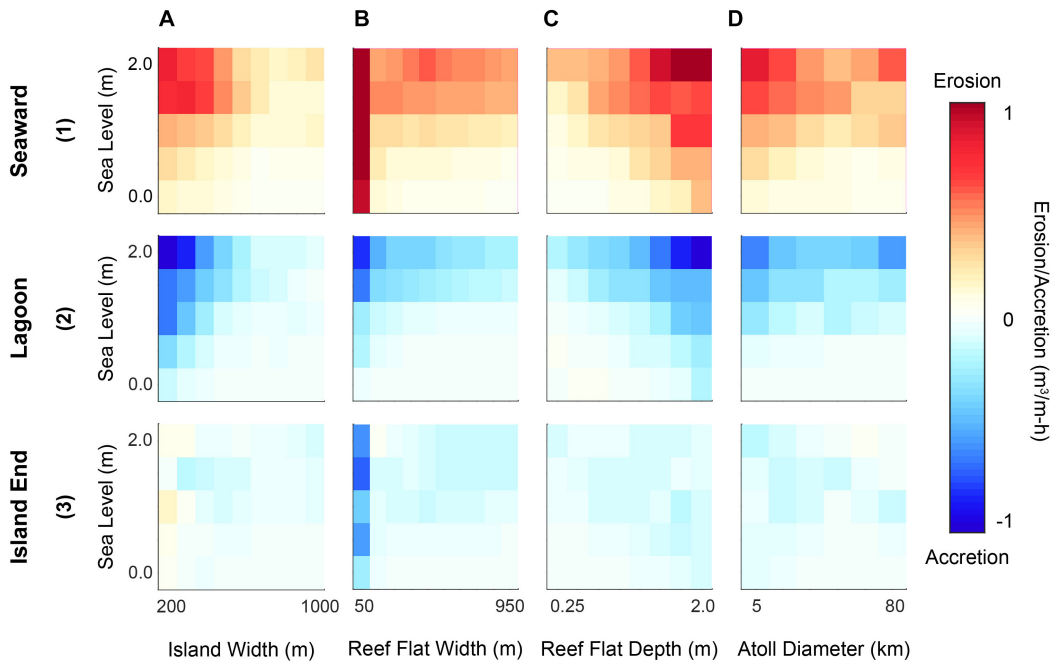

FIGURE 2 | Relative changes in shoreline erosion/accretion magnitudes with morphological parameter (x-axes) and SLR (y-axes) for the windward island. Rows describe (1) seaward, (2) lagoon, and (3) island end shorelines; columns denote morphological parameters **(A)** island width, **(B)** reef flat width, **(C)** reef flat depth, and **(D)** atoll diameter. Red indicates net erosion and blue net accretion, with increasing color intensity indicating greater magnitude. The color ramp is linear, but absolute magnitudes are unlisted to address only relative changes.

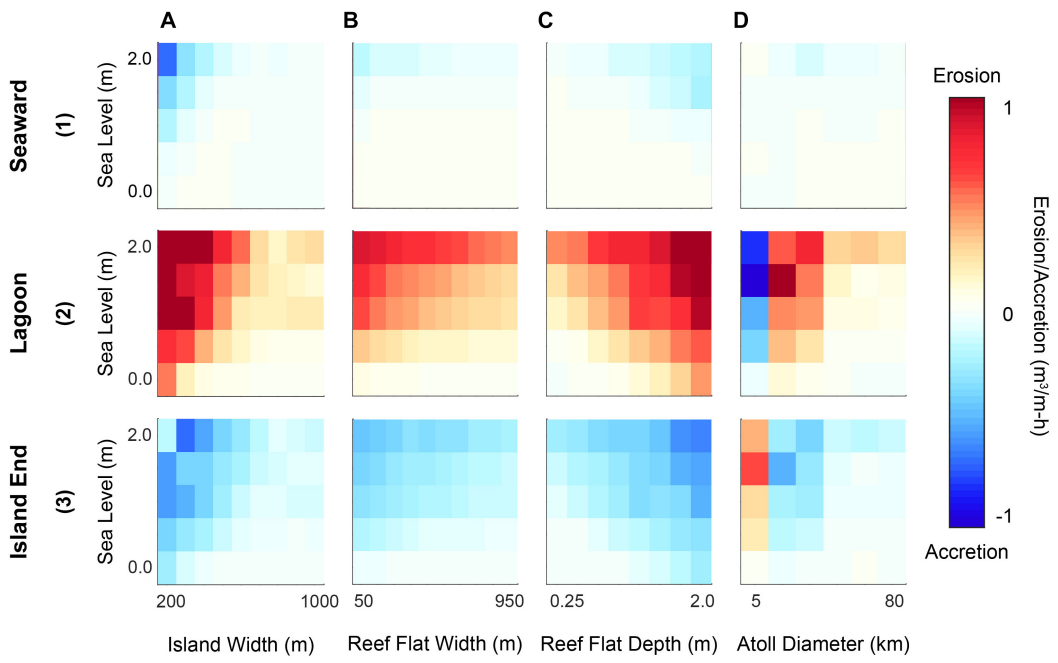

FIGURE 3 | Relative changes in shoreline erosion/accretion magnitudes with morphological parameter (x-axes) and SLR (y-axes) for the leeward island. Rows describe **(1)** seaward, **(2)** lagoon, and **(3)** island end shorelines; columns denote morphological parameters **(A)** island width, **(B)** reef flat width, **(C)** reef flat depth, and **(D)** atoll diameter. Red indicates net erosion and blue net accretion, with increasing color intensity indicating greater magnitude. The color ramp is linear, but absolute magnitudes are unlisted to address only relative changes.

Oblique Islands

Seaward shorelines demonstrated similar trends to the windward islands' seaward shorelines, as all were projected to be erosive over the range of morphologic variations. Smaller island widths (<1 km, **Figure 4A1**), narrower reef flats (<500 m, **Figure 4B1**), deeper reef flats (>1 m, **Figure 4C1**), and smaller atoll diameters (<20 km, **Figure 4D1**) had more erosion. Medium-sized (20–40 km) atolls generally displayed less erosion than other diameters. The greatest magnitude of erosion occurred with deep and narrow reef flats. The lagoon shoreline exhibited similar trends to the windward island lagoon shoreline, being accretive over the range of morphologic variations. Smaller island widths (**Figure 4A2**), narrower reef flats (**Figure 4B2**), deeper reef flats (**Figure 4C2**), and smaller atoll diameters (**Figure 4D2**) had greater accretion. Both small and large atoll diameters had greater accretion than middling sizes. The greatest magnitude of accretion occurred with narrow island widths. Leeward island end shorelines were accretive under all modeled morphologies. Larger island widths (**Figure 4A3**), narrower reef flats (**Figure 4B3**), deeper reef flats (**Figure 4C3**), and smaller atoll diameters (**Figure 4D3**) displayed increased accretion. The greatest magnitude of accretion occurred with deep reef flats. This was the only shoreline in the study where larger island widths were associated with a greater magnitude of shoreline change. Windward island end shorelines were erosive under all morphologies. Smaller island widths (**Figure 4A4**), narrower reef flats (**Figure 4B4**), deeper reef flats (**Figure 4C4**), and smaller atoll diameters (**Figure 4D4**) had increased erosion, with the greatest magnitude occurring with deep reef flats.

DISCUSSION

The results are discussed at two scales. The first focuses on how individual morphological parameters affect alongshore transport gradients from an atoll-scale to island-scale parameters (i.e., the island width). The second section considers these parameters together: including how they may influence the morphological evolution of individual islands and enable a relativistic classification of island shoreline stability with SLR.

The Influence Morphological Parameters

Atoll Diameter

Atolls with smaller diameters (5–10 km) were projected to have greater shoreline erosion than comparably larger atolls. Wave refraction around the atoll and wave shadowing by the

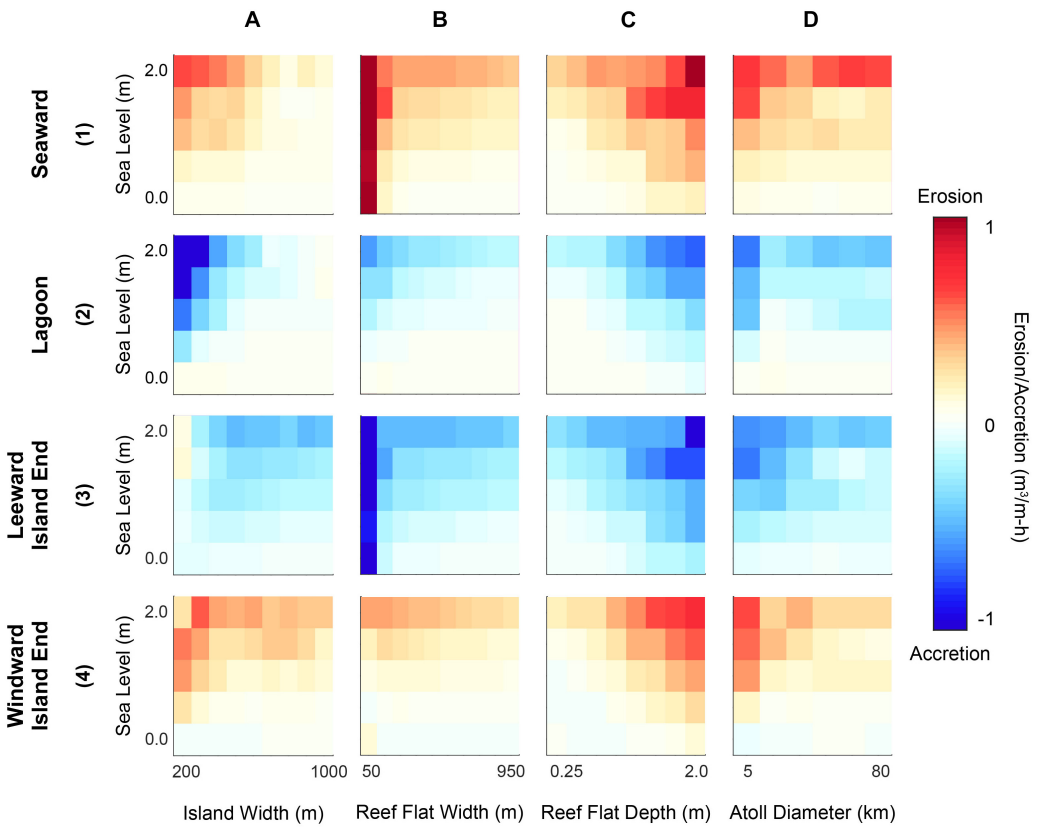

FIGURE 4 | Relative changes in shoreline erosion/accretion magnitudes with morphological parameter (x-axes) and SLR (y-axes) for the oblique island. Rows describe **(1)** seaward, **(2)** lagoon, **(3)** leeward island end, and **(4)** windward island end shorelines; columns denote morphological parameters **(A)** island width, **(B)** reef flat width, **(C)** reef flat depth, and **(D)** atoll diameter. Red indicates net erosion and blue net accretion, with increasing color intensity indicating greater magnitude. The color ramp is linear, but absolute magnitudes are unlisted to address only relative changes.

windward island (**Figure 1D**) likely account for these differences. Mandlier and Kench (2012) observed that changing the aspect ratio of an oblate coral reef platform affected wave refraction and convergence patterns; the patterns are likely similar for a circular platform with a central lagoon. On smaller atolls, the reef flat and islands have greater curvature, increasing refraction, directing wave energy toward the island shorelines that would normally be bypassed near the island ends. Additionally, a windward island that covers a greater fraction of atoll circumference, such as in the smallest diameter model, will cause a wave shadow that affects incident wave energy along the leeward island, changing transport gradient. For atoll diameters greater than or equal to 10 km, the leeward island's transport gradients reverse, indicating that it is no longer in the northern island's shadow. At the largest atoll diameter range, wave refraction is less, striking seaward shorelines closer to perpendicular, and reduced reef frictional dissipation from traversing a shorter (non-refracted) distance across the reef flat. These results indicate that atoll size is a crucial model parameter, and transport patterns projected for a smaller atoll may not necessarily scale to a larger atoll.

Reef Flat Width

Narrower reef flats were projected to exhibit greater erosion with SLR. Narrower fringing reef flats lead to increased nearshore H_s because less wave energy is attenuated through frictional dissipation (Lowe et al., 2005; Grady et al., 2013; Ferrario et al., 2014; Quataert et al., 2015), resulting in greater transport gradients between the seaward and lagoon shorelines. Very narrow reef flats (<50 m) along windward and oblique islands often generated comparably high magnitude erosion due to the coarseness of the model resolution and smoothing resulting in a poorer representation of the very narrow reef within the wave model. However, this result does follow reports of narrower reef flats allowing more energy to reach shore (e.g., Quataert et al., 2015), reducing wave refraction, and resulting in greater alongshore transport. For leeward islands, very narrow reef flats do not have a similar effect waves that reach leeward islands lose much of their energy as they traverse the northern reef platform width before crossing the lagoon or are refracted around the atoll to intersect the southern shoreline. However, the trend between wider reef flats and more reduced alongshore erosion was greatest on leeward islands. Waves that reach lagoon shorelines of leeward islands traverse the total reef platform and the lagoon before reaching shore. When crossing the reef flat, these waves refract, traveling a greater distance than the platform width. As a result, changes in reef flat width are magnified in these conditions.

Reef Flat Depth

Increasing reef flat depth reduces depth-limited breaking at the reef crest, and frictional energy dissipation, thus increasing sediment transport potential. Conversely, shallower reef flats afford more protection from wave attack and reduce erosion. Previous studies have observed increased shoreline erosion with increasing reef depths in the Seychelles due to reef degradation (Sheppard et al., 2005) and in models of fringing reef sediment dynamics in Hawaii (Storlazzi et al., 2011; Grady et al., 2013).

Island Width

Narrower islands lead to greater nearshore H_s and increased transport in all scenarios. Alongshore sediment erosion and deposition around an atoll island is dominated by the alongshore wave energy gradient with sediment migrating from regions of high energy to low (Kench and Brander, 2006; Kench et al., 2006, 2009; Beetham and Kench, 2014; Smithers and Hoeke, 2014). A wider island decreases the energy (and sediment transport) gradient from the seaward to lagoon shorelines, because the approximately same change in alongshore energy is divided over a longer alongshore distance. A secondary impact is that for a given reef flat width, wider islands result in a wider reef platform. The reef flat width was held constant at 250 m within the model, so the reef platform width varied along with island width which resulted in increased energy dissipation and less sediment transport (Grady et al., 2013). Island width had a stronger impact on erosion magnitudes than reef flat widths except for narrow (<150 m) reef flat widths; this implies that under the range of conditions studied here, alongshore distance affects the energy gradient more than incident wave energy dissipation provided by the reef under the control scenario.

Implications for Atoll Island Stability

With SLR, all shorelines exhibited an intensification of a preexisting alongshore erosion/accretion patterns. Mandlier and Kench (2012) found that with increased water depths, the wave convergence zones that help form reef islands migrate from the windward side of a reef platform to the leeward side, increasing erosion along the windward shoreline of an island. This process manifests within the modeled results as an intensification of erosion along the windward and oblique islands' seaward shorelines and the leeward island's lagoon shoreline. Following the migration of the wave convergence zone, model results indicate that windward islands would erode along the seaward shoreline (**Figure 5**), with its sediment being transported to the island ends and the lagoon shorelines in accordance with observational studies (e.g., Webb and Kench, 2010), which would widen these beaches. However, other studies have found conflicting results. Yates et al. (2013) observed windward islands accreting along their seaward shorelines on Manihi Atoll; Woodroffe (2008) describes seaward shorelines as long-term sediment sinks and erosion along these shorelines as ephemeral. Additionally, Shope et al. (2017) found that with SLR, modeled windward islands eroded along seaward shoreline and lagoon shorelines, accreting at the islands' ends and parts of the shoreline with a wider reef flat. Similarly, the oblique islands would extend leeward along the reef rim as the leeward beaches build out and toward the lagoon (**Figure 5**) as the transport gradient between the seaward and lagoon shorelines is intensified. Leeward island transport patterns were more complex. Leeward islands receive wave energy from waves that refract around the atoll and smaller waves that are able to bypass the reef rim, which mobilize sediment along the seaward and lagoon shorelines, respectively (**Figure 1D**). However, there is generally an asymmetry in this energy resulting in net accretion along the island ends and seaward shorelines as observed at Funafuti

(Webb and Kench, 2010) and Manuae (Yates et al., 2013) Atolls and modeled at Wake and Midway Atolls (Shope et al., 2017). As sea level increases, so does the energy gradient asymmetry following the leeward migration of the wave convergence zone (Mandlier and Kench, 2012), increasing accretion along the island ends and seaward shoreline. As a result, with SLR, leeward islands would become longer, as sediment is redistributed to the ends, and narrower as transport gradients on the lagoon and seaward shorelines to the island ends intensify (**Figure 5**). Many atoll islands have remained morphologically stable during recent observational periods (e.g., Webb and Kench, 2010; Purkis et al., 2016), though there are exceptions such as Farol Island, Rocas Atoll (Costa et al., 2017). However, studies analyzing island response from relatively low SLR rates of the past century (∼ 0.2 m of SLR) may not accurately portray how islands will respond in the near future (by 2100) to greater SLR rates (∼0.5–2.0 m by 2100; Church et al., 2013; Kopp et al., 2014; Slangen et al., 2014) and elevations similar to those at the time of island formation (Dickinson, 2004; Kench et al., 2005).

While these patterns held true in most cases, some atoll configurations were found to be more resistant to intensification with SLR than others. Wide islands (>500 m) with comparably shallow (<1 m) and wide (>500 m) reef flats were more resistant to enhanced erosion and accretion magnitudes with SLR (**Figure 5**). Shallow, wide reef flats provide protection from incident wave attack regardless of island configuration, and wider islands result in comparably less transport potential regardless of atoll morphology. Shoreline stability responds complexly to changing atoll diameter. The most stable (smallest transport gradients/erosion magnitudes) configuration for windward and oblique islands is a wide island (>500 m) on a small-diameter (<20 km) atoll, whereas leeward island shorelines tend to be more stable when the atoll diameter is greater than 40 km. A simple implication is that, smaller, narrower (generally uninhabited) islands are likely to see more alongshore transport with SLR than larger, wider (generally inhabited) islands. Yates et al. (2013) observed significant erosional response to SLR at two narrow, uninhabited islands on Manuae Atoll. On the other hand, inhabited islands tend to be wider (resistant to transport gradient changes, **Figures 2–4**) as there is greater space and more freshwater resources (Bailey et al., 2010). Additionally, as SLR always resulted in a proportionally larger intensification of transport gradients compared to varying morphologies alone. A morphologically stable island with high SLR could experience greater erosion than an unstable island without SLR.

It is important to note that the projection of shoreline change in **Figure 5** does not incorporate how the island planform area may change due to increased overwash and inundation with SLR (e.g., Storlazzi et al., 2015). Increased overwash coupled with the limited sediment production in an atoll environment could dramatically alter the island morphology and position on the reef platform, likely narrowing the islands as they build vertically from overland sediment deposition (Smithers and Hoeke, 2014) and migrate toward the lagoon. The assumption of a constant

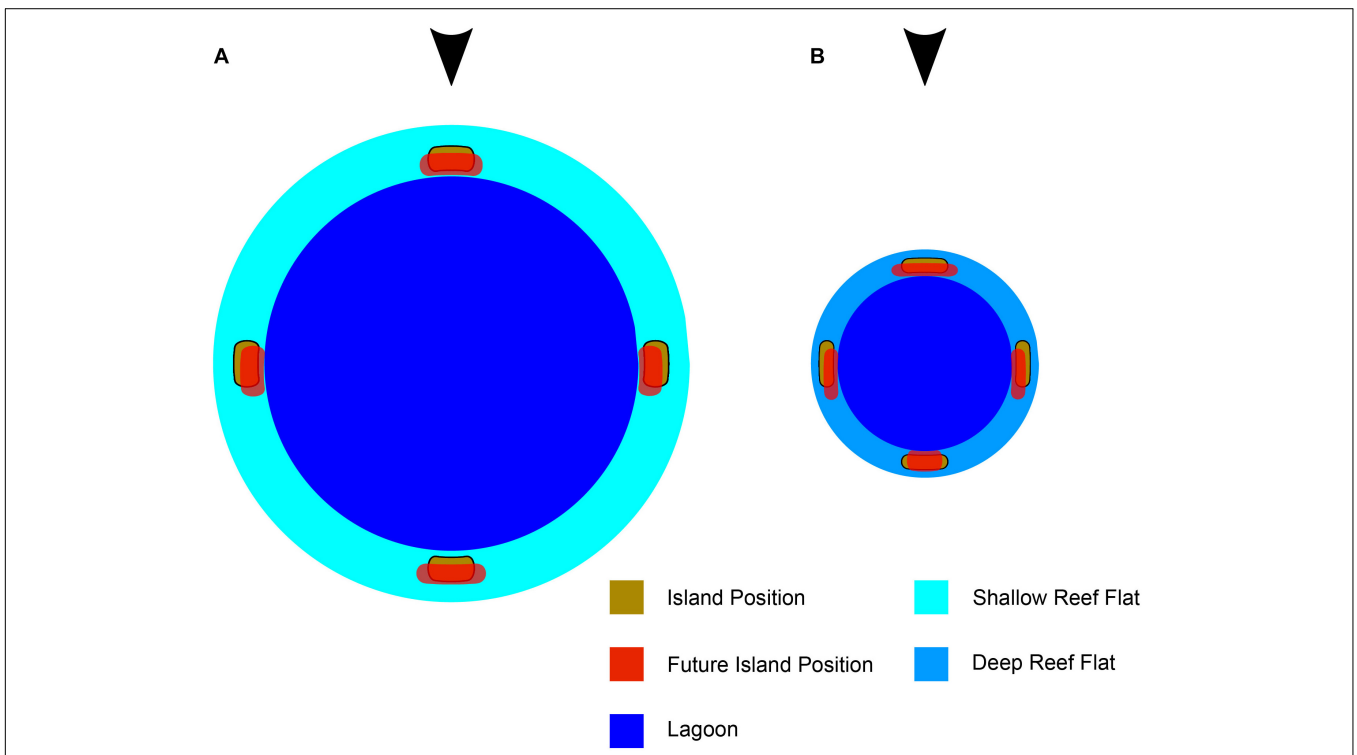

FIGURE 5 | Schematic atoll island shoreline response to SLR, with waves approaching from the top of the diagram. **(A)** Relatively resistant atoll (shallow, wide fringing reef flat; large atoll; wide islands). **(B)** Relatively susceptible atoll (deep, narrow fringing reef flat; small atoll, narrow islands). Initial island positions are shown in gold, with future positions overlain in red.

sediment supply also ignores how the islands may change in the future due to new sediment influx and deposition into the lagoon or off the reef platform. Finally, as incident wave energy is the primary driver of the CERC transport formula, larger wave conditions at the model boundary (increased H_s or T_p) would increase sediment mobilization and smaller waves would decrease sediment mobilization. This change increase or decrease calculated erosion and accretion magnitudes, respectively.

Comparing these stability scenarios with observational studies is difficult due to the influence of other sediment transport controls, such as wave climate, shoreline composition, or smaller water level variations. Holistic projections of island morphological change should not be considered independently from these other transport controls. One atoll location could have all the morphological hallmarks of greater instability, but its wave climate may be less energetic, its shorelines composed beach rock or armor, or its sediment production smaller when compared to a more "stable" scenario.

CONCLUSION

The morphology of an atoll and its islands impacts nearshore wave-energy gradients that drive alongshore morphological change. Because atoll islands are generally dynamic features (Kench and Brander, 2006; Rankey, 2011) and these alongshore wave-energy gradients will increase with SLR, future island alongshore transport patterns will change considerably. Schematic, physics-based modeling can help elucidate the control of individual morphological characteristics on potential alongshore transport changes that future SLR may bring. Additionally, one can evaluate an individual atoll island's relative proclivity for enhanced alongshore sediment transport with SLR, regardless of *in situ* data availability. The strongest modeled morphological controls on alongshore sediment transport are the island width and reef flat depth; reef flat width and atoll diameter play an important but lesser role. Atoll islands that are most susceptible to enhanced transport gradients with SLR (shoreline instability) are narrow (<500 m), located on small atolls (<20 km), with narrow (<500 m), and deep (>1 m) reef flats. Relative to incident wave direction, windward and oblique islands shorelines are projected to extend toward the lagoon, retreating from the reef rim following SLR-enhanced transport gradients. Leeward islands are expected to become longer and narrower as sediment is redistributed along the island ends. In general, these most susceptible islands are likely to be uninhabited, due to limited water resources and opportunity for infrastructure development. Even so, as SLR is expected to accelerate at unprecedented rates over the next century, many atoll islands will likely see increased coastal change and threatened coastal infrastructure.

While this methodology is useful for a first-order analysis, future efforts should address many of the aforementioned limitations and improve the accuracy of schematic atoll models. A numerical, coupled hydrodynamic and sediment transport model is necessary to accurately simulate wave-driven alongshore transport around an atoll island and capture the complexities that govern shoreline evolution. A vital addition would be to incorporate cross-shore wave models that can simulate infragravity waves and their associated run-up. A model that incorporates long period waves would be able to accurately simulate overwash and vertical island accretion from successive onshore transport events to build a more complete picture of how islands may respond to changing sea levels and varying morphologies.

AUTHOR CONTRIBUTIONS

JS constructed and ran schematic atoll models, analyzed model results, and wrote most of the manuscript. CS provided guidance, additional analysis, and edited and contributed to the final manuscript.

FUNDING

This project was funded by the USGS's Coastal and Marine Geology Program and Department of Defense's Strategic Environmental Research and Development Program (SERDP) under RC-2334. Funding was also provided by the Dr. Earl H. Myers and Ethel M. Myers Oceanographic and Marine Biology Trust and Wells Fargo Coastal Sustainability Fellowship.

ACKNOWLEDGMENTS

This work was carried out under the USGS's Coral Reef Project as part of an effort in the United States and its trust territories to better understand the effect of geologic and oceanographic processes on coral reef systems and the USGS's Coastal Climate Impacts to the Project to understand the impact of climate change on U.S. and U.S.-affiliated island shorelines. Neil Ganju (USGS) contributed numerous excellent suggestions and a timely review of our work. Thanks to Tony Kimmet of the USDA-NRCS-National Geospatial Center of Excellence for imagery acquisition. Use of trademark names does not imply USGS endorsement of products. Data used in this study can be found and downloaded at: Shope and Storlazzi, 2019, http://doi.org/10.5066/P9U28JFO.

REFERENCES

Adams, P. N., Inman, D. L., and Lovering, J. L. (2011). Effects of climate change and wave direction on longshore sediment transport patterns in Southern California. *Clim. Change* 109, 211–228. doi: 10.1007/s10584-011-0317-0

Ashton, A. D., and Murray, A. B. (2006). High-angle wave instability and emergent shoreline shapes: 1. modeling of sand waves, flying spits, and capes. *J. Geophys. Res. Earth Surf.* 111:F04011. doi: 10.1029/2005JF000422

Bailey, R. T., Jenson, J. W., and Olsen, A. E. (2010). Estimating the ground water resouces of atoll islands. *Water* 2, 1–27. doi: 10.3390/w2010001

Beetham, E. P., and Kench, P. S. (2014). Wave energy gradients and shoreline change on vabbinfaru platform. Maldives. *Geomorphology* 209, 98–110. doi: 10.1016/j.geomorph.2013.11.029

Beetham, E., Kench, P. S., O'Callaghan, J., and Popinet, S. (2016). Wave transformation and shoreline water level on Funafuti Atoll, Tuvalu. *J. Geophys. Res. Oceans* 121, 311–326. doi: 10.1002/2015JC011246

Booij, N., Ris, R. C., and Holthuijsen, L. H. (1999). A third-generation wave model for coastal regions - 1. model description and validation. *J. Geophys. Res. Oceans* 104, 7649–7666. doi: 10.1029/98JC02622

Cheriton, O. M., Storlazzi, C. D., and Rosenberger, K. J. (2016). Observations of wave transformation over a fringing coral reef and the importance of low-frequency waves and offshore water levels to runup, overwash, and coastal flooding. *J. Geophys. Res. Oceans* 121, 3121–3140. doi: 10.1002/2015JC011231

Church, J. A., Clark, P. U., Cazenave, A., Gregory, J. M., Jevrejeva, S., Levermann, A., et al. (eds) (2013). "Sea Level Change," in *Climate Change 2013: The Physical Science Basis. Contribution of Working Group I to the Fifth Assessment Report of the Intergovernmental Panel on Climate Change*, (Cambridge: Cambridge University Press).

Costa, M. B., Macedo, E. C., and Siegle, E. (2017). Planimetric and volumetric changes of reef islands in response to wave conditions. *Earth Surf. Process. Landforms.* 42, 2663–2678. doi: 10.1002/esp.4215

Dickinson, W. (2004). Impacts of eustasy and hydro-isostasy on the evolution and landforms of Pacific atolls. *Palaeogeogr. Palaeoclimatol. Palaeoecol.* 213, 251–269. doi: 10.1016/j.palaeo.2004.07.012

Dickinson, W. R. (2009). Pacific atoll living: how long already and until when. *GSA Today* 19:4. doi: 10.1130/GSATG35A.1

Ferrario, F., Beck, M. W., Storlazzi, C. D., Micheli, F., Shepard, C. C., and Airoldi, L. (2014). The effectiveness of coral reefs for coastal hazard risk reduction and adaptation. *Nat. Commun.* 5:3794. doi: 10.1038/ncomms4794

Ford, M. (2012). Shoreline changes on an urban atoll in the Central Pacific Ocean: Majuro Atoll, Marshall Islands. *J. Coast. Res.* 28, 11–22. doi: 10.2112/JCOASTRES-D-11-00008.1

Ford, M., Becker, J., and Merrifield, M. (2013). Reef flat wave processes and excavation pits: observations and implications for Majuro Atoll, Marshall Islands. *J. Coast. Res.* 29, 545–554. doi: 10.2112/JCOASTRES-D-12-00097.1

Gourlay, M. R. (1996). Wave set-up on coral reefs. S. set-up on reefs with various profiles. *Coast. Eng.* 28, 17–55. doi: 10.1016/j.marpolbul.2010.06.023

Grady, A. E., Moore, L. J., Storlazzi, C. D., Elias, E., and Reidenbach, M. A. (2013). The influence of sea level rise and changes in fringing reef morphology on gradients in alongshore sediment transport. *Geophys. Res. Lett.* 40, 3096–3101. doi: 10.1002/grl.50577

Grigg, R. W. (1982). Darwin point: a threshold for atoll formation. *Coral Reefs* 1, 29–34. doi: 10.1007/BF00286537

Grothe, P. R., Taylor, L. A., Eakins, B. W., Carignan, K. S., Lim, E., Warnken, R. R., et al. (2010a). *Digital Elevation Models of Midway Island: Procedures, Data Sources and Analysis, NOAA Technical Memorandum NESDIS NGDC-33*. Boulder, CO: Dept. of Commerce, 24.

Grothe, P. R., Taylor, L. A., Eakins, B. W., Carignan, K. S., Warnken, R. R., Lim, E., et al. (2010b). *Digital Elevation Models of Wake Island: Procedures, Data Sources and Analysis, NOAA Technical Memorandum NESDIS NGDC-32*. Boulder, CO: Dept. of Commerce, 22.

Harney, J. N., and Fletcher, C. H. I. I. I. (2003). A budget of carbonate framework and sediment production, Kailua Bay, Oahu Hawaii. *J. Sed. Res.* 73, 865–868. doi: 10.1306/051503730856

Hoeke, R., McInnes, K., and O'Grady, J. (2015). Wind and wave setup contributions to extreme sea levels at a tropical high island: a stochastic cyclone simulation study for Apia. *Samoa. J. Mar. Sci. Eng.* 3, 1117–1135. doi: 10.3390/jmse3031117

Hoeke, R. K. (2010). *An Investigation of Wave-Dominated Coral Reef Hydrodynamics*. Ph. D thesis, James Cook University, Townsville.

Hoeke, R., Storlazzi, C., and Ridd, P. (2011). Hydrodynamics of a bathymetrically complex fringing coral reef embayment: wave climate, in situ observations, and wave prediction. *J. Geophys. Res.* 117:C04018. doi: 10.1029/2010JC006170

Hoeke, R. K., McInnes, K. L., Kruger, J. C., McNaught, R. J., Hunter, J. R., and Smithers, S. G. (2013). Widespread inundation of Pacific islands triggered by distant-source wind-waves. *Glob. Planet. Change* 108, 128–138. doi: 10.1016/j.gloplacha.2013.06.006

Kench, P. S., and Brander, R. W. (2006). Response of reef island shorelines to seasonal climate oscillations: South Maalhosmadulu atoll, Maldives. *J. Geophys. Res.* 111:F01001. doi: 10.1029/2005JF000323

Kench, P. S., Brander, R. W., Parnell, K. E., and McLean, R. F. (2006). Wave energy gradients across a Maldivian atoll: implications for island geomorphology. *Geomorphology* 81, 1–17. doi: 10.1016/j.geomorph.2006.03.003

Kench, P. S., McLean, R. F., and Nichol, S. L. (2005). New model of reef-island evolution: Maldives, Indian Ocean. *Geology* 33, 145–148.

Kench, P. S., Nichol, S. L., Smithers, S. G., McLean, R. F., and Brander, R. W. (2008). Tsunami as agents of geomorphic change in mid-ocean reef islands. *Geomorphology* 95, 361–383. doi: 10.1016/j.geomorph.2007.06.012

Kench, P. S., Parnell, K. E., and Brander, R. W. (2009). Monsoonally influenced circulation around coral reef islands and seasonal dynamics of reef island shorelines. *Mar. Geol.* 266, 91–108. doi: 10.1016/j.margeo.2009.07.013

Komar, P. D. (1971). The mechanics of sand transport on beaches. *J. Geophys. Res.* 76, 713–721. doi: 10.1029/jc076i003p00713

Komar, P. D. (1998). *Beach Processes and Sedimentation*. Upper Saddle River, NJ: Prentice-Hall.

Kopp, R. E., Horton, R. M., Little, C. M., Mitrovica, J. X., Oppenheimer, M., Rasmussen, D. J., et al. (2014). Probabilistic 21st and 22nd century sea-level projections at a global network of tide-gauge sites. *Earth's Future* 2, 383–406. doi: 10.1002/2014EF000239

Lowe, R. J., Falter, J. L., Bandet, M. D., Pawlak, G., Atkinson, M. J., Monismith, S. G., et al. (2005). Spectral wave dissipation over a barrier reef. *J. Geophys. Res.* 110:C04001.

Mandlier, P. G., and Kench, P. S. (2012). Analytical modelling of wave refraction and convergence on coral reef platforms: implications of island formation and stability. *Geomorphology* 159, 84–92. doi: 10.1016/j.geomorph.2012.03.007

McLean, R., and Kench, P. (2015). Destruction or persistence of coral atoll islands in the face of 20th and 21st century sea-level rise? *WIRES Clim. Change* 6, 445–463. doi: 10.1002/wcc.350

Montaggioni, L. F. (2005). History of Indo-Pacific coral reef systems since the last glaciation: development patterns and controlling factors. *Earth Sci. Rev.* 71, 1–75. doi: 10.1016/j.earscirev.2005.01.002

Ohde, S., Greaves, M., Masuzawa, T., Buckley, H. A., Van Woesik, R., Wilson, P. A., et al. (2002). The chronology of funafuti atoll: revisiting an old friend. *Proc. R. Soc. Math. Phys. Eng. Sci.* 458, 2289–2306. doi: 10.1098/rspa.2002.0978

Pelnard-Considere, R. (1956). *Essai de Theorie de L'evolution des Formes de Rivage en Plages de Sable et de Galets, in 4th Journees de l'Hydraulique, Les Energies de la Mer, III*. Grenoble: La Houille Blanche, 289–298.

Pequignet, A. C., Becker, J. M., Merrifield, M. A., and Boc, S. J. (2011). The dissipation of wind wave energy across a fringing reef at Ipan. Guam. *Coral Reefs* 30, 71–82. doi: 10.1007/s00338-011-0719-5

Purkis, S. J., Gardiner, R., Johnston, M. W., and Sheppard, C. R. C. (2016). A half-century of coastline change in Diego Garcia - the largest atoll island in the Chagos. *Geomorphology* 261, 282–298. doi: 10.1016/j.geomorph.2016.03.010

Quataert, E., Storlazzi, C., van Rooijen, A., Cheriton, O., and van Dongeren, A. (2015). The influence of coral reefs and climate change on wave-driven flooding of tropical coastlines. *Geophys. Res. Lett.* 42, 6407–6415. doi: 10.1002/2015GL064861

Rankey, E. C. (2011). Nature and stability of atoll island shorelines: gilbert Island chain, Kiribati, equatorial Pacific: atoll shoreline change, equatorial Pacific. *Sedimentology* 58, 1831–1859. doi: 10.1111/j.1365-3091.2011.01241.x

Ris, R. C., Holthuijsen, L. H., and Booij, N. (1999). A third-generation wave model for coastal regions - 2. verification. *J. Geophys. Res. Oceans* 104, 7667–7681. doi: 10.1029/1998JC900123

Rosati, J. D., Walton, T. L., and Bodge, K. (2002). "Longshore sediment transport," in *Coastal Engineering Manual, part II, Coastal Sediment Processes*, ed. D. B. King (Washington, D. C: Army, U. S., Corps of Eng.).

Roy, P., and Connell, J. (1991). Climatic-change and the future of atoll States. *J. Coast. Res.* 7, 1057–1075.

Sheppard, C., Dixon, D. J., Gourlay, M., Sheppard, A., and Payet, R. (2005). Coral mortality increases wave energy reaching shores protected by reef flats: examples from the Seychelles. *Estuar. Coast. Shelf Sci.* 64, 223–234. doi: 10.1016/j.ecss.2005.02.016

Shope, J. B., Storlazzi, C. D., Erikson, L. H., and Hegermiller, C. A. (2016). Changes to extreme wave climates of islands within the Western Tropical Pacific

throughout the 21st century under RCP 4.5 and RCP 8.5, with implications for island vulnerability and sustainability. *Glob. Planet. Change* 141, 25–38. doi: 10.1016/j.gloplacha.2016.03.009

Shope, J. B., Storlazzi, C. D., and Hoeke, R. K. (2017). Projected atoll shoreline and run-up changes in response to sea-level rise and varying large wave conditions at wake and Midway Atolls, Northwestern Hawaiian Islands. *Geomorphology* 295, 537–550. doi: 10.1016/j.geomorph.2017.08.002

Shope, J. B., and Storlazzi, C. D. (2019). *Physics-Based Numerical Model Simulations of Wave Propagation Over and Around Theoretical Atoll and Island Morphologies for Sea-Level Rise Scenarios: U.S. Geological Survey Data Release*. Available at: http://doi.org/10.5066/P9U28JFO

Slangen, A. B. A., Carson, M., Katsman, C. A., van de Wal, R. S. W., Khol, A., Vermeersen, L., et al. (2014). Projecting twenty-first century regional sea-level changes, Cliatic. *Change* 124, 317–332. doi: 10.1007/s10584-014-1080-9

Smith, E. R., Wang, P., Ebersole, B. A., and Zhang, J. (2009). Dependence of Total longshore sediment transport rates on incident wave parameters and breaker type. *J. Coast. Res.* 25, 675–683. doi: 10.2112/07-0919.1

Smithers, S. G., and Hoeke, R. K. (2014). Geomorphological impacts of high-latitude storm waves on low-latitude reef islands — observations of the december 2008 event on Nukutoa, Takuu, Papua New Guinea. *Geomorphology* 222, 106–121. doi: 10.1016/j.geomorph.2014.03.042

Storlazzi, C. D., Elias, E., Field, M. E., and Presto, M. K. (2011). Numerical modeling of the impact of sea-level rise on fringing coral reef hydrodynamics and sediment transport. *Coral Reefs* 30, 83–96. doi: 10.1007/s00338-011-0723-9

Storlazzi, C. D., Elias, E. P. L., and Berkowitz, P. (2015). Many Atolls may be uninhabitable within decades due to climate change. *Sci. Rep.* 5:14546. doi: 10.1038/srep14546

Taebi, S., and Pattiaratchi, C. (2014). Hydrodynamic response of a fringing coral reef to a rise in mean sea level. *Ocean Dyn.* 64, 975–987. doi: 10.1007/s10236-014-0734-5

Vousdoukas, M. I., Velegrakis, A. F., and Plomaritis, T. A. (2009). Beachrock occurrence, characteristics, formation mechanisms and impacts. *Earth Sci. Rev.* 85, 23–46. doi: 10.1016/j.earscirev.2007.07.002

Webb, A. P., and Kench, P. S. (2010). The dynamic response of reef islands to sea-level rise: evidence from multi-decadal analysis of island change in the Central Pacific. *Glob. Planet. Change* 72, 234–246. doi: 10.1016/j.gloplacha.2010.05.003

Woodroffe, C., McLean, R., Smithers, S., and Lawson, E. (1999). Atoll reef-island formation and response to sea-level change: West Island, Cocos (Keeling) Islands. *Mar. Geol.* 160, 85–104. doi: 10.1016/S0025-3227(99)00009-2

Woodroffe, C. D. (2008). Reef-island topography and the vulnerability of atolls to sea-level rise. *Glob. Planet. Change* 62, 77–96. doi: 10.1016/j.gloplacha.2007.11.001

Yates, M. L., Le Cozannet, G., Garcin, M., Salaï, E., and Walker, P. (2013). Multidecadal Atoll Shoreline change on Manihi and Manuae, French Polynesia. *J. Coast. Res.* 289, 870–882. doi: 10.2112/JCOASTRES-D-12-00129.1

Conflict of Interest Statement: The authors declare that the research was conducted in the absence of any commercial or financial relationships that could be construed as a potential conflict of interest.

frontiers in Earth Science

ORIGINAL RESEARCH
published: 14 May 2019
doi: 10.3389/feart.2019.00103

Shoreline Dynamics Along a Developed River Mouth Barrier Island: Multi-Decadal Cycles of Erosion and Event-Driven Mitigation

Christopher J. Hein[1], Andrew R. Fallon[1], Peter Rosen[2], Porter Hoagland[3], Ioannis Y. Georgiou[4], Duncan M. FitzGerald[5], Michael Morris[6], Sarah Baker[7,8], George B. Marino[7,9] and Gregory Fitzsimons[10]*

[1] Department of Physical Sciences, Virginia Institute of Marine Science, William & Mary, Williamsburg, VA, United States, [2] College of Science, Northeastern University, Boston, MA, United States, [3] Marine Policy Center, Woods Hole Oceanographic Institution, Falmouth, MA, United States, [4] Department of Earth and Environmental Sciences, The University of New Orleans, New Orleans, LA, United States, [5] Department of Earth & Environment, Boston University, Boston, MA, United States, [6] Storm Surge: The Merrimack Valley Coastal Adaptation Workgroup, Newburyport, MA, United States, [7] Department of Geology, William & Mary, Williamsburg, VA, United States, [8] Department of Earth and Ocean Sciences, University of North Carolina Wilmington, Wilmington, NC, United States, [9] Department of Geography, University of South Carolina, Columbia, SC, United States, [10] Graduate School of Education, University of Massachusetts Lowell, Lowell, MA, United States

OPEN ACCESS

Edited by:
Clara Armaroli, University of Ferrara, Italy

Reviewed by:
Edward Anthony, Aix-Marseille Université, France
Yann Balouin, Bureau de Recherches Géologiques et Minières, France

***Correspondence:**
Christopher J. Hein
hein@vims.edu

Specialty section:
This article was submitted to Interdisciplinary Climate Studies, a section of the journal Frontiers in Earth Science

Received: *15 January 2019*
Accepted: *24 April 2019*
Published: *14 May 2019*

Citation:
Hein CJ, Fallon AR, Rosen P, Hoagland P, Georgiou IY, FitzGerald DM, Morris M, Baker S, Marino GB and Fitzsimons G (2019) Shoreline Dynamics Along a Developed River Mouth Barrier Island: Multi-Decadal Cycles of Erosion and Event-Driven Mitigation. Front. Earth Sci. 7:103. doi: 10.3389/feart.2019.00103

Human modifications in response to erosion have altered the natural transport of sediment to and across the coastal zone, thereby potentially exacerbating the impacts of future erosive events. Using a combination of historical shoreline-change mapping, sediment sampling, three-dimensional beach surveys, and hydrodynamic modeling of nearshore and inlet processes, this study explored the feedbacks between periodic coastal erosion patterns and associated mitigation responses, focusing on the open-ocean and inner-inlet beaches of Plum Island and the Merrimack River Inlet, Massachusetts, United States. Installation of river-mouth jetties in the early 20th century stabilized the inlet, allowing residential development in northern Plum Island, but triggering successive, multi-decadal cycles of alternating beach erosion and accretion along the inner-inlet and oceanfront beaches. At a finer spatial scale, the formation and southerly migration of an erosion "hotspot" (a setback of the high-water line by ∼100 m) occurs regularly (every 25–40 years) in response to the refraction of northeast storm waves around the ebb-tidal delta. Growth of the delta progressively shifts the focus of storm wave energy further down-shore, replenishing updrift segments with sand through the detachment, landward migration, and shoreline-welding of swash bars. Monitoring recent hotspot migration (2008–2014) demonstrates erosion (>30,000 m^3 of sand) along a 350-m section of beach in 6 months, followed by recovery, as the hotspot migrated further south. In response to these erosion cycles, local residents and governmental agencies attempted to protect shorefront properties with a variety of soft and hard structures. The latter have provided protection to some homes, but enhanced erosion elsewhere. Although the local community is in broad agreement about the need to plan for long-term coastal changes associated with sea-level rise and increased storminess, real-time responses have involved reactions mainly to short-term

(<5 years) erosion threats. A collective consensus for sustainable management of this area is lacking and the development of a longer-term adaptive perspective needed for proper planning has been elusive. With a deepening understanding of multi-decadal coastal dynamics, including a characterization of the relative contributions of both nature and humans, we can be more optimistic that adaptations beyond mere reactions to shoreline change are achievable.

Keywords: tidal-inlet dynamics, beach erosion, coastal adaptation, developed beach, shoreline change

INTRODUCTION

Developed beaches exist in a dynamic, coupled state, impacted by natural forcings (e.g., waves, tides, and storms) acting upon sedimentary landscapes that reflect the legacy of millennia of climate change and hundreds of years of local and distant human alterations (**Figure 1**). For example, the delivery of river-derived sediment to the coast has been altered by land-use/land-cover changes, sediment quarrying and mining, embankment installation, land reclamation and river engineering, and damming (e.g., Wang et al., 2007; Milliman and Farnsworth, 2011; Yang et al., 2011; Frings et al., 2015). Coupled with long-term impacts from accelerating sea-level rise (Nerem et al., 2018), updrift shoreline hardening, and storms which are likely increasing in both frequency and intensity (Donnelly et al., 2015), human alterations have caused widespread beach erosion and land loss (e.g., Inman and Jenkins, 1984; Jiménez and Sánchez-Arcilla, 1993; Van Rijn, 2011; El Mrini et al., 2012; Houston and Dean, 2015). Along beaches where development has encroached upon backbarrier or ocean-front shores, this erosion is responsible for *ca.* $500 million per year in property losses (land losses and structure damages) in the United States alone (The Heinz Center, 2000; NOAA Office of Ocean and Coastal Resource Management, 2013).

When natural processes place human populations and infrastructure at risk, the traditional response is to try to mitigate damages to property and communities. Coastal communities may be forced to respond to erosional conditions triggered by global-scale climate change either by *reacting* in the short-term or by *adapting* in the long-term. Short-term reactions have occurred typically at timescales of years to decades, involving the emplacement of artificial hard-protection structures [jetties, groins, sea walls, bluff-stabilization measures, breakwaters, etc.; see Pilkey and Wright (1988), French (2001), and Taylor et al. (2004) for discussion of engineering approaches and environmental consequences] and application of soft engineering solutions (beach nourishment, scraping, and draining). In contrast, longer-term adaptation, including possibly a retreat from the coast, often has been seen as a policy of last resort, to be avoided at all cost. Adaptation to a changing coastal landscape would involve accepting the loss of infrastructure, proactively moving infrastructure, or encouraging flooding of low-lying areas to promote creation of wetlands and riparian zones as a "natural" defense (Cooper and McKenna, 2008).

In high-density urban areas, the values of human welfare and protected infrastructure typically outweigh the costs of emplacing hard structures (e.g., New Orleans, Greater New York area; Granja and Carvalho, 2000; Cooper and McKenna, 2008). The same cannot always be said for more vulnerable, but often less economically relevant, coasts situated distal to major urban centers; these nonetheless may be of high ecological value (Armaroli et al., 2012). Unfortunately, a clear understanding of the natural system, including potential changes to ecosystem services, often has been lacking in these decision-making processes (Gowan et al., 2006). As a result, the first option is generally physical intervention, often using some of the same techniques responsible for disrupting natural sedimentation patterns in the first place. These interventions have largely disrupted the natural pathways for redistribution of sediments within the littoral zone (Pilkey and Clayton, 1989; Nordstrom, 2000; Charlier et al., 2005; Defeo et al., 2009), resulting in localized erosion and deposition hotspots, modification of overall beach geomorphology (McLachlan, 1996; Fallon et al., 2015) and increased risk of local flooding (Bernatchez et al., 2011).

Here, we present the results of a case study of beach morphologic change over timescales of months to multiple decades along one such developed and stabilized beach-inlet system: Plum Island and the Merrimack River Inlet, Massachusetts (United States). Using a combination of historical shoreline-change mapping, sedimentology, monthly three-dimensional beach surveys, and hydrodynamic modeling of nearshore and inlet processes, we reconstruct the causes for alternating erosion and accretion along this inlet-beach system, and explore the history of reactionary, and occasionally counter-intuitive, community responses to these changes.

A COUPLED RIVER-MOUTH INLET AND BEACH: PLUM ISLAND, MASSACHUSETTS (UNITED STATES)

Coastal Geologic Setting

Plum Island is a 13-km long, mixed-energy, tide-dominated barrier island located along the formerly glaciated western coast of the Gulf of Maine (**Figure 2**). To the north, the island abuts the Merrimack River, which has a seasonal discharge ranging from 50 m^3/s during late summers to 1,500 m^3/s during spring freshets (Ralston et al., 2010). Behind Plum Island are a number of small estuaries that feed into the Great Marsh and Plum Island Sound (Hein et al., 2012). The mean tidal range near the mouth of the Merrimack River is 2.5 m, reaching a maximum of 4 m during spring tides (Ralston et al., 2010), and in the

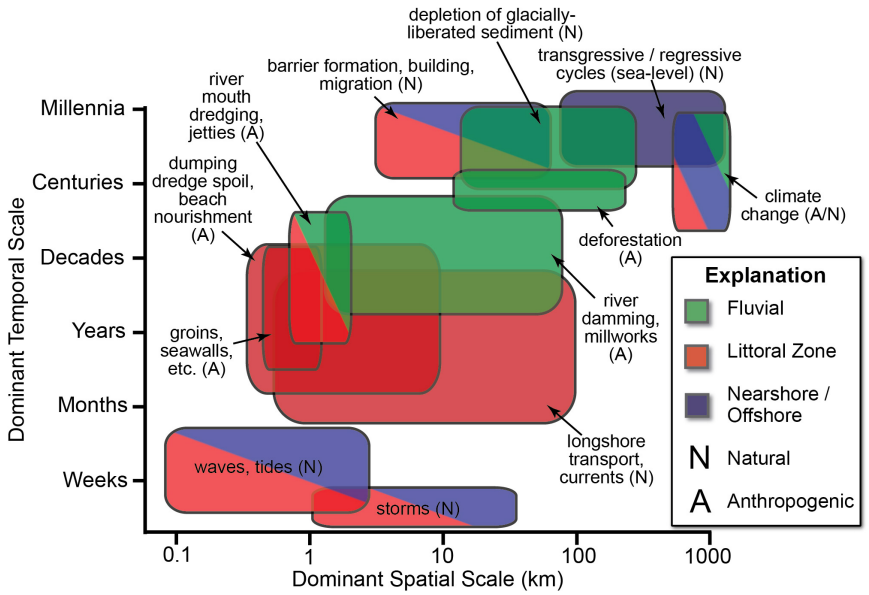

FIGURE 1 | Conceptual model of the natural and anthropogenic factors influencing sediment delivery to and along coastal zones across spatial and temporal scales.

backbarrier, tidal range is attenuated by 10–15% (Zhao et al., 2010). Tidal currents near the mouth of the river and tidal inlet system commonly exceed ∼1 m/s (Ralston et al., 2010). Along the coast, Zhao et al. (2010) reported residual currents nearing 1 m/s directed south around the Merrimack River ebb-tidal delta, which in turn cause a recirculation zone in the nearshore areas of Plum Island. Residual currents in the central portion of the island reach ∼0.3 m/s directed toward the north, and increase to *ca.* 0.5–0.7 m/s in the northern portion of the island, near the Merrimack River mouth. The average significant wave height along this coast is *ca.* 1 m (Abele, 1977) and predominant waves are from the east-southeast (90–180°) during low-energy periods (late spring through summer). However, dominant wave energy is associated with the passage of *ca.* 15–20 extratropical storms (northeast storms, or "nor'easters") during winter and early spring, producing waves from the northeast (0–90°) with offshore wave heights of 4–8 m (Li et al., 2018). A wave analysis for these large storms (Woods Hole Group, 2017) revealed that the highest energy events (42% of total; wave heights of ∼6–8 m) approach from 55–100 azimuth degrees.

Plum Island built from sediment derived from nearshore marine deposits and upstream glacial-fluvial deposits sourced from the Merrimack River, which disgorges through the Merrimack River Inlet at the northern end of the barrier. The geologic evolution of Plum Island was strongly influenced by a complex sea-level history that resulted from the combined forcings of global eustatic sea-level rise and regional glacio- and hydro-isostatic adjustments (Hein et al., 2012, 2014). Plum Island stabilized in its modern position about 3,500–4,000 years ago, following a deceleration of relative sea-level rise to near modern rates, and has since undergone 3,000 years of aggradation, elongation, and progradation within a regime of relative stability (non-migration) (Hein et al., 2012).

Shoreline-Change and Sediment-Transport Patterns

Over centennial timescales, Plum Island remains relatively stable, eroding at the statistically insignificant rate of 0.09 ± 0.60 m yr^{-1} (Executive Office of Energy and Environmental Affairs [EOEEA], 2010; Thieler et al., 2013). This largely reflects the continued input of sand-sized sediment from the Merrimack River (average freshwater discharge = 6.5 km^3 yr^{-1}; Milliman and Farnsworth, 2011). Headed in the White Mountains of New Hampshire (**Figure 2A**), this river drains regions dominated by granitic plutons that have been eroded to quartzose, sandy glacial deposits (FitzGerald et al., 2005; Hein et al., 2014). The Merrimack River empties into a drowned river valley that contains extensive tidal flats composed of sand and mud. Sediment discharge (largely sand and fine gravel) is episodic, dominated by high-discharge events associated with the passage of hurricanes and extratropical storms (Hill et al., 2004) and by spring freshets produced by melting snow accompanying high precipitation events (FitzGerald et al., 2002; Brothers et al., 2008). Ebb-dominated bedforms at the inlet and southeasterly oriented sandwaves on the ebb delta indicate seaward and southerly sand transport. This corroborates sedimentologic evidence of a southerly fining trend across the ebb delta (FitzGerald et al., 1994) and is supported by simulated residual currents within the inlet and around the ebb-delta showing strong currents to the east (∼0.3–0.4 m/s) and south (∼1 m/s), respectively (Zhao et al., 2010).

The southern ∼10 km of Plum Island (**Figure 2B**) is preserved from development as part of the Parker River National Wildlife Refuge (PRNWR; United States Fish and Wildlife Federation) and the Sandy Point State Reservation (Commonwealth of Massachusetts), which together draw nearly 250,000 recreational

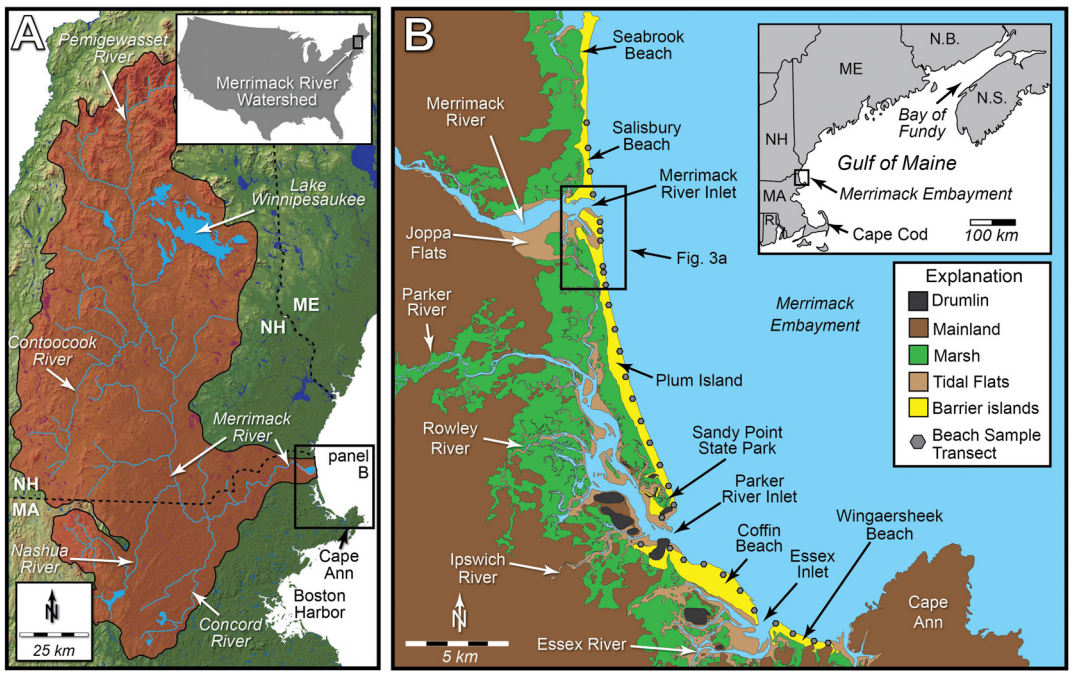

FIGURE 2 | Study area: Plum Island, MA. **(A)** Drainage basin of the Merrimack River, which delivers an average annual bedload (sand) volume of 4.16 × 10^4 m^3/yr to the coast since at least the mid-1900s (Hein et al., 2012). Modified from Hein et al. (2014). **(B)** The mixed-energy, tide-dominated coast of the Merrimack Embayment in northern Massachusetts, United States (western Gulf of Maine), showing locations of beach sediment sampling transects. Modified from Hein et al. (2012).

visitors each year (Sexton et al., 2012). However, over the past century, the northern 3 km of Plum Island—that bordering the Merrimack River Inlet—have been developed extensively with *ca.* 1200 residential properties and >100 roads (Fallon et al., 2017) as parts of the towns of Newburyport (northern half, including the inlet-facing "Reservation Terrace" beach) and Newbury (southern *ca.* 2.3 km of ocean-facing beach) (**Figure 3A**). Historically, the Merrimack River Inlet underwent a series of major ebb-delta breaching events on an approximate centennial timescale in response to the development of a hydraulically inefficient southerly deflection of the main ebb channel caused by a longshore transport driven by dominant northeast storms (Nichols, 1942; FitzGerald, 1993; Watts and Zarillo, 2013; Hein et al., 2016). Sand released from inlet channel-margin linear bars and swash bars during the most recent of these events in the early 1800s migrated onshore, eventually welding to Plum Island. By 1851, the remnant ebb-delta sand shoals formed a narrow, northward-elongating, subaerial, arcuate bar ("New Point"), which has since elongated to the north and prograded, largely in response to artificial stabilization of the inlet mouth, enhancing sediment delivery through a local reversal of longshore transport immediately downdrift of the inlet (FitzGerald, 1993; Hein et al., 2016). Navigation hazards associated with these inlet dynamics prompted the United States Army Corps of Engineers (USACE) to construct two inlet-stabilizing jetties, beginning in 1883 and completed in 1905 (South Jetty) and 1914 (North Jetty). These have required semi-regular maintenance, including 14 times between 1900 and 1938 (United States Army, Corps of Engineers [USACE], 1973) and again in the 1960s and 2013–2014 (Li et al., 2018). The USACE continues to dredge the Merrimack River Inlet on roughly a decadal basis (Plumb, 2010), removing over the last *ca.* 100 years an annual average of 4.16 × 10^4 m^3 of fine sand to fine gravel (Hein et al., 2012).

METHODS

Historical Shoreline-Change Mapping

Following the methodology of Thieler et al. (2013), historical high-water line (HWL) positions were mapped at 1:1000 scale along the northern, developed, ocean-facing 2.9 km of Plum Island for 19 time periods between 1912 and 2018 (**Supplementary Table S1**), and for 22 time periods between 1912 and 2018 along the 1.5 km long inlet-facing beach ("Reservation Terrace"; **Supplementary Table S2**). Historical shorelines (pre-satellite imagery) were derived from digitization of georeferenced NOAA T-sheets. Early T-sheets mark only the drawn boundary of land and water, interpreted as a HWL, but with a higher error than other mapping approaches (Thieler et al., 2013). Two techniques were used to consistently identify the HWL on recent (1970s to present) satellite and georeferenced aerial imagery. First, where possible, the division between dark and light sands on the beach was mapped, indicating the extent of wave run-up during the previous high tide. In the cases where the sand division was either not apparent or the imagery resolution was too poor, the HWL was mapped as the seaward edge of the wrack line.

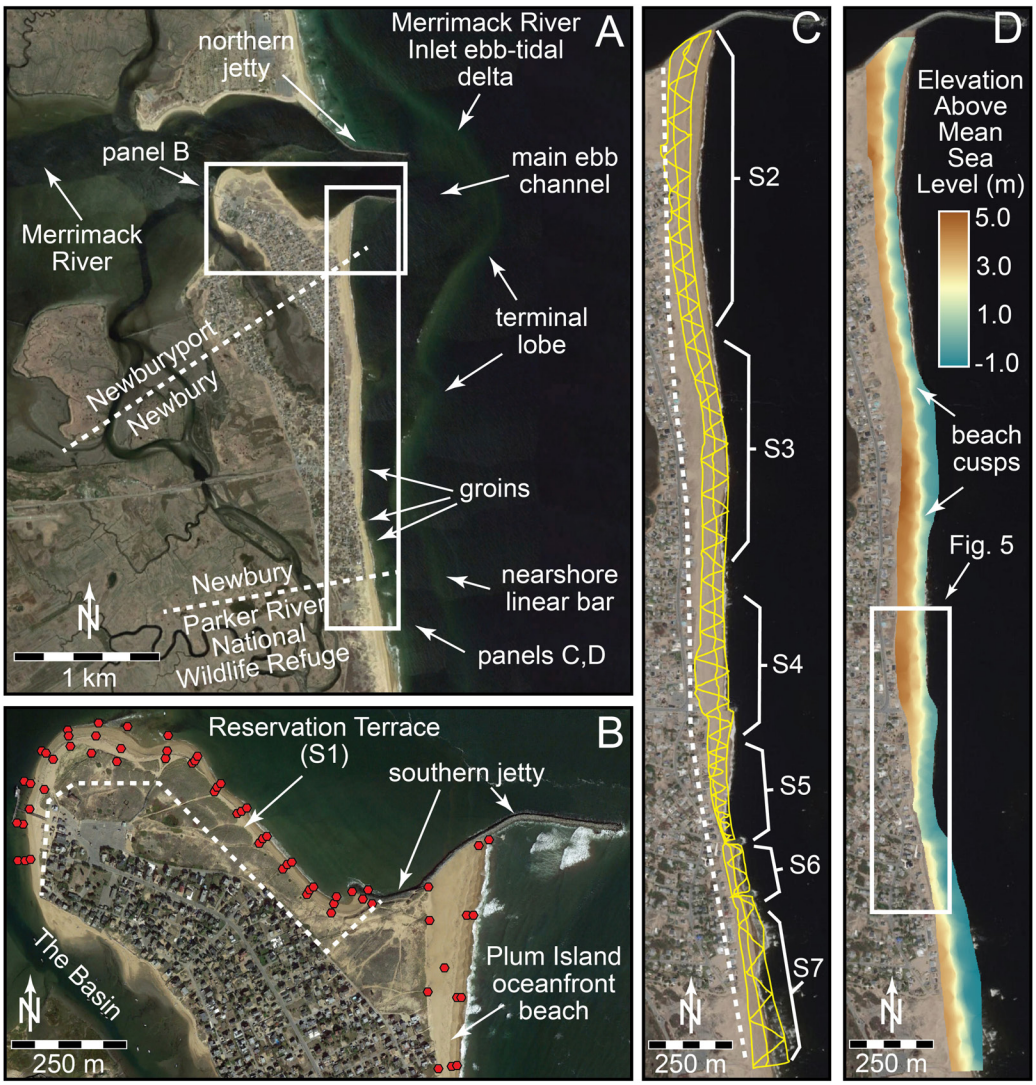

FIGURE 3 | (A) Overview map of northern Plum Island and the Merrimack River Inlet. Background Landsat image: April 27, 2016, from Google Earth™. **(B)** Reservation Terrace, located within the Merrimack River Inlet, west-northwest of the southern jetty. Locations of dune toe, mid-beach, and low-tide-terrace samples are shown as red polygons. Background Landsat image is from October 05, 2016, 3 months following sample collection. **(C)** RTK-GPS transects from May 06, 2014 survey. **(D)** Post-processed, interpolated digital terrain model for May 06, 2014. Background in **(C,D)** is 60 cm resolution 2018 Landsat ArcGIS Basemap imagery. Dashed white lines in **(B,C)** demark landward extent of beach area mapping (**Figure 4C**). Beach sectors (S) shown in **(B,C)** are: (S1) Reservation Terrace; (S2) Right Prong; (S3) Salient; (S4) Center Island; (S5) Annapolis Way; (S6) Fordham Way; and (S7) Refuge.

Along both the northern oceanfront Plum Island beach and Reservation Terrace, we also calculated the beach area between the HWL and a baseline landward of the landward-most mapped historical shorelines (proximal to the seaward extent of development) for each year between 1952 and 2018 (**Figures 3B,C**, **4**). Beach volumes at each time step were then estimated using the United States Army Corps of Engineers guideline that 1 ft^2 (0.93 m^2) of beach area equals 1 yd^3 (0.76 m^3) of sand (**Figure 4C**).

Mapping uncertainties (**Supplementary Tables S1, S2**) are estimated based on mapping resolution, historical uncertainty, and, if applicable, rectification image uncertainty, following the methods of Hapke et al. (2011) and Thieler et al. (2013). These are treated as a compilation for each shoreline, thereby creating a single uncertainty value for each paleo-shoreline position. Horizontal shoreline mapping uncertainty is in a range of 0.5–4.3 m, depending on the source. Notably, even the larger error value is well within the range of horizontal shoreline position change (10 s of meters between mapped years).

Beach Surveys

Short-term shoreline-change analysis was conducted via real-time kinematic geographic positioning system (RTK-GPS) surveys collected monthly between December 2013 and January 2015, and a final survey in March 2015. Continuous horizontal and vertical position data along and across the northern, 2.8 km

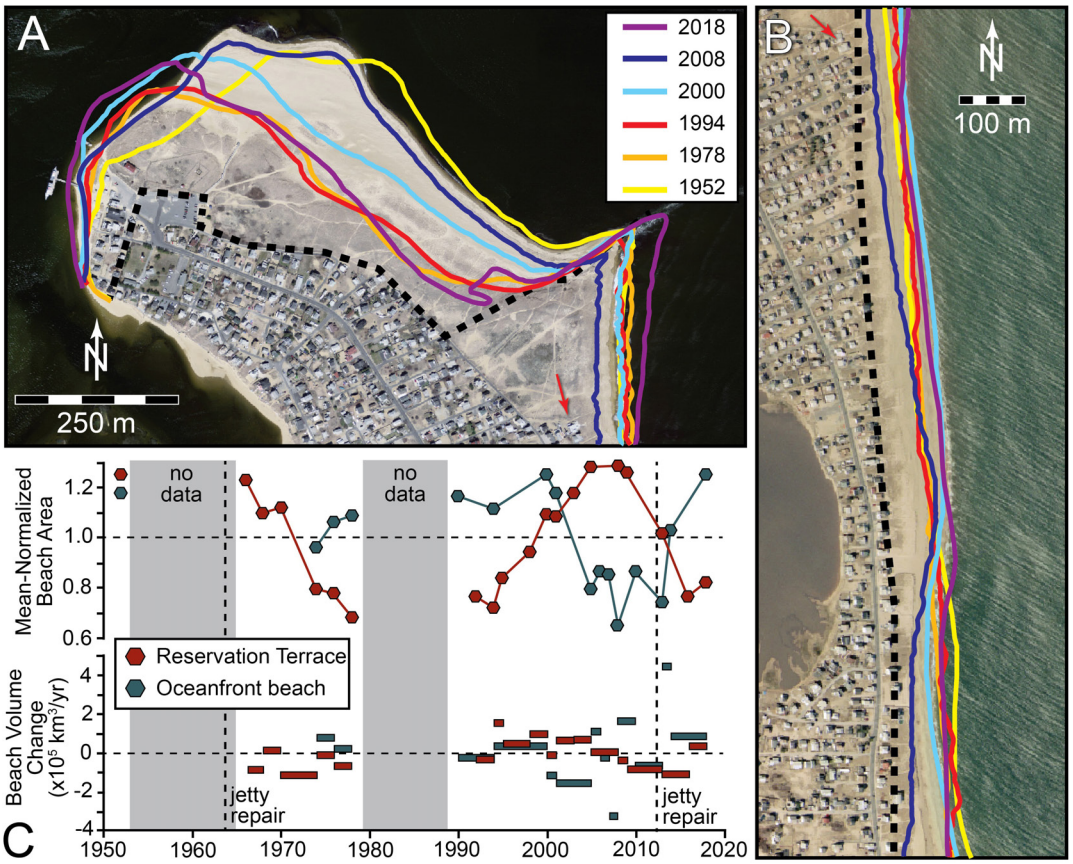

FIGURE 4 | Historical shorelines (1952–2018) along **(A)** Reservation Terrace (S1); and **(B)** the Right Prong (S2), Salient (S3), and northern Center Island (S4) portions of Plum Island beach, overlain on 2008 and 2001 imagery (times of near-maximum beach extent for each region), respectively. Scales of **(A,B)** are the same and red arrow in each points to the same house. Changes in beach area through time (**C**, top) are normalized to long-term mean area of mapped beach extents [dashed black line in **(A,B)**]. Annual beach volume fluxes are calculated following the United States Army Corps of Engineers beach area-volume guideline (1 ft^2 beach area = 1 yd^3 sand).

of ocean-fronting Plum Island beach was collected using a Topcon Hiper II RTK-GPS (**Figure 3C**). Each survey consisted of approximately shore-parallel transects along three primary cross-shore slope knickpoints: dune toe, mid-beach (beach berm, where applicable), and low-tide terrace. These were connected through oblique, crossing tie lines (**Figure 3C**). Survey point spacing was 1 m; each survey consisted of *ca.* 15,000 discrete data points. Resulting RTK-GPS data were post-processed (data reduction, base-station correction) and then interpolated via variogram-based kriging [model based on the spatial autocorrelation between data points to account for directional biases (e.g., seaward-sloping beach face); Stein, 2012] in a GIS framework to develop three-dimensional Digital Terrain Models (DTMs) of the survey area. DTMs from each of the 15 months were used to calculate sediment budgets and analyze hotspot-associated and seasonal variations in beach morphology. All DTMs were clipped to the same spatial extent (0.25 km^2: 2.9 km along shore, 50–150 m cross-shore; **Figure 3D**), equivalent to the maximum common area mapped in all 15 surveys. Beach volumes at each time step were calculated as the difference between the beach elevation surface and a horizontal plane (clipped to same extent) at 1.0 m below mean sea level (lowest mapped elevation of low-tide terrace).

Monthly RTK-GPS data have an average error of 0.028 m horizontally and 0.048 m vertically from sampling. Root mean square errors for DTM-based beach sediment volumes is 0.013–0.021, depending on the survey month, reflecting the density of data collected for each survey and along-shore consistency in beach morphology. DTM sediment volume errors are *ca.*±25,000 m^3, less than 5% of the minimum monthly beach volume (605,000 m^3). Volume changes of <10% (given an assumed maximum beach volume error of ±5%) are considered insignificant and omitted from analysis.

Sediment Sampling

Near-surface sediments were sampled from the northern, developed, oceanfront Plum Island beach monthly along five transects between June 2014 and December 2014, concurrent with beach surveys. These transects were re-occupied during a supplemental August 2015 sampling period, during which additional samples were collected at *ca.* 1 km intervals (27 transects total) along the full length of the ocean-facing Plum

Island beach and from adjacent beaches (Castle Neck, Coffins Beach, Wingaersheek Beach) (**Figure 2B**). A final set of surface samples was collected in July 2016 along 21 transects (spacing: *ca.* 100 m) from Reservation Terrace (**Figure 3B**). Samples (*ca.* 100 g dry sand) were collected from 10 cm below the sediment surface from three stations along each transect: central low-tide terrace, beach berm, and the base of the foredune. Where no berm or other break-in-slope was present, samples were collected from the approximate midpoint between the low tide line and the foredune toe.

Samples were dried, split, and organic debris and shell hash were removed by hand-picking. Textural analysis was conducted using a Rapid Sediment Analyzer (settling tube), which estimates grain-size distributions from −1 to 4 φ in 0.125 φ bins based on Stokes' settling velocities. Grain-size statistics were calculated as per Folk (1968).

Hydrodynamic Modeling

A hydrodynamic model (Delft3D; Lesser et al., 2004), previously developed and validated with deployments in Plum Island Sound, was used to provide time-dependent water level and current velocities in the vicinity of the Merrimack River Inlet. The model resolution varies from *ca.* 2 km offshore, to 20 m in Plum Island Sound. For this effort, we added a higher-resolution nested domain covering the study focus (northern 3 km of Plum Island and along Reservation Terrace) to examine the role of nearshore waves on observed erosional trends. Selected storm wave conditions, derived from analysis of offshore waves, were simulated to evaluate wave transformation over the nearshore bars and in the inlet, and to elucidate mechanisms that contribute to Plum Island and Reservation Terrace erosion.

RESULTS: SHORELINE CHANGE ON NORTHERN PLUM ISLAND FROM MONTHS TO DECADES

Developed portions of Newbury and Newburyport (northern Plum Island) are sub-divided into seven shoreline sectors, from north to south (**Figures 3B,C**): (S1) Reservation Terrace (beach inside the Merrimack River Inlet; 1,100 m); (S2) Right Prong (850 m); (S3) Salient (600 m); (S4) Center Island (450 m); (S5) Annapolis Way (150 m); (S6) Fordham Way (150 m); and (S7) Refuge (300 m).

Multi-Decadal Shoreline Change

Beaches of Reservation Terrace and oceanfront Plum Island have each undergone periods of advance and retreat since the 1960s (**Figure 4**). (Low data density prior to this time does not allow for full analysis of decadal shoreline-change trends). Along Reservation Terrace (**Figure 4A**), the shoreline has migrated such that the undeveloped portion of the Plum Island beach within the Merrimack River Inlet has three times changed in area by a factor of two since the 1960s (**Figure 4C**), such that the shoreline was in nearly identical positions in 1966 and 2005 and in 1976 and 2018. Although we are unable to locate high-quality shoreline data (high-resolution satellite imagery, shoreline position maps, and aerial imagery) for the 1980s, low-resolution satellite imagery available through the Google Earth Engine[1] reveal little shoreline change along Reservation Terrace during this period. Erosion of the northeast-facing, eastern Reservation Terrace beach by up to *ca.* 250 m is commonly associated with the growth of the smaller, northwestern beach by up to *ca.* 150 m. However, erosive periods represent a net volume loss of an estimated 8.0×10^5 m^3 of sand from Reservation Terrace as compared with periods of near-maximum beach area.

Area change along the oceanfront Plum Island beach (**Figure 4B**) is similarly cyclical since the 1950s. During most of this time, it is characterized by a stable (non-migrating) dune fronted by a 50–150 m supratidal beach. Erosion of the beach of up to 120 m has occurred a number of times in the past, including in 1912, 1952, and 1974–1976 (Fallon et al., 2015). Our data best capture this as a widespread erosion event between 2008 and 2014 (**Figure 4C**) when the oceanfront beach volume was reduced by up to $\sim 8.3 \times 10^5$ m^3 from its 1990s long-term mean. Following each period of erosion, this shoreline has returned to a long-term, steady state position, during which periods the beach is generally straight and near its maximum width. In contrast, periods of retreat are rarely uniform along the beach. For example, in 1952, an apparent period of near-maximum beach area (**Figure 4C**), the beach extended up to 150 m from the dune toe (nearly double its 2018 width) near Center Island (S4), but was at its narrowest (*ca.* 60 m narrower than in 2018) along much of the Right Prong (S2) and Refuge (S7) section of beach. Most commonly, retreat takes the form of a southerly migrating erosion "hot spot" (*cf.* Kraus and Galgano, 2001), in which more severe (up to 100 m in width) erosion is focused along a beach length of *ca.* 300–800 m. These are best captured in shoreline data from 1974 to 1978 (**Figure 5A**) and in the more recent 2008–2018 period (**Figure 5B**). In both instances, a section of Center Island (S4) beach 300 m (2008) to 450 m (1974) long retreated by 90–100 m from its pre-erosion HWL position. Over the following 4–5 years, this hotspot migrated *ca.* 600 m south along Annapolis Way (S5), eventually becoming pinned north of the Annapolis Way Groin. During the more severe 2013–2018 erosion period, erosion extended to south of the Fordham Way Groin, the southern-most on the island (**Figure 5B**).

Short-Term Beach Volume Changes

During the course of the 16 months of beach surveys conducted between December 2013 and March 2015, the volume of the oceanfront Plum Island beach within the study area changed by 9.5×10^5 m^3. The largest change occurred during a period marked by the impact of several nor'easters between November and December 2014 when all sectors of the oceanfront beach experienced erosion; this was followed by a near complete recovery during the relatively calm period between December 2014 and January 2015 (**Figure 6A**). Normalizing the volume of each subsection of the beach by the volumetric change of the entire beach for that same time period (**Figure 6B**) allows us to account for changes in beach volume in response to seasonality

[1] https://earthengine.google.com/

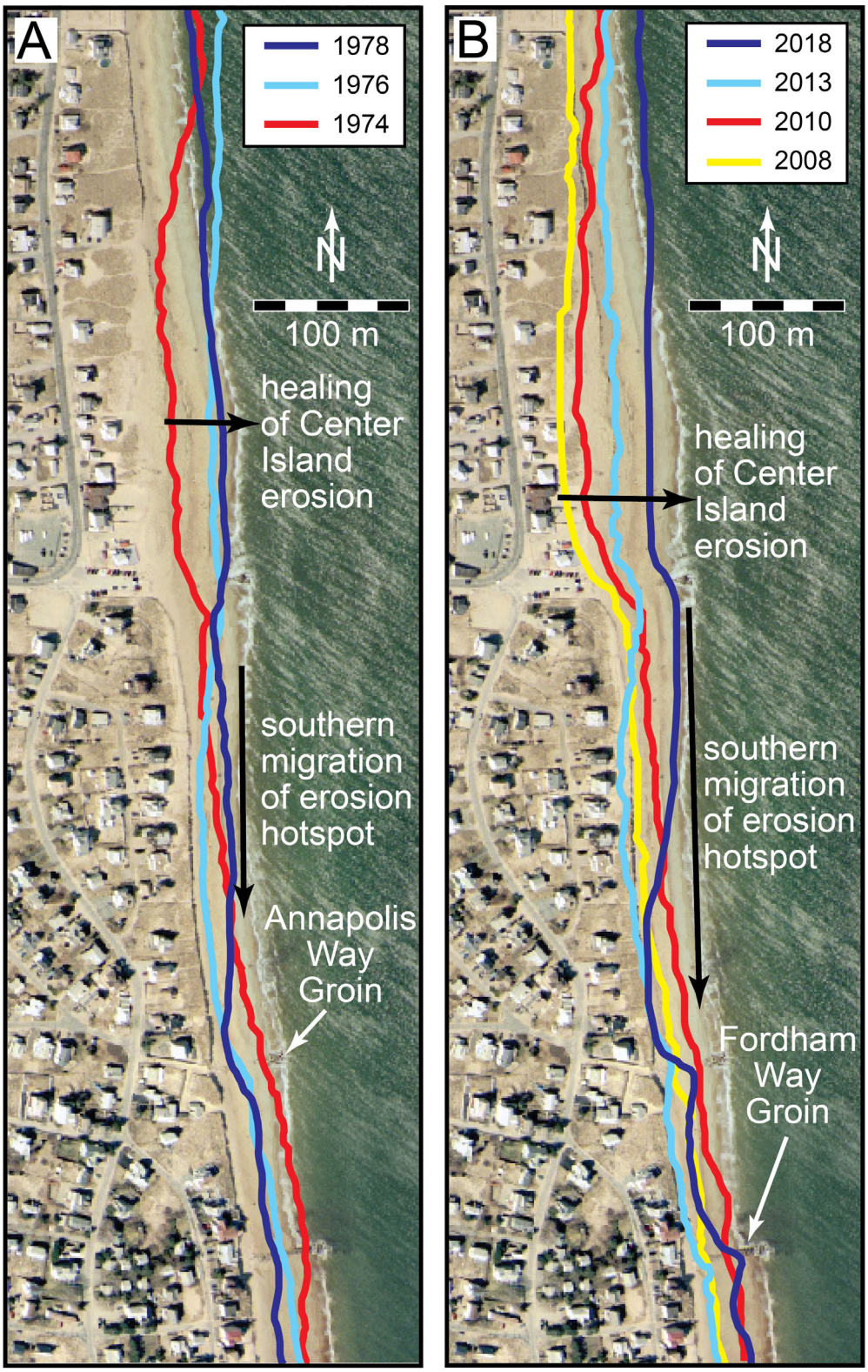

FIGURE 5 | Two phases of erosion hotspot formation and southerly migration along Plum Island beach, as captured in historical high-water shorelines between 1974 and 1978 **(A)** and 2008 and 2018 **(B)**. Background imagery is 2001 color orthophotos from MassGIS (Commonwealth of Massachusetts EOEA).

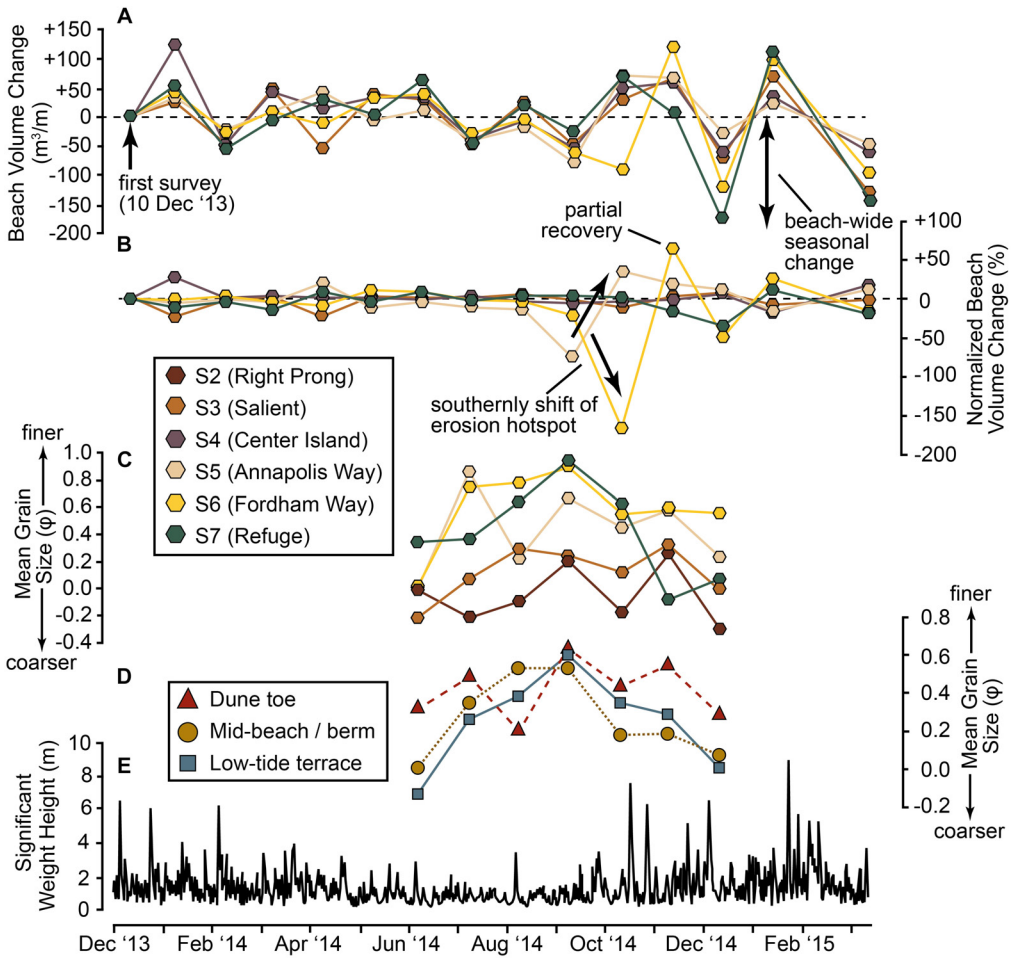

FIGURE 6 | Short-term changes along the northern, ocean-facing Plum Island. **(A)** Monthly change (difference from previous survey) in beach volume per meter alongshore for northern Plum Island sectors S3–S7. **(B)** Monthly percent change (difference from previous survey) in beach volume, normalized by volumetric change across the full northern 2.8 km of Plum Island (sectors S2–S7). **(C)** Average (three sampling stations per transect) monthly mean grain size at each sector. **(D)** Average (for sectors S2, S3, S5–S7) monthly mean grain size at each sampling point along transects. **(E)** Significant wave height data are from Jeffery's Ledge Buoy (NOAA NDBC Station 44098).

and storm impacts (which would be expected to impact the whole beach equally) and examine short-term alongshore trends in erosion and accretion. This reveals that the largest month-to-month changes for the Salient (S3), Center Island (S4), Annapolis Way (S5), Fordham Way (S7), and Refuge (S7) sections are 70 m^3/m (January 2015), 140 m^3/m (January 2014), −75 m^3/m (September 2014), 175 m^3/m (November 2014) and −139 m^3/m (March 2015), respectively. Most notably, between August and September 2014, the beach fronting Annapolis Way (S5) experienced *ca.* 25,500 m^3 (70 m^3/m) of accretion as the Fordham Way beach immediately to the south (S6) simultaneously experienced ca. 12,000 m^3 (87 m^3/m) of net sediment loss (**Figure 6B**). In the months that followed, the beach fronting Annapolis Way continued to grow: between September 2014 and March 2015, *ca.* 30,000 m^3 (82 m^3/m) of sediment accreted along Annapolis Way (**Figure 7**). The beach fronting Fordham Way also grew through deposition of *ca.* 8,000 m^3 (57 m^3/m) of sand during this period, notably along the low-tide terrace, despite the impact of eight storms with wave heights >4 m between September and March surveys (**Figure 7**).

Beach and Dune Sedimentologic Patterns

Mean grain size for dune toe, mid-beach, and low-tide terrace beach samples along each of the 53 sampling transects ranged from 2.11 to −0.46 φ (0.23–1.37 mm), 2.08 to −1.08 φ (0.24–2.11 mm), and 2.22 to −0.09 φ (0.21–1.06 mm), respectively. Nearly all samples show a moderate to high degree of maturity, with insignificant differences between mean and median sizes and sorting values (0.032–0.88) between moderately and very well sorted. Dune samples are, as anticipated, the finest of the three samples taken from along most transects, but beach and low-tide terrace samples become finer than dune sands along Coffins and Wingaersheek beaches (**Figure 8**). A single

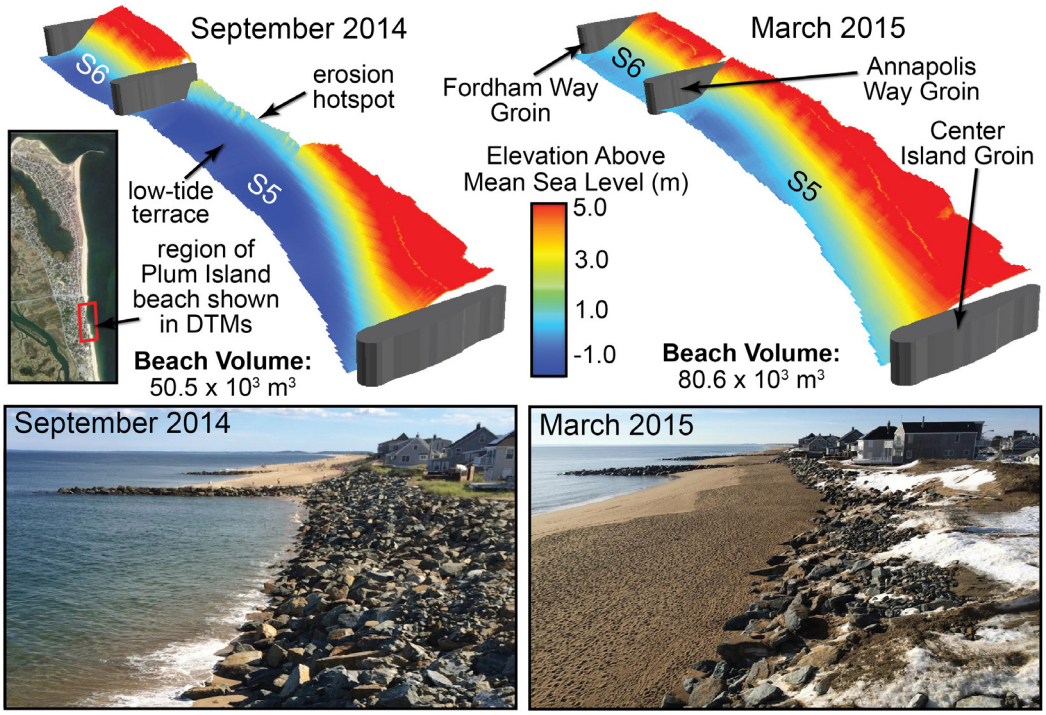

FIGURE 7 | Short-term migration of the erosion "hotspot" to the south along the northern Plum Island beach (see location, **Figure 3D**) in 2014 (approximately same time as shown in **Figure 6**) to 2015. Digital topographic models **(top)** are derived from RTK-GPS surveys (**Figures 3C,D**). Photos **(bottom)** are taken at the same period of the tidal cycle (mid- to high tide) looking south, standing along Annapolis Way beach toward Fordham Way beach.

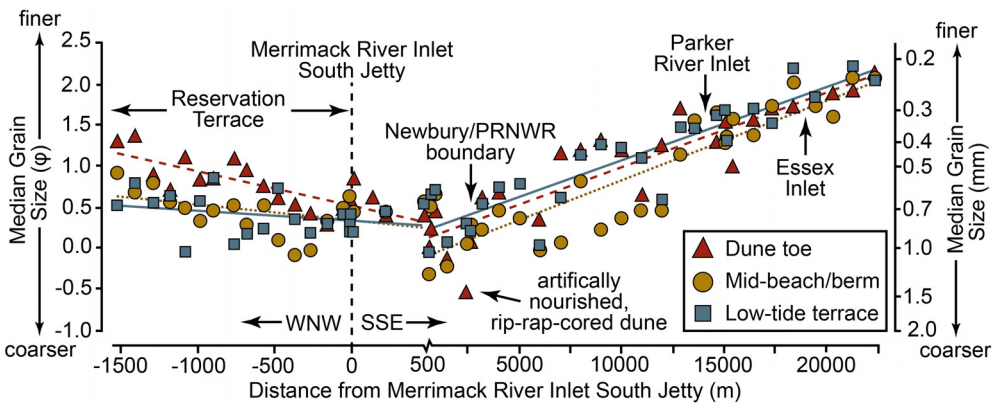

FIGURE 8 | Spatial textural trends in each dune, mid-beach/berm, and low-tide terrace sediment samples collected in August 2015 (south of Merrimack River Inlet) and July 2016 (Reservation Terrace). Note change in axis scale at +500 m.

sample composed of very coarse sand was sampled from the base of an artificially nourished dune along Annapolis Way. The coarsest beach samples are found *ca.* 500 m south of the Merrimack River Inlet South Jetty (within the Right Prong beach [S2]). Dune, beach, and low-tide terrace samples generally fine with increasing distance south of the mouth of this point, and to the west of the Merrimack River Inlet along Reservation Terrace (**Figure 8**). Whereas beach and dune samples gradually fine and show increased maturity (semi-rounded to rounded quartz grains, decreasing rock fragments) to the west along Reservation Terrace beach (S1), low-tide terrace samples are more spatially heterogeneous. In particular, several of the coarsest low-tide terrace samples, collected from the northwest corner of Reservation Terrace, contain abundant coarse (<1 mm diameter) rock fragments, a characteristic not observed along any oceanfront Plum Island samples.

Seasonal variations in grain size were also observed along the northern, developed oceanfront Plum Island beach (S2–S7): sediments fined during the late summer period marked by low wave energy (July to September) and then coarsened between

September and December, notably along the low-tide terrace and mid-beach (**Figures 6C,D**). In particular, a substantial coarsening is observed along all transects coincident with the period of high wave energy and erosion between November and December 2014 sampling periods. All samples in northern Plum Island remained moderately well to very well sorted (sorting: 0.16–0.85) during the entire sampling period.

Hydrodynamic Modeling

Simulations show that wave transformation across the nearshore bars is controlled by the elevation of the bar crest and bar continuity. The distal ebb delta and terminal lobe bar control wave transmission, while the terminal lobe continuity controls wave refraction (**Figure 9A**). Storm waves are attenuated by more than 50–60% over the terminal lobe (**Figure 9A**); the corresponding wave period is reduced by *ca.* 0.5 s. In the vicinity of the low longshore bar crest leading toward the bar gap, wave transmission is higher: here, wave attenuation is <30% and wave period is nearly unchanged (**Figure 9A**). Storm waves with northeasterly and southeasterly approach refract differentially across the bar (**Figures 9B,C**), causing the persistence of large wave-height gradients regardless of the deep-water wave angle (**Figure 9D**). In the vicinity of the hotspot, significant wave height gradients are approximately 0.5 m.

DISCUSSION

Inlet Dynamics and the Shifting Shorelines of Plum Island

Sediment-Transport Dynamics at the Engineered Merrimack River Mouth

Modern bedload sediment delivered to the Merrimack River Inlet from the river itself ranges in size from fine to coarse sand and granules (FitzGerald et al., 2002). Seaward of the inlet jetties, the inlet ebb-tidal delta extends in a southerly direction and is characterized by southerly- and ebb-oriented sandwaves indicative of southerly sediment migration. This corroborates sedimentologic evidence showing a southerly fining trend in grab samples collected across the ebb delta and a general trend of increasing textural and mineralogical maturity to the south, away from the Merrimack River, reflecting winnowing and differential transportation of finer sand grains by wave action (FitzGerald et al., 1994, 2002). Our results confirm the spatial continuity of this trend: beach and dune sand transition from very coarse sand proximal to the inlet to fine sand along the length of the barrier-island chain. Dominant southerly transport is further evidenced by the growth of recurved spits on the downdrift ends of Plum Island (Sandy Point State Park) and Crane Beach (Farrell, 1969) and an increase in the spacing of offshore contours to the south along the chain (Smith, 1991), indicating net deposition along the southern coast of the embayment (Hubbard, 1976; Barnhardt et al., 2009).

Proximal to the Merrimack River Inlet (i.e., along the northern, developed coast of Plum Island), transport patterns are more complex. A combination of prevailing southerly winds and waves and refraction of northeast storm waves around the Merrimack River Inlet ebb-tidal delta creates a seasonally migrating nodal zone, north of which net transport is to the north, toward the inlet (FitzGerald, 1993). Sediment textural trends (**Figure 8**) indicate that the long-term position of this nodal zone is *ca.* 500 m south of the South Jetty, near the center of the Right Prong beach sector (S2). However, sediment accumulation south of the groins (and attendant erosion along the north side), as far south as Annapolis and Fordham ways (S5 and S6; 2,300 m south of the South Jetty), demonstrates the seasonal (or longer) dominance of northerly transport along the Newburyport and northern Newbury beaches.

The South Jetty of the Merrimack River Inlet presents a barrier to northward-migrating sand at the northern end of the Right Prong (S1) beach. This section of beach grew rapidly in the years following jetty construction: erosion in 1912 was the most severe to date along S3–S7, but the beach proximal to the jetty was its widest on record during this time. This section of beach also grew during the period of hotspot erosion along beach sectors S4, S5, and S6 in 1974–1978. However, the primary control on the volume of the Right Prong (S2) beach is the continuity of the South Jetty itself: occasional degradation of this jetty has allowed for the transport of sand over and through the wall, and to Reservation Terrace (**Figure 10**). This sand transport pattern is evident in sediment textural data (**Figure 8**) and in the apparent anti-phasing of beach widths along both Reservation Terrace and the oceanfront beach (**Figure 4**): since the 1960s, beach area along Reservation Terrace changes in unison with, but in the opposite direction of, that of the oceanfront beach. This timing is not coincidental: the South Jetty was twice repaired and rebuilt, once in the mid-1960s and again in 2013–2014. The most recent construction re-built the jetty to its designed height of *ca.* 4.8 m above mean sea level. Repairs in the 1960s was followed within years by rapid (between 1966 and 1978) areal loss of nearly 90,000 m^2 of beach (equivalent sand volume: *ca.* 7.3×10^5 m^3) from Reservation Terrace; in the latter third of this period (1974–1978) alone, the oceanfront Plum Island beach grew by 25,000 m^2 (equivalent sand volume: *ca.* 2.0×10^5 m^3). This trend repeated itself in the 1990s to 2000s as the jetty slowly degraded and Reservation Terrace grew by 91,500 m^2 (equivalent sand volume: *ca.* 7.5×10^5 m^3) as the Plum Island oceanfront beach lost *ca.* 7.3×10^5 m^3 of sand between 1994 and 2008 (**Figure 4**). Following jetty repair, the Right Prong (S2) beach rapidly grew as Reservation Terrace (S1) approached its minimum mapped extent (**Figure 10C**).

This more recent cycle of erosion and accretion along Reservation Terrace and the Plum Island oceanfront beach demonstrates that these beaches are not a simple closed littoral cell in which sand is exchanged between the beaches through ebb-currents within the inlet and wave action along the oceanfront beach. Most importantly, reversal of the recent erosion-accretion cycle (2008–2009) pre-dated jetty repair (2013–2014) by 5 years, possibly reflecting a decrease in the frequency of storms or high-water events capable of delivering sand across the jetty between 2008 and 2013. Additionally, although the volumes of sand lost (gained) from Reservation Terrace and those gained (lost)

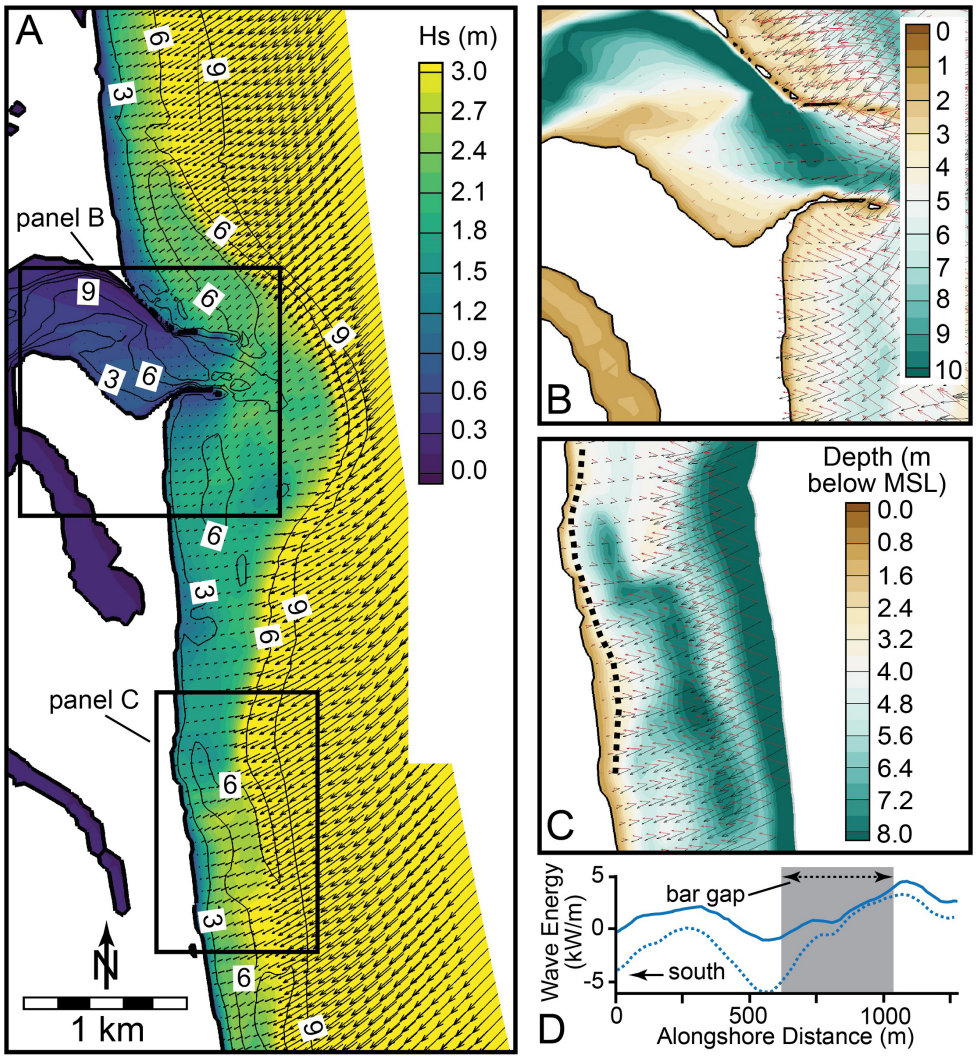

FIGURE 9 | Hydrodynamic model results. **(A)** Significant wave height distribution resulting from a storm wave (H_s ~5 m; T_s ~12 s) approaching from the northeast (*ca.* 45 compass degrees). Vectors show wave energy transport direction (a proxy for sand transport), and solid black lines show depth in meters below mean sea level (MSL). Wave energy transport resulting from two storm wave conditions are shown in the vicinity of the Reservation Terrace **(B)** and the 2008–2018 erosional hotspot **(C)**. For one storm event, waves approach is from the northeast (*ca.* 45 compass degrees; black vectors), and for one they approach from the southeast (*ca.* 135 compass degrees; red vectors). Contours show depth in meters below MSL, and both offshore waves are similar (H_s ~5 m; T_s ~12 s). **(D)** Alongshore variation of wave-energy transport through the erosional hotspot [along transect shown as black dashed line in **(C)**] for each of the two events (NE approach: solid line, SE approach: dashed line).

from the oceanfront Plum Island beach are nearly identical over decadal times (**Figure 4C**), there is no clear evidence that all sand eroded from Plum Island beach is reworked to the north and through the jetty, even during times of disrepair. In fact, textural trends (**Figure 8**) indicate that the long-term oceanfront nodal zone is located only 500 m south of the jetty, and thus the section of beach impacted by northerly long-term transport is restricted to only beach sector S2. Restricting the region of analysis of oceanfront shoreline change to only S2 would decrease the 1994–2008 beach loss volume to *ca.* 3.7×10^5 m^3, or only half of the volume gained along Reservation Terrace during that same time. Nonetheless, there is abundant evidence (e.g., accumulation of sand to the south, and erosion to the north, of Annapolis and Fordham Way groins, as well as the presence in 2008 at the South Jetty of remnants of coir logs originally placed along Center Island) that, at least during periods of hotspot erosion, the nodal point is as much as 2 km down-beach from the South Jetty (see section "Hotspot Migration and the Merrimack Inlet Ebb-Tidal Delta"). Finally, in spite of a clear westward fining trend along Reservation Terrace away from the jetty, the presence of coarse, immature sand along the northern low-tide terrace and mid-beach reveals the occurrence of some exchange of sediment between the Merrimack River and the Reservation Terrace beach. Hence, sediment delivered to Reservation Terrace is not solely derived from the oceanfront beach. The Merrimack River Inlet has also undergone routine dredging throughout both

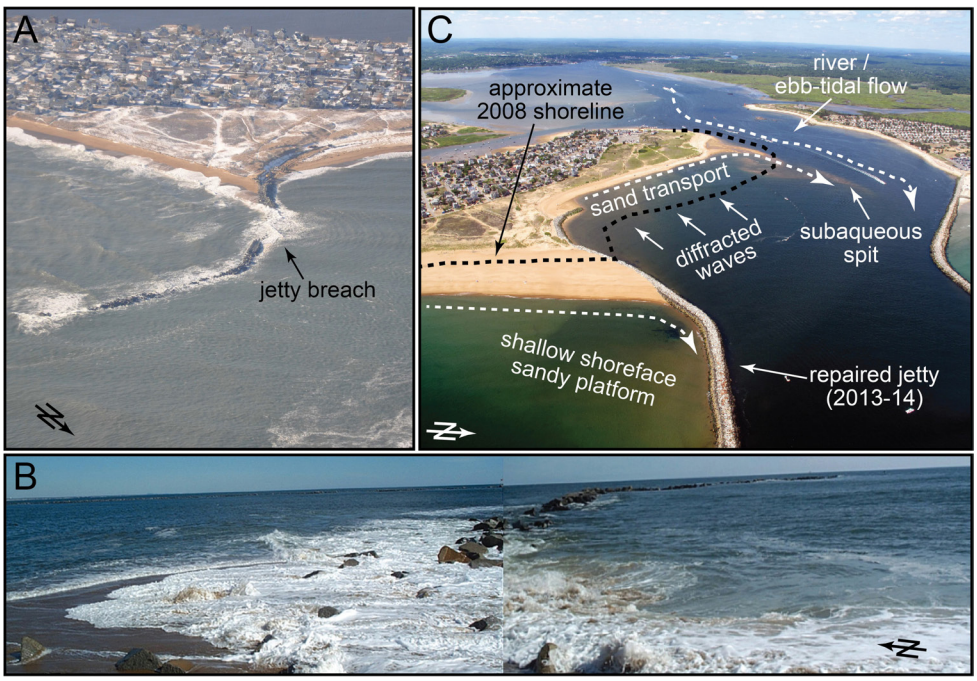

FIGURE 10 | Merrimack River Inlet jetty sediment transport. **(A)** Refracted northeast storm waves propagate through a beach in the South Jetty during high tide (credit: R. Barrett, Plum Island Taxpayer's Association, December 28, 2012). **(B)** Merged panoramic of waves delivering sediment through the breach in the South Jetty to proximal Reservation Terrace (credit: M. Morris, March 06, 2008). **(C)** Aerial view of northern Plum Island following jetty repair showing erosional beach of Reservation Terrace and growth of oceanfront beach south of Merrimack River Inlet South Jetty (credit: P. Rosen, July 27, 2016).

periods, including the removal of 5.4×10^5 m^3 of sediment during the 1960s and 1970s period of erosion along Reservation Terrace. Yet, no such dredging immediately preceded erosion along Reservation Terrace in 2008: the most recent prior river-mouth dredging was the removal of ∼11,000 m^3 of sand in 1999, followed by removal of another ∼11,000 m^3 in 2010, coincident with this period of erosion alone Reservation Terrace (pers. com., 2010, E. O'Donnell, Chief, Navigation Section, USACE New England District).

Thus, at least some portion of shoreline change along Reservation Terrace is in response to conditions unassociated with direct human activities within the Merrimack River Inlet (i.e., jetty degradation and repair). In particular, diffraction and refraction of waves entering the Merrimack River Inlet create turbulent wave conditions in the entrance channel and westerly longshore currents along the northeast-facing Reservation Terrace shoreline (Li et al., 2018). New modeling results (**Figure 9B**) indicate that, regardless of the wave approach, wave angles and thus wave energy—and therefore resulting sediment transport along the Reservation Terrace shoreline—are similar. This suggests that, once the sand is transported over the jetty to the Reservation Terrace beach, waves rework that sand until in equilibrium with the dominant wave approach. This process in combination with strong, river-influenced ebb currents (Li et al., 2018) forms a clockwise sand circulation pattern within the southwestern portion of the inlet. Sand, including sediment originating from the oceanfront Plum Island beach through breaches in the jetty, is transported along Reservation Terrace to the west by waves, aided likely by flood tidal currents. Upon reaching the northwest corner of Reservation Terrace, this sand is then carried by ebb currents to the northeast along the margin of the Merrimack River channel, forming a linear, 300–500 m long, northeast-oriented subaqueous channel-margin spit (**Figure 10C**). This feature persists regardless of the configuration of Reservation Terrace, with its orientation shifting between *ca.* 12 and 42 compass degrees. This sand gyre is corroborated by modeling studies: a 1:75-scale (undistorted) physical model of the Merrimack River Inlet (Curren and Chatham, 1979), bathymetry change analysis (Li et al., 2018) and more recent numerical models that build on the Haas and Hanes (2004) model (Woods Hole Group, 2017) and the Coastal Modeling System (CMS) Flow and Wave models (Li et al., 2018). Changes in offshore wave climate and/or the orientation of the Merrimack River thalweg are likely to alter the magnitude of the transport system and ultimately, the rate in which sand is transferred between the estuary and the Reservation Terrace beach. These are likely to be partly responsible for observed changes in the width and volume of Reservation Terrace.

Hotspot Migration and the Merrimack Inlet Ebb-Tidal Delta

In addition to long-term changes in beach volume associated with sediment exchange with Reservation Terrace, the northern-most, inlet-proximal 3 km of the Plum Island oceanfront beach is characterized by shorter-term periods of formation and longshore migration of a 300–800 m long, 80–100 m wide,

erosion hotspot. This hotspot was observed in the 1950s, 1974–1976, and 2008–2018 (**Figure 11**) and forms with an apparent cyclicity of *ca.* 25–40 years (Fallon et al., 2015). Southerly migration of the hotspot occurs as a threshold process: the hotspot will be situated for several years immediately north of Center Island Groin (e.g., **Figure 11B**) and then, following a period of partial beach recovery (commonly associated with low wave energy), it will shift south by several hundred meters during one or more high-energy events, becoming pinned north of Annapolis Way Groin (**Figure 11D**). This process later repeats as the hotspot shifts to front Fordham Way and the groin at its southern end (**Figure 11F**). Here, we demonstrate that this hotspot forms and migrates along the beach in response to morphologic changes and sediment transport patterns of Merrimack River Inlet and its associated ebb-tidal delta (**Figure 12**).

We observed a longshore shift in the erosion hotspot along Annapolis and Fordham ways during the latter half of our beach surveys (**Figures 6B**, **7**). In September 2014, the beach volume along Annapolis Way (S5), which had been artificially armored with rip-rap in 2013, was at the minimum observed throughout the study period. No beach sand was present above the mid-tide line. By late October 2014, this section of beach had grown by nearly 26,000 m^3, the HWL had prograded 20 m seaward of the revetment, and a new beach berm and dune toe had formed. At the same time, the

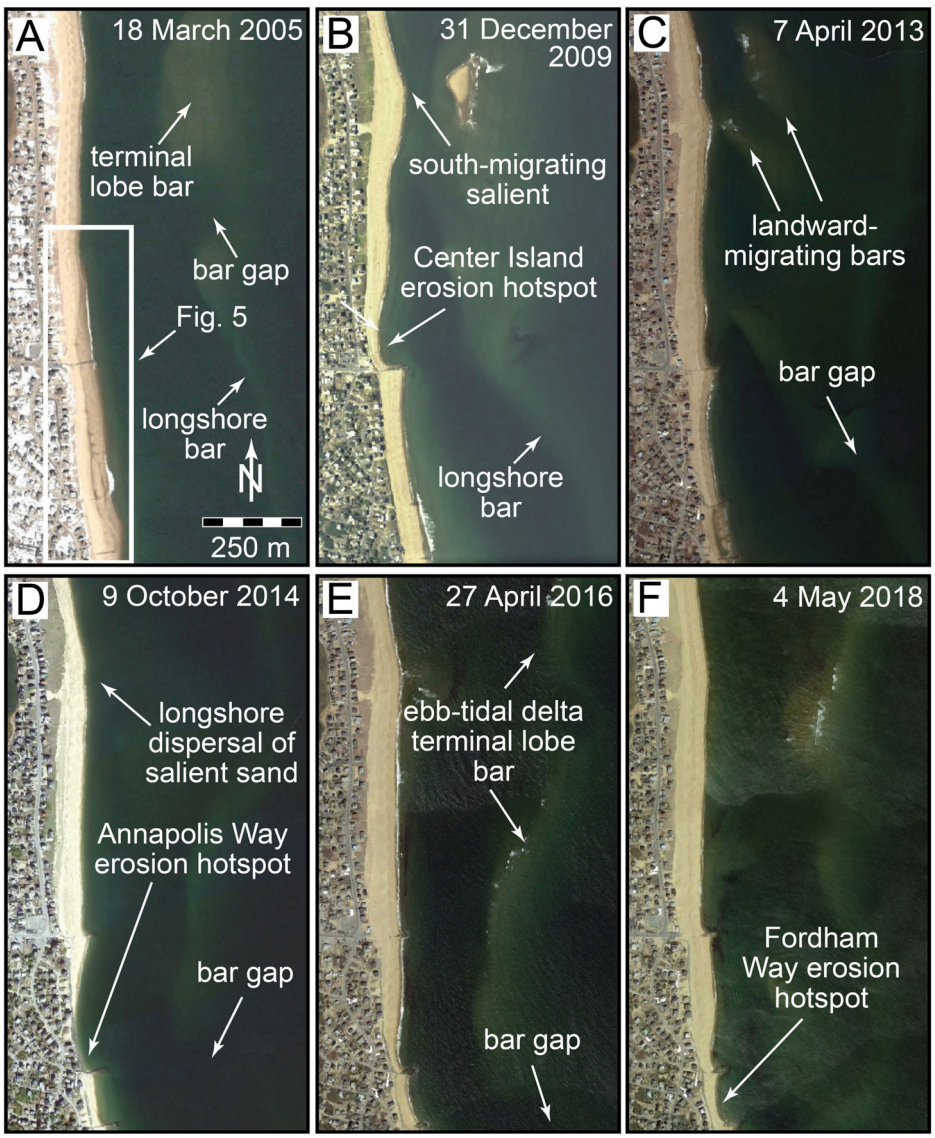

FIGURE 11 | Formation and long-term migration of the Plum Island erosion hotspot along Center Island and Annapolis Way between 2005 **(A)** and 2018. This current phase of erosion initiated north of the Center Island Groin in 2007, and was followed by gradual southerly migration of the erosion hotspot to north of the Annapolis Way Groin between 2009 **(B)** and 2014 **(C,D)** and then between the Annapolis Way and Fordham Way groins between 2014 and 2018 **(D–F)**. All imagery from Google, TerraMetrics except: **(A)** MassGIS (Commonwealth of Massachusetts EOEA) and **(B)** USDA Farm Service Agency.

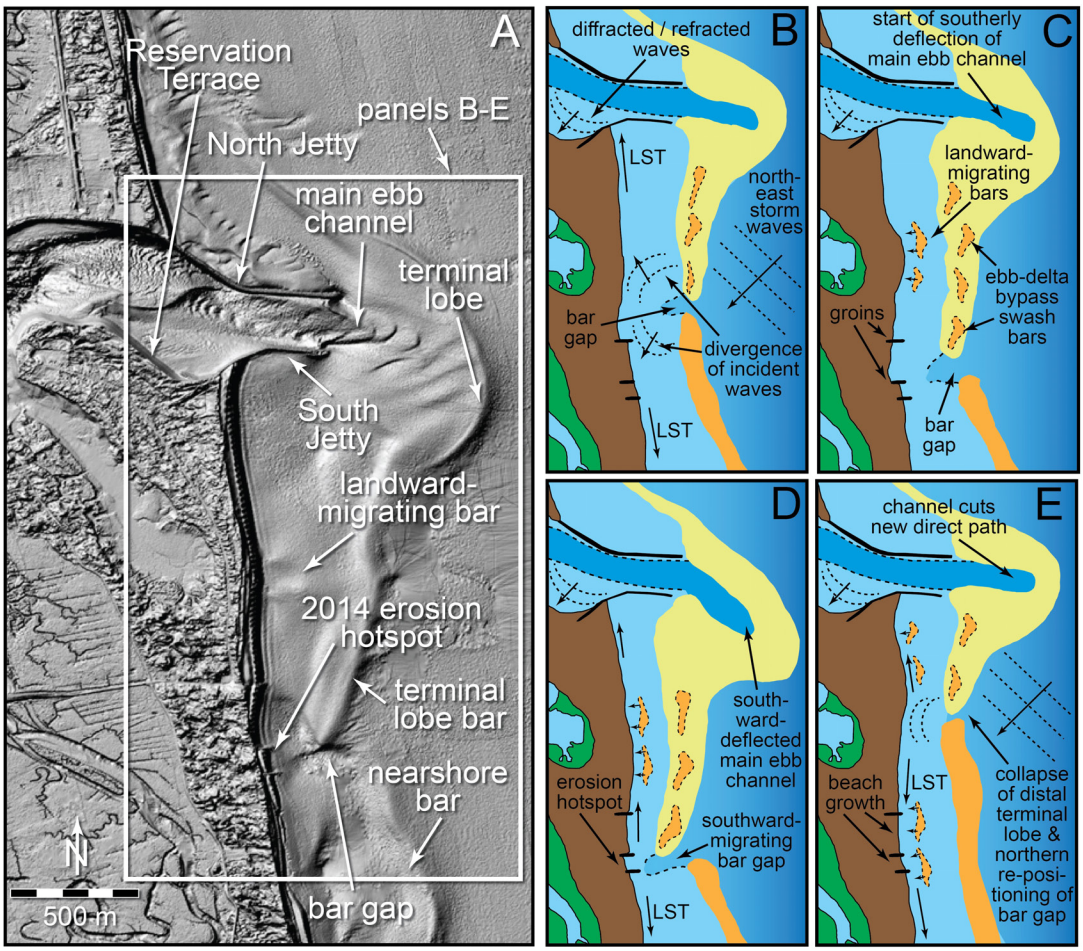

FIGURE 12 | Conceptual model of hotspot formation, growth, and downdrift migration along Plum Island oceanfront beach. **(A)** Hillshaded and interpolated 2014 LiDAR data of northern Plum Island (data source: United States Army, Corps of Engineers [USACE], 2014) highlighting primary features shown in conceptual model; image corresponds (approximate) with panel **(C)**. Note that morphologies shown in **(B–E)** are based on **(A)** and imagery in **Figure 10**, but are diagrammatic in nature, with less visible changes (e.g., migration of main ebb channel) exaggerated. Data shown in **(A)** was used for hydrodynamic model (**Figure 9**) grid.

Fordham Way Beach (S6) had lost *ca.* 12,000 m^3 of sand. Although the entirety of the oceanfront beach grew during this period (**Figure 6A**), Annapolis Way (S5) beach gained nearly 50% more sand with respect to the overall beach-sector volume than the oceanfront beach as a whole (**Figure 6B**). Several months later (November to December 2014), the Refuge section of the beach (S7) experienced its largest relative sand loss (~82,000 m^3) during the study period, and Fordham Way experienced its second largest relative loss; these both preferentially recovered in December 2014 to January 2015. From these observations, an overall pattern emerges of localized ("hotspot") erosion imprinted upon seasonal to sub-seasonal beach morphologic changes. At any given time during its *ca.* 5–10 years cycle of growth and migration, this hotspot may be more or less severe than at other times (**Figures 8**, **11**), but during periods when the beach is at its narrowest [generally following high-energy or high-water (extreme high tides such as occurred in August 2014) events], the 300–800 m long hotspot becomes most apparent.

The eastern-most portion of the terminal lobe of the Merrimack River Inlet ebb-tidal delta is >12 m in relief, reaches depths of <3 m, is situated nearly 450 m south of the South Jetty, and extends >2 km alongshore (**Figures 3A**, **12A**). It becomes closer to the shoreline to the south, from >450 m along the Right Prong (S2) section of the beach to <200 m near Center Island (S4). The crest of this bar is commonly within 1 m of mean sea level and monthly visual observations coinciding with beach surveys throughout 2014 reveal that the bar was often subaerially exposed at low tide (see also **Figures 11B,F**). Sand is delivered to the Salient section (S3) of Plum Island beach from the ebb-tidal delta through onshore bar migration along this portion of the terminal lobe (**Figures 11B,C**, **12A,C**). The southern end of the terminal lobe bar coincides with a *break-in-the-bar* (*cf.*, Kraus and Galgano, 2001) or *bar gap*, and start of a secondary, low-relief (2–3 m above surrounding seafloor; maximum heights reaching *ca.* 3.5 m below mean sea level) subtidal bar (**Figure 12A**). This feature extends nearly continuously, *ca.* 100–200 m offshore of the low-tide terrace,

along the entire southern 15 km of Plum Island. Water depths at a bar gap, a relatively short (commonly <100 m) cavity between the terminal lobe and nearshore bars (**Figures 11**, **12**), can be several meters greater than over the adjacent bars (over which storm waves will shoal and break). This opening is most likely related to inlet sediment bypassing, a process commonly associated with the formation and landward migration of swash bars, the width and length of which vary with the size of a given inlet and volume of sand that is bypassed (FitzGerald et al., 2000; Kraus, 2000; Ridderinkhof et al., 2016). It is common to have several bars independently migrating onshore, along the ebb-tidal delta swash platform, and along the landward beach. This creates a dynamic downdrift end of the ebb-tidal delta terminal lobe bar, and incomplete welding with the lower-relief subtidal longshore bar. The associated bar gap allows propagation of larger waves onshore, thereby focusing wave energy along the beach immediately landward of the break. Model results (**Figure 9**) demonstrate that, regardless of the offshore wave angle, wave refraction and diffraction through the bar gap promote a divergence of incident waves and promote transport to the north, forming a short-term (during period of hotspot activity) nodal point immediately south of the hotpot. North-directed tidal residual currents (Zhao et al., 2010) promote transport and act to efficiently move sand to the north. If the bar resides in a single location for a long enough period, these mechanisms will starve the onshore beach of sand, resulting in erosion. In contrast, wave shoaling across the terminal lobe nearshore bar (north of the hotspot) and refraction around this bar dissipate energy landward of the bar, allowing for sand deposition, as evidenced by a significant (*ca.* 30–40%) reduction in wave heights along beach segments north of the hotspot (**Figure 9D**). In a fashion similar to a tombolo, the beach accretes in this region. Continued sediment delivery to the northern 1.5–2.5 km of the oceanfront beach by refracted/diffracted waves traveling to the north from the hotspot-associated nodal point allows for accretion proximal to the South Jetty, and for delivery of sand across the jetty to Reservation Terrace.

Satellite imagery over the course of the most recent period of hotspot formation and migration (**Figure 11**) reveals that southerly growth of the ebb-tidal delta progressively shifts toward the southern end of the terminal lobe, and the bar gap. The focus of storm wave energy, and thus the erosion hotspot, migrates further down-shore in response (**Figures 12B–D**). Coincident with this, the salient (focal point for onshore bar migration from the terminal lobe) also shifts south, replenishing up-drift beach segments with sand through the detachment, landward migration, and shoreline-welding of ebb delta-associated swash bars (**Figure 12C**). Eventually, easterly realignment of the main ebb channel to a more hydraulically efficient pathway (**Figure 12E**) through breaching (process of *outer channel shifting*; FitzGerald, 1993; FitzGerald et al., 2000, 2012) reconfigures the terminal lobe and rapidly shifts the bar gap to the north. This process can release large volumes of sand in the form of swash bars, which migrate landward, welding to the beach and contributing sand north and south to the longshore transport system.

This form of hotspot-style erosion associated with inlet outer channel shifting (or larger-scale ebb-delta breaching) is common to many tidal inlets, both jettied and unstructured (**Table 1**). For example, along northern Assateague Island (Maryland, United States), Kraus (2000) documented a *ca.* 40 years cycle of downdrift beach erosion and accretion associated with sand bypassing of the adjacent Ocean City Inlet. By contrast, along the beach downdrift of the Guadiana Estuary (Portugal), erosion and accretion cycles associated with sediment bypassing range from 15 to 25 years (Garel et al., 2014). The jetties at Guadiana Estuary are more than twice the length of those at the Merrimack River Inlet, forcing the Guadiana Inlet ebb tidal delta further offshore, and increasing the length of beach affected by these erosional cycles to more than 3 km (as compared with a maximum of only *ca.* 2.5 km along northern Plum Island). In fact, Fenster and Dolan (1996) demonstrated that inlet processes can dominate shoreline morphology up to nearly 4.5 km downdrift of the tidal inlet, and influence shoreline behavior >10 km from the inlet, at least in wave-dominated settings. Thus, the processes observed along the Plum Island beach are not unique to this site, or even to engineered inlets. However, here they have been met by a series of reactionary responses to short-term erosion associated with a lack of a collective consensus for best management and a longer-term perspective needed for proper planning and adaptation.

A Developed Coast in Peril

Reactionary Erosion Mitigation Along Plum Island's Beaches

The coastal region surrounding Plum Island was first settled by Europeans in the late 17th century, and by the early 1800s the Merrimack River port along the mainland town of Newburyport had become commercially viable (Labaree, 1962). Installation of the Plum Island Turnpike in the early 1800s allowed for access to the island and the development of the Plum Island Hotel, the only permanent structure on Plum Island for nearly a century (Currier, 1896). In the late 19th century, the installation of the 500–700 m long Merrimack River Inlet jetties halted centennial-scale river-mouth migration and ebb-tidal-delta breaching which had previously caused near-complete erosion of the northern 2 km of the island (Hein et al., 2016). The stabilization of the island afforded by these jetties fostered extensive residential development (*ca.* 1200 homes and >100 roads; Fallon et al., 2017), which continues to yield significant benefits to homeowners and vacationers and contributes to local and state tax bases.

In spite of their benefits, the Merrimack River Inlet jetties shifted the inlet ebb-tidal delta seaward into deeper water, initiating the cycle of erosion and accretion along the developed section of Plum Island. This hazard drew the attention of property owners, local governments, and state and federal agencies. In response, a variety of mitigation strategies have been employed to protect private properties (**Figure 13**), but most have found limited success. The first of many beach nourishment projects was conducted in 1953 by the Division of Waterways of the Massachusetts Department of Public Works, through the

TABLE 1 | Examples of shoreline erosion and accretion associated with inlet processes at engineered and unstructured inlets.

Site	Coastal setting	Hard structures	Erosion patterns	Citations
Unstructured inlets				
Sea Island, Georgia (United States)	Tides: 2–3 m; Waves: ~1 m	None	Erosion at proximal end of spit during mature ebb delta; erosion at distal end of inlet during youthful ebb-tidal delta (one channel)	Oertel, 1977
Price Inlet, South Carolina (United States)	Tides: 1.5 m tides; Waves: 1.3 m	None	Short-term accretionary patterns of 4–7 years of ebb-tidal delta breach to onshore welding.	FitzGerald, 1984
Regnéville Inlet, West Cotentin Coast, Normandy (France)	Tides: 11 m avg; Waves: 0.5 m typical, up to 2 m during intense storms	None	Beach erosion associated with migration of swash bars onshore (bar located 400 m offshore results in 80 m of erosion), followed by accretion post-welding	Robin et al., 2009
Northeast New Zealand	Tides: 1.0–2.5 m; Waves: 0.5–1.5 m	Small jetties on two inlets, primarily natural system	Inlets relatively stable due to headland sheltering; only subtle changes to inlet throat; limited downdrift erosion	Hume and Herdendorf, 1992
Structured inlets				
John's Pass, Florida (United States)	Tides: ~0.8 m; Waves: 0.2–0.3 m	2 jetties	lLarge ebb-tidal delta, but largely stable inlet and beach	Wang and Beck, 2012
Blind Pass, Florida (United States)	Tides: ~0.8 m; Waves: 0.2–0.3 m	2 jetties	Inlet migration with downdrift erosion	Wang and Beck, 2012
Murrells, Little River, Charleston Harbor Inlets, South Carolina (United States)	Tides: 1.5 m; Waves: 1.0–1.5 m	2 jetties at each of three sites	Development of ebb-tidal delta at each inlet *ca.* 5 years following jetty construction: formed offshore of pre-jetty locations; cycles of erosion and accretion associated with onshore bar welding at Murrells and Little River inlets	Hansen and Knowles, 1988
Ocean City Inlet, Maryland (United States)	Tides: 0.65 m; Waves: 0.5–1.0 m	2 jetties	Severe downdrift erosion; bypassing and attachment of ebb shoals once every 40+ years	Kraus, 2000
Moriches Inlet, New York (United States)	Tides: ~1 m; Waves: ~1.1–1.3 m	2 jetties: 432 m long each	Multiple arcs of erosion, decreasing in magnitude with distance from inlet	Galgano, 2009
Shinnecock Inlet, New York (United States)	Tides: 0.88 m; Waves: 1–1.6 m	2 jetties	Erosion/accretion of adjacent shoreline dependent on longshore sediment availability and alterations of position of migratory bars and attachment points	Buonaiuto and Bokuniewicz, 2008
Merrimack River Inlet, Massachusetts (United States)	Tides: 2.7 m; Waves: 0.4–1.0 m	2 jetties: 500 and 980 m	Formation and southerly migration of 300–800 m long, 80–100 m wide erosion hotspot every 25–40 years along downdrift beach	This study
Saco Bay, Maine (United States)	Tides: 3.0–3.5 m; Waves: 1.0–1.5 m	2 jetties (1,400 and 1,800 m); 3 km rip-rap revetment along downdrift beach	5–6 km of downdrift beach experiences erosion at 2–3 m/yr	Dickson et al., 2009
Grays Harbor Estuary, Washington (United States)	Tides: 3.0–3.5 m; Waves: 2.1 m	2 jetties: 3,000 and 2,700 m	Accretion of 10–100 m/yr along up- and down- drift beaches for 40 years following jetty construction, followed by erosion (4 m/yr) of downdrift beach; updrift beach continued to accrete at ~10 m/yr	Buijsman et al., 2003
Guadiana Estuary (Portugal)	Tides: 2 m; Waves: ~1 m	2 jetties: one 1,340 m disconnected subaqueous jetty; one 2,040 m subaerial jetty	>3 km of downdrift island impacted by cycles of erosion associated with sediment bypassing	Garel et al., 2014
Texel Inlet (Netherlands)	Tides: 1.4 m; Waves: 1.3 m	stone revetments	Some erosion on the downdrift beach (undeveloped and poorly monitored)	Elias and van der Spek, 2006
Lido Inlet, Northern Adriatic Coast (Italy)	Tides: ~0.6 m; Waves: <0.5 m	2 jetties	Ebb-tidal delta destroyed by jetty construction and not reformed, likely due to dredging activity; accretion along updrift beach at 5–15 m/yr.	Fontolan et al., 2007
Currumbin Creek (Australia)	Tides: 1 m; Waves: up to 8 m	Seawall/groin and jetty	Pre-engineering: 7 years sediment bypassing cycle; Post-structures: minimal bypassing and recirculation in the inlet; little downdrift beach erosion	Castelle et al., 2007

placement of 4.3 × 10^5 m^3 of fine sand (extracted from The Basin; see location **Figure 3**) along a 900 m section of beach. This action was followed by additional nourishments in 1957, 1973, 1987, 1999, and 2010 (Haddad and Pilkey, 1998; Plumb, 2010). Additional soft-stabilization approaches have included emplacement of a 200 m wall of 7,000 sand bags by the Massachusetts National Guard in January of 1976 (these were lost in a storm the following month; Macone, 2008).

More recently, in response to localized erosion at the start of the most recent period of hotspot erosion, the Town of Newbury (with funding from the Commonwealth of Massachusetts) placed "geotubes" (in 2008), hay bales, and large sand-filled, coir (coconut-fiber) rolls (2009–2010) along the dune toe of Center Island (S4) beach (**Figure 13B**). Even though it is only partially effective and likely temporary, as much as 13% of the assessed value of proximate properties can be attributed to this soft-structure (Fallon et al., 2017). At the same time, along Annapolis Way (S5), property owners instituted a controversial (e.g., Executive Office of Energy and Environmental Affairs [EOEEA], 2010) program of periodic beach scraping to create sacrificial dunes in advance of storm impacts (**Figure 13C**). Although these were destroyed by waves within days, a similar approach was undertaken along Reservation Terrace (S1) in 2018 in response to ongoing erosion threats to homes that had been fronted by 200 m of beach as recently as 2008.

More permanent shoreline-stabilization measures have also been instituted, including the installation of short sections of rip-rap seawalls in the late 1970s (later re-exposed by erosion; see **Figure 13A**) and, along Reservation Terrace, the USACE lengthened the South Jetty landward and armored the nearby beach with nearly 6,400 metric tons of stone following the loss of one of a United States Coast Guard building in 1969. At the same time, the City of Newburyport constructed a concrete wall fronting the northern line on homes along much

FIGURE 13 | Examples of erosion and mitigation responses along Plum Island. **(A)** Erosion in 2010 along central Center Island (S4) exposes stabilizing footings for housing structure (deck) (credit: C. Hein, March 23, 2010). **(B)** Sand-filled coir logs placed along dune toe at southern Center Island (S4) (credit: C. Hein, March 23, 2010). **(C)** Beach scraping (building artificial dunes with sand pushed landward from the low-tide terrace and beach berm) in advance of nor'easter (credit: C. Walth, July 11, 2011). **(D)** Construction of rip-rap revetment along Annapolis Way (credit: B. Connors, April 2013). **(E)** View north along Annapolis Way section of Plum Island Beach. Not visible in photo in far distance is a crane repairing the Merrimack River Inlet South Jetty (credit: G. Clifford, December 16, 2013).

of Reservation Terrace. However, the primary and longest-lasting approach has been the construction of rip-rap groins along the oceanfront beach. Between 1954 and 1967, the Commonwealth of Massachusetts constructed a series of seven groins, each 50–75 m long. Of these, the Fordham Way, Annapolis Way, and Center Island groins (**Figure 13**) serve as temporary pinning points for the southerly migrating erosion hotspot. Four other groins, spaced at *ca.* 400 m between the Center Island Groin and the South Jetty, are buried by sand. The USACE, which had earlier advised against emplacement of groins (United States Army, Corps of Engineers [USACE], 1952), recommended that these be extended to at least 300 m in length in order for them to intersect the nearshore bar and more effectively trap sand (United States Army, Corps of Engineers [USACE], 1967); no such modifications were made. These groins serve to "pin" the southerly migrating erosion hotspot, focusing higher wave energy associated with the break-in-bar along a narrower section of the beach, thereby contributing to erosion today.

In response to the most recent phase of hotspot erosion along Annapolis and Fordham ways (S5, S6) in 2013–2014, local homeowners collectively funded the construction of rip-rap revetments along *ca.* 500 m of dune toe fronting 16–18 plots/properties (**Figures 13D,E**). This action challenged rules embodied in the Commonwealth's Wetlands Protection Act (WPA), as implemented through the municipal conservation commissions. In the vicinity of Annapolis and Fordham Ways, those rules classify the beach and foredune as a "coastal dune" resource, thereby barring modifications to the dune, such as the placement of protective structures. While Commonwealth officials have expressed their disapproval over the revetment construction, local homeowners, backed by the Pacific Legal Foundation, which litigates issues that threaten the underpinnings of private property rights, have threatened to go to court should the Commonwealth act to force the removal of the revetment (Graikoski and Hoagland, 2017).

While protecting adjacent properties, the revetment has exacerbated hotspot erosion by enhancing wave scour at its base. As a result, subaerial beach is absent along this stretch of coast during periods of more intense erosion [e.g., December 2013 (**Figure 13E**) to September 2014 (**Figure 7**)]. Additionally, this has removed a sediment source (dune erosion) from the littoral system, and along with a steeper nearshore beach slope, likely enhancing erosion in proximal stretches of the Plum Island beach. A similar scenario is observed along Saco Bay (Maine, United States), where a rip-rap revetment was installed in response erosion at an average rate of 2.5 m/yr along the 5–6 km downdrift of the jettied Saco River mouth. Here, beach armoring led to a reduction in longshore sediment supply, causing rapid erosion at the downdrift end of the revetment, and the need to lengthen the revetment multiple times (Dickson et al., 2009).

Long-Term Mitigation and Adaptation Planning in the Absence of Collective Consensus

Hurricanes are likely to increase in frequency and magnitude (Emanuel, 2013; Kossin et al., 2010, 2014; Knutson et al., 2015), decrease in forward speed (Gutmann et al., 2018; Kossin, 2018), and track further northward along the United States East Coast (Garner et al., 2017) in response to climate change. Although it is unclear whether northeast storms will undergo a similar increase in intensity, it is likely that this overall enhanced storm climate will produce larger storm surges and higher wave conditions. Along Plum Island, these factors, coincident with more frequent flooding associated with an acceleration in sea-level rise (Talke et al., 2018), will increase storm-related beach erosion, dismantlement of coastal structures, and wave overtopping of the South Jetty, likely resulting in enhanced fluxes of sand to Reservation Terrace from the Plum Island oceanfront beach.

The planning for adaptation and mitigation along Plum Island oceanfront and Reservation Terrace beaches to these predicted changes is hampered by the complexity of the timescales and patterns of erosion along these beaches, leading to a lack of any unified understanding, policy, or response to erosion when it does threaten structures. Instead, mitigation has been entirely reactionary in nature, responding to individual storm events, rather than the longer-term trends in beach erosion and accretion associated with sediment fluxes between the Reservation Terrace and oceanfront beaches, and hotspot migration along the southern oceanfront beach. As a result of a confluence of interests and human actions—large public infrastructure expenditures, highly valued real estate, environmental concerns for preserving the barrier beach, and the adherence to public trust doctrine—the Commonwealth, pressured by interest groups, has consistently attempted to attempt to stave off or mitigate coastal change along Plum Island (Gurley, 2015). Only recently has Massachusetts—which does not have a master plan for organized coastal retreat—begun incorporating climate change into the Commonwealth's hazard mitigation and adaptation planning, including through a $2.4 billion bond package in the 2019 budget (Rios, 2018). However, counteracting any state-level initiatives are growing revenues generated from property taxes in the City of Newburyport and Town of Newbury, which have factored significantly into local governmental decision-making in relation to further infrastructure development and beach protection. For example, as recently as 2006 the City of Newburyport, in concert with the Commonwealth Department of Environmental Protection, constructed a city water and sewage project connecting Plum Island with mainland Newburyport, at a cost of *ca.* $25 million (Gurley, 2015). Damage to the sewer system on Plum Island during a series of northeast storms in February 2015 eventually resulted in a $5.5 million settlement to the City for repair (Boute, 2016).

Lacking consensus management at the governmental level, local citizens, commonly with support from local or state governmental officials, have organized several education and planning initiatives. For example, the *Merrimack River Beach Alliance*, co-chaired by a state senator, was formed in 2008 to promote the preservation of Plum Island and Salisbury Beach (located north of the Merrimack River Inlet; see **Figure 1**), largely through soft and hard engineering interventions funded at the state and federal level. More recently, *Storm Surge: The Merrimack Valley Coastal Adaptation Workgroup*, was formed in Spring 2013, largely in response to the controversial

shoreline-hardening along Annapolis and Fordham ways. This organization seeks to encourage, educate, and support local communities to prepare for the impacts of climate change (sea-level rise and storms), with a particular focus on long-term adaptation and retreat planning. Although largely educational, the chair of this group (a co-author of this manuscript) is also leading development of the City of Newburyport's climate adaptation plan in his role as co-chair of the City's Climate Resiliency Committee. Incorporation of plans for managed retreat of shoreline property holders in this local plan, as well as state-level initiatives (e.g., Coastal Erosion Commission Commonwealth of Massachusetts [CEC], 2015), while unpopular with many local residents (Shi and Huang, 2018), mark a major change in attitudes toward human habitation of Plum Island, but one lacking precedent and a clear future. Within the context of Plum Island's unique dynamic coastal environment, these efforts comprise a general approach to the engagement of scientists with stakeholders in the optimistic expectation that a more informed community can debate the merits of the full array of potential adaptive responses, both in the short- and long-term.

CONCLUSION: SUSTAINABLE MANAGEMENT OF AN ENGINEERED RIVER-MOUTH BEACH

More than 200 years of human alteration of the lower Merrimack River and Plum Island beaches have produced a sizable tax base and recreation site for the Town of Newbury, City of Newburyport, and their citizens. However, unintended consequences associated with the same shoreline hardening structures that stabilized the northern 3 km of the island have led to periods of severe erosion, threatening both public and private homes and infrastructure. Both refraction of northeast storm waves around the Merrimack River Inlet ebb-tidal delta and strong southeast swell produce a local reversal of net southerly longshore transport. During these conditions, which can be enhanced at times of spring tides, breaking waves overtop the rock structure, transporting sand across the landward end of the South Jetty, feeding the inner-inlet beach (Reservation Terrace). While this reversal, combined with tidal- and wave- induced currents inside the inlet, can lead to accretion of *ca.* 7.5×10^5 m^3 of sand along the Reservation Terrace beach, it is largely at the expense of the oceanfront beach to the south.

Superimposed on the local transport system are smaller-scale variations in wave energy along the shore, which correspond to shifting configuration of the ebb-delta platform. This process creates southerly migrating erosion hotspots (setback of the high-water line by ∼100 m) that, when active, can focus severe erosion on a small portion of the developed beach, while leaving other areas stable or accretionary. These hotspots can last 5–10 years in an aperiodic pattern, and associated beach volume changes associated can be more than 30% of those measured over multi-decadal cycles along the inner-inlet Reservation Terrace beach.

Variability in the timescales and patterns of beach erosion at Plum Island has contributed to the lack of any unified understanding, policy, or response to erosion when it does threaten structures. The responses have been reactionary and short-term in nature: beginning in the late 1950s and early 1960s, a range of beach structures, including groins and riprap seawalls were constructed as a result of an erosional cycle; many have been lost to erosion since then. Local citizen-led response to the most recent erosional period has been even more controversial, comprising the installation of rip-rap revetments along the dune toe fronting nearly two blocks of homes (including in front of lots where houses previously lost to erosion have been replaced by much larger structures, and a single empty lot from which a house had been moved landward) between 2013 and 2015. This action may have exacerbated beach erosion even while protecting adjacent homes, representing a challenge to the Commonwealth's wetlands protection policies. The two local municipalities, Newbury and Newburyport, benefit significantly from property taxes on highly valued coastal properties, and they face conflicting motivations for responding to the threats of shoreline change (Fallon et al., 2017).

The Plum Island case serves as just one example of how humans have greatly altered sediment transport dynamics along an inlet-associated coastal beach but have failed to develop sustainable strategies to balance the dynamic, interacting natural and human processes that were the consequence. Although communities on Plum Island and surrounding towns now have recognized the need to plan for long-term coastal changes associated with climate change, real-time mitigation continues to be reactive, responding to short-term (<5 years) erosion threats. A collective consensus for best management is lacking, and the development of a longer-term perspective needed for proper planning and adaptation has been elusive. With a deepening understanding of the coastal dynamics on Plum Island, including a characterization of the relative contributions of both nature and humans, we can be more optimistic that adaptations beyond mere reactions to shoreline changes are achievable.

AUTHOR CONTRIBUTIONS

CH, PR, and PH designed the study and obtained the funding. AF, SB, and GM conducted field data collection and laboratory analyses as part of graduate masters (AF) and undergraduate senior (SB and GM) theses at the Virginia Institute of Marine Science and William & Mary, respectively. IG conducted hydrodynamic modeling. DF, MM, and GF provided scientific, local, and historical input. CH drafted the manuscript with contributions from all co-authors.

FUNDING

This work was supported financially by the National Science Foundation (NSF) Coastal SEES program (awards OCE 1325430 and OCE 1325366). PH also received partial support through the NSF Coupled Natural-Human Systems program (award AGS 1518503) and the Northeast Regional Sea Grant and Woods

Hole Sea Grant Programs (NOAA Cooperative Agreement award NA14OAR4170074).

ACKNOWLEDGMENTS

We acknowledge Mr. Bob Connors (Plum Island resident) and Ms. Nancy Pau (Parker River National Wildlife Refuge) for beach access and logistical support. We thank Z. Hughes, J. Connell, C. Shuman, and J. Shawler for field and lab support. This is contribution 3825 of the Virginia Institute of Marine Science.

SUPPLEMENTARY MATERIAL

The Supplementary Material for this article can be found online at: https://www.frontiersin.org/articles/10.3389/feart.2019.00103/full#supplementary-material

REFERENCES

Abele, R. W. Jr. (1977). *Analysis of Short-Term Variations in Beach Morphology (and Concurrent Dynamic Processes) for Summer and Winter Periods, 1971-72, Plum Island, Massachusetts*. Fort Belvoir, VA: U.S. Army, Corps of Engineers, Coastal Engineering Research Center.

Armaroli, C., Ciavola, P., Perini, L., Calabrese, L., Lorito, S., Valentini, A., et al. (2012). Critical storm thresholds for significant morphological changes and damage along the Emilia-Romagna coastline. Italy. *Geomorphology* 143, 34–51. doi: 10.1016/j.geomorph.2011.09.006

Barnhardt, W., Andrews, B., Ackerman, S., Baldwin, W., and Hein, C. (2009). *High Resolution Geologic Mapping of the Inner Continental Shelf: Cape Ann to Salisbury Beach Massachusetts*. Reston, VA: U.S. Department of Interior.

Bernatchez, P., Fraser, C., Lefaivre, D., and Dugas, S. (2011). Integrating anthropogenic factors, geomorphological indicators and local knowledge in the analysis of coastal flooding and erosion hazards. *Ocean Coast. Manage.* 54, 621–632. doi: 10.1016/j.ocecoaman.2011.06.001

Boute, B. J. (2016). *Plum Island Sewer System Failure Settled for $5.5m*. Available at: https://www.bostonglobe.com/metro/2016/09/01/settlement-reached-over-plum-island-sewer-system-failure/0uODn33qF5VcDXPOA1ERJL/story.html. (accessed September 5, 2016)

Brothers, L. L., Belknap, D. F., Kelley, J. T., and Janzen, C. D. (2008). Sediment transport and dispersion in a cool-temperate estuary and embayment, Saco River estuary, Maine, USA. *Mar. Geol.* 251, 183–194. doi: 10.1016/j.margeo.2008.02.004

Buijsman, M. C., Sherwood, C. R., Gibbs, A. E., Gelfenbaum, G., Kaminsky, G. M., Ruggiero, P., et al. (2003). *Regional Sediment Budget of the Columbia River Littoral Cell, USA Analysis of Bathymetric- and Topographic-Volume Change*. Reston, VA: U.S. Department of Interior.

Buonaiuto, F. S. Jr., and Bokuniewicz, H. J. (2008). Hydrodynamic partitioning of a mixed energy tidal inlet. *J. Coastal Res.* 24, 1339–1348. doi: 10.2112/07-0869.1

Castelle, B., Bourget, J., Molnar, N., Strauss, D., Deschamps, S., and Tomlinson, R. (2007). Dynamics of a wave-dominated tidal inlet and influence on adjacent beaches, Currumbin Creek, Gold Coast, Australia. *Coast. Eng.* 54, 77–90. doi: 10.1016/j.coastaleng.2006.08.007

Charlier, R. H., Chaineux, M. C. P., and Morcos, S. (2005). Panorama of the history of coastal protection. *J. Coastal Res.* 21, 79–111. doi: 10.2112/03561.1

Coastal Erosion Commission Commonwealth of Massachusetts [CEC] (2015). *Report of the Coastal Erosion Commission, Volume 1: Findings and Recommendations*. Available at: https://www.mass.gov/files/documents/2016/12/vl/cec-final-report-dec2015-v1.pdf (accessed August 09, 2017).

Cooper, J. A. G., and McKenna, J. (2008). Social justice in coastal erosion management: the temporal and spatial dimensions. *Geoforum* 29, 294–306. doi: 10.1016/j.geoforum.2007.06.007

Curren, C. R., and Chatham, C. E. (1979). *Design for Wave Protection and Erosion Control; Hydraulic Model Investigation*. Vicksburg: USACE Waterways Experiment Station.

Currier, J. J. (1896). *"Ould Newbury": Historical and Biographical Sketches*. Boston: Damrell and Upham.

Defeo, O., McLachlan, A., Schoeman, D. S., Schlacher, T. A., Dugan, J., Jones, A., et al. (2009). Threats to sandy beach ecosystems: a review. *Estuar. Coast. Shelf S.* 81, 1–12. doi: 10.1016/j.ecss.2008.09.022

Dickson, S. M., Slovinsky, P. A., Kelley, J. T., Belknap, D. F., and Brothers, L. L. (2009). "Coastal storms, sediment budgets, and mitigating engineering in Saco Bay," in *Proceedings of the Northeast Geological Society of America Field Trip Guide*, (Reston, VA: U.S. Dept. of the Interior), 16.

Donnelly, J. P., Hawkes, A. D., Lane, P., MacDonald, D., Shuman, B. N., Toomey, M. R., et al. (2015). Climate forcing of unprecedented intense-hurricane activity in the last 2000 years. *Earth's Future* 3, 49–65. doi: 10.1002/2014EF000274

El Mrini, A., Anthony, E. J., Maanan, M., Taaouati, M., and Nachite, D. (2012). Beach-dune degradation in a Mediterranean context of strong development pressures, and the missing integrated management perspective. *Ocean Coast. Manage.* 69, 299–306. doi: 10.1016/j.ocecoaman.2012.08.004

Elias, E. P. L., and van der Spek, A. J. F. (2006). Long-term morphodynamic evolution of Texel Inlet and its ebb-tidal delta (The Netherlands). *Mar. Geol.* 225, 5–21. doi: 10.1016/j.margeo.2005.09.008

Emanuel, K. A. (2013). Downscaling CMIP5 climate models shows increased tropical cyclone activity over the 21st century. *Proc. Natl. Acad. Sci. U.S.A.* 110, 12219–12224. doi: 10.1073/pnas.1301293110

Executive Office of Energy and Environmental Affairs [EOEEA] (2010). *Beach Scraping Report*. Byfield, MA: EOEEA.

Fallon, A. R., Hein, C. J., Rosen, P. S., and Gannon, H. L. (2015). "Cyclical shoreline erosion: the impact of a jettied river mouth on the downdrift barrier island," in *Proceedings of the Coastal Sediments '15*, (San Diego, CA).

Fallon, A. R., Hoagland, P., Jin, D., Phalen, B., Fitzsimons, G., and Hein, C. J. (2017). Adapting without retreating: responses to shoreline change on an inlet-associated coastal beach. *Coast. Manage.* 45, 360–383. doi: 10.1080/08920753.2017.1345607

Farrell, S. C. (1969). "Growth cycle of a small recurved spit, Plum Island, Massachusetts," in *Coastal Environments: Northeastern Massachusetts and New Hampshire*, (Amherst, MA: University of Massachusetts, Geology Department, Field Trip Guidebook 1969), 316–336.

Fenster, M., and Dolan, R. (1996). Assessing the impact of tidal inlets on adjacent barrier island shorelines. *J. Coastal Res.* 12, 294–310.

FitzGerald, D. M. (1984). Interactions between the ebb-tidal delta and landward shoreline: price Inlet, South Carolina. *J. Sediment. Petrol.* 54, 1303–1318.

FitzGerald, D. M. (1993). Origin and stability of tidal inlets in Massachusetts. *Coast. Estuar. Stud.* 44, 1–61. doi: 10.1029/ce044p0001

FitzGerald, D. M., Buynevich, I. V., Fenster, M. S., Kelley, J. T., and Belknap, D. F. (2005). "Coarse grained sediment transport in northern New England Estuaries: a synthesis," in *High Resolution Morphodynamics and Sedimentary Evolution of Estuaries*, eds D. M. FitzGerald and J. Knight (New York, NY: Springer), 195–214.

FitzGerald, D. M., Buynevich, I. V., and Hein, C. J. (2012). "Morphodynamics and facies architecture of tidal inlets and tidal deltas," in *Principles of Tidal Sedimentology*, eds R. A. Davis and R. W. Dalrymple (New York: Springer), 301–333. doi: 10.1007/978-94-007-0123-6_12

FitzGerald, D. M., Buynevich, V. I, Davis, R. A. Jr., and Fenster, M. S. (2002). New England tidal inlets with special reference to riverine-associated inlet systems. *Geomorphology* 48, 179–208. doi: 10.1016/S0169-555X(02)00181-2

FitzGerald, D. M., Kraus, N. C., and Hands, E. B. (2000). *Natural Mechanisms of Sediment Bypassing at Tidal Inlets*. Vicksburg: USACE Research and Development Center.

FitzGerald, D. M., Rosen, P. S., and van Heteren, S. (1994). "New England barriers," in *Geology of Holocene Barrier Island Systems*, ed. R. A. Davis (Berlin: Springer-Verlag), 305–394.

Folk, R. L. (1968). *Petrology of Sedimentary Rocks*. Austin, TX: Hemphill Publishing Company.

Fontolan, G., Pillon, S., Delli Quadri, F., and Bezzi, A. (2007). Sediment storage at tidal inlets in northern Adriatic lagoons: ebb-tidal delta morphodynamics,

conservation and sand use strategies. *Estuar. Coast. Shelf S.* 75, 261–277. doi: 10.1016/j.ecss.2007.02.029

French, P. W. (2001). *Coastal Defences: Processes, Problems and Solutions*. London: Routledge.

Frings, P. J., Clymans, W., Fontorbe, G., Gray, W., Chakrapani, G., Conley, D. J., et al. (2015). Silicate weathering in the Ganges alluvial plain. *Earth Planet. Sci. Lett.* 427, 136–148. doi: 10.1016/j.epsl.2015.06.049

Galgano, F. A. (2009). Beach erosion adjacent to stabilized microtidal inlets. *Middle States Geogr.* 42, 18–32.

Garel, E., Sousa, C., Ferreira, O., and Morales, J. A. (2014). Decadal morphological response of an ebb-tidal delta and down-drift beach to artificial breaching and inlet stabilisation. *Geomorphology* 216, 13–25. doi: 10.1016/j.geomorph.2014.03.031

Garner, A. J., Mann, M. E., Emanuel, K. A., Kopp, R. E., Lin, N., Alley, R. B., et al. (2017). Impact of climate change on New York City's coastal flood hazard: increasing flood heights from the preindustrial to 2300 CE. *Proc. Natl. Acad. Sci. U.S.A.* 114, 11861–11866. doi: 10.1073/pnas.1703568114

Gowan, C., Stephenson, K., and Shabman, L. (2006). The role of ecosystem valuation in environmental decision making: hydropower relicensing and dam removal on the Elwha River. *Ecol. Econ.* 56, 508–523. doi: 10.1016/j.ecolecon.2005.03.018

Graikoski, M., and Hoagland, P. (2017). Comparing policies for encouraging retreat from the Massachusetts coast. *Sea Grant Law Pol. J.* 8:1.

Granja, H. M., and Carvalho, G. S. (2000). Inland beach migration (beach erosion) and coastal zone management: the experience of the north-west coast of Portugal. *Period. Biol.* 201, 413–424.

Gurley, G. (2015). *Plum Island at Risk: CommonWealth*. Available at: http://commonwealthmagazine.org/environment/plum-island-at-risk/ (accessed April 29, 2016)

Gutmann, E. D., Rasmussen, R. M., Liu, C., Ikeda, K., Bruyere, C. L., Done, J. M., et al. (2018). Changes in hurricanes from a 13-yr convection-permitting pseudo–global warming simulation. *J. Clim.* 31, 3643–3657. doi: 10.1175/JCLI-D-17-0391.1

Haas, K. A., and Hanes, D. M. (2004). Process based modeling of total longshore sediment transport. *J. Coast. Res.* 20, 853–861. doi: 10.2112/1551-5036(2004)20%5B853:pbmotl%5D2.0.co;2

Haddad, T. C., and Pilkey, O. H. (1998). Summary of the New England beach nourishment experience (1935-1996). *J. Coast. Res.* 14, 1395–1404.

Hansen, M., and Knowles, S. C. (1988). "Ebb-tidal delta response to jetty construction at three South Carolina inlets," in *Hydrodynamics and Sediment Dynamics of Tidal Inlets*, eds D. G. Aubrey and L. Weishar (New York, NY: Springer), 364–381. doi: 10.1007/978-1-4757-4057-8_20

Hapke, C. J., Himmelstoss, E. A., Kratzmann, M. G., List, J. H., and Thieler, E. R. (2011). *National Assessment of Shoreline Change: Historical Shoreline Change along the New England and Mid-Atlantic Coasts*. Reston, VA: U.S. Department of Interior, 1–66.

Hein, C. J., FitzGerald, D. M., Buynevich, I. V., van Heteren, S., and Kelley, J. T. (2014). Evolution of paraglacial coasts in response to changes in fluvial sediment supply. *Geol. Soc.* 388, 247–280. doi: 10.1144/sp388.15

Hein, C. J., FitzGerald, D. M., Carruthers, E. A., Stone, B. D., Barnhardt, W. A., and Gontz, A. M. (2012). Refining the model of barrier island formation along a paraglacial coast in the Gulf of Maine. *Mar. Geol.* 307–310, 40–57. doi: 10.1016/j.margeo.2012.03.001

Hein, C. J., Fitzsimons, G. G., FitzGerald, D. M., and Fallon, A. R. (2016). Records of migration and ebb-delta breaching at historic and ancient tidal inlets along a river-fed paraglacial barrier island. *J. Coastal Res.* 75, 228–232. doi: 10.2112/SI75-46.1

Hill, H. W., Kelley, J. T., Belknap, D. F., and Dickson, S. M. (2004). The effects of storms and storm-generated currents on sand beaches in Southern Maine, USA. *Mar. Geol.* 210, 149–168. doi: 10.1016/j.margeo.2004.05.008

Houston, J. R., and Dean, R. G. (2015). Erosional impacts of modified inlets, beach encroachment, and beach nourishment on the east coast of Florida. *J. Coastal Res.* 32, 227–240. doi: 10.2112/JCOASTRES-D-15-00105.1

Hubbard, D. K. (1976). "Changes in inlet offset due to stabilization," in *Proceedings of the 15th International Conference on Coastal Engineering*, (Honolulu).

Hume, T. M., and Herdendorf, C. E. (1992). Factors controlling tidal inlet characteristics on low drift coasts. *J. Coastal Res.* 8, 355–375.

Inman, D. L., and Jenkins, S. A. (1984). "The Nile littoral cell and man's impact on the coastal zone of the southeastern Mediterranean," in *Proceedings of the 19th International Conference on Coastal Engineering*, (Houston, TX), 1600–1617.

Jiménez, J. A., and Sánchez-Arcilla, A. (1993). Medium-term coastal response at the Ebro delta. Spain. *Mar. Geol.* 114, 105–118. doi: 10.1016/0025-3227(93)90042-T

Knutson, T. R., Sirutis, J. J., Zhao, M., Tuleya, R. E., Bender, M., Vecchi, G. A., et al. (2015). Global projections of intense tropical cyclone activity for the late twenty-first century from dynamical downscaling of CMIP5/RCP4. 5 scenarios. *J. Clim.* 28, 7203–7224. doi: 10.1175/JCLI-D-15-0129.1

Kossin, J. P. (2018). A global slowdown of tropical-cyclone translation speed. *Nature* 558, 104–108. doi: 10.1038/s41586-018-0158-3

Kossin, J. P., Camargo, S. J., and Sitkowski, M. (2010). Climate modulation of North Atlantic hurricane tracks. *J. Clim.* 23, 3057–3076. doi: 10.1175/2010JCLI3497.1

Kossin, J. P., Emanuel, K. A., and Vecchi, G. A. (2014). The poleward migration of the location of tropical cyclone maximum intensity. *Nature* 509, 349–352. doi: 10.1038/nature13278

Kraus, N. C. (2000). Reservoir model of ebb-tidal shoal evolution and sand bypassing. *J. Waterw. Port Coast.* 126, 305–313. doi: 10.1061/(asce)0733-950x(2000)126:6(305)

Kraus, N. C., and Galgano, F. A. (2001). *Beach Erosional Hot Spots: Types, Causes, and Solutions*. Vicksburg: USACE Research and Development Center.

Labaree, B. W. (1962). *Patriots and Partisans: The Merchants of Newburyport*. Cambridge: Harvard University Press, 1764–1815.

Lesser, G. R., Roelvink, J. A., van Kester, J. A. T. M., and Stelling, G. S. (2004). Development and validation of a three-dimensional morphological model. *Coast. Eng.* 51, 883–915. doi: 10.1016/j.coastaleng.2004.07.014

Li, H., Brown, M., Beck, T., Frey, A., Rosati, J., Habel, M., et al. (2018). *Merrimack Estuary and Newburyport Harbor Sediment Management Studies*. Vicksburg: USACE Research and Development Center.

Macone, J. (2008). *'How Many Times are We Going to Save Something?' Beach Erosion, Regrowth, an Endless Pattern*. Newburyport, MA: The Daily News of Newburyport.

McLachlan, A. (1996). Physical factors in benthic ecology: effects of changing sand particle size on beach fauna. *Mar. Ecol. Prog. Ser.* 131, 205–217. doi: 10.3354/meps131205

Milliman, J. D., and Farnsworth, K. L. (2011). *River Discharge to the Coastal Ocean*. Cambridge: Cambridge University Press.

Nerem, R. S., Beckley, B. D., Fasullo, J. T., Hamlington, B. D., Masters, D., and Mitchum, G. T. (2018). Climate-change–driven accelerated sea-level rise detected in the altimeter era. *Proc. Natl. Acad. Sci. U.S.A.* 115, 2022–2025. doi: 10.1073/pnas.1717312115

Nichols, R. L. (1942). Shoreline changes on Plum Island, Massachusetts. *Am. J. Sci.* 240, 349–355. doi: 10.2475/ajs.240.5.349

NOAA Office of Ocean and Coastal Resource Management (2013). *Beach Nourishment: A Guide for Local Government Officials. National Oceanographic and Atmospheric Administration*. Available at: https://coast.noaa.gov/archived/beachnourishment/html/human/law/index.htm (accessed September 10, 2015).

Nordstrom, K. F. (2000). *Beaches and Dunes on Developed Coasts*. Cambridge: Cambridge University Press.

Oertel, G. F. (1977). Geomorphic cycles in ebb deltas and related patterns of shore erosion and accretion. *J. Sed. Res.* 47, 1121–1131. doi: 10.1306/212F72F2-2B24-11D7-8648000102C1865D

Pilkey, O. H., and Clayton, T. D. (1989). Summary of beach replenishment experience on U.S. East Coast barrier islands. *J. Coastal Res.* 5, 147–158.

Pilkey, O. H., and Wright, H. L. (1988). Seawalls versus beaches. *J. Coastal Res.* 4, 41–64.

Plumb, T. (2010). *Making a Mighty Effort to Hold Back the Hungry Sea*. Boston, MA: Boston Globe.

Ralston, D. K., Geyer, W. R., Lerczak, J. A., and Scully, M. (2010). Turbulent mixing in a strongly forced salt wedge estuary. *J. Geophys. Res.* 115:C12. doi: 10.1029/2009JC006061

Ridderinkhof, W., de Swart, H. E., van der Vegt, M., and Hoekstra, P. (2016). Modeling the growth and migration of sandy shoals on ebb-tidal deltas. *J. Geophys. Res.* 121, 1351–1372. doi: 10.1002/2016JF003823

Rios, S. (2018). *Entrench Or Retreat? That Is the Question On Plum Island*. Available at: https://www.wbur.org/news/2018/08/02/plum-island-climate-change-entrench-retreat (accessed August 3, 2018)

Robin, N., Levoy, F., Monfort, O., and Anthony, E. (2009). Short-term to decadal-scale onshore bar migration and shoreline changes in the vicinity of a megatidal ebb delta. *J. Geophys. Res.* 114, 1–13. doi: 10.1029/2008JF001207

Sexton, N. R., Dietsch, A. M., Don Carlos, A. W., Koontz, L., Solomon, A. N., and Miller, H. M. (2012). *National Wildlife Refuge Visitor Survey 2010/2011: Individual Refuge Results for Parker River National Wildlife Refuge*. Reston, VA: U.S. Department of Interior.

Shi, W., and Huang, J.-C. (2018). Correcting on-site sampling bias: a new method with application to recreation demand analysis. *Land Econ.* 94, 459–474. doi: 10.3368/le.94.3.459

Smith, J. B. (1991). *Morphodynamics and Stratigraphy of Essex River Ebb-Tidal Delta: Massachusetts*. Vicksburg: USACE.

Stein, M. L. (2012). *Interpolation of Spatial Data: Some Theory for Kriging*. New York, NY: Springer Science & Business Media.

Talke, S. A., Kemp, A. C., and Woodruff, J. (2018). Relative sea level, tides, and extreme water levels in Boston Harbor from 1825 to 2018. *J. Geophys. Res.* 123, 3895–3914. doi: 10.1029/2017JC013645

Taylor, J. A., Murdock, A. P., and Pontee, N. I. (2004). A macroscale analysis of coastal steepening around the coast of England and Wales. *Geogr. J.* 170, 179–188. doi: 10.1111/j.0016-7398.2004.00119.x

The Heinz Center (2000). *Evaluation of Erosion Hazards*. Washington, DC: The H. John Heinz Center for Science, Economics and the Environment.

Thieler, R. E., Smith, T. L., Knisel, J. M., and Sampson, D. W. (2013). *Massachusetts Shoreline Change Mapping and Analysis Project, 2013 Update*. Reston, VA: U.S. Department of Interior, 1–16.

United States Army, Corps of Engineers [USACE] (1952). *Office of the Division Engineer, New England Division: Beach Erosion Control Report on Cooperative Study of Plum Island*. Plum Island, MA: USACE.

United States Army, Corps of Engineers [USACE] (1967). *New England Division: Small Beach Erosion Control Project*. Plum Island, MA: USACE.

United States Army, Corps of Engineers [USACE] (1973). *New England Division: Small Beach Erosion Control Project*. Plum Island Beach, MA: USACE.

United States Army, Corps of Engineers [USACE] (2014). *2014 USACE NAE Topobathy Lidar*. Newbury, MA: USACE. Available at: https://inport.nmfs.noaa.gov/inport/item/49777 (accessed July 20, 2015).

Van Rijn, L. C. (2011). Coastal erosion and control. *Ocean Coast. Manag.* 54, 867–887. doi: 10.1016/j.ocecoaman.2011.05.004

Wang, H., Yang, Z., Saito, Y., Liu, J. P., Sun, X., and Wang, Y. (2007). Stepwise decreases of the Huanghe (Yellow River) sediment load (1950-2005): impacts of climate change and human activities. *Glob. Planet. Chang.* 57, 331–354. doi: 10.1016/j.gloplacha.2007.01.003

Wang, P., and Beck, T. M. (2012). Morphodynamics of an anthropogenically altered dual-inlet system: John's Pass and Blind Pass, west-central Florida, USA. *Mar. Geol.* 291, 162–175. doi: 10.1016/j.margeo.2011.06.001

Watts, I. M., and Zarillo, G. A. (2013). "Macroscale geomorphic evolution of an inlet," in *Proceedings of the 7th International Conference on Coastal Dynamics*, (Arcachon), 1881–1892.

Woods Hole Group (2017). *Great marsh Resiliency Project Wave Analysis and Numerical Modeling*. Falmouth: Woods Hole Group.

Yang, S. L., Milliman, J. D., Li, P., and Xu, K. (2011). 50,000 dams later: erosion of the Yangtze River and its delta. *Glob. Planet. Chang.* 75, 14–20. doi: 10.1016/j.gloplacha.2010.09.006

Zhao, L., Chen, C., Vallino, J., Hopkinson, C., Beardsley, R. C., Lin, H., et al. (2010). Wetland-estuarine-shelf interactions in the Plum Island Sound and Merrimack River in the Massachusetts coast. *J. Geophys. Res.* 115:C10. doi: 10.1029/2009JC006085

Conflict of Interest Statement: The authors declare that the research was conducted in the absence of any commercial or financial relationships that could be construed as a potential conflict of interest.

frontiers in Earth Science

ORIGINAL RESEARCH
published: 28 May 2019
doi: 10.3389/feart.2019.00125

The Risk Reduction Benefits of the Mesoamerican Reef in Mexico

Borja G. Reguero[1], Fernando Secaira[2], Alexandra Toimil[3], Mireille Escudero[4], Pedro Díaz-Simal[3], Michael W. Beck[1,2], Rodolfo Silva[4], Curt Storlazzi[5] and Iñigo J. Losada[3]*

[1] Institute of Marine Sciences, University of California, Santa Cruz, Santa Cruz, CA, United States, [2] The Nature Conservancy, Mérida, Mexico, [3] Environmental Hydraulics Institute "IHCantabria", Universidad de Cantabria, Santander, Spain, [4] Instituto de Ingeniería, Universidad Nacional Autónoma de México, Mexico City, Mexico, [5] United States Geological Survey, Pacific Center, Santa Cruz, CA, United States

Coastal development and climate change are dramatically increasing the risks of flooding, erosion, and extreme weather events. Coral reefs and other coastal ecosystems act as natural defenses against coastal hazards, but their degradation increases risk to people and property. Environmental degradation, however, has rarely been quantified as a driver of coastal risk. In Quintana Roo, Mexico, a region on the Mexican Caribbean coast with an annual tourism economy of 10 billion USD, coral reefs constitute a natural barrier against flooding from hurricanes. This study spatially quantifies the risk reduction benefits of the Mesoamerican Reef in Quintana Roo for people, buildings, and hotel infrastructure. The risk reduction benefits are substantial. For example, the reefs prevented 43% additional damage during Hurricane Dean in (2007) and provide nowadays hazard risk reduction for 4.3% of the people, 1.9% of the built capital, and 2.4% of the hotel infrastructure, per year. The annual benefits are estimated in 4,600 people, 42 million USD damage prevention for buildings, and 20.8 million USD for hotel infrastructure. The study also compares the risk reduction of coral reefs with (i) the protection offered by dunes and (ii) the increase in coastal risk from sea-level rise (SLR). The risk reduction of dunes is more critical where there are no coral reefs offshore and for small return-periods storms. Sea-level rise, however, will make the more frequent storms more impactful and will drive significant increases in annual expected damages across the region. However, we demonstrate that, in coral reef environments, the contribution of reef degradation to coastal risk is larger than the expected increase in risk from SLR. However, the spatial distribution of the risk reduction benefits from reefs differs for people and infrastructure, and in particular for hotels, which receive the most protection from reefs. Furthermore, many sections present larger benefits than the typical costs of restoration. This valuation makes a compelling case for protecting and maintaining this natural infrastructure for its risk reduction service, but also allows the development of piloting innovative strategies, such as risk finance and insurance strategies, that can align environmental and risk management goals.

Keywords: coastal risk, coral reefs, flood risk, environmental degradation, sea-level rise, losses and damages

OPEN ACCESS

Edited by:
Christophe Viavattene, Middlesex University, United Kingdom

Reviewed by:
Hyoungsu Park, Oregon State University, United States
Elizabeth Christie, University of Cambridge, United Kingdom

****Correspondence:***
Borja G. Reguero
breguero@ucsc.edu

Specialty section:
This article was submitted to Geohazards and Georisks, a section of the journal Frontiers in Earth Science

Received: *19 February 2019*
Accepted: *09 May 2019*
Published: *28 May 2019*

Citation:
Reguero BG, Secaira F, Toimil A, Escudero M, Díaz-Simal P, Beck MW, Silva R, Storlazzi C and Losada IJ (2019) The Risk Reduction Benefits of the Mesoamerican Reef in Mexico. Front. Earth Sci. 7:125. doi: 10.3389/feart.2019.00125

INTRODUCTION

People and assets in the coastal zones are increasingly exposed to the impact of hazards such as flooding and erosion. The combined effect of demographic concentration in low-elevation coastal zones (Silva et al., 2014; Neumann et al., 2015; Reguero et al., 2015) and the added threats of climate change such as sea-level rise (SLR) (Church et al., 2013) or increasing wave action from a more powerful global wave climate (Reguero et al., 2019) are ever putting coastal areas at an increasing risk. Climate change is a risk multiplier to coastal communities and economies (Hallegatte et al., 2013; Wong et al., 2014; Storlazzi et al., 2018). Addressing current and future coastal risk requires urgent action to mitigate the impacts from coastal hazards and increase the resilience of coastal communities.

Comprehensive risk management involves assessing risk and identifying ways to manage it (i.e., risk avoidance, risk transfer, risk reduction or risk retention). Such approaches aim at building long-term resilience in relation to extreme and slow onset events (UNFCCC, 2013). The Paris Agreement (article 8) reaffirmed the Warsaw International Mechanism for Loss and Damage as the main vehicle to avert, minimize and address loss and damage associated with climate change impacts, including extreme weather events and slow onset events (UNFCCC, 2015). Therefore, comprehensive risk management strategies need to be informed by the attribution of losses and damages to the different drivers of risk so that they can be better linked to strategies and actions and insurance and risk transfer (Briggs et al., 2015; Mechler and Schinko, 2016). However, research has been very limited on how the threats to coastal ecosystems can be linked with the risk of SLR and damaging storms on people and infrastructure. Furthermore, existing approaches currently largely overlook drivers of risk such as environmental degradation, whose contribution to risk, from a loss and damage perspective, is currently unapprised.

It is increasingly recognized that coastal ecosystems represent a natural infrastructure that provides coastal protection. However, their degradation is rarely appraised as an important driver of coastal risk to people and property. Coral reefs, for example, serve as natural, highly efficient submerged breakwaters that provide flood reduction benefits through wave breaking and wave energy attenuation (Lowe et al., 2005; Monismith, 2007; Ferrario et al., 2014). These protective services, however, depend on reef parameters such as depth, width, structural complexity and roughness, which are intimately related to the health of the coral (Harris et al., 2018). Yet, reefs continue degrading all around the world, from increasing temperatures, storm damage and poor management (Bellwood et al., 2004). The widespread loss of reef-building corals leads to loss of architectural complexity and 'reef flattening' (Alvarez-Filip et al., 2009), which affects the capacity of coral reefs for dissipating wave energy (Quataert et al., 2015; Harris et al., 2018) and keeping pace with the rising sea levels (Graham et al., 2015; Perry et al., 2018). Climate change through SLR, higher waves, and coral degradation will further increase wave runup in reef environments (Quataert et al., 2015). These factors jeopardize the substantial global risk reduction services that coastal communities receive from coral reefs at present (Beck et al., 2018).

Mainstreamed coastal policy and management approaches largely do not account for the contribution of environmental reef degradation to coastal risk. It is also broadly unknown whether the magnitude of this contribution relative to other threats such as SLR or the protection offered by other natural defenses, like dunes, which are more generally recognized for their coastal protection service and managed and restored accordingly. Only recently has research started to establish the risk reduction benefits of ecosystems (Narayan et al., 2017; Beck et al., 2018; Menéndez et al., 2018; Reguero et al., 2018b), but their combined effect, e.g., reefs acting with beach and dune systems, have only been assessed in terms of wave attenuation (e.g., Guannel et al., 2016) and not in terms of coastal risk, i.e., probability of socioeconomic losses, which are the metrics directly related to risk management strategies. These factors make it difficult to assess how these natural barriers work together for reducing risk to people and property and how intertwined their services are, while also hampering their consideration in risk management strategies.

This study focuses on the Mesoamerican Reef (MAR hereafter), the largest coral reef barrier in the western hemisphere. Understanding coastal flood risk and evaluating the risk reduction service of the MAR is critical not only for its conservation, but also for coastal risk management. The MAR precedes the eastern coastline of the state of Quintana Roo, Mexico, home to 1.5 million people (INEGI, 2015) and whose tourism sector contributes a 1.34% to Mexico's Gross Domestic Product. In Quintana Roo, uncontrolled and intense coastal development since the 1970s, particularly in Cancun, Cozumel, Isla Mujeres, Playa del Carmen and along the Mayan Riviera (Cancun to Tulum coastal stretch), have altered the natural coastal system and hence the resilience to extreme natural phenomena (Escudero-Castillo et al., 2014a). The area is also exposed to hurricanes and storms that produce recurrent flooding and erosion of settlements and assets on the beach front (Escudero-Castillo et al., 2014a; Mendoza et al., 2015), while anthropogenic interventions and degradation of ecosystems over wide extensions of these coasts have also driven chronic erosion and increased vulnerability to extreme weather events that put the people and the state's economy at risk (Escudero-Castillo et al., 2014a,b, 2018). However, the MAR is increasingly threatened by pollution, storm damage, ocean acidification, rising sea surface temperatures, disease outbreaks and unsustainable management practices (Mcfield et al., 2018). These factors put at risk the structural complexity and roughness of this natural barrier and jeopardize its capacity to dissipate wave energy.

This article addresses these questions and represents an advancement in how to account for the different drivers of coastal risk. The study focuses on assessing (i) how much and (ii) where the MAR prevents hurricane-flood damages to people and infrastructure, or in an equivalent manner, how reef degradation could increase coastal risk. This service is also compared relative to (iii) the protection offered by dunes, which are acknowledged and hence maintained and

restored for their protection service, and (iv) the increased risk from SLR through its contribution to extreme flooding from hurricanes.

MATERIALS AND METHODS

Overview

This study quantifies the coastal flood risk reduction provided by the MAR for people, buildings (or built capital), and hotel infrastructure in Quintana Roo, Mexico. To assess this risk reduction benefits, we followed the expected damage cost avoided approach that estimates the benefits by their avoided flood damages. The main steps are described below and represented in **Figure 1**. Coastal flood risk is defined by the hurricane-induced flood hazard and their damage to people and built infrastructure. The flood hazard is defined from a synthetic generation of storms (∼15,000 storms) based on the historical distribution of hurricanes in the Caribbean. The effect of reefs on flooding is modeled through a numerical model that accounts for the complex transformation of waves in reef environments. The flood damages for each storm are quantified based on the flood heights of each storm and using vulnerability curves that relate the intensity of flooding with the degree of damage to the infrastructure. Risk is then quantified as the statistical description of these damages in terms of people affected and dollar-value damaged (buildings and hotels) and for different probabilities. The economic impacts include both direct and indirect losses. The flood risk reduction benefit of the MAR is estimated by calculating the difference in damages between two scenarios: current coral reefs and a scenario that assumes degraded coral reefs.

This approach follows and advances methods recently used to assess the risk reduction benefits of ecosystems (Beck et al., 2018; Menéndez et al., 2018). However, in this study, the risk reduction of the MAR is also compared with two other drivers of risk: (i) the increased hurricane flood risk produced by SLR and (ii) the effect of losing the dunes. The effect in risk of SLR is modeled by including local SLR projections to each hurricane. The effect of dunes on risk is estimated in a similar manner as applied to coral reefs (**Figure 1**).

Hurricane Flood Hazard

The probability of damages to people and buildings was calculated by generating synthetic hurricanes in the Caribbean. A stochastic generation of storms was needed because is not possible to calculate statistics of losses from a single damage scenario or a limited number of historical storms, where probability would remain uncertain (Resio and Irish, 2015). The simulations of ∼15,000 synthetic storms were generated based on the historical storms (∼900 historical storms) using a stochastic simulation of origins and wind speeds and modeling the hurricane tracks through random walks. The analysis of storms was carried out with the open-source CLIMADA risk model using the hurricane and coastal modules (Reguero et al., 2018b; Aznar-Siguan and Bresch, 2019).

For each of the synthetic storms, we calculated the wind, wave, and surge fields using global bathymetry from GEBCO and ETOPO in deep waters (National Oceanic, and Atmospheric Administration [NOAA], 2006) and the parametrical models implemented in CLIMADAś coastal module, following methods previously used in Reguero et al. (2018b). For the wind field, the model uses a non-symmetric fields model (Bretschneider, 1990). Wind waves generated by the wind field are calculated as the average of two different models (Young, 1988; Bretschneider, 1990). The storm surge was calculated by linearly adding the barometric surge and wind setup produced by the storm (Dean and Dalrymple, 1991). The rise of water above astronomical on the forereef takes into account the combined effects of direct onshore and alongshore wind stress on the surface of the water. The shear stress produced by the wind on the sea surface generates an elevation of the water level at the coastline, which can be described by the long wave equation, resolved on coastal transects (Dean and Dalrymple, 1991). Storm surges values were also obtained with the modeled surges from the MATO hydrodynamic model (Posada et al., 2008) as applied in Escudero-Castillo et al. (2014b), using surge levels calculated stationary conditions of winds to interpolate surge levels for any storm. The final storm surge values were calculated as the mean value of the surge levels from the analytical solution and the numerical simulations. These simplified approaches include uncertainty, particularly in nearshore areas, although they are a good estimate at the forereef. The significant wave height and surge levels offshore associated with a 100-year return period were compared with existing estimates of surge levels for the region of up to 2 m in Valdez (2010) and significant wave heights up to 15 m in Meza-Padilla et al. (2015), showing a good agreement (**Supplementary Figure 1**).

Modeling Flooding and the Effect of Reefs

Given the scope of the study and the availability of data, the flooding analysis had to be limited to the section of Quintana Roo with available information on coral reef presence and bathymetry. The region of study is shown in **Figure 2** and comprises the mainland section of the MAR, but leaves out the island of Cozumel and other sections offshore and northwards where the coral reef bathymetry does not exist. For this region, high resolution bathymetry and coral cover data were available via CONABIO (Comisión Nacional para el Conocimiento y Uso de la Biodiversidad) from the 'Sistema Nacional de Información sobre Biodiversidad'[1], which provides 4-m resolution bathymetry and seabed cover from Cabo Catoche to Xcalak. The fore reef and beach profiles were assumed equal for all the coastal transects, based on mean slope values observed in the region (Escudero-Castillo et al., 2014b, 2018).

Flooding inland and the effect of reefs were modeled through XBeach, a wave propagation model that is able to calculate wave runup onshore but also the contribution to flooding of time-dependent long waves, which are particularly important in the surf zone of reef environments. This model has been

[1]http://www.conabio.gob.mx/informacion/gis/

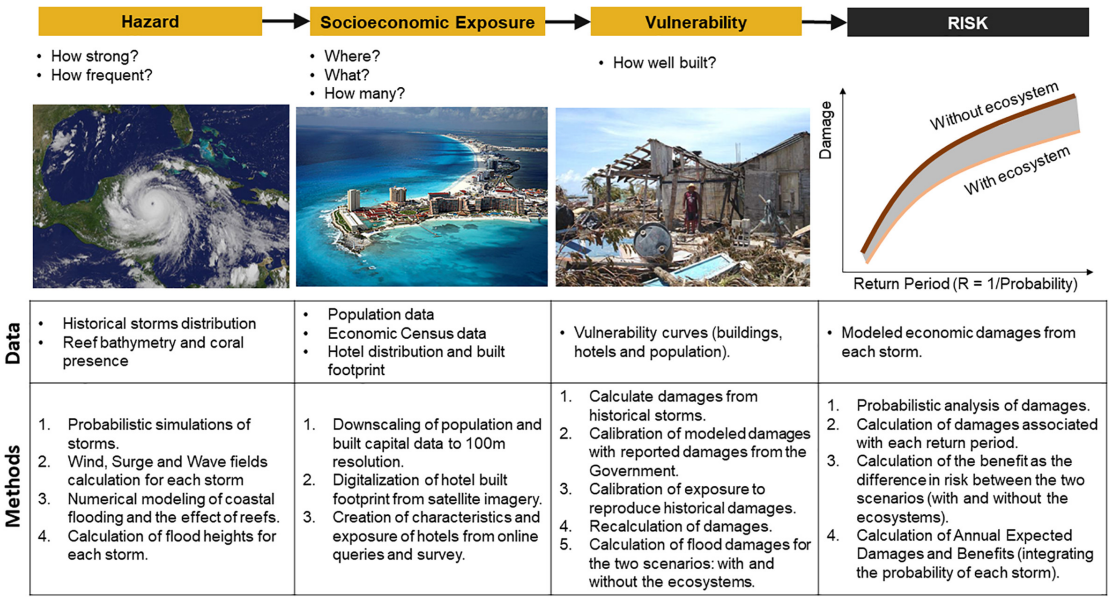

FIGURE 1 | Key steps and critical data needed to quantify risk. Source: adapted from Reguero et al. (2018b). Image 1: NASA GOES *Blue Marble imagery by NASA's Earth Observatory Team*. Image 2: Wikimedia Commons, by http://www.safainla.us/. Image 3: CENAPRED, (2007).

extensively validated for reef environments (van Dongeren et al., 2013; Quataert et al., 2015). The numerical model was run in coastal transects (a total of 2,515 transects), every 200 m along the coast (see **Figure 2**), with variable friction and in surf-beat mode. The application of a one-dimensional model neglects some of the dynamics that occur on natural reefs, such as lateral flow. However, it does represent a conservative estimate for infragravity generation and wave runup, as the forcing is shore-normal. In this case, the coastline and reef configuration show near-normally offshore waves (e.g., **Figure 2**). The friction coefficients were set based on a calibration of the model based on field data from (Quataert et al., 2015), and defined based on the seabed type classification for the region. The incident wave friction coefficient (f_w) and the current and infragravity wave friction coefficient (c_f), were applied to incorporate the effect of the roughness of the sea bottom on the decay of incident waves (van Dongeren et al., 2013). Coral reefs were given a value of f_w of 0.3, whereas the rest of seabed types were given a friction value of 0.1. The current and infragravity wave friction coefficient, c_f, varied from 0.01 for sand to 0.15 for rocky coral reefs, whereas algae were given a value of 0.03. Although the effect of seagrasses and algae was considered in the modeling, they provide less flood attenuation than coral reefs and their contribution was not isolated. However, research shows that in other areas they can also contribute to coastal protection, erosion control in particular (James et al., 2019). Examples of the transects with different bathymetric configurations are given in **Figure 3**.

The numerical model was run shore-normal, at each coastal transect for a subset of wave heights (H_s) covering the range between 1 and 10 m by 1 m increments, and sea levels ranging from 0 to 4 m (combination of mean sea level and storm surge) by 1 m increments. The modeled peak wave periods varied between 5 and 12 s. The peak wave period was set constant due to computation limitations and because the effect of wave heights is more dominant on wave runup than the effect of wave periods. We selected 9.6 s for all simulations, which represents the 80% percentile of the peak periods calculated for all historical storms across the region. However, larger wave periods generate larger runup, and therefore this approach can be considered conservative for large wave periods at the cost of overestimating runup for sea-dominated storms. Nevertheless, storms with low periods also present smaller wave heights, which is the most influential variable for wave runup. The direction of waves was also considered orthogonal to each transect in the fore reef.

The flood levels onshore were reconstructed from the numerical simulations using multidimensional interpolation techniques based on radial basis functions that have been successfully applied to wave climate downscaling and wave overtopping in similar applications (Camus et al., 2011a,b; Guanche et al., 2013). The flooding levels onshore were interpolated using radial basis functions, which were trained taking as inputs the different wave heights, and surge levels at the forereef, and outputs the flooding levels simulated with the numerical model. This approach provided flooding levels for all the storms in each coastal transect. However, the approach does not consider horizontal effects in the propagation and flooding.

The scenario of a degraded reef from storm damage, pollution, and other factors was simulated assuming flattened and deeper reefs (Yates et al., 2017). The degraded reef was simulated by specifying in the numerical model: (1) an increase in depth for the reefs of 1 m; and (2) reduced coral reef friction, assumed to be the same than the default sand values, per (Storlazzi et al., 2017).

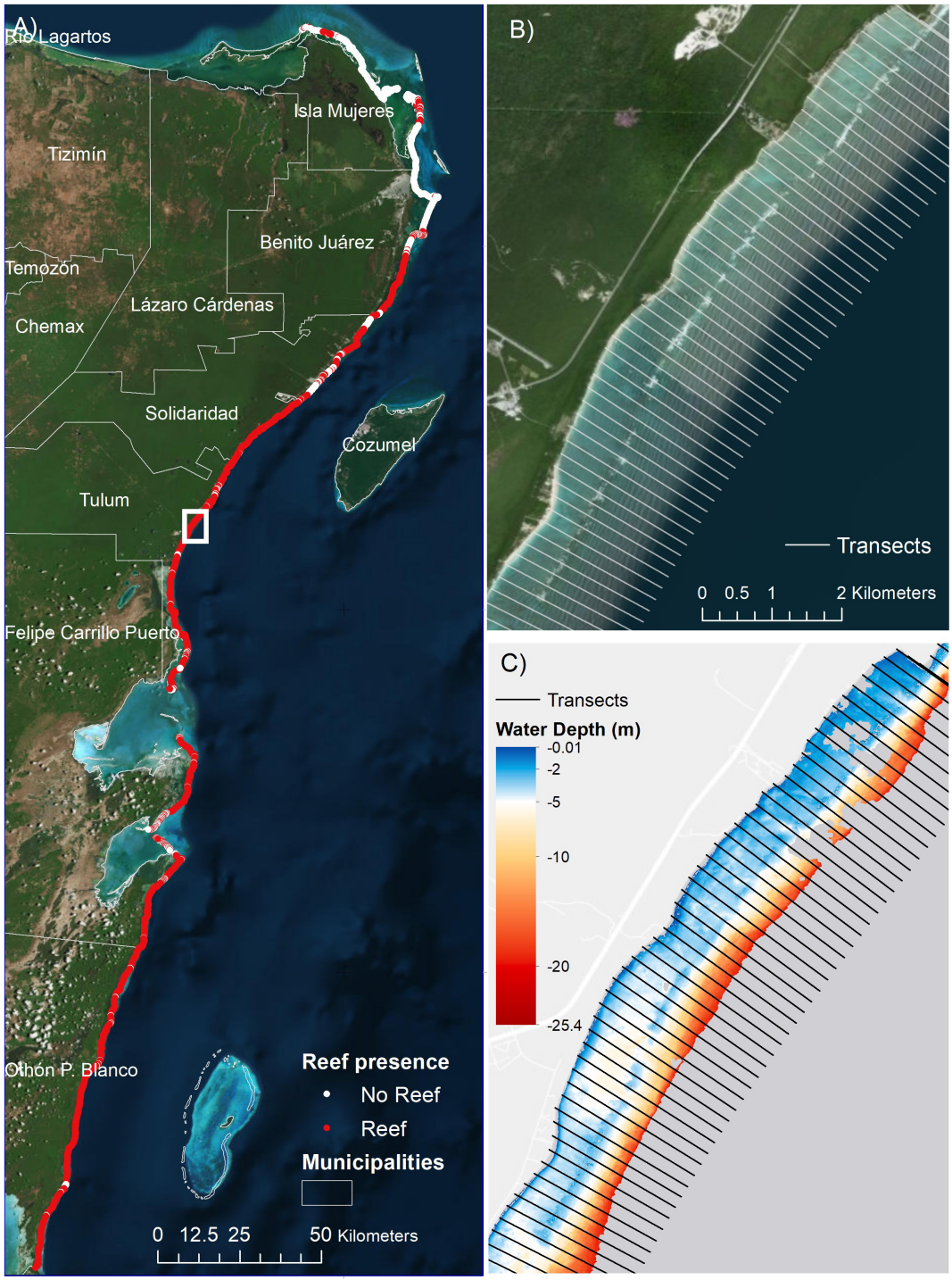

FIGURE 2 | Region of study and coastal transects. **(A)** Region of study, reef presence and costal transects coverage; **(B)** detail of coastal transects and satellite image showing the reef crest; and **(C)** details of bathymetry and coastal transects. The transects in **(B,C)** are spaced 200 m apart. The location for **(B,C)** is indicated in **(A)**. Colors in **(C)** indicate water depths, in meters.

These assumptions are based on observed changes in degraded reefs. Observations in changes in seafloor elevation and volume for coral reefs in the Atlantic, Pacific, and Caribbean over the last several decades show significant regional loss of seafloor elevation and volume and are indicative of potential future changes in reefs (Yates et al., 2017). Evidences also show substantial flattening of reefs across the Caribbean as architectural complexity had declined non-linearly with the near disappearance of the most

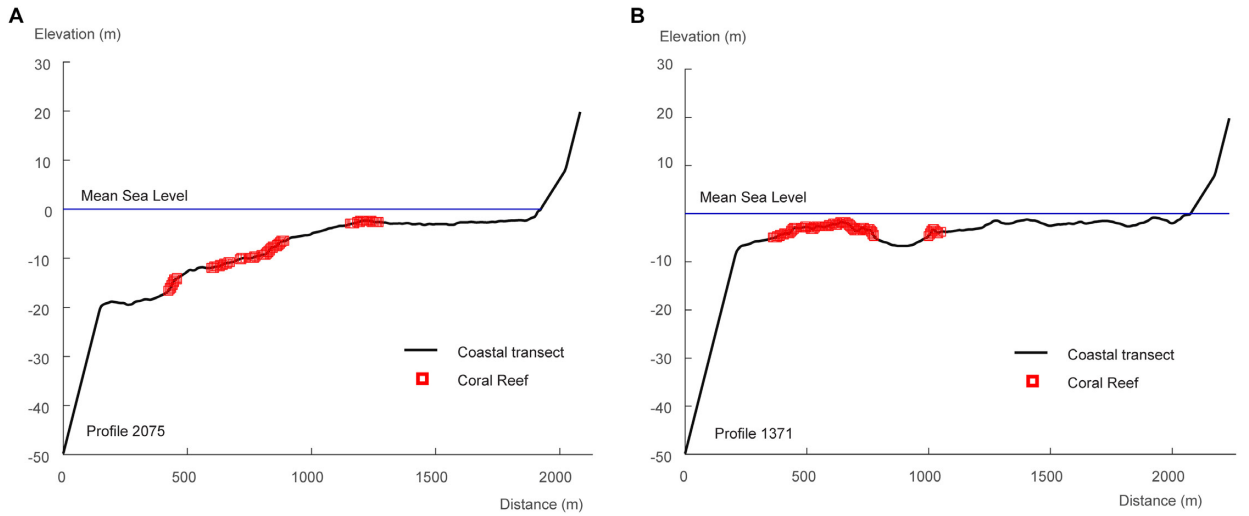

FIGURE 3 | Two examples of coastal transects for the reef model. The transect in panel **(A)** presents a deeper reef section, while panel **(B)** shows another transect with a shallower reef crest, followed by a reef lagoon.

complex reefs since 1969 (Alvarez-Filip et al., 2009). The loss of friction represents a severe flattening of the reef and reef matrix degradation, which are translated into frictional loss assuming that the reef will show a similar friction as the no-reef parts of the profile.

Calculating People and Assets Damaged

To calculate the consequences of flooding, data on people; built capital, which comprises residential, commercial and other infrastructure; and hotels were analyzed in spatial units of approximately 5 km and counted by ground elevations using the Shuttle Radar Topography Mission (SRTM) Digital Elevation Model, with a horizontal resolution of 90 m and vertical resolution of 1 m (Rabus et al., 2003; Farr et al., 2007). The total counts of people, built capital, and hotel infrastructure were then distributed between the coastal transects to infer damages by interpolating the flood levels with the potential socioeconomic exposure.

Population data were obtained from the WorldPop dataset with a spatial resolution of 100 m (Lloyd et al., 2017), represented in **Figure 4**. The spatial distribution and total counts of people were compared by municipalities with local census data and show a good agreement (**Supplementary Figure 2**). Built capital, or the value of buildings, was calculated based on global data from the 2015 Global Assessment Report (GAR) on Disaster Risk Reduction (UNISDR, 2015). The GAR data, with 5-km spatial resolution, were downscaled to a resolution of 100 m using the population data and the government economic census that provides values of the residential, industrial, services and government buildings. The methods are based on approaches previously applied for risk quantification in data-poor environments (Reguero et al., 2015; Beck et al., 2018; Menéndez et al., 2018). To do this, first the residential capital stock per capita was calculated using data from GAR's Capital Stock and population (UNISDR, 2015). Second, the per capita values were resampled to a resolution of 100 m and multiplied by the 100 m-resolution population data (**Figure 4**). The industrial and commercial stocks were obtained similarly by dividing the urban and rural industrial capital from GAR by the total number of workers from the government census. The distribution of the different types of built capital is shown in **Figure 5**.

Impact on hotel infrastructure was calculated independently from built capital. Information on hotels was obtained from the economic census (INEGI, 2015) and online sources (Tripadvisor and Expedia) to create a database of hotel location, ranking, number of rooms, range and average prices, and other variables such as number of employees. The built footprint of each hotel along the coastline was digitized from Google Earth and satellite imagery in ArcMap (image available on May 2016). Hotels were classified into four categories based on their star rating. A predominance of 3.5- to 5-star hotels was observed in the northern coast of Quintana Roo, whereas the southern coast presents a high density of lower hotel rating, 2.5- to 3-stars. The hotel distribution and number of rooms are represented in **Figure 6**.

To calculate the damages from flooding, the damage of each single storm is calculated by multiplying the value of exposure (dollar-value) by a percentage of property damaged, which is determined based on the flood heights generated by each storm at each coastal transect. The percentage of damage is determined from vulnerability curves for each type of asset (people, built capital, and hotels). For buildings, vulnerability curves were obtained by taking the average damage degree obtained from all the curves in the HAZUS-FEMA database (Scawthorn et al., 2006a,b) for each type of building: residential, commercial, and industrial types, respectively (see **Supplementary Figure 3**). For hotels, local vulnerability curves were developed based on historical damages for hurricanes Wilma and Dean, obtained from the Mexican National Center for Prevention of Disasters

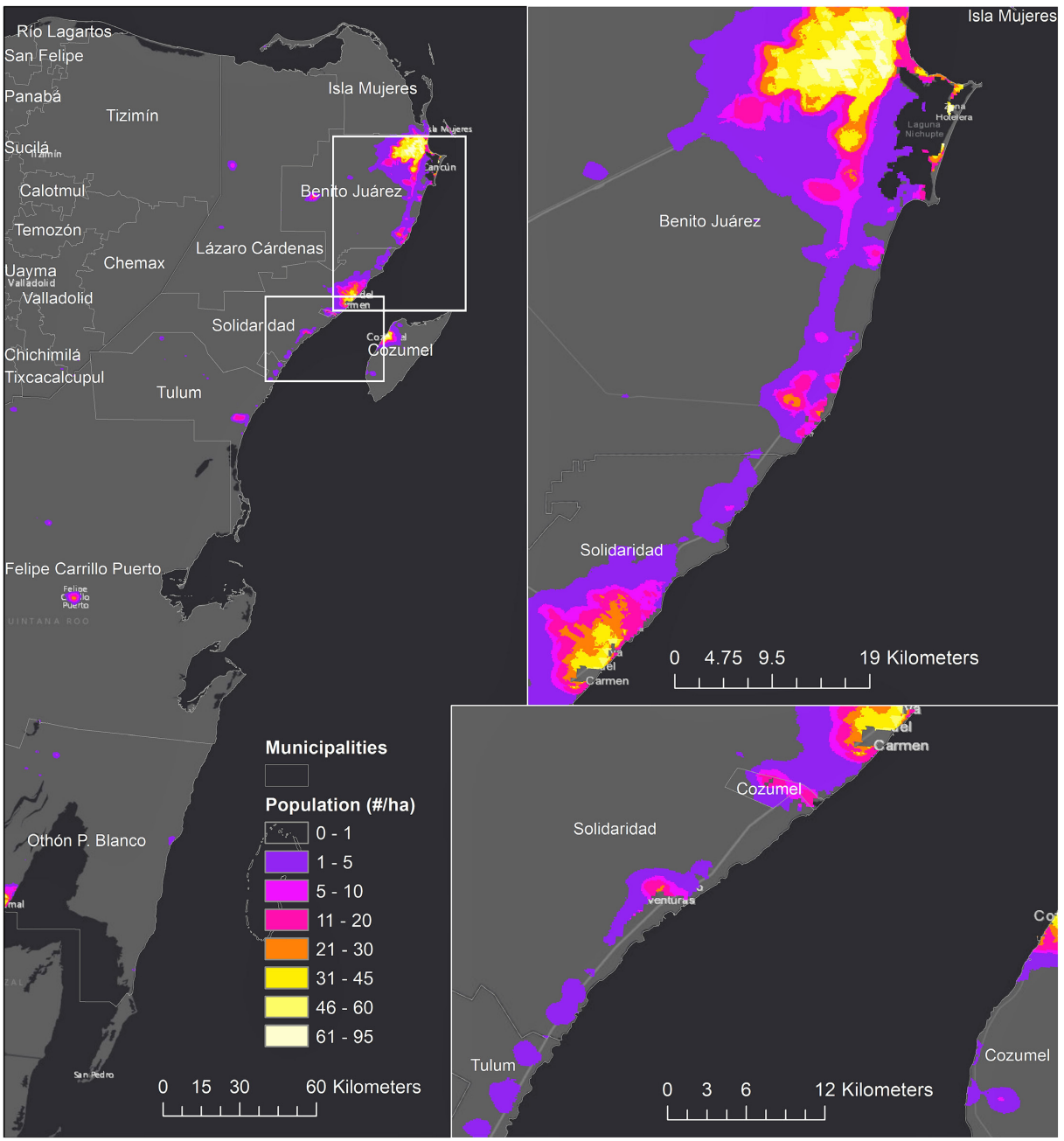

FIGURE 4 | Population distribution. Values are expressed in number of people per hectare.

(CENAPRED) and the Economic Commission for Latin America and the Caribbean (CEPAL). Damage costs were expressed in US Dollars (USD) per square meter of the flood plain as a function of the hotel star-rating, using the reported losses in terms of number of damaged hotel rooms after each event and the estimated surface area of each hotel room (see **Supplementary Figure 4**).

Given the uncertainties in the risk modeling (e.g., exposure data, hazard definition, flooding approach, and vulnerability curves), the model was calibrated to represent the reported losses for historical hurricanes, which are surveyed and reported after each storm season by the CENAPRED. The exposure was calibrated over the region so that the modeled direct losses for Hurricane Dean would match the official economic damages reported by the Government for the same storm. Hurricane Dean was selected between the available historical events with official damage estimates as a benchmark because its damages (∼214 million USD in 2007) were predominantly driven by coastal flooding and impacted significant residential infrastructure, as opposed to other storms, such as Wilma and Emily in 2005,

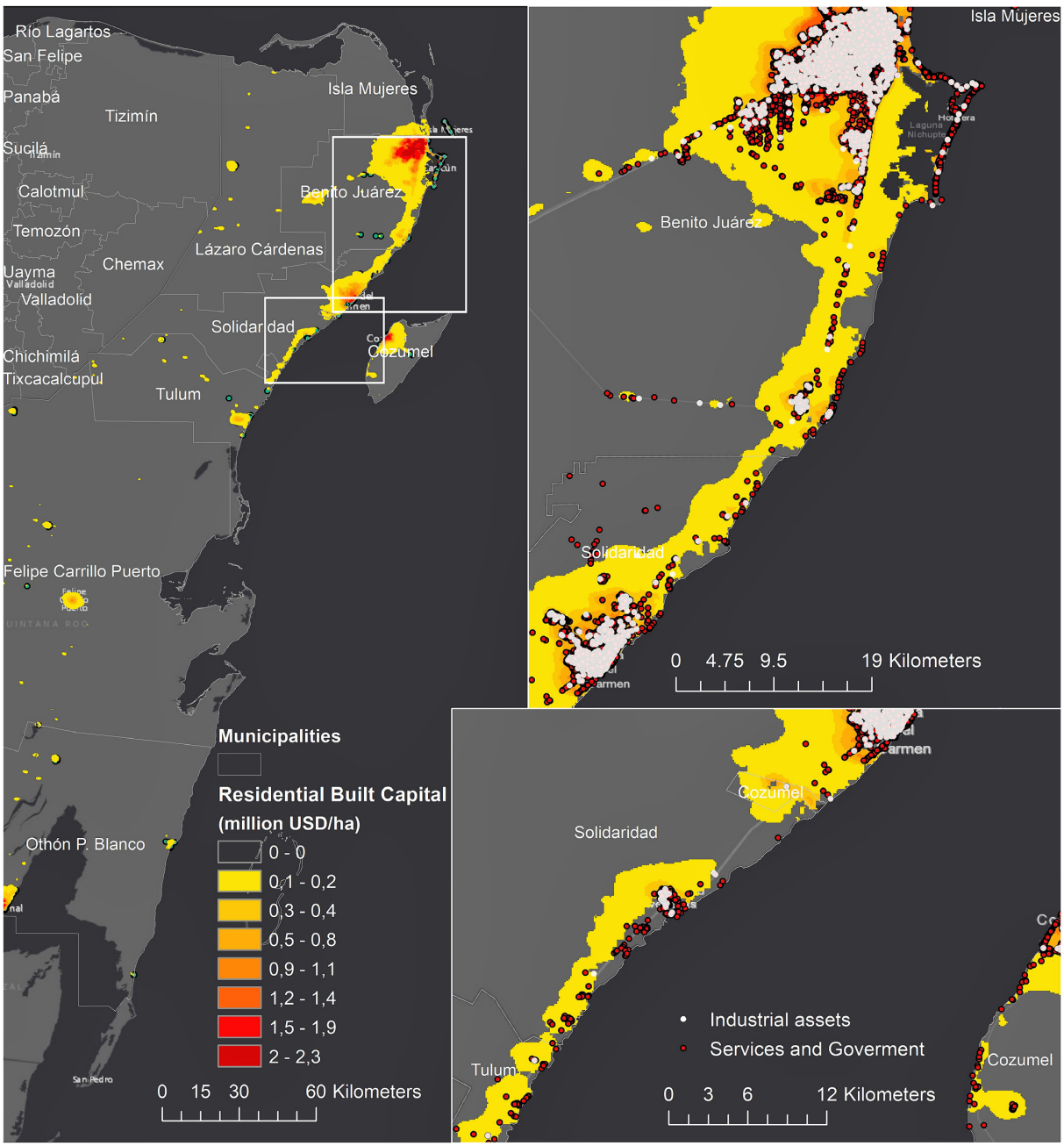

FIGURE 5 | Distribution of built capital. Values are expressed in million USD value per hectare.

where a significant fraction of the damages were caused by wind and rainfall and the losses were mostly concentrated on the tourism sector.

Estimating Indirect Damages

We also estimated indirect damages, which are economic losses caused by the consequences of physical destruction caused by flooding such as business interruption, tourism impact, etc. Estimates of the indirect damages were based on the review of impacts of historical storms in the region produced annually by CENAPRED. Indirect damages were calculated by multiplying the modeled direct damages with an average ratio of indirect over direct damages for three historical Hurricanes: Emily in (2005), Wilma in (2005), and Hurricane Dean in (2007). Values of direct and indirect damages for the three storms were obtained from CENAPRED reports and converted to USD for each corresponding year using historical conversion rates and then to USD-value in 2015 correcting for the historical buying power.

According to surveys from the Government, Hurricane Dean in (2007) produced 40% additional damages in indirect impacts

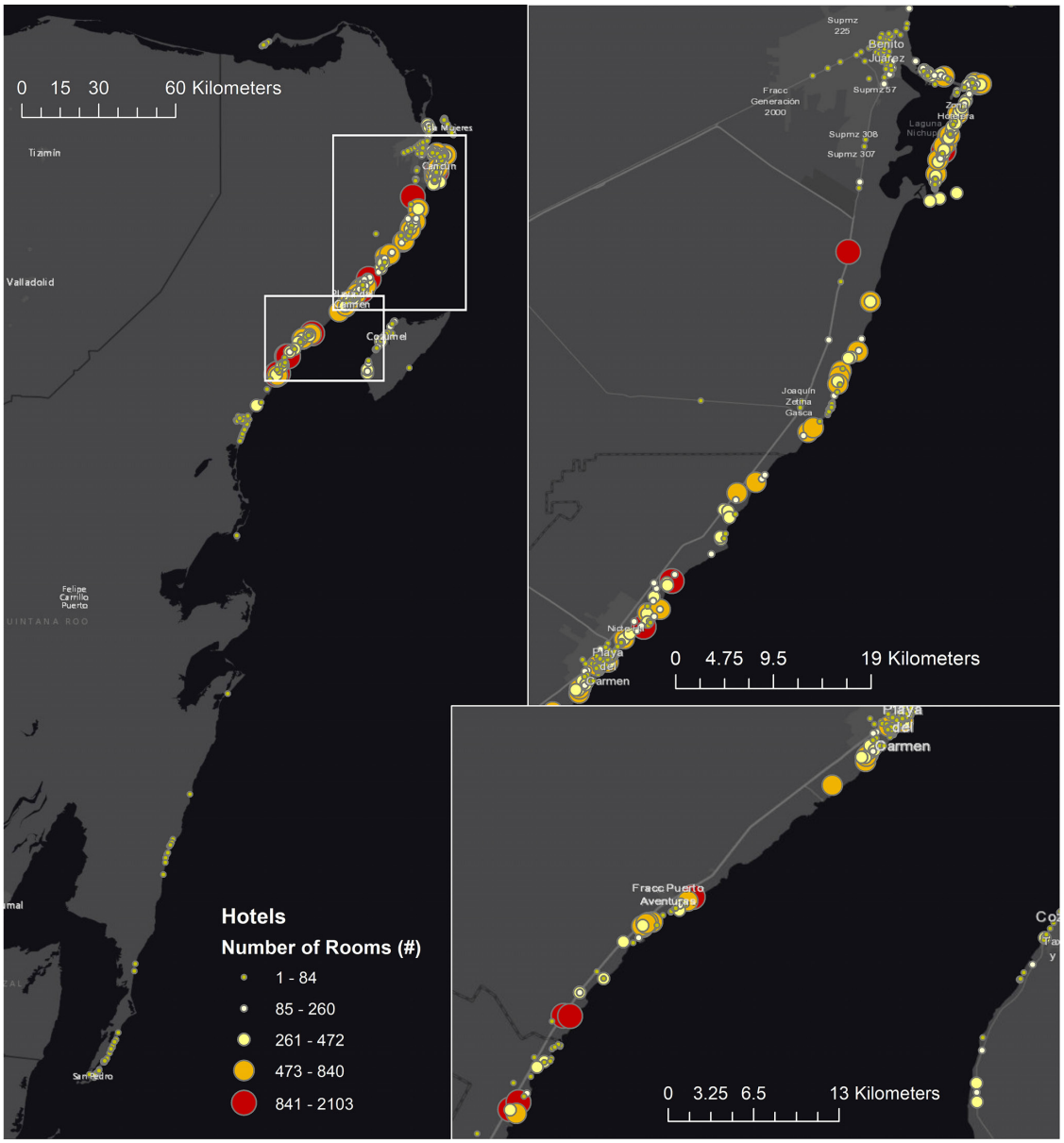

FIGURE 6 | Hotel distribution in Quintana Roo coastal zone by the number of rooms.

(0.4 factor), Wilma in (2005) had three times more indirect damages than direct damages, and Emily in (2005) produced 1.6 times more indirect damages than direct damages. Based on these measured values, the indirect damages are on average 1.6 times the direct damages, although it shows a large range of variation. However, evidence suggests that the proportion of indirect impacts increases in larger disasters, as seen with Hurricane Wilma in comparison with Emily, although both impacted the same region. This is because business interruption and other indirect effects are proportionally larger after stronger storms. However, in absence of better data, here we used the average factor, x1.6, and applied it linearly to all the storms although we acknowledge that the indirect damages may constitute a larger fraction of total losses in larger disasters than in smaller ones.

Calculation of Reef Benefits

The flood risk reduction from coastal ecosystems was estimated through the avoided damage or expected damage function methods (Samonte-Tan et al., 2007; Barbier, 2015). The approach compares the additional people and property affected if existing coastal ecosystems were lost. This approach, therefore, represents the risk reduction benefits of the protection that ecosystems offer, but it can also be seen as the increase in risk from environmental degradation. Risk is described using (i) an estimate of the annual average costs of flooding, or annual expected damage (AED), and

(ii) the damages associated with different storm return periods (i.e., the average recurrence interval, in years, of each event). The damages for the different return periods are interpolated from the damage exceedance frequency curve at each coastal transect using the probability associated to different return periods. The damage probability distributions were calculated through cumulative frequency analysis of all the damages produced by storms at each location. The AED is calculated by weighting the loss of each storm by its probability of occurrence. The economic risk reduction benefits are provided in 2015 USD and risk reduction for the population in total number of people protected.

The Effect of Dunes in Coastal Risk

The risk reduction service of the MAR was compared with the relative contribution of dunes for flood risk reduction to better understand the reef's relative importance for flood prevention across the region. The effect of the dunes was estimated by including the dune height in the flood model and calculating flooding damages only if the dune heights were overtopped. The effect of dunes in coastal risk was calculated by comparing the simulated losses with and without dunes.

Dune elevation and width were estimated from Lidar data provided by the INEGI (Instituto Nacional de Estadística y Geografía de México) for the year 2007, with a horizontal resolution of 5 m. Dune heights vary between 0.5 and 4 m (**Supplementary Figure 5**). However, in contrast with the reef bathymetry, the Lidar topographic data did not cover the entire region (only from Punta Nizuc to south of Punta Maroma). The remaining dune elevations were estimated from satellite imagery and associating the elevation from similar sections of beach and dunes covered in the Lidar data.

Lack of data in dune vegetation did not allow considering the effect of dune vegetation in attenuating the wave run up and overtopping, although recent research shows that it can provide a reduction of wave-run up erosion of 40% (Feagin et al., 2019). Erosion of dunes under large storms was also not considered although it could reduce the effectiveness of dunes should they breach. For these reasons, the valuation for dunes carries higher uncertainty than for the MAR and is only used for comparative purposes.

The Effect of Sea-Level Rise in Coastalz Risk

The effect of SLR was including in the flood model as a static increase in the mean sea level in every storm. The damage from each coastal storm was recalculated similarly to the without SLR scenarios, at each coastal transect and using a new mean sea level that corresponded to a SLR projection by the end of the 21st century. The new simulated damages were analyzed statistically to define losses associated with different return periods, as applied to the risk without SLR. The local SLR was obtained from the mean value of the Representative Concentration Pathway (RCP) 4.5 by the end of the 21st century and interpolated at each coastal transect (Church et al., 2013). The RCP4.5 projects a mean SLR for Quintana Roo of ∼0.5 m (with lower and upper bounds of projections being 0.29 and 0.75 m, respectively), whereas the average estimate for the RCP 8.5 is 0.7 m. The assumption of the RCP 4.5 is, therefore, a conservative one. The SLR was used to recalculate the flooding of all hurricanes. Other effects of climate change, such as changes in the hurricane intensity or frequency, were not included to isolate the effect of SLR in flooding and compare its effect on risk with reef degradation. Once the projected flood heights were calculated, the assessment of flood risk followed the same approach as above.

The effect of SLR was studied in terms of changes in damages (changes in losses and people impacted for different probabilities), but also in terms of changes in the flood hazard (i.e., variations in total water levels onshore) because the reef provides different flood attenuation depending on the specific wave and sea level conditions of each storm. To assess the effect of SLR in the flood hazard, we calculated attenuations for each storm under two scenarios of mean sea level: present sea level and sea-level rise, as:

Attenuation = [flood level without the reef for storm i]/[flood level with the reef for storm i] – 1.

The attenuation values were summarized by the mean and the 25- and 75% percentiles, to then calculate the ratio between the mean attenuation with sea-level rise and with present sea level.

RESULTS

Flood Hazard Damage Prevention by the Mesoamerican Reef in Quintana Roo

Distribution of People and Economic Exposure in the Study Area

38% of the total of 1.5 million people living in the State of Quintana Roo, 570,670 people, live in the coastal zone, defined as the flood-prone area close to the shoreline and below 20 m in elevation. The population and infrastructure located in the study area (with coral reef and bathymetry data) totals 307,640 people and over 3.3 billion USD in built capital, concentrated primarily in the northern portion of Quintana Roo (**Figures 4**, **5**). However, only 26% of the built capital (869 million USD) and 34% of these people (105,800) are located inshore of a coral reef. For example, Cancun, the most intensively developed area, is not protected by reefs (Escudero-Castillo et al., 2018). However, the fraction of hotel infrastructure situated onshore of coral reefs is comparatively larger than for other types of buildings; 63% of the hotel infrastructure is inshore of coral reefs (**Figure 6**).

Historical Hurricanes

The MAR has provided significant protection against historical hurricanes. During Hurricane Dean in (2007), which made landfall on the Yucatan Peninsula as a powerful Category 5 storm and produced ∼175 million 2015 USD in direct damages (CENAPRED), the MAR prevented 43% of additional flood damage (**Table 1**). For hurricanes Wilma (category 5 at landfall, 2005) and Emily (category 4, 2005), coral reefs prevented 11 and 9% of flood damages respectively (**Table 1**). The damage prevention provided by coral reefs was lower for Hurricanes Wilma and Emily because they affected the northern portion of the State, which includes Cancun that is intensely developed but

TABLE 1 | Socioeconomic benefits from the Mesoamerican Reef for historical hurricanes.

Storm	Modeled people flooded (#)	People protected by reefs (#)	% of modeled impact	Modeled damage to built capital (million USD)	Benefit of protection (million USD)	% of modeled impact	Modeled damage to hotels (million USD)	Benefit of protection (million USD)	% of modeled impact
Hurricane Dean in 2007	21,015	13,799	65.7%	174.9	119.2	68.2%	46.9	43.2	92.1%
Emily in 2005	124,537	13,683	11.0%	1,439.6	155.8	10.8%	179.6	82.1	45.7%
Wilma in 2005	168,859	15,766	9.3%	2,075.9	181.0	8.8%	265.5	91.8	34.6%

Benefits are calculated as the differences between the modeled impact (in number of people and dollar-value) with and without the reef. The percentages are calculated by dividing the savings over the modeled impact.

not directly protected by reefs, and they were also characterized by strong rainfall (Escalante-Mancera et al., 2009; Silva et al., 2009). Meanwhile, Hurricane Dean impacted the southern section and affected predominantly residential houses and coastal population, while most of the damages were directly produced by coastal flooding.

For the same reasons, the estimates of people protected for reefs are also higher for Hurricane Dean; the MAR prevented ∼66% more people from being affected by flooding (**Table 1**). Despite the different characteristics and exposure distribution of the three storms impact areas, the MAR protected consistently between 13,688 and 15,766 people from flooding during those storms. The protection for hotels, however, was significantly larger than for people and built capital. The estimated benefits for hotels in flood damage prevention range from 34.6% from Wilma to 92.1% for Dean, valued at 43.2 and 91.8 million USD respectively (**Table 1**). The economic protection of the MAR for hotels was also higher for Hurricanes Emily and Wilma than for Dean because the distribution of hotels is closer to the coastline than other buildings and coastal communities (**Figure 6**).

Probabilistic Coastal Risk Reduction

The risk reduction benefits of the MAR are also assessed probabilistically across storms frequency. The risk is described by the direct damages to people, building and hotel infrastructure across return periods, and also calculated as AEDs. The risk reduction potential of the reefs is represented in **Figure 7** and summarized in **Table 2**. The modeled damages with current reef condition and with degraded reefs for population, built capital and hotel infrastructure are included in **Supplementary Tables 1–3**. The results for people (**Figures 7a,d** and **Table 2**) indicate that reefs protect ∼4,600 people per year on average, which represents 4.3% of the people living inshore of a reef. The people protected is twice as much for a 1-in-100-year event. However, if reefs were degraded, the AED could more than double (increase of 195%), and the 1-in-100-year would affect 41.7% more people.

In terms of built capital (**Figures 7b,e**, **Table 2**, and **Supplementary Table 2**), the MAR protects 1.9% of the total built capital value behind reefs per year. Its value is estimated in ∼16 million USD per year in direct avoided flood damages, but assuming average ratios of indirect damages, reefs provide an additional protection of ∼26 million USD in averted indirect losses per year. Overall, this totals an estimated value of 42 million USD savings in flood protection per year. However, reef degradation could more than double AED (increase of 178%), while the 1-in-100-year risk would increase by 74%, by ∼100.7 million USD of additional damage (**Figure 7b** and **Table 2**).

Hotels benefit most from the effects of the MAR on flood prevention; the modeled direct losses and the benefits for the hotel infrastructure are provided in **Table 2** and **Supplementary Table 3**. Hotels receive ∼21 million USD per year in direct averted flood damages (without accounting for indirect damages). However, reef degradation could more than double the AED (∼173% increase; **Figure 7f** and **Table 2**); from 12 million USD per year to 33 million USD per year. The 1-in-100-year flood risk would increase by 91%, or by ∼323 million USD (**Figure 7c** and **Table 2**). These benefits relative to the built capital value in the coastal zone represent between 2.4% per year to 50% of the built capital for a 1-in-500-year flood damage (**Table 2** and **Supplementary Tables 1–4**).

Spatial Distribution of Risk Reduction Benefits

The spatial distribution of the annual expected benefits for people, built capital and hotel infrastructure, respectively, are shown in **Figures 8–10** The maps identify where this protection is more valuable and reveals that the most protection to economic assets and people do not always coincide.

The benefits for people are concentrated in the urban areas of Puerto Morelos (in Benito Juarez) and south of Cancun (**Figure 8**). However, protection for the built capital also concentrates in Playa del Carmen. This difference demonstrates the protection in Playa del Carmen is not only for residential buildings, but also to commercial and other buildings. In that region, there are benefits of more than 0.5 million USD for 200-m long sections of reef, which represents over 2,500 USD per alongshore linear meter of reef, per year. However, the comparison with the benefits for hotel infrastructure indicates a different pattern. The protection of MAR is more homogenous along the coastline and concentrates the largest benefits in the district of Solidaridad, followed by Playa del Carmen.

Risk Reduction Effects of Dunes

To better understand the risk reduction of the MAR with respect to other drivers of risk, we compare the coral reefs' benefits with the risk reduction provided by dunes. The dunes are assumed to provide protection up to the elevation they are overtopped during a storm or hurricane. Their risk reduction benefit is determined by comparing two scenarios: with and without dunes, as applied to coral reefs.

The risk at present and the risk reduction benefits of dunes are presented in **Supplementary Table 4**. Regionally, the annual

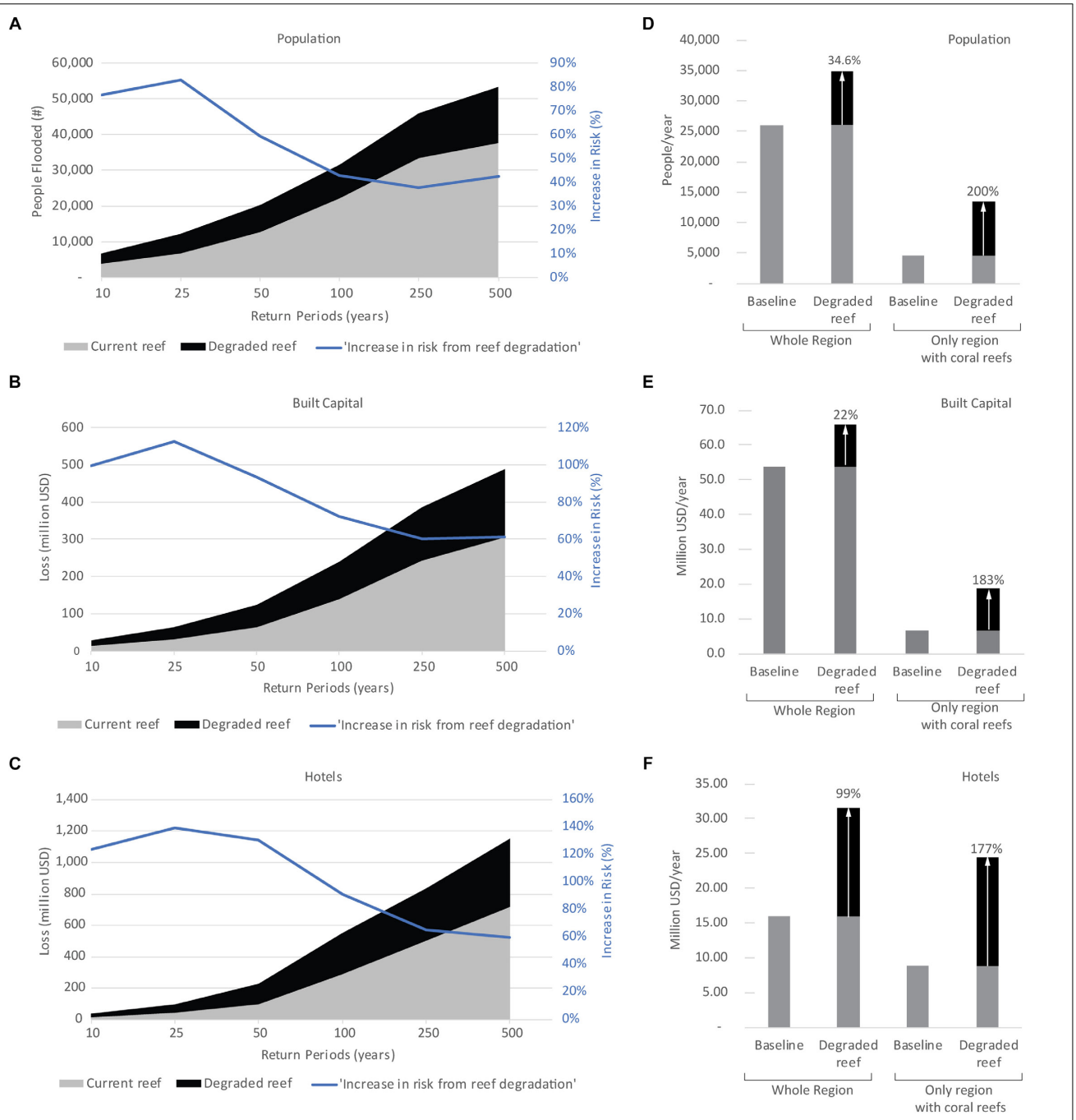

FIGURE 7 | Coastal risk and the risk reduction of the Mesoamerican Reef. Risk is represented as people flooded **(a,d)**, damages to built capital **(b,e)**, and damages to hotel infrastructure **(c,f)**. The difference in the graphics (in black) represents the protection offered by the Mesoamerican Reef. Risk is represented across return periods **(a–c)** and in terms of annual expected damages (AEDs) **(d–f)**. A return period of *n* years represents a probability of occurrence of 1/ *n* years. The increase in risk, showed by a solid blue line in the left panels, indicates how much risk will increase from reef degradation, in percentage over the baseline risk, or risk with 'current reef' (gray shading). It is calculated as the benefit (black shading) divided over the baseline risk (gray shading). For **(d–f)**, the bars on the left represent flood risk for the whole of the region, whereas the bars on the right represent only the values for the subset of transects with coral reefs (excluding transects with no coral reefs). The annual percent increase in losses is annotated in each case and calculated with respect to the baseline scenario. Values for each type of population, built capital and hotel infrastructure are included in **Supplementary Tables 1**–**3**, respectively.

benefit of the dunes in Quintana Roo is estimated at more than 16.7 million USD per year. Considering only sections with coral reefs, the annual benefit for built capital provided by dunes is 4.7 million USD, whereas the risk reduction benefit from reefs for the same region is four times larger, over 16.6 million USD per year.

TABLE 2 | Population, built capital, and hotel infrastructure protected by reefs.

Risk reduction offered by the mesoamerican reef	Annual expected damage	Storm return period					
		10 years	25 years	50 years	100 years	250 years	500 years
Risk reduction benefit offered by reefs							
Population (#)	4,586	2,677	5,140	6,941	8,796	10,784	13,478
Built capital (million USD)	16.3	13.8	33.8	56.8	100.7	130.7	171.7
Hotel infrastructure (million USD)	20.8	20.8	58.4	130.5	262.6	332.1	431.5
Percentage increase in risk compared to baseline risk							
Population	195.5%	74.4%	81.1%	57.9%	41.7%	33.5%	37.8%
Built capital	178.2%	96.9%	111.7%	91.4%	74.0%	56.0%	57.5%
Hotel Infrastructure	173.3%	123.8%	139.2%	131.0%	91.2%	65.6%	60.0%
Percentage increase in risk compared to the total exposure in the coastal zone							
Population (*)	4.3%	2.5%	4.9%	6.6%	8.3%	10.2%	12.7%
Built capital (**)	1.9%	1.5%	3.8%	6.5%	11.6%	15.1%	19.8%
Hotel infrastructure (**)	2.4%	2.4%	6.7%	15.0%	30.2%	38.2%	49.7%

Annual Expected Damage is calculated as the probability of each storm and the associated losses. Disaggregated figures and damages with current reef condition and with degraded reefs for population, built capital and hotels can be found in ***Supplementary Tables 1–3****, respectively. (*) Population living behind reefs: 105,800; (**) Built capital behind reefs: 858 million USD.*

TABLE 3 | Increase in risk for built capital from reef degradation and sea level rise.

Built capital (million USD) protected in sections with reefs	Annual expected damage	Storm return period					
		10 years	25 years	50 years	100 years	250 years	500 years
Damage with current reef condition (baseline)	12.0	16.8	41.9	99.6	287.8	506.0	719.2
Contribution of losing the reef	20.8	20.8	58.4	130.5	262.6	332.1	431.5
Contribution of sea level rise	32.5	16.0	28.8	59.1	129.1	162.6	201.9
Contribution of reef degradation and sea level rise	74.0	49.0	122.5	219.9	431.1	533.5	667.9

However, the risk reduction benefits of dunes are most critical where there is no coral reef offshore and for small return-period storms. For example, for sections with both ecosystems, coral reef degradation would represent a 99% increase in the 1-in-10-year risk, but dunes loss would represent a 264% increase. Dunes provide 27.3 million USD protection across the region for the same storm probability, whereas the benefits of the reefs are 13.8 million USD (**Supplementary Tables 2**, **4**). However, for the 1-in-100-year storm, the benefit of dunes is 14.8 million USD, compared to 100.7 million USD from reefs, as reefs keep attenuating waves and flooding during intense storms, whereas dunes are overtopped.

Effects of Sea-Level Rise on Coastal Risk

Corals reefs provide significant flood reduction along the Quintana Roo coastline. The percentage increase in flood risk with degraded reefs is shown in **Figure 11**. The average increase in flooding varies from 20 to 120% between transects, with a mean value of 48%, depending on different geomorphology but also the different hurricanes' waves and surges for each storm along the shoreline. The mean values across the region of the 25- and 75-percentiles are 33.5 and 63.4%, respectively. However, the reefs attenuate flood levels for specific storms up to 140%, as shown by the 75-percentile of flood attenuation.

Rising sea levels and climate change will have a significant negative impact on the ability of coral reefs to mitigate the effects of coastal hazards in the future (Quataert et al., 2015). In principle, the contribution of SLR would render reefs less effective, as the water depth increases with all the remaining factors unchanged. In general, reefs will be less effective (ratio below the 1-value in **Figure 11b**), although there are also instances where reefs will provide more effective flood reduction with SLR (ratio above 1), as shown in **Figure 11b**. This can be explained by the different reef bathymetric configurations and their effects on flooding (e.g., Baldock et al., 2014).

The contribution of the reef degradation is larger than the increase in risk caused by SLR for population, built capital, and hotel infrastructure at risk (**Figure 12**). For example, for a 1-in-10-year probability, SLR contributes 20.8 more million USD in risk to built capital versus 16.0 million USD of SLR (**Table 3**).

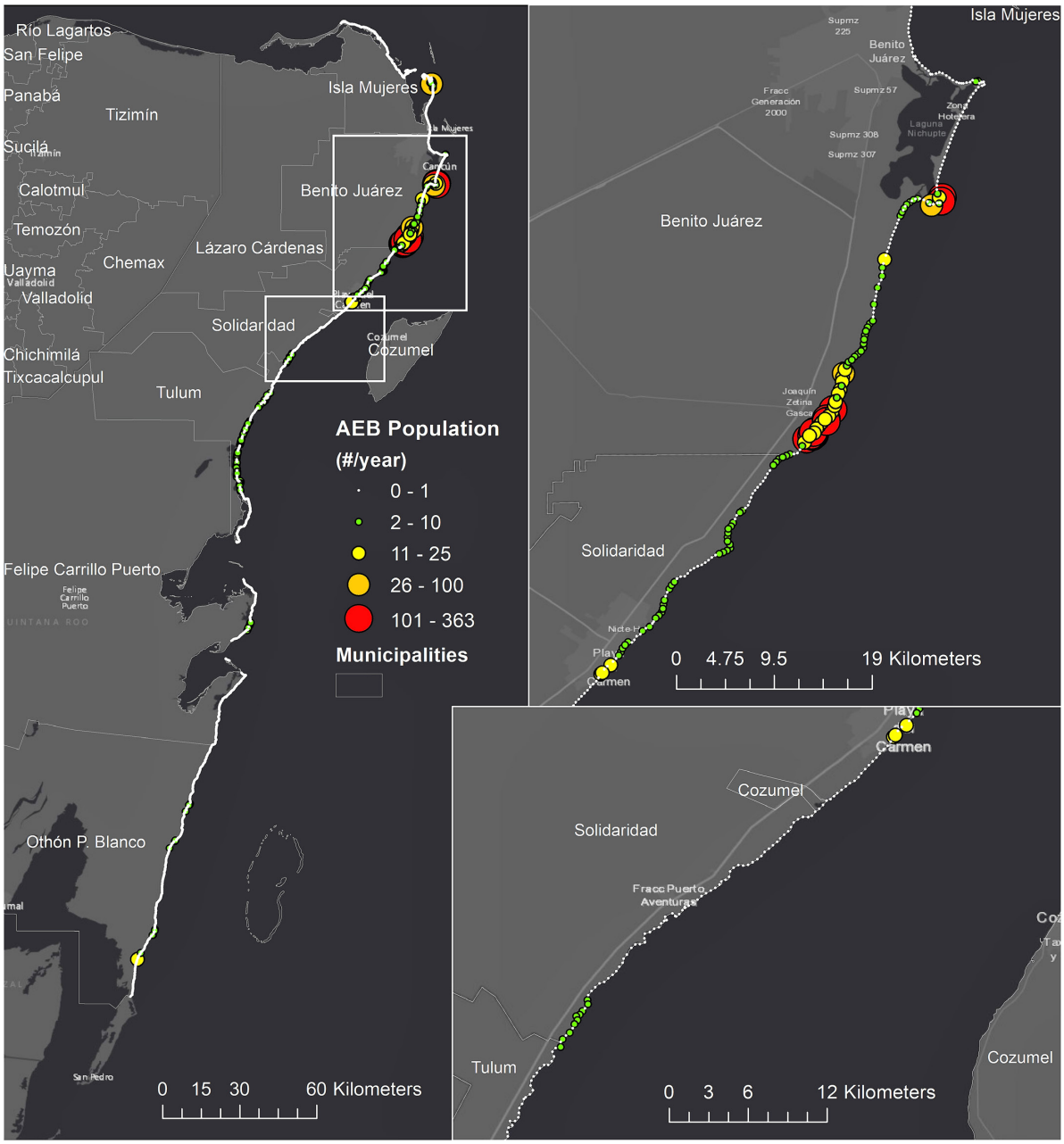

FIGURE 8 | People protected from flooding per year. The points represent the annual expected benefit to people, in each coastal transect spaced 200-m along the coastline.

However, in terms of AED, the contribution of SLR is larger than coral reef degradation (32.5 versus 20.8 million USD increase in risk). Furthermore, the combined contribution of SLR and reef degradation leads to damages larger than the linear addition of each driver. These two reasons point to SLR as a major driver of more recurrent damages. Indeed, SLR is the largest contributor to risk overall. Sea-level rise would increase hurricane flood risk by a factor of 1.8 times, from 72.3 million USD to 204.2 million USD, for a modest (+0.5 m, RCP 4.5) increase in the mean sea level.

DISCUSSION

By integrating economic, ecological, and hydrodynamic models, this study shows the spatial risk reduction benefits of the MAR, locally and regionally. The MAR provides substantial risk reduction benefits for people, the buildings, and hotels in Quintana Roo, particularly for low-return-periods storms (e.g., Hurricane Dean). The benefit of coral reefs to built capital, for example, varies from 100 to 60% as returns periods increase (**Figure 7** and **Table 2**). This is because reefs increase their benefit

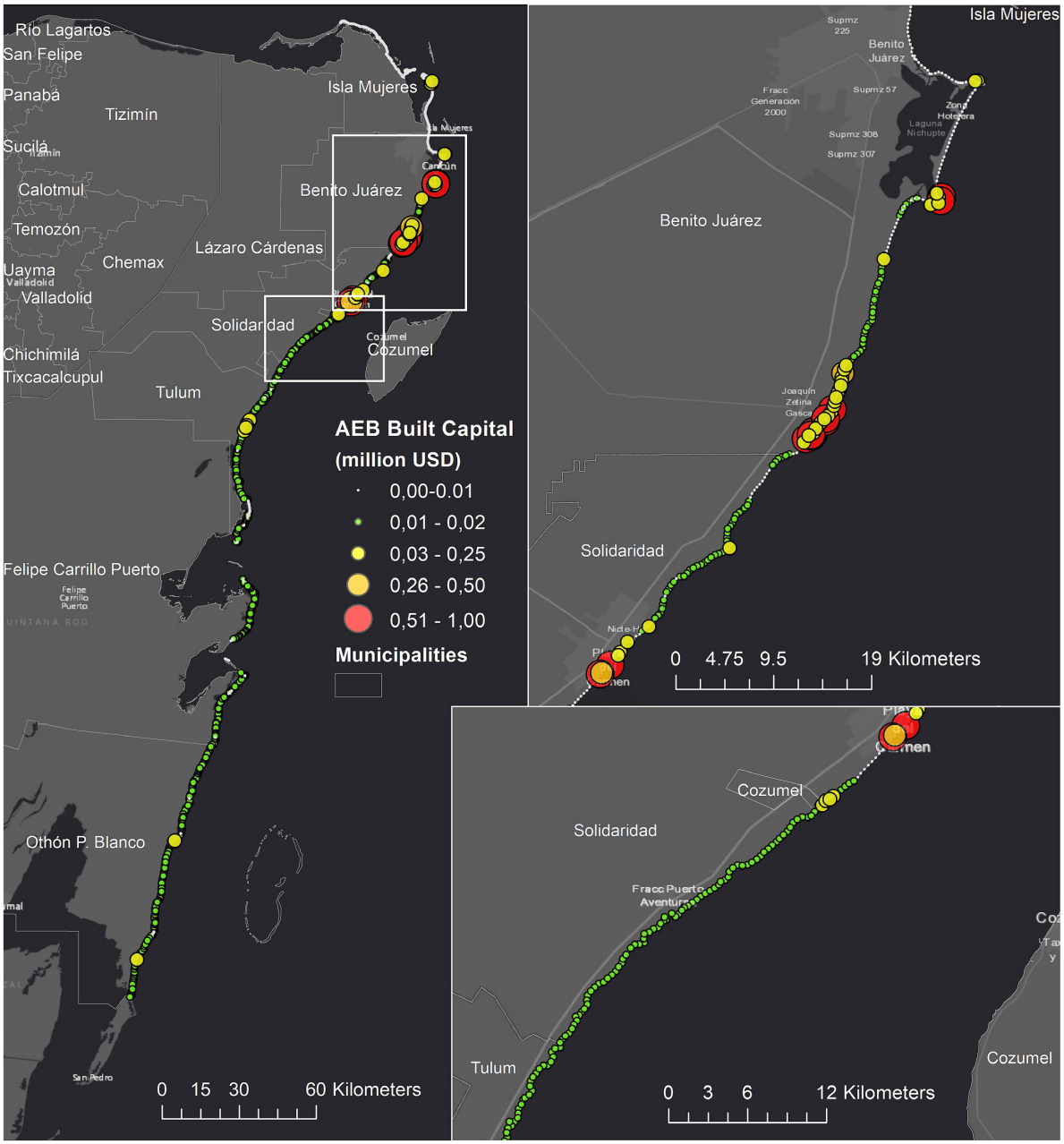

FIGURE 9 | Built capital protected from flooding per year. The points represent the annual expected benefit to built capital, in each coastal transect spaced 200-m along the coastline.

with larger waves, but they become less effective with higher water levels during the most intense and damaging events.

However, areas where reefs provide the most economic valuable protection do not always coincide with areas where people are protected the most, in particular for hotels, which for their location receive the largest protection from reefs. The spatial differences depend on the storm hazard (waves and sea levels); coral reefs presence, local water depth and friction; and the assets concentration on the coast. These spatial differences in flood prevention for the hotel infrastructure, the built capital, and people (**Figures 10–12**) differ, which has implications for coastal management and policy and may inform restoration strategies. These differences are relevant when determining where to maintain the natural protection offered by the reefs, for example through restoration, and who benefits most.

Explicit valuations of their protection services are particularly critical for coral reefs. As compared to other coastal ecosystems, quantifying their role in flood reduction require numerical models able to resolve complex processes at sufficient resolution (e.g., Quataert et al., 2015; Harris et al., 2018). Because reefs

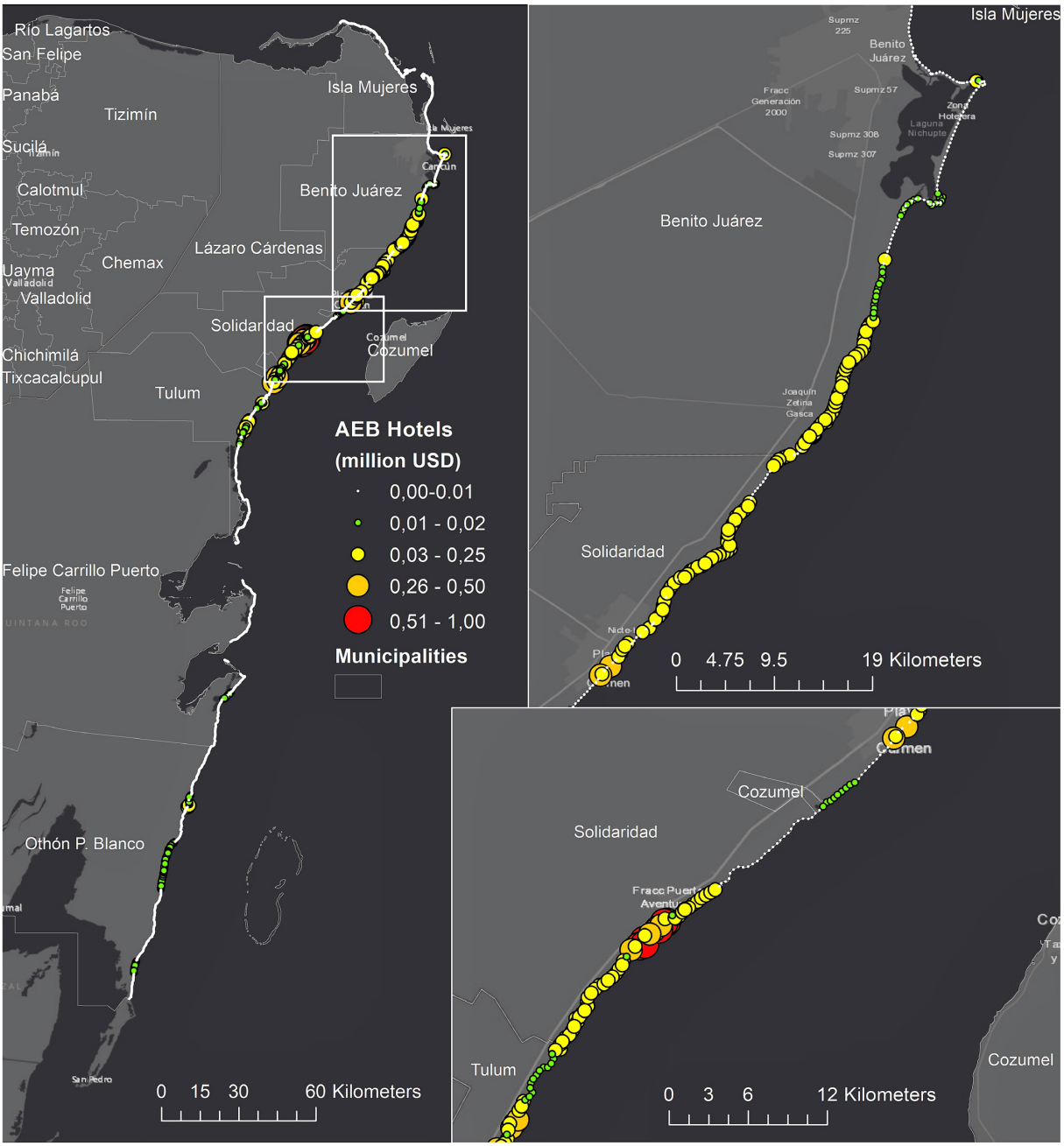

FIGURE 10 | Hotel capital protected from flooding per year. The points represent the annual expected benefit to hotels, in each coastal transect spaced 200-m along the coastline.

are under water, it has also been more challenging to make the connection between coral reef degradation and coastal risk increase than for other defenses or drivers of risk (e.g., Reguero et al., 2018a). For example, the loss of dunes, or intertidal habitats such as mangroves and marshes, is visibly apparent and hence communities recognize connections between habitat loss and flood damage. This has started to allow large-scale restoration practices and national policies. This study shows that spatial quantitative risk assessments are nowadays possible so reefs can be considered and maintained as a natural infrastructure for their services to communities and property.

Dunes also provide critical coastal protection in Quintana Roo. Topo-bathymetric data and the numerical modeling performed for the case of the coast of Quintana Roo, shows that, in general, when beaches have less protection from coral reefs, the dunes are higher and they are composed of coarser sand (Ruiz de Alegria-Arzaburu et al., 2013; Martínez et al., 2014). However, behind reefs, dunes are lower, and the sediment is finer

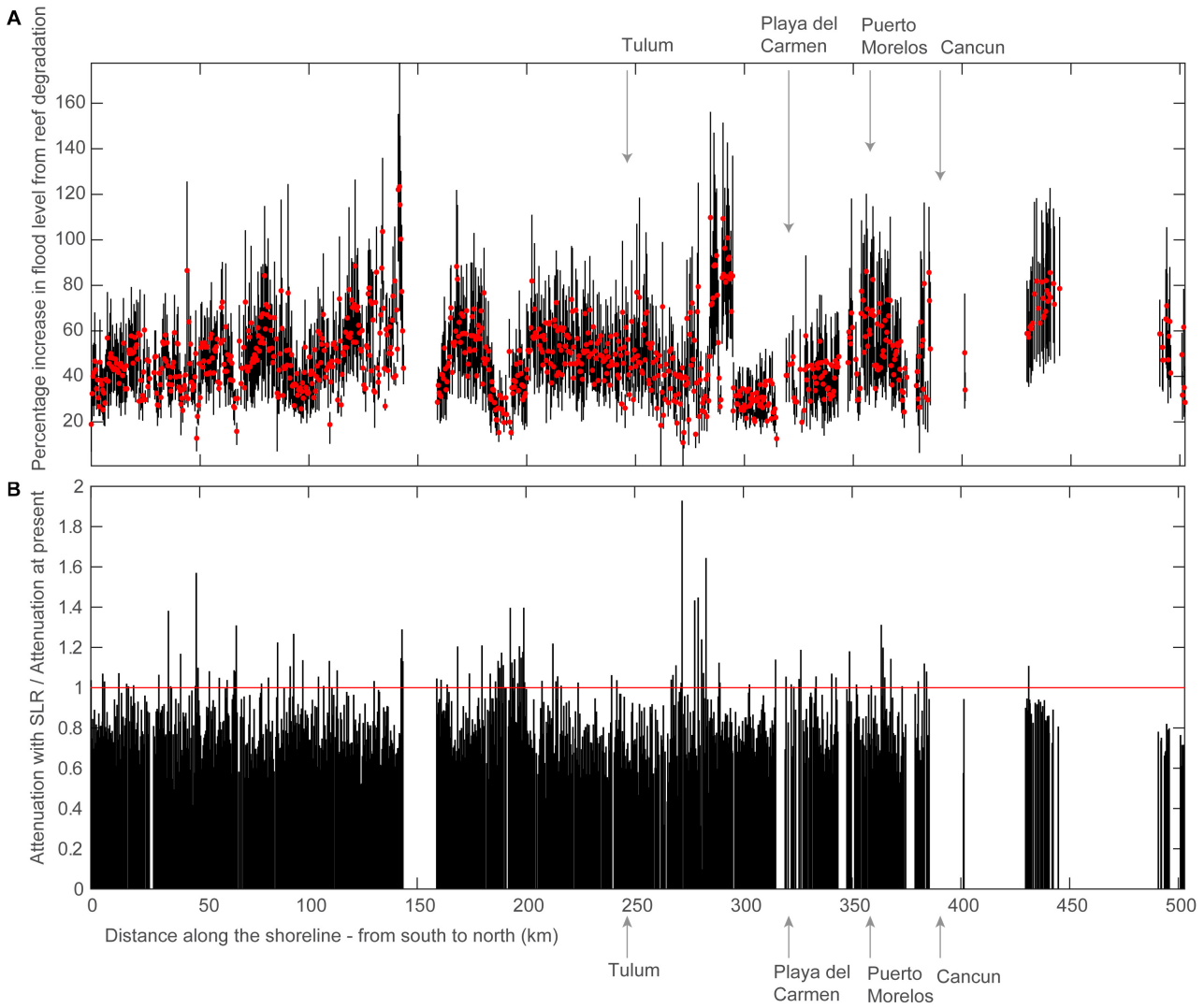

FIGURE 11 | Alongshore distribution in flood protection provided by coral reefs in Quintana Roo. **(a)** Flood reduction provided by the Mesoamerican Reef. The lines represent the range between the 25 and 75% percentiles of flood levels for each coastal transect. The red dots represent the mean value of flood reduction provided by the reef. **(b)** The ratio in flood reduction with sea-level rise (SRL) relative to present sea level. The local SLR was obtained from the mean value of the Representative Concentration Pathway 4.5 by the end of the 21st century. The gaps represent no reef sections.

(Ruíz Cavazos et al., 2010). In sections without reefs in Puerto Morelos, longshore sediment transport is more intense and hence maintaining the beach width requires more input of sand (James et al., 2019). This behavior has important implications for coastal management: if coral reef degradation reduces the effect of reefs in the surf zone (e.g., dissipation of wave energy), the sediment transport will intensify, and beaches will require more sand to be maintained and even larger volumes of sediment to build dunes to reduce risk.

The comparison of the risk reduction from dunes and coral reefs reveals also important takeaways. This is the first time a study assesses and compares these natural infrastructures in terms of their contribution to coastal damage prevention. Although the analysis for dunes can be considered less rigorous than for reefs, given limitations on data and the simplified assumptions on their protective mechanisms (e.g., no consideration of important factors such as vegetation effect and erosion of beach and dunes), the comparison provides interesting insights into the complementary of these natural defenses. First, we identified the protection dunes offer larger protection than reefs for storms with higher probabilities. However, in sections with reefs, the annual risk reduction benefit of reefs largely exceeds those from dunes. This is explained by the effect of reefs on reducing flooding but also changes in dune heights in sections with reefs. Granulometric analyses in the region have shown that dunes behind reefs tend to be lower and sediment finer because the reef protection reduces surf zone dynamics and the movement of sediment that can be mobilized by the wind to grow dunes (Ruíz Cavazos et al., 2010). These results point out that both features are part of a whole

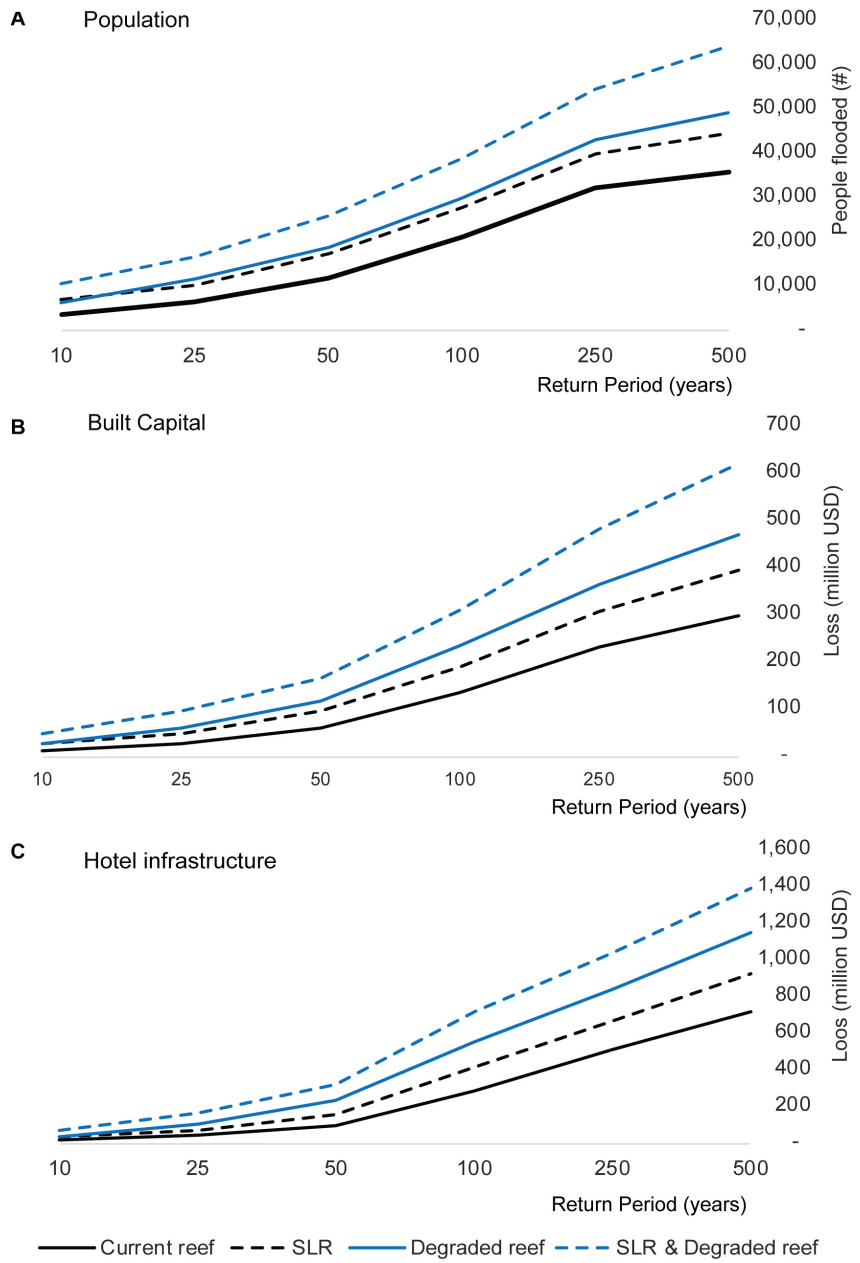

FIGURE 12 | Coastal risk increases with degradation of reefs and Sea-Level Rise (SLR). Risk is represented as **(a)** people flooded, **(b)** damages to built capital, and **(c)** damages to hotel infrastructure for various return periods. The risk from SLR is indicated by dashed lines. The local SLR was obtained from the mean value of the Representative Concentration Pathway 4.5 by the end of the 21st century. The risk from reef degradation is indicated in blue.

interconnected system and their location and properties are linked to each other.

This analysis also shows that these increases in coastal risk could be coupled with the significant impacts of a SLR and lead to compounding effects later in the century. We find that SLR increases notably the annual risk because it will produce greater impacts from storms. Furthermore, here we considered conservative estimates of SLR of ∼0.5 m, although the projected values by the end of the century could reach 1 m of SLR (Church et al., 2013). Furthermore, we demonstrated that in coral reef environments, the contribution of reef degradation to coastal risk can exceed the contribution of these increases due to SLR. However, adaptation strategies still put the main focus on SLR adaptation while losing this natural infrastructure can be as damaging or more. The effect of reef degradation on coastal risk could also be more aggravated considering recent research that shows increasing power in the ocean waves associated to global warming (Reguero et al., 2019), which could both affect

reef integrity but also enhance flooding. Therefore, the protective service of coral reefs becomes even more valuable with the rising threats of climate change.

These estimates also make a compelling case for present-day investments in coral reef management and conservation. We found benefits at certain sections of over 0.5 million USD per year in direct loss prevention. For reef sections of 200 m, this represents 2,500 USD per alongshore linear meter of reef. The median cost per meter of reef restoration has been estimated in 1,290 USD per meter from a global review of projects (Ferrario et al., 2014). This means that this natural infrastructure, if well-maintained, provides on an annual basis a risk reduction that is equally or more valuable than the cost of restoring the reef to maintain this protection. Furthermore, a constructed pilot case in Grenada of a hybrid restoration project that included the construction of artificial submerged structures cost ∼3,300 USD per alongshore linear meter (Reguero et al., 2018a). For this type of interventions, the annual benefits of reefs will also balance the costs over a 2-year period. In the MAR section of Quintana Roo, these results and approach can also help identify priority sites for conservation and restoration for coastal protection, either as 'stand-alone' solutions, or part of hybrid approaches that combine natural defenses, like coral reef restoration and dune rehabilitation, with built infrastructure.

Although the risk model was calibrated to represent the losses from historical storms, the results are affected by different uncertainty factors that are worth highlighting and could be improved with better data and modeling. The main factors for uncertainty include: offshore bathymetry data and parametric models for waves and surge definition; limited data on beach and dune topography and vegetation; a 90 m elevation model; lack of consideration of relevant process in dunes such as erosion by storms or wave runup attenuation by vegetation; simplified approach for flooding; asset distribution and economic value; and specific vulnerability curves for the buildings in the region. However, the analysis can also be considered conservative in the degree and the effects of reef degradation. Our scenarios do not assume that reefs will disappear altogether under a business-as-usual global climate emission scenario. The without reefs scenario assumes modest effects of degradation of 1 m change in reef profile (reef coral living layer and reef substrate), although similar flattening of coral reefs has been observed globally and could be accelerated by other threats in the MAR (Yates et al., 2017). Furthermore, this study did not analyze the effect of the reef on coastal erosion prevention, but this is likely to be a major benefit, particularly for the tourism sector. Research indicates that reefs can deter shoreline erosion through wave attenuation, energy dissipation and shifting, and sediment transport control (Reguero et al., 2018a).

Reefs provide a substantial first line of defense from coastal hazards and should be better managed for this benefit. Risk financing and insurance are critical in absorbing financial losses in the wake of disasters and natural catastrophes, and therefore, significant opportunities for restoration may lie in risk financing associated to the reefs' risk reduction service. Furthermore, in the wake of several destructive hurricanes in 2017, there is a growing need for policies that encourage the conservation and restoration of habitats that provide coastal protection, in the places where their degradation could represent significant increases in coastal risk to coastal communities and economies. Valuations of the protection services from coastal habitats in risk metrics as shown in this study could inform decisions to meet multiple objectives in risk reduction and environmental management.

Indeed, based on the MAR's risk reduction service in Mexico, the government and private industry are taking action to protect and provide innovative finance for coral reefs to mitigate coastal hazards and support tourism. In Quintana Roo, the government, hotel owners, The Nature Conservancy, and the local science community are piloting a pioneering strategy to confront these threats based on the socioeconomic benefits the coral reefs provide. This partnership has established a Coastal Zone Management Trust that can fund ongoing maintenance of coral reefs and beaches and purchase insurance to ensure these vital ecosystems are restored after extreme storms. This mechanism will provide financial protection to maintain the flood risk prevention reefs provide to people, built capital, and hotels in Quintana Roo. However, there is an opportunity to advance such innovations elsewhere too, through investment in risk financing for climate resilience (which could also include other ecosystem services). There is a large and growing pool of funding for natural infrastructure for risk reduction (Colgan et al., 2017), including innovative mechanisms for coral reefs (ICRI, 2018). New technologies and data can also inform these mechanisms and help monitor changes in the coastal landscape. However, only through risk-based valuations can coral reefs be incorporated in innovative risk finance to build the resilience of ecosystems and the economies they support.

DATA AVAILABILITY

All datasets generated for this study are included in the manuscript and/or the **Supplementary Files**.

AUTHOR CONTRIBUTIONS

BR, IL, and MB conceived and designed the analysis. BR and PD-S developed the methodology for economic exposure. AT and ME performed the exposure and geospatial analysis. BR and CS developed the reef modeling framework and simulations. BR, FS, RS, and MB discussed the results and contributed to the final manuscript discussion. BR wrote the manuscript. All authors provided critical feedback and helped shape the research, analysis and manuscript.

FUNDING

Funding for this work was provided by The Nature Conservancy and The Kingfisher Foundation.

ACKNOWLEDGMENTS

We sincerely thank the different organizations that provided data and information that enable this analysis, and the different donors and funding sources that supported this work. We especially thank different agencies from the Government of Mexico that provided crucial data for the analysis: 'Comisión Nacional para el Conocimiento y Uso de la Biodiversidad' (CONABIO), 'Instituto Nacional de Estadística y Geografía' (INEGI), and 'Centro Nacional de Prevención de Desastres' (CENAPRED). We also thank Sean Vitousek for the useful comments provided.

SUPPLEMENTARY MATERIAL

The Supplementary Material for this article can be found online at: https://www.frontiersin.org/articles/10.3389/feart.2019.00125/full#supplementary-material

REFERENCES

Alvarez-Filip, L., Dulvy, N. K., Gill, J. A., Côté, I. M., and Watkinson, A. R. (2009). Flattening of Caribbean coral reefs: region-wide declines in architectural complexity. *Proc. Biol. Sci.* 276, 3019–3025. doi: 10.1098/rspb.2009.0339

Aznar-Siguan, G., and Bresch, D. N. (2019). CLIMADA – a global weather and climate risk assessment platform. *Geosci. Model Dev. Discuss.* 2019, 1–18. doi: 10.5194/gmd-2018-338

Baldock, T. E., Golshani, A., Callaghan, D. P., Saunders, M. I., and Mumby, P. J. (2014). Impact of sea-level rise and coral mortality on the wave dynamics and wave forces on barrier reefs. *Mar. Pollut. Bull.* 83, 155–164. doi: 10.1016/j.marpolbul.2014.03.058

Barbier, E. B. (2015). Valuing the storm protection service of estuarine and coastal ecosystems. *Ecosyst. Serv.* 11, 32–38. doi: 10.1016/j.ecoser.2014.06.010

Beck, M. W., Losada, I. J., Menéndez, P., Reguero, B. G., Díaz-Simal, P., and Fernández, F. (2018). The global flood protection savings provided by coral reefs. *Nat. Commun.* 9:2186. doi: 10.1038/s41467-018-04568-z

Bellwood, D. R., Hughes, T. P., Folke, C., and Nystrom, M. (2004). Confronting the coral reef crisis. *Nature* 429, 827–833. doi: 10.1038/nature02691

Bretschneider, C. L. (1990). "Tropical cyclones," in *Handbook of Coastal & Ocean Engineering*, eds J. B. Herbich and C. L. Bretschneider (Houston: Gulf Pub. Co.), 249–303.

Briggs, S., Kennel, C. F., and Victor, D. G. (2015). Planetary vital signs. *Nat. Clim. Chang.* 5:969. doi: 10.1038/nclimate2828

Camus, P., Mendez, F. J., and Medina, R. (2011a). A hybrid efficient method to downscale wave climate to coastal areas. *Coast. Eng.* 58, 851–862. doi: 10.1016/j.coastaleng.2011.05.007

Camus, P., Mendez, F. J., Medina, R., and Cofiño, A. S. (2011b). Analysis of clustering and selection algorithms for the study of multivariate wave climate. *Coast. Eng.* 58, 453–462. doi: 10.1016/j.coastaleng.2011.02.003

Church, J. A., Clark, P. U., Cazenave, A., Gregory, J. M., Jevrejeva, S., Levermann, A., et al. (2013). "Sea level change," in *The Physical Science Basis: Contribution of Working Group I to the Fifth Assessment Report of the Intergovernmental Panel on Climate Change*, eds T. F. Stocker, D. Qin, G.-K. Plattner, and M. Tignor (Cambridge: Cambridge University Press).

Colgan, C. S., Beck, M. W., and Narayan, S. (2017). *Financing Natural Infrastructure for Coastal Flood Damage Reduction*. London: Lloyd's Tercentenary Research Foundation.

Dean, R. G., and Dalrymple, R. A. (1991). *Water Wave Mechanics for Engineers and Scientists*. Singapore: World Scientific.

Escalante-Mancera, E., Silva, R., Mendoza, E., Mariño-Tapia, I., and Ruiz-Renteria, F. (2009). Análisis de la variación del nivel del mar y de las corrientes inducidas por el huracán wilma en puerto morelos, quintana roo. *Rev. Ing. Hidráulica en México* 24, 111–126.

Escudero-Castillo, M., Felix-Delgado, A., Silva, R., Mariño-Tapia, I., and Mendoza, E. (2018). Beach erosion and loss of protection environmental services in Cancun. *Mexico. Ocean Coast. Manag.* 156, 183–197. doi: 10.1016/j.ocecoaman.2017.06.015

Escudero-Castillo, M., Mendoza, E., Silva, R., and Villatoro, M. (2014a). Comparative risk assessment at isla del carmen and cancun, mexico. *Coast. Eng. Proc.* 1:10. doi: 10.9753/icce.v34.management.10

Escudero-Castillo, M., Silva, R., and Mendoza, E. (2014b). Beach erosion driven by natural and human activity at isla del carmen barrier island, mexico. *J. Coast. Res.* 62–74. doi: 10.2112/SI71-008.1

Farr, T. G., Rosen, P. A., Caro, E., Crippen, R., Duren, R., Hensley, S., et al. (2007). The shuttle radar topography mission. *Rev. Geophys.* 45:33. doi: 10.1029/2005RG000183

Feagin, R. A., Furman, M., Salgado, K., Martinez, M. L., Innocenti, R. A., Eubanks, K., et al. (2019). The role of beach and sand dune vegetation in mediating wave run up erosion. *Estuar. Coast. Shelf Sci.* 219, 97–106. doi: 10.1016/j.ecss.2019.01.018

Ferrario, F., Beck, M. W., Storlazzi, C. D., Micheli, F., Shepard, C. C., and Airoldi, L. (2014). The effectiveness of coral reefs for coastal hazard risk reduction and adaptation. *Nat. Commun.* 5:3794. doi: 10.1038/ncomms4794

Graham, N. A. J., Jennings, S., MacNeil, M. A., Mouillot, D., and Wilson, S. K. (2015). Predicting climate-driven regime shifts versus rebound potential in coral reefs. *Nature* 518, 94–97. doi: 10.1038/nature14140

Guanche, Y., Camus, P., Guanche, R., Mendez, F. J., and Medina, R. (2013). A simplified method to downscale wave dynamics on vertical breakwaters. *Coast. Eng.* 71, 68–77. doi: 10.1016/j.coastaleng.2012.08.001

Guannel, G., Arkema, K., Ruggiero, P., and Verutes, G. (2016). The power of three: coral reefs, seagrasses and mangroves protect coastal regions and increase their resilience. *PLoS One* 11:e0158094. doi: 10.1371/journal.pone.0158094

Hallegatte, S., Green, C., Nicholls, R. J., and Corfee-Morlot, J. (2013). Future flood losses in major coastal cities. *Nat. Clim. Chang.* 3, 802–806. doi: 10.1038/nclimate1979

Harris, D. L., Rovere, A., Casella, E., Power, H., Canavesio, R., Collin, A., et al. (2018). Coral reef structural complexity provides important coastal protection from waves under rising sea levels. *Sci. Adv.* 4:eaao4350. doi: 10.1126/sciadv.aao4350

ICRI (2018). *Innovations for Coral Finance*. Tokyo: ICRI.

INEGI (2015). *Principales Resultados de la Encuesta Intercensal 2015*. Mexico: Instituto nacional de estadistica y geografia.

James, R. K., Silva, R., van Tussenbroek, B. I., Escudero-Castillo, M., Mariño-Tapia, I., Dijkstra, H. A., et al. (2019). Maintaining tropical beaches with seagrass and algae: a promising alternative to engineering solutions. *BioScience* 69, 136–142. doi: 10.1093/biosci/biy154

Lloyd, C. T., Sorichetta, A., and Tatem, A. J. (2017). High resolution global gridded data for use in population studies. *Sci. Data* 4:170001. doi: 10.1038/sdata.2017.1

Lowe, R. J., Falter, J. L., Bandet, M. D., Pawlak, G., Atkinson, M. J., Monismith, S. G., et al. (2005). Spectral wave dissipation over a barrier reef. *J. Geophys. Res. Ocean* 110, 5–20. doi: 10.1029/2004JC002711

Martínez, M. L., Moreno-Casasola, P., Espejel, I., Orocio Jimenez, O. A., and Infante Mata, N. (2014). *Diagnóstico General de las Dunas Costeras de México*. México, D.F: Comisión Nacional Forestal.

Mcfield, M., Kramer, P., Alvarez-Filip, L., Drysdale, I., Marisol, R.-F., Giro, A., et al. (2018). *2018 Mesoamerican Reef Report Card*. doi: 10.13140/RG.2.2.19679.36005

Mechler, R., and Schinko, T. (2016). Identifying the policy space for climate loss and damage. *Science* 354, 290–292. doi: 10.1126/science.aag2514

Mendoza, E., Silva, R., Enriquez-Ortiz, C., Mariño-Tapia, I., and Felix, A. (2015). "Analysis of the hazards and vulnerability of the cancun beach system," in *Extreme Events: Observations, Modeling, and Economics, Chapter: Analysis of the Hazards and Vulnerability of the Cancun Beach System*, eds M. Chavez, M. Ghil, and J. Urrutia-Fucugauchi (Hoboken: John Wiley & Sons, Inc), doi: 10.1002/9781119157052.ch10

Menéndez, P., Losada, I. J., Beck, M. W., Torres-Ortega, S., Espejo, A., Narayan, S., et al. (2018). Valuing the protection services of mangroves at national scale: the Philippines. *Ecosyst. Serv.* 34, 24–36. doi: 10.1016/j.ecoser.2018.09.005

Meza-Padilla, R., Appendini, C., and Pedrozo-Acuña, A. (2015). Hurricane-induced waves and storm surge modeling for the Mexican coast. *Ocean Dyn.* 65, 1199–1211. doi: 10.1007/s10236-015-0861-867

Monismith, S. G. (2007). Hydrodynamics of coral reefs. *Annu. Rev. Fluid Mech.* 39, 37–55. doi: 10.1146/annurev.fluid.38.050304.092125

Narayan, S., Beck, M. W., Wilson, P., Thomas, C. J., Guerrero, A., Shepard, C. C., et al. (2017). The value of coastal wetlands for flood damage reduction in the Northeastern USA. *Sci. Rep.* 7:9463. doi: 10.1038/s41598-017-09269-z

Neumann, B., Vafeidis, A. T., Zimmermann, J., and Nicholls, R. J. (2015). Future coastal population growth and exposure to sea-level rise and coastal flooding - a global assessment. *PLoS One* 10:e0118571. doi: 10.1371/journal.pone.0118571

National Oceanic, and Atmospheric Administration [NOAA] (2006). *ETOPO2v2 Global Gridded 2-minute Database*. Silver Spring, MD: NOAA.

Perry, C. T., Alvarez-Filip, L., Graham, N. A. J., Mumby, P. J., Wilson, S. K., Kench, P. S., et al. (2018). Loss of coral reef growth capacity to track future increases in sea level. *Nature* 558, 396–400. doi: 10.1038/s41586-018-0194-z

Posada, G., Silva, R., and de Brye, S. (2008). Three dimensional hydrodynamic model with multiquadtree meshes. *Am. J. Environ. Sci.* 4, 245–258. doi: 10.3844/ajessp.2008.245.258

Quataert, E., Storlazzi, C., van Rooijen, A., Cheriton, O., and van Dongeren, A. (2015). The influence of coral reefs and climate change on wave-driven flooding of tropical coastlines. *Geophys. Res. Lett.* 42, 6407–6415. doi: 10.1002/2015GL064861

Rabus, B., Eineder, M., Roth, A., and Bamler, R. (2003). The shuttle radar topography mission—a new class of digital elevation models acquired by spaceborne radar. *ISPRS J. Photogramm. Remote Sens.* 57, 241–262. doi: 10.1016/S0924-2716(02)00124-127

Reguero, B. G., Beck, M. W., Agostini, V. N., Kramer, P., and Hancock, B. (2018a). Coral reefs for coastal protection: a new methodological approach and engineering case study in Grenada. *J. Environ. Manage.* 210, 146–161. doi: 10.1016/j.jenvman.2018.01.024

Reguero, B. G., Beck, M. W., Bresch, D. N., Calil, J., and Meliane, I. (2018b). Comparing the cost effectiveness of nature-based and coastal adaptation: a case study from the gulf coast of the United States. *PLoS One* 13:e0192132. doi: 10.1371/journal.pone.0192132

Reguero, B. G., Losada, I. J., Díaz-Simal, P., Méndez, F. J., and Beck, M. W. (2015). Effects of climate change on exposure to coastal flooding in latin america and the caribbean. *PLoS One* 10:e0133409. doi: 10.1371/journal.pone.0133409

Reguero, B. G., Losada, I. J., and Méndez, F. J. (2019). A recent increase in global wave power as a consequence of oceanic warming. *Nat. Commun.* 10:205. doi: 10.1038/s41467-018-08066-8060

Resio, D. T., and Irish, J. L. (2015). Tropical cyclone storm surge risk. *Curr. Clim. Chang. Reports* 1, 74–84. doi: 10.1007/s40641-015-0011-19

Ruíz Cavazos, D., Ruíz Martínez, G., Mendoza, E., and Silva, R. (2010). *Distribución del Sedimento en las Costas de Yucatán y Quintana Roo XXI Congreso Nacional de Hidráulica*. Guadalajara: AMH.

Ruiz de Alegria-Arzaburu, A., Mariño-Tapia, I., Enriquez, C., Silva, R., and González-Leija, M. (2013). The role of fringing coral reefs on beach morphodynamics. *Geomorphology* 198, 69–83. doi: 10.1016/j.geomorph.2013.05.013

Samonte-Tan, G. P. B., White, A. T., Tercero, M. A., Diviva, J., Tabara, E., and Caballes, C. (2007). Economic valuation of coastal and marine resources: bohol marine triangle. *Philippines. Coast. Manag.* 35, 319–338. doi: 10.1080/08920750601169634

Scawthorn, C., Blais, N., Seligson, H., Tate, E., Mifflin, E., Thomas, W., et al. (2006a). HAZUS-MH flood loss estimation methodology. I: overview and flood hazard characterization. *Nat. Hazards Rev.* 7, 60–71. doi: 10.1061/(ASCE)1527-698820067:2(60)

Scawthorn, C., Flores, P., Blais, N., Seligson, H., Tate, E., Chang, S., et al. (2006b). HAZUS-MH flood loss estimation methodology. II. damage and loss assessment. *Nat. Hazards Rev.* 7, 72–81. doi: 10.1061/(ASCE)1527-698820067:2(72)

Silva, R., Mendoza, E., Escalante, E., Mariño, I., and Ruiz, F. (2009). Oleaje inducido por el huracán wilma en puerto morelos, quintana roo, méxico. *Rev. Ing. Hidraúlica en México XXIV* 24, 93–109.

Silva, R., Martínez, M. L., Hesp, P. A., Catalán, P., Osorio, A., Martell, R., et al. (2014). Present and future challenges of coastal erosion in latin America. *J. Coast. Res.* 71, 1–16. doi: 10.2112/SI71-001.1

Storlazzi, C. D., Gingerich, S. B., van Dongeren, A., Cheriton, O. M., Swarzenski, P. W., Quataert, E., et al. (2018). Most atolls will be uninhabitable by the mid-21st century because of sea-level rise exacerbating wave-driven flooding. *Sci. Adv.* 4:eaa9741. doi: 10.1126/sciadv.aap9741

Storlazzi, C., Reguero, B., Lowe, E., Shope, J., Gibbs, A., Beck, M., et al. (2017). Rigorously valuing the role of coral reefs in coastal protection: an example from Maui. *Hawaii, USA. Coast. Dyn.* 2017:035.

UNFCCC (2013). *Warsaw International Mechanism for Loss and Damage*. Bonn: UNFCCC.

UNFCCC (2015). *Paris Agreement*. Bonn: UNFCCC

UNISDR (2015). *2015 Global Assessment Report on Disaster Risk Reduction*. Geneva: UNISDR

Valdez, G. D. (2010). *Análisis del Peligro por Marea de Tormenta en el Golfo de México. Tesis Maestría (Maestría en Ingeniería Civil)-UNAM*. México: Instituto de Ingeniería.

van Dongeren, A., Lowe, R., Pomeroy, A., Trang, D. M., Roelvink, D., Symonds, G., et al. (2013). Numerical modeling of low-frequency wave dynamics over a fringing coral reef. *Coast. Eng.* 73, 178–190. doi: 10.1016/j.coastaleng.2012.11.004

Wong, P. P., Losada, I. J., Gattuso, J.-P., Hinkel, J., Khattabi, A., McInnes, K. L., et al. (2014). "Coastal systems and low-lying areas," in *Climate Change 2014: Impacts, Adaptation, and Vulnerability. Part A:Global and Sectoral Aspects. Contribution of Working Group II to the Fifth Assessment Report of theIntergovernmental Panel on Climate Change*, eds V. R. Barros, D. J. Dokken, K. J. Mach, M. D. Mastrandrea, T. E. Bilir, M. Chatterjee, (Cambridge: Cambridge University Press), 361–409.

Yates, K. K., Zawada, D. G., Smiley, N. A., and Tiling-Range, G. (2017). Divergence of seafloor elevation and sea level rise in coral reef ecosystems. *Biogeosciences* 14, 1739–1772. doi: 10.5194/bg-14-1739-2017

Young, I. (1988). Parametric hurricane wave prediction model. *J. Waterw. Port Coastal Ocean Eng.* 114, 637–652. doi: 10.1061/(ASCE)0733-950X1988114:5(637)

Conflict of Interest Statement: The authors declare that the research was conducted in the absence of any commercial or financial relationships that could be construed as a potential conflict of interest.

frontiers in Earth Science

ORIGINAL RESEARCH
published: 31 July 2019
doi: 10.3389/feart.2019.00187

Multi-Decadal to Short-Term Beach and Shoreline Mobility in a Complex River-Mouth Environment Affected by Mud From the Amazon

Morgane Jolivet[1], Edward J. Anthony[1,2], Antoine Gardel[1] and Guillaume Brunier[3]*

[1] USR LEEISA, CNRS, Ifremer, Université de Guyane, Cayenne, French Guiana, [2] UM 34 CEREGE, Aix-Marseille University, CNRS, IRD, INRA, Collège de France, Aix-en-Provence, France, [3] Laboratoire des Sciences de l'Environnement Marin (LEMAR), UMR 6539 (UBO/CNRS/IRD/Ifremer), Institut Universitaire Européen de la Mer, Plouzané, France

On the 1500 km-long mud-dominated Guianas coast of South America, between the mouths of the two mega-rivers, the Amazon and the Orinoco, debouch numerous small rivers draining the humid tropical/equatorial Guiana Shield. The geomorphic development of the mouths of these rivers reflects interactions among water discharge, fluvial sediment load, and the alongshore migration of Amazon-derived mud banks alternating with inter-bank areas. The mouth of the Maroni River, astride the French Guiana-Suriname border, shows advanced estuarine infill and geomorphic development characterized by a western (downdrift) side comprising numerous recent cheniers and an eastern (updrift) side bound by an old (>2000 years B.P.) chenier. A multi-decadal analysis of the beach bounding this chenier shows little net overall mobility notwithstanding significant decadal to sub-decadal variation. The overall stability reflects the diversion of sand supply from the Maroni River toward the downdrift coast and limited sand supply by the smaller Mana River further east, and the south bank of which was contiguous with this beach. The variability in beach multi-decadal mobility reflects the influence, on waves, of alongshore-migrating banks (strong wave dissipation, limited beach mobility) and inter-bank areas (limited wave dissipation, larger beach mobility), highlighted by a comparison, in the current bank phase, of offshore and inshore waves. Erosion of the beach between 2011 and 2017 coincides with the sealing of the mouth of the Mana by muddy progradation in 2011 and mouth relocation several kilometers eastward. The morphodynamics of the beach and shorter-term fluctuations in budget are related to: (1) interaction with estuarine sand dunes mobilized by strong tidal currents on the adjacent shallow shoreface, (2) the influence of the Maroni channel, and (3) rapid encroachment of the leading edge of the shore-attached mud bank on the eastern part of the beach. The beach morphodynamics and evolution highlight, thus, embedded levels of influence: the Maroni at the local scale, and the net westward sediment-transport system and bank and inter-bank alternations that affect the Guianas coast at a regional scale. The recent erosion poses a threat to the local communities by reducing beach space available for recreation and turtle-nesting.

Keywords: river mouth, estuarine beach, Amazon-Orinoco coast, mud bank, beach morphodynamics

OPEN ACCESS

Edited by:
Derek W. T. Jackson, Ulster University, United Kingdom

Reviewed by:
Rory Patrick Flood, Queen's University Belfast, United Kingdom
Christopher John Hein, College of William & Mary, United States

****Correspondence:***
Morgane Jolivet
morgane.jolivet@etu.univ-guyane.fr

Specialty section:
This article was submitted to Geohazards and Georisks, a section of the journal Frontiers in Earth Science

Received: *21 May 2019*
Accepted: *03 July 2019*
Published: *31 July 2019*

Citation:
Jolivet M, Anthony EJ, Gardel A and Brunier G (2019) Multi-Decadal to Short-Term Beach and Shoreline Mobility in a Complex River-Mouth Environment Affected by Mud From the Amazon. Front. Earth Sci. 7:187. doi: 10.3389/feart.2019.00187

INTRODUCTION

The Guianas coast of South America is a unique system in the world characterized by large-scale muddy sedimentation in spite of the exposure of the coast to waves from the Atlantic (**Figure 1A**). The mud is organized into a series of large banks that migrate along the coast under the influence of waves and currents, separated by "inter-bank" zones (Anthony et al., 2010). In this system, the inner part of a mud bank can weld onto the coast, creating new land that can be rapidly colonized by mangroves, whereas in inter-bank zones, higher incident wave energy can lead to intense shoreline erosion. Inter-bank erosion is mitigated, where beaches (cheniers) composed of sand and/or shells occur (Augustinus, 1978; Augustinus et al., 1989; Prost, 1989; Anthony et al., 2019). Cheniers are wave-reworked coarse-grained deposits resting stratigraphically on a muddy substrate (Otvos, 2018).

There has been significant progress in unraveling the characteristics of mud banks (Abascal Zorrilla et al., 2018; Abascal Zorrilla, 2019) and their interaction with the Amazon-Orinoco coast (Anthony et al., 2010, 2014). Within this overwhelmingly mud-and mangrove-dominated 1500 km-long coast, cheniers are restricted in their development, and the mechanisms and pathways of sand supply responsible for their formation are still not clear because of this pervasive influence of mud. Cheniers are, nevertheless, an important resource. In addition to their role in coastal protection, they serve as zones of rural settlements and urban development, and as pathways for road and communication networks. Active cheniers assure recreational and ecological functions and services, notably by providing nesting sites for marine turtles and habitat for shorebirds and other wildlife. They also provide ready access to the sea for fishermen in this mud-dominated setting.

Although sandy deposits, and locally shells, may form secondary sources reworked from inner shoreface deposits or from pre-existing cheniers attacked by erosion, the primary source of sand for the development of the cheniers on the Guianas coastal plain is the local rivers (Anthony et al., 2013, 2014). Between the two big Amazon and Orinoco Rivers occur numerous smaller rivers (**Figure 1A**) reflecting the rainy tropical/equatorial catchments draining the Guiana Shield. In French Guiana, the heavy-mineral signatures of beach (chenier) sands are typical of the basement rocks drained by these local rivers (Pujos et al., 2000). The capacity of these rivers to supply sand to the coast depends on their ability to limit large-scale sedimentation of Amazon mud at their mouths. The smaller river mouths are commonly diverted by capes built from mud supplied by the Amazon (Augustinus, 1978; Plaziat and Augustinus, 2004; Gardel et al., 2019). Beaches are rare on this muddy coast and are systematically found downdrift (west to northwest) of river mouths on the east-west to southeast-northwest trending Amazon-Orinoco coast, thus highlighting the importance of the regional longshore sand transport induced by waves from a relatively constant north to east quadrant (**Figure 2**). These beaches (cheniers) commonly run alongshore for a few kilometers to tens of kilometers, before petering out to give way to the more common muddy mangrove-colonized shorelines. The variability in the lengths of such cheniers reflects sand supply volume from updrift and interruptions by mud-bank attachment to the shore that lead to chenier isolation inland (Anthony et al., 2019). Coasts updrift of many river mouths are generally, thus, characterized by muddy shorelines impinging directly on the east (or southeast) bank, forming a continuous mangrove-colonized fringe that may line the estuarine reaches of the Guiana rivers for several kilometers upstream.

Among the larger rivers is the Maroni (68,700 km^2; mean discharge: 1700 m^3/s), between French Guiana and Suriname, characterized by a large funnel-shaped, sand-filled shallow estuary mouth, reflecting significant fluvial bedload supply (**Figure 1B**). The Maroni is a good example of a river that has supplied sand for downdrift sandy chenier construction in Suriname (Anthony et al., 2019). The east shore of the Maroni exhibits, however, a sandy beach fronting the village of Yalimapo, in contrast to the common pattern of pervasive muddy sedimentation. This beach was considered as one of the most important turtle-nesting sites on the Guianas coast (Peron, 2014), and still is the most important recreational beach in western French Guiana. This beach was hitherto linked to the south bank of the Mana River (**Figure 1B**), a smaller river (catchment size: 12,090 km^2; mean discharge: 320 m^3/s) diverted westward by a large muddy cape, Pointe Isère (Plaziat and Augustinus, 2004) that has been largely eroded over the last five decades (Jolivet et al., 2019). The gradual impingement of a large mud bank has been accompanied, in 2011, by sealing of the ancestral mouth of the Mana by mud and deflection of the present mouth of this river several kilometers east of the village of Awala, which is now completely isolated from the sea by the shore-attached remnant of Pointe Isère (**Figure 1B**).

In this paper, we analyze, from a combination of remote sensing and field datasets, this updrift sandy beach and show how its morphodynamics and short (seasonal) to medium-term (multi-decadal) evolution have been modulated by the interplay of fluvial sand supply, river-mouth processes, mud-bank sedimentation, updrift muddy erosion of Pointe Isère, and wave dampening. The study highlights the morphodynamic and sedimentary interactions between a sandy beach and estuarine infill. It also brings out complex multi-decadal regional shoreline change in a context associated with bank sedimentation and inter-bank erosion under the overarching influence of mud supply from the Amazon.

MATERIALS AND METHODS

We combined a mesoscale temporal (1955–2017) analysis of shoreline change in the vicinity of the river mouth with a short-term approach based on field experiments conducted in 2017–2018 (**Figure 3**). Except where specified otherwise, all the data generated by the study were archived and analyzed using MATLAB software.

Multi-Decadal Shoreline Change

Multi-decadal shoreline change covering the beach (**Figure 3B**) was analyzed from ten very-high resolution (0.4–1.5 m) aerial photographs covering 56 years (1955–2012). These included

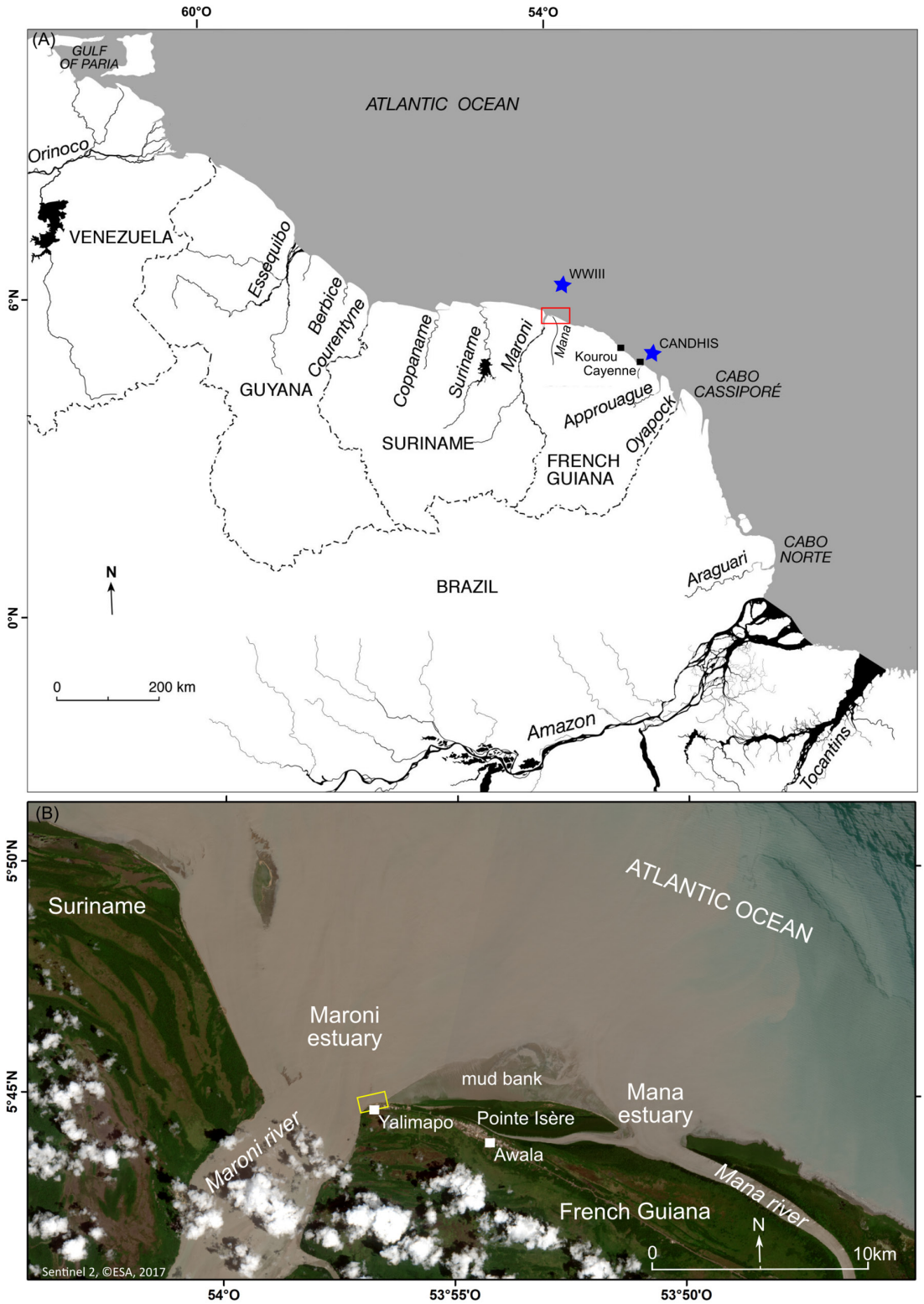

FIGURE 1 | (A) Map of the Guianas coast between the deltas of the Amazon and Orinoco Rivers, and study area (red box). Also shown are several smaller rivers, among which the Maroni, and the Mana in western French Guiana. **(B)** SENTINEL 2 satellite image showing a close-up view of the mouth of the Maroni River and the neighboring Mana River, the former mouth of which (located at Awala) has been sealed by shore-attached mud following erosion of much of Pointe Isère, a mud cape extant since at least the mid-19th century. Yellow box shows aerial and ground photos on **Figure 5**.

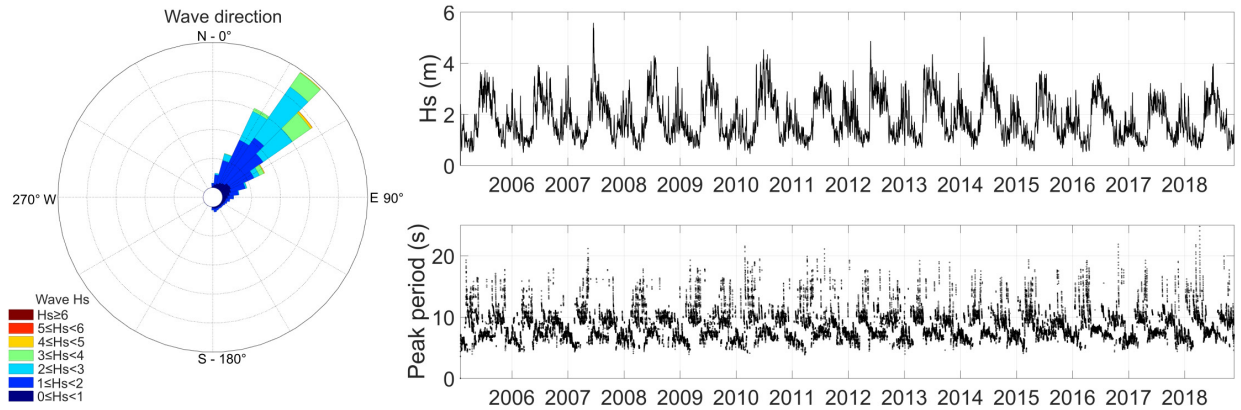

FIGURE 2 | Three hour averages of wave-climate parameters, H_s and T_s, derived from a 13 year (2006–2018) record of data extracted from the Wave Watch III model (WWIII, NOAA) for a point (5°54′14.85′′N, 53°48′7.96′′W) 20 km offshore of the mouth of the Maroni (see **Figure 1A**).

three ortho-photographs and seven photographs in silver-print and digital format. This dataset was complemented for the most recent period (2011–2017) by four PLEIADE and SPOT6/7 satellite images, both with a very high resolution of 50 cm (**Supplementary Table S1**). The aerial photographs were georeferenced using a second-order polynomial transformation following generation of >500 ground control points (GCPs) and were then merged in order to obtain orthomosaics. As a reference, we used the Universal Transverse Mercator zone 22 North on the World Geodetic System 1984 ellipsoid. To quantify shoreline change, the limit between land and sea was first identified using beach sand vegetation, which stands out in good contrast with non-vegetated areas on French Guiana beaches (Anthony et al., 2002). This delimitation was facilitated by the high resolution of the images. Statistical analyses of shoreline variations were then conducted using the Digital Shoreline Analysis System DSAS v4.4 tool with Arcgis (Thieler et al., 2017). The analysis consisted of a total of 500 transects spaced 10 m apart and drawn perpendicular to a baseline (**Figure 3B**). The accuracy of the derived shoreline changes depends on a combination of errors from image resolution (50 cm), vectoring (50 cm), and geo-referencing. Given the large number (10–15) of images for each date, we calculated the average of the root mean square errors derived from geo-referencing for each date, and obtained a global mean of 8 m for all dates. We then combined these three sources of error to obtain a total accuracy rounded to ±10 m. The recent period of observation (post 2011) corresponded to one of gradual impingement of a large mud bank migrating westwards toward Suriname (Jolivet et al., 2019). The leading edge of this shore-welded mud was determined from the satellite images.

Field Surveys

River-Mouth Bathymetric Surveys

A bathymetric survey of the entire Maroni estuary was conducted in May 2017 (**Figure 3A**) using a Valeport Midas echosounder with a single beam dual-frequency (33–210 kH) and integrated DGPS. The GPS precision is ±2 m and that of the echosounder 0.01 m. Hydromagic software was used for synchronization of the data with the GPS positions. The survey was conducted along transects across the estuary at a spacing of 2 km, resulting in the generation of a digital elevation model (DEM) with 200 m-cells. The transect spacing was reduced to 40 m in a 2.5 km-wide zone offshore of Yalimapo, resulting in a DEM with 80 m cells (**Figure 3A**). Two bathymetric surveys were further conducted in April and October 2018 based on transects spaced 15–45 m along the beach and running offshore for 200–300 m (**Figure 3B**). The echosounder was synchronized with RTK-GPS with ±1 to 2 cm for X, Y coordinates and ±2 to 3 cm for the Z coordinate. From the corrected data, DEMs with 20 m-cells were computed using the ANUDEM interpolation (Hutchinson et al., 2011).

Beach Photogrammetric Surveys

Four photogrammetric surveys, aimed at highlighting beach morphological changes, sediment transport patterns, and short-term fluctuations in the beach sediment budget, were conducted using a motorized ultralight aircraft on May 29, June 28, September 11, and November 21, 2018 (**Figure 3B**). The frequency was designed to capture seasonal beach changes. In order to obtain as large a spatial coverage as possible (notably including the beach shoreface) all the surveys were conducted during spring low tides. Aerial photographs were obtained with a Sony Alpha7R camera with a 32 mega-pixel capacity, fixed on the wing of a motorized ultralight. Ground-size pixels, ground distances, and numbers of photographs per survey are shown in **Supplementary Table S2**.

The images acquired were analyzed using the structure-from-Motion (SfM) workflow (Westoby et al., 2012), with stereo pair-alignment based on GCPs deployed on the beach. The GCPs were made of 50 × 50 cm strips of linoleum painted with a black and white checker pattern, and their centers were accurately geo-referenced with a Trimble Real Time Kinetics (RTK) DGPS. The SfM-photogrammetry workflow was operated using Agisoft Photoscan Professional Software and the dense point cloud processed with CloudCompare free software. The coordinates of the GCPs were used in the dense point cloud construction to obtain X, Y, Z references. We adopted the

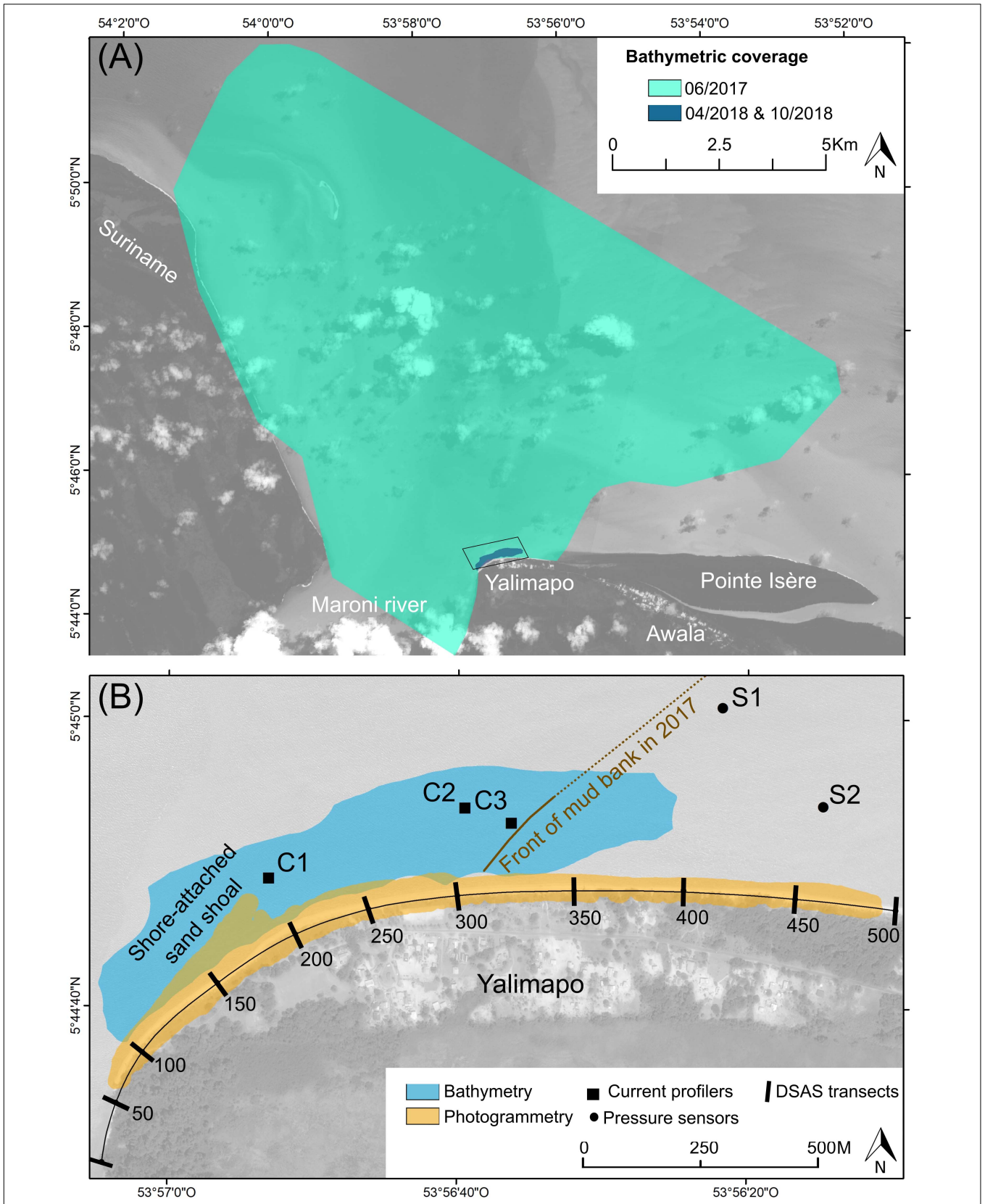

FIGURE 3 | Map of the Maroni estuary showing area of bathymetric coverages in 2017 and location of study area (rectangle) **(A)**; instrument deployment points, transects of multi-decadal (1955–2017) shoreline analysis, and areas of photogrammetric and bathymetric coverages in 2018 **(B)**.

Universal Transverse Mercator zone 22 North on the World Geodetic System 1984 ellipsoid as our project coordinate system. We obtained 4 DEMs with a 0.50 cm optimal resolution, and compared them for the quantification of temporal changes in morphology and sediment budgets.

In order to assess the quality of our DEMs, elevations were obtained from ground truth points (GTPs) and transects using RTK-DGPS (**Supplementary Table S2**). We used the same linoleum strips for the GTPs as those used for the GCPs, but the GTP and transect data were not used in the SfM workflow for DEM construction. The RTK base station was deployed on a IGN (French ordnance datum) benchmark, with an *X*, *Y* error of 5 cm and a *Z* error of 0.5 cm. The constructor error margin for the RTK-DGPS is ±1 to 2 cm for *X*, *Y* coordinates and ±2 to 3 cm for the *Z* coordinate. The comparison between our GTPs and control transects with our DEMs highlight errors close to 5 cm for *Z* (**Figure 3**). We applied a total error margin, inclusive of the RTK-DGPS error, of 5 cm to our DEM results. Beach profiles and DEM differentials, named differences of DEMs (DoDs), were established from the 2D and 3D data yielded by these surveys. We did not collect data on beach grain-size characteristics. Peron (2014) conducted a detailed analysis of grain sizes on the beach between Awala and Yalimapo, and showed a fine to coarse sand range largely dominated by quartz (>90%).

Wave and Current Measurements

In order to monitor the wave conditions prevailing over the estuarine beach shoreface, two NKE–SP2T pressure sensors (S1, S2) were deployed (**Figure 3B**) from 10/09/2018 to 15/09/2018 in the course of a spring-to-neap tide cycle on a transect running from the intertidal zone to subtidal shoreface-attached mud. The sensors sampled continuously at 2 Hz. Wave characteristics were evaluated using linear wave theory which is commonly employed for wind waves in shallow water. Wave spectra were calculated over bursts of 20 min using Fast Fourier transforms. A correction factor was applied with a cutoff at 0.5 Hz to account for the non-hydrostatic pressure field. For each burst, significant wave heights (Hs) and peak periods (Tp) were calculated in the spectral window [0.02; 0.5] Hz. A limit of 0.05 Hz was set between the gravity and infra-gravity wave domains. The pressure sensor accuracy is 0.02 m, and wave heights under this value were neglected.

There are no offshore wave data available in the study area. We resorted to wave records (June 2016 to May 2018, but with gaps) from a buoy deployed off Cayenne, 205 km east of the mouth of the Maroni (**Figure 1A**), beyond the shelf zone of mud-bank influence, by CANDHIS, the French National In Situ Wave Data Archive (Centre d'Archivage National des Données de Houle In Situ[1]).

In order to gauge the influence of the Maroni estuary and tidal currents on the shoreface of the beach, we measured current velocities from 07/09/2017 to 08/09/2017. Three Nortek Aquadopp current profilers were deployed off the beach (**Figure 3B**). C1 was deployed in a side-looking position 60 cm above the bed at the edge of the main Maroni channel cutting across the large sand bank that has largely infilled the estuary. C2 and C3 were deployed further east over the estuarine sand bank in an up-looking position and 50 cm from the bed. C3 was moored at the limit between estuarine sand and the mud bank. The frequency of acquisition was 1 MHz with 30 cm bins for C1, and 2 MHz with 10 cm bins for C2 and C3. The instruments were set with a burst measurement of 60 s at 5 min intervals. Mean current directions were averaged for each vertical bin over 7.5 s and interpolated between bins. We discarded data closest to the bed (from 0 to 0.065 m) because of potential contamination by side-lobe interference. Compass precision after calibration was around ±2°.

RESULTS

Multi-Decadal Shoreline Change

The data on the multi-decadal shoreline evolution highlight significant mobility over the 62 year period of analysis (1955–2017), but much of this mobility is encompassed in the aerial photographic coverage between 1955 and 1987, strongly declining thereafter (**Figure 4B1**). The overall mobility over the entire period of observation exceeds 100 m at transects 105–127, but is within the error margin (±10 m) for 23% of the transects, and barely exceeds this margin (±10–20 m) for another 20% (**Figure 4C**). The area of beach represented by the transects (75–230) evincing the largest mobility appears to be related to a change in the orientation of the Maroni river-mouth east bank shoreline and to be linked to a shore-attached shoal (**Figure 3B**). This is a multi-decadal feature identifiable on aerial photographs and in the field at low tide.

The latest period (2011–2017) has been dominantly characterized by erosion (83% of transects), peaking at nearly 40 m at transects 94 to 95 (**Figure 4B2**), and marking a clear turn-around from advance to retreat in this area. This period has also been characterized by the gradual encroachment of the front of the shore-attached mud bank on the beach, by nearly 1.5 km between 2011 and 2017 (**Figure 4B2**). This encroachment has resulted in increasing inland isolation of the eastern part of the beach and the village of Awala, hitherto situated on the beach, by a dense forest of *Avicennia germinans* mangroves (**Figure 5**), and the present length of exposed beach has been reduced by about 50%.

Estuarine Bathymetry and Shoreface Currents

The Maroni estuary is characterized by a wide, relatively shallow platform (**Figure 6**) with large areas ranging in depth from 2 to 4 m below French hydrographic datum (0 m). The platform is cut by a moderately deep (down to −10 m) and relatively straight single channel running north-northeast. The grain size (sand or mud) of the platform was mapped from the echo-sounder frequency signal (33 MHz = sand; 210 MHz = mud). Although much of the platform is sandy, a large area east of the channel is composed of mud, highlighting the encroachment of the leading edge of a mud bank, parts of which have welded ashore (**Figure 5**).

[1] http://candhis.cetmef.developpement-durable.gouv.fr/

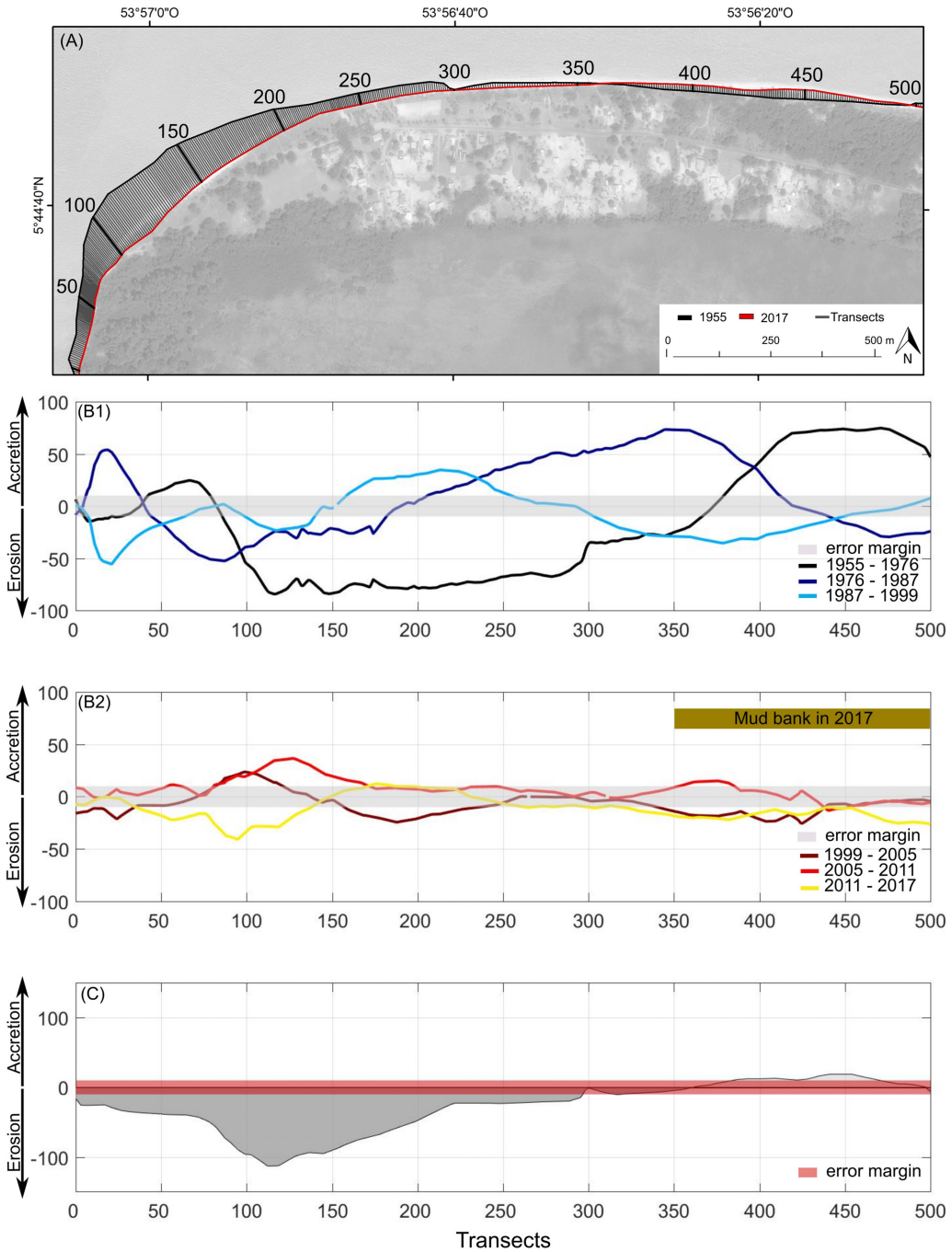

FIGURE 4 | Mobility of Yalimapo beach between 1955 and 2017: **(A)** transects; **(B)** shoreline change between 1955 and 1999 **(B1)**, and between 1999 and 2017 **(B2)**; **(C)** net shoreline variation over the period 1955–2017.

The beach shoreface bathymetry highlights several features (**Figure 7**): (1) the proximity of the Maroni channel to the beach in areas corresponding to transects 0 to 125 (**Figure 4A**); (2) the shallow (−1 m below 0 datum) shoreface expression of the intertidal beach-attached shoal mentioned above (**Figure 2**), and shoreface deepening northeast of this feature; and (3) a second zone of more extensive shallowing (with large areas <1 m below 0 datum) corresponding to the shore-attached mud bank (**Figures 7A1,A2,B**). During the field experiments in 2017 and 2018, the intertidal beach-attached shoal was characterized by abundant dunes composed of medium to coarse quartz sand with broken shells (**Figure 8B**). The dunes migrated over a hard pavement of packed coarse sand. Based on the terminology of Ashley (1990), these dunes are medium-sized

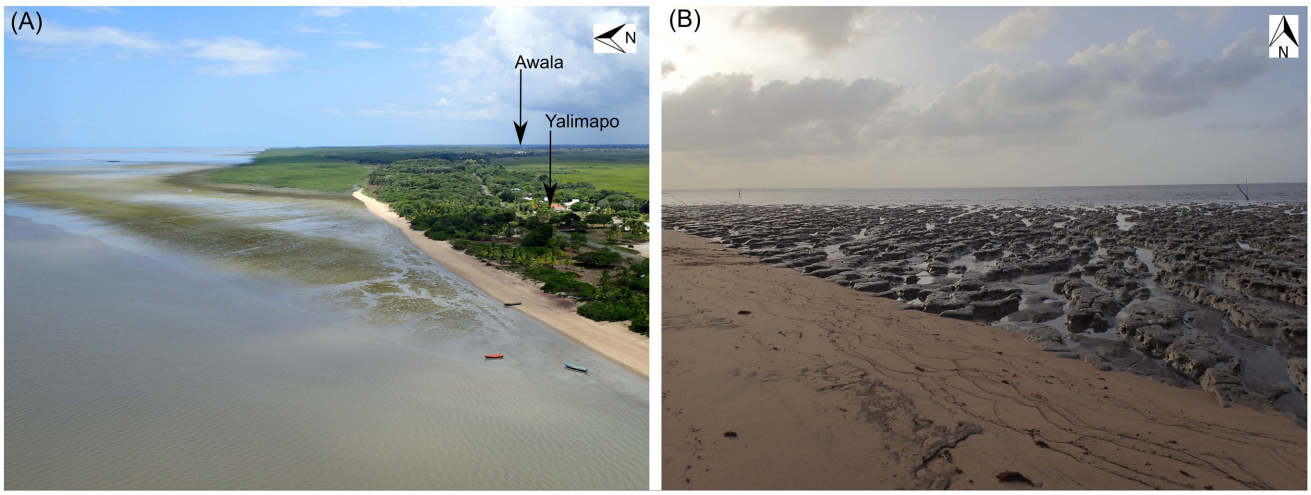

FIGURE 5 | Encroachment of a shore-attached mud bank on Yalimapo beach (see **Figure 1B**) since 2014, resulting in increasing inland isolation of the eastern part of the beach and of the hitherto beach-front village of Awala **(A)**, and reworked shoreface mud in front of the beach **(B)**. The mud bank is progressively colonized by an advancing front of *Avicennia germinans* mangroves.

(0.5–2 m), 2D to 3D forms. They evinced net eastward migration under the influence of the strong tidal currents described below.

The comparison of the DEMs shows that mild erosion has prevailed near the estuarine channel, although parts of the shoreface mud bank also exhibit lowering between 10/2017 and 04/2018 (**Figure 7B**). Overall, the innermost muddy shoreface in contact with the beach in its eastern part exhibits stability or mild accretion.

The currents measured during the survey are shown in **Figure 8A**. The largest current speeds were measured at C1. Directions were clearly bidirectional and controlled by the tide. Speeds were high, attaining a peak of 1.7 m/s in the upper part of the water column but systematically before high water, whereas the lowest speeds (0.2–0.7 m/s) occurred at high and low water. Currents flowed toward the northwest (300–275°) during the flood and to south-southeast (100–150°) during the ebb. C2 showed similar directions but speeds were less. C3 was dominated by currents flowing toward west-northwest (250°) during the flood, and east-northeast (60°) during the ebb.

Short-Term Beach Morphodynamics and Sediment Budget

There is a marked difference in wave heights and periods between the offshore wave characteristics and the data recorded by the pressure sensors inshore (**Figure 9**). The largest Hs values (**Figure 9A1**) in winter (December to March) may correspond to northern hemisphere winter storms with relatively long-period waves (>12 s). Much of the spectrum corresponds to trade-wind waves with periods of 5 to 12 s (**Figure 9A2**).

Inshore wave heights recorded during the field experiments in September 2018 were much lower, <0.25 m, and only exceeded 0.45 m (**Figure 9B2**) in the course of one semi-diurnal tide (**Figure 9B1**). The 2018 experiment showed wave periods (6–12 s) characteristic of the trade-wind wave regime, in addition to locally generated wind waves. The energy spectrum shows a dominant gravity component (**Figure 9B4**).

The DoDs constructed from the photogrammetric data are shown in **Figure 10A**, together with the corresponding sediment budget changes, which highlight net sand loss over the 8 month survey period. The three maps show overall beach sand loss in the March–June 2017 DoD, almost completely mirrored by accretion in the following June–September DoD, and a more alongshore variable pattern in the September–November 2018 DoD (**Figure 10A**). The latter shows a clear accretion in the eastern half of the beach where erosion had prevailed over the period 2011–2017 (**Figure 4B2**), accretion along much of the rest of the beach, but loss on the upper beach. This variability is also evinced by the beach profiles depicted in **Figure 10B**. They show a relatively steep beach, characterized by an upper beach scarp. Profile sediment loss between March and June 2018 had been partially recovered by November 2018, except for the central profile P5. Profile P2, linking the beach and the shore-attached shoal, showed significant mobility.

DISCUSSION

Beaches flanking river mouths are commonly an outgrowth of accumulation of bedload that leads to river channel infill through both lateral accretion of the channel margins and vertical sedimentation (Anthony, 2009). Lateral accretion commonly forms tidal flats that may constitute a low-tide terrace generally flanked by estuarine beaches (e.g., Nordstrom, 1992; Jackson et al., 2002). The west bank of the Maroni River (Suriname) shows a much more prograded chenier plain than the east bank (French Guiana) on which is located the beach studied here. This difference in chenier plain growth in the vicinity of the mouth of the Maroni (**Figure 1B**) highlights the westward transport of sandy sediments from this river (and others) consistent

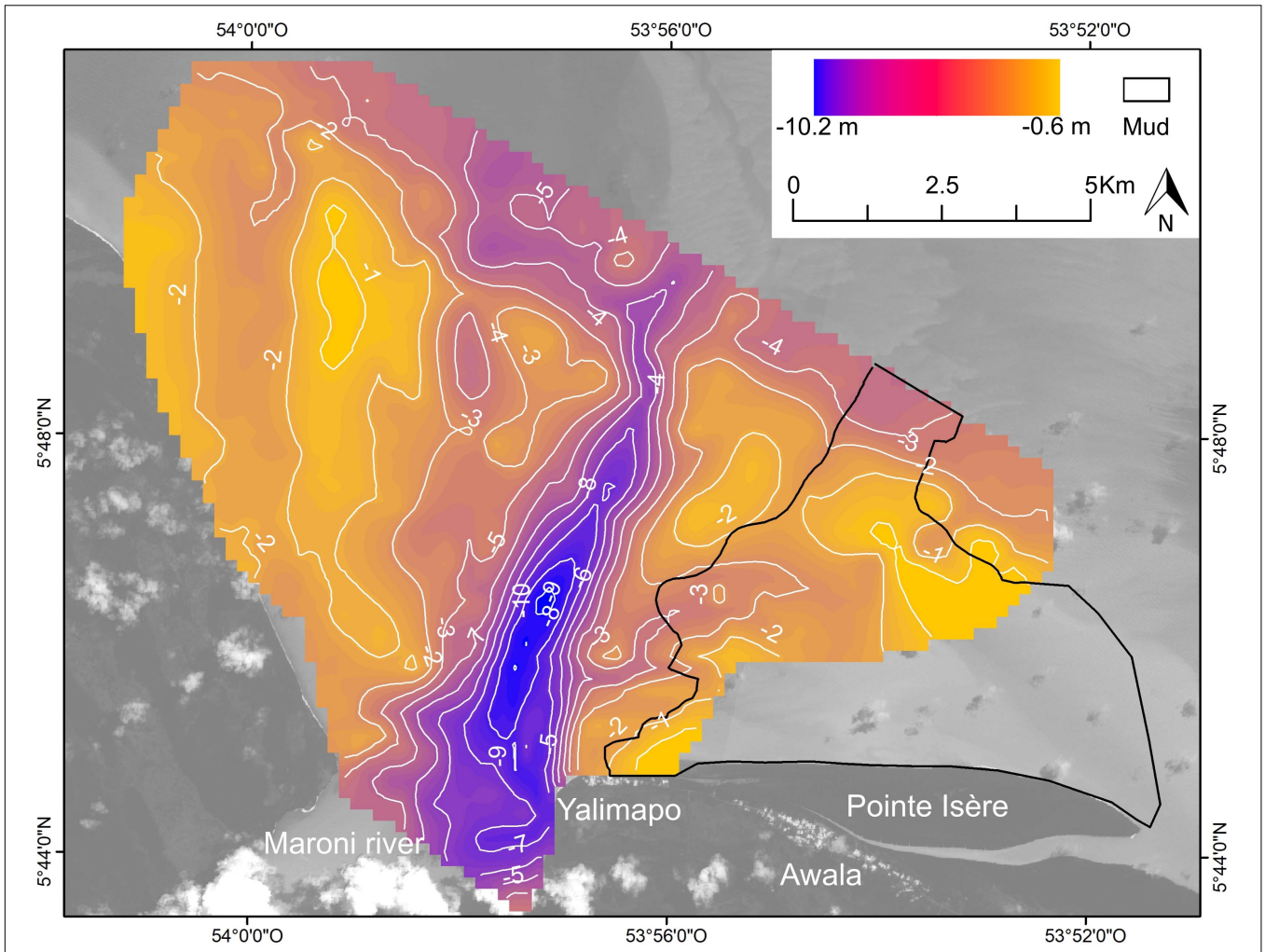

FIGURE 6 | Bathymetry of the Maroni estuary showing advanced sandy infill and a single estuarine channel. Mud (enclosed area) is associated with encroachment, from the east, of a mud bank over the sandy estuarine infill.

with the regional wave forcing from the north to northeast quadrant (Anthony et al., 2019; Gardel et al., 2019). It also highlights the limited supply of sand from the former diverted estuarine reach of the neighboring Mana River (**Figure 1B**). The Maroni river-mouth east-bank beach does not seem to be an outgrowth of the advanced estuarine infill of the Maroni estuary (**Figure 6**) but is part of an old chenier shoreline associated with the Mana River, which now exits several kilometers to the east of the Maroni (**Figure 1B**). This is attested by relatively old (>2000 years B.P.) optically stimulated luminescence ages obtained about 200 m behind the present beach (Brunier et al., 2019). The distribution of the chenier ages and the presence of Pre-Columbian settlements in Yalimapo (Gérard Collomb, pers.com, June 2019) suggest relative stability of the beach over a long timescale. The short-term (2018 field surveys) also show a fluctuating pattern of accretion and erosion (**Figures 7**, **10**), although the net negative sediment budgets are consistent with the recent prevailing erosional trend (2011–2017). The two points that can be drawn from this are: (1) the extent to which both the meso-scale and short-term patterns of evolution of the beach are controlled by the template set by mud banks impinging on the Maroni estuary, and (2) the mechanisms that regulate beach adjustment to this template. The implications of the recent eastward shift of the Mana outlet will be discussed later.

The multi-decadal mobility of the beach showed relatively large variability between 1955 and 1999, followed by more muted changes since. The large variability between 1955 and 1999 mirrored significant shoreline changes east of Yalimapo associated with the almost total demise of Pointe Isère (**Figure 11**), the large mud cape that had diverted the Mana River westwards up to 2011, and since at least the 19th Century (Plaziat and Augustinus, 2004). This erosion included pulses of reworking of inland cheniers behind Pointe Isère between 1972, 1979, and 2001–2011 (Jolivet et al., 2019), as the muddy cape was progressively eroded, and some of the reworked sand from Pointe Isère transported toward the mouth of the Maroni River (**Figure 11B**). It is interesting to note that erosion has been prevalent over much of the beach in the last few years

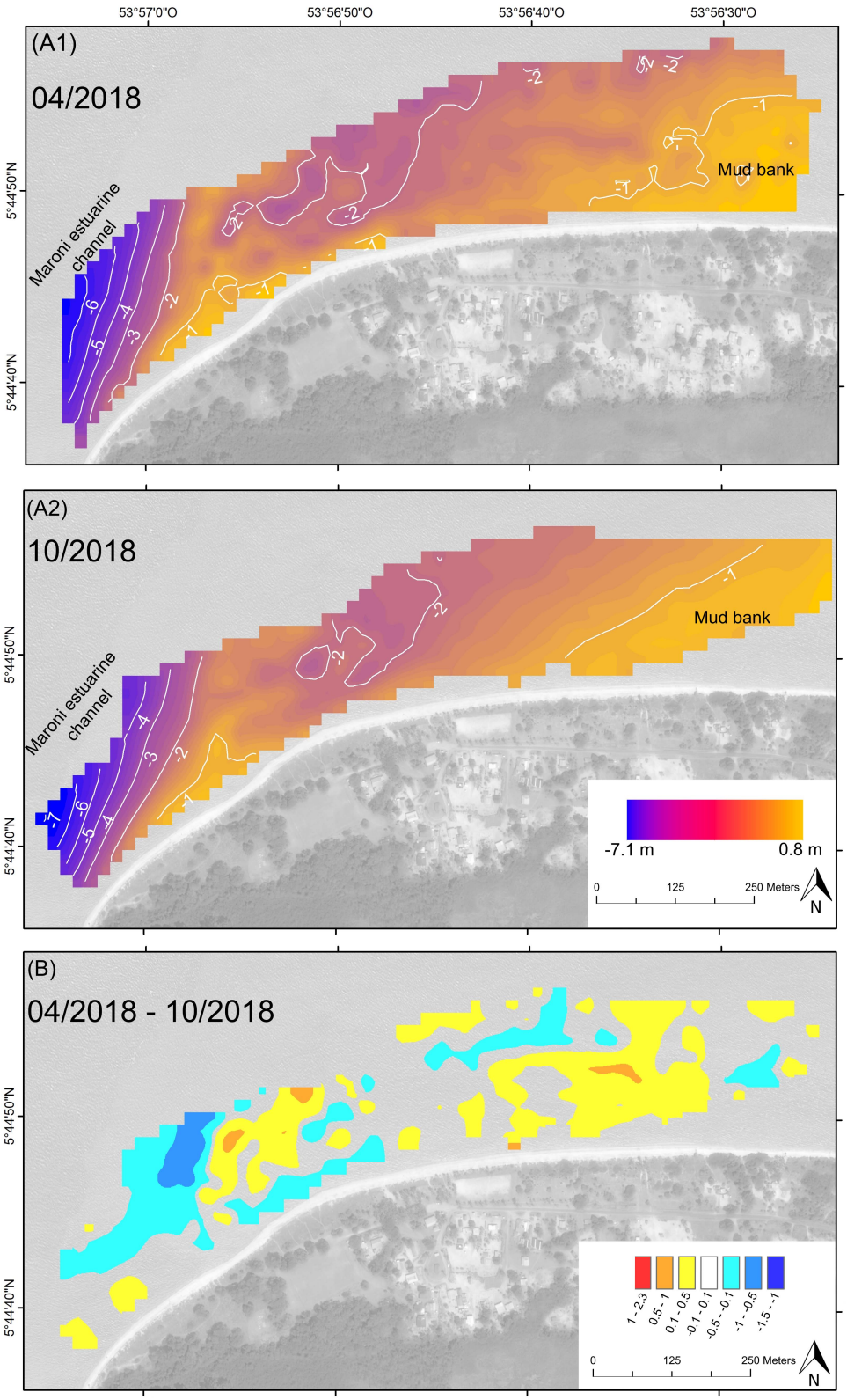

FIGURE 7 | DEMS of shoreface bathymetry adjacent to the beach **(A1,A2)**, and DoD over the study period, showing sediment loss close to the Maroni estuarine channel **(B)**.

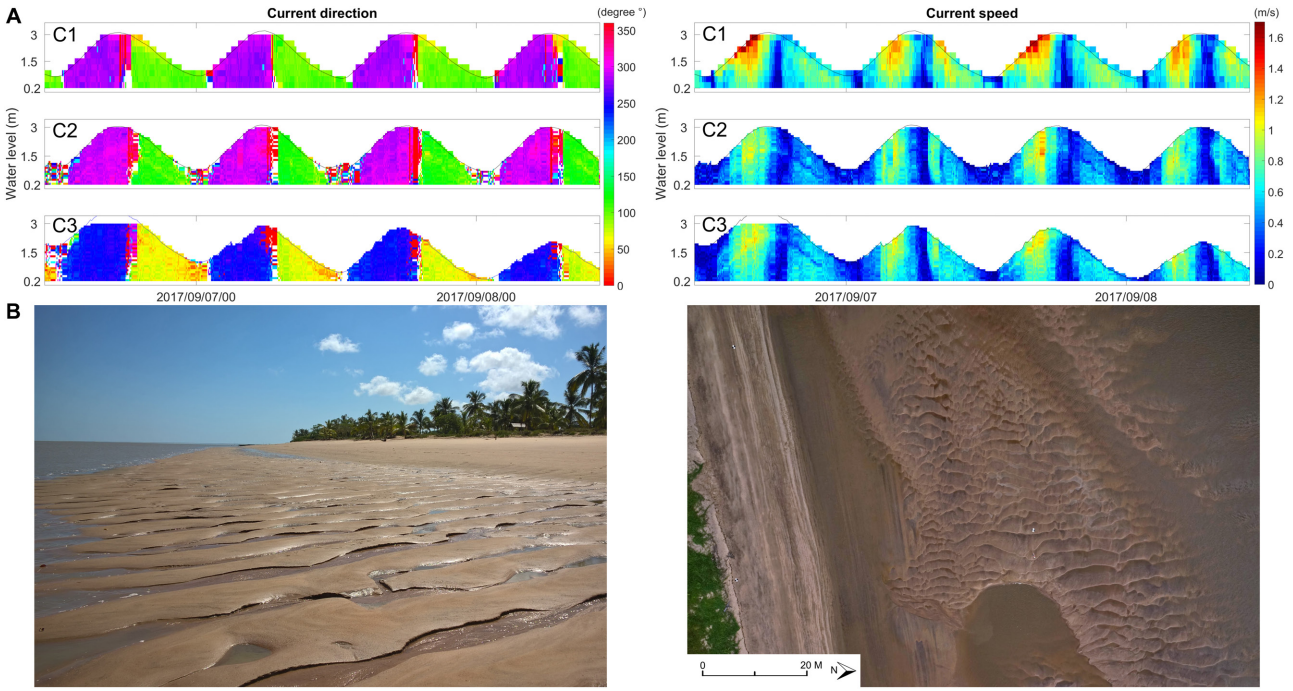

FIGURE 8 | Currents measured near the beach (see **Figure 2**) over several tidal cycles **(A)** and photographs of bedforms (2D to 3D dunes) on the shoreface adjacent to the beach **(B)**.

(2011–2017, **Figure 4B2**), and in 2018 (**Figure 10**), generating anxiety regarding loss of land, threats to beach tourism, and diminishing space for nesting marine turtles in Yalimapo. However, given the large past shoreline mobility, prediction of the time frame over which erosion will prevail is hazardous. The reasons for the current prevalent erosion likely reside in modifications of alongshore sand transport on the beach generated by impingement of the mud bank on the eastern part of the beach (**Figures 4B2**, **6**, **10**, **11C**). This is an outgrowth of the multi-decadal demise of Pointe Isère. Jolivet et al. (2019) documented the sealing of the former mouth of the Mana and the marked eastward shift of the present mouth of the river as a result of the shore-attachment of the bank east of Yalimapo, thus depriving the beach of potential sand supply by this river. These mesoscale changes reflect the utility of adopting a more regional, large-scale (big picture) approach in order to better elucidate local shoreline change.

Overall shoreline change has been most important in the zone where the east bank of the Maroni estuary joins the beach, between transects 75 and 220 (**Figure 4**). A likely explanation for this local variability is that of mobility of the main Maroni estuarine channel in adjustment to pervasive mud supply and attendant changes in hydrodynamics induced by mud banks. This is reflected in the extremely high turbidity values within the channel resulting from the impingement of the present large mud bank (Sottolichio et al., 2018). Transects 0 to 200 correspond to the most constricted part of the estuary and where the main Maroni estuarine channel is in direct contact with the intertidal beach (**Figure 7**). In addition to (or as a result of) this channel proximity, much of the shoreline mobility in this sector has been engendered by the migration of the beach-attached shoal identified from both ground and aerial photographs (not shown here). The formation of this shoal was probably initially due to expansion of the fluvial-tidal hydraulic jet of the Maroni with widening of the estuary where the beach changes its orientation to eastward, to form part of the south bank of the hitherto diverted Mana River (**Figure 1B**). Sand shoal formation of this type is akin to that of a flying spit (Zenkovich, 1967), or a banner bank (Dyer and Huntley, 1999), although the latter type of bank is generally associated with headlands.

The short-term data further highlight this mesoscale variability and show the seasonal cut-and-fill signature typical of the trade wind-wave-influenced French Guiana beaches during inter-bank phases (Dolique and Anthony, 2005), when mud banks do not affect the coast, or of many other tropical beaches with a well-defined seasonal trade-wind or monsoon wave regime (e.g., Tamura et al., 2010; Pereira et al., 2016; Anthony et al., 2017; Arrifin et al., 2018). The beach underwent significant sand loss (**Figure 10**; $-14{,}579$ m^3) in response to the high waves that prevailed between March and June 2018 (**Figure 9A**). Filtering of wave energy does occur, as shown by the pronounced difference between, on the one hand, both the modeled offshore wave data provided by the WWIII model (**Figure 2**) and the CANDHIS buoy data (**Figure 9A**), and, on the other, data recorded by the pressure sensors near the beach (**Figure 9B**). Filtering is caused by the mud banks migrating alongshore but also by the large estuarine sand bank that is infilling the mouth of the Maroni. This filtering effect is proportional to

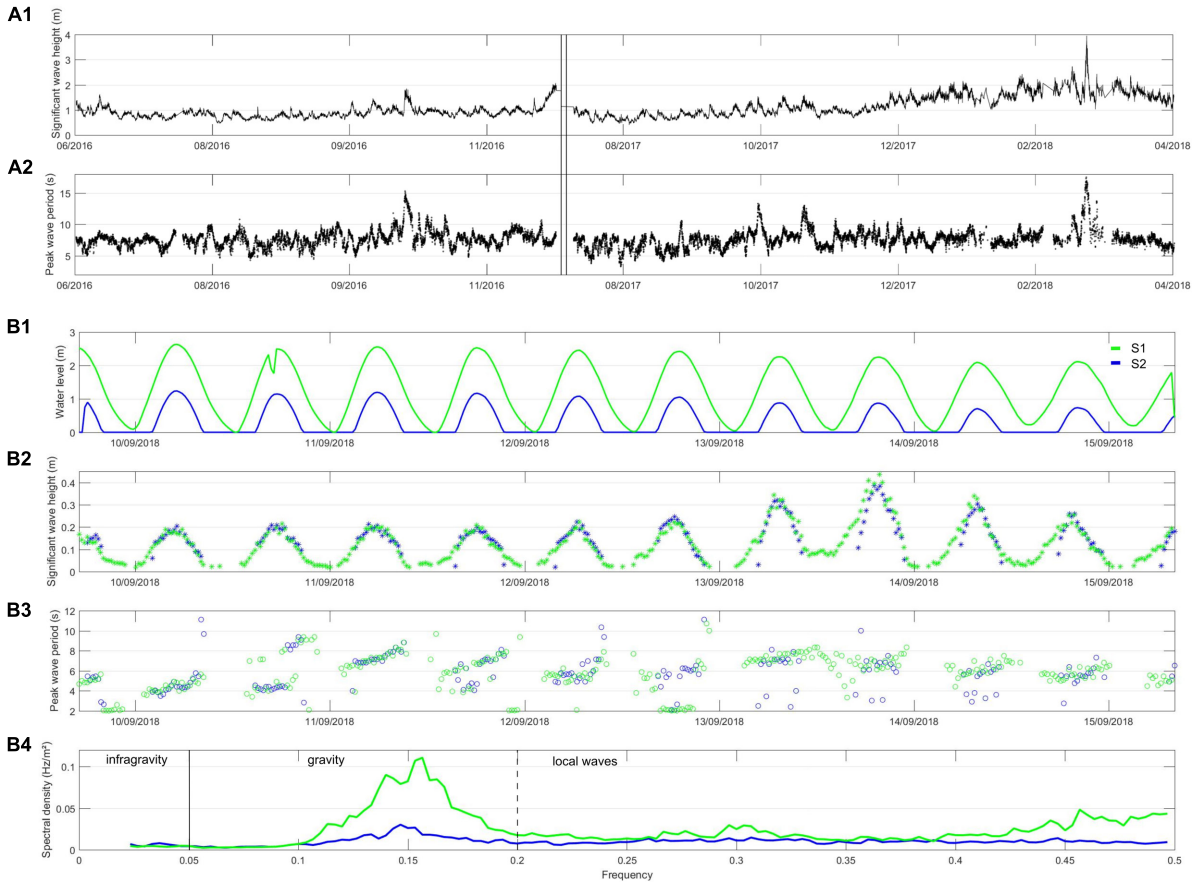

FIGURE 9 | Hydrodynamic conditions during the course of the field experiments. From top to bottom: offshore significant wave heights **(A1)** and periods **(A2)** measured by the CANDHIS buoy offshore of Cayenne (see **Figure 1A**); water levels measured by the pressures sensors **(B1)**; inshore wave heights **(B2)** and periods **(B3)** measured by the pressure sensors (see **Figure 2**); and examples of bursts of wave energy spectral density **(B4)**.

wave energy, and large waves succeed in impacting the beach, as seen from field observations, especially during large spring tides. The high waves between March and June 2018 (**Figures 2**, **9A**) also included equinoctial spring tides during which high-tide dissipation was less. The estuarine sheltering effect from exposure to waves, which commonly results in short-fetch waves, is an overarching influence of estuaries on beach morphodynamics (Jackson et al., 2002).

Wave measurements conducted on other beaches in the Guianas both in the vicinity of river mouths and well away from these river mouths show that incident wave energy is strongly modulated temporally and alongshore by the presence of banks (low waves) or their absence (high waves associated with inter-bank phases), resulting in large short- to mesoscale (>decade) shoreline mobility (Anthony et al., 2002). It is not clear from the available data whether this meso-scale wave variability has also been the case on the beach at Yalimapo but the commonality of this pattern on various other beaches in the Guianas suggests this likelihood, which is also reflected in the multi-decadal variability in beach mobility.

As shown in **Figure 10**, short-term beach morphological change has been quite variable notwithstanding the ambient low wave-energy context, possibly reflecting a further influence of: (1) progressive impingement on the eastern part of the beach, of shore-attached mud (**Figure 10A**), (2) sand exchanges between the estuarine bank and the beach, notably in the shore-attached shoal area (Profile P2, **Figure 10B**), and (3) antecedent beach profile characteristics in feeding back on morphological change. Estuarine beaches are commonly characterized by a relatively wide low gradient terrace, or "low tide terrace," across which sediment mobilization may occur under relatively high energy (wave) conditions (Jackson et al., 2002). These beaches also commonly exhibit the following features: (1) longshore and transverse bars and biogenic features; (2) swash bars; (3) vegetation and wrack accumulations on the intertidal foreshore; (4) pebbles and/or shells; and (5) small aeolian dunes.

On the Maroni mouth beach, the low-tide terrace corresponds to the adjoining estuarine sand bank (transects 175–500) but the features and patterns of sediment mobilization prevailing on this beach do not correspond to those enumerated above. Low wind speeds, high ambient humidity, and rapid growth and spread of creeping grasses on the backshore considerably limit aeolian activity on the beaches of the Guianas (Anthony et al., 2014). The sediment mobility on the beach is regulated by strong

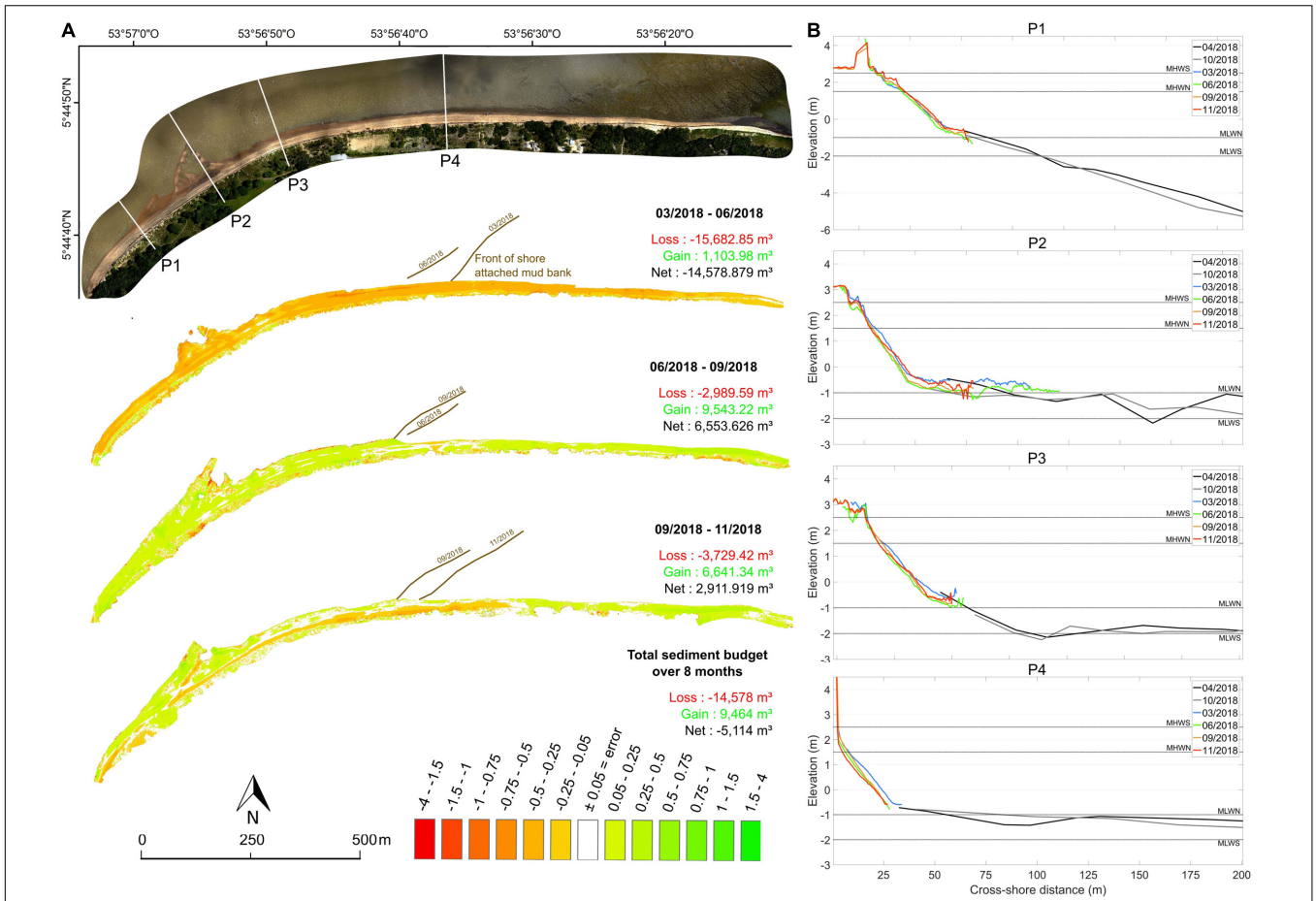

FIGURE 10 | High-density orthophotograph assemblage (March 2018) and three DoDs of the beach obtained from SfM photogrammetry in 2018, together with net budget estimations **(A)**, and examples of beach and shoreface profiles **(B)**.

alongshore tidal currents (**Figure 8A**) that generate important tidal bedforms, notably the 2D–3D hydraulic dunes (**Figure 8B**). The beach, which is also devoid of aeolian activity, clearly interacts with the strong tidal currents which are typically of a standing tide (notably at C1), and with these bedforms, especially in the shoal-attached area. The high current speeds during the rising tide associated with such a standing tide act not only on the bedforms of the shallow shoreface but also on the adjacent beach face. The estuarine sand bank serves as both a sand source and sink, resulting in the pulses of accretion and erosion evinced by the beach, which were further modulated, up to 2011, by limited sand supply by the Mana River. This relationship is, thus, mediated by the energetic tidal currents and by dissipation of waves over the terrace. Jackson and Nordstrom (1992) showed that under the extremely dissipative conditions prevailing on the low-tide terrace, beach profile change becomes restricted to the steep foreshore. This appears to be the case in the study area where the upper beach tends to show a scarped reflective profile (**Figure 10B**).

Tidal modulation of waves has been shown to be an important component of the hydrodynamics of Guiana beaches, generated by ambient permanent shoreface mud during both bank and inter-bank phases (Anthony et al., 2019). Field measurements at Yalimapo clearly highlight this tidal modulation and show that high-tide waves are generated by a mix of both trade-wind waves (6–12 s) and short-fetch local sea breezes that generate choppy conditions with periods that do not exceed 5 s (**Figure 9**). Field observations further show that waves are only active on the upper beach, resulting in local high-tide scarping (**Figure 10B**). Spring tides no doubt reinforce the high-tide scarping and low-tide dissipation. Under these erosive conditions, downslope transfer of beach sand to the estuarine sand bank is assured by the prevalence of steep reflective beach profiles, which function in a positive short-term morphodynamic feedback loop that maintains profile steepness and recession seen in the short-term (2018) data of parts of the beach (**Figure 10B**).

The timescales and relationships involved in the multi-decadal evolution and short-term morphodynamics of the beach at Yalimapo, French Guiana, are conceptualized in **Figure 12**. The net westward sediment transport system and influence of bank and inter-bank alternations that affect the Guianas coast at a regional scale affect the beach and the dynamics of the mouth of the Maroni River. The latter further influences variations in beach morphology and stability through estuarine

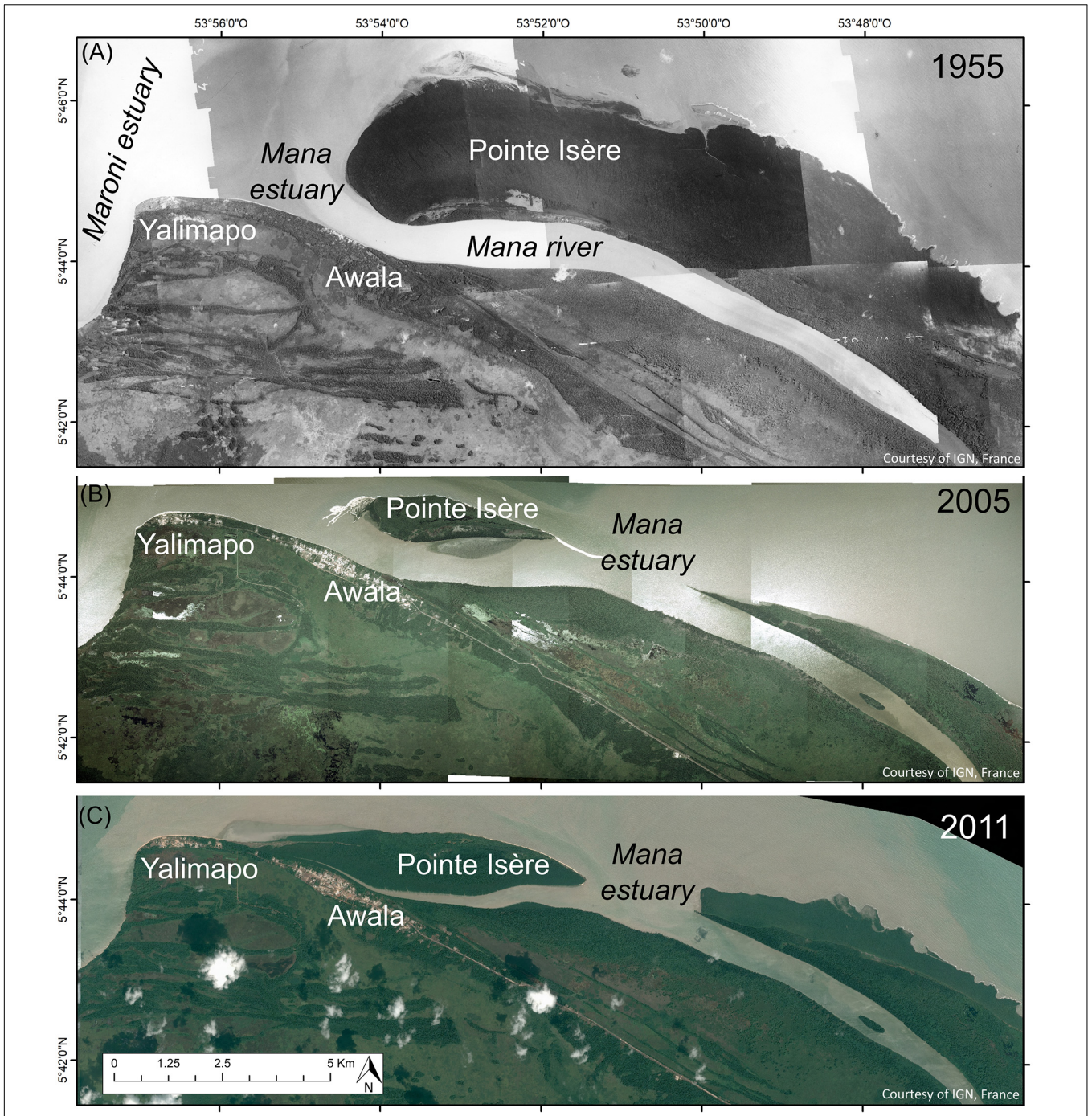

FIGURE 11 | Rapid shoreline changes associated with erosion of much of the mud cape of Pointe Isère between 1955 and 2005 **(A,B)** and closure of the former mouth of the Mana River between Awala and Yalimapo by shore-welded mangrove-colonized mud that has isolated the beach at Awala from the sea **(C)**.

channel mobility, dissipation of waves by the large estuarine sand sink that is infilling this river mouth, and tidal currents and bedforms.

It is important to note that the erosion that has prevailed along much of the beach in the last few years (2011–2017, **Figure 4B2**), and in 2018 (**Figure 10**) is having deleterious ecological and sociological effects in the coastal settlements of Awala and Yalimapo (**Figure 1**) (population in 2018: 1400). The beach was, up to the 1990s, one of the most important turtle-nesting sites on the South American coast, and as the available beach space has receded due to mud encroachment, the number of turtle landings has diminished drastically (Peron, 2014). The villages

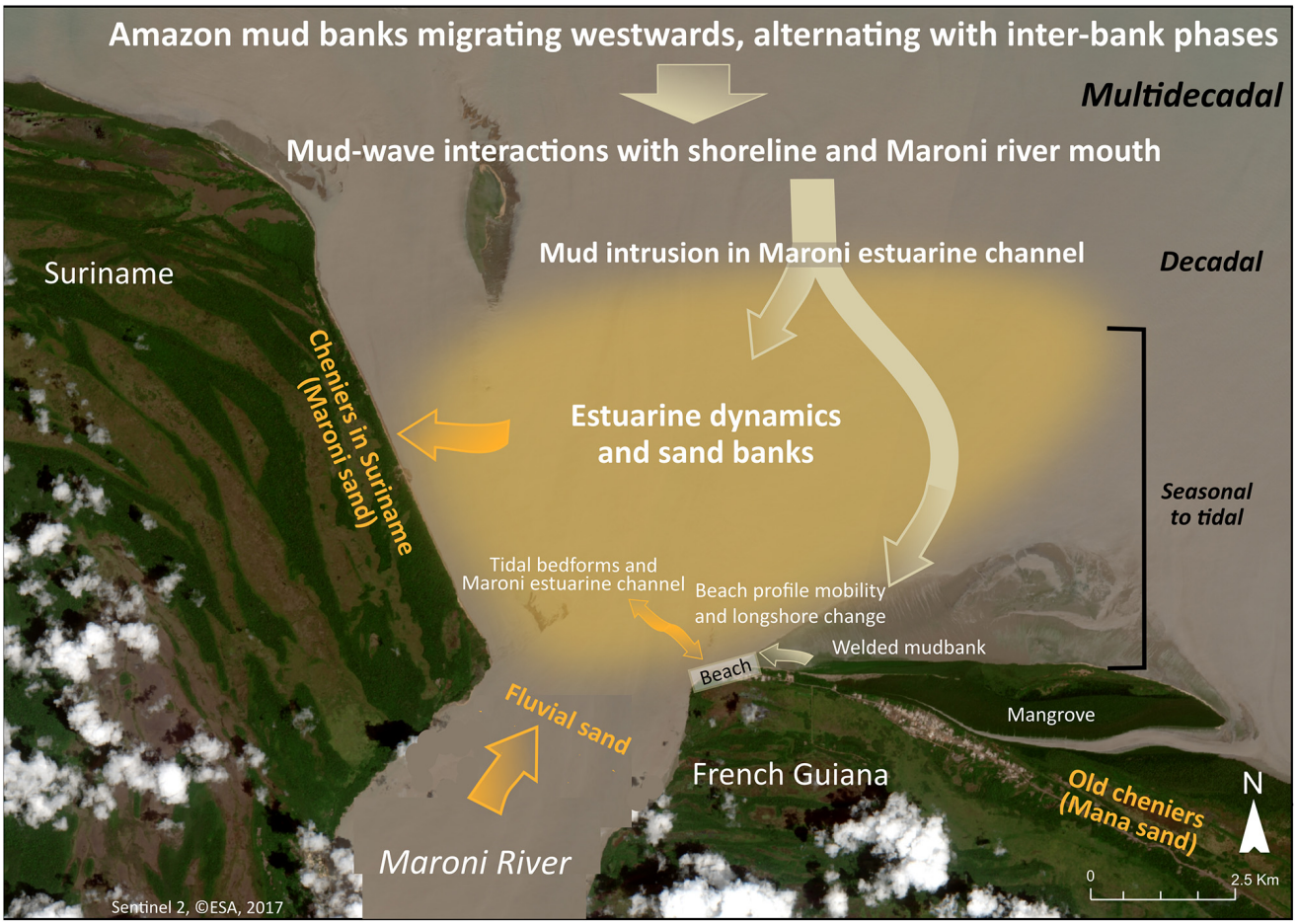

FIGURE 12 | Conceptual model of multi-decadal to short-term changes at Yalimapo beach, French Guiana. The morphology and dynamics of the beach are influenced, at embedded spatial (regional to local) and temporal (multi-decadal to daily) timescales, by the relationship and interactions among various sediment bodies and forces. These are the regional mud banks migrating under wave and wind influence at > decadal to multi-decadal timescales westward from the Amazon to the Orinoco, wave dissipation by these banks and by the large estuarine sand bank infilling the mouth of the Maroni River, and at a timescale of several years, mud intrusion into the mouth of the Maroni and local welding of mud released by the banks onto the beach. Seasonal modulation of wave activity, the local influence of the main Maroni estuarine channel, strong tidal currents on the inner shoreface adjacent to the beach, and sand exchanges, at fortnightly tidal to semi-daily scales between beach and inner-shoreface tidal bedforms, are reflected in beach profile and alongshore mobility at the local scale.

are inhabited by indigenous Kali'na populations that became sedentary in the late 1940s. Risks posed by shoreline mobility in the Guianas prior to this sedentary lifestyle were accommodated by population mobility to safer areas. Present fears in reaction to the on-going coastal changes concern loss of land, large-scale mangrove development, threats to beach recreation, and to revenue from tourism related to nesting marine turtles. Prior to encroachment of the bank that has welded onshore, Awala had access to the sandy beach and benefited, like Yalimapo, from the advantages of beach-related recreation and tourism. This has been the only accessible sandy beach in western coastal French Guiana (total population in 2018: 60,000), an area of very rapid demographic growth. Much of this tourism is related to turtle-watching during the nesting season. The now completely mud-bound beach of Awala implies that the village is presently totally deprived of revenue from tourism, and direct access to the sea for fishermen has been shut off by a wide mangrove front (**Figure 5A**). The decrease in the number of turtle landings is also depriving neighboring Yalimapo (**Figure 5A**), now the only available beach spot in western French Guiana, of much-needed tourist revenue. Given the large past shoreline mobility, prediction of the time frame over which erosion will continue to prevail is hazardous.

CONCLUSION

The multi-decadal evolution and short-term morphodynamics of the beach at Yalimapo, French Guiana, illustrate the influence of the dynamics of the mouth of the Maroni River at the local scale, and the net westward sediment transport system and influence of bank and inter-bank alternations that affect the Guianas coast at a regional scale. The influence of the Maroni is reflected in variations in beach morphology and stability induced by channel

dynamics, tidal currents and bedforms, and dissipation of waves by the large estuarine sand sink that is infilling this river mouth. The bank and inter-bank fluctuations have determined multi-decadal beach mobility through their influence on the wave regime and in mediating sand supply alongshore. These two scales of analysis show how local changes are embedded in, and overprinted by, the pervasive influence of changing mud-bank and inter-bank phases alongshore, a hallmark of the 1500 km-long Guianas shoreline. Changes resulting from these controls include complete isolation of the village of Awala from the sea by mangrove-colonized mud, disastrous for tourism, fishing activities in terms of access to the sea, and to beach recreation. The shortening of the beach as a result of mud encroachment now poses a threat to the village of Yalimapo, the only site in western French Guiana with a still available sandy beach. Reduction of the available beach space is having negative ecological and socio-economic consequences. This reduction is detrimental to turtle-landings on the beach for nesting, the number of which has diminished dramatically over the last decade, and to the income generated by beach tourism geared toward watching turtles nest. It is also nefarious to beach recreation and to fishing.

DATA AVAILABILITY

All datasets generated for this study are included in the manuscript/**Supplementary Files**.

AUTHOR CONTRIBUTIONS

MJ, EA, and AG designed the project, conducted the field work, analyzed the data, and wrote the manuscript. GB participated in the field work and data analyses.

FUNDING

We acknowledge financial support from the European Regional Development Fund for the project OYAMAR. Additional funding was provided within the framework of the projects GUIABEACH, GUIACHENIER, MORPHOMAR, and DYALOG supported by the "Pépinière Interdisciplinaire de Guyane" of the CNRS.

ACKNOWLEDGMENTS

The Direction de l'Environnement, de l'Aménagement et du Logement (DEAL Guyane) provided access to the CANDHIS offshore wave data. Aerial photographs were provided free of charge by the IGN (French National Institute for Geographic and Forest Information), and downloaded from the website https://remonterletemps.ign.fr/. PLEIADE and SPOT 6/7 images were provided by CNES (distribution Spot Image S.A.). We thank Tanguy Maury and Sylvain Morvan for help during the field work. This is a contribution from the National Observation Service DYNALIT site of Awala-Yalimapo in western French Guiana, and from the French GDR LIGA researcher network. We thank the two reviewers for their constructive suggestions for improvement. MJ acknowledges a Ph.D. grant from the Université de Guyane.

SUPPLEMENTARY MATERIAL

The Supplementary Material for this article can be found online at: https://www.frontiersin.org/articles/10.3389/feart.2019.00187/full#supplementary-material

TABLE S1 | Inventory of aerial photographs and satellite images used in the study.

TABLE S2 | Summary of items concerned by the four photogrammetric surveys.

REFERENCES

Abascal Zorrilla, N. (2019). *Dynamics of the Amazonian mud Bank System Through Spatial Observation and Hydro-Sedimentary Modeling: Application to the Coastal Domain of French Guiana*. Ph.D thesis, Université de Guyane, Cayenne, French Guiana.

Abascal Zorrilla, N., Gensac, E., Vantrepotte, V., Huybrechts, N., and Gardel, A. (2018). Interest of Landsat8-OLI derived SPM maps for monitoring the subtidal extension of Amazonian mud banks (French Guiana). *Remote Sens.* 10:1733. doi: 10.3390/rs10111733

Anthony, E. J. (2009). *Shore Processes and Their Palaeoenvironmental Applications. Developments in Marine Geology*. Amsterdam: Elsevier Science.

Anthony, E. J., Brunier, G., Gardel, A., and Hiwat, M. (2019). Chenier morphodynamics and degradation on the amazon-influenced coast of Suriname, South America: implications for beach ecosystem services. *Front. Earth Sci.* 7:35. doi: 10.3389/feart.2019.00035

Anthony, E. J., Dussouillez, P., Dolique, F., Besset, M., Brunier, G., Nguyen, V. L., et al. (2017). Morphodynamics of an eroding beach and foredune in the mekong river delta: implications for deltaic shoreline change. *Cont. Shelf Res.* 147, 155–164. doi: 10.1016/j.csr.2017.06.018

Anthony, E. J., Gardel, A., Dolique, F., and Guiral, D. (2002). Short-term changes in the plan shape of a sandy beach in response to sheltering by a nearshore mud bank, Cayenne, French Guiana. *Earth Surface Process. Landforms* 27, 857–866. doi: 10.1002/esp.357/full

Anthony, E. J., Gardel, A., and Gratiot, N. (2014). Fluvial sediment supply, mud banks, cheniers and the morphodynamics of the coast of South America between the Amazon and Orinoco river mouths. *Geol. Soc.* 388, 533–560. doi: 10.1144/sp388.8

Anthony, E. J., Gardel, A., Gratiot, N., Proisy, C., Allison, M. A., Dolique, F., et al. (2010). The amazon-influenced muddy coast of south america: a review of mud bank-shoreline. *Earth Sci. Rev.* 103, 99–121. doi: 10.1016/j.earscirev.2010.09.008

Anthony, E. J., Gardel, A., Proisy, C., Fromard, F., Gensac, E., Peron, C., et al. (2013). The role of fluvial sediment supply and river-mouth hydrology in the dynamics of the muddy, Amazon-dominated Amapá–Guianas coast, South America: a three-point research agenda. *J. South Am. Earth Sci.* 44, 18–24. doi: 10.1016/j.jsames.2012.06.005

Arrifin, E. H., Sedrati, M., Akhir, M. F., Daud, N. R., Yaacob, R., and Husain, M. L. (2018). Beach morphodynamics and evolution of monsoon-dominated coasts in kuala terengganu, malaysia: perspectives for integrated management. *Ocean Coast. Manag.* 63, 498–514. doi: 10.1016/j.ocecoaman.2018.07.013

Ashley, G. M. (1990). Classification of large-scale subaqueous bedforms; a new look at an old problem. *J. Sediment. Res.* 60, 160–172.

Augustinus, P. G. E. F. (1978). *The Changing Shoreline of Surinam (South America)*. Ph.D. thesis, University of Utrecht, Utrecht.

Augustinus, P. G. E. F., Hazeloff, L., and Kroon, A. (1989). The chenier coast of Suriname: modern and geological development. *Mar. Geol.* 90, 269–281. doi: 10.1016/0025-3227(89)90129-1

Brunier, G., Tamura, T., Anthony, E. J., Gardel, A., Dussouillez, P., Todisco, D., et al. (2019). "OSL chronology of sandy cheniers in French Guiana," in *Proceedings of the 1st Latin American Physics of Estuaries and Coastal Oceans Conference – LAPECO*, Florianopilis.

Dolique, F., and Anthony, E. J. (2005). Short-term profile changes of sandy pocket beaches affected by Amazon-derived mud, Cayenne, French Guiana. *J. Coast. Res.* 21, 1195–1202. doi: 10.2112/04-0297.1

Dyer, K. R., and Huntley, I. A. (1999). The origin, classification and modelling of sand banks and ridges. *Cont. Shelf Res.* 19, 1285–1330. doi: 10.1016/s0278-4343(99)00028-x

Gardel, A., Anthony, E. J., Jolivet, M., Huybrechts, N., Lesourd, N., Santos, V., et al. (2019). "Sediment fluxes in the Maroni River mouth, South America: interactions with mud banks and adjacent coasts," in *Proceedings of the 1st Latin American Physics of Estuaries and Coastal Oceans Conference – LAPECO*, Florianopilis.

Hutchinson, M. F., Xu, T., and Stein, J. A. (2011). "Recent progress in the ANUDEM elevation gridding procedure," in *Geomorphometry 2011*, eds T. Hengel, I. S. Evans, J. P. Wilson, and M. Gould (Redlands, CA: International Society for Geomorphometry), 19–22.

Jackson, N. F., Nordstrom, K. F., Eliot, I., and Masselink, G. (2002). 'Low energy' sandy beaches in marine and estuarine environments: a review. *Geomorphology* 48, 147–162. doi: 10.1016/s0169-555x(02)00179-4

Jackson, N. L., and Nordstrom, K. F. (1992). Site-specific controls on wind and wave processes and beach mobility on estuarine beaches. *J. Coast. Res.* 8, 88–98.

Jolivet, M., Gardel, A., and Anthony, E. J. (2019). Multi-decadal changes on the mud-dominated coast of western French Guiana: implications for mesoscale shoreline mobility, river-mouth deflection, and sediment sorting. *J. Coast. Res.* 82, (in press).

Nordstrom, K. F. (1992). *Estuarine Beaches*. London: Elsevier, 225.

Otvos, E. G. (2018). "Cheniers," in *Encyclopaedia of Coastal Science*, eds C. Finkl and C. Makowski (Cham: Springer), doi: 10.1007/978-3-319-48657-4_67-5

Pereira, L. C. C., Vila-Concejo, A., and Short, A. D. (2016). "Coastal morphodynamics processes on the macro-tidal beaches of Pará state under tidally-modulated wave conditions," in *Brazilian Beach Systems*, eds A. D. Short and A. H. F. Klein (Cham: Springer), 95–124. doi: 10.1007/978-3-319-30394-9_1

Peron, C. (2014). *Dynamique Littorale et Comportement de ponte des tortues marines en Guyane française*. Ph.D thesis, Université du Littoral Côte d'Opale, Dunkerque.

Plaziat, J. C., and Augustinus, P. G. E. F. (2004). Evolution of progradation/erosion along the French Guiana mangrove coast: a comparison of mapped shorelines since the 18th century with Holocene data. *Mar. Geol.* 208, 127–143. doi: 10.1016/j.margeo.2004.04.006

Prost, M. T. (1989). Coastal dynamics and chenier sands in French Guiana. *Mar. Geol.* 90, 259–267. doi: 10.1016/0025-3227(89)90128-X

Pujos, M., Pons, J. C., and Parra, M. (2000). Les minéraux lourds des sables du littoral de la Guyane française : bilan sur l'origine des dépôts de la plate-forme des Guyanes. *Oceanol. Acta* 24, S27–S35.

Sottolichio, A., Gardel, A., Huybrechts, N., Maury, T., Morvan, S., and Lesourd, S. (2018). "Patterns of circulation and fine sediment dynamics in a tropical estuary under Amazon influence (Maroni Estuary, French Guyana)," in *Proceedings of the PECS 2018 Physics of Estuaries and Coastal Seas Meeting 2018*, Galveston, TX.

Tamura, T., Horaguchi, K., Saito, Y., Nguyen, V. L., Tateishi, M., Ta, T. O. K., et al. (2010). Monsoon-influenced variations in morphology and sediment of a mesotidal beach on the Mekong River delta coast. *Geomorphology* 116, 11–23. doi: 10.1016/j.geomorph.2009.10.003

Thieler, R. E., Himmelstoss, E. A., Zichichi, J. L., and Ergul, A. (2017). *The Digital Shoreline Analysis System (dsas) version 4.0: An Arcgis Extension for Calculating Shoreline Change*. Reston, VA: U.S. Geological Survey.

Westoby, M. J., Brasington, J., Glasser, N. F., Hambrey, M. J., and Reynolds, J. M. (2012). 'Structure-from-Motion' photogrammetry: a low-cost, effective tool for geoscience applications. *Geomorpholohy* 179, 300–314. doi: 10.1016/j.geomorph.2012.08.021

Zenkovich, V. P. (1967). *Processes of Coastal Development*. New York, NY: Interscience Publishers.

Conflict of Interest Statement: The authors declare that the research was conducted in the absence of any commercial or financial relationships that could be construed as a potential conflict of interest.

frontiers in Earth Science

ORIGINAL RESEARCH
published: 06 August 2019
doi: 10.3389/feart.2019.00190

Coastal Impact From High-Energy Events and the Importance of Concurrent Forcing Parameters: The Cases of Storm Ophelia (2017) and Storm Hector (2018) in NW Ireland

Emilia Guisado-Pintado[1,2]* *and Derek W. T. Jackson*[2]

[1] Department of Physical Geography and Regional Geographic Analysis, University of Seville, Seville, Spain, [2] School of Geography and Environmental Sciences, Ulster University, Coleraine, United Kingdom

OPEN ACCESS

Edited by:
Christina Robyn Magill,
Macquarie University, Australia

Reviewed by:
Linlin Li,
National University of Singapore, Singapore
Pushpa Dissanayake,
University of Kiel, Germany

***Correspondence:**
Emilia Guisado-Pintado
eguisado@us.es

Specialty section:
This article was submitted to Geohazards and Georisks, a section of the journal Frontiers in Earth Science

Received: 15 February 2019
Accepted: 05 July 2019
Published: 06 August 2019

Citation:
Guisado-Pintado E and Jackson DWT (2019) Coastal Impact From High-Energy Events and the Importance of Concurrent Forcing Parameters: The Cases of Storm Ophelia (2017) and Storm Hector (2018) in NW Ireland. Front. Earth Sci. 7:190. doi: 10.3389/feart.2019.00190

Infrequent but high energy storm events can radically modify coastlines, at times displacing significant sediment volumes and changing shoreline configuration. More frequent and stronger Atlantic storms over the last 40 years have heightened the potential risk to coastal environments, population and infrastructure. Understanding local environmental forcing conditions and associated variables involved in coastal impact and response, can better inform future coastal management planning. This study examines the coastal impacts of two separate storms that occurred at Five Finger Strand, on the northwest Irish coast, in late 2017 (Storm Ophelia) and mid-2018 (Storm Hector). Using forcing parameters (wind speed and direction, wave heights and wave run up) along with 3D topographic surveys, impacts are examined for both storm events. For Storm Ophelia, shore-oblique to shore-parallel waves (2 m in height) coincident with low tide (~0.8 m) were recorded. This resulted in minimal erosional impact which was corroborated by a new proxy storm impact index, "Storm Dune Trimming" (value of >0.03) as well as a sediment displacement volume of 8,300 m^3, largely confined to the intertidal area with only limited foredune edge erosion. Storm Hector, on the other hand, a lower energy event than Storm Ophelia, resulted in much more pronounced sediment displacement (13,400 m^3 in the intertidal area) and significantly more dune scarping (Storm Dune Trimming >0.09) due to better synchronicity of forcing factors such as high tide level, high wave heights and onshore wind direction. We conclude that storm energy is not always a direct indicator of coastal impact and that synchronicity of local forcing factors and antecedent beach conditions appears to be the most relevant in actual coastal response on sandy beaches. This study, therefore shows the importance of particular environmental parameters and their simultaneous timing in forcing change and is an important insight into which parameters may be more risk-relevant in producing erosion along many sandy, dune-fringed coasts of NW Europe.

Keywords: Five Finger Strand, dune scarp, synchronicity, forcing factors, run up, storm impact, erosion

INTRODUCTION

Storm impact along sandy coasts globally is driven by various local factors, including accommodation space and physical forcing parameters which help drive coastal dynamics (Cooper and Orford, 1998). The extent and range of impact variability can be high, even over small coastal stretches and minor morphologic alterations to beaches as result of dune vegetation, soil development and slope changes can influence beach response (Carter and Stone, 1989). Other characteristics of the subaerial beach, such as the elevation of the dune toe, foredune height, and the presence of nearshore subaqueous sandbars help determine the response of local morphology alongshore (Splinter et al., 2018). Changes in frequency and occurrence of storm-groups (Ferreira, 2006), as well as storm clusters (Dissanayake et al., 2015) can also intensify coastal morphological impacts.

The majority of storms impacting the Atlantic coastline of Europe form in the western mid-latitude wind belts as extratropical storms (Lozano et al., 2004). This movement of cyclones aligns along track corridors (Hayden, 1981) and displays an inter-annual variability (Schmith et al., 1998). Winter climate and storm occurrence and its corresponding relationship with large-scale patterns of atmospheric variability, such as the North Atlantic Oscillation (NAO), have been widely studied (Hurrell, 1995; Dawson et al., 2002). Indeed, a strong relationship was found between wave climate variability in the North Atlantic region and the NAO index (Dawson et al., 2002, 2004; Dodet et al., 2010). Studies from Lambert (1996) and Schinke (1993) have shown that more intense storm events have occurred since 1970 in the northern hemisphere. The Global Tropical and Extratropical Cyclone Climatic Atlas data (GTECCA, 1996) was used to show that storms normally originate from the west, with most focussing SW of Iceland (Lozano et al., 2004). In a comparative study, Feser et al. (2015) also found that from early 70s until the mid-1990s, there has been increased storm activity over the North Atlantic area (north of 55–60°) in agreement with the variability long-term proxies including the NAO.

Strong coastal storms particularly affect the western/north-western coasts of Ireland (Cooper et al., 2004; Backstrom et al., 2015). Historically, both its hard coasts (Scheffers et al., 2009, 2010; Erdmann et al., 2017) and sandy coasts (Cooper et al., 2004; Kandrot et al., 2016) are influenced by remnants of Atlantic Hurricanes reaching Ireland. Events such as the 1839 'Night of the big wind' (Shields and Fitzgerald, 1989) a Category 3 Hurricane and 1961's Hurricane Debbie (Hickey and Connolly-Johnston, 2012), demonstrate the potential impacts of receiving these events. More recently, Loureiro and Cooper (2019) show that in Ireland there is a strong relationship between positive phases of the NAO and highly energetic winters, with a greater number of storms per winter over the past 67 winters. For this period, they conclude that winters in the northwest coast of Ireland are becoming stormier.

The western coast of Ireland has therefore become attuned to generally high-energy wave settings, with localised sediments adjusted to this elevated energy forcing. In this regard, these beaches therefore usually require an amalgamation of forcing events to provoke substantial impact (Cooper and Jackson, 2003) with extreme storms resulting in dramatic shoreline erosional responses. These impacts manifest as rapid erosion of foredunes but are typically followed by shoreline readjustment (Cooper et al., 2007) and sediment recirculation within coastal cells with sand being returned to the coast in post-storm recovery periods (e.g., Backstrom et al., 2015).

In this study, we focus on two recent storm events that reached the coast of Ireland in the 2017–2018 period. Storm Ophelia arrived to the western coast of Ireland on the 16th October 2017 which at landfall was a "post-tropical storm" but was earlier labelled as a Category 3 hurricane (NOAA, 2017), the most eastern Category 3 Atlantic hurricane recorded (NOAA, 2017; United Kingdom Meteorological Office, 2017). This high-energy storm produced sustained winds of more than 34 knots and induced significant wave heights of 26.1 m at the Kinsale gas platform located at −100 m depth (Met EIREANN, 2017). Secondly, we examine Storm Hector, an unusually energetic summertime storm generated from a deep low-pressure system that was deflected toward the northeast to Ireland by a strong jet stream. It made landfall early on the 14th June 2018 with mean wind speeds between 65 and 80 km/h, with the highest recorded gusts reaching 111 km/h at Mace Head, Co. Galway (around 3:00 am) (Met EIREANN, 2017).

Coastal response to events like these, as well as post-storm recovery behaviour, have been shown to be spatially highly variable, even between adjacent coastal sites (Guisado-Pintado et al., 2014) and can be attributed to differences in local hydrodynamic regimes (Burvingt et al., 2017). Beach morphology (Haerens et al., 2012), regional and local geology (Jackson et al., 2005; Jackson and Cooper, 2009) all dictate site-specific response. Some studies (e.g., Karunarathna et al., 2014) have shown that beach and dune erosion from a clustering of storms could be more impactful than an isolated, single event with similar overall energy. However, the final impact could be strongly influenced by the chronology and sequence of storms in a cluster (Dissanayake et al., 2015). Further, the complex interplay between variables such as offshore wave height and pre-existing bathymetry often controls the coastal response (Coco et al., 2014). Forcing factors such as wave heights coinciding with higher water levels during storms, has been shown to dictate actual coastal damage-response (Masselink et al., 2016a,b) and further changes in dune morphology, based on the relative tidal range reached (Costas et al., 2005). Additionally, the orientation of a coastline compared to the storm direction and average winds, can also influence the incoming wave angle approach, inducing shelter effects and helping force the beach/dune into transporting sediment into the cross-shore and alongshore dimension (Castelle et al., 2015). Finally, the physical characteristics of beach-dune systems such as their dune toe elevation and overall dune height (Houser, 2013), the presence of subtidal sandbars and beach-slope's angle, can in combination, induce a physical response (Splinter et al., 2018).

The objective of this study is to investigate the associated coastal impacts from two storm events with different energy levels such as Storm Ophelia (October 2017) and Storm Hector (June 2018). We focus on morphological changes within an

intertidal zone and dune edge that occurred on the north-western sandy beach of Five Finger Strand during the storm peaks of both events. The direction of the storm, its intensity (significant wave height, wave period and speed of winds), storm duration locally, tidal stage and water level surge, as well as the intertidal morphology under pre- and post-storm conditions are examined. To better understand the forcing and response of dune coasts under particular conditions, we propose and test a new impact index "Storm Dune Trimming" which examines the potential dune trimming of specific storm events. We compare the actual local impact induced by both storm events to demonstrate the importance of synchronicity of forcing parameters in determining coastal impact response.

STUDY AREA

Western Irish coastlines are defined by hard geology with a cover of glacial materials, providing important sedimentary sources for its beaches (Burningham and Cooper, 2004). Basaltic headlands and cliffs punctuate the coast, while sandy beaches and large coastal dunes are present in coastline re-entrants (Jackson et al., 2005). Only 44% of its coastline can be classified under a high energy category (Devoy, 2008).

Five Finger Strand is situated on the Inishowen penninsula in County Donegal, western Ireland (**Figure 1A**). The beach, 1.7 km long and 350 m wide, is backed by a vegetated sand dune system that can reach heights of around 25 m with an average dune toe height that ranges from 2.0 to 3.0 m relative to mean sea level (**Figure 2B**). Its beach is classed as dissipative (Wright and Short, 1984) and runs north to south between Five Fingers rocks and Lagg Point at Trawbreaga Bay (**Figure 1A**). In the south, a tidal inlet presents a large ebb tide delta system with a concomitant, ebb channel. Sand shifts between the ebb tidal delta, estuary and the beach/dune system, driven through tidal inlet changes (Cooper et al., 2007; O'Connor et al., 2011). Nearshore intertidal bars are also present at Five Fingers Strand and their dynamics show clear seasonal and inter-annual variability (Jackson et al., 2016). Typically, during winter time (Oct-Feb) the site's northern beach and dune profiles (P1-3 in **Figure 1B**) displays quite flat topography with little to no bar formation, thereby rendering the beach and dune toe edge more exposed to higher energy storms and surges during the region's storm season. Conversely, in spring and summer, bars start to reform (and migrate toward the nearshore) along the northern profiles, as there is enough accommodation for them after the beach flattens earlier in the year. Conversely, the southern part of the Strand (P4-P5 in **Figure 1B**) are devoid of nearshore bars for most seasons and only in late summer does an infrequent nearshore bar form which is preceded by an intertidal channel. The beach sediment is carbonate-rich terrigenous sand (mean grain size 0.3 mm and largely homogenous across this zone) with a subordinate gravel component overlying a cobble/gravel base of glacial sediments.

Ireland's west coast beaches are largely meso-tidal (2–4 m) environments. Five Finger strand has a spring tidal-range of 3.5 m with average significant wave heights around 2.2 m and wave periods of 9 s, with predominant winds from the southwest (Jackson et al., 2005, 2016). Dominant swell wave approach is from the west and southwest and fully refracted within the headland-embayment system (Jackson et al., 2016; Guisado-Pintado and Jackson, 2018). Five Finger strand is therefore a high energy Atlantic beach system that has been modally adjusted to a large swell wave environment that undergoes important morphological changes over various spatial and temporal scales (Cooper et al., 2007; Guisado-Pintado et al., 2017).

STORM OPHELIA AND STORM HECTOR CHARACTERISTICS

Storm Ophelia

The remnants of Hurricane Ophelia struck the British Isles in mid-October 2017 under the status of an extra-tropical storm. The Hurricane developed originally southwest of the Azores from a persistent low-pressure system, allowing it to travel to north-eastern Europe (NOAA, 2017). Storm Ophelia reached Ireland on the 16th October and was re-classified as a "post-tropical" cyclone (Guisado-Pintado and Jackson, 2018) but still retained gusts of up to 130 km/h were recorded. Storm Ophelia made landfall at 10am (1100 UTC) October 16th.

Storm Ophelia's highest gust was 156 km/h with a SSE direction, which was recorded in Roche's Point (Co. Cork) at 10:59 am, further north at Malin Head (Co. Donegal), a maximum wind gust of 106 km/h was reached at 19:30 h on the 16th of October with an overall direction of SSW. Storm Ophelia, despite initial expectations, lost its energy as it travelled north toward the study site. Around Malin Head (**Figure 3A**) significant wave heights ranged from 1.78 m on the 16th October at 9:00 am to 1.28 m when the storm had passed the study site (18th October) as shown in **Figure 3C**, with associated 4–5 s wave periods. The maximum wave height, 2.22 m, was reached at 6:00 pm (17th October, **Figure 3B**). Wave direction varied from 170 (S) to 220 (SW) during the storm event, which is parallel to main beach orientation of the study site.

Storm Hector

Storm Hector occurred in the second half of June 2018 and was formed by an unusually strong jet stream forced by a cold air mass from Polar Regions meeting a warm air mass from the tropics. The storm reached the western Ireland coast on Wednesday the 14th June around midnight, producing 2 days of gales on the 13th and 14th, followed by frontal systems crossing toward Scotland on the 20th June.

Storm Hector's highest gust was 61 knots (113 km/h), the highest June gust since 2005. The month's highest 10-minute mean wind speed was 48 knots (89 km/h), and its highest June 10-min wind speed since 2005.[1] In Northern Ireland, gusts of 64 knots (119 km/h) and 60 knots (111 km/h) were recorded.[2]

[1]Met Eireann June report (2018).
[2]UK Met Office June report (2018).

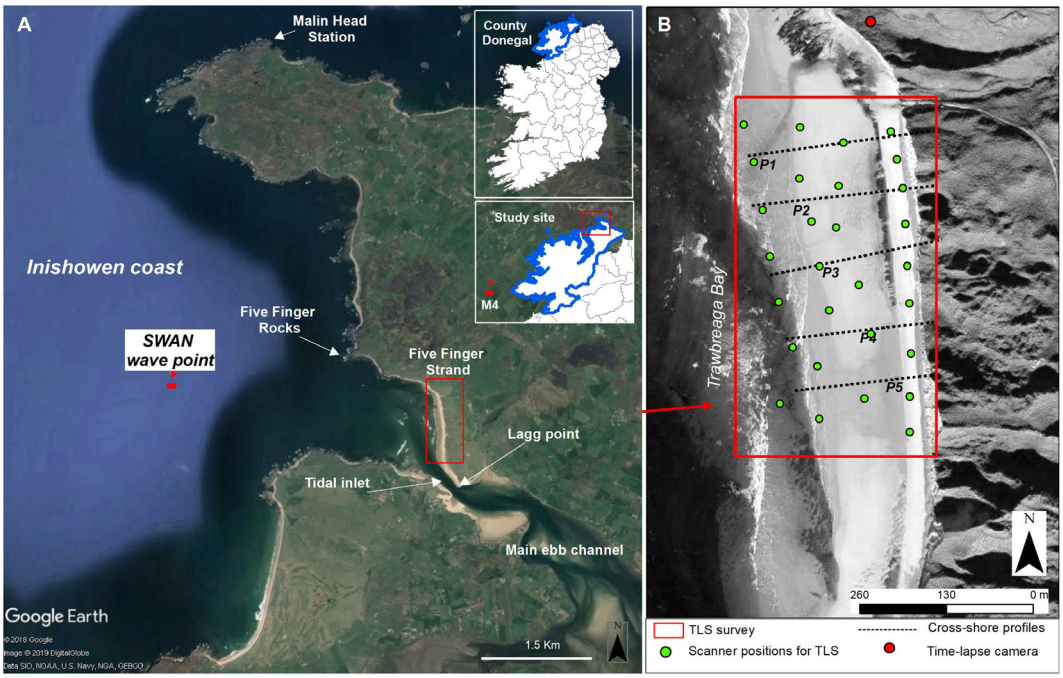

FIGURE 1 | (A) General location of the western coast of Ireland and the Five Finger site showing the M4 wave buoy position and SWAN grid point location. **(B)** Map of study area in north-western Ireland showing location of the TLS survey, time lapse camera and cross-shore profiles.

The strongest winds from Storm Hector over the northern coast of Ireland were coincident with high spring tides, leading to coastal flooding and wave overtopping in many coastal areas of Co. Donegal and Co. Galway. Storm Hector arrived at the study site around 3:00 am on the 14th of June (H_s = 2.5 m) and lasted until the 15th June 6:00 am were significant wave heights dropped below 2.5 m (**Figures 3E,F**). The storm had reached a maximum significant wave height of 4.0 m south of Malin Head (14th June 9:00 am) (**Figure 3D**). Mean wave period of 6 s were recorded closest to the study site. While offshore, the Marine Institute M4 buoy (54.99°N 9.9°W), recorded a wave height of 6.53 m (T = 8.9 s) at 9:00 am on the 14th of June. The storm showed a mean wave direction of 220–270° (W and WSW), perpendicular to the main coast orientation.

METHODS

Wave and wind data have been analysed as Storm Ophelia and Storm Hector moved over Ireland's western coastline, with particular reference to Five Finger Strand, using hourly data from various meteorological stations over a 24-h period encompassing both storms. To investigate the response at Five Finger Strand beach and dune system detailed before and after topographic data were acquired using a Terrestrial Laser Scanner (TLS) to quantify changes in the intertidal and subaerial beach areas as well as across the beach/dune topography (**Table 1**). Continuous monitoring of derived wave run-up and further storm-dune interactions during the occurrence of both events was carried out using a fixed, time-lapse camera over-looking the site.

Hydrodynamic Conditions During the Events

Offshore and Nearshore Modelled Wave Conditions

Modelled wave conditions at intermediate depths (−20 m) for analysing wave forcing close to the site was performed using the East Atlantic SWAN Wave Model output from Ireland's Marine Institute. The model uses the nearshore wave model SWAN (Booij et al., 1999; Ris et al., 1999) at a 0.025 degrees resolution (1.5 km) for a domain covering the Irish waters. The Global Forecast System (GFS) by the National Center for Environmental Prediction (NCEP) and the Fleet Numerical Meteorology and Oceanography Center (FNMOC) through Wave Watch 3 data model, provide boundary conditions. The model provides 3-hourly significant wave height (H_s), wave period (T) and wave direction (D). The nearest grid point to the site (55.332°N, 7.40°W; −20 m depth and located 2.7 km offshore) was used for extracting wave forcing (see **Figure 1A**). Wave analysis covered periods from pre-storm TLS surveys of the beach, from the 19th September 2017 until Storm Ophelia and from the 30th of March 2018 until the occurrence of Storm Hector respectively.

Water Levels and Wind Forcing

Tide levels were extracted every 6 min from the Malin Head tide gauge at 55.37°N, −7.33°W (see **Figure 1A**). The tidal dataset was combined with the height of the dune toe, taken previously from the TLS and GPS data along the back-beach (**Figure 2D**), and used to assess potential erosion of dune toe areas. Total water levels were calculated as the combination of the tide level and run up heights (Ruggiero et al., 2001;

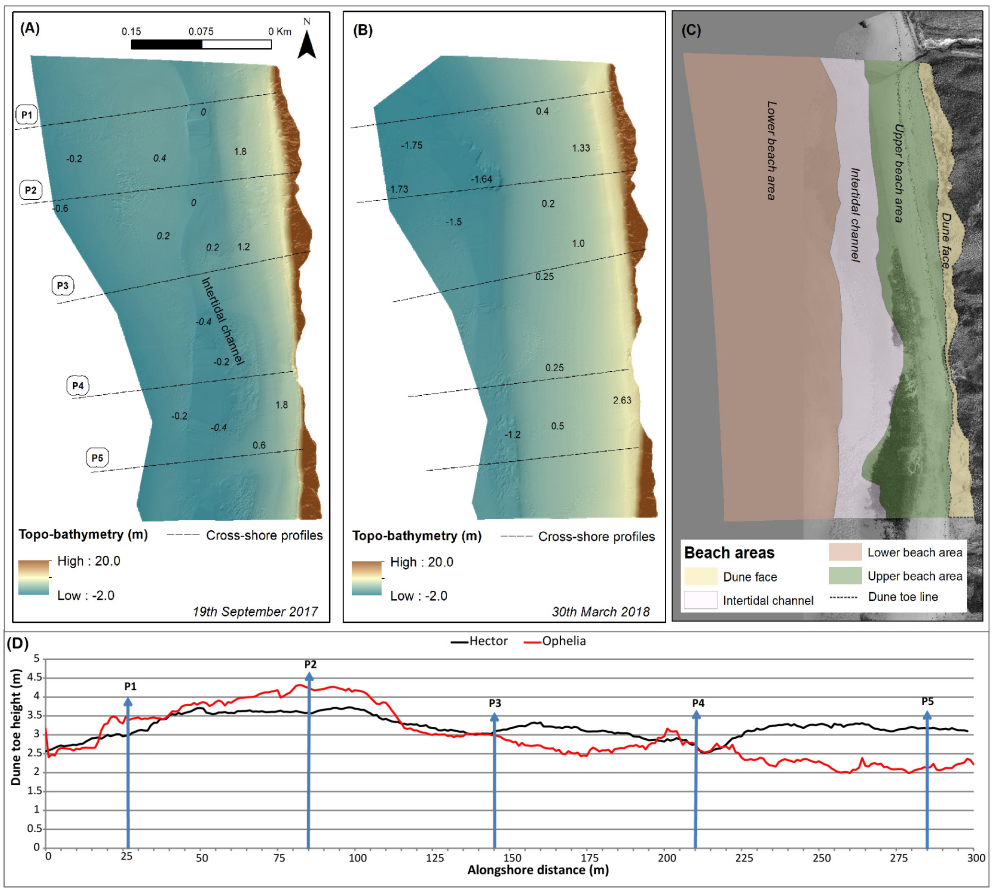

FIGURE 2 | Pre-Storm Ophelia **(A)** and Storm Hector **(B)** topo-bathymetries extracted from TLS surveys with numbers representing depths. Note differences in antecedent conditions of the submerged and subaerial beach at Five Finger Strand. **(C)** shows the subzones used for comparisons in the DoD analysis. **(D)** shows an alongshore section of dune toe height before Storm Ophelia (partially adapted from Guisado-Pintado and Jackson, 2018) and Storm Hector where the blue arrows represent the cross-shore profiles.

Young et al., 2016; Castelle et al., 2017). Stockdon et al. (2006)'s formula for dissipative beaches discerned that the level was exceeded by 2% of waves (R2%).

Real-time wave run-up and dune toe encroachment monitoring was supplemented by a fixed, time-lapse camera system (Brinno TLC200) set to capture images twice an hour. As a result, images spanning the whole monitoring period and particularly during the occurrence of the storm events (see **Tables 1**, **2**) helped (qualitatively) to image features such as sand lags/deposits and actual run-up encroachments.

Additionally, the wind regime was assessed during the passage of both storm events using the Malin Head meteorological station (shown in **Figure 1A**) operated by Met Eireann: The Irish Meteorological Service. Ten-minute average wind speeds (knots), wind direction (degrees) and Mean Sea Level Pressure (hPa) were extracted to examine wind forcing (speed and direction) during storms Ophelia and Hector.

Characterisation of Storm Events

Storm thresholds are usually site specific, with wind speed-based values ranging from 7.6 to 15.3 m/s in Atlantic coastal areas (Lozano et al., 2004). Here, we define storm events as those with a peak significant wave heights (H_s) above 10% exceedance of wave height, previously determined as being $H_s > 3$ m (Guisado-Pintado and Jackson, 2018). To determine the storm duration we used the 5% of exceedance meaning that a wave induced storm is noted only when H_s exceeds the 5% exceedance wave height (Masselink et al., 2016a,b) and ends with it falls below this limit. For the study site, the 5% exceedance wave height was set at $H_s = 2$ m. A minimum threshold for storm duration of 12 h was considered (to guarantee the events extend over high tide).

Given that storm events can differ significantly in terms of duration, wave power and morphological impact, the use of environmental proxies help to classify and compare storm events for a specific site. Proxies allow analysis of the variation in storms and their geomorphological impact, based on variables such as the frequency, duration, wave power and category (e.g., Dolan and Davies, 1992; Rangel-Buitrago and Anfuso, 2011). Two proxies were used to characterise storm climate during the study period: the *Storm Severity Index* (SSI) and the *Storm Impact Potential* (SIP) both developed by Zãinescu et al. (2017).

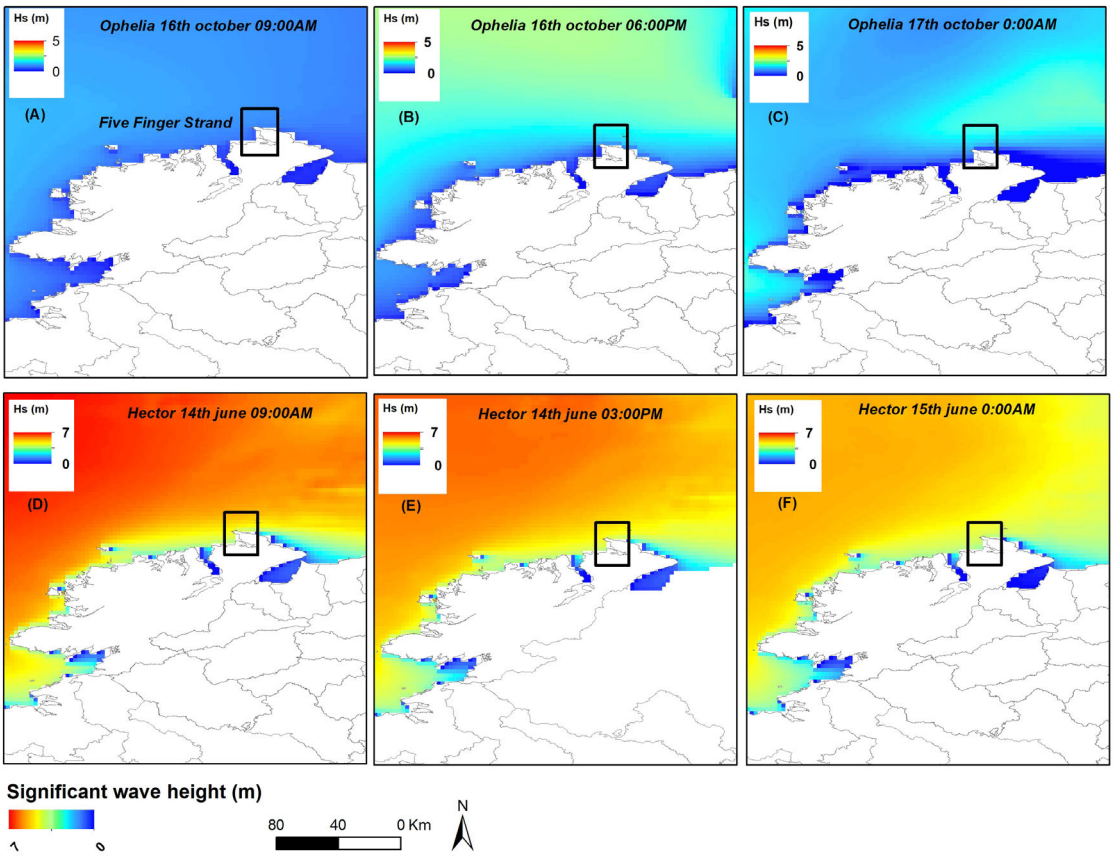

FIGURE 3 | Spatial and temporal evolution of Storm Ophelia **(A–C)** and Storm Hector **(D–F)** as they moved across the northwest coast of Ireland. Location map highlights the study site (black square) and hydrodynamic conditions (Significant wave heights) from the Marine Institute East Atlantic SWAN wave model.

In addition, a new index called *Storm Dune Trimming* (SDT) is proposed here to account for the potential dune trimming of a specific storm event.

The SSI quantifies the total energetic strength of an individual storm, based on the wind speed and its duration, and is based on work by Lamb and Frydendahl (1991):

$$SSI = \sum (V^3 \times T)/10^3 \quad (1)$$

Where: V = wind speed and T = total duration of a given speed (h).

In order to measure the potential coastal impact of a storm, the morphologic index (SIP) was used as it accounts for the angle of wind direction (α) and the shoreline orientation (θ) itself, which in the case of Five Finger is mostly N-S. Maximum impact is therefore assumed for storms from the NW to SW (i.e., for angles between 200° and 300°) for this site. Lower impacts correspond to storms that approach the coast with a longshore or slightly oblique strike to the shore direction (N–NNW; S–SSW). For this proxy, offshore wind directions are not taken into consideration.

$$SIP = \sum (V^3 \times T \times \sin(\alpha - \theta))/10^3 \quad (2)$$

Where: V = wind speed and T = total duration of a given speed (h).

Finally, the Storm Dune Trimming (SDT) proxy is designed to estimate the total water level (water level and run up) reached by a storm and thus the potential dune impact. The proxy is a measure of the number of hours for which total water levels of a specific onshore storm event is above the average and lower dune toe height.

$$SDT = \sum (TWL^3 \times Th \times \sin(\alpha - \theta))/10^3 \quad (3)$$

Where: TWL = total water level, Th = total duration of wave height above dune toe (h) and α = wave direction.

Topographical Change Analysis

Topographic changes, driven by the storm events, both in the intertidal area and subaerial beach, were quantified using a FARO Focus 3D × 330 TLS. The TLS survey produced a dense point cloud, extending from the dune toe toward the intertidal environment. Surveys were undertaken during low tide conditions, revealing a large part of the intertidal area to around −1.5 m (see **Figures 2A,B**) and ranging landward over front sections of the dunes (up to +20 m).

TABLE 1 | Main characteristics of the storm events studied and the topographic surveys performed to monitor geomorphological impact.

Storm event	Pre-storm TLS and topographic survey	Post-storm TLS and topographic survey	Time after event	Scan stations
Ophelia (16th–17th October 2018)	19th September 2017	18th October 2017	24 h	29 scans
Hector (13th–15th June 2018)	30th March 2018	26th June 2018	11 days	31 scans

TABLE 2 | Storm characteristics for each surveyed period pre- and post-Ophelia and Hector storms.

Storm events		Wave conditions	Duration	Mean wave direction	Maximum TWL
Pre- Storm Ophelia	S1	Maximum H_s = 4.62 m; T = 8.74 s	108 h	318°	2.30 m
	S2	Maximum H_s = 3.66 m; T = 9.67 s	75 h	325°	2.44 m
	S3	Maximum H_s = 3.84 m; T = 11.23 s	36 h	324°	1.86 m
Storm Ophelia	S4	Maximum H_s = 2.24 m; T = 5.3 s	12h	326°	1.40 m
Pre- Storm Hector	S1	Maximum H_s = 3.07; T = 9.87 s	15 h	340°	2.30 m
	S2	Maximum H_s = 4.96; T = 10.64 s	57 h	336°	2.02 m
Storm Hector	S3	Maximum H_s = 4.06; T = 6.59 s	21 h	340°	2.92 m

Topographic surveys were performed along the northern section of Five Finger Strand (**Figure 1B**), selecting a 420 m × 250 m area of interest (≈105,000 m^2). For Storm Ophelia pre- and post-storm surveys were 6 weeks apart (Guisado-Pintado and Jackson, 2018), whereas for Storm Hector a pre-storm survey was carried out 13 weeks before the event and the post-storm took place 8 days after the event (**Table 1**). A total of 29 scan station locations were established across the site for each event, ensuring good coverage. We used 6 target spheres as reference Ground Control Points (G) (**Figure 1B**) georeferenced into the Irish National Grid coordinate system using a RTK dGPS (Trimble 5800) with an accuracy of 0.03 m in x, y and z.

TLS-generated Point Clouds were post-processed to create Digital Surface Models (DSMs) from pre- and post- conditions of the storm events. The Geomorphic change detection (GCD) add-in in ArcGIS (Wheaton et al., 2010) allowed surface volume variations (DEM of Difference, DoD) and topographical comparisons (vertical changes) of each pair of surveys. The total volumetric change (dQ_{total} in m^3) relates to the difference in volume of the post- and pre-storm surface utilising the DEM, and areal change (dA_{total} m^2) is the amount of area undergoing erosion/deposition after each event and over subsequent TLS surveys during the recovery process. To guarantee the quantification of morphological changes at different beach sections as well as the comparison of driven impacts of both events (storms Ophelia and Hector), four zones were delimited following Guisado-Pintado and Jackson (2018). These relate to (1) lower areas from mean sea level (MSL) to lowest level surveyed by TLS, (2) an intertidal channel, (3) between MSL and the shoreline (dune toe) and; (4) the upper area from the shoreline to the top of the dune edge (**Figure 2C**). Finally, five cross-shore profiles (**Figures 1**, **2**) extracted from DTM surveys where analysed to assess alongshore and cross-shore morphological changes between the two storm events.

RESULTS

Wind Forcing

Wind is one of the main environmental variables that dictates the characteristics of locally generated waves at the coast, with speed and direction of wind critical in driving potential beach impacts from a storm. Wind patterns and resulting wave climates during storms Ophelia and Hector were significantly different, with storm events that occurred between the pre- and post TLS surveys also being dissimilar in power, orientation and duration.

During Storm Ophelia, winds reached a maximum of 38 knots (70 km/h) at Malin Head station which were sustained for around 3 h (**Figure 4A**). However, as shown in **Figure 4B**, the wind direction was mostly shore-parallel and varied from a predominantly southern direction (about 180°) to SSW (220°) as the storm passed through the site (17th October 2017 at around 18:00 h). At Malin Head during the passage of the Storm Ophelia, sea level pressure reached a minimum of 979 hPa (**Figure 4C**). Storm Hector's pattern was somewhat different. A maximum wind speed of 37 knots was recorded during the storm but lasted for only 1 h (see **Figure 4A**), although sustained winds over 18 knots were recorded for the remainder of the storm. Predominantly *onshore* winds with an average direction of 220–270° (WSW) were recorded over the site during the passage of Storm Hector. Minimum pressure at sea level never fell below 985 hPa (**Figure 4C**). In both cases, mean wind speeds during the storms were around 27 knots at Malin Head station (**Figure 4A**) and changes in wind orientation conditions produced a 5–10 knots decrease in wind speeds (**Figures 4A,B**).

Wave Climate and Storm Occurrence: Evolution and Characterisation

The hourly evolution of Storm Ophelia along the western seaboard of Ireland (**Figures 3A–C**) reveals that the storm's intensity gradually dissipated as it travelled north, whereas during Storm Hector energy conditions reached their maximum level at northern Irish latitudes as the storm moved toward the western seaboard (**Figures 3D–F**. In the case of Storm Ophelia, and according to Guisado-Pintado and Jackson (2018), three storm wave events (onshore directed with orientation varying from 318° to 324°) were recorded in between topographic and TLS surveys and before the occurrence of Storm Ophelia (see **Table 2** and **Figure 5A**). The peak of the first storm (S1) occurred on the

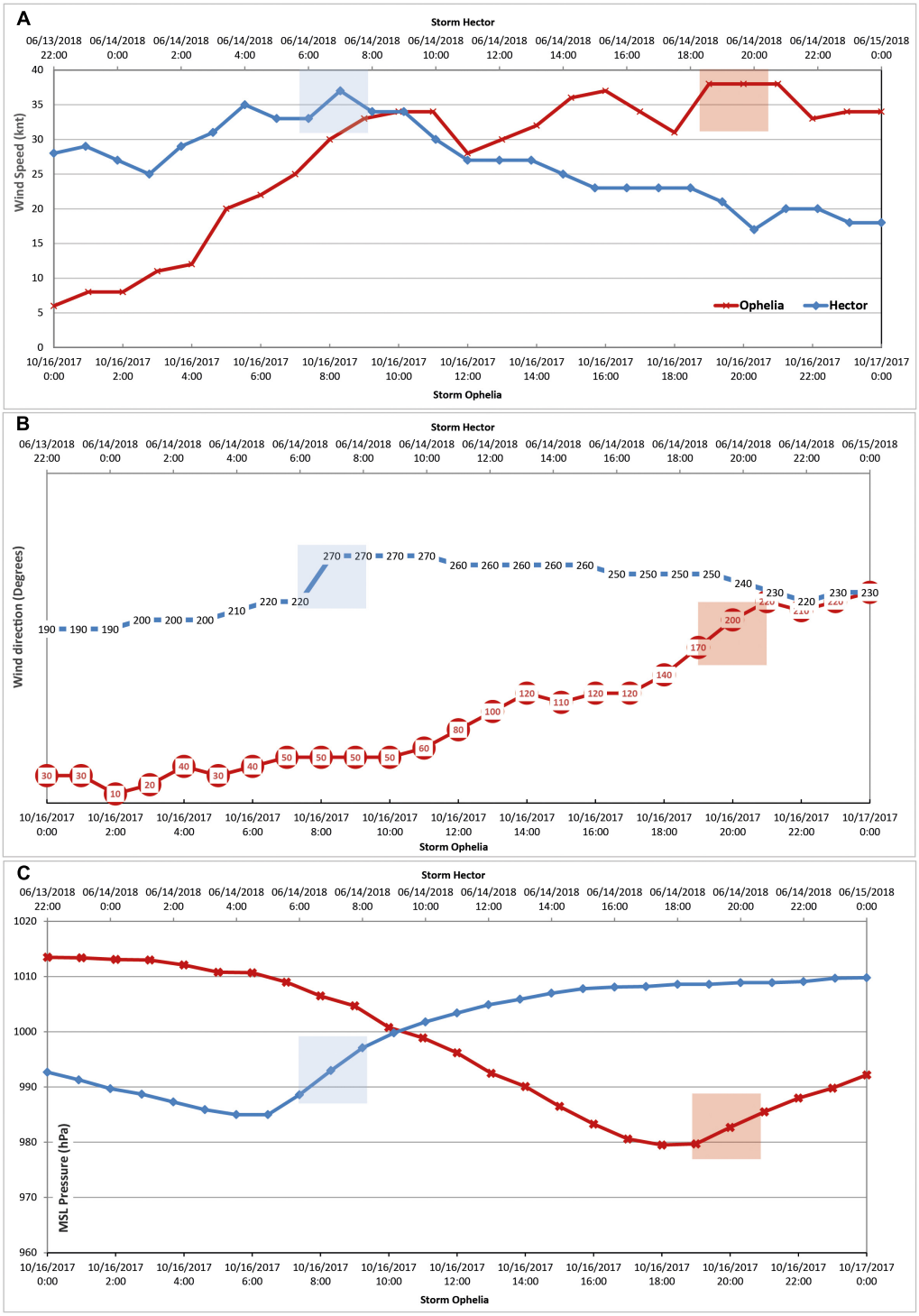

FIGURE 4 | Time-series of wind conditions during both storm events at Malin Head Station. From above **(A)** 10-min wind speed (knots), **(B)** wind direction (degrees) and **(C)** Mean sea level pressure (hPa). Red and blue boxes represent Storm Ophelia and Storm Hector coincidence at Five Finger Strand respectively.

2nd Oct at 03:00 am during high tide (1.21 m), producing a total water level (TWL) of 2.13 m. A second highest synchronisation between wave height and water levels took place on the 4th October between 16:30 and 18:00 h, where TWL peaked to 2.2 m (see **Figure 5C**). The second storm (S2: 10th Oct 18:00 h) began 5 days later and over its duration was coincident with several cycles of high tide (1.47 m) resulting in a maximum TWL of 2.5 m and thus above average dune toe height (2 m

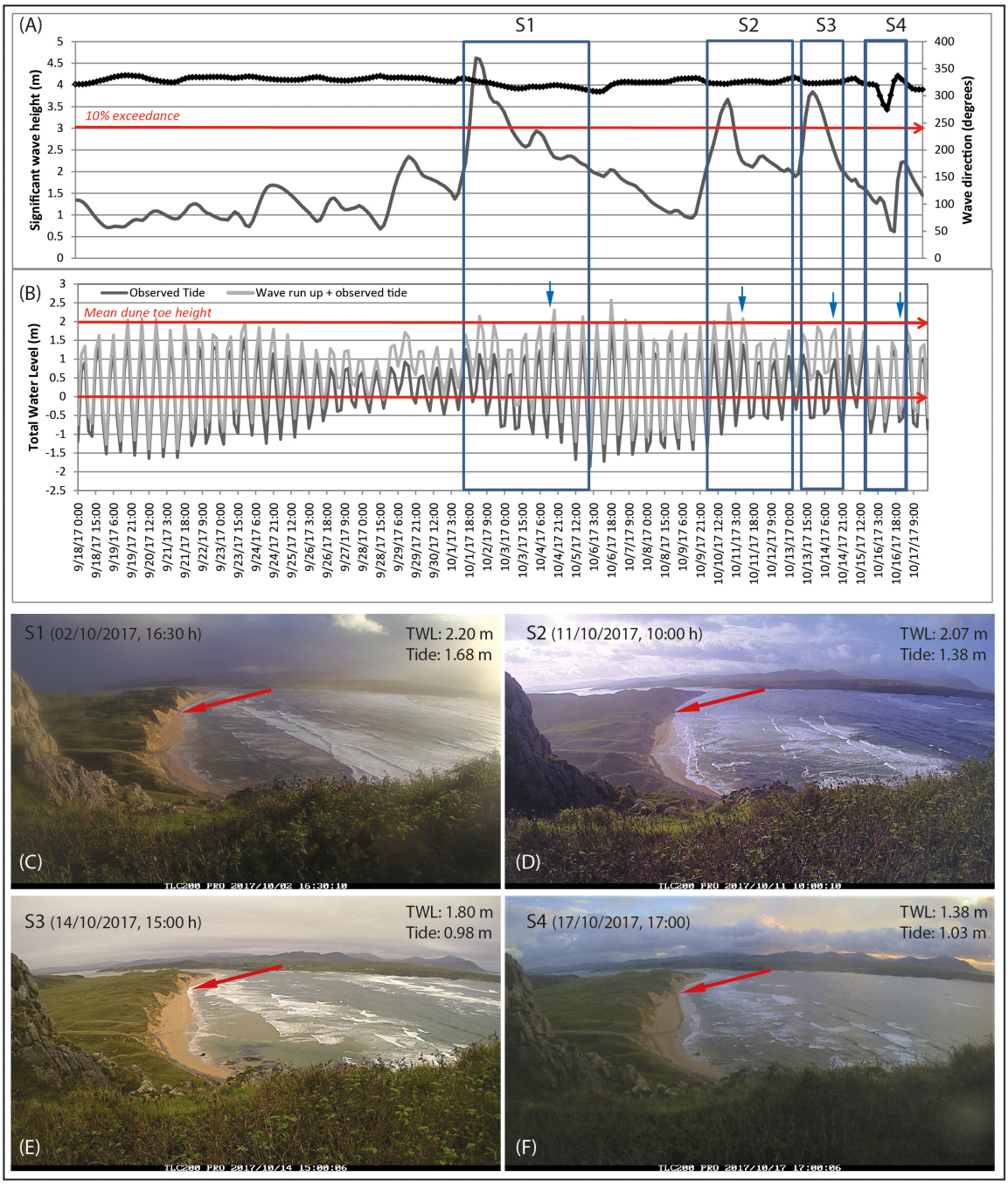

FIGURE 5 | (A) Shows the wave climate time-series spanning Storm Ophelia where the left Y-axis accounts for H_s (grey line) and right Y-axis represents wave direction in degrees (top black line). Graph **(B)** represents the Total Water Level (TWL) based on wave run-up for each storm event (from Guisado-Pintado and Jackson, 2018) where blue arrows show the water level position from the time-lapse camera pictures. Squares highlight storm events that occurred between TLS/topographic surveys with S4 corresponding to Storm Ophelia. Pictures **(C–F)** show corresponding time-lapse images where peak storm wave height and/or the highest synchronisation of both wave height and water level during each storm analysed (S1–S4). Note that red arrows point to the maximum wave run up.

height as shown in **Figure 2D**). S2 peaked during the night of 10th October at 9:00 pm and couldn't be recorded by the TLC but hours later (11th October between 09:00 and 10:00 am) a second peak resulted in TWL of 2.07 m as evidenced in **Figure 5D**, affecting the dune toe line in the most southern sections. Six hours after the end of S2, a third storm occurred (S3: 13th Oct 15:00 h). S3 presented two peaks, one on the 14th at midnight with a maximum TWL of 1.86 m and a second the 14th at midday where TWLs were around 1.8 m, in both cases below mean dune toe height (**Figure 5E**). Twenty-four hours

after the end of S3, at 3:00 am, Storm Ophelia struck south western Ireland. At the Five Finger site, on the 16th October at around 6:00 pm, the storm was coincident with a low tide, producing TWLs up to 1.4 m and hence below the average height of the dune toe at the time as shown in **Figure 5F**. Given the fast tracking speed of Storm Ophelia, sustained high wave energy conditions were limited and the average significant wave height was <2.5 m at Five Fingers Strand. Interestingly, using the standard storm analysis, which includes a certain threshold criteria (duration and 10% of exceedance of significant wave height), Storm Ophelia may not actually be characterised as a storm 'event'. On the other hand, two of the three storm events (S1 and S2) that impacted Five Finger before Storm Ophelia, had the potential to produce dune trimming and shoreline retreat with the calculated TWLs (**Figure 5B**) and observed time-lapse images (**Figures 5C,D**). Neither Storm Ophelia nor the preceding storm (S3), however, had synchronised conditions (coincident with high tide and sustained onshore winds) with which to impact the dunes.

Storm Hector hit the western coast of Ireland during the 14th of June 2018. As the storm travelled north it increased in strength and the strongest winds were recorded across Northern Ireland before spreading eastwards across Scotland, northern England and north Wales. The storm lasted for 21 h and a maximum wave height of 4.06 m was recorded for the site. At the peak of the storm (14th June at 06:00 am), maximum water levels of 2.92 m were reached, given its coincidence with spring tide (2.21 m) and provoking the storm surge surpassing the average dune toe height for the site (**Figure 2D**). Wave run-up, as recorded by the time-lapse camera (see **Figure 6D**), reached the dune toe across the beach. However, in the spring of 2018, two other storms preceded Storm Hector at the site (**Figure 6A** and **Table 2**). The first storm (S1) began on the 17th April with its peak coincident with high tide (1.37 m) although TWLs achieved (2.3 m) were slightly below average dune toe height for north sectors but could have affected the dune toe in southern areas (see **Figure 6B**). One month later, S2 began on the 9th of May and lasted for 57 h. Despite its duration, the storm was coincident with neap tides and although morphological changes in the intertidal and supratidal occurred, wave run-up did not effectively reach the dune base. The peak of S2 occurred at 3:00 am on the 10th of May with a TWL of 2.02 m. A second peak took place 12 h later, resulting in maximum water levels below dune toe (TWL = 1.59 m) as can be seen in the time-lapse image (**Figure 6C**).

A key aspect of our study is the use of storm proxies to examine individual storm events in terms of intensity, duration and potential morphological impact. Resulting proxies were calculated for the seven events: three preceding events before Storm Ophelia, Ophelia itself, two storms preceding Storm Hector and for Storm Hector. **Table 3** shows calculated proxies and some significant differences between storm events. Previous to Storm Ophelia, S1 displayed the greater SSI and SIP values, inducing significant dune trimming (SDT = 0.11) due to both its duration (more 100 h) and its coincidence with several cycles of high tides. Similarly, S2, which occurred 10 days before Storm Ophelia, had a Storm Severity Index of 721 with a strong potential morphological impact (SIP = 566.12) and impacted the dunes as confirmed with the SDT value and TLC images (**Figure 5D**). On the other hand, S3 and Storm Ophelia resulted in lower values of SSI and SIP. In both cases, storm duration was too short to cause morphological impact in the intertidal and dune field (SDT < 0.05), although Storm Ophelia with shore-parallel winds could have had an important role in sediment transport across the base of the frontal dune line and supratidal areas.

Storm proxies for the events preceding Storm Hector as well as Storm Hector itself, show that despite S2 (May 2018) presenting similar and greater values of SSI and SIP respectively than Storm Hector, the effective morphological impact on the dunes and subaerial beach was minor (SDT = 0.01). The S2 had an overall duration of 60 h but it coincided with neap tides resulting in lower TWLs. On the contrary, Storm Hector despite it only lasting a third of S2 duration, was synchronised with Spring tides resulting in a SDT of 0.9 and thus giving dune toe erosion (**Table 3** and **Figure 6C**).

Morphological Changes and Beach/Dune Response Patterns

The analysis of the morphological response from both events was carried out using two pairs of DTMs from TLS point clouds at 0.5 m resolution. As described by Guisado-Pintado et al. (2019), this method helps compare topographic and volumetric changes between surveys across a beach/dune continuum. Total volumetric change (dQ_{total} in m^3) relates to a difference in volume between the post- and pre-storm periods using the DEM, whereas areal change (dA_{total} m^2) is the area with erosion/deposition.

The morphological response after Storm Ophelia shows that volumetric differences are significantly focussed in the alongshore, with a distinct North-South picture revealed (**Figure 7A**). The blue colour scale shows areas where deposition (gains) is prevalent, with a deposition volume of +9,464 m^3 covering 0.39 km^2 (around 38% of the surface) and located around the intertidal channel with a net gains in volume of +7,309 m^3 (**Figure 9B**) for the whole area (Guisado-Pintado and Jackson, 2018). This deposition is particular evident across profiles P1 and P2 and P4 where the differences in elevation are around +0.5 m. Red areas represent erosion/sediment loss and is represented by 62% of the total surface area. A total volume of 15,481 m^3, representing 0.66 km^2, is ubiquitous over the lower (−7,140 m^3) and upper beach area (−6,040 m^3; **Figure 9B**) and represents −0.8 m in elevation change around profiles P3 and P5, as shown in **Figures 8C,E**. Finally, the southern dune face (at P4 and P5), where the minimum dune toe heights are found, accounts for a loss of −1,860 m^3 due to dune trimming during the previous storms (around 0.5 m change in elevation) as shown in **Figures 7A**, **8D,E**.

For Storm Hector, the spatial topographic changes detected in the DoD analysis suggest that a northern lobe of sand was stripped and relocated to the middle-north of the study area (**Figure 7B**), whereas southern profiles underwent erosion (**Figures 8D,E**). A general lowering of the southern area (≈ −0.20 m of elevation change) and across all zones is found

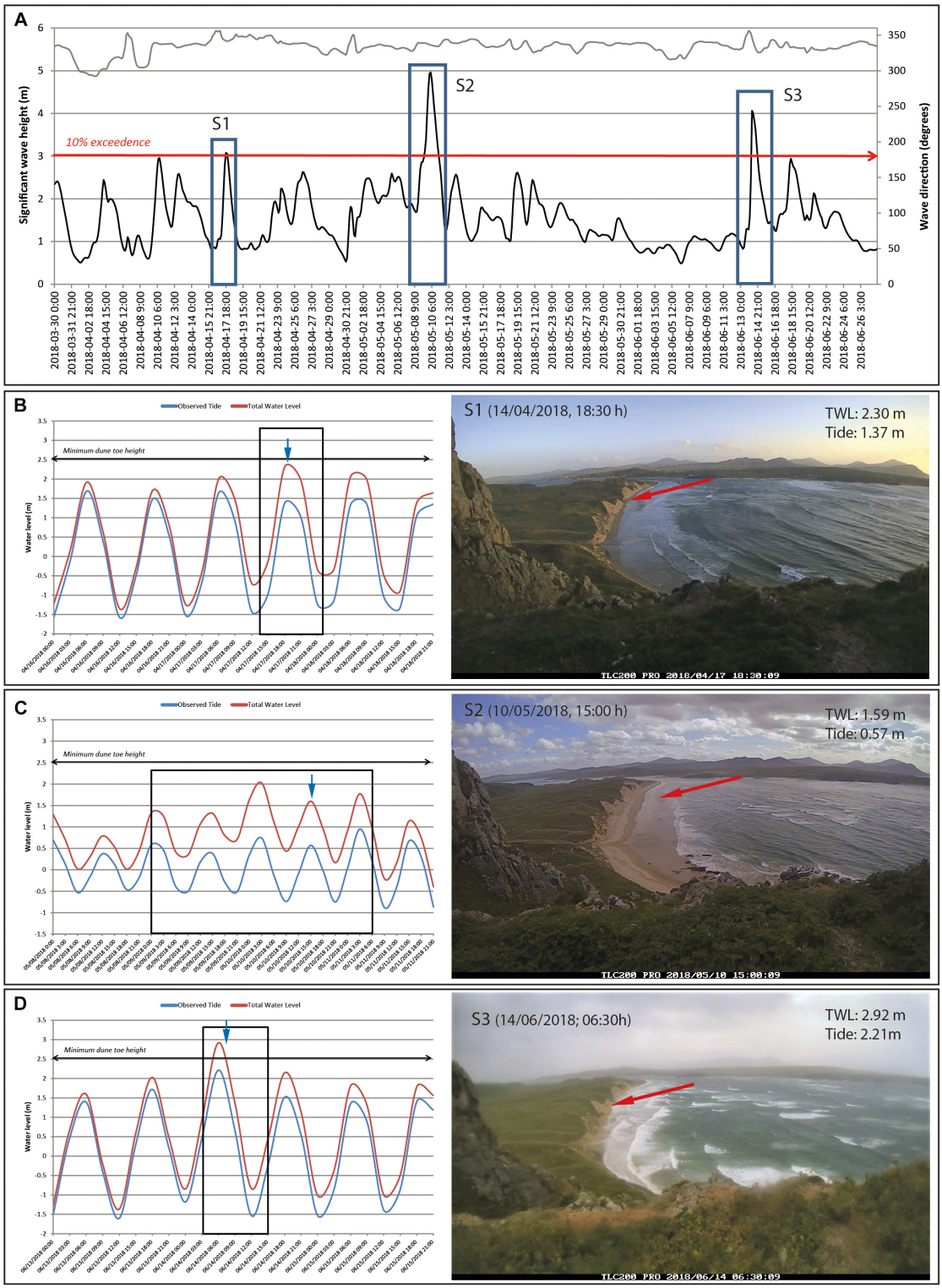

FIGURE 6 | Wave climate time series spanning Storm Hector **(A)**, where the left Y-axis accounts for H_s (black line) and right Y-axis represents wave direction in degrees (top grey line). Note that in this panel black empty squares highlight storm events occurring between TLS/ topographic surveys (S3 corresponds to Storm Hector). **(B–D)** represent measured water levels and calculated Total Water Level (TWL) based on wave run-up for each storm event considered (left hand). On the right, time-lapse images representing either the storm's wave height peak or the highest synchronisation of both wave height and water level during each storm analysed (S1–S3). Note that red arrows point to the maximum wave run up reached.

TABLE 3 | Calculated proxies for each storm recorded at the study site.

Storm events		Storm Severity Index (SSI)	Storm Impact Potential (SIP)	Storm Dune Trimming (SDT)
Pre-Storm Ophelia	S1	1718.65	1298.00	0.11
	S2	721.80	566.12	0.10
	S3	194.22	85.40	0.04
Storm Ophelia	S4	114.71	95.72	0.02
Pre-Storm Hector	S1	50.80	44.80	0.03
	S2	323.00	219.00	0.01
Storm Hector	S3	357.00	159.00	0.09

(with a net loss of −7,400 m^3, **Figure 9C**) and 97% of area experiencing erosion. Further north (P1-P2), the blue colour scale indicate areas of deposition (gains) which dominates 86.5% of the northern part of the study site, with a total volume of deposition of +14,300 m^3. Across this area, changes in elevation reach up to +0.45 m, particularly across P1 as shown in **Figure 8A**. The area comprising the dunes shows a pattern of the higher portions of dune with erosion (red) suggesting that sediment had slumped to the base of dune (blue) with an exception at P3 (**Figure 8C**). This result is in line with previous results that showed that a maximum TWL of 3 m was above dune toe height in the majority of the coastal stretch (except around P1 and P2), invoking dune trimming during the storm. Finally, it is clear that sediment gains occurred in the lower beach (75% deposition with an average volume of 10,000 m^3, **Figure 9C**) and in the dune area (91% deposition at P1 and P5 as in **Figures 8A,E**) whereas losses are evident in the upper beach around the southern part of the study site (P3–P5), where it accounts for −3,900 m^3 (60% of the zone experienced lowering), and in the intertidal area (**Figure 9B**), except at P3 which small changes are detected.

Overall morphological changes induced by the seven storms analysed represent a positive net volume difference of 772 m^3 in the lower beach area and 6,596 m^3 in the intertidal as shown in **Figure 9A**. Negative net volume differences are found in the upper beach area, where after the balance of the erosion and deposition induced by the storms, represents a net volume of –6,859 m^3. Finally, the dune facing area shows the smallest net volume difference accounting for the comparison of the two DoD with a value of +244 m^3.

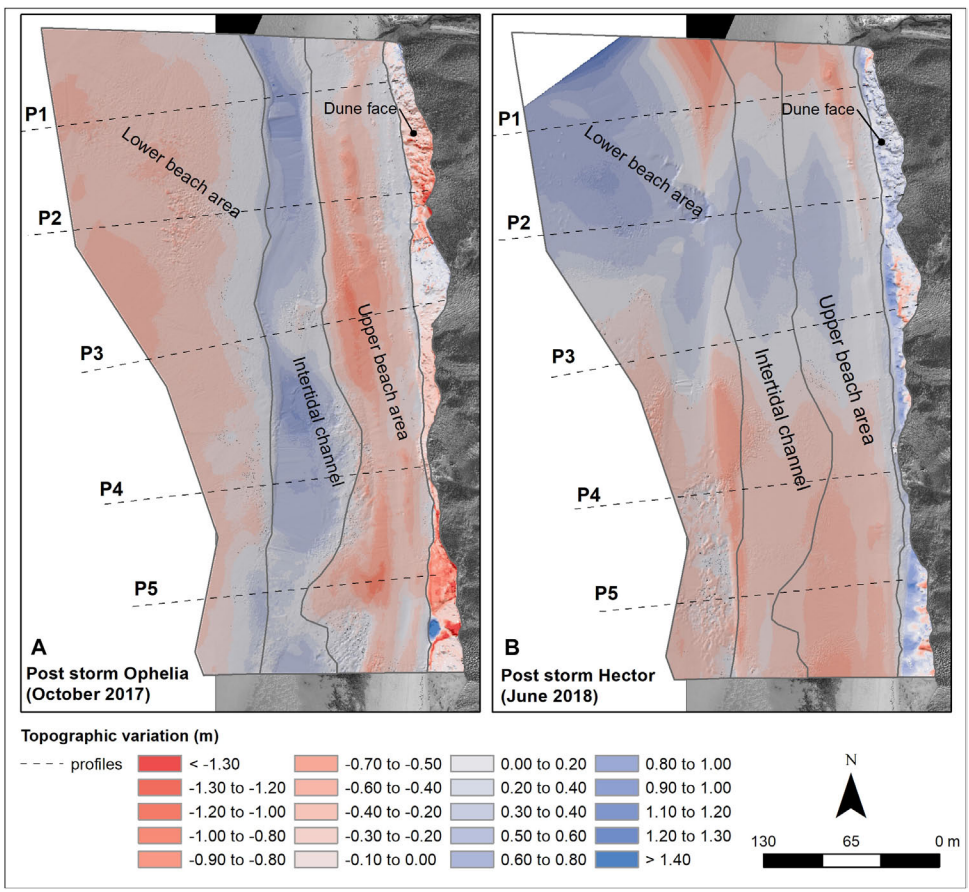

FIGURE 7 | Spatial representation of topographic changes measured pre- and post-Storm Ophelia **(A)** and Storm Hector **(B)** at the study site. Four zones (dune face, upper beach, intertidal channel and lower beach area) are defined where topographic changes are evident. Note that cross-shore profiles are represented with black dashed lines.

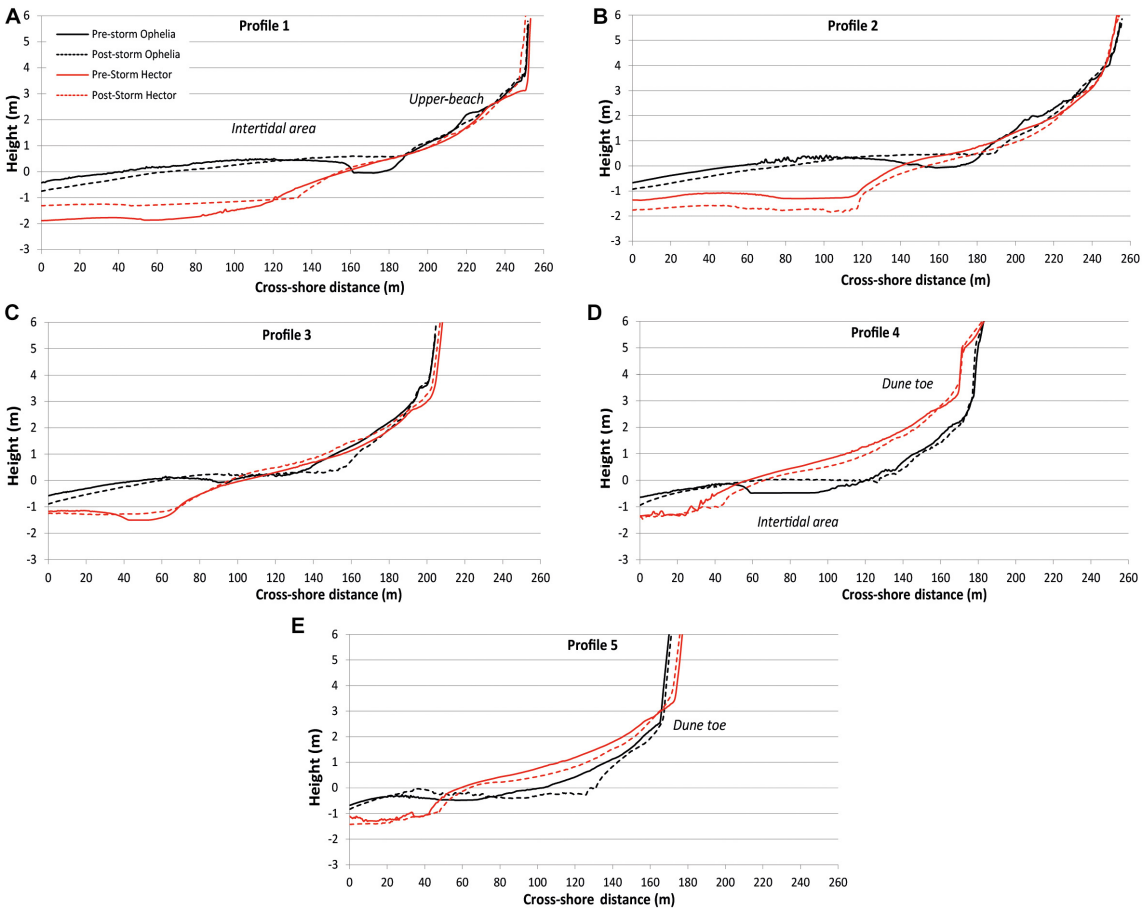

FIGURE 8 | Diagrams **(A–E)** correspond to five cross-shore profiles used to compare topographic changes (see **Figure 1B**). Pre-Storm Ophelia is represented by the black line and post-Storm with a black dashed line. Red line corresponds to pre-Storm Hector and the post-Storms profile is shown with a dashed red line.

DISCUSSION

Understanding the response of sandy coastlines to high-energy storm events is important for effective coastal management. Many studies have deliberated on their actual impact, defining a whole suite of outcomes from a range of forcing factors available from site to site and event type (Coco et al., 2014; Guisado-Pintado et al., 2014, Loureiro et al., 2014; Backstrom et al., 2015; Burvingt et al., 2017). Storm duration and intensity are now established as key variables in dictating the degree of change that may occur along sandy beach and dune coastlines (Dolan and Davies, 1992; Masselink et al., 2016a,b) but to date, these are largely generalisations with only a limited number of studies comparing storm response and effective combinations of driving factors for beach/dune response (Castelle et al., 2015; Phillips et al., 2017, Guisado-Pintado and Jackson, 2018; Splinter et al., 2018). The examination of antecedent surface changes and the definition of storm thresholds is extremely relevant to anticipate subsequent responses (Gervais et al., 2012) as storm buffering and shoreline response are a direct result of intertidal configuration. A paucity of studies on these dynamic systems is caused by the requirement for regular pre- and post-storm environmental monitoring to gather an appropriate range of information required at sufficient spatial and temporal levels. Poor temporal data on beach and dune topography, hydrodynamic and atmospheric variables at most coastal sites means that insufficient time-series' are available for adequate analysis of process-responses mechanisms driving changes.

Here, using two high-energy storm events, we show that the occurrence of what are deemed automatically as impact storms may not always play out as predicted. We isolated a number of key environmental variables under pre-storm and post-storm periods from both Storm Ophelia (October 2017) and Storm Hector (June 2018) to provide a range of conditions and responses to better examine which parameters may prove more effective at inducing (or not) changes on the sandy intertidal and back-beach areas of a beach/dune site in NW Ireland along a high-energy coastline.

The work highlights the importance of having a set of synchronised environmental variables that, when combined, can have a highly significant impact in driving actual morphological changes on sandy beaches and dunes. The use of two separate and quite different storm events provides a range

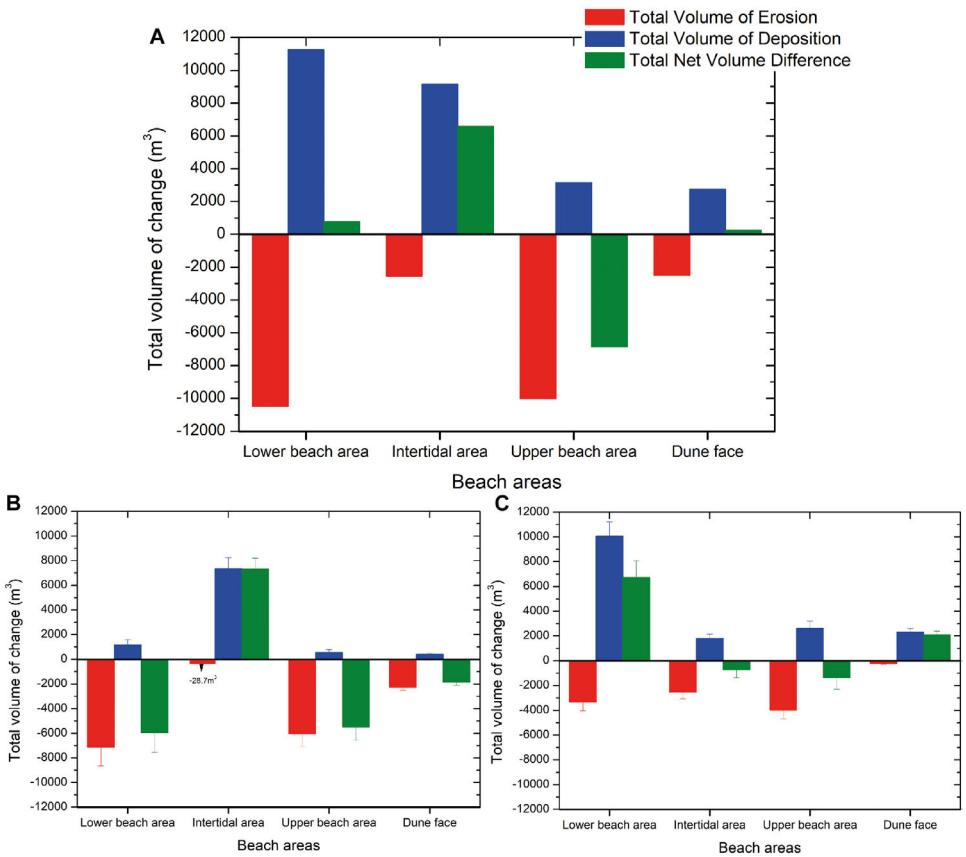

FIGURE 9 | Total volumetric changes (m^3) detected from DoD analysis corresponding to the combined effect of both main storms **(A)**. The bars show the budget segregation at defined beach areas for comparative purposes. Graphs **(B,C)** represent the volumetric changes induced by Storm Ophelia (from Guisado-Pintado and Jackson, 2018) and **(C)** Storm Hector respectively with errors bars.

of forcing parameters to better examine those more effective parameters at play.

Storm Duration

The duration of a storm (effectively the speed of the storm track) largely commands how long the high magnitude event will retain those energy levels at a particular site and thereby enhances the coincidence with high-tide. Storm Ophelia for example, was a rapidly tracking event, albeit of very high energy levels, which passed over the site relatively quickly, reducing its impact compared to Storm Hector which pushed its energy into a more temporally concentrated period to create more sustained conditions. Storms that are 'held' in place longer will naturally coincide with the regular high tide level cycles at sites and therefore impact, particularly dune toe erosion from wave run-up processes, will be magnified (e.g., Cooper et al., 2004). This 'held' erosive phase unfolded during Storm Hector, where we saw much more dune toe erosion than with Storm Ophelia (see **Figure 7**). The Storm Dune Trimming index (SDT) value for Storm Hector for example, was over four times greater than during Storm Ophelia, indicating that the storm was coincident with high tide levels (**Figure 6D**). Similarly, Storm Hector had a Storm Severity Index (SSI) over three times that of Storm Ophelia (**Table 3**) which suggests that overall, this induced a more severe morphological impact on the beach/dune which is in line with **Figure 7B**, where substantial changes in topography are more evident. In this sense, the proposed proxy seems to represent quite well the potential dune trimming from a storm event. Furthermore, storm events that occurred before Storm Ophelia (i.e., S1 and S2) showed high values of SSI, SIP and STD, suggesting that some of the intertidal changes observed in the post-storm survey could be associated with the passages of these two high-energy events as suggested by Guisado-Pintado and Jackson (2018).

Sediment and Spatial Surface Changes

The Storm Impact Potential (SIP) of Storm Hector was 1.67 times that of Storm Ophelia's suggesting a much more effective sediment movement and displacement of intertidal and supratidal beach sand under Storm Hector conditions. This again is likely due to Storm Hector being effectively held over the site longer and forming a more effective direction (onshore winds with W to SW orientation) than Storm Ophelia, which gave time for waves to modify topography.

Comparison of pre- and post-Storms Ophelia and Hector surface topographies and their cross-shore profiles, the two major

storms (**Figures 7**, **8**), show localised displacement patterns that illustrate interesting responses of the beach surface. This finding indicates where waves have preferentially stripped and deposited sand as result of forcing in pre-storm and during storm conditions. For Storm Ophelia, the upper and lower sections of the beach show strong erosional patterns, with a central band of deposition running along North to South as previously discussed by Guisado-Pintado and Jackson (2018). For Storm Hector, sediment has been removed primarily from the northern and southern sections (upper and lower beach as seen in P2, P4 and P5) and then relocated further to the middle of the beach (around P3), depositing and building up the beach surface local to the erosion (**Figures 7B**, **8C**). Further erosional lowering of the intertidal beach is then evident, again in the southern sections of the site (**Figures 8D,E**). Storm Hector's 'held' position may have allowed more focussing of wave energy with a more onshore component of the storm compared to Storm Ophelia given that storm duration was coincident with onshore winds that were highly synchronised with high tide levels at the site. This resulted in a significant change on the front dunes, undergoing sediment loss due to dune toe trimming and resultant collapse that can be seen as depositional areas (91% of deposition) in the DoD (**Figures 7B**, **9C**). In the case of Storm Ophelia, cross-shore sediment transport processes seem to be responsible for sediment lost in the upper beach and in the intertidal channel whereas morphological changes observed along the dune face are indicative of alongshore processes and exchanges. This finding shows that alongshore dune retreat is heterogeneous and driven by particular dune morphology present, antecedent beach volumes and likely nearshore bathymetric configurations.

Further, the observed vertical dune face differences in P4 (**Figure 8D**) between Storm Ophelia and Storm Hector seems to be the result of large-scale slumping and sediment cascading down the front dune face. Sediment is then re-worked and trimmed vertically to create the new profile found around the time of the Storm Hector event. In Profile 5 (**Figure 8E**), the lateral retreat of the dune face is due to wave erosion of the dune toe and sediment being moved offshore onto the back beach profile (vertical accretion pattern compared to Storm Ophelia cross-shore profiles). However, the changes found in the same profile, for instance the offset of P5, is likely the result of all intervening (smaller) storm and lower energy events occurring in the time period between the field campaigns (September 2017 to June 2018) and not just the product of the two storms, particularly Hector.

Differences in the alongshore response to high-energy events have been widely discussed. Several authors have argued that this range of responses can play out at different scales, from meters up to 1 km, depending on a combination of physical and dynamic variables (Harley et al., 2009, Gervais et al., 2012; Haerens et al., 2012; Houser, 2013; Loureiro et al., 2014; Splinter et al., 2018). A myriad of physical static factors such as coastline orientation and exposure to predominant wave direction, existence of emerged landforms (capes and rocky headlands), submerged morphological features (nearshore bars), underlying geological control (Jackson et al., 2005; Jackson and Cooper, 2009) as well as antecedent morphology conditions (e.g., beach slope, intertidal channels), and dynamic environmental variables such as wave height and tidal levels, wind speed, direction and duration and the synchronicity of all of them can lessen or enhance actual beach response. In terms of quantification of areal and volumetric changes (**Figure 9**), a noticeable variability alongshore (**Figure 7**) and in the cross-shore (**Figure 8**) exists. In Storms Ophelia and Hector, post-storm topography, an alongshore variability pattern is evident whereas the spatial configuration of sediment exchanges and actual distribution are dissimilar. This result suggests the important role of environmental variables (particularly wave energy and run up) not only in the generation of morphological changes but in the reorganising of sediment into different available spaces (Coco et al., 2014) along and across the beach/dune system. This is particularly the case for pre-Storm Hector intertidal beach configuration where summer conditions may have accentuated morphology by the presence of nearshore bars (qualitative TLC imagery reinforces the presence of bars).

Pre-event "Storms" and Adjustment of Antecedent Topography

Pre-storm events (S1-S2 for Storm Ophelia) may also have played a very important role in sculpting the intertidal topography so they cannot be ignored in the analysis. As a result, their cumulative effect may have added significantly to the actual Storm Ophelia event. Two of the three pre-Ophelia events have significantly higher SSI and SIPs and resulting SDTs than Storm Ophelia, sometimes by a huge margin. In addition, two of these events coincided with high tide and thus TWLs reached were above mean dune toe heights (**Figures 5C,D** and **Table 2**), particularly along the southern part of the site. Likewise, the two preceding storms of Storm Hector were (combined) at or exceeding the values of its SSI and SIP, albeit resulting in half of the SDT of the Storm Hector event itself, potentially due to neither of them accounting for TWL above the mean dune toe height or neither of them lasted beyond a high tide cycle whereas Storm Hector did (**Figure 6D** and **Table 2**). This highlights the importance of any pre-events that help adjust the antecedent surface beach conditions and possibly dictating future beach response, depending on pre-established surface heterogeneity.

It must also be recognised that any post-storm recovery of the intertidal and dune toe area may restore the beach topography into somewhat different configurations than its previous form and therefore subsequent hydrodynamics may undergo a different set of behavioural patterns than that of previous events.

CONCLUSION

Using two, quite different high-energy storm events, a range of conditions and responses has enabled examination of the relative importance of forcing factors on shoreline change dynamics on sandy beach and dune systems. In order to fully assess beach response several key parameters, deemed significant in driving

coastal changes, including storm duration and orientation, storm track line speed, local wave height and tidal water levels were isolated and analysed. Field observations and modelling results show that synchronicity of variables is crucial in driving the effectiveness of those storm-induced changes along sandy, dune-fringed coastlines.

Antecedent intertidal beach configuration, as well as pre-storm clustering events, appears to play important roles in dictating coastal response. Using a Storm Severity Index (SSI) and Storm Impact Potential (SIP) to characterise what the site was subjected to, does not necessarily always result in actual dune retreat, with field observations showing that effective storm dune trimming might not materialise if other factors such as high tide and storm duration are not synchronised. However, the new proxy Storm Dune Trimming index resulted in an accurate proxy for potential and effective wave run-up and subsequent dune trimming, as qualitatively demonstrated by time-lapse camera images collected during the storms.

The study shows that for a more complete understanding of coastal response we need to have a myriad of forcing and response data captured over sufficient time periods, before, during and after high-energy events. Despite having an intensively monitored site such as in this study, understanding detailed relationships between forcing dynamics and actual coastal response is fraught with difficulties, with various feedbacks active in the system, which ultimately complicates the final storm-response of the beach/dune zone. Even with very high-energy events such as Storm Ophelia, anticipated to cause significant coastal impact, a much smaller event such as Storm Hector proved to be much more effective at causing morphological (SIP and SDT) change due to having better synchronicity of forcing factors.

Ultimately, the study confirms that having higher frequency monitoring at sites goes some way toward bridging the gaps in our understanding of coastal response to storm activity. This will help improve how such systems need to be managed in the future. The coastal-dune response observed in this research provides regional and local coastal managers with an estimation of the degree of impact that can be expected with the passage of these types of high-energy storms and should inform coastal risk actions and plans along sandy, dune-fringed coastlines.

DATA AVAILABILITY

The datasets generated for this study are available on request to the corresponding author.

AUTHOR CONTRIBUTIONS

EG-P and DJ designed the experiments and contributed meaningfully to the manuscript writing. EG-P was in charge of data analysis and results description, and production of figures. DJ carried out the fieldwork as well as significantly contributed to the results, analysis, and discussion.

FUNDING

This work is a contribution to the Natural Environment Research Council grant NE/F019483/1 and to the UNESCO IGCP Project 639 "Sea Level Change from Minutes to Millennia."

ACKNOWLEDGMENTS

We wish to thank the Irish Marine Institute for providing access to hydrodynamic data (measured water levels and modelled parameters including significant wave height, mean wave direction and mean wave period) for the study site location. We would also like to acknowledge the Met Éireann (The Irish Meteorological Service) for the meteorological data at the Malin Head station. Thanks are also extended to David Rogers for his invaluable help in fieldwork and in the post-processing of topographic field data and to the Ulster University for supporting the research and providing the fieldwork equipment. We also thank the two reviewers whose suggestions and comments helped to improve the manuscript enormously.

REFERENCES

Backstrom, J., Jackson, D. W. T., Cooper, J. A. G., and Loureiro, C. (2015). Contrasting geomorphological storm response from two adjacent shorefaces. *Earth Surf. Process. Landf.* 40, 2112–2120. doi: 10.1002/esp.3788

Booij, N., Ris, R. C., and Holthuijsen, L. H. (1999). A third-generation wave model for coastal regions. Model description and validation. *J. Geophys. Res.* 104, 7649–7666. doi: 10.1029/98jc02622

Burningham, H., and Cooper, J. A. G. (2004). "Morphology and historical evolution of north-east Atlantic coastal deposits: the west Donegal estuaries, north-west Ireland," in *Proceedings of the STRAEE Workshop (WINTER 2004)*, Vol. 41. (Ferrara), 148-159.

Burvingt, O., Masselink, G., Russell, P., and Scott, T. (2017). Classification of beach response to extreme storms. *Geomorphology* 295, 722–737. doi: 10.1016/j.geomorph.2017.07.022

Carter, R. W. G., and Stone, G. W. (1989). Mechanisms associated with the erosion of sand dune cliffs, Magilligan, Northern Ireland. *Earth Surf. Process. Landf.* 14, 1–10. doi: 10.1002/esp.3290140102

Castelle, B., Bujan, S., Ferreira, S., and Dodet, G. (2017). Foredune morphological changes and beach recovery from the extreme 2013/2014 winter at a high-energy sandy coast. *Mar. Geol.* 385, 41–55. doi: 10.1016/j.margeo.2016.12.006

Castelle, B., Marieu, V., Bujan, S., Splinter, K. D., Robinet, A., Sénéchal, N., et al. (2015). Impact of the winter 2013–2014 series of severe Western Europe storms on a double-barred sandy coast. Beach and dune erosion and megacusp embayments. *Geomorphology* 238, 135–148. doi: 10.1016/j.geomorph.2015.03.006

Coco, G., Senechal, N., Rejas, A., Bryan, K. R., Capo, S., Parisot, J. P., et al. (2014). Beach response to a sequence of extreme storms. *Geomorphology* 204, 493–501. doi: 10.1016/j.geomorph.2013.08.028

Cooper, J. A. G., and Jackson, D. W. T. (2003). "Geomorphological and dynamic constraints on mesoscale coastal response to storms, Western Ireland," in *Proceedings 6th International Symposium on Coastal Engineering and Science of Coastal Sediment Processes*, (Florida: American Society of Civil Engineers), 1–13.

Cooper, J. A. G., and Orford, J. D. (1998). Hurricanes as agents of mesoscale coastal change in western Britain and Ireland. *J. Coast. Res.* 26, 123–128.

Cooper, J. A. G., Jackson, D. W. T., Navas, F., McKenna, J., and Malvarez, G. (2004). Identifying storm impacts on an embayed, high-energy coastline: examples from western Ireland. *Mar. Geol.* 210, 261–280. doi: 10.1016/j.margeo.2004.05.012

Cooper, J. A. G., McKenna, J., Jackson, D. W. T., and O'Connor, M. (2007). Mesoscale coastal behavior related to morphological self-adjustment. *Geology* 35, 187–190.

Costas, S., Alejo, I., Vila-Concejo, A., and Nombela, M. A. (2005). Persistence of storm-induced morphology on a modal low-energy beach: a case study from NW-Iberian Peninsula. *Mar. Geol.* 224, 43–56. doi: 10.1016/j.margeo.2005.08.003

Dawson, A., Elliott, L., Noone, S., Hickey, K., Holt, T., Wadhams, P., et al. (2004). Historical storminess and climate 'see-saws' in the North Atlantic region. *Mar. Geol.* 210, 247–259. doi: 10.1016/j.margeo.2004.05.011

Dawson, A. G., Hickey, K., Holt, T., Elliott, L., Dawson, S., Foster, I. D. L., et al. (2002). Complex North Atlantic Oscillation (NAO) index signal of historic North Atlantic storm-track changes. *Holocene* 12, 363–369. doi: 10.1191/0959683602hl552rr

Devoy, R. J. N. (2008). Coastal vulnerability and the implications of sea-level rise for Ireland. *J. Coast. Res.* 24, 325–341. doi: 10.2112/07a-0007.1

Dissanayake, P., Brown, J., Wisse, P., and Karunarathna, H. (2015). Effects of storm clustering on beach/dune evolution. *Mar. Geol.* 370, 63–75. doi: 10.1016/j.margeo.2015.10.010

Dodet, G., Bertin, X., and Taborda, R. (2010). Wave climate variability in the North-East Atlantic Ocean over the last six decades. *Ocean Model.* 31, 120–131. doi: 10.1016/j.ocemod.2009.10.010

Dolan, R., and Davies, R. E. (1992). An intensity scale for Atlantic Coast Northeast Storms. *J. Coast. Res.* 8, 840–853.

Erdmann, W., Kelletat, D., and Kuckuck, M. (2017). Boulder ridges and washover features in Galway Bay, Western Ireland. *J. Coast. Res.* 33, 997–1021. doi: 10.2112/jcoastres-d-16-00184.1

Ferreira, Ó (2006). The role of storm groups in the erosion of sandy coasts. *Earth Surf. Process. Landf.* 31, 1058–1060. doi: 10.1002/esp.1378

Feser, F., Barcikowska, M., Krueger, O., Schenk, F., Weisse, R., and Xia, L. (2015). Storminess over the North Atlantic and northwestern Europe—A review. *Quart. J. R. Meteorol. Soc.* 141, 350–382. doi: 10.1002/qj.2364

Gervais, M., Balouin, Y., and Belon, R. (2012). morphological response and coastal dynamics associated with major storm events along the gulf of lions coastline. France. *Geomorphology* 14, 69–80. doi: 10.1016/j.geomorph.2011.07.035

GTECCA (1996). *Global Tropical and Extratropical Cy-clone Climatic Atlas 2.0*. Asheville, NC: NOAA.

Guisado-Pintado, E., Jackson, D. W. T., Cooper, J. A. G., and O'Connor, M. (2017). Storm impacts on a high energy sandy beach system, northwest Ireland: short (event) to long term (decadal) behaviour. *Geophys. Res. Abstr.* 19:10267.

Guisado-Pintado, E., and Jackson, D. W. T. (2018). Multi-scale variability of storm Ophelia 2017: the importance of synchronised environmental variables in coastal impact. *Sci. Total Environ.* 630, 287–301. doi: 10.1016/j.scitotenv.2018.02.188

Guisado-Pintado, E., Jackson, D. W. T., and Rogers, D. (2019). 3D mapping efficacy of a drone and terrestrial laser scanner over a temperate beach-dune zone. *Geomorphology* 328, 157–172. doi: 10.1016/j.geomorph.2018.12.013

Guisado-Pintado, E., Malvárez, G., Navas, F., and Carrero, R. (2014). "Spatial distribution of storm wave energy dissipation for the assessment of beach morphodynamics," in *Proceedings of the 13th International Coastal Symposium*, Durban, 259–265. doi: 10.2112/si70-044.1

Haerens, P., Bolle, A., Trouw, K., and Houthuys, R. (2012). Definition of storm thresholds for significant morphological change of the sandy beaches along the Belgian coastline. *Geomorphology* 143-144(Suppl. C), 104–117. doi: 10.1016/j.geomorph.2011.09.015

Harley, M. D., Turner, I. L., Short, A. D., and Ranasinghe, R. (2009). "An empirical model of beach response to storms - Se Australia," in *Proceedings of the 19th Conference Coasts and Ports 2009 in a Dynamic Environment, Engineers*, Wellington.

Hayden, B. (1981). Secular variation in atlantic coast extratropical cyclones. *Mon. Weather Rev.* 109, 159–167. doi: 10.1175/1520-0493(1981)109<0159:sviace>2.0.co;2

Hickey, K. R., and Connolly-Johnston, C. (2012). "The impact of hurricane debbie (1961) and Hurricane Charley (1986) on Ireland," in *Advances in Hurricane Research - Modelling, Meteorology, Preparedness and Impacts*, ed. K. Hickey (Rijeka: InTech).

Houser, C. (2013). Alongshore variation in the morphology of coastal dunes: Implications for storm response. *Geomorphology* 199, 48–61. doi: 10.1016/j.geomorph.2012.10.035

Hurrell, J. W. (1995). Decadal trends in the north atlantic oscillation: regional temperatures and precipitation. *Science* 269, 676–679. doi: 10.1126/science.269.5224.676

Jackson, D. W. T., and Cooper, J. A. G. (2009). Geological control on beach form: accommodation space and contemporary dynamics. *J. Coast. Res.* 56, 69–72.

Jackson, D. W. T., Cooper, J. A. G., and del Rio, L. (2005). Geological control of beach morphodynamic state. *Mar. Geol.* 216, 297–314. doi: 10.1016/j.margeo.2005.02.021

Jackson, D. W. T., Cooper, J. A. G., O'Connor, M., Guisado-Pintado, E., Loureiro, C., and Anfuso, G. (2016). Field measurements of intertidal bar evolution on a high-energy beach system. *Earth Surf. Process. Landf.* 41, 1107–1114. doi: 10.1002/esp.3920

Kandrot, S., Farrell, E., and Devoy, R. (2016). The morphological response of foredunes at a breached barrier system to winter 2013/2014 storms on the southwest coast of Ireland. *Earth Surf. Process. Landf.* 41, 2123–2136. doi: 10.1002/esp.4003

Karunarathna, H., Pender, D., Ranasinghe, R., Short, A. D., and Reeve, D. E. (2014). The effects of storm clustering on beach profile variability. *Mar. Geol.* 348, 103–112. doi: 10.1016/j.margeo.2013.12.007

Lamb, H., and Frydendahl, K. (1991). *Historic Storms of the North Sea, British Isles and Northwest Europe*. Cambridge: Cambridge University Press.

Lambert, S. J. (1996). Intense extratropical northern hemisphere winter cyclone events: 1899–1991. *J. Geophys. Res.* 101, 21319–21325. doi: 10.1029/96jd01653

Loureiro, C., and Cooper, J. A. G. (2019). Temporal variability in winter wave conditions and storminess in the northwest of Ireland. *Ir. Geogr.* 51, 1–16. doi: 10.2014/igj.v51i2.1369

Loureiro, C., Ferreira, O., and Cooper, J. A. G. (2014). Non-uniformity of storm impacts on three high-energy embayed beaches. *J. Coast. Res.* 70, 326–331. doi: 10.2112/si70-055.1

Lozano, I., Devoy, R. J. N., May, W., and Andersen, U. (2004). Storminess and vulnerability along the Atlantic coastlines of Europe: analysis of storm records and of a greenhouse gases induced climate scenario. *Mar. Geol.* 210, 205–225. doi: 10.1016/j.margeo.2004.05.026

Masselink, G., Castelle, B., Scott, T., Dodet, G., Suanez, S., Jackson, D. W. T., et al. (2016a). Extreme wave activity during 2013/2014 winter and morphological impacts along the Atlantic coast of Europe. *Geophys. Res. Lett.* 43, 2135–2143. doi: 10.1002/2015GL067492

Masselink, G., Scott, T., Poate, T., Russell, P., Davidson, M., and Conley, D. (2016b). The extreme 2013/2014 winter storms: hydrodynamic forcing and coastal response along the southwest coast of England. *Earth Surf. Process. Landf.* 41, 378–391. doi: 10.1002/esp.3836

Met EIREANN (2017). Observational Records: Provisional Quick Observational Facts of Land and Marine Observations on STORM OPHELIA, 2017. Available at: https://www.met.ie/news/display.asp?ID=463 (accessed November 20, 2018).

NOAA (2017). *National Hurricane Center: Post-Tropical Cyclone Ophelia Discussion Number 28 NWS*. Silver Spring, MA: NOAA.

O'Connor, M. C., Cooper, J. A. G., and Jackson, D. W. T. (2011). Decadal behavior of tidal inlet–associated beach systems, Northwest Ireland, in relation to climate forcing. *J. Sediment. Res.* 81, 38–51. doi: 10.2110/jsr.2011.3

Phillips, M. S., Harley, M. D., Turner, I. L., Splinter, K. D., and Cox, R. J. (2017). Shoreline recovery on wave-dominated sandy coastlines: the role of sandbar morphodynamics and nearshore wave parameters. *Mar. Geol.* 385, 146–159. doi: 10.1016/j.margeo.2017.01.005

Rangel-Buitrago, N., and Anfuso, G. (2011). An application of dolan and davis (1992) classification to coastal storms in SW spanish littoral. *J. Coast. Res.* 64, 1891–1895.

Ris, R. C., Holthuijsen, L. H., and Booij, N. (1999). A third-generation wave model for coastal regions: 2. Verification. *J. Geophys. Res.* 104, 7667–7681. doi: 10.1029/1998jc900123

Ruggiero, P., Komar, D., McDougal, W. G., Marra, J. J., and Beach, R. A. (2001). Wave runup, extreme water levels and the erosion of properties backing beaches. *J. Coast. Res.* 17, 407–419.

Scheffers, A., Kelletat, D., Haslett, S., Scheffers, S., and Browne, T. (2010). Coastal boulder deposits in Galway Bay and the Aran Islands, western Ireland. *Zeitschrift for Geomorphologie* 54, 247–279. doi: 10.1127/0372-8854/2010/0054s3-0027

Scheffers, A., Scheffers, A., Kelletat, D., and Browne, T. (2009). Wave-emplaced coarse debris and megaclasts in Ireland and Scotland: boulder transport in a high-energy littoral environment. *J. Geol.* 117, 553–573. doi: 10.1086/600865

Schinke, H. (1993). On the occurrence of deep cyclones over Europe and the North Atlantic in the period 1930-1991. *Beitr. Phys. Atmos.* 66, 223–237.

Schmith, T., Kaas, E., and Li, T. S. (1998). Northeast Atlantic winter storminess 1875–1995 re-analysed. *Clim. Dyn.* 14, 529–536. doi: 10.1007/s003820050239

Shields, L., and Fitzgerald, D. (1989). The 'Night of the Big Wind' in Ireland, 6–7 January 1839. *Ir. Geogr.* 22, 31–43. doi: 10.1080/00750778909478784

Splinter, K. D., Kearney, E. T., and Turner, I. L. (2018). Drivers of alongshore variable dune erosion during a storm event: observations and modelling. *Coast. Eng.* 131, 31–41. doi: 10.1016/j.coastaleng.2017.10.011

Stockdon, H. F., Holman, R. A., Howd, A., and Sallenger, A. H. Jr. (2006). Empirical parameterization of setup, swash, and runup. *Coast. Eng.* 53, 573–588. doi: 10.1016/j.coastaleng.2005.12.005

United Kingdom Meteorological Office (2017). *Ex-Hurricane Ophelia Report*. Available at: https://www.metoffice.gov.uk/climate/uk/interesting/2017-ophelia (accessed November 20, 2018).

Wheaton, J. M., Brasington, J., Darby, S. E., and Sear, D. A. (2010). Accounting for uncertainty in DEMs from repeat topographic surveys: improved sediment budgets. *Earth Surf. Process. Landf.* 35, 136–156.

Wright, L. D., and Short, A. D. (1984). Morphodynamic variability of surf zones and beaches. *Mar. Geol.* 56, 93–118. doi: 10.1016/0025-3227(84)90008-2

Young, A. P., Guza, R. T., O'Reilly, W. C., Burvingt, O., and Flick, R. E. (2016). Observations of coastal cliff base waves, sand levels, and cliff top shaking. *Earth Surf. Process. Landf.* 41, 1564–1573. doi: 10.1002/esp.3928

Zăinescu, F. I., Tătui, F., Valchev, N. N., and Vespremeanu-Stroe, A. (2017). Storm climate on the danube delta coast: evidence of recent storminess change and links with large-scale teleconnection patterns. *Nat. Hazards* 87, 599–621. doi: 10.1007/s11069-017-2783-9

Conflict of Interest Statement: The authors declare that the research was conducted in the absence of any commercial or financial relationships that could be construed as a potential conflict of interest.

frontiers in Earth Science

ORIGINAL RESEARCH
published: 20 August 2019
doi: 10.3389/feart.2019.00211

Seasonal Variability of Forces Controlling Sedimentation in the Sundarbans National Forest, Bangladesh

R. P. Hale[1], C. A. Wilson[2] and E. J. Bomer[2]*

[1] Department of Ocean, Earth and Atmospheric Sciences, Old Dominion University, Norfolk, VA, United States, [2] Department of Geology and Geophysics, Louisiana State University, Baton Rouge, LA, United States

Southwest Bangladesh, located on the Ganges-Brahmaputra-Meghna delta, is experiencing the impacts of sea level rise (SLR) due to processes at both the local and global scale. In particular, regional alterations of the hydrodynamic network, due to embankment construction, have drastically altered effective SLR, placing millions of inhabitants at risk of prolonged inundation, and threatening the world's largest continuous mangrove stand, the Sundarbans National Forest (SNF). In order to effectively employ landscape recovery solutions, an understanding of local sediment transport and deposition is critical. This field-based study investigates the sediment dynamics between the mangrove platform and tidal channels of the SNF using data from a variety of instruments and sediment samples collected within a forested sub-basin (~20 km^2) fed by a major tidal channel. We observe profound seasonal variability within the sub-basin, with the wet season exhibiting a deeper and longer inundation of the mangrove platform and greater suspended sediment concentrations (SSC). Further, there exists a trend of decreasing SSC and median grain size from the perimeter of the SNF to the interior, and decreasing SSC from the tidal channel to the platform at both locations. We project seasonal platform sedimentation rates ranging from 0.17 ± 0.16 cm in the dry season to 1.8 ± 0.35 cm in the wet season. Importantly, the annual deposition rate measured at either location is sufficiently rapid to keep pace with observed rates of effective SLR published in other studies (~1.0–1.7 cm/year). Based on our results, it appears that many controls on sedimentation are both covariant and of similar importance to land aggradation in the SNF. While inundation depth and frequency will likely increase under future SLR scenarios, sediment supply is threatened by India's proposed River Linking Project, which could decrease the sediment loads of the Ganges and Brahmaputra Rivers by as much as 75 and 25%, respectively. These rivers provide the sediment for the entire delta, and we predict that with decreasing SSC, some regions—particularly interior sediment-depleted regions—may begin to deteriorate and become submerged, including within the SNF.

Keywords: hydrodynamics, Bangladesh, sediment transport, seasonal variability, mangrove forest

OPEN ACCESS

Edited by:
Denise Reed,
The University of New Orleans,
United States

Reviewed by:
Julian David Orford,
Queen's University Belfast,
United Kingdom
Hans Middelkoop,
Utrecht University, Netherlands

****Correspondence:***
R. P. Hale
rphale@odu.edu

Specialty section:
This article was submitted to Quaternary Science, Geomorphology and Paleoenvironment, a section of the journal Frontiers in Earth Science

Received: *27 November 2018*
Accepted: *31 July 2019*
Published: *20 August 2019*

Citation:
Hale RP, Wilson CA and Bomer EJ (2019) Seasonal Variability of Forces Controlling Sedimentation in the Sundarbans National Forest, Bangladesh. Front. Earth Sci. 7:211. doi: 10.3389/feart.2019.00211

INTRODUCTION

Mangrove forests provide a variety of societal benefits, including storm-surge buffering (e.g., Badola and Hussain, 2005), economic stimulus from ecotourism (e.g., Satyanarayana et al., 2012), land stability and erosion minimization (e.g., Carlton, 1974; Saenger and Siddiqi, 1993), and carbon sequestration (e.g., Mcleod et al., 2011; Ray et al., 2011; Alongi, 2012; Twilley et al., 2018). As populations around the world move toward coastlines and either alter landscapes or eradicate mangroves altogether, it is imperative that we understand how these systems behave under pseudo-natural conditions to help protect these valuable resources. This study will focus on a portion of the Sundarbans National Forest (SNF), a relatively pristine mangrove forest located in southwestern Bangladesh (**Figure 1**). The total extent of the Sundarbans reaches across political boundaries into India, expressing a continuum of fluvial and tidal forces with increased distance from the modern Ganges-Brahmaputra-Meghna River mouth (Allison and Kepple, 2001; Rogers et al., 2013; Flood et al., 2015, 2018). Immediately to the north of the SNF is an inhabited region where the construction of earthen embankments ("polders") has resulted in a substantial modification of the tidal prism, leading to tidal amplification and extensive network reorganization (e.g., Pethick and Orford, 2013; Wilson et al., 2017). While attributed to anthropogenic modification, this tidal amplification also impacts the SNF, and—coupled with eustatic sea-level change and compaction—has resulted in an effective sea level rise of 0.7 cm/year at the southern coast, increasing to 1.7 cm/year near the city of Khulna, which enhances flood risk across the entire tidal deltaplain (**Figure 1**; Steckler et al., 2010; Pethick and Orford, 2013). Furthermore, the National River Linking Project (NRLP) proposed by India is expected to reduce freshwater discharge of the Ganges River by 24%, with a corresponding reduction in sediment load by 39–75% if fully implemented (Higgins et al., 2018). Those authors further predict a reduction in delta-wide aggradation from 0.36 to 0.25 cm/year under this scenario. Given that >60% of the sediment deposited in the SNF is recently derived from the mainstem Ganges-Brahmaputra-Meghna (Allison and Kepple, 2001; Rogers et al., 2013), we expect the impacts of this decrease in sediment supply to be particularly acute in the SNF.

Several recent investigations have investigated the health and stability of the SNF platform elevation in the face of locally accelerated relative sea level rise (e.g., Rogers et al., 2013; Auerbach et al., 2015; Bomer et al., in review). These previous efforts have addressed the timing of seasonal sedimentation, and estimated deposition rates of 1.0 ± 0.9, 1.1 ± 1.0, and 1.32–2.16 ± 0.17–0.26 cm/year, respectively. Collectively, these studies demonstrate that at present, there is sufficient sediment being delivered to the SNF for the vertical accretion to keep pace with rates of local sea level rise, and that the platform is maintaining its elevation relative to mean high water. However, knowledge gaps remain concerning what controls sediment delivery and accumulation within the SNF, and how this varies spatially. To address this need, this study investigates sediment delivery and deposition within a sub-basin in the SNF, and how we might expect similar regions to respond given changes to these functions. Specifically, we combine data from acoustic and optical instrumentation with physical sediment samples to address seasonal changes in: (i) tidal channel suspended sediment concentrations (SSC), water velocity, and grain size; and (ii) platform inundation depth, duration, and grain size. These specific parameters have been identified as especially important in controlling wetland sedimentation in zero-dimensional, mass-balance models of marsh growth and mangrove sediment dynamics (e.g., Krone, 1987; Allen, 1990; French, 1993; Furukawa and Wolanski, 1996; Furukawa et al., 1997; Temmerman et al., 2004; Capo et al., 2006; Horstman et al., 2015).

STUDY AREA

The SNF is the largest continuous mangrove stand in the world, with a total area of ∼10,000 km^2 comprised of several major tidal channels separated by vegetated sub-basins (**Figure 1**). This project focuses on a ∼20-km^2 sub-basin in north-central SNF, immediately adjacent to the human-modified agricultural region, ∼100 km inland from the Bay of Bengal (**Figure 1**). Water and sediment are primarily delivered to this region by a tidal channel extending from the Sutarkhali River, called the Sorbathkhali, which lies between two primary conduit channels that connect this region to the broader Ganges-Brahmaputra-Meghna river system: the Pussur and Shibsa Rivers (**Figure 1**). The majority of freshwater and sediment are delivered to the region by inland advection from the Bay of Bengal during the southwest monsoon season (July to September; e.g., Barua, 1990; Barua et al., 1994; Allison and Kepple, 2001; Rogers et al., 2013; Shaha and Cho, 2016; Hale et al., 2019). As a result, the entire SNF is characterized by fresh water (∼0 PSU) from July to late November, and brackish to saline waters (∼20–30 PSU) for the remainder of the year (Shaha and Cho, 2016; Ayers et al., 2017). Accompanying the fresh water is a substantial change in local suspended sediment concentration (SSC), which varies by a factor of five or more from dry-season minima (∼0.2 g/l) in June to Monsoon maxima (>1.5 g/l) in September (Hale et al., 2019). These previous studies provide an excellent backdrop for the research presented here, which focuses on the specific processes responsible for delivering sediment from the major tidal channels onto the mangrove forest platform within the SNF.

The specific focus of this study is on two areas within a representative ∼20-km^2 sub-basin in the SNF, supplied with sediment and water by a single channel, the Sorbothkhali (**Figure 1**). The Sorbathkhali is ∼90 m wide at its diversion from the Sutarkhali River, with typical thalweg depths ranging from 7 to 10 m. The channel narrows and shoals with distance away from this junction, to a width of ∼15 m and depth of ∼0 m at most interior reaches during spring low tides. While the absolute platform elevation is difficult to constrain owing to seasonal variability and limited benchmark availability, the average inundation depth has previously been reported as ∼0.3 m (Auerbach et al., 2015). Assuming that the Sorbathkhali channel is the conduit for the majority of flooding water (Auerbach et al., 2015), approximately 6×10^6 m^3 of water is conveyed during spring tides (e.g., Auerbach et al., 2015; Bomer et al., in review).

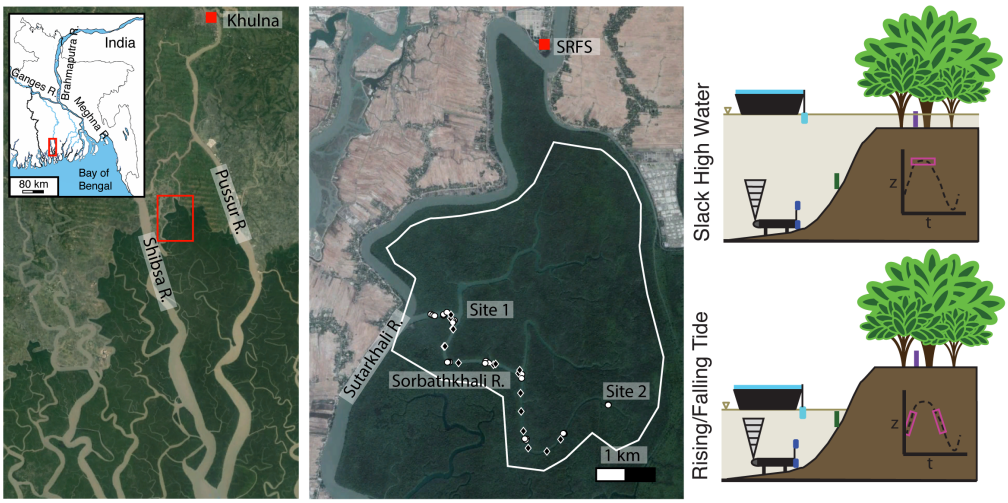

FIGURE 1 | Satellite images of the study area, highlighting the Sundarbans mangrove forest (dark green) and representative sub-basin (red box) located proximal to the heavily modified polder region (light green-tan). Middle image is a zoom of the sub-basin, highlighting the location of the long-term sensors at the Suterkhali Reserve Forestry Station (SRFS), Sites 1 and 2 where single-day measurements were made seasonally, and sediment grab locations for the wet (diamond) and dry (circle) seasons. An approximate boundary for this sub-basin is sketched in white. Right-hand panel depicts the experimental design at Sites 1 and 2, demonstrating the relative locations of the ADCP measurements (gray triangle), channel-bottom measurements (blue), channel-surface measurements (cyan), channel-bank velocities (green), and platform measurements (purple). Satellite imagery via (Google Earth, 2015, 2017).

The primary vegetation here is the endangered mangrove *Heritiera fomes*, locally known as the Sundri, which can grow to a maximum height of 25 m and prefers freshwater. Other species found in this region, presented using their local names, include Gewa, Bain, Pussur, and Kakra (Ghosh et al., 2016).

MATERIALS AND METHODS

This study benefits from the use of a variety of datasets. Long-term seasonal changes were measured using a Schlumberger conductivity, temperature, depth (CTD) sensor continuously deployed in a channel adjacent to the SNF at the Sutarkhali Forest Ranger Station (SFRS) from October 2017 to March 2018 (**Figure 1**). In addition, suspended sediment concentration was recorded ∼30 cm above bed (cmab) using a Fisher Scientific optical backscatter sensor 3 + (OBS). The OBS was calibrated to SSC using a method described by Hale et al. (2019). In short, water samples were collected at the same time and depth as OBS readings, prior to the long-term instrument deployment. Known sample volumes were then filtered using 0.4 mm glass-fiber filters to determine SSC. A linear relationship between measured OBS response and filtered SSC was then derived.

Within the SNF, discrete observations were made during individual spring tide cycles during both the wet and dry seasons at two locations within the sub-basin: an exterior site approximately 1 km from the confluence with the Sutarkhali River (Site 1; **Figure 1**), and an interior site approximately 5 km further into the forest (Site 2; **Figure 1**). These locations were selected based on their relative proximity to the sediment source (the Sutarkhali River), and correspond to the locations used in a companion study of platform accumulation (Bomer et al., in review). Wet season measurements were collected in October 2017 and dry season observations took place in March 2018. On each survey day, measurements began as close to low tide as possible, and continued through the entire period of platform inundation. Due to daylight constraints, our results are focused primarily during the rising limb, slack high, and onset of the ebb portions of the tidal cycle, with limited observations at the termination of the falling limb. While the specifics of each survey day varied slightly due to instrumentation and environmental conditions, the general approach included: near-bottom measurements of water depth, velocity profiles (50–250 cmab), temperature, and SSC (5 cmab); water-surface measurements of temperature, conductivity, and SSC, and; measurements of water depth and SSC from the forest platform during periods of inundation (**Figure 1**). Velocity profiles were measured using an acoustic Doppler current profiler (ADCP), which measured velocity in 10-cm bins extending from 50 to 250 cmab. Measurements were collected at 1 Hz in 512-second bursts every 10 min, with the burst-averaged velocities reported herein. During the dry season, additional water velocity measurements were made further up the bank using a tilt current meter deployed ∼1.25 m below the platform elevation. Platform measurements occurred at distances of ∼50 m and ∼90 m from the creek bank for Sites 1 and 2, respectively, at the locations of the sediment elevation tables used in a concurrent study by Bomer et al. (in review; **Figure 1**). Efforts were made to ensure that the exact locations of instrument deployment were consistent across seasons. Surface water samples were also collected every 30–60 min to calibrate optical instrumentation measuring SSC, using the method described previously in this section.

We used the observed reduction in platform SSC to estimate the deposition (dz) associated with individual tidal cycles, according to the following equation:

$$dz = \left[(SSC1 - SSC2) \times h\right] / \rho_p$$

where *SSC1* and *SSC2* are the pre-slack-water maximum and post-slack-water minimum SSC (kg/m^3), h is the maximum inundation depth (m), and ρ_p is the bulk density of the platform (kg/m^3). All values used for this calculation are described in **Table 1**.

In addition to the observations made using acoustic and optical instrumentation, sediment samples were collected from the platform at Sites 1 and 2, and at locations spaced throughout the sub-basin at approximately 400-m intervals in between sites, with repeat sampling in March 2015 and October 2015 (**Figure 1**). Platform samples used to measure grain size were composed of the seasonally deposited sediment recovered from the sediment tiles deployed as part of a companion study by Bomer et al. (in review). Channel samples (n = 40) were collected at or near low tide, and an effort was made to collect sediment from the mid/upper bank, as well as the channel center (presumptive thalweg) at each station. To the best of our ability, we scraped the upper ∼1 cm of these samples to represent the recently transported material. All samples were measured for their particle size distribution using a Malvern Mastersizer 2000 laser diffraction particle size analyzer, after a ∼0.5 g subsample was immersed in sodium hexametaphosphate and sonified to disaggregate particles. For simplicity, the median grain size (D50) is presented in this study. Finally, sediment dry bulk density was calculated as the quotient of dry sediment weight over volume, using sediment from the upper 10 cm of cores collected at sites 1 and 2.

RESULTS

Multi-Year Observations From Channel Adjacent to SNF

Tidal-channel water depth at Suterkhali Reserve Forestry Station (SRFS) demonstrates a strong semi-diurnal signal, and pronounced spring-neap variability (**Figure 2A**). Peak water levels were higher in the wet season than the dry by ∼25 cm, while the water level minimum during the dry-season observations was ∼33 cm lower than that of the wet season (**Figures 2A,D**).

Conductivity during our study period began to increase in early November, reaching a maximum of ∼6 PSU in early January, before apparently dropping to ∼3 PSU until recovery in March (**Figure 2B**). An important caveat here is that the CTD was covered in encrusting worms upon recovery. Conductivity during the dry-season field work, as measured by replacement sensors not subjected to long-term deployment, was closer to 15 PSU (**Figure 2B**). We suggest that the observed salinity decrease that began in early 2018 is the product of biofouling.

Although the OBS record is incomplete because of deployment challenges in this harsh environment, we can see that SSC at SFRS ranged from 0.05 to ∼1.0 g/l during the wet season field work, and decreased to a minimum of 0.01–0.15 g/l

TABLE 1 | Values of water level, SSC, and velocity measured during the single-day observations.

		Site 1 - Wet	Site 2 - Wet	Site 1 - Dry	Site 2 - Dry
Tide data	Absolute max (m)	4.881	4.885	4.667	4.532
	Absolute min (m)	0.741	0.594	0.191	0.343
	Range (m)	4.14	4.291	4.476	4.189
Platform data	Inundation time (min)	266	321	122	105
	Inundation depth (cm)	38.8	42.7	6	7.5
	Mean SSC (g/l)	0.27	0.22	0.08	0.05
	Flood-max SSC (g/l)	0.39	0.33	0.2	0.06
	Ebb-min SSC (g/l)	0.14	0.15	0	0.03
	Sediment dry bulk density (kg/m^3)	1100	670	760	700
	Predicted seasonal deposition (cm)	1.6	2.1	0.3	0.06
	Measured vertical accretion (Bomer et al., in review) (cm)	1.93 ± 0.46	0.94 ± 0.24	1.07 ± 0.25	0.81 ± 0.28
Channel surface	Mean SSC (g/l)	0.52	0.50	0.32	0.10
	Max SSC (g/l)	0.86	0.79	0.64	0.55
Channel bottom	Mean SSC (g/l)	0.62	na	0.41	0.11
	Max SSC (g/l)	0.90	na	0.66	0.46
	Flood Umax (m/s)	0.64	0.44	0.45	0.30
	Ebb Umax (m/s)	0.24	0.25	0.30	0.69
	Re* (average)	0.27		0.48	
	θ_t (average)	1.25		0.47	

Note the general trends of decreasing SSC, inundation depth, and inundation duration from wet to dry season at both Sites, and the generally higher SSC observed at Site 1 vs. Site 2, NA: NA stands for not applicable, as the instrument was not monitoring at that time/location.

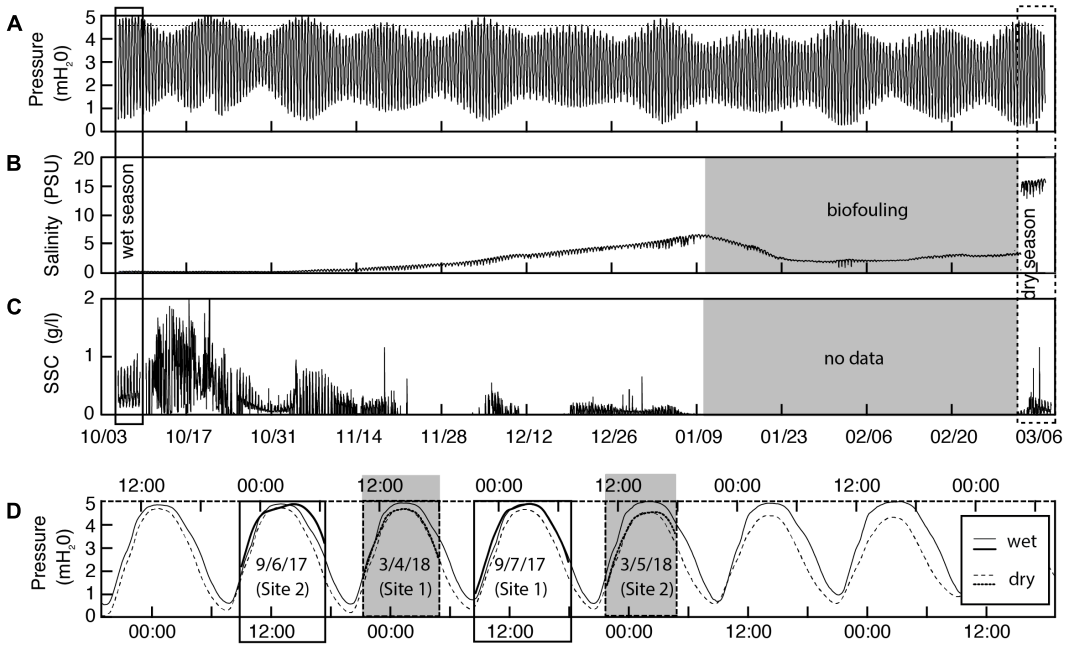

FIGURE 2 | Long-term observations of pressure **(A)**, conductivity **(B)**, and SSC **(C)** at SRFS, and focused observations of water level during the single-day observation periods at Sites 1 and 2 **(D)**. Wet and dry field seasons are outlined by solid and dashed boxes. Notice the general decrease in water level and SSC, and increase in conductivity during the dry season. The dashed line in panel **(A)** is the platform elevation at Site 1 for reference. For panel **(D)**, dashed and light solid lines are from SRFS, while dark solid lines are from Sites 1 and 2.

in early January, at which point the sensor appears to have been completely buried before being re-exposed in March. SSC during the dry season field work ranged from 0.01 to 0.3 g/l (**Figure 2C**).

Single-Day Hydrodynamics and Sediment Dynamics Within the SNF

Tidal range remained relatively constant during the days during which discrete sampling took place (**Figures 2A,D**). As measured at the SRFS, the tidal range during Site 1 sampling days was 4.14 and 4.48 m for wet and dry seasons, respectively (**Table 1** and **Figure 3**). Similarly, Site 2 sampling days exhibited tidal ranges of 4.29 and 4.19 m for the wet and dry seasons, respectively.

Despite the similarity of tidal range, the platform inundation depth and duration were drastically different as a result of the overall drop in absolute water levels during the dry season (**Figure 2A**). Site 1 was inundated for 266 min during the wet season survey day, and to a maximum depth of 0.39 m (**Table 1**). The same location was inundated for 122 min during the dry season, to a maximum depth of 0.06 m, which correspond to reductions of 54 and 84%, respectively (**Table 1** and **Figure 3** columns I, III). At Site 2, the platform was inundated for 321 min, to a maximum depth of 0.43 m during the wet season. During the dry season, on the other hand, the inundation duration reduced 67% to 105 min, and inundation depth reduced 81% to 0.08 m (**Table 1** and **Figure 3** columns II, IV). On the platform, average SSC was substantially greater during the wet season than the dry season at both locations. At Site 1, we observed an average SSC of 0.27 g/l during the wet season, versus 0.08 g/l during the dry season. Site 2 was similarly dramatic, with average SSC dropping from 0.22 to 0.05 g/l between seasons (**Table 1** and **Figure 3**).

Water velocities were faster during the wet season than the dry season, although not substantially. At Site 1 within the channel, the maximum depth-averaged flooding velocity was 0.64 m/s during the wet season, compared to 0.45 m/s during the dry season, a 30% reduction (**Table 1** and **Figure 3**). Moving further into the sub-basin at Site 2, the depth-averaged velocity reduced ∼47% from 0.44 m/s in the wet season to 0.30 m/s in the dry season (**Table 1** and **Figure 3**). One complication with the burst-averaged velocities presented here is that during ebbing tides at Site 1, the interplay between two channels (**Figure 1**) sets up ∼30-m-wide eddies, resulting in rapid flow reversals on ∼1-minute time scales. Because the burst length is ∼8.5 min, the burst-averaged velocity (**Figure 3**) is considerably lower than the instantaneous velocity. We do not observe this complication during flooding tides at Site 1, because flow is divergent rather than convergent, preventing eddy formation. At Site 2, the single channel results in uniformly directed currents, with ebb tide burst-averaged velocities that are faster than at Site 1 (**Figure 3**).

Average near-bed SSC reduced 33% from 0.62 to 0.41 g/l from wet to dry seasons at Site 1 (**Table 1** and **Figure 3**). Unfortunately, near-bed SSC was not measured at Site 2 in the wet season. During conditions of reduced water velocity observed during the dry season, near-bed SSC was ∼0.11 g/l. SSC at the water surface was substantially greater during the wet season than the dry season at both locations. From the OBS, wet season mean SSC was 0.52 and 0.50 g/l at Sites 1 and 2, respectively. During

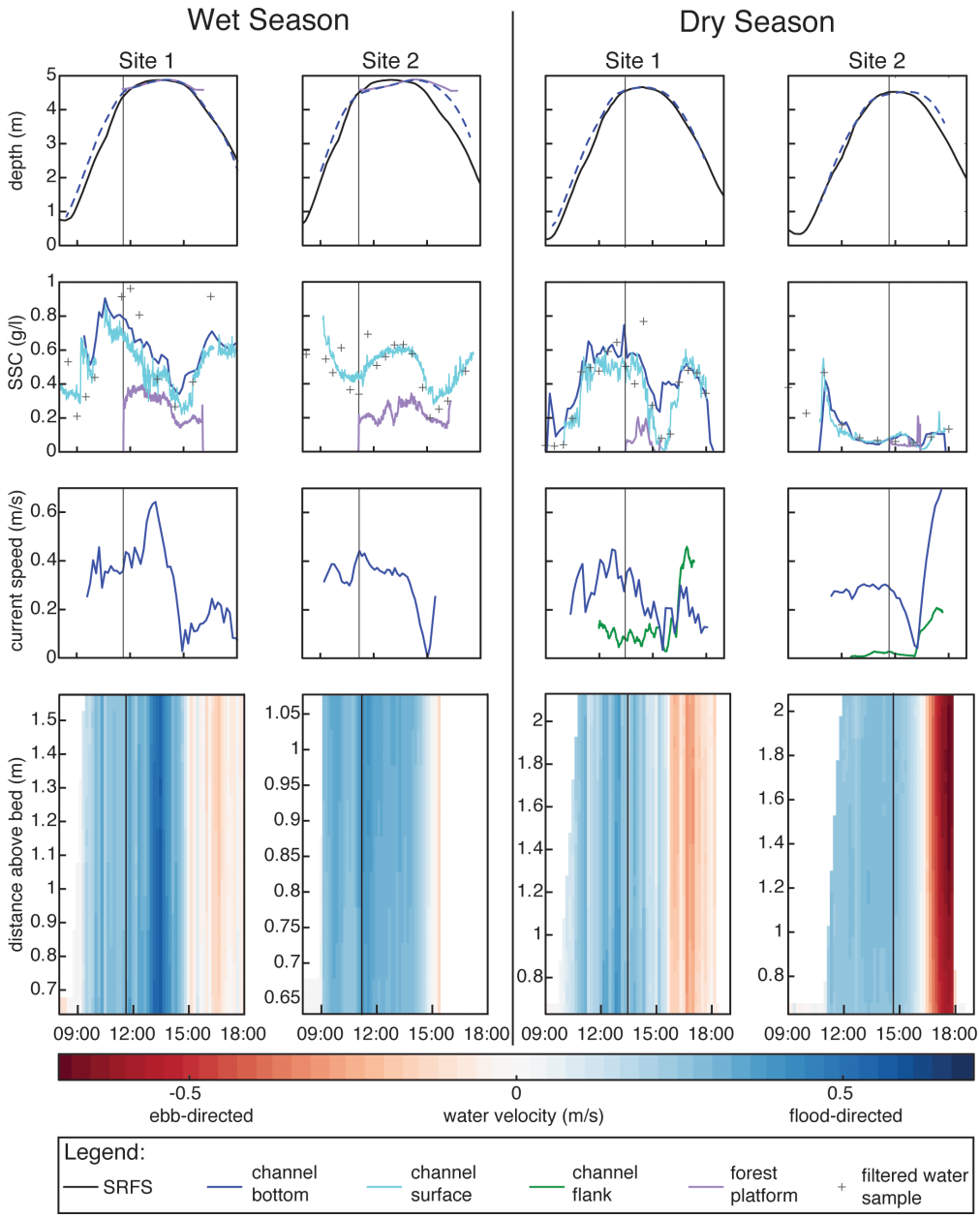

FIGURE 3 | Observations from the single-day experiments, including depth (relative to SRFS), SSC, and water velocity within the tidal channel. In general, we observe a decrease in both flood-oriented current velocity and SSC within the tidal channel from Site 1 to Site 2 (exterior to interior of the sub-basin), and from wet season to dry season. Vertical black line corresponds to the timing of platform inundation, as measured by the platform OBS.

the dry season, the same locations exhibited mean SSC of 0.32 and 0.10 g/l, representing reductions of 38 and 80% (**Table 1** and **Figure 3**). SSC maxima at the channel surface were greatest during the wet season, although the relative decrease during the dry season was not as drastic as for the mean. Max SSC during the wet season were 0.86 g/l (Site 1) and 0.79 g/l (Site 2), compared to dry season SSC of 0.64 and 0.55 g/l at the same locations, for respective reductions of 26 and 30% (**Table 1** and **Figure 3**). In each case, the decrease in SSC within the SNF is smaller than at the longer-term observation station SRFS, where SSC maxima during the wet season field work were ∼0.8 g/l, vs. ∼0.4 g/l dry season (**Figure 1**).

Sediment Grain Size

Median grain size on the platform decreases from 31 μm at the confluence with the Sutarkhali River to 15 μm near Site 2 (**Figure 4**). Within the channel, samples collected near Site 1 exhibit median diameters ranging from 13 to 30 μm, while samples near Site 2 are uniformly finer grained (∼19 μm). Interestingly, there is no obvious difference between samples

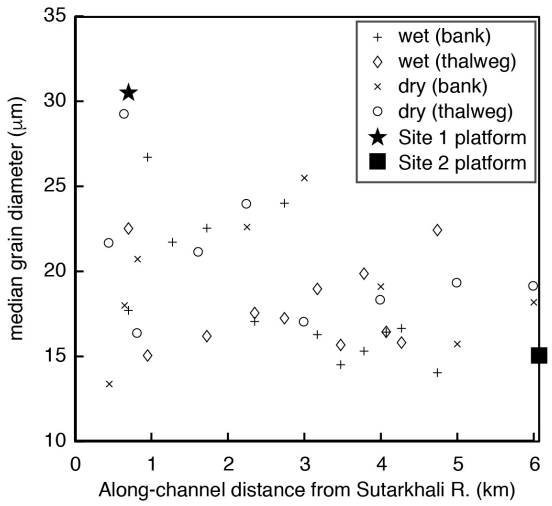

FIGURE 4 | Median grain diameter within the sub-basin plotted against distance from the Sutarkhali River, the conduit for both sediment and water. There is no obvious trend according to season or sample elevation within the channel, although there is a weak trend of decreasing grain size with distance inland.

collected in the thalweg vs. the channel flank, nor is there a discernible change between seasons (**Figure 4**).

DISCUSSION

The field instrument deployment strategy used in this study is admittedly limited in both temporal and spatial coverage due to access issues, safety concerns, and available resources. That said, we are able to provide measurements of sediment in the tidal channels at two locations within this sub-basin, paired with observations on the mangrove platform 50–90 m inland (**Figure 1**). In doing so, we can address sedimentation conditions in the best-case scenario (wet season at Site 1), and a substantially less-optimal example (dry season at Site 2). Finally, extrapolating from a handful of tidal cycles to a year's worth of deposition will never capture the full range of sedimentary or diagenetic processes, even if our measurements occur during periods corresponding to the annual minima and maxima for conditions related to sedimentation (**Figure 2**). Instead, as we demonstrate in the following sections, we are encouraged that based on the similarity of our extrapolated deposition rates, and those observed by previous and concurrent studies (Rogers et al., 2013; Bomer et al., in review), we appear to be measuring and comparing the appropriate controlling forces. Future research in this area should build upon these initial observations to develop numerical simulations (*sensu* Horstman et al., 2015) that will help explain both spatial and temporal variability that this study can not address.

Sedimentation Controls

A persistent challenge in untangling the controls on sedimentation is that they are often covariant. This is clearly the case on the platform in the SNF, as the dry season features less-frequent and shallower inundation depths, shorter inundation durations, and lower SSC (**Table 1** and **Figure 3**), all of which likely combine to reduce seasonal deposition. One parameter that remains consistent across seasons is the grain size distribution, which controls settling velocity and therefore the efficiency of sediment delivery to and across the platform (**Figure 4**). Our laboratory analysis of particle sizes, however, ignores the potential for sediment aggregation as a result of either biological processes or the electrochemical properties of fine-grained particles in salt water (e.g., Mietta et al., 2009; Manning et al., 2013). Aggregates (loosely cohesive packets of fine-grained sediment and organic matter) can behave like coarser particles in the water column, requiring additional turbulence to be advected upward, and settling more rapidly during periods of slack water (Manning et al., 2013). We might expect, therefore, that surface SSC in the dry-season channel is reduced more rapidly at slack water than during the wet-season. This effect can be observed most clearly in the time series observations of SSC at Site 1 during the wet and dry seasons (**Figure 3**). During the monsoon, there is relatively little difference between SSC at the channel surface and bottom, suggesting a well-mixed water column, and relatively little settling by what we assume to be disaggregated sediment particles. While the lowest values of SSC are observed near slack-high tide (**Figure 3**), there is generally poor correlation between velocity and SSC (**Figure 5**). During the dry season, on the other hand, not only is there a stronger coupling between SSC and velocity (**Figure 5**), but while near-bed SSC reduces by ∼60% to ∼0.2 g/l, surface SSC decreases to effectively 0 g/l (**Figure 3**). Similarly, wet season SSC on the platform at Site 1 is 61% lower than SSC in the channel at the onset of inundation (0.26 g/l vs. 0.67 g/l; **Figure 3**). During the dry season, the reduction from channel to platform is closer to 90% (0.50 to 0.05 g/l; **Figure 3**). In each case, the implication is that not only is the overall sediment supply reduced during the dry season, but the sediment in suspension is actually largely unavailable to nourish platform interiors within vegetated sub-basins (here extending ∼6 km from the main Sutarkhali channel). This observation does not discount the presence of biological aggregation, however, we interpret the enhanced dry-season settling as indicative of the relatively greater importance of electrochemical processes here.

Based on our observations of environmental conditions, we expect substantially more sediment to be deposited on the platform during the wet season than the dry season. At a fundamental level, we observe that the platform floods more frequently and to greater depth because of the seasonal water-level setup (∼25 cm; **Figure 2**), and the water flooding the platform is carrying dramatically more sediment in suspension (0.22–0.27 vs. 0.05–0.08 g/l; **Table 1** and **Figures 3**, **5**). These conditions should promote enhanced deposition, as described by Rogers et al. (2013). In their study of deposition rates at the same locations as this study, Bomer et al. (in review) also observe substantially more frequent and prolonged inundation during the wet season. Those authors measured an average vertical accretion of 1.44 ± 0.35 cm during the wet season (typically measured in October), compared to 0.94 ± 0.27 cm during

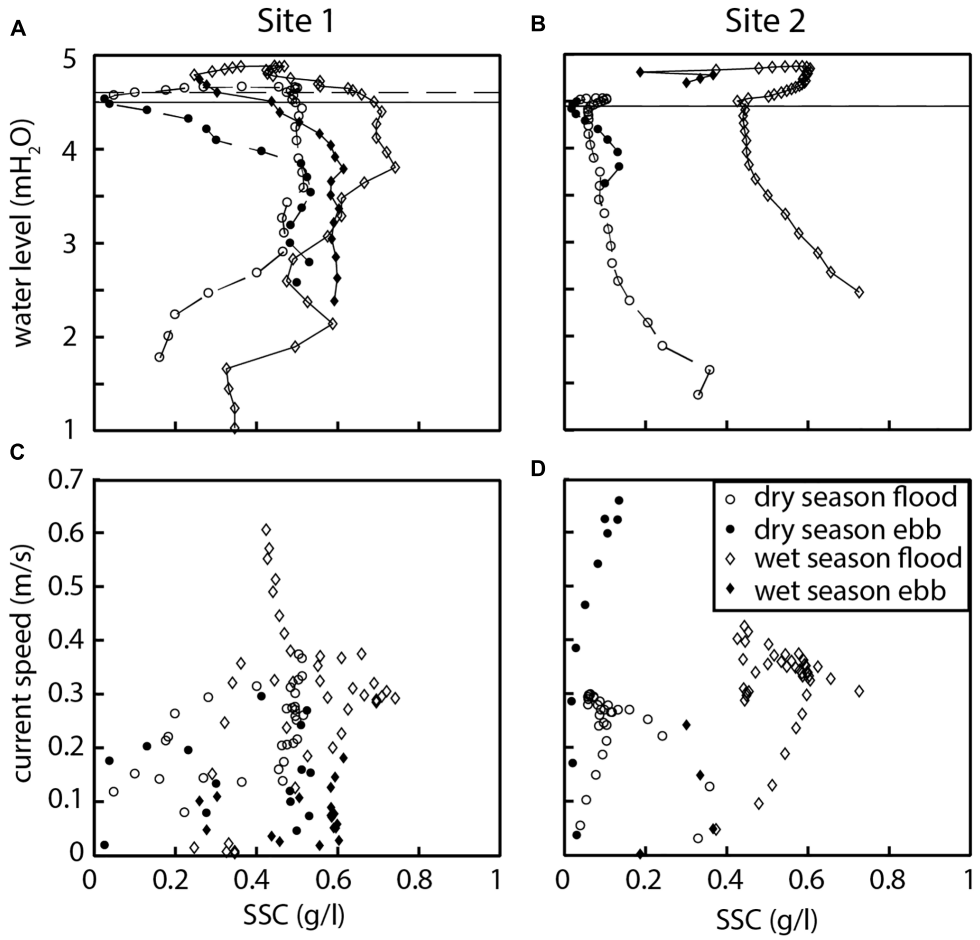

FIGURE 5 | Water level against tidal-channel SSC **(A,B)** and depth-averaged current speed against tidal-channel SSC **(C,D)**, for Site 1 (left) and Site 2 (right). SSC maxima occur immediately prior to inundation at Site 1, and near water-level minima at Site 2. SSC is generally higher during flood currents (open symbols), however, current speed is a poor predictor of SSC in either season.

the dry season (typically measured in March–May), with no significant difference between the groups.

As described in the section "Materials and Methods," we estimate the amount of sediment deposited on each tidal cycle, assuming that the difference between the maximum flood-limb SSC and the minimum ebb-limb SSC is the product of deposition. This assumption is supported by a comparison of the settling velocities of the particles at each site, to the depth of the water column at each location. Based on Gibbs et al. (1971), we would expect the median grain size particles at Site 1 (31 μm) and Site 2 (14 μm) to settle at rates of 0.085 and 0.023 cm/s, respectively. These values are likely conservative, as mud particles often aggregate or flocculate as described above, settling at faster rates than the constituent particles (Mietta et al., 2009). Based on these conservative settling rates and the inundation depths described in **Table 1**, we would expect that during the wet season, the water column at Site 1 could be evacuated of sediment in as few as 7 min during slack high water, while Site 2 might require as long as 30 min of placid conditions. According to our velocity measurements in the tidal channel – a much more dynamic environment – near-slack conditions ($U < 0.10$ m/s) persist for ∼40 min at each location, offering ample time for sediment to settle from suspension (**Figure 3**). Previous research has demonstrated the effectiveness of pneumatophores at trapping sediment, with the mangrove platform often serving as a one-way pump for fine-grained material (Wolanski, 1995; Furukawa et al., 1997; Victor et al., 2004). As such, conditions promoting sediment accumulation are unlikely to improve with increased distance from the channel. Our observations should therefore be considered a "best-case" scenario. Locations further from the sediment source are unlikely to demonstrate deposition rates faster than those estimated here, given the well-understood process of reduced SSC with distance from source both from the literature (e.g., Delaune et al., 1978; Reed, 1988; Christiansen et al., 2000), and between Site 1 and Site 2 in this study (**Figure 3**).

To estimate deposition on the platform during a single tidal cycle, we can begin with an examination of the observations made at Site 1 during the wet season, where we observe a maximum SSC of 0.39 g/l during the flood limb, and a minimum SSC of 0.14 g/l on the ebb. Interestingly, this reduction in SSC

(0.25 g/l) is almost identical to the difference back-calculated by Auerbach et al. (2015), when considering sediment deposition in the adjacent poldered region. Assuming that the SSC we measured near the platform bed was consistent throughout the ∼0.39 m water column, 97.5 g/m^2 of sediment would come out of suspension at slack high water. Dry bulk density for surface samples collected at Site 1 is 1100 kg/m^3 in the wet season, and the resulting quotient suggests deposition of 8.7×10^{-3} cm per inundation cycle (**Table 1**). While this value may appear unimpressive, the significance is gained when we extrapolate based on the number of inundation periods that occur under similar conditions of SSC and depth. If we assume, for example, that this location is influenced by similar peak monsoon forces for 90 days (180 inundation periods) per year, we would expect deposition of ∼1.6 cm during that time frame (**Table 1**); similar to the average deposition of 1.1 cm/wet season observed by Rogers et al. (2013). The same location we would expect an order of magnitude lower deposition (0.3 cm) based on the conditions observed during the dry season (**Table 1**). Predicted deposition rates at Site 2 are similar to Site 1, ranging from 2.1 to 0.06 cm/season for the wet and dry seasons, respectively (**Table 1**). Of course, these estimates assume that the entire decrease in SSC at slack high tide is a result of deposition, that there is no subsequent erosion, and that this accounts for all of the deposition that occurs during a given inundation cycle. These assumptions are justified based on our calculations of settling times (<10 min), our observations of little to no sediment resuspension on the platform (**Figure 3**), and the observations of Furukawa et al. (1997) who describe sediment trapping by pneumatophores. We concede here, however, that these back-of-the-envelope calculations only apply directly to the interior of the vegetated platform proximal to (50–90 m) the channel margin, as it is readily accepted that sediment accumulation decreases – often exponentially – with distance from the channel edge (Delaune et al., 1978; Reed, 1988; Christiansen et al., 2000). For the wet season, at least, our average predicted deposition (1.8 cm; **Table 2**) compares favorably with the measurements made by Bomer et al. (in review; 1.4 cm; **Table 2**). Our dry-season prediction (0.3 cm) on the other hand, is much lower than was observed by Bomer et al. (in review; 0.9 cm; **Table 2**). Again, our observations are from individual days extrapolated across an entire season, so a one-for-one comparison is likely not reasonable. Furthermore, Bomer et al.'s (in review) measurements of seasonal sediment deposition were typically made in September-October (wet season) and March-May (dry season); periods of time that were sensibly based on the Ganges-Brahmaputra river discharge. As we can see in this study, however, monsoon-like conditions (nearly fresh water, elevated SSC, higher water levels) persist in the tidal channels well into November (**Figure 2**), allowing for the potential of additional deposition that would be attributed to the dry season in that study. Additionally, in this analysis we are assuming that conditions remain similar throughout either the monsoon or dry season, which we know to be a simplification (**Figure 2**). We are nevertheless encouraged by the similarities between our calculation and measurements from previous research, and look forward to future colleagues extending these results with a full-scale numerical simulation, the likes of which was outside the scope of the present research.

TABLE 2 | Predicted change in seasonal deposition according to the projected changes in suspended sediment supply and fresh water due to the IRLP, as described by Higgins et al. (2018).

	Wet Season Average (cm)	Dry Season Average (cm)
Measured vertical accretion (Bomer et al., in review)	1.4	0.9
Predicted deposition (this study)	1.8	0.2
14% reduction in sediment supply	1.6	<0.2
18% reduction in sediment supply	1.4	<0.1
18% reduction in sediment + 1 month shorter freshwater conditions	1.0	<0.1

Comparison Between Locations

In addition to the profound seasonal changes observed at our study locations, there are also important distinctions from within our sub-basin that help us better understand how sediment dynamics evolve within Ganges Brahmaputra tidal sub-basins as a whole. One factor is platform elevation, which is not only different between Sites 1 and 2, but the magnitude of this difference appears to change across seasons. To assess this variability, we adjust the inundation depth by the difference in the absolute magnitude of tide height as measured at SFRS (**Figure 5**). During the wet season, the platform elevation at Site 2 is approximately 4 cm lower than Site 1. During the dry season, this difference extends to 15 cm (**Figure 5**). This calculation relies on the assumptions that the instrument deployment locations are identical across seasons, as is the modification of the tidal waveform between SRFS and the study sites. Given the similarities between the relative inundation depths at each site across seasons, we consider these assumptions to be valid. We suggest that sediment texture plays an important role in controlling platform elevation. In short, the finer grains present at Site 2 (15 vs. 30 μm; **Figure 4**) are more susceptible to compaction from dewatering, which would be particularly important during the dry season when inundation frequency and duration are reduced (e.g., Knott et al., 1987; Nuttle and Hemand, 1988; Nuttle et al., 1990; Bomer et al., in review). This is further supported based on our observations of sediment dry bulk density at the platform surface, which is ∼35% greater at Site 1 than Site 2 (means of 935 and 685 kg/m^3, respectively, **Table 1**), and which also increases by ∼10% from the wet to dry seasons at Site 2 (876 and 968 kg/m^3, respectively), suggesting that compaction is taking place.

Another factor driving the sediment dynamics is proximity to large conduit channels, particularly during the dry season when SSC delta-wide are lower (Barua, 1990; Hale et al., 2019). As described above, we observe relatively little difference between the in-channel SSC at Sites 1 and 2 during the wet season (**Figure 3**). In contrast, there is a dramatic difference between the two sites during the dry season, with substantially less SSC

at the interior location (Site 2). The reason for this may be similar to the difference in the observed reduction of SSC from channel to platform described in section "Sedimentation Controls" above, where an overall decrease in material availability, and increased settling velocities due to salinity-induced flocculation combine to reduce the travel distance for a given particle. While this may seem relatively intuitive, this provides the first empirical evidence for this phenomenon within the SNF. This has very important implications as tidal river management (TRM) projects are being implemented in the poldered region with the goal of combating some of the deleterious side effects of the embankments. With TRM, periodic breaches of the polder wall reconnect sub-basin land with the tidal channel to accelerate land accretion (Khadim et al., 2013; Hossain et al., 2015). Based on our observations, TRM effectiveness would change dramatically based not only on the season, but also the distance from the larger tidal channels. We expect this concept to be explored in greater detail in the near future.

Beyond the obvious elevation difference observed in the sub-basin between Sites 1 and 2, and their relative distances from the Sutarkhali channel, they also exhibit fundamentally different behavior between channel hydrodynamics and sediment transport. In neither location is velocity a strong predictor of SSC (**Figure 5**). Indeed, the strongest correlation occurs at Site 2 during the dry season, where velocity explains ∼35% of the in-channel SSC variance. This weak relationship might suggest that at each site, local resuspension plays a less important role in controlling in-channel SSC than advection from up- or down-stream sources. While this may be true, the roles of local resuspension and advection are likely much more nuanced.

A comparison of the Shields parameter (θ_t) and roughness Reynolds number (Re_*) reveals that with the exception of slack high water, the critical shear stress for resuspension is always exceeded (**Table 1**; Shields, 1936; Miller et al., 1977). Here, shear velocity was determined calculated as the quotient of von Kármán's constant divided by the slope of the curve of velocity versus the natural log of depth, as described by the Law of the Wall. We performed these calculations using data from the relatively quiescent dry season; the stronger velocities observed during the wet season would only serve to enhance shear in the water column and stress on the bed. Of course, evaluating the Shields parameter in fine-grained systems can be fraught, however, our primary reason for using it here is to highlight an interesting difference in the timing of SSC maxima observed at our two field locations. At Site 1, the maximum flood-limb SSC occurs immediately prior to platform inundation during both the wet and dry season (**Figure 5**). This region is characterized by broad (∼15 m-wide), muddy banks, which can continuously provide sediment for resuspension as they inundate, assuming sufficiently strong shear velocities. In contrast, peak flood-limb SSC at Site 2 is observed near the lowest water levels, long before any material in suspension could be delivered to the platform. The channel has narrowed substantially at this distance inland, and is completely drained during spring low tides during the wet and dry seasons. The banks here are not as wide as at Site 1 and are heavily vegetated, which can baffle near-bed flow as the water elevation rises, thereby preventing additional erosion (Furukawa and Wolanski, 1996). **Figure 3** compares the average current speed from the upward-looking ADCP (located on the channel bottom), with the velocity on the channel flank, ∼1.25 m below the platform elevation, during the dry season. While the flood velocities in the channel were similar at the two locations, the velocities on the bank were dramatically different. At Site 2, the maximum flooding velocity on the bank was 0.03 m/s, a full order of magnitude lower than the fastest channel velocity, and unlikely to resuspend bank sediment. In contrast, Site 1 demonstrated bank velocities as fast as 0.15 m/s, which is 34% as fast as the channel velocity, and certainly capable of resuspension (**Figure 3**). This additional source of sediment is one of several mechanisms that help to explain the increased deposition seen at Site 1 relative to Site 2, as observed by Bomer et al. (in review; **Table 1**).

Spatio-Temporal Variability and Future Implications

Interestingly, the deposition rates determined by this and other recent studies (e.g., Rogers et al., 2013; Auerbach et al., 2015; Bomer et al., in review) are similar to the local deposition rates observed across the entire Holocene (0.7–1.0 cm/year; Ayers et al., 2016). Further to the west, where sedimentation has been reduced as a result of the eastward migration of the Ganges River over the past 4000 years, the long-term deposition rates are closer to 0.1–0.2 cm/year (Flood et al., 2015). It would be an oversimplification to imply that this spatial variability stems exclusively from a moving sediment supply. Many boundary conditions, including upstream sediment supply, reservoir construction, sea level, and polder construction have all played a role in effecting delta-wide sedimentation. Nevertheless, the area that has been subject to the most-dramatic decrease in sediment supply (western delta plain) also demonstrates a reduced accumulation rate. This provides important context for the effects of a reduced sediment supply to the SNF—which we can augment with our observed differences between wet season and dry season SSC and sedimentation.

For example, consider the possible impacts of a reduced sediment discharge associated with India's planned dams and diversions through the NRLP on sedimentation in the SNF: if fully implemented, one result would be a reduction in the annual suspended sediment load of the Ganges and Brahmaputra rivers by 39–75% and 9–25%, respectively, with the majority of this reduction occurring during the wet season (Higgins et al., 2018). Collectively, this amounts to a reduction in the total suspended sediment load by 14–18%. Rogers et al. (2013) estimate that approximately two thirds of the sediment deposited each monsoon season is of recent (<6 month) Ganges-Brahmaputra origin, with the remainder being sourced from antecedent shelf and floodplain deposits. Using the more optimistic estimate of sediment load reduction (14%), average wet-season deposition is reduced from 1.8 to ∼1.6 cm (**Table 2**). Using instead the high-end estimate for total sediment

load reduction, wet-season deposition decreases further to ∼1.4 cm (**Table 2**). In both scenarios, dry season deposition is <0.2 cm (**Table 2**). Of course, by reducing the freshwater discharge of these rivers by 24 and 6% respectively, we can also expect the effective duration of monsoon-like conditions to be reduced by a month or more (Higgins et al., 2018). Indeed, if we rework our initial estimate of deposition to reflect a substantially shorter monsoon season (i.e., from 3 to 2 months, or 180 platform-inundating events to 120), wet-season deposition drops to 1.2 cm. With less sediment being delivered to the region, a smaller freshwater contribution to the wet season water levels, and a longer duration of conditions that do not favor sedimentation, we expect sedimentation rates within the SNF to be reduced as a result of a fully implemented IRLP. Further, we expect the combined effects of these impacts to result in a greater reduction in sedimentation than any factor acting in isolation. Using the combined worst-case scenario of maximum suspended load reduction and a shortened wet season, our estimate of deposition drops to <1 cm (**Table 2**). Without adequate sedimentation to offset the regional relative and effective rates of SLR, the SNF may drown in place as predicted by Loucks et al. (2010). Importantly, our analysis neglects the possibility of sediment supplied by channel scouring downstream of the dams associated with the IRLP, similar to the scenario on the Mississippi River described by Nittrouer and Viparelli (2014). That said, as we discussed in the previous sections, the majority of the platform is being supplied with silt and finer-grained sediment, as coarser grains are incapable of being transported to the platform interior. As such, this remains an important area of future research.

CONCLUSION

Sedimentation in the SNF is controlled by a combination of independent factors, including maximum water depth, sediment particle size, inundation duration, and SSC. Understanding the interaction of each of these parameters, as well as their relative importance, is critical to understanding the health and sustainability of the SNF and tidal deltaplain as a whole. Furthermore, the SNF stands out as a natural case study to contrast with the adjacent, heavily modified poldered region, where significant change is necessary to ensure continued habitability. In this study, we observe two overarching trends from a tidal sub-basin located in the SNF. First, we see that environmental conditions during the wet season are substantially more conducive to sediment deposition, with more-frequent and deeper inundation of the platform by fresh water enriched with suspended sediment. The apparent importance of salinity on controlling the formation of aggregates was a particularly interesting find with delta-wide implications in the face of future changes to the fresh water supply. Second, we see that the location proximal to the larger tidal channel (Site 1) exhibits greater SSC values, coarser grain size, and sits at a higher elevation than the location deeper in the forest (Site 2), regardless of season. Despite this, predicted monsoon deposition is actually greater at Site 2 than Site 1, largely because of the lower sediment bulk density (**Table 1**). This combination is particularly interesting, as it suggests that the coarser grains at Site 1 are building a more-stable platform capable of maintaining a higher elevation along the perimeter of SNF sub-basins, while the finer-grained interior is subject to more-intense compaction and dewatering. We must be cautious, therefore, in extrapolating our measurements from channel margins to span the entire lower delta, as the inaccessible interior regions may be more vulnerable to changes in sediment supply. We should also consider these results in practical applications like TRM, and ensure that sites selected for sluice gates have a sediment supply that is both robust and sufficiently coarse to build lasting platforms. Perhaps more important than the observations of the modern conditions are the implications of these observations in the context of scenarios for reduced sediment supply in response to upstream river damming and diversions. In the worst case, where sediment delivery is reduced by 14–18%, and the duration of fresh water conditions is shortened by one month or more, we predict deposition rates ∼50% lower than are currently observed. Not only will this diminish the effectiveness of land reclamation strategies such as TRM, these rates are below those of local effective sea level rise, resulting in a threat to the continued viability of the SNF. Elevated SSC and fresh water conditions not only appear critical to the delivery of sediment from the tidal channels to the mangrove platform, but are also most likely to be affected by changes to the fresh water or sediment discharges of the larger Ganges and Brahmaputra rivers.

AUTHOR CONTRIBUTIONS

RH was responsible for study design and acquiring funding. RH, CW, and EB conducted the field work. RH drafted the initial report, which was subsequently revised by all authors, each of who contributed to the intellectual content.

FUNDING

This work was supported by the National Science Foundation (Coastal SEES- #1600319) and CRDF Global (OISE-17-63730-0).

ACKNOWLEDGMENTS

The local access was granted by Abu Naser Hossain of the Forestry Crime Department, and accommodations arranged by Nasrul Islam Bachchu of Pugmark Tours. The authors extend their deepest gratitude to the captains and crew of the M/V Bawali, M/L Mawali, and M/L Sundari Trawler for their patience and support. We would like to thank Md. Saddam Hossain, Abdullah Al Nahian, and Sourov Bijoy Datta for logistics and field support and Dr. Steven Goodbred, two reviewers, and the editor for their comments that substantially improved the manuscript.

REFERENCES

Allen, J. R. L. (1990). Salt-marsh growth and stratification: a numerical model with special reference to the Severn Estuary, Southwest Britain. *Mar. Geol.* 95, 77–96. doi: 10.1016/0025-3227(90)90042-i

Allison, M., and Kepple, E. (2001). Modern sediment supply to the lower delta plain of the Ganges-Brahmaputra River in Bangladesh. *Geo Mar. Lett.* 21, 66–74.

Alongi, D. M. (2012). Carbon sequestration in mangrove forests. *Carbon Manag.* 3, 313–322. doi: 10.4155/cmt.12.20

Auerbach, L. W., Goodbred, S. L. Jr., Mondal, D. R., Wilson, C. A., Ahmed, K. R., Roy, K., et al. (2015). Flood risk of natural and embanked landscapes on the Ganges–Brahmaputra tidal delta plain. *Nat. Clim. Change* 5, 153–157. doi: 10.1038/nclimate2472

Ayers, J. C., George, G., Fry, D., Benneyworth, L., Wilson, C., Auerbach, L., et al. (2017). Salinization and arsenic contamination of surface water in southwest Bangladesh. *Geochem. Trans.* 18:4. doi: 10.1186/s12932-017-0042-3

Ayers, J. C., Goodbred, S. L., George, G., Fry, D., Benneyworth, L., Hornberger, G., et al. (2016). Sources of salinity and arsenic in groundwater in southwest Bangladesh. *Geochem. Trans.* 17:4. doi: 10.1186/s12932-016-0036-6

Badola, R., and Hussain, S. A. (2005). Valuing ecosystem functions: an empirical study on the storm protection function of Bhitarkanika mangrove ecosystem, India. *Environ. Conserv.* 32, 85–92. doi: 10.1017/s0376892905001967

Barua, D. K. (1990). Suspended sediment movement in the estuary of the Ganges-Brahmaputra-Meghna river system. *Mar. Geol.* 91, 243–253. doi: 10.1016/0025-3227(90)90039-m

Barua, D. K., Kuehl, S. A., Miller, R. L., and Moore, W. S. (1994). Suspended sediment distribution and residual transport in the coastal ocean off the Ganges-Brahmaputra river mouth. *Mar. Geol.* 120, 41–61. doi: 10.1016/0025-3227(94)90076-0

Capo, S., Sottolichio, A., Brenon, I., Castaing, P., and Ferry, L. (2006). Morphology, hydrography, and sediment dynamics in a mangrove estuary: the Konkoure Estuary, Guinea. *Mar. Geol.* 230, 199–215.

Carlton, J. M. (1974). Land-building and stabilization by mangroves. *Environ. Conserv.* 1, 285–294. doi: 10.1017/s0376892900004926

Christiansen, T., Wiberg, P. L., and Milligan, T. G. (2000). Flow and sediment transport on a tidal salt marsh surface. *Estuar. Coast. Shelf Sci.* 50, 315–331. doi: 10.1006/ecss.2000.0548

Delaune, R. D., Patrick, W. H., and Buresh, R. J. (1978). Sedimentation rates determined by 137Cs dating in a rapidly accreting salt marsh. *Nature* 275, 532–533. doi: 10.1038/275532a0

Flood, R. P., Barr, I. D., Welte, G. J., Roberson, S., Russel, M. I., Meneely, J., et al. (2018). Provenance and depositinal variability of the Thin Mud Facies in the lower Ganges-Brahmaputra delta, West Bengal Sundarbans, India. *Mar. Geol.* 395, 198–218. doi: 10.1016/j.margeo.2017.09.001

Flood, R. P., Orford, J. D., McKinley, J. M., and Roberson, S. (2015). Effective grain size distribution analysis for interpretation of tidal-deltaic facies: West Bengal Sundarbans. *Sediment. Geol.* 318, 58–74. doi: 10.1016/j.sedgeo.2014.12.007

French, J. R. (1993). Numerical simulation of vertical marsh growth and adjustment to accelerated sea-level rise, north Norfolk, UK. *Earth Surf. Process. Landf.* 18, 63–81. doi: 10.1002/esp.3290180105

Furukawa, K., and Wolanski, E. (1996). Sedimentation in mangrove forests. *Mangroves and Salt Marshes* 1, 3–10. doi: 10.1023/A:1025973426404

Furukawa, K., Wolanski, E., and Mueller, H. (1997). Currents and sediment transport in mangrove forests. *Estuar. Coast. Shelf Sci.* 44, 301–310. doi: 10.1006/ecss.1996.0120

Ghosh, M. K., Kumar, L., and Roy, C. (2016). Mapping long-term changes in mangrove species composition and distribution in the sundarbans. *Forests* 7:305. doi: 10.3390/f7120305

Gibbs, R. J., Matthews, M. D., and Link, D. A. (1971). The relationship between sphere size and settling velocity. *J. Sediment. Res.* 41, 7–18.

Google Earth (2015). *Google Earth V 7.1.8.3036. Southern Bangladesh. TerraMetrics 2019.* (accessed February 2, 2018).

Google Earth (2017). *Google Earth V 7.1.8.3036. Southern Bangladesh. Digital Globe 2019.* (accessed February 2, 2018).

Hale, R. P., Bain, R., Goodbred, S. Jr., and Best, J. (2019). Observations and scaling of tidal mass transport across the lower Ganges-Bramaputra delta plain: implications for delta management and sustainability. *Earth Surf. Dynam.* 7, 231–245, doi: 10.5194/esurf-7-231-2019

Higgins, S., Overeem, I., Rogers, K., and Kalina, E. (2018). River linking in India: downstream impacts on water discharge and suspended sediment transport to deltas. *Elem. Sci. Anth.* 6:20. doi: 10.1525/elementa.269

Horstman, E. M., Dohmen-Janssen, C. M., Bouma, T. J., and Hulscher, S. J. M. H. (2015). Tidal-scale flow routing and sedimentation in mangrove forests: combining field data and numerical modelling. *Geomorphology* 228, 244–262. doi: 10.1016/j.geomorph.2014.08.011

Hossain, F., Khan, Z. H., and Shum, C. K. (2015). Tidal river management in Bangladesh. *Nat. Clim. Change* 5:492. doi: 10.1038/nclimate2618

Khadim, F. K., Kar, K. K., Halder, P. K., Rahman, M. A., and Morshed, A. M. (2013). Integrated water resources management (IWRM) impacts in south west coastal zone of Bangladesh and fact-finding on tidal river management (TRM). *J. Water Resour. Protect.* 5:953. doi: 10.4236/jwarp.2013.510098

Knott, J. F., Nuttle, W. K., and Hemond, H. F. (1987). Hydrologic parameters of salt marsh peat. *Hydrol. Process.* 1, 211–220. doi: 10.13287/j.1001-9332.201704.033

Krone, R. B. (1987). "A method for simulating historic marsh elevations," in *Coastal Sediments*, ed. N. C. Krause (New York, NY: ASCE), 316–323.

Loucks, C., Barber-Meyer, S., Hossain, M. A. A., Barlow, A., and Chowdhury, R. M. (2010). Sea level rise and tigers: predicted impacts to Bangladesh's Sundarbans mangroves. *Clim. Change* 98, 291–298. doi: 10.1007/s10584-009-9761-5

Manning, A. J., Spearman, J. R., Whitehouse, R. J., Pidduck, E. L., Baugh, J. V., and Spencer, K. L. (2013). "Flocculation dynamics of mud: sand mixed suspensions," in *Sediment Transport Processes and Their Modeling Applications*, ed. A. J. Manning (London: InTechOpen).

Mcleod, E., Chmura, G. L., Bouillon, S., Salm, R., Björk, M., Duarte, C., et al. (2011). A blueprint for blue carbon: toward an imporved understanding of the role of vegetated coastal habitats in sequestering CO2. *Front. Ecol. Environ.* 9, 552–560. doi: 10.1890/110004

Mietta, F., Chassagne, C., Manning, A. J., and Winterwerp, J. C. (2009). Influence of shear rate, organic matter content, pH and salinity on mud flocculation. *Ocean Dyn.* 59, 751–763. doi: 10.1007/s10236-009-0231-4

Miller, M. C., McCave, I. N., and Komar, P. (1977). Threshold of sediment motion under unidirectional currents. *Sedimentology* 24, 507–527. doi: 10.1111/j.1365-3091.1977.tb00136.x

Nittrouer, J. A., and Viparelli, E. (2014). Sand as a stable and sustainable resource for nourishing the Mississippi River delta. *Nat. Geosci.* 7, 350–354. doi: 10.1038/NGEO2142

Nuttle, W. K., and Hemand, H. F. (1988). Salt marsh hydrology: implications for biogeochemical fluxes to the atmosphere and estuaries. *Glob. Biogeochem. Cycles* 2, 91–114. doi: 10.1029/gb002i002p00091

Nuttle, W. K., Hemond, H. F., and Stolzenbach, K. D. (1990). Mechanisms of water storage in salt marsh sediments: the importance of dilation. *Hydrol. Process.* 4, 1–13. doi: 10.1002/hyp.3360040102

Pethick, J., and Orford, J. D. (2013). Rapid rise in effective sea-level in southwest Bangladesh: its causes and contemporary rates. *Glob. Planet. Change* 111, 237–245. doi: 10.1016/j.gloplacha.2013.09.019

Ray, R., Ganguly, D., Chowdhury, C., Dey, M., Das, S., Dutta, M. K., et al. (2011). Carbon sequestration and annual increase of carbon stock in a mangrove forest. *Atmos. Environ.* 45, 5016–5024. doi: 10.1016/j.atmosenv.2011.04.074

Reed, D. J. (1988). Sediment dynamics and deposition in a retreating coastal salt marsh. *Estuar. Coast. Shelf Sci.* 26, 67–79. doi: 10.1016/0272-7714(88)90012-1

Rogers, K. G., Goodbred, S. L. Jr., and Mondal, D. R. (2013). Monsoon sedimentation on the 'abandoned'tide-influenced Ganges–Brahmaputra delta plain. *Estuar. Coast. Shelf Sci.* 131, 297–309. doi: 10.1016/j.ecss.2013.07.014

Saenger, P., and Siddiqi, N. A. (1993). Land from the sea: the mangrove afforestation program of Bangladesh. *Ocean Coast. Manag.* 20, 23–39. doi: 10.1016/0964-5691(93)90011-m

Satyanarayana, B., Bhanderi, P., Debry, M., Maniatis, D., Foré, F., Badgie, D., et al. (2012). A socio-ecological assessment aiming at improved forest resource management and sustainable ecotourism development in the mangroves of Tanbi Wetland National Park, The Gambia, West Africa. *Ambio* 41, 513–526. doi: 10.1007/s13280-012-0248-7

Shaha, D. C., and Cho, Y. K. (2016). Salt plug formation caused by decreased river discharge in a multi-channel estuary. *Sci. Rep.* 6:27176. doi: 10.1038/srep27176

Shields, A. (1936). "Application of similarity principles nad turbulence research to bed-load movement," in *Mitteilungen der Preussischen Versuchsanstalt fur*

Wasserbau und Schifbau, Berlin, eds W. P. Ott and J. C. van Uchelen (Pasadena, CA: California Institute of Technology).

Steckler, M. S., Nooner, S. L., Akhter, S. H., Chowdhury, S. K., Bettadpur, S., Seeber, L., et al. (2010). Modeling Earth deformation from monsoonal flooding in Bangladesh using hydrographic, GPS, and Gravity Recovery and Climate Experiment (GRACE) data. *J. Geophys. Res.* 115. doi: 10.1029/2009JB007018

Temmerman, S., Govers, G., Wartel, S., and Meire, P. (2004). Modelling estuarine variations in tidal marsh sedimentation: response to changing sea level and suspended sediment concentrations. *Mar. Geol.* 212, 1–19. doi: 10.1016/j.margeo.2004.10.021

Twilley, R. R., Rovai, A. S., and Riul, P. (2018). Coastal morphology explains global blue carbon distributions. *Front. Ecol. Environ.*. 16, 503–508. doi: 10.1002/fee.1937

Victor, S., Golbuu, Y., and Wolanski, E. (2004). Fine sediment trapping in two mangrove-fringed estuaries exposed to contrasting land-use intensity, Palau, Micronesia. *Wetlands Ecol. Manage* 12, 277–283. doi: 10.1007/s11273-005-8319-1

Wilson, C., Goodbred, S., Small, C., Gilligan, J., Sams, S., Mallick, B., et al. (2017). Widespread infilling of tidal channels and navigable waterways in human-modified tidal deltaplain of southwest Bangladesh. *Elem. Sci. Anth.* 5:78. doi: 10.1525/elementa.263

Wolanski, E. (1995). "Transport of sediment in mangrove swamps," in *Asia-Pacific Symposium on Mangrove Ecosystems. Developments in Hydrobiology*, Vol. 106, eds Y. S. Wong and N. F. Y. Tam (Dordrecht: Springer).

Conflict of Interest Statement: The authors declare that the research was conducted in the absence of any commercial or financial relationships that could be construed as a potential conflict of interest.

frontiers in Earth Science

ORIGINAL RESEARCH
published: 30 August 2019
doi: 10.3389/feart.2019.00203

From Hazard to Consequences: Evaluation of Direct and Indirect Impacts of Flooding Along the Emilia-Romagna Coastline, Italy

Clara Armaroli[1], Enrico Duo[1] and Christophe Viavattene[2]*

[1] Department of Physics and Earth Sciences, University of Ferrara, Ferrara, Italy, [2] Flood Hazard Research Centre, Middlesex University of London, London, United Kingdom

Managing coastal flood risk at the regional scale requires a prioritization of economic resources along the shoreline. Advanced modeling assessment and open-source tools are now available to support transparent and rigorous risk evaluation and to inform managers and stakeholders in their choices. However, the issues lay in data availability and data richness to estimate coastal vulnerability and impacts. The Coastal Risk Assessment Framework (CRAF) has been developed as part of the Resilience Increasing Strategies for Coasts - Toolkit (RISC-KIT) EU FP7 project. The framework provides two levels of analysis. In the first phase, a coastal index approach is applied to identify a restricted number of potential critical areas for different hazards (i.e., erosion and flooding). In the second phase, an integrated hazard and impact modeling approach is applied in the critical areas to assess the direct and indirect impacts of storm events using a matrix-based approach and a systemic analysis. The framework was tested on the coastline of the Emilia-Romagna region (northern Italy) for two probabilistic coastal storms with representative return periods of 10 and 100 years. In this work, the application of the second phase of the CRAF is presented for two sites, Lido degli Estensi-Spina (Ferrara province) and Milano Marittima (Ravenna province). The hazard modeling of floods was implemented using a coupling between XBeach and Lisflood-FP. The Integrated Disruption Assessment (INDRA) model was applied to quantify direct and indirect impacts. The impact assessment focused on household's financial recovery, business disruption and financial recovery, transport network disruption and risk to life. The considered business sector comprised the key economic activities related to the sun-and-beach tourism, which is one of the main drivers of the regional economy. A Multi-Criteria Analysis was applied to support decision-makers to identify the most critical site. The importance of detailed physical and socio-economic data collected at the regional and local levels is highlighted and discussed, together with the importance to involve different stakeholders in the process (e.g., through interviews and surveys). The limitations of the applied approach due to data quality and availability and to the assumptions introduced in the hazard and disruption models are highlighted.

Keywords: coastal risk, vulnerability, exposure, INDRA model, Lisflood, XBeach, storm, inundation

OPEN ACCESS

Edited by:
Carmine Galasso,
University College London,
United Kingdom

Reviewed by:
Raffaele De Risi,
University of Bristol, United Kingdom
Maria Pregnolato,
University of Bristol, United Kingdom
Mohammad Heidarzadeh,
Brunel University London,
United Kingdom
Rui Figueiredo,
University of Porto, Portugal

****Correspondence:***
Clara Armaroli
clara.armaroli@unife.it

Specialty section:
This article was submitted to Geohazards and Georisks, a section of the journal Frontiers in Earth Science

Received: *28 February 2019*
Accepted: *25 July 2019*
Published: *30 August 2019*

Citation:
Armaroli C, Duo E and Viavattene C (2019) From Hazard to Consequences: Evaluation of Direct and Indirect Impacts of Flooding Along the Emilia-Romagna Coastline, Italy. Front. Earth Sci. 7:203. doi: 10.3389/feart.2019.00203

INTRODUCTION

Coastal areas represent one of the most vulnerable environments worldwide due to the high population density and the pressure of human activities. Sea level rise and increased storminess due to climate change is consequently expected to increase coastal flooding and intensify the frequency and magnitude of coastal impacts, posing a threat to coastal communities. The population exposed to coastal flooding is predicted to increase to up to 1.52–3.65 million by the end of the century (Vousdoukas et al., 2018b). In parallel, the present expected annual damage of 1.25 billion Euro is projected to increase, ranging between 93 and 961 billion Euro by the end of the century, thus increasing of two or three orders of magnitude the present expected annual damage (Vousdoukas et al., 2018b). In terms of vulnerability, one fourth of low coastal areas are retreating globally (Luijendijk et al., 2018) and the total amount of eroded land is twice that which is gained (Mentaschi et al., 2018). The IPCC (2018) report highlights that risks can be reduced if proper and effective adaptation and mitigation options are activated. Additionally, the Science for Disaster Risk Management report (Poljanšek et al., 2017) states that "*The discrepancies in data quality are sometimes asserted an excuse to delay risk analysis and modeling, but it is infinitely better to embark on a risk assessment and analysis process from the outset than wait until better data become available. A "1-in-100 event" could happen tomorrow, it is better to have tried, and commit resources to develop a greater understanding of the risks as far as possible now (and so identify key weaknesses and data gaps) than postpone action until better data are collected.*" Therefore, greater effort should focus on using the best available data and information to carry out comprehensive impact assessments of different hazards. This will provide decision makers with a better idea of the most probable consequences so that they can take action and implement new measures or improve those already in place. Decision makers should also be informed of the uncertainties associated with data and processes used in the quantification of the impact of extreme events.

Whereas risk can be defined by a simple product equation of the hazard probability and its consequences, its quantification remains complex. Assessing the consequences requires the evaluation of hazard intensities together with the direct exposure of assets and their vulnerability (Gouldby et al., 2005). Coastal hazards are of a different nature and intensities and can vary through time (Zscheischler et al., 2018). They can also impact in combination (multi-hazards). Exposure analysis requires the georeferenced mapping of both the built and the natural environment. Land use maps are static by nature and used as such in impact assessment. Yet, the exposed assets may vary by their activities in the short term (e.g., seasonal) or by type in the long term, as land use changes. Vulnerability is even more ambitious to define as it varies through time and includes the intrinsic nature of each exposed element, even for the well-studied flood depth-damage curves where much debate exists on which method provides the most accurate estimation (Jongman et al., 2012). The estimation of indirect and systematic impacts is often avoided biasing decision making toward the direct impacts (Meyer et al., 2013), but must be now encouraged (UNISDR, 2015). Indeed, the impacts of an extreme event can generate effects that last for many weeks or years after the event, and even be permanent, and affect areas and activities that are located far from the coastline and from the impacted site. As a result of difficulties in computing and retrieving the necessary information with a sufficient level of accuracy and reliability, the evaluation of certain consequences is often avoided or implemented by using simple methodologies at large scales, undermining the analysis of critical differences in the impact assessment (Viavattene et al., 2018).

Recent research activities have shown important advancement in risk assessments. Several studies focus on the definition of hazard scenarios, discussing their potential impacts (e.g., Villatoro et al., 2014; Ruol et al., 2018; Favaretto et al., 2019). Most of risk assessment studies combine the hazard evaluation, obtained with various hazard models, with exposure maps to infer the number and nature of probable affected assets (e.g., Perini et al., 2016; Aucelli et al., 2017). Other studies include vulnerability concepts (e.g., Torresan et al., 2012). The obtained results should be considered as an indication of the potential risk, rather than a proper quantification of the risk. Some studies present valuable approaches, combining hazard, vulnerability, and exposure of coastal areas (e.g., Zanuttigh et al., 2014; Erikson et al., 2018). Significant improvements in risk assessment science were delivered by multi-disciplinary projects such as, e.g., THESEUS (Zanuttigh, 2011), MICORE (Ferreira et al., 2009; Ciavola et al., 2011), and RISC-KIT (Van Dongeren et al., 2018). Specifically, the RISC-KIT Project[1] (Van Dongeren et al., 2018) developed management tools with the aim to support coastal administrations to perform proper risk and impact assessment, improving the prevention and preparedness phases of the disaster management cycle. The tools were developed to derive a comprehensive analysis of multiple hazards and systemic impacts (Van Dongeren et al., 2018).

The Coastal Risk Assessment Framework (CRAF; Viavattene et al., 2018) is the RISC-KIT regional risk assessment tool aiming to determine where critical coastal sectors (hotspots) are located and where coastal managers should act first, therefore prioritizing their (usually limited) resources. The framework is composed of two phases. A first screening of the coast (Phase 1) that includes the computation of a coastal index based on the identification of exposure indicators and hazard indicators to provide a shortlist of critical sites (hotspots). Subsequently, hotspots are ranked (Phase 2) by applying a risk assessment utilizing more complex hazard models at the local scale (i.e., XBeach, Roelvink et al., 2009; Lisflood-FP, Bates and De Roo, 2000) and the Integrated Disruption Assessment model (INDRA, Viavattene et al., 2015[2], 2018). The second phase is carried out to compare the selected hotspots in order to define the most critical one at the regional level.

This paper presents the implementation of CRAF Phase 2 for flooding at two coastal hotspots in the Emilia-Romagna (Italy) coast that were identified as critical through CRAF Phase 1 analysis (Armaroli and Duo, 2018). Beyond this, the paper

[1] www.risckit.eu

[2] http://www.risckit.eu/np4/file/383/RISC_KIT_D2.3_CRAF_Guidance.pdf

highlights the importance of the quality of the input data for the proper application of an impact assessment, as well as discusses how data quality, hazard modeling uncertainties and damage functions selection could affect the reliability of the final results. The paper discusses the influence of data quality for the interpretation of the results and to identify the most critical hotspot, among the ones selected in CRAF Phase 1, in the context of an urbanized and highly touristic regional coast.

CASE STUDY

The Emilia-Romagna Region (RER hereafter) coastline, facing the north Adriatic Sea in Italy, stretches over 130 km and is composed of low-lying sandy beaches mostly of a dissipative nature (**Figure 1**, Perini et al., 2016). The majority of landward territories are below mean sea level, with the lower values registered in the Ferrara Province. The coastal area is heavily urbanized, especially in the central-southern parts (**Figure 1**). A large number of hard protection structures had been constructed starting from the late 1970s in order to protect the coast from erosion and inundation (60% of the regional coastline is protected by hard structures; Perini et al., 2016). There are few pristine sites that are located in natural parks of the Natura 2000 network. The parks represent the only remaining coastal areas where flora and fauna are preserved from anthropisation. However, the vicinity of the natural sites to heavily exploited areas makes them fragile and exposed to degradation.

The tidal regime is microtidal ranging between 30–40 and 80–90 cm at neap and spring conditions, respectively (Perini et al., 2016). The coastline is exposed to storms from the E-NE and SE directions. Prevailing winds are from the same directions (Bora and Scirocco, respectively) and are able to generate significant storm waves and high surge levels, although the modal wave regime is of low energy (91% of Hs below 1.25 m; Ciavola et al., 2007). The 1-in-1 year return period wave height is 3.3 m with a peak period of 7.7 s (Armaroli et al., 2009). Storm tides represent a threat for the coastal area because they can double the tidal effect (1-in-10 years return period surge ∼1 m, Masina and Ciavola, 2011) and are mainly associated with SE winds. Subsidence rates exacerbate the exposure of coastal lands to the impact of storms. Subsidence affects the whole coastline to varying degrees and is the result of the natural compaction of alluvial sediments that compose the Po River plain and of human activities, such as groundwater and natural gas extraction (Teatini et al., 2005; Taramelli et al., 2015; Perini et al., 2017; Antonellini et al., 2019). The peak values are registered at the coast near Ravenna (2 cm/year).

The main coastal hazards are beach erosion and inundation that cause sediment loss and beach width reduction, along with damages to coastal structures and infrastructures. A major event occurred on 5–7 February 2015 (Hs = 4.6 m, Tp = 9.9 s, wave dir = ENE – measured at the Cesenatico wave rider buoy at the peak of the storm; max water level = 1.2 m measured at Porto Corsini tide gauge, **Figure 1**; Duo et al., 2018). This caused the extensive inundation of landward areas and impressive beach erosion. Perini et al. (2015a,b) report that the inundated area was, in several localities, comparable to the 100 years return period flood extension computed by the regional authorities in the framework of the EU Floods Directive (Perini et al., 2016, 2017), while in other locations it appeared to be closer to the 10 years return period flood map (Duo et al., 2018). In some coastal towns located in the Ravenna Province a flood water level of up to 2 m was measured (Perini et al., 2015a,b). The event was followed by extraordinary interventions to repair the damages and nourish the shores with 1.2 million cubic meters of sand taken from offshore deposits. The Italian and Regional Governments allocated 20 million Euro to finance the interventions[3].

The coastal area is very important for the regional economy as it includes a large number of activities related to the sun-and-beach tourism. The tourist presence in 2017 (between January and December) in the Riviera (the coastal area of the Emilia-Romagna region) was almost 7 million visitors. The summer period only (May–September) registered almost 5.5 million visitors[4]. Tourism represents 11% of the Regional GDP, with the Riviera as the main driver of the leisure industry. The leisure industry is represented by the "chain" that includes accommodations, concessions (areas occupied by permanent structures, located on the rear part of the beach, that are granted to private entities who pay a yearly fee to the State to be allowed to use the public land for entrepreneur activities) and facilities such as sun-chairs and umbrellas, restaurants, bars, gym, changing cabinets, showers, etc.

Two coastal hotspots were selected to evaluate the direct and indirect impacts of extreme events. The hotspots were identified through the application of the first phase of the Coastal Risk Assessment Framework developed in the RISC-KIT project (for more details on the project refer to Van Dongeren et al., 2018; for CRAF phase 1 application along the Emilia-Romagna coastline refer to Armaroli and Duo, 2018). The identified hotspots are the Lido degli Estensi-Lido di Spina coastal area (hereafter referred to as HS1, Ferrara province, **Figure 1**) and Milano Marittima (HS2, Ravenna province, **Figure 1**). Both locations experienced impacts in February 2015 (see Duo et al., 2018 for HS1; Perini et al., 2015a,b for HS2). Furthermore, HS1 and HS2 were identified by local end-users as the areas where a more detailed evaluation of the direct and indirect impacts caused by extreme events should be carried out. Herein, the impacts of flooding are discussed.

HS1 – Lido degli Estensi-Lido di Spina

The coastal villages of Lido degli Estensi and Lido di Spina are located in the Ferrara province (**Figure 1**). The area is bounded by the Porto Garibaldi jetty in the northern part. The analyzed beach extends southward by almost 4 km. The beach is composed of fine to medium sand and is very dissipative. The shore at Lido degli Estensi has a maximum width of 250 m, one of the largest of the regional coastline. The sand

[3]https://www.ferraraitalia.it/ripascimento-della-costa-aggiudicata-la-gara-per-20-milioni-79268.html

[4]https://www.ucer.camcom.it/osservatori-regionali/os-turistico/pdf17/2017-rapporto-consuntivo-turismo-er.pdf

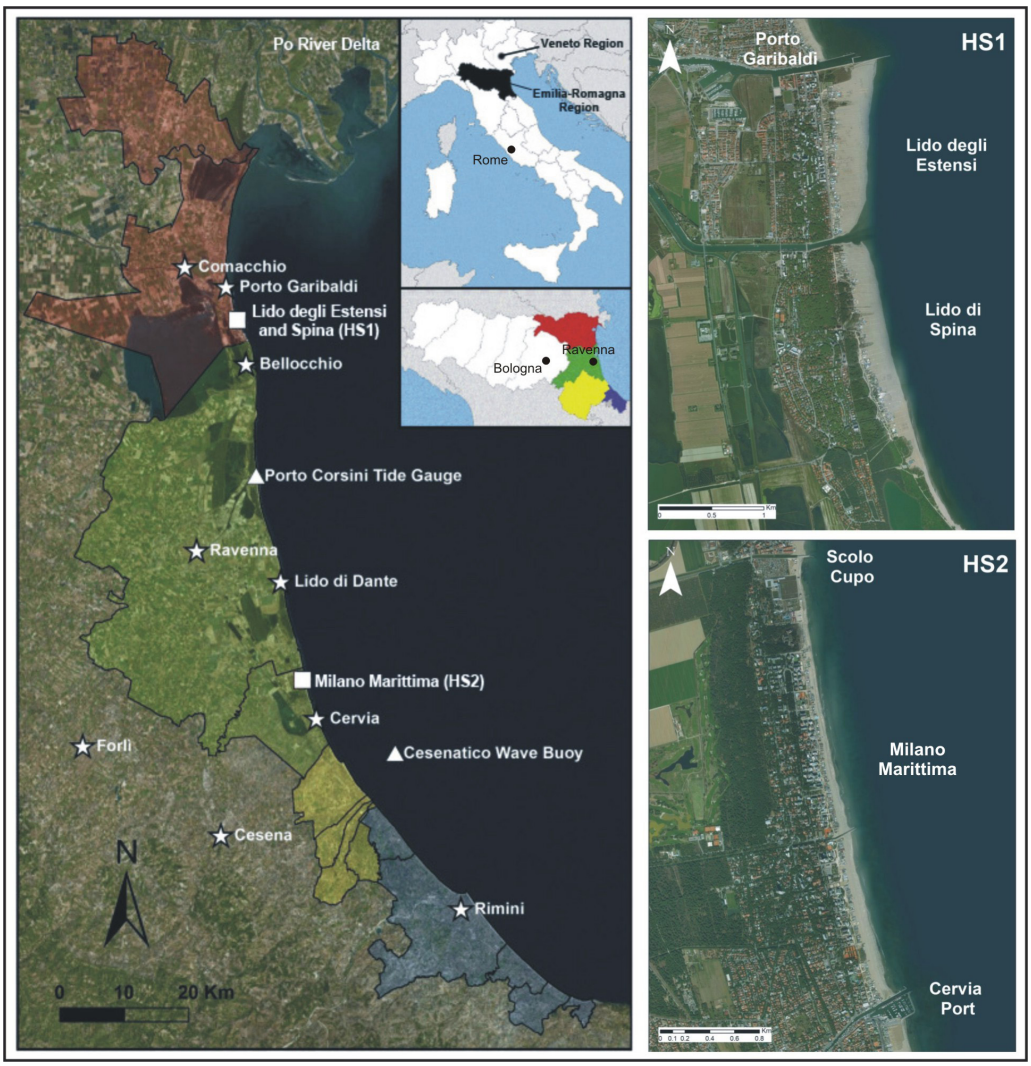

FIGURE 1 | Coastal area of the Emilia Romagna region. The localities cited in the text are indicated. On the right: Lido degli Estensi-Lido di Spina (HS1) and Milano Marittima (HS2). The different colors in the inset indicate the four coastal provinces (modified from Armaroli and Duo, 2018).

accumulation is due to interruption of longshore sediment transport caused by the Porto Garibaldi jetty that was built in the early 1940s to protect the mouth of the navigation channel of Porto Garibaldi. The backshore is urbanized, and the beach is predominantly occupied by bathing establishments with some remaining dunes in-between structures. The economic activities of the area are based on fishery, aquaculture, agriculture, summer (coastal) leisure activities and eco-tourism (the site is located in the Po Delta Park that is part of the Natura 2000 network).

HS2 – Milano Marittima

The Milano Marittima site is in the Ravenna province (**Figure 1**). The beach is almost 5 km long and comprised between the artificial canal "Scolo Cupo" in the north and the Cervia port in the south. The beach width is between 50 and 100 m. It is dissipative with fine to medium sand. The area in 1943 was characterized by large dune fields and few buildings, especially located in the southern part of the site. Starting from the early 1970s, HS2 was occupied by many buildings and infrastructure and development increased until the late 1980s, along with the destruction of the coastal dunes and occupation of the rear part of the beach with concessions. At present the site is one of the most attractive for summer tourism along the regional coastal area. The number of second homes is large as well as hotels and other types of accommodation. The main economic activity is the summer tourism.

METHODS AND DATA

The second phase of the CRAF is aimed at the comparison between coastal hotspots, that were identified in the first phase of the framework (see, as an example, Armaroli and Duo, 2018),

in terms of direct and indirect impacts. In this section, the methodology for the assessment of the impact of extreme coastal flood events is presented. It consists of two main parts: the hazard and the impact modules. The hazard (see Inundation Modeling and Extreme Events Selection) is assessed through numerical models forced with literature-based design extreme events. The risk assessment is completed through the application of the Integrated Disruption Assessment (INDRA) module (see The Integrated Disruption Assessment (INDRA) Module) able to quantify direct (see Direct Impacts) and indirect (see Indirect Impacts) impacts. The comparison between hotspots is done through a Multi Criteria Analysis [see Multi Criteria Analysis (MCA)] which is based on the involvement of regional and local stakeholders.

Inundation Modeling and Extreme Events Selection

The hazard modeling is implemented through a model chain coupling XBeach (Roelvink et al., 2009) 1D profiles with a 2D Lisflood-FP (Bates and De Roo, 2000; Bates et al., 2005) model of the hinterland (**Figure 2**). The XBeach model computes the hydro-morphodynamics of the profile for a given extreme forcing event. The discharge time series of the profiles, that are calculated considering the morphodynamic feedback of the profile, are therefore used as input for the Lisflood model that computes the inundation maps (i.e., water depth, velocity and flood-depth velocity). Specifically, the link between the two models is implemented through Matlab scripts that read the discharge timeseries calculated by the XBeach model for each profile and process them to provide water discharges. For each profile, the position (P) where the discharge time series is read by the scripts, is located around 10 m inland from the location where beach erosion interrupts. Since each profile is representative of a beach sector with a specific length (L), the discharge time series for the Lisflood model are corrected taking into account the length of each sector. Additionally, in order to avoid localized massive and unrealistic amounts of water pouring into the Lisflood domain at the discharge location (P), the localized discharge is distributed between equally spaced points in each sector, considering the cell size of the Lisflood model grid and the length (L) of the sector.

The characteristics of the topo-bathymetric dataset are presented in **Table 1**. Different datasets from different sources and with different resolutions (Lidar flights and multibeam surveys) are merged (covering the emerged and submerged beach) to obtain a uniform topo-bathymetric model of the area in order to run the numerical model. A large number of XBeach profiles are selected (90 for HS1; 106 for HS2) in order to describe in details the morphology of the beach and the backshore, as it represents a dominant factor for the inundation modeling. Each profile is representative of a uniform coastal sector, with lengths ranging from 9 to 98 m for HS1, and from 7 to 109 m for HS2. Representative cross-shore profiles along the regional coastal area are presented in Armaroli and Duo (2018), in their Figure 2. The water level and wave time series are designed as triangular shapes (e.g., McCall et al., 2010) based on the parameters presented by Perini et al. (2016). The forcing levels in deep water were calculated as the sum of the high tide and storm surge components while wave data are used as they appear in **Table 2**. The direction of each storm is not considered, thus meaning that the direction of wave propagation is assumed to be perpendicular to the coast. The results of the model chain are post-processed to provide the inundation maps of each event in terms of maximum water depth and flood depth-velocity. The main parameters used in the model chain (XBeach-Lisflood) are summarized in **Table 3** (Bates and De Roo, 2000; Bates et al., 2005; Roelvink et al., 2009). XBeach automatically defines the time step depending on the Courant–Friedrichs–Lewy number (CFL) that is set as default (0.7). The time step for LISFLOOD is also set as default (10 s).

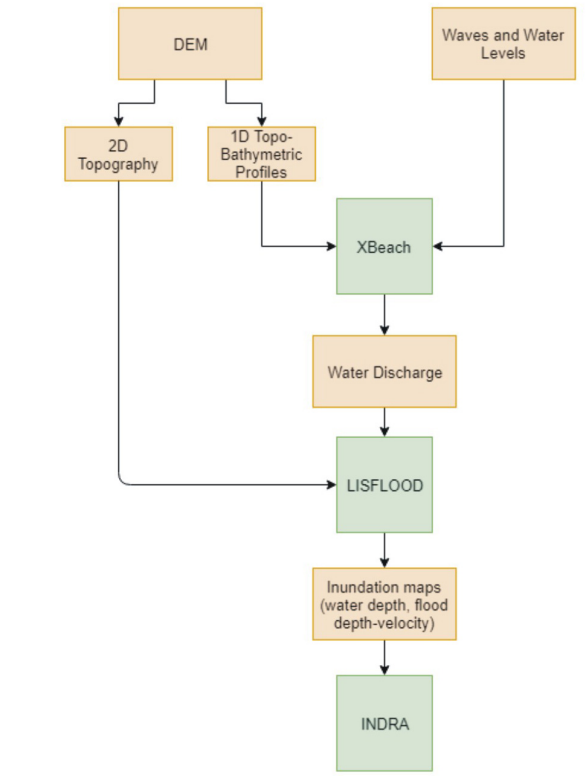

FIGURE 2 | Hazard assessment process and link between XBeach and Lisflood models.

TABLE 1 | Topo-bathymetric dataset, input for the XBeach (1D Topo-bathymetric profiles) and Lisflood (2D Topography) models.

Hotspot ID	Area	Type	Period	Merged dataset resolution
HS1	Inland	Lidar	October 2014	1 m × 1 m
	Nearshore	Bathymetric Lidar	2012	5 m × 5 m
	Offshore	Multibeam	2013	5 m × 5 m
HS2	Emerged	Lidar	2012	1 m × 1 m
	Submerged	Bathymetric Lidar	2012	5 m × 5 m

TABLE 2 | Parameters of the selected extreme events: 10 and 100 years return period storms (T10 and T100, adapted from Perini et al., 2016).

ID	Scenario	RP [years]	Storm Surge [m]	High Tide [m]	Wave Setup [m]	TWL [m]	Hs [m]	Tp [seconds]	Dur [days]
T10	Freq.	10	0.79	0.4	0.3	1.75	4.7	8.9	1.75
T100	Low Freq.	100	1.02	0.4	0.39	1.81	5.9	9.9	2.3

Water levels, wave characteristics and duration of each event.

TABLE 3 | Modified parameters from the default settings for both models (XBeach and Lisflood) used for the analysis.

Model	Parameters	Grid resolution
XBeach (1D)	Average sediment grain size (D50): 0.00023 m	Surf and emerged area: ∼1 m
	Factor related to the effect of the wave form on the sediment transport (facua): 0.1	Offshore area: ∼20 m
	Morphological acceleration factor (morfac): 5	
	Interval time of output (tintm): 1800 s	
Lisflood-FP (2D)	Infiltration rate (infiltration): 0.00003 m/s	3 m × 3 m

The Integrated Disruption Assessment (INDRA) Module

The direct and indirect impacts of the simulated coastal events are assessed with the INDRA model (Integrated Disruption Assessment). The INDRA model (Viavattene et al., 2018) produces as outputs eight regional standardized indicators for a multi-criteria analysis, i.e., risk to life, ecosystem recovery, household displacement, household financial recovery, business financial recovery, regional business disruption, regional utilities disruption, regional transport service disruption (**Figure 3**) (for more detailed information on methods see Viavattene et al., 2015). The INDRA model code[5] and CRAF application manual are available online as public deliverables of the RISC-KIT project (Viavattene et al., 2015[6]). However, a brief summary of the main equations and assumptions used in the model are presented in the following sections. For other applications of the model in different case study sites the reader is invited to refer to Christie et al. (2018), De Angeli et al. (2018), and Ferreira et al. (2018).

The calculation of each indicator requires the collection of specific data on exposed assets and their characteristics. The estimation of the direct impacts requires the geolocation of assets (land uses and networks) and vulnerability indicators such as flood depth damage curves. A common five-point scale (None, Low, Medium, High, and Very High Impact) is used to measure the direct impacts; each scale being associated with a hazard intensity threshold level (e.g., flood depth, flood depth-velocity, flood duration, erosion distance).

Additional inputs are then required for estimating the resulting indirect impacts. As such, empirical or synthetic data are necessary to estimate, e.g., the time spent by households in alternative accommodation according to the severity of an event. Information on penetration rate of insurance is required to estimate the financial recovery of households and businesses. INDRA also aims to estimate the loss of services over time using network analysis. It requires an evaluation of reinstatement time (e.g., required logistic and repair time for an asset to be operational) and of their dependencies for the considered assets (e.g., business supply chain, utility networks).

INDRA aims to compare indicators and hotspots rather than absolutely quantifying the losses. Therefore, the indicators are scaled regionally from 0 to 1 (from no regional impact to all region been impacted). The indicators are then combined by weighted summation using Multi Criteria Analysis (MCA). The MCA approach is considered here as an appropriate and widely used method to support transparent decision-making between various stakeholders (Janssen, 2001; Belton and Stewart, 2002; Hajkowicz and Higgins, 2008). It permits stakeholders perspectives to be reflected on the indicators and consensus to be reached on the selected hotspot(s).

The approach adopted in INDRA recognizes the existing issues of inconsistent units and of data collection and availability, and the model was developed to increase flexibility and the ease of use in the context of scarce or rich data being available. To maintain a degree of transparency and to support the stakeholders in their selection, a Data Quality Score is included in the approach. It consists of scoring between 1 and 5 the different input data (From "1 - Data available and of sufficient quality" to "5 - No data available, based on multiple assumptions"). The scoring is carried out through an expert judgment approach, meaning that the level of quality is assigned by who carries out the analysis and collects the information, i.e., who is aware of the quantity and quality of the included information and datasets.

Data Input for the INDRA Model

The INDRA model is applied to evaluate the direct and indirect impacts of two extreme events selected as representative of the 10 and 100 years return period storms. At the regional and hotspots scales households, businesses, risk to life, transport networks are included in the impact assessment. Ecosystems, including agricultural areas, were considered as negligible with the end-users and were scored to 0 by default in the impact assessment model. Indeed, the coastal zone includes large agricultural areas and two important natural parks. However, the analysis carried out builds on the awareness that, although coastal managers recognize the importance of natural sites, especially in a coastline where pristine lands are rare and protected, they have to "*face the reality*" (Martinez et al., 2018). In fact, the majority of human and economic resources are spent for the protection and maintenance of one of the most important economic sectors of the Region, i.e.,

[5]http://www.risckit.eu/np4/383.html, T6

[6]http://www.risckit.eu/np4/file/383/RISC_KIT_D2.3_CRAF_Guidance.pdf

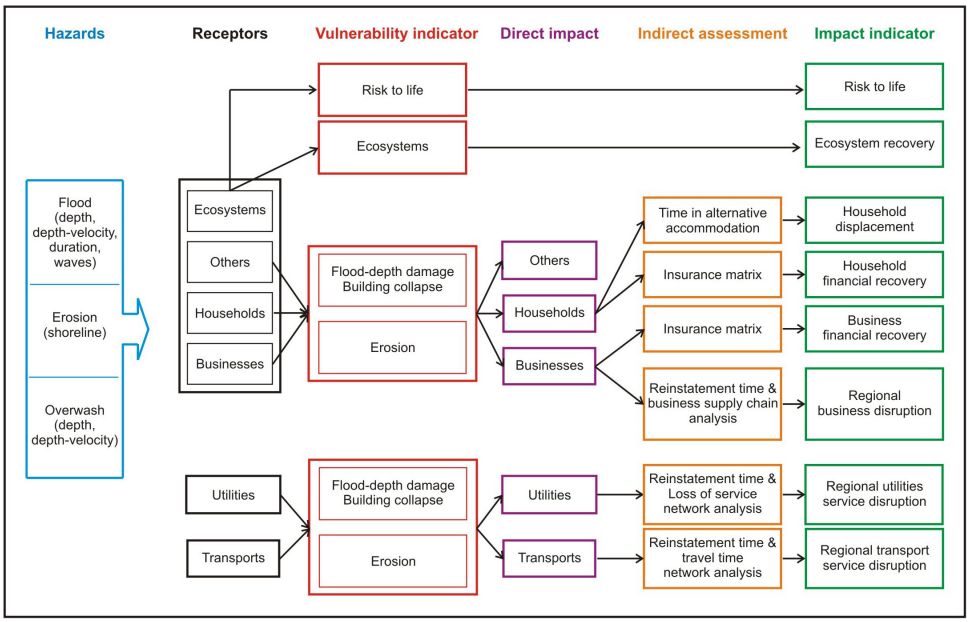

FIGURE 3 | Impact assessment process of the INDRA model (modified from Viavattene et al., 2018).

tourism in coastal villages and towns where hotels, concessions, shops and many other facilities are located. Utilities are not taken into account as in the first phase of the CRAF it was found that important electricity stations, aqueducts and wastewater treatment plants are not exposed (Armaroli and Duo, 2018).

Direct Impacts

Direct impacts represent the category of losses associated with a physical contact with the water. They mainly concern assets and people and are treated differently in the model. In the next paragraphs the method used to evaluate direct impacts to assets (see Direct Impacts to Assets) and people (see Direct Impacts to People) is presented. An additional section (see Direct Impact to Other Structures) regarding the direct impact to other structures, such as schools and cultural heritage sites identified in the two hotspots, is included.

Direct Impacts to Assets

Impact indicators related to assets are evaluated by estimating the direct damages to buildings and other assets using flood-depth damage curves and a building collapse matrix (**Figure 3**). Such evaluation requires the identification and location of each asset. Buildings are identified using 2016 cadastral maps provided by regional managers, updated with more recent information where necessary. The polygon features are firstly converted into points calculating the centroid of each polygon and then the points manually checked and corrected. The cadastral maps do not provide a description of the mapped elements and are classified by default as residential building. For the purpose of this study only residential buildings, hotels, concessions, camping sites, cultural heritage buildings and schools have been classified according to their type, but the rest of non-residential properties (e.g., public offices, shops, restaurants) remained classified as residential properties. Such information is unavailable and will require additional local surveys. Therefore, the assessment probably overestimates the number of impacted residential properties and underestimates that of non-residential properties, with the exception of the typologies listed above (hotels, concessions, cultural heritage buildings, and schools). For estimating the regional indicators all regional assets have to be represented in the model. However, only the exposed assets have to be represented individually for the impact assessment. Therefore, all the assets potentially non-exposed (i.e., outside the hotspots area) are aggregated. The mapped assets in each hotspot are the ones falling inside flood-prone areas derived from the modeling chain (i.e., potentially affected). The transport network includes both roads and railways and are mapped at the regional level on the basis of data provided by regional managers that has been checked and manually corrected and simplified.

Table 4 includes the vulnerability functions used to evaluate the direct impacts. The flood-damage curve utilized to compute the direct impacts is adapted from the study by Scorzini and Frank (2017). The curve was constructed considering the damages to residential properties caused by a river flooding that occurred in Veneto in 2010, the Region that borders Emilia-Romagna in the north. The decision to use flood-damage curves for river flooding comes from the fact that similar curves for marine flooding are not available for Italian coastlines. The chosen curve is the one developed for single-family detached buildings, that shows the highest derivative. The thresholds summarized in **Table 4** are defined following the approach adopted by Sanuy et al. (2018) for the Italian site Lido degli

TABLE 4 | Vulnerability indicators for the direct impact of flooding and corresponding references.

Land use types	Hazard component	Th 1 Low	Th 2 Medium	Th 3 High	Th 4 Very High	Reference and comments
Residential, hotels, concessions, camping	flood depth (fd, m)	0	0.3	0.7	9999	Fd curve (single-family detached, "worst case") by Scorzini and Frank (2017)
Residential, hotels, concessions, camping	flood depth velocity (fdv, m^2/s)	9999	9999	3	7	Based on building collapse matrix (coastal vulnerability indicator (CVI), library RISC-KIT project[1]; Karvonen et al., 2000)
Road and railway networks	flood depth (fd, m)	0.3	9999	9999	9999	The 0.3 m is considered as an average flood depth for which transports section will be closed (based on Penning-Rowsell et al., 2013)

[1]*Available at http://www.risckit.eu/np4/383.html. Th1, 2, 3, and 4 refer to the threshold values used to represent the impact level (low, medium, high, and very high, respectively).*

Estensi-Spina (Ferrara province, **Figure 1**), which includes part of HS1. In Sanuy et al. (2018), site-specific damage levels are defined based on the damage factor value (here translated into water depths following the adopted curve) in agreement with regional coastal managers.

The thresholds used for building collapse (Karvonen et al., 2000) and direct impacts to the transport network (Penning-Rowsell et al., 2013) are the default values included in the model, because it was not possible to retrieve such information from local, regional or national sources (database, literature, reports). The hazard input in the INDRA model is in the form of a grid with flood depths (fd) and flood depths-velocities (fdv) associated to each cell of the grid. In case that low depths (e.g., 0.3 m < fd < 0.7 m, medium impact, **Table 4**) but high velocities occur (i.e., the product flood depth*velocity is e.g., above the 3 m^2/s threshold according to **Table 4**, which means high impact) the model considers the worst condition (i.e., high impact). The overall Data Quality for assessing the direct impact is scored 3.

Direct Impacts to People

Loss of life and injuries may result from extreme events. However, the causes vary and, often, are a combination of multiple determinants such as lack of warning, time, type of flooding, surrounding environment, structure collapse, individual behavior (Jonkman et al., 2008). A simplified method applicable to regional scale is considered in the model. Risk to life is evaluated with the matrix produced for the FLOODSITE project by Priest et al. (2007). The matrix includes simple and easy-to-access information such as flood-depth velocities and the nature of the area in terms of building materials, number of stories and type of property (the matrix is also presented in Christie et al., 2018 in their Table 8). There are three levels of vulnerability (low, medium, and high) associated to different buildings' characteristics: multi-storey apartments and masonry concrete and brick properties (low), typical residential area with mixed types of properties (medium) and mobile homes, campsites, bungalows and poorly constructed properties (high). It must be noted that the method does not preclude the consideration of other determinants such as the presence of vulnerable population group or flood warning. The matrix was built taking into account the comprehensive review by Jonkman et al. (2008) of different risk models and provides a risk to life score ranking from 0 (no risk to life) to 4 (very high risk to life). Residential buildings and hotels are associated with the low vulnerability class, concessions to medium and camping sites to high. The surface (in km^2) of each vulnerability class in each hotspot is presented in **Table 5** with the associated impact thresholds. The model associates to each property the flood depth-velocity obtained from the hazard modeling to derive a risk to life score. The scores from each building are then aggregated and normalized to calculate a Regionalized Risk to Life Indicator.

Direct Impact to Other Structures

The direct impact to schools, cultural heritage buildings and camping sites is evaluated considering the same thresholds defined for other assets (**Table 4**). In HS1 there is one school located not far from the beach and in front of the navigation channel of Porto Garibaldi. In HS2 four schools are identified and two cultural heritage sites represented by the Varese and Montecatini summer colonies built in 1938–1939 that are part of the regional cultural heritage. The financial recovery for schools and cultural heritage sites is set to be fully compensated because they are public properties. It should be underlined that the colonies represent an important part of the historical heritage of the region, but they are abandoned and not utilized because the investments needed to restore the buildings would be very high.

Indirect Impacts

Household Displacement

According to the analysis of recent storm events that caused the evacuation of the population (in 1999 and 2015), household displacement is not a major issue when storm events occur. Specifically, households are displaced for few days and mostly as a precautionary measure, especially where there is a river flooding hazard[7,8] (Perini et al., 2011).

The storm that occurred on 6–7 November 1999 caused extensive beach erosion along the whole coastal area and

[7]http://www.comune.ra.it/Notizie-di-copertina/Maltempo-il-diario-delle-comunicazioni-di-servizio.-L-impegno-di-Comune-Istituzioni-e-mondo-imprenditoriale-per-far-fronte-all-emergenza

[8]http://protezionecivile.regione.emilia-romagna.it/argomenti/piani-sicurezza-interventi-urgenti/speciali/febbraio-2015-emergenza-neve-e-mareggiate/febbraio-2015-emergenza-neve-e-mareggiate

TABLE 5 | Site vulnerability classes and related impact thresholds according to fdv values for the risk to life assessment on the basis of the risk to life matrix (Priest et al., 2007; Christie et al., 2018).

Site vulnerability	Low (fdv m^2/s)	Medium (fdv m^2/s)	High (fdv m^2/s)	Very High (fdv m^2/s)	Site vulnerability in HS1 (km^2)	Site vulnerability in HS2 (km^2)
Low	<0.25	0.5–1.1	NA	>7	0.38	0.44
Medium	<0.25	0.5–1.1	1.1–7	>7	0.03	0.02
High	<0.25	0.25–0.5	0.5–1.1	>1.1	0.14	0.09

The surface extension of each vulnerability class in each hotspot is included. fdv, flood depth-velocity.

inundation (Perini et al., 2011). It is reported that 50 residents of Cesenatico (Forlì-Cesena province, **Figure 1**) were evacuated. The event that occurred on 5–6 February 2015 was one of the most intense ever registered since 1966 (i.e., the most intense storm occurred along the RER coast; Duo et al., 2018) and caused severe damages and inundation along the whole regional area. According to newspapers articles, around 400 people were evacuated from their homes, but mostly as a preventive measure due to the high elevation, above the alert level, of the freshwater inside canals and rivers. Marine flooding affected several villages, and 20 families were evacuated from their homes in Lido di Savio (Ravenna province, **Figure 1**). The information was provided by end-users and stakeholders during a consultation that took place in October 2015 with ten stakeholders (representatives of Land Use planners, Civil Protection, Forest Rangers, Academics, Regional Meteo Agency, Po Delta Regional Park, Comacchio Municipality) and by examining local and regional newspapers' articles. People were evacuated after the peak of the storm and, after two/three days, they were allowed to go back home. Damages to households consisted of deposition of mud and sand on ground floors, and damage to goods and furniture located in the lower floors.

A comprehensive review of past events centered on household displacement is not available. Such information is difficult to recover. In the catalog of past storm events that affected the regional coastal area between 1946 and 2010, produced for the Micore EU project[9] (Perini et al., 2011), the information on displacement is limited, especially that related to the duration. Also, for the 2015 storm, information is difficult to find for the whole regional area (not even the Regional Civil Protection official report gives detailed information, especially on the duration of the displacement and exact location[10]). Therefore, it was decided to consider that households are not displaced. The Data Quality for displacement is considered as poor (3).

Household and Business Financial Recovery

Financial recovery mechanisms may include compensation provided by both national and regional governments and also by private insurance companies. They can be in the form of reimbursements, direct payments, tax breaks or as coverage on a standard insurance policy.

In Italy, marine flooding is currently excluded from private residential insurance policy. Large debate at the political level occurred between 2012 and 2014 on the proposal to make compulsory the insurance for inundation of households for all the areas included within hazard zones. However, any decision has been currently postponed and the principal financial recovery mechanism in place is governmental compensation.

Therefore, the financial recovery mechanism for private properties that was considered in the model is the compensation that is provided if a disastrous event occurs and only if the regional government declares the "natural disaster state." If this is declared, the regional government can have access to specific national and regional funds that are allocated to compensate areas that are affected by catastrophic events (e.g., the 2012 earthquake that occurred in the RER region; the 2015 storm event in the northern Adriatic). Therefore, compensation is provided only for high and very high hazards and depends on the magnitude and extent of the impacts. In **Table 6** the insurance figure for residential properties and business activities is presented. For households, 15% are associated to NoI (Not Insured, to include a certain percentage of households that do not access compensations due to bureaucratic obstacles and/or non-eligibility for compensations), 85% NoILcomp (Not Insured, Low compensation, because we are taking into account extreme events).

TABLE 6 | Financial recovery mechanisms in relation to the scores of the direct impact on properties and business activities.

Assets	Distribution (from 0 to 1)	Direct impact on properties			
		Low	Medium	High	Very high
Households					
No Insurance (NoI)	0.15	2	3	4	5
No Insurance but access to large government compensation scheme (NoILcomp)	0.85	1	1	2	3
Household Financial Recovery Score (Hfri)		1.15	1.3	2.3	3.3
Business (hotels, concessions)					
Business Not Insured but Self-insured (BNoISelf)	1	1	2	3	4
Business Financial Recovery Score (Bfri)		1	2	3	4

[9] www.micore.eu

[10] http://protezionecivile.regione.emilia-romagna.it/argomenti/piani-sicurezza-interventi-urgenti/speciali/febbraio-2015-emergenza-neve-e-mareggiate/febbraio-2015-emergenza-neve-e-mareggiate

We have interviewed the President of the Consortium of economic activities (concessions and hotels) located in the coastal area of the Ferrara Province and he stated that: "there are no insurance companies that offer policies that cover the risk of inundation and erosion." Furthermore, he stated that "our consortium has created a guarantee fund to collect money from the associated partners (a sort of auto-taxation) that is used to finance different activities, among which there is the compensation to entrepreneurs whose enterprise was affected by inundation and erosion. The fund is not large enough to fully compensate each entrepreneur, especially if the coast (beach and related structures) was largely damaged, but it is possible to obtain partial compensation. The central and regional governments do not include businesses in the compensations provided in the aftermath of a catastrophic event. Compensation are only meant to refund households." Nevertheless, the compensation provided by the private fund is negligible (max 5000 Euro[11]) when compared to true damages of very high impact events.

In **Table 6**, 100% business activities are associated to BNoISelf (Business Not Insured, Self-insured) because marine inundation is not covered by insurance companies for economic activities in Italy. Nevertheless, after the 2015 storm (Duo et al., 2018), the regional authorities have mediated between representatives of economic activities and lending institutions in order to find an agreement on soft loans to entrepreneurs affected by the event. Some economic support initiatives were also activated by the regional government[12]. Overall a Data Quality Score of 3 is attributed to the insurance matrix.

The INDRA model assigns the Household or Business Financial Recovery Score for each property according to the level of direct impact. For each asset a scale of recovery (from 1 = Full financial recovery – recovery with no/few adverse impacts to 5 = Very low financial recovery is possible – major and permanent changes to associated activities) is attributed based on international analyses of the commonly adopted approaches (Priest, 2014). The Regionalized Business Financial Recovery Indicator (I_{Bfr}) is then calculated following **Table 7**. A similar approach is applied for Household.

Transport Network Disruption

Transport disruption is an important issue along the regional coastline. If we consider the regional scale, the motorway that connects the eastern regions of Italy (i.e., the regions that face the Adriatic Sea) to the northern regions runs along the coastline and in its southern part is located close to the coast (**Figure 4**). For this reason, if flooding occurs in the southern part of the regional coastline, and if the motorway and railway lines are affected, the disruption can potentially become massive for the national transport system. On the other hand, in the two selected hotspots the transport networks are represented by local roads and by a limited portion of the regional railway line in HS2. The impact assessment is carried out considering a boundary that includes the whole regional area and that extends landward up to Bologna (**Figure 4**), in order to take into account the most important routes and junctions.

Accessibility is considered in the model as the principal "product" of the transportation system (Demirel et al., 2015) and its loss a good indicator of the disruption for regional analysis. Accessibility can be reduced by the loss of access to certain sites and by longer journey to reach certain sites. Two indicators, a connectivity ratio (Weighted Disconnection between nodes, WD2/WD1) and a time ratio (Time Lengthening between nodes, TL1/TL2), are therefore estimated by network analysis and combined to calculate a Weighted Disconnection and Time Lengthening Indicator transport (WDTL) by comparing the situation before (1) and after the event (2) (Sohn, 2005; Demirel et al., 2015; Mattsson and Jenelius, 2015, **Table 7**). The connectivity ratio estimates the loss of connectivity to places weighted by importance based on stakeholders' inputs. The importance of a place permits to incorporate in the assessment the relative loss of the option to go from one place to another, such as the access to locations that provide essential services or important economy activities compared to uninhabited locations. WD1 represents the number of nodes accessible from each node before the disruption, WD2 the number of accessible nodes after the disruption. TL2 and TL1 represents the sum of network's shortest possible travel times after (2) and before (1) the disruption (**Table 7**). The WDTL and related ratios are calculated following **Table 7**. WDTL is then integrated over time to better consider flood duration and repair time to return to normal condition.

For the present analysis, we have taken into account: local roads in the two selected hotspots, two important regional roads, part of the motorway (where it is located close to the coast, i.e., southern part of the regional coastline), the main provincial roads that connect the coastal villages to the main regional and national roads and the national and regional railway lines. A Data Quality Score of 2 is given to the input information for the transport network disruption.

Business Disruption

The business sector along the RER coastline is represented by the sun-and-beach tourism and, specifically, by the concessions that offer a large number of services to their clients. There are many hotels along the whole regional coastline and most of them offer special prices in nearby concessions.

Business disruption is firstly represented by the damage, and time for repair, to concessions and hotels that can negatively affect the whole hotspot area. A business supply chain approach derived from graph theory approaches is then used to model the principal business facilities in form of nodes and the business interactions or exchanges in form of arcs (Wagner and Neshat, 2010; Kim et al., 2015). The daily disruption (I_{BD}, **Table 7**) is estimated as a reduction in the supply capacity of each of its nodes due to the flooding of premises weighted by their relative economic importance (**Table 7**). In INDRA

[11] http://www.confesercentiferrara.it/mareggiate-un-aiuto-da-confesercenti/

[12] http://www.comune.ra.it/Notizie-di-copertina/Maltempo-il-diario-delle-comunicazioni-di-servizio.-L-impegno-di-Comune-Istituzioni-e-mondo-imprenditoriale-per-far-fronte-all-emergenza

TABLE 7 | Descriptions and formulas of the main indicators and parameters calculated by the INDRA model for business financial and household recovery, risk to life and transport and business disruption.

Indicator/Parameter	Formula	Description
Regionalized Business Financial Recovery Indicator (I_{Bfr})	$I_{Bfr} = \frac{\sum_{i=0}^{n} Bfr_i}{\sum_{i=0}^{n} 5}$	n: all business properties in the region; Bfr_i: Business Financial Recovery Score for each i business property (scores' values in **Table 6**).
Regionalized Household Financial Recovery Indicator (I_{Hfr})	$I_{Hfr} = \frac{\sum_{i=0}^{n} Hfr_i}{\sum_{i=0}^{n} 5}$	n: all household properties in the region; Hfr_i: Household Financial Recovery Score for each i household property(scores' values in **Table 6**).
Regionalized Risk to Life Indicator (I_{Rtl})	$I_{RtL} = \frac{\sum_{i=0}^{n} (S_i \cdot RtL_i)}{\sum_{i=0}^{n} (S_i \cdot 4)}$	n: number of land use receptors; Si: Surface area; RtL_i: Risk to Life Score of area i (max value = 4)
Weighted Disconnection and Time Lengthening Indicator for transport (WDLT)	$WDTL = \frac{WD2}{WD1} \cdot \frac{TL1}{TL2}$	WD2/WD1: connectivity ratio; TL1/TL2: time ratio.
Connectivity to places before the disruption weighted by importance (WD1)	$WD1 = \sum_{i_{d1}=1}^{N} \left(\sum_{j_{d1}=1}^{n_{i_{d1}}} W_{j_{d1}} \right)$	n_{id1}: the number of nodes which are accessible from the node i_{d1}, before the disruptive event; W_{jd1}: the weight of the node j_{d1} which belongs to the set of the nodes that are accessible from the node i_{d1}, before the disruptive event.
Connectivity to places after the disruption weighted by importance (WD2)	$WD2 = \sum_{i_{d2}=1}^{N} \left(\sum_{j_{d2}=1}^{n_{i_{d2}}} W_{j_{d2}} \right)$	n_{id2}: the number of nodes which are accessible from the node i_{d2}, after the disruptive event; W_{jd2}: the weight of the node j_{d2} which belongs to the set of the nodes that are accessible from the node i_{d2}, after the disruptive event.
Sum of network's shortest possible travel time before the disruption (TL1)	$TL1 = \sum_{i_{l1}=1}^{N} \left(\sum_{j_{l1}=1}^{n_{i_{l1}}} T_{i_{l1}j_{l1}} \right)$	T_{il1jl1}: the travel time for the fastest route from the node i_{l1} to the node j_{l1} before the occurrence of the disruptive event, if this route remains accessible; n_{il1}: the number of nodes that remain accessible from the node i_{l1} after the occurrence of the disruptive event.
Sum of network's shortest possible travel time after the disruption (TL2)	$TL2 = \sum_{i_{l2}=1}^{N} \left(\sum_{j_{l2}=1}^{n_{i_{l2}}} T_{i_{l2}j_{l2}} \right)$	T_{il2jl2}: the travel time for the fastest route from the node i_{l2} to the node j_{l2}, only if it remains possible to go from the node i_{l2} to the node j_{l2} after the occurrence of the disruptive event; n_{il2}: the number of nodes that remain accessible from the node i_{l2}, after the occurrence of the disruptive event.
Business Daily disruption (I_{BD})	$I_{BD} = 1 - \frac{1}{\sum We} \sum_{i=1}^{d} \left(We_i \cdot \frac{Cimp_i}{Cnorm_i} \right)$	d: number of supply nodes; $Cimp_i$: supply capacity of the node i, in impacted supply chain; $Cnorm_i$: supply capacity of the node i, in normal supply chain; We_i: relative economic importance weighting factor for node i.

each asset can be associated with a node of the modeled supply chain and attributed a supply capacity. As such, the supply capacity of the non-flooded assets can be aggregated for each node (Cimp) and compared to its supply capacity in normal condition (Cnorm) to derive the I_{BD} at each simulation step.

Sun-umbrellas are included in the supply chain because they represent an important tourist and economic activity, as described in the field site description. The supply chain goes from "umbrellas" to hotels and concessions and from concessions to "umbrellas." If the beach (available space for setting up umbrellas) or concessions are impacted, umbrellas and associated services will not be available for the tourists. The hotels are also negatively affected as people are not prone to go to local towns where services provided by concessionaires are not available on the beach. Because the inputs are based on many assumptions a Data Quality Score of 5 is given to the information for the business disruption.

Multi Criteria Analysis (MCA)

The INDRA model includes an MCA analysis to evaluate which of the selected hotspots is the most critical. In the present study it is decided to weight (in percentages) the different elements exposed to storms (i.e., Risk to Life, Household financial, Household displacement, Business financial, Business disruption, Transport, Ecosystems, Agricultural areas) through the consultation of end-users. The values are chosen on the basis of a discussion carried out with three stakeholders (a regional land use planner, a stakeholder working with the regional civil protection and a coastal manager). They were asked to score the elements listed above according to their own perception/opinion of the importance of each component. The listed values in **Table 8** are obtained by first computing the mean values of the three values provided by the stakeholders, one for each component, and then through an agreement on the rounded values. The final values are then used in the weighted summation of the indicators to obtain a final score for each considered extreme

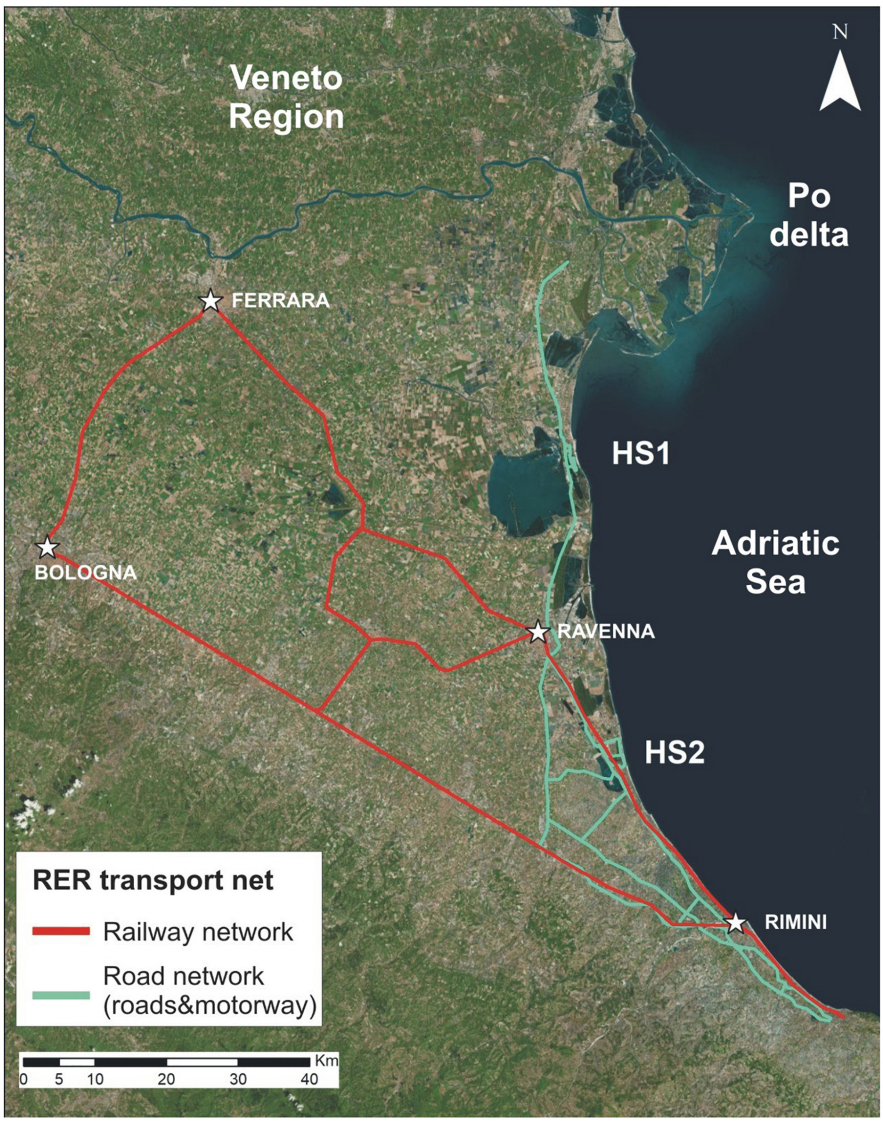

FIGURE 4 | Schematic of the transport network at the regional level.

event (equation 1):

$$MCA\ score = \sum_{i=1}^{8} \frac{W_i}{100} \cdot I_i \qquad (1)$$

where W_i = Weighted value obtained for each indicator (**Table 8**), I_i = Indicator Value (obtained using **Table 7** formulas, specifically I_{Bfr}, I_{Hfr}, I_{Rtl}, WDTL, I_{BD}; for displacement, agriculture and ecosystem indicators a 0 value is considered)

The consultation with regional and local stakeholders provides the figure about the level of awareness on coastal issues related to the impact of storms and how the issues are perceived and managed (Martinez et al., 2018). The involvement of the end-users is a fundamental step in the CRAF application, because it drives the selection of hotspots to be compared in phase 2 and the final ranking of the selected sites according to the MCA analysis of INDRA.

RESULTS

The direct impact on assets of any type is large for both events in HS2 (**Figures 5**, **6**) with flood depths up to 1.6 m. HS1, on the contrary, is not impacted by the T10 event while T100 generates some impacts, but still very limited. On **Figures 5**, **6** the identified assets of any type and the flooding extension, flood depth and flood depth-velocity values are presented. It is important to note that none of the assets experiences a very high impact (i.e., building collapse, **Figure 6**).

HS1 presents very few residential buildings and business activities that are impacted under both scenarios. In HS2 most

TABLE 8 | List of indicators and associated weights.

Indicator	Value
Risk to Life	30
Household financial	10
Household displacement	10
Business financial	10
Business disruption	15
Transport	10
Ecosystems	10
Agricultural areas	5

of the exposed assets are affected by T100, with a significant percentage of assets in the medium and high impact levels (**Figure 7**). It should be underlined that schools are also impacted in HS2. Specifically, the four identified schools experience impact levels from 1 to 3, depending on their location. The colonies are impacted by the T100 event but the impact level is low.

The increased number of affected properties, associated with a significant change in the distribution of the severity of impacts from T10 to T100, leads to a reduced financial recovery of many households and businesses. A high proportion of households will be covered by compensation and will recover based on the government response. For businesses, the recovery is worsened by the absence of insurance or compensation. In HS2, the higher severity of impact may lead to a significant number of businesses expecting difficulties in recovering financially. As it was expected, the percentage of impacted business activities in the two hotspots increases between T10 and T100. Nevertheless, the percentage of affected businesses in HS1, with any impact level, for T100 is 25% of the identified activities while in HS2 the percentage rises to 92%. Furthermore, most of them experience medium and high severity impacts.

The final scores of the MCA in HS1 for the T100 event provide a value of business financial recovery equal to 0.003. This value indicates a high-level of recovery for the region as very few of the 3456 businesses identified at the regional level are impacted. Household financial recovery (2.5e-5) and risk to life (2.5e-4) values are also negligible to the low exposure level. The transport network is not impacted, while business disruption equals 0.006. The total MCA score is 0.001 considering the weighted values presented in **Table 8**. For HS2, on the contrary, risk to life is 0.007 and household financial recovery is 0.008 for the 66428 residential properties identified at the regional level. Business financial recovery is 0.022 reflecting a locally significant exposure, combined with a lack of insurance coverage. Transport disruption is not significant, while business disruption is 0.048. The total MCA score is 0.012, therefore one order of magnitude higher than HS1, but the regional impact remains low overall.

DISCUSSION

This study represents one of the first attempts at the national level to provide an evaluation that quantifies the direct and indirect impacts to different assets, along coastal areas, generated by marine storms only. A previous study by De Angeli et al. (2018) evaluated the impact of marine and river flooding in the Liguria region (Italy), on the basis of comparable assumptions presented here. In fact, the methodology was developed for the RER coastline in the RISC-KIT project and then applied similarly at the two Italian case study sites. The evaluation is very much influenced by the quality of the input data. In the present paper the analysis is carried out including all the available information and the most up to date databases that are accessible at the regional and national level. Nevertheless, a lot of information is not available, and many assumptions are applied in order to produce the risk assessment.

The hazard modeling includes several limitations determined by the numerical approach, the assumptions and data availability. Beyond the fact that numerical models present intrinsic limitations, several simplifications are applied in this study. First, the morphodynamic behavior of the beach is represented by 1D profiles that, although computationally faster, do not represent the 2D nature of the phenomena. Furthermore, the forcing probabilistic extreme events are defined with information extracted from the literature. This choice was made because the selected information are commonly used at the regional level to define design extreme events for different purposes (e.g., Armaroli et al., 2009; Perini et al., 2016). A comprehensive assessment should include the evaluation of the combined probability of occurrence of waves and surge levels to define the forcing components for different return periods. The direction of the storm is assumed to be perpendicular to the coast, thus leading to a possible overestimation of the flood extension. An additional limitation on the forcing input is represented by the use of symmetric triangular synthetic storms to describe the temporal evolution of the event. Although it is a commonly adopted approach in numerical coastal studies (e.g., McCall et al., 2010; Plomaritis et al., 2018; Sanuy et al., 2018), it represents another source of uncertainty. Finally, the numerical models are applied in default mode, except for the parameters previously described. It was demonstrated that the hazard modeling input (and, therefore, the output flood maps) can act as important factors affecting the overall uncertainty of flooding risk assessments (e.g., Vousdoukas et al., 2018a). On the other hand, other studies (e.g., Apel et al., 2009; De Moel and Aerts, 2011) conclude that it does not represent a dominant factor, when compared with the uncertainty due to the assumptions on the impact assessment component. In particular, De Moel and Aerts (2011) quantify that the variation of the final damage assessment induced by the uncertainty related to the damage model are comparable (or higher) to that of a uniform variation of $\sim$1.1 m in flood water depth. Being these uncertainty magnitudes for flood depth estimates rather improbable (see, as an example, the performance of the hazard models in Apel et al., 2009), the design- and default-based hazard modeling applied in this study can be assumed to represent a meaningful approach, especially considering the comparative nature of the CRAF 2 approach.

On the other hand, the direct impact assessment is affected by large uncertainties (Jongman et al., 2012) that propagate

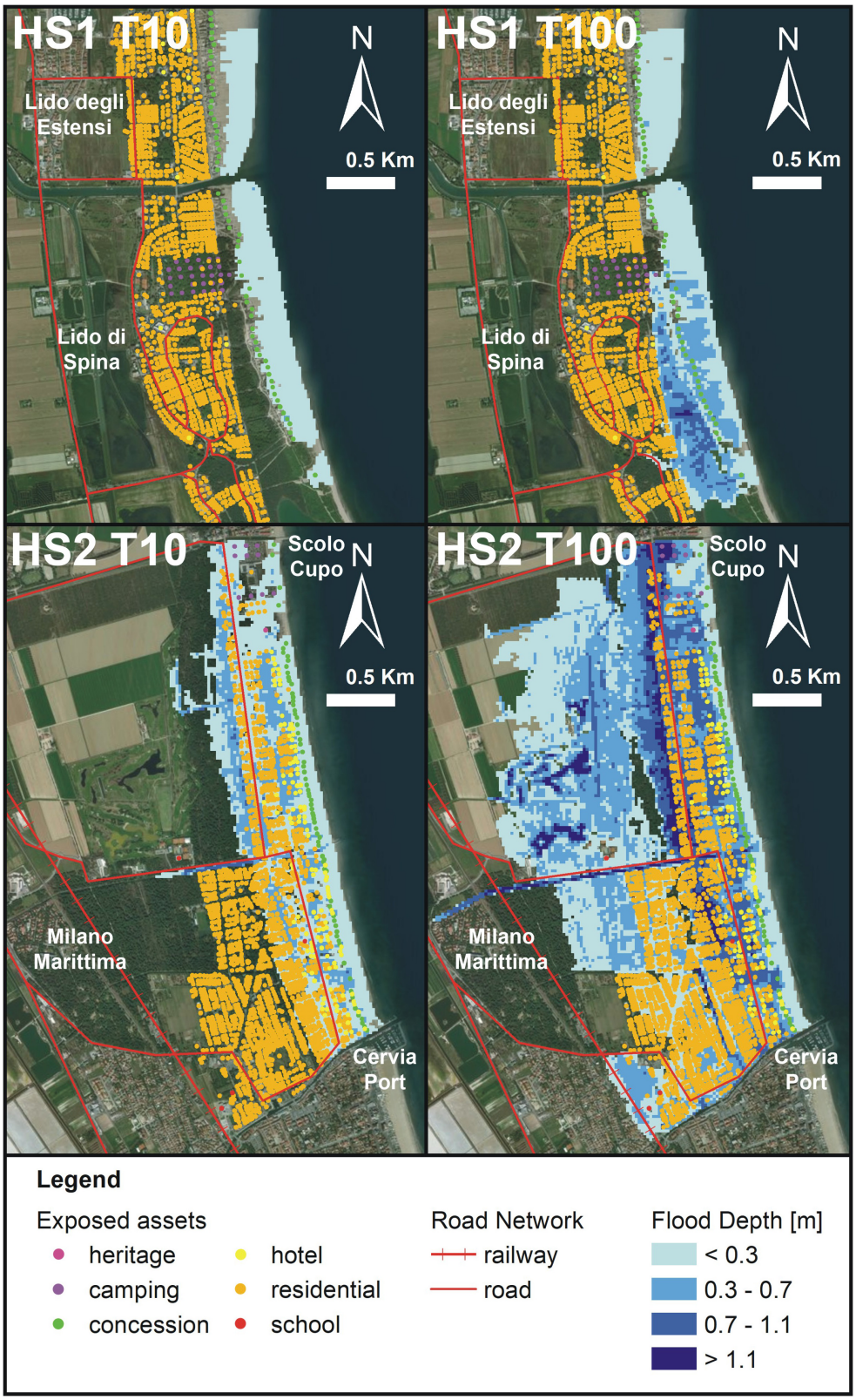

FIGURE 5 | Identified assets and transport network in the two selected hotspots (HS1, Lido degli Estensi-Lido di Spina; HS2, Milano Marittima) and flooding extension. Flood depth calculated through the hazard modeling chain presented in **Figure 2** for the two selected storms (T10 and T100) in the two hotspots: HS1, upper figures; HS2, lower figures. The selected classes for the visualization of flood depth values are chosen on the basis of the thresholds presented in **Table 4**.

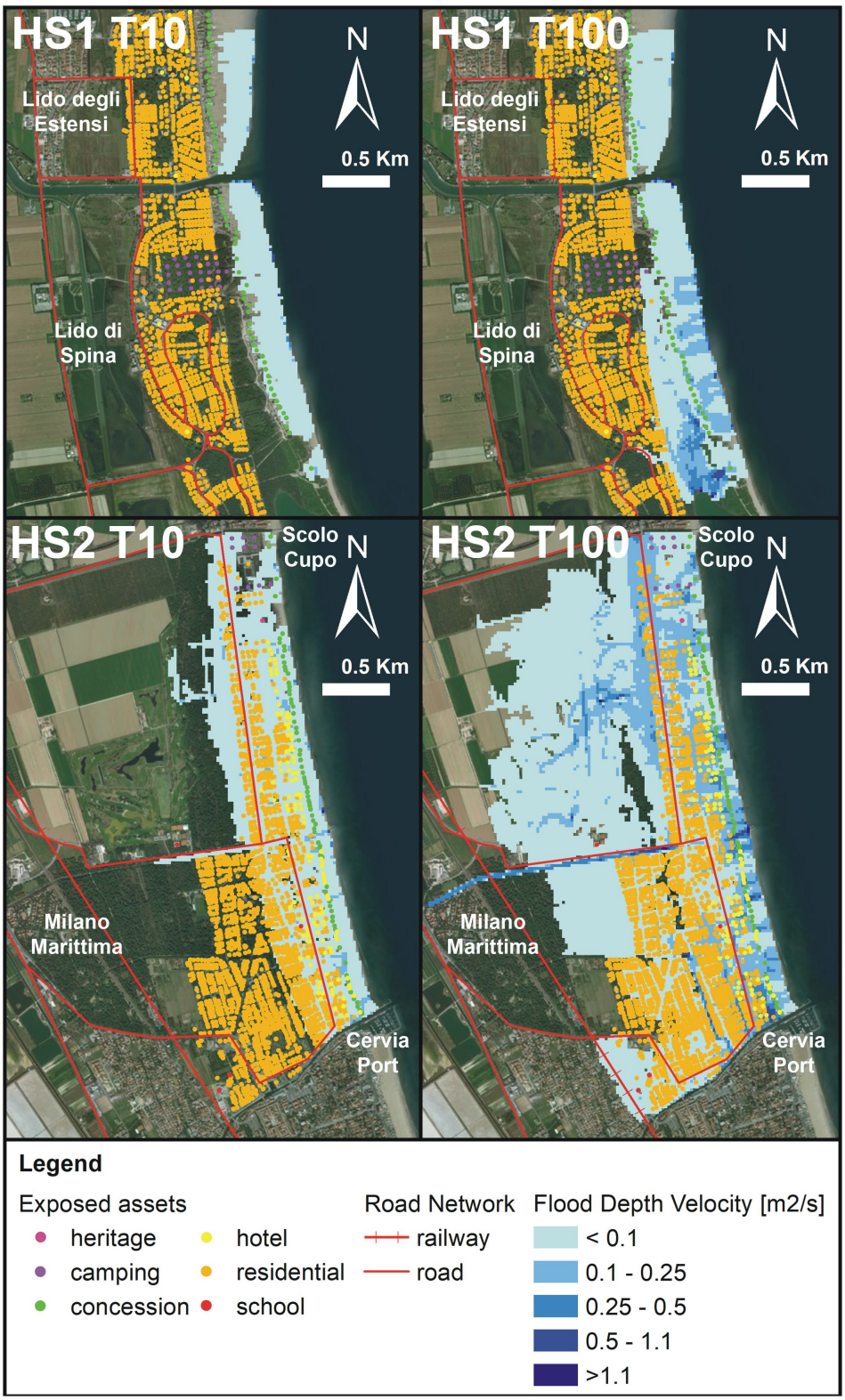

FIGURE 6 | Identified assets and transport network in the two selected hotspots (HS1, Lido degli Estensi-Lido di Spina; HS2, Milano Marittima) and flooding extension. Flood depth-velocity calculated through the hazard modeling chain presented in **Figure 2** for the two selected storms (T10 and T100) in the two hotspots: HS1, upper figures; HS2, lower figures. The selected classes for the visualization of flood depth-velocity values are chosen on the basis of the risk to life matrix and also presented in **Table 5**.

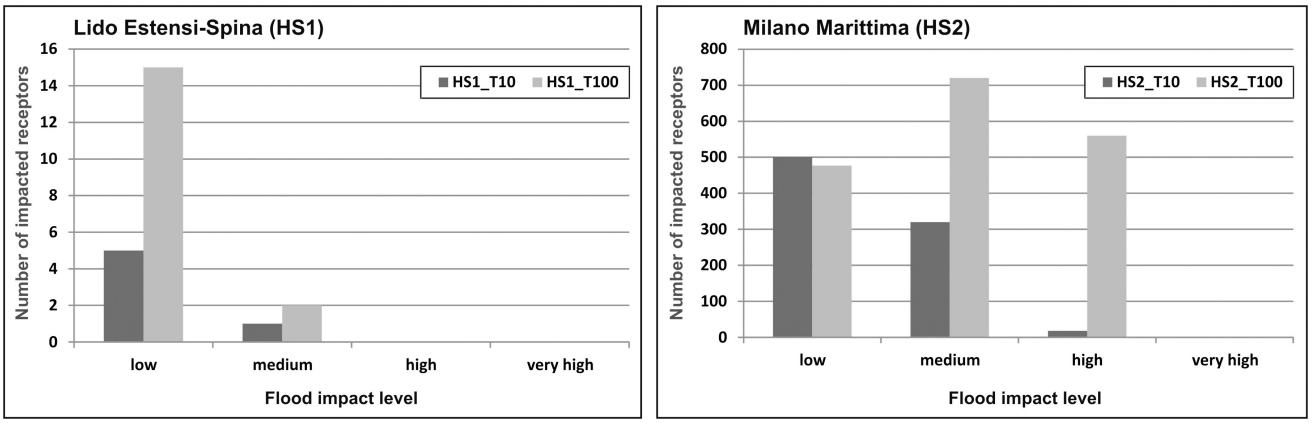

FIGURE 7 | Distribution of impact severity to the selected assets per scenarios (T10 and T100) in the two hotspots: Lido degli Estensi-lido di Spina, HS1 and Milano Marittima, HS2.

to the final damage estimations. It was demonstrated that the uncertainty related to this component represents a dominant factor affecting the overall uncertainty of damage assessments (De Moel and Aerts, 2011), especially when damage calculations are applied in deterministic ways (Figueiredo et al., 2018). Additionally, damage models are generally site-dependent. Therefore, transferability to locations where such data is not available remains an important issue, although the utilization of curves developed in different countries is a common practice (Scorzini and Frank, 2017). The definition of the land use or building category is also fundamental, however, such specific data is difficult to obtain. The type of flood hazard and related damage models are also important, as marine floods are different from fluvial ones in terms of consequences to buildings (e.g., salinity, short-period waves). These aspects contribute to lower the predictive skills of damage models (Figueiredo et al., 2018). The damage curve used in this study (adapted from Scorzini and Frank, 2017) was developed for residential buildings, for a fluvial flood occurred in Veneto in 2010. The Emilia-Romagna region borders the Veneto region to the north and has comparable architectural, as well as economic, characteristics. Therefore, spatial transferability of the damage curve does not represent an issue. On the other hand, the uncertainty on direct impact evaluation is mostly represented by the use of average depth-damage curves developed for fluvial inundations and the lack of building typology (e.g., single- or multi- storey; with/without basement). It is worth mentioning that the selection of the curve was made in agreement with the regional coastal managers and that all the limitations were discussed with them, in the framework of the RISC-KIT project. The proper selection of direct damage models is a persisting problem in the literature. Whereas an uplift factor could be considered in further studies to better reflect additional damages associated with saline and wave conditions, specific building-type depth-damages curves and appropriate cadastral maps remain to be developed and applied to marine conditions. Furthermore, no differentiation was possible on the type of residential building because of the lack of available data. Additionally, the curve is also applied to commercial activities, since a specific model was not available. As deterministic approaches based on flood damage curves showed limitations and low predictive skills, recent approaches are moving toward probabilistic (e.g., Dottori et al., 2016) or model-ensemble approaches (Figueiredo et al., 2018). The damage is, therefore, calculated using different damage models in order to produce a distribution of possible damages and, at the same time, to quantify the uncertainty of the outcomes. Figueiredo et al. (2018) provide a methodology to score a dataset of damage models that can also be applied for deterministic approaches, to select the most suitable one. The score assignment is based on the expert judgment of the main properties of the models, such as the type of physical variables included, the degree of characterization of the assets, the similarity of the context where the model has to be applied with the study site where the model was built, the correspondence between the analyzed flood and the type of flood used to build the model and the type of variable used to quantify the output damage (i.e., damage factor or monetary damage). Following the example of damage model properties proposed in Figueiredo et al. (2018) in their Figure 3, the curve applied in the present study scores 0.59e-2, or 0.44e-2, depending on the fact that the regional contexts (i.e., Veneto and Emilia-Romagna) are considered comparable or not. The scores are medium-low values if compared to the scoring (from 0.15e-2 to 3.34e-2) of models assessed in Figueiredo et al. (2018).

A site-specific damage model would undoubtedly represent the best option. Therefore, regional coastal managers should prioritize the collection and analysis of the necessary information to produce reliable damage models. At present, there is not an official regional (or national) standard for data collection in the aftermath of an extreme coastal event, in order to measure flood levels and identify, collect and rigorously catalog the losses in monetary terms or structural/content damage. Standard data-collection protocols should be based on scientific studies already available at local level (e.g., Duo et al., 2018), in order to collect the necessary information that is of foremost importance to develop damage models.

The assets' location is very well defined, but other characteristics are assumed to be uniform or are associated with default values defined at European level or for other EU countries (Jongman et al., 2012). The elevation above the ground of both buildings and roads is set to 0 m. Clearly this is not the real situation for all the identified assets. However, the definition of the correct elevations would require very detailed data collection on the ground. The presence of underground garages or basements should be identified for each asset and included in the input data. The time required to collect such data is large and raises a question about the feasibility of such in-depth inspection of critical areas. It could be performed for areas with a limited extent and/or number of assets, but for hotspots with many buildings and a large flooding extension it is less realistic. An alternative of an in-depth inspection of critical areas is the development in collaboration with architects, civil engineers, land use planner of a national or regional dataset of properties' typology which better reflects fundamental structural differences and construction. This could be then integrated in the current land use information to better support risk assessment.

The consultation of stakeholders with different roles is fundamental to properly define the variables to be included in the model, taking into account the information that correctly describe the characteristics of the study area. In fact, the insurance figure included in the model is based on both a comprehensive desktop research and interview of an informed person (President of the Consortium of economic activities, i.e., concessions and hotels) who provided useful information to define the level of insurance according to the level of impact. The same applies to the household displacement. The decision to exclude displacement from the evaluation derives from the consultation of regional managers and thanks to the historical storm database (Perini et al., 2011). The lack of well documented impacts of past events, as such, limits the possibility to use post-events survey to estimate future risk and the coastal community resilience. This is aggravated by the rapid changes in urbanization, livelihood and in the environment. Working with the coastal communities to develop plausible "what-if" scenarios and to collect relevant socio-economic data could complement this lack of information as well as building community resilience.

The supply chain presented in the paper is surely one of the most important economic activities at the regional level. However, it does not fully represent the complexity of the local economy and the connection with other businesses such as restaurants, local commerce and producers, highly dependent for their annual incomes on the seasonal touristic activity level. The identification of the most significant business sectors and the linkage between the different parts of the identified sectors requires much effort for data collection and construction of the correct supply chain and paths of "goods" exchange (represented here by hotels, concessions and umbrellas customers). The involvement of informed stakeholders is also needed to properly design the supply chain. A better understanding of the coping strategies is also required to better assess differences in businesses recovery time. The quantification of direct and indirect impacts to the economic sector is important for a comprehensive risk assessment but still in its infancy, as demonstrated in the present paper.

CONCLUSION

This paper includes the analysis of direct and indirect impacts generated by flooding in two coastal villages located in the Emilia-Romagna coastline (Italy): Lido degli Estensi-Spina (HS1) and Milano Marittima (HS2) (**Figure 1**). The evaluation was carried out taking into account two extreme events with return periods of 10 and 100 years through a modeling chain that included a morphological numerical model (XBeach) and an inundation model (Lisflood-FP). The flooding hazard assessment was then used to quantify direct and indirect impacts for different assets. The INDRA (Integrated Disruption Assessment) model (Viavattene et al., 2018), developed in the RISC-KIT project (Van Dongeren et al., 2018), was used to quantify the impacts, to define the level of recovery of the analyzed assets after the events and the probable disruption of the transport network and of the business supply chain. The data input for the impact assessment was performed utilizing the best available information and through consultations with different stakeholders. An evaluation of the data quality was carried out to underline the strengths and limitations of the applied methodology.

The results showed that HS2 is the most critical site, with many assets highly impacted in both scenarios (**Figures 5**, **6**). The results are consistent with the historical information on past events that affected the regional coastline (Perini et al., 2011). Furthermore, the site is one of the most vulnerable of the RER coast. Nevertheless, the present work quantifies the damage and identifies a certain level of disruption, with some sectors (i.e., business activities) being more severely affected, in the case of an extreme event occurrence, because of a lack of flood-related insurance coverage. These results are in accordance with the observed consequences of storms. The most affected assets are the concessions that represent a pivotal element of the business supply chain.

The evaluation of the quality of the data identified the business supply chain as largely based on general assumptions (DQS = 5), while the direct impacts, household displacement and insurance matrix have a higher quality, but still poor (DQS = 3). The input information with the best quality is the transport network disruption (DQS = 2). As discussed, the evaluation of the impacts is largely affected by the quality of the input information. The outcomes should be evaluated taking into account the uncertainty/limitations of the adopted approach in terms of hazard modeling and damage functions selection that are presented and largely examined.

The study represents a first and important step toward the quantification of risk, properly and fully characterized. However, it underlines that comprehensive data collection should be carried out to better characterize the risk at the regional level and that a wider involvement of stakeholders should also be foreseen.

DATA AVAILABILITY

The datasets generated for this study are available on request to the corresponding author.

AUTHOR CONTRIBUTIONS

CA wrote the manuscript with the contribution of ED and CV. CA collected the information on assets to perform the direct and indirect impact assessment, including the insurance figure, displacement information, reinstatement and recovery times, the interview to stakeholders, and mapping of the assets in GIS. CV supervised the data collection and defined the final quality scores in agreement with CA and ED. CA ran the INDRA model. ED designed the forcing input data and ran the hazard models, providing the flood maps. CV is one of the main designers of the INDRA model (provided by the Middlesex University of London in the RISC-KIT project). CV analyzed the results of the INDRA model together with CA. CA, ED, and CV equally contributed to the literature review, and "Introduction," "Discussion," and "Conclusion" sections.

FUNDING

The research leading to these results has received funding from EU H2020 Program under grant agreement no. 700099 (Anywhere: Enhancing emergency management and response to extreme weather and climate events).

ACKNOWLEDGMENTS

The authors are very grateful to Prof. Sally J. Priest and Prof. Paolo Ciavola for providing valuable comments and suggestions on the manuscript and for the grammar and language corrections. The authors would like to thank Dott.ssa Luisa Perini, Dr. Lorenzo Calabrese, and Dott. Paolo Luciani of SGSS for providing LU/LC maps, cadastral maps, and Lidar data. The authors would like to thank ENI for providing Lidar and Multibeam data. The authors would also like to thank all the interviewed stakeholders for their availability and for the valuable information provided, without which it would not have been possible to carry out the analysis. The authors are very grateful to the four reviewers for their valuable comments and suggestions that helped to significantly improve the manuscript.

REFERENCES

Antonellini, M., Giambastiani, B. M. S., Greggio, N., Bonzi, L., Calabrese, L., Luciani, P., et al. (2019). Processes governing natural land subsidence in the shallow coastal aquifer of the Ravenna coast. Italy. *CATENA* 172, 76–86. doi: 10.1016/j.catena.2018.08.019

Apel, H., Aronica, G. T., Kreibich, H., and Thieken, A. H. (2009). Flood risk analyses—how detailed do we need to be? *Nat. Hazards* 49, 79–98. doi: 10.1007/s11069-008-9277-8

Armaroli, C., Ciavola, P., Masina, M., and Perini, L. (2009). Run-up computation behind emerged breakwaters for marine storm risk assessment. *J. Coast. Res.* 56, 1612–1616.

Armaroli, C., and Duo, E. (2018). Validation of the coastal storm risk assessment framework along the emilia-romagna coast. *Coast. Eng.* 134, 159–167. doi: 10.1016/j.coastaleng.2017.08.014

Aucelli, P. P. C., Di Paola, G., Incontri, P., Rizzo, A., Vilardo, G., Benassai, G., et al. (2017). Coastal inundation risk assessment due to subsidence and sea level rise in a Mediterranean alluvial plain (Volturno coastal plain – southern Italy). *Estuar. Coast. Shelf S.* 198, 597–609. doi: 10.1016/j.ecss.2016.06.017

Bates, P., and De Roo, A. P. (2000). A simple raster-based model for flood inundation simulation. *J. Hydrol.* 236, 54–77. doi: 10.1016/S0022-1694(00)00278-X

Bates, P. D., Dawson, R. J., Hall, J. W., Horritt, M. S., Nicholls, R. J., Wicks, J., et al. (2005). Simplified two-dimensional numerical modelling of coastal flooding and example applications. *Coast. Eng.* 52, 793–810. doi: 10.1016/j.coastaleng.2005.06.001

Belton, S., and Stewart, T. S. (2002). *Multiple Criteria Decision Analysis. An Integrated Approach*. Massachusetts: Kluwer Academic Publishers.

Ciavola, P., Ferreira, O., Haerens, P., Van Koningsveld, M., and Armaroli, C. (2011). Storm impacts along European coastlines. Part 2: lessons learned from the MICORE project. *Environ. Sci. Policy* 14, 924–933. doi: 10.1016/j.envsci.2011.05.009

Christie, E. K., Spencer, T., Owen, D., McIvor, A. L., Möller, I., and Viavattene, C. (2018). Regional coastal flood risk assessment for a tidally dominant, natural coastal setting: North Norfolk, southern North Sea. *Coast. Eng.* 134, 177–190. doi: 10.1016/j.coastaleng.2017.05.003

Ciavola, P., Armaroli, C., Chiggiato, J., Valentini, A., Deserti, M., Perini, L., et al. (2007). Impact of storms along the coastline of Emilia-Romagna: the morphological signature on the Ravenna coastline (Italy). *J. Coast. Res.* SI 50, 540–544.

De Angeli, S., D'Andrea, M., Cazzola, G., Dolia, D., Duo, E., and Rebora, N. (2018). Coastal risk assessment framework: comparison of modelled fluvial and marine inundation impacts. bocca di magra, ligurian coast, Italy. *Coast. Eng.* 134, 229–240. doi: 10.1016/j.coastaleng.2017.09.011

De Moel, H., and Aerts, J. C. J. H. (2011). Effect of uncertainty in land use, damage models and inundation depth on flood damage estimates. *Nat. Hazards* 58, 407–425. doi: 10.1007/s11069-010-9675-6

Demirel, H., Kompil, M., and Nemry, F. (2015). A framework to analyze the vulnerability of European road networks due to Sea-Level Rise (SLR) and sea storm surges. *Transport. Res. A Policy Pract.* 81, 62–76. doi: 10.1016/j.tra.2015.05.002

Dottori, F., Figueiredo, R., Martina, M. L. V., Molinari, D., and Scorzini, A. R. (2016). INSYDE: a synthetic, probabilistic flood damage model based on explicit cost analysis. *Nat. Hazards Earth Syst. Sci.* 16, 2577–2591. doi: 10.5194/nhess-16-2577-2016

Duo, E., Trembanis, A. C., Dohner, S., Grottoli, E., and Ciavola, P. (2018). Local-scale post-event assessments with GPS and UAV-based quick-response surveys: a pilot case from the Emilia–Romagna (Italy) coast. *Nat. Hazards Earth Syst. Sci.* 18, 2969–2989. doi: 10.5194/nhess-18-2969-2018

Erikson, L., Barnard, P., O'Neill, A., Wood, N., Jones, J., Finzi Hart, J., et al. (2018). Projected 21st century coastal flooding in the southern california bight. part 2: tools for assessing climate change-driven coastal hazards and socio-economic impacts. *J. Mar. Sci. Eng.* 6:76. doi: 10.3390/jmse6030076

Favaretto, C., Martinelli, L., and Ruol, P. (2019). Coastal flooding hazard due to overflow using a level II method: application to the venetian littoral. *Water* 11:134. doi: 10.3390/w11010134

Ferreira, O., Viavattene, C., Jiménez, J. A., Bolle, A., das Neves, L., Plomaritis, T. A., et al. (2018). Storm-induced risk assessment: evaluation of two tools at the regional and hotspot scale. *Coast. Eng.* 134, 241–253. doi: 10.1016/j.coastaleng.2017.10.005

Ferreira, Ó., Ciavola, P., Armaroli, C., Balouin, Y., Benavente, J., Del Río, L., et al. (2009). Coastal storm risk assessment in Europe: examples from 9 study sites. *J. Coast. Res.* 56, 1632–1636.

Figueiredo, R., Schröter, K., Weiss-Motz, A., Martina, M. L. V., and Kreibich, H. (2018). Multi-model ensembles for assessment of flood losses and associated uncertainty. *Nat. Hazards Earth Syst. Sci.* 18, 1297–1314. doi: 10.5194/nhess-18-1297-2018

Gouldby, B., Samuels, P., Klijn, F., van Os, A., Sayers, P., and Schanze, J. (2005). *Language of Risk - Project Definitions EU Floodsite Project*. Available at: http://www.floodsite.net/html/partner_area/project_docs/FLOODsite_Language_of_Risk_v4_0_P1.pdf (accessed February 8, 2019).

Hajkowicz, S., and Higgins, A. (2008). A comparison of multiple criteria analysis techniques for water resource management. *Eur. J. Oper. Res.* 184, 255–265. doi: 10.1016/j.ejor.2006.10.045

IPCC (2018). "Summary for policymakers in global warming of 1.5°C. An IPCC Special Report on the impacts of global warming of 1.5°C above pre-industrial levels and related global greenhouse gas emission pathways," in *The Context of Strengthening the Global Response to the Threat of Climate Change, Sustainable Development, and Efforts to Eradicate Poverty*, eds P. Masson-Delmotte, et al. (Geneva: World Meteorological Organization), 32.

Janssen, R. (2001). On the use of multi-criteria analysis in environmental impact assessment in the Netherlands. *J. Multi-Criteria Decis. Anal.* 10, 101–109. doi: 10.1002/mcda.293.abs

Jongman, B., Kreibich, H., Apel, H., Barredo, J. I., Bates, P. D., Feyen, L., et al. (2012). Comparative flood damage model assessment: towards a European approach. *Nat. Hazards Earth Syst. Sci.* 12, 3733–3752. doi: 10.5194/nhess-12-3733-2012

Jonkman, S. N., Vrijling, J. K., and Vrouwenvelder, A. C. W. M. (2008). Methods for the estimation of loss of life due to floods: a literature review and a proposal for a new method. *Nat. Hazards* 46, 353–389. doi: 10.1007/s11069-008-9227-5

Karvonen, T., Hepojoki, A., Huhta, H.-K., and Louhio, A. (2000). *The Use of Physical Models in Dam-Break Analysis RESCDAM Final Report*. Helsinki: Helsinki University.

Kim, Y., Chen, Y.-S., and Linderman, K. (2015). Supply chain network disruption and resilience: a network structural perspective. *J. Oper. Manag.* 33-34, 43–59. doi: 10.1016/j.jom.2014.10.006

Luijendijk, A., Hagenaars, G., Ranasinghe, R., Baart, F., Donchyts, G., and Aarninkhof, S. (2018). The state of the world's beaches. *Sci. Rep.* 8:6641. doi: 10.1038/s41598-018-24630-6

Martinez, G., Armaroli, C., Costas, S., Harley, M. D., and Paolisso, M. (2018). Experiences and results from interdisciplinary collaboration: utilizing qualitative information to formulate disaster risk reduction measures for coastal regions. *Coast. Eng.* 134, 62–72. doi: 10.1016/j.coastaleng.2017.09.010

Masina, M., and Ciavola, P. (2011). Analisi dei livelli marini estremi e delle acque alte lungo il litorale ravennate. *Studi Costieri* 18, 87–101.

Mattsson, L.-G., and Jenelius, E. (2015). Vulnerability and resilience of transport systems – a discussion of recent research. *Transp. Res.* 81, 16–34. doi: 10.1016/j.tra.2015.06.002

McCall, R. T., Van Thiel de Vries, J. S. M., Plant, N. G., Van Dongeren, A. R., Roelvink, J. A., Thompson, D. M., et al. (2010). Two-dimensional time dependent hurricane overwash and erosion modeling at Santa Rosa Island. *Coast. Eng.* 57, 668–683. doi: 10.1016/j.coastaleng.2010.02.006

Mentaschi, L., Vousdoukas, M. I., Pekel, J.-F., Voukouvalas, E., and Feyen, L. (2018). Global long-term observations of coastal erosion and accretion. *Sci. Rep.* 8:12876. doi: 10.1038/s41598-018-30904-w

Meyer, V., Becker, N., Markantonis, V., Schwarze, R., van den Bergh, J. C. J. M., Bouwer, L. M., et al. (2013). Review article: assessing the costs of natural hazards – state of the art and knowledge gaps. *Nat. Hazards Earth Syst. Sci.* 13, 1351–1373. doi: 10.5194/nhess-13-1351-2013

Penning-Rowsell, E. C., Priest, S., Parker, D., Morris, J., Tunstall, S., Viavattene, C., et al. (2013). *Flood and Coastal Erosion Risk Management A Manual for Economic Appraisal*. London: Routledge.

Perini, L., Calabrese, L., Deserti, M., Valentini, A., Ciavola, P., and Armaroli, C. (2011). *Le mareggiate e gli impatti sulla costa in Emilia-Romagna 1946–2010*. Bologna: ARPA Emilia-Romagna.

Perini, L., Calabrese, L., Lorito, S., and Luciani, P. (2015a). "Coastal flood risk in Emilia-Romagna (Italy): the sea storm of February 2015," in *Proceedings of the Coastal and Maritime Mediterranean Conference*, 3rd Edn, eds D. Levacher, M. Sanchez, P. Ciavola, and E. Raymond (Ferrara).

Perini, L., Calabrese, L., Lorito, S., and Luciani, P. (2015b). *Il rischio da mareggiata in Emilia-Romagna: l'evento del 5-6 Febbraio 2015. il Geologo. 53, 8–17.* Available at: http://www.geologiemiliaromagna.it/il-geologo-anno-xv-2015-n-53/ (accessed January 30, 2019).

Perini, L., Calabrese, L., Luciani, P., Olivieri, M., Galassi, G., and Spada, G. (2017). Sea-level rise along the Emilia-Romagna coast (Northern Italy) in 2100: scenarios and impacts. *Nat. Hazards Earth Syst. Sci.* 17, 2271–2287. doi: 10.5194/nhess-17-2271-2017

Perini, L., Calabrese, L., Salerno, G., Ciavola, P., and Armaroli, C. (2016). Evaluation of coastal vulnerability to flooding: comparison of two different methodologies adopted by the Emilia-Romagna region (Italy). *Nat. Hazards Earth Syst. Sci.* 16, 181–194. doi: 10.5194/nhess-16-181-2016

Plomaritis, T. A., Costas, S., and Ferreira, Ó (2018). Use of a Bayesian network for coastal hazards, impact and disaster risk reduction assessment at a coastal barrier (Ria Formosa, Portugal). *Coast. Eng.* 134, 134–147. doi: 10.1016/j.coastaleng.2017.07.003

Poljanšek, K., Marin Ferrer, M., De Groeve, T., and Clark, I. (eds) (2017). *Science for Disaster Risk Management 2017: Knowing Better and Losing Less*. Luxembourg: Publications Office of the European Union.

Priest, S., Wilson, T., Tapsell, S., Penning-Rowsell, E., Viavattene, C., and Fernandez-Bilbao, A. (2007). *Building a Model to Estimate Risk to Life for European Flood Events – Final Report. FLOODsite project report T10-07-10*. Wallingford: HR Wallingford.

Priest, S. J. (2014). Review of International Flood Insurance and Recovery Mechanisms: Implications for New Zealand and the Resilience of Older People. Research Report for the Community Resilience and Good Ageing: Doing Better in Bad Times Project. Available at: http://resilience.goodhomes.co.nz/publications/ (accessed August 1, 2019).

Roelvink, D., Reniers, A., van Dongeren, A., van Thiel de Vries, J., McCall, R., and Lescinski, J. (2009). Modelling storm impacts on beaches, dunes and barrier islands. *Coast. Eng.* 56, 1133–1152. doi: 10.1016/j.coastaleng.2009.08.006

Ruol, P., Martinelli, L., and Favaretto, C. (2018). Vulnerability analysis of the venetian littoral and adopted mitigation strategy. *Water* 10:984. doi: 10.3390/w10080984

Sanuy, M., Duo, E., Jäger, W. S., Ciavola, P., and Jiménez, J. A. (2018). Linking source with consequences of coastal storm impacts for climate change and risk reduction scenarios for Mediterranean sandy beaches. *Nat. Hazards Earth Syst. Sci.* 18, 1825–1847. doi: 10.5194/nhess-18-1825-2018

Scorzini, A., and Frank, E. (2017). Flood damage curves: new insights from the 2010 flood in Veneto. Italy. *J. Flood Risk Manage.* 10, 381–392. doi: 10.1111/jfr3.121633

Sohn, J. (2005). Evaluating the significance of highway network links under the flood damage: an accessibility approach. *Transp. Res. A Policy Pract.* 40, 491–506. doi: 10.1016/j.tra.2005.08.006

Taramelli, A., Di Matteo, L., Ciavola, P., Guadagnano, F., and Tolomei, C. (2015). Temporal evolution of patterns and processes related to subsidence of the coastal area surrounding the Bevano River mouth (Northern Adriatic) – Italy. *Ocean Coast. Manage.* 108, 74–88. doi: 10.1016/j.ocecoaman.2014.06.021

Teatini, P., Ferronato, M., Gambolati, G., Bertoni, W., and Gonella, M. (2005). A century of land subsidence in Ravenna. *Italy. Environ. Geol.* 47, 831–846. doi: 10.1007/s00254-004-1215-9

Torresan, S., Critto, A., Rizzi, J., and Marcomini, A. (2012). Assessment of coastal vulnerability to climate change hazards at the regional scale: the case study of the North Adriatic Sea. *Nat. Hazards Earth Syst. Sci.* 12, 2347–2368. doi: 10.5194/nhess-12-2347-2012

UNISDR (2015). *Disaster Risk Reduction and Resilience in the 2030 Agenda for Sustainable Development*. Available at: https://www.unisdr.org/files/46052_disasterriskreductioninthe2030agend.pdf (accessed February 8, 2019).

Van Dongeren, A., Ciavola, P., Martinez, G., and Viavattene, C. (2018). Introduction to RISC-KIT: resilience increasing strategies for coasts. *Coast. Eng.* 134, 2–9. doi: 10.1016/j.coastaleng.2017.10.007

Viavattene, C., Jiménez, J. A., Ferreira, O., Priest, S., Owen, D., and McCall, R. (2018). Selecting coastal hotspots to storm impacts at the regional scale: a coastal risk assessment framework. *Coast. Eng.* 134, 33–47. doi: 10.1016/j.coastaleng.2017.09.002

Viavattene, C., Jiménez, J. A., Owen, D., Priest, S., Parker, D., Micou, P., et al. (2015). *Coastal Risk Assessment Framework Tool*. London: Middlesex University research.

Villatoro, M., Silva, R., Méndez, F. J., Zanuttigh, B., Pan, S., Trifonova, E., et al. (2014). An approach to assess flooding and erosion risk for open beaches in a changing climate. *Coast. Eng.* 87, 50–76. doi: 10.1016/j.coastaleng.2013.11.009

Vousdoukas, M. I., Bouziotas, D., Giardino, A., Bouwer, L. M., Mentaschi, L., Voukouvalas, E., et al. (2018a). Understanding epistemic uncertainty in large-scale coastal flood risk assessment for present and future climates. *Nat. Hazards Earth Syst. Sci.* 18, 2127–2142. doi: 10.5194/nhess-18-2127-2018

Vousdoukas, M. I., Mentaschi, L., Voukouvalas, E., Bianchi, A., Dottori, F., and Feyen, L. (2018b). Climatic and socioeconomic controls of future coastal flood risk in Europe. *Nat. Clim. Change* 8, 776–780. doi: 10.1038/s41558-018-0260-4

Wagner, S. M., and Neshat, N. (2010). Assessing the vulnerability of supply chains using graph theory. *Int. J. Prod. Econ.* 126, 121–129. doi: 10.1016/j.ijpe.2009.10.007

Zanuttigh, B. (2011). Coastal flood protection: what perspective in a changing climate? The THESEUS approach. *Environ. Sci. Policy* 14, 845–863. doi: 10.1016/j.envsci.2011.03.015

Zanuttigh, B., Simcic, D., Bagli, S., Bozzeda, F., Pietrantoni, L., Zagonari, F., et al. (2014). THESEUS decision support system for coastal risk management. *Coast. Eng.* 87, 218–239. doi: 10.1016/j.coastaleng.2013.11.013

Zscheischler, J., Westra, S., van den Hurk, B. J. J. M., Seneviratne, S. I., Ward Philip, J., Pitman, A., et al. (2018). Future climate risk from compound events. *Nat. Clim.Change* 8, 469–477. doi: 10.1038/s41558-018-0156-3

Conflict of Interest Statement: The authors declare that the research was conducted in the absence of any commercial or financial relationships that could be construed as a potential conflict of interest.

frontiers in Earth Science

ORIGINAL RESEARCH
published: 13 September 2019
doi: 10.3389/feart.2019.00242

The Role of Detailed Geomorphic Variability in the Vulnerability Assessment of Potential Oil Spill Events on Mixed Sand and Gravel Beaches: The Cases of Two Adriatic Sites

Edoardo Grottoli[1,2]* *and Paolo Ciavola*[2]

[1] School of Geography and Environmental Sciences, Ulster University, Coleraine, United Kingdom, [2] Department of Physics and Earth Science, University of Ferrara, Ferrara, Italy

OPEN ACCESS

Edited by:
Denise Reed,
University of New Orleans,
United States

Reviewed by:
Jacqui Michel,
Research Planning, Inc.,
United States
Ping Wang,
University of South Florida,
United States
Mark Kulp,
University of New Orleans,
United States

***Correspondence:**
Edoardo Grottoli
e.grottoli@ulster.ac.uk

Specialty section:
This article was submitted to Geohazards and Georisks, a section of the journal Frontiers in Earth Science

Received: 03 June 2019
Accepted: 30 August 2019
Published: 13 September 2019

Citation:
Grottoli E and Ciavola P (2019) The Role of Detailed Geomorphic Variability in the Vulnerability Assessment of Potential Oil Spill Events on Mixed Sand and Gravel Beaches: The Cases of Two Adriatic Sites. Front. Earth Sci. 7:242. doi: 10.3389/feart.2019.00242

The role of short- to medium-term geomorphic variation is analyzed in two Italian mixed sand and gravel beaches to better understand how it could affect vulnerability assessments of oil spill events. The study sites, Portonovo and Sirolo, are in one of the most congested areas for oil transportation in the Adriatic Sea (Ancona port). A "snapshot" situation populated with field data collected in April 2015 is compared to a "changing" situation built with previous field datasets (topographic surveys and surface sediment samplings) available for the two beaches. According to the ESI guidelines established by the National Oceanic and Atmospheric Administration [NOAA], 2002, both Portonovo and Sirolo can be ranked as ESI 5 or 6A in most of the cases. Sediment size resulted in the most decisive factor for the ESI assessment. As consequence of the bimodal direction of storms, the high geomorphic variability on the two sites is mainly related to storm berms which lead to rapid burial processes on both beaches. In oil spill circumstances, burial is considered the most alarming factor, especially on microtidal mixed beaches that develop storm berms so high and close to the shoreline. A quantification of the maximum potential depth reachable by the oil in the beach body is therefore needed for the most dynamic beaches; this could be achieved with repeated field measurements to be performed in the period between two consecutive ESI updates (5–7 years) and the addition of an appendix in the ESI maps dealing with the geomorphic characteristics of the beach. The significance of a changing ESI rank is that the authorities in charge of responding to the oil spill could be improperly prepared for the conditions that exist at a spill site if the geomorphology has changed from when it was first given an ESI rank.

Keywords: oil spill, mixed beaches, coarse-grained beaches, storm berm, burial, ESI

INTRODUCTION

Despite the increasing exploitation of renewable energies, oil is currently one of the most adopted energy sources in the world (British Petroleum [BP], 2018). Its transportation is still necessary by tankers across the sea and its extraction by means of offshore platforms is quite common, creating the potential for oil spills whether offshore or toward the coasts. The coastal value from ecological, socioeconomic, and cultural points of view is threatened by several pollution sources, and among them oil represents one of the most harmful (Santos and Andrade, 2009). Thanks to the implementation of satellite and SAR images, oil spill monitoring has recently received more attention from the scientific community (Fiscella et al., 2000; Brekke and Solberg, 2005; Gambardella et al., 2010; Xu et al., 2014). Improvements in remote sensing have allowed better identification of oil in water environments, but the many possible background interferences and the absence of *ad hoc* sensors to detect oil in the water still represent limitations (Fingas and Brown, 2018). When an oil spill reaches the coast, several factors dealing with the physical nature and the hydrodynamics of the site can signal the persistence of oil in the coastal environment. The first attempts of classification for oil spill vulnerability were proposed by Gundlach and Hayes (1978) and Michel et al. (1978). Those efforts were improved through the years (Jensen et al., 1998) and finally merged into the most comprehensive tool known so far to asses coastal vulnerability to oil spill, which is the Environmental Sensitivity Index (ESI) established by the National Oceanic and Atmospheric Administration (National Oceanic and Atmospheric Administration [NOAA], 2002). The aim of the ESI guidelines is to generate vulnerability maps for water environments potentially affected by oil spill events. Fattal et al. (2010) conceptually defined the coastal vulnerability to oil spill as the combination of (1) shoreline type (substrate, sand grain size, tidal range), (2) exposure to wave and tidal energy, (3) the biological sensitivity index (Nansingh and Jurawan, 1999), (4) the analysis of oil persistence on the shoreline, (5) crisis management, and (6) the value of business activities affected by the oil spill. In the European context there are no tools like ESI maps, but some studies have been led to propose an index for marine-spill risk along the entire European coastline (Fernández-Macho, 2016). At the scale of the Adriatic Sea, the SHAPE project built an atlas as a tool for storing, visualizing and managing data useful to implement the Integrated Coastal Zone Management (ICZM) and Maritime Spatial Planning (MSP) policies, among which the oil spill vulnerability assessment is also present[1]. An oil spill forecasting system was set up for seven specific oil platforms in the Italian seas by Ribotti et al. (2019), including three sites in the Adriatic Sea. In the Adriatic Sea there is also the oil platform closest to the coast (Sarago Mare platform), which is also 30 km SE from the study area of the present paper. Coastal hazard assessments were modeled by Olita et al. (2019) for some Italian oil platforms, and the largest hazard value resulted from the Sarago Mare platform. According to Fernández-Macho (2016), Italy occupies the fourth place in Europe for oil spill vulnerability, even though the Ancona area (namely the study site of this paper) turned out to be quite low. As stated by Pourvakhshouri and Mansor (2003), the priority in the case of an oil spill affecting a coastal environment is to stop the dispersion of pollutants in the beach and through the adjacent water column. According to Kirby and Law (2010), an effective response to an oil spill at sea must include a well planned and executed post-incident assessment of environmental contamination and damage. For all these reasons it is crucial to understand and recognize the morpho-sedimentary dynamics of beaches. The vulnerability assessment should provide guidelines to help the local authorities in taking the proper decision to contrast the oil spill consequences (Pourvakhshouri and Mansor, 2003). As stated by Aps et al. (2014), beaches cannot be simply considered from a statistical point of view, and coastal morphodynamics is an important factor to take into account in the vulnerability assessment for oil spill events. The crucial role of field measurements for evaluating ESI was already recognized by Nelson and Grubesic (2018), as they helped to decrease observational error when only remote sensing data are used. According to González et al. (2009), to minimize the impact of oil spill on beaches it is crucial to understand the modal state of the beach and its morphodynamics variability through time; the authors also highlight the importance of the beach limits (lateral and the cross-shore), which confine the water circulation and the oil transport on the beach. The ESI scale of National Oceanic and Atmospheric Administration [NOAA] (2002) still represent an impressive and comprehensive tool to assess the susceptibility to spilled oil along coastal habitats, and it represents something that still must be reproduced at a European or worldwide context. Nevertheless, an improvement on the "shoreline type" classification is possible to better adopt ESI on a more local scale and in coastal environments amply different from oceanic coasts.

The aim of this paper is to adopt the ESI guidelines of National Oceanic and Atmospheric Administration [NOAA] (2002) for two mixed sand and gravel beaches in the microtidal environment of the Adriatic Sea (Italy). Comparing a one-time ("snapshot") situation with sequential field measurements from the same sites ("changing" situation), we want to demonstrate the crucial role of rapid geomorphic and surface sediment changes in the vulnerability assessment of mixed beaches for oil spill events. Substantial changes within relatively short time frames can take place in mixed sand and gravel beaches, therefore they may require different consideration in the preparedness and response to oil spill events.

Study Area

The study area is represented by two mixed sand and gravel beaches located on the eastern side of Conero Headland, which represents a rare case of high coast for the flat and sandy Italian side of the Adriatic Sea. Typical wave directions recorded by the Ancona offshore wave buoy (**Figure 1A**) between 1999 and 2006 are from SE (20%) and NE (16%) which also correspond to the main directions of storms (SE driven by "Scirocco" wind and NE driven by "Bora" wind). The significant wave height is usually between 0.25 and 2 m (80% of the time), less than 0.25 m for the 10% and higher than 2 m for the last 10%

[1] www.shape-ipaproject.eu

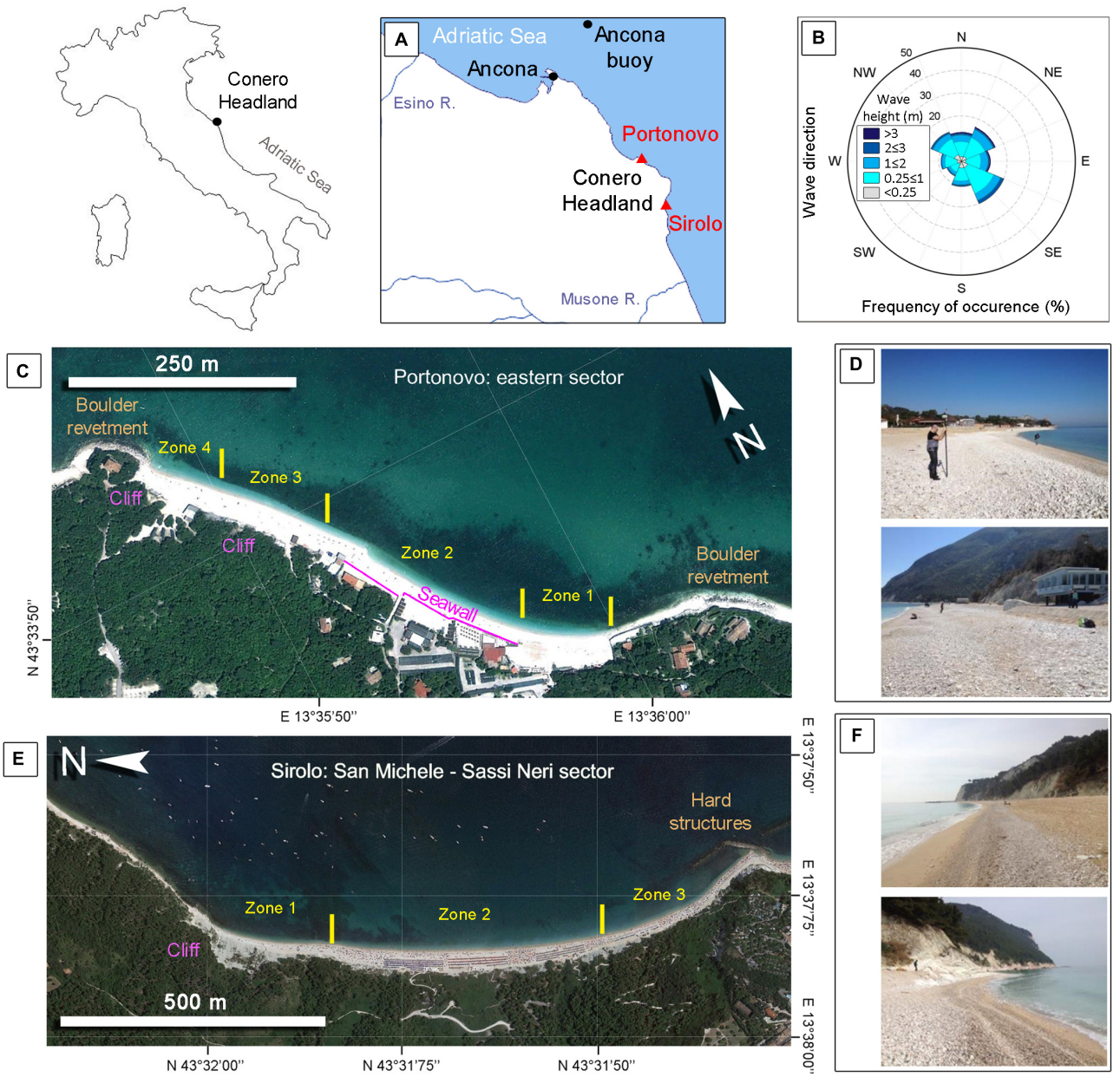

FIGURE 1 | Study sites: **(A)** Location; **(B)** Multiyear wave climate for Portonovo and Sirolo (recording period from 1999 to 2006). Wave data recorded by ISPRA buoy of Ancona (Bencivenga et al., 2012); **(C)** Zone subdivision in Portonovo; **(D)** Beach sediments in Portonovo in April 2015; **(E)** Zone subdivision in Sirolo; **(F)** Beach sediments in Sirolo in April 2015.

(Bencivenga et al., 2012; **Figure 1B**). The littoral transport is directed northward given the dominant influence of easterly winds (Colantoni et al., 2003; Regione Marche, 2005). The first site is Portonovo, a 500 m long and 20–50 m wide beach, orientated NW–SE. The beach is limited on both longshore sides by historical buildings protected at their bases by boulder-mound revetments (**Figure 1C**). The southern portion of the beach is slightly embayed and wider, whereas the central sector is the narrowest since the backshore is limited by a seawall protecting the local restaurants. The northern side is limited landward by a natural cliff made of limestone and marls, which also represents the only source of sediments for the beach (Grottoli et al., 2015). This cliff, locally reaching 12 m in elevation, is actually material that has fallen from Conero Headland in the Middle Ages (1249 circa; Montanari et al., 2016; **Figure 1C**). The grain size of beach sediment ranges from medium sand to cobbles, with a prevalent fraction of pebbles. Between 2006 and 2010, local authorities injected circa 18500 m^3 of nourishment material made of alluvial sediments (D_{50} = 10–50 mm, limestone) to prevent beach erosion. The framework involved all the beaches

of Portonovo, and the exact quantity deployed on the study site is unknown even though most of the nourishment material was deployed outside this sector, namely in the western part of the town (personal communication by local authorities, i.e., Regione Marche). The gravel fraction usually occupies the swash zone, with granules and fine pebbles normally found on the fair-weather berm and in the swash zone and cobbles and boulders usually found on the step zone. The beachface typically slopes at 0.2 (11°), whereas the seabed seaward of the step is approximately 0.01 (0.5°), as typically on the northern part of Adriatic seabed (Grottoli et al., 2017). According to the Jennings and Shulmeister (2002) classification of gravel beaches, Portonovo is a mixed sand and gravel beach (MSG) since a complete intermixing of sandy and gravelly sediments occurs (**Figure 1D**). The second study site is Sirolo (San Michele-Sassi Neri beach), which is located 5 km south from Portonovo. Here the beach is 1.2 km long and 30–40 m wide: it can be considered a natural embayed pocket beach since the cliff of Conero Headland confines the beach both alongshore and landward. The southernmost edge of the beach is also limited by hard structures (**Figure 1E**). The beach is N–S orientated, with the beachface typically sloping at 0.16 (9°) whereas the seabed seaward of the step is approximately 0.01 (0.5°; Grottoli et al., 2017). As in Portonovo, the only sediment source for Sirolo is represented by the limestone cliff behind the beach: small rockfalls occur during major storms or after heavy rainfall. Gravel nourishment was also undertaken in Sirolo by local authorities: between 2009 and 2011, 156000 m^3 of alluvial material (D_{50} = 6–12 mm, limestone) were deposited on the beachface to counter coastal erosion (Regione Marche, 2005). According to the Jennings and Shulmeister (2002) classification, Sirolo is a mixed sand and gravel beach (MSG). Like in Portonovo, here the beach surface looks extremely heterogeneous due to the intermixing of sand and gravel (**Figure 1F**). The swash zone is populated by granules and fine pebbles. The two study sites are in a semidiurnal tidal regime with the maximum excursion at spring tide of 0.47 m and a maximum record of 0.58 m (Colantoni et al., 2003).

MATERIALS AND METHODS

In order to highlight the role of geomorphic variability in estimating the ESI for oil spill vulnerability of Portonovo and Sirolo beaches, a "snapshot" situation, obtained from direct field measurements (topographic survey and surface sediment sampling) performed in April 2015, was compared with a series of previous field datasets from the same study sites which represented a "changing" situation.

Environmental Sensitivity Index Guidelines for Oil Spill Vulnerability

In 2002, National Oceanic and Atmospheric Administration (NOAA) established the ESI guidelines in order to create vulnerability maps of the United States in the case of oil spill events (National Oceanic and Atmospheric Administration [NOAA], 2002). The aim of this classification is to collect all the critical resources and natural characteristics of each water environment (fluvial, lacustrine, and estuarine) to assess its potential oil spill vulnerability. According to National Oceanic and Atmospheric Administration [NOAA] (2002), coastal habitats are vulnerable to oil spills. The classification requires three different details to complete ESI maps: (i) type of shoreline; (ii) biological resources; and (iii) human-use resources. This study is only focused on the "type of shoreline" to better characterize the geomorphic contribution to its assessment. The type of shoreline according to National Oceanic and Atmospheric Administration [NOAA] (2002) is controlled by the following factors: (i) beach exposure to waves and tides; (ii) beach slope; (iii) substrate type (i.e., sediment grain size, mobility, penetration, and/or burial and trafficability); and (iv) biological productivity and sensitivity. Concerning wave and tide exposure, National Oceanic and Atmospheric Administration [NOAA] (2002) distinguishes three categories. High-energy shorelines (1A–2B) are regularly exposed to large waves or strong tidal currents during all seasons. Medium-energy shorelines (3A–7) often have seasonal patterns in storm frequency and wave size. Low-energy shorelines (8A–10E) are sheltered from wave and tidal energy, except during unusual or infrequent events. Beach slope is meant as the inclination of the intertidal zone. The slope categories are steep (>30°), moderate (between 5° and 30°), and flat (<5°), but more accurate subdivision is made for each vulnerability rank. The substrate type can be classified as bedrock (permeable or impermeable, depending upon the presence of surface deposits on top of the bedrock); sediments, which are divided by grain size; and man-made materials (basically riprap or seawalls). The fourth factor concerning the biological productivity and sensitivity was not considered in this work. A comprehensive description of each vulnerability rank is listed in **Table 1** and is available in National Oceanic and Atmospheric Administration [NOAA] (2002). Each vulnerability level, which is characterized by different sediment sizes, beach slope and hydrodynamics, has important implications for the penetration of oil and its burial by beach sediments. Sediment size and its mixing also affect trafficability of cleaning equipment, making cleaning operations different for each environment. The higher the ESI rank, the more sensitive the environment is to oil (National Oceanic and Atmospheric Administration [NOAA], 2002).

Geomorphic Situation of April 2015 (Snapshot Situation)

To assess the oil spill vulnerability of the two beaches according to ESI guidelines (National Oceanic and Atmospheric Administration [NOAA], 2002), *in situ* investigations were performed in April 2015. Beach topography was measured by means of an RTK-GNSS (Trimble R6, ± 4 cm of accuracy). In Portonovo, a network of 50 cross-shore profiles, spaced 10 m apart, were surveyed. In Sirolo 18 cross-shore profiles, 50 m spaced, were measured. At the same time, surface sediment samplings were also performed in both beaches: a total of 51 samples along 14 profiles were collected (3–4 samples for each profile) at Portonovo beach: this sampling grid unfortunately covers only half the beach (zone 1 and 2 of **Figure 1C**) since it represents a previous sampling grid that was chosen to be

TABLE 1 | Environmental Sensitivity Index shoreline classification for vulnerability assessment of oil spill events (National Oceanic and Atmospheric Administration [NOAA], 2002; modified).

ESI rank	Estuarine environment
1A	Exposed rocky shores
1B	Exposed, solid manmade structures
1C	Exposed rocky cliffs with boulder talus base
2A	Exposed wave-cut platforms in bedrock, mud, or clay
2B	Exposed scarps and steep slopes in clay
3A	Fine- to medium-grained sand beaches
3B	Scarps and steep slopes in sand
3C	Tundra cliffs
4	Coarse-grained sand beaches
5	Mixed sand and gravel beaches
6A	Gravel beaches (granules and pebbles)
6B	Riprap, Gravel Beaches (cobbles and boulders)
6C	Riprap
7	Exposed tidal flats
8A	Sheltered scarps in bedrock, mud, or clay; Sheltered rocky shores (impermeable)
8B	Sheltered, solid man-made structures; Sheltered rocky shores (permeable)
8C	Sheltered riprap
8D	Sheltered rocky rubble shores
8E	Peat shorelines
9A	Sheltered tidal flats
9B	Vegetated low banks
9C	Hypersaline tidal flats
10A	Salt- and brackish-water marshes
10B	Freshwater marshes
10C	Swamps
10D	Scrub-shrub wetlands; Mangroves
10E	Inundated low-lying tundra

maintained. In Sirolo, 26 samples were collected along nine profiles (three samples for each profile). Grain size analyses were performed by means of dry sieving with 1-phi intervals, to be consistent with previous sediment datasets. Grain size parameters (mean diameter and sorting) were computed following Folk and Ward's (1957) method by means of GRADISTAT 8.0 software (Blott and Pye, 2001). Topographic and surface sediment data collected in April 2015 have been used to describe the oil spill vulnerability in a "snapshot" situation as if an oil pollution would reach the beaches at that time.

Geomorphic Variability From Previous Data (Changing Situation)

The analysis of the short- to medium-term changing situation was undertaken thanks to previous datasets on both beaches. At Portonovo beach, topographic data, gathered following the same profile network used in April 2015, were available from March 2012 to February 2014 (approximately 23 months). Surface sediment samples were also available from March 2012 to April 2013 (approximately 13 months) from the same sampling grid of April 2015 (zone 1 and 2 of Portonovo beach, **Figure 1C**). To properly estimate the ESI rank of Portonovo, only the dates when both topographic and grain size data were available have been considered. In Sirolo, topographic data were available from March 2012 to October 2012 (approximately 8 months) recorded on the same profile network used in April 2015. No sediment samples were available apart from April 2015 in this site, so ESI estimation from previous datasets has been done only considering slope data. Both beaches were divided in zones (**Figures 1C,E**) according to recurrent morpho-sedimentary features observed from previous data. The subdivision will be useful to test and discuss if temporal morpho-sedimentary changes in those zones may vary the vulnerability rank. A more detailed use of ESI both in time and space can represent a chance to improve ESI guidelines from a geomorphic point of view. Topographic measurements, sediment samplings and grain size analyses were performed with the same methodology used for the dataset of April 2015 which is described in the previous paragraph.

RESULTS

ESI Shoreline Classification of April 2015 (Snapshot Situation)

In April 2015, Portonovo beach had an average slope in the intertidal zone of 13° (0.23), hence the whole beach could be alternatively considered as rank 5 or 6A according to the National Oceanic and Atmospheric Administration [NOAA] (2002) guidelines on beach slope (**Table 2**). The average grain size (mean diameter, Mz) was 11.6 mm (medium pebbles) and the material was generally poorly sorted (σ1 = 1.1 phi). The sand-gravel ratio for the whole beach is 0.19, therefore only one sixth of the beach is sandy and the rest is gravelly. According to grain size data and ESI guidelines by National Oceanic and Atmospheric Administration [NOAA] (2002), Portonovo beach can be classified as rank 5 (mixed beaches, **Table 2**). Following the zone subdivision showed in **Figure 1C**, Portonovo beach can be classified most of the time both as rank 5 and 6A if only the slope of the intertidal zone is considered (**Table 2**). On the other hand, if only grain size is considered, Portonovo beach can be classified always as rank 5 (mixed beaches; **Table 2**). In the same period, Sirolo beach had an average slope of 10° (0.18) in the intertidal zone, hence the beach could be classified alternatively as rank 5 or 6A according to the National Oceanic and Atmospheric Administration [NOAA] (2002) guidelines on beach slope. The average grain size (mean diameter, Mz) was 6.12 mm (fine pebbles) and the material was generally poorly sorted (σ1 = 1.2 phi). The sand-gravel ratio for the whole beach is 0.44, therefore only one third of the beach is sandy and the rest is gravelly. According to these data and the ESI guidelines by National Oceanic and Atmospheric Administration [NOAA] (2002), Sirolo beach can be classified as rank 5 (mixed beaches). Following the zone subdivision shown in **Figure 1E**, Sirolo beach can be classified most of the time both as rank 5 and 6A if only the intertidal beach slope is considered (**Table 2**). If only grain size is considered, Sirolo beach can be classified as rank 5 (mixed beaches) in zone 2 and 3 and as rank 6A (gravel beach – granules

TABLE 2 | The National Oceanic and Atmospheric Administration [NOAA] (2002) classification for Portonovo and Sirolo according to field data of April 2015.

		Sediment					Slope (intertidal zone)		
					Vulnerability (NOAA 2002)			Vulnerability (NOAA 2002)	
		Field data			Rank 5	Rank 6A	Field data	Rank 5	Rank 6A
		Ave. Mz (mm)	Ave. σ1 (phi)	S/G ratio	≥20% gravel	100% gravel	Ave. β (°)	8° < β < 15°	10° < β < 20°
Portonovo April 10, 2015	Zone 1	10.33	1.13	0.33	x		15	x	x
	Zone 2	12.80	1.05	0.11	x		13	x	x
	Zone 3			NA			16		x
	Zone 4			NA			10	x	x
Sirolo April 11, 2015	Zone 1	10.20	1.30	0.00		x	9	x	
	Zone 2	3.74	1.12	0.62	x		10	x	x
	Zone 3	4.42	1.23	1.00	x		12	x	x

and pebbles) in zone 1 giving the absence of sandy samples and therefore a zero sand-gravel ratio (**Table 2**).

ESI Shoreline Classification From Previous Data (Changing Situation)

According to previous sediment analyses (six samplings over 13 months), Portonovo beach can always be classified as rank 5 (mixed beaches), except for one case relating to zone 1 (the southernmost) in April 2013 (**Table 3**) when the area was gravelly (rank 6A, gravel beaches made by granules and pebbles). According to previous slope data of the intertidal zone (six surveys over 13 months), Portonovo beach can be classified alternatively as rank 5 or 6A in 50% of cases (**Table 3**). In 15% of cases, the intertidal beach slope is so high that the vulnerability rank is 6A (gravel beaches – granules and pebbles) whereas in the remaining 35% of cases the beach is ranked as 5 (mixed beaches; **Table 3**). In Sirolo, where only slope data were available, the beach showed a wider range of vulnerability levels (**Table 4**). In two surveys (March and October 2012) the central part of the beach is alternatively classifiable as rank 5 or 6A, whereas the southernmost area (zone 3) can be classified as rank 4 (coarse-grained sand beaches) and the northernmost area (zone 1) can be ranked as rank 1C (exposed rocky cliffs with boulder talus base; **Table 4**). In April 2012 the beach can be basically classified as rank 5 or 6A (**Table 4**).

DISCUSSION

Environmental Sensitivity Index guidelines by National Oceanic and Atmospheric Administration [NOAA] (2002) were conceived to rapidly and widely asses the oil spill vulnerability for the large variety of water environments of the United States. The ESI guidelines remain a strong and exhaustive tool to assess oil spill vulnerability not only in the United States since they are also considered valid tools in different coastal environments worldwide (Hanna, 1995; Castanedo et al., 2009; Pincinato et al., 2009; Bello Smith et al., 2011; Aps et al., 2014, 2016) and take part in more comprehensive analyses of oil spill vulnerability (Fattal et al., 2010; Frazão Santos et al., 2013; Romero et al., 2013). The typical publication scale of ESI maps established by National Oceanic and Atmospheric Administration [NOAA] (2002) is 1:50000, which means that Sirolo would barely be represented by 2 cm on the map (**Figure 1E**), and Portonovo, with its entire length, would be only 1 cm (**Figure 1C**). Given the large scales adopted by NOAA, in many cases a remote interpretation of beach geomorphology and sediment characteristics is adequate in assessing the ESI rank, but sometimes this may lead to important mistakes like the case of the SHAPE project (see footnote 1), which assessed the two study sites of the present paper as sandy beaches. This is another reason why the geomorphic study presented here can be considered as detailed, and morphodynamic monitoring through time is crucial to correctly assess oil spill vulnerability, particularly on mixed beaches. NOAA is clearly aware of the factors contributing to spatial error in ESI estimation as explained by National Oceanic and Atmospheric Administration [NOAA] (2002). Understanding detailed geomorphic and grain size variability is crucial to correctly assessing the oil spill vulnerability of beaches that are, as a matter of fact, constantly changing landforms. Apart from the pure cartographic output, NOAA provides site-specific information for each rank represented in an ESI map (i.e., National Oceanic and Atmospheric Administration [NOAA], 2007). If more than one ESI rank is ascribable to a coastal site, both shoreline symbols are used [for example a riprap behind a sand beach; National Oceanic and Atmospheric Administration [NOAA] (2002)], but this means that both types of beach coexist at the same time. Some coastal areas can change dramatically with the season and this is the reason why NOAA in the past prepared seasonal summary maps at larger scales (namely 1:250000 to 1:50000; Jensen et al., 1998), but again the detail of geomorphic changes would be missed in beaches like Portonovo or Sirolo. Changes in the grain size and beach topography are particularly impressive on mixed beaches, and as already stated by Kirk (1980), the most complex aspects of mixed beaches relate to sediment characteristics and the way in which processes and

TABLE 3 | The National Oceanic and Atmospheric Administration [NOAA] (2002) classification for Portonovo according to previous sediment and slope datasets.

		Sediment					Slope (intertidal zone)		
					Vulnerability (NOAA 2002)			Vulnerability (NOAA 2002)	
		Field data			Rank 5	Rank 6A	Field data	Rank 5	Rank 6A
		Ave. Mz (mm)	Ave. σ1 (phi)	S/G ratio	≥20% gravel	100% gravel	Ave. β (°)	8° < β < 15°	10° < β < 20°
(01) March 28, 2012	Zone 1	5.43	1.06	0.30	x		10	x	x
	Zone 2	10.89	1.15	0.23	x		15	x	x
	Zone 3	NA							
	Zone 4	NA							
(02) April 18, 2012	Zone 1	6.65	1.03	0.45	x		18		x
	Zone 2	4.88	0.89	0.45	x		10	x	x
	Zone 3	NA							
	Zone 4	NA							
(03) May 28, 2012	Zone 1	6.60	0.82	0.59	x		14	x	x
	Zone 2	11.18	0.83	0.27	x		8	x	
	Zone 3	NA					12	x	x
	Zone 4	NA					12	x	x
(04) October 2, 2012	Zone 1	8.58	0.88	0.12	x		9	x	
	Zone 2	5	1.01	0.54	x		8	x	
	Zone 3	NA					16		x
	Zone 4	NA					19		x
(05) December 20, 2012	Zone 1	9.59	0.75	0.12	x		11	x	x
	Zone 2	5.76	1.13	0.49	x		9	x	
	Zone 3	NA					8	x	
	Zone 4	NA					8	x	
(06) April 22, 2013	Zone 1	27.24	0.71	0.00		x	15	x	x
	Zone 2	6.19	1.25	0.32	x		9	x	
	Zone 3	NA					11	x	x
	Zone 4	NA					15	x	x

TABLE 4 | The National Oceanic and Atmospheric Administration [NOAA] (2002) classification for Sirolo according to previous slope datasets.

		Slope (intertidal zone)				
		Field data	Vulnerability (NOAA 2002)			
			Rank 4	Rank 5	Rank 6A	Rank 1C
		Ave. β (°)	5° < β < 15°	8° < β < 15°	10° < β < 20°	β < 30°
(01) March 31, 2012	Zone 1	23				x
	Zone 2	15		x	x	
	Zone 3	7	x			
(02) April 19, 2012	Zone 1	10		x	x	
	Zone 2	9		x		
	Zone 3	11		x	x	
(03) October 6, 2012	Zone 1	22				x
	Zone 2	11		x	x	
	Zone 3	6	x			

sources interact to redistribute the sediments within the beach. Given the dramatic changes that a mixed sand and gravel beach can experience, an exhaustive comprehension of how a beach behaves, at least in the short period, is crucial. Aps et al. (2014) found that an extra factor should be considered by the National Oceanic and Atmospheric Administration [NOAA] (2002) classification, which is the dynamicity of a beach. In a beach of Ruhnu Island (Estonia) they found an increase after 6 years in the ESI rank from 3 to 6 because of the concomitant effect of seasonal storms and sediment deficit that no longer could

nourish the beach. The surface sandy layer of the beach was then eroded, transforming it into a gravel beach (**Figures 2A1,2**). A similar layout was also experienced in Portonovo in only 3 months after the subsequent occurrence of comparable storms from opposite directions (**Figures 2B1,2**, **6**). Thanks to both topographic and sediment data previously available, the four zones of Portonovo have always been ascribable to ESI 5 or 6A, and the grain size factor that better defined the ESI is 5. On the other hand, the wider vulnerability rank ascribable to Sirolo beach is mainly due to the only slope data available from previous surveys; instead, when grain size data are also available (see April 2015; **Table 2**), a better discrimination of its vulnerability is possible. Bello Smith et al. (2011) highlighted that the National Oceanic and Atmospheric Administration [NOAA] (2002) classification is hardly applicable to microtidal beaches because beach slope is likely overrated if compared to the wider oceanic beaches. The higher sandy fraction and the consequent gentle slope of its intertidal zone are the main reasons to assess Sirolo as ESI 5 in most cases. The least alarming area of Sirolo beach in the case of an oil spill event is the northernmost (zone 1; **Figure 1E**): here the narrow beach, basically comprised by the cliff and a boulder talus base, could be easily cleaned by the normal swash fluxes and wave energy (as also reported by National Oceanic and Atmospheric Administration [NOAA] (2002) for rank 1C). Unfortunately, the fact that the dataset of the two beaches is not fully comparable forced the authors to formulate their belief mainly on the more complete dataset collected for Portonovo beach. No repeated sediment sampling was undertaken in Sirolo beach as the dataset we used was originally collected for a morphodynamics study. Nevertheless, the slope variability documented for Sirolo beach is still valuable in determining the maximum potential oil depth reachable in this beach.

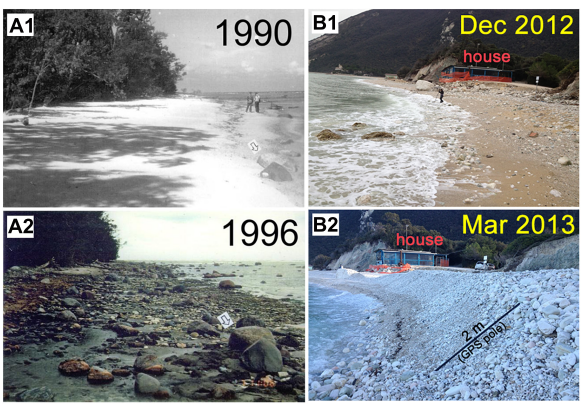

FIGURE 2 | (A1,2) Comparison of the same beach portion of Ruhnu Island (Estonia) after 6 years (modified from Aps et al., 2014) and **(B1,2)** the same beach portion in Portonovo (zone 4) after 3 months. The beach portion of Portonovo is shown after two storms driven from opposite directions (**B1** storm from NE, **B2** storm from SE). The high dynamism associated both with burial and the variation of sediment size can be noticed comparing all the frames.

TABLE 5 | Vertical extents of oil penetration, sediment mobility, and burial (or erosion) of the different vulnerability levels according to ESI guidelines by National Oceanic and Atmospheric Administration [NOAA] (2002).

	Rank 1	Rank 4	Rank 5	Rank 6
Oil penetration	0 (impermeable substrate)	0.25	0.50	1
Sediment mobility (mixing depth)	–	0.20	High during storms	High during storms
Burial/Erosion	–	Rapid during a single tidal cycle	Rapid during storms	Rapid during storms

Only the levels ascribable to Portonovo and Sirolo are shown. Values are given in meters.

The most important information in the case of an oil spill event is the burial and penetration of oil in the beach body. National Oceanic and Atmospheric Administration [NOAA] (2002) gives some important implications for each ESI regarding burial (or erosion), penetration of oil and sediment mobility (**Table 5**). Given the mixture of sediments of Sirolo and Portonovo beaches, burial and penetration can be particularly rapid and could easily increase the oil persistence in the beach body, leading to potential long-term biological impacts and making cleanup procedures much more difficult and intrusive (National Oceanic and Atmospheric Administration [NOAA], 2002). As showed in **Table 5**, many indications given by National Oceanic and Atmospheric Administration [NOAA] (2002) are only general or qualitative, and this makes sense from their point of view given the wide application of the ESI classification. An opportunity for improvement is a quantification of the maximum potential depth, which is reachable by the oil, but this implies the collection and the analysis of site-specific data.

Given its predominant gravelly fraction, Portonovo is constantly affected by rapid burial (**Figures 2B1,2**), which can be led not only by severe storms as already documented by Grottoli et al. (2017), who analyzed the storm response of the beach with a typical wave climate for the area. The high dynamicity of Portonovo was also experienced with low energy conditions which generated 0.5 m of burial due to the formation of the fair-weather berm in the intertidal zone (Grottoli et al., 2019). Nevertheless, storm berms represent the most dangerous geomorphic factors in the case of an oil spill event that reaches the beach. In Portonovo, the highest storm berms were always observed after storms coming from the SE ("Scirocco" wind; **Figure 3**). Due to its orientation (NW–SE), the beach is largely exposed to incident storm waves coming both from the SE and NE, but SE waves, due to the smaller accommodation space of zones 3 and 4 (**Figure 3**), can pile up larger sediments (pebbles and cobbles) in storm berms from 1 to 3 m high (**Figures 3B,D,F**). In sites like Portonovo (**Figures 3**, **4**) the beach limits are crucial, not only in confining the water circulation in the case of an oil spill (González et al., 2009) but, primarily, for increasing the chances of significant burial in case of severe storms (i.e., Hs of 3.5–5 m, an approximate energy of 600–800 m^2h and at least 30 h of storm conditions; Grottoli et al., 2017). The strong

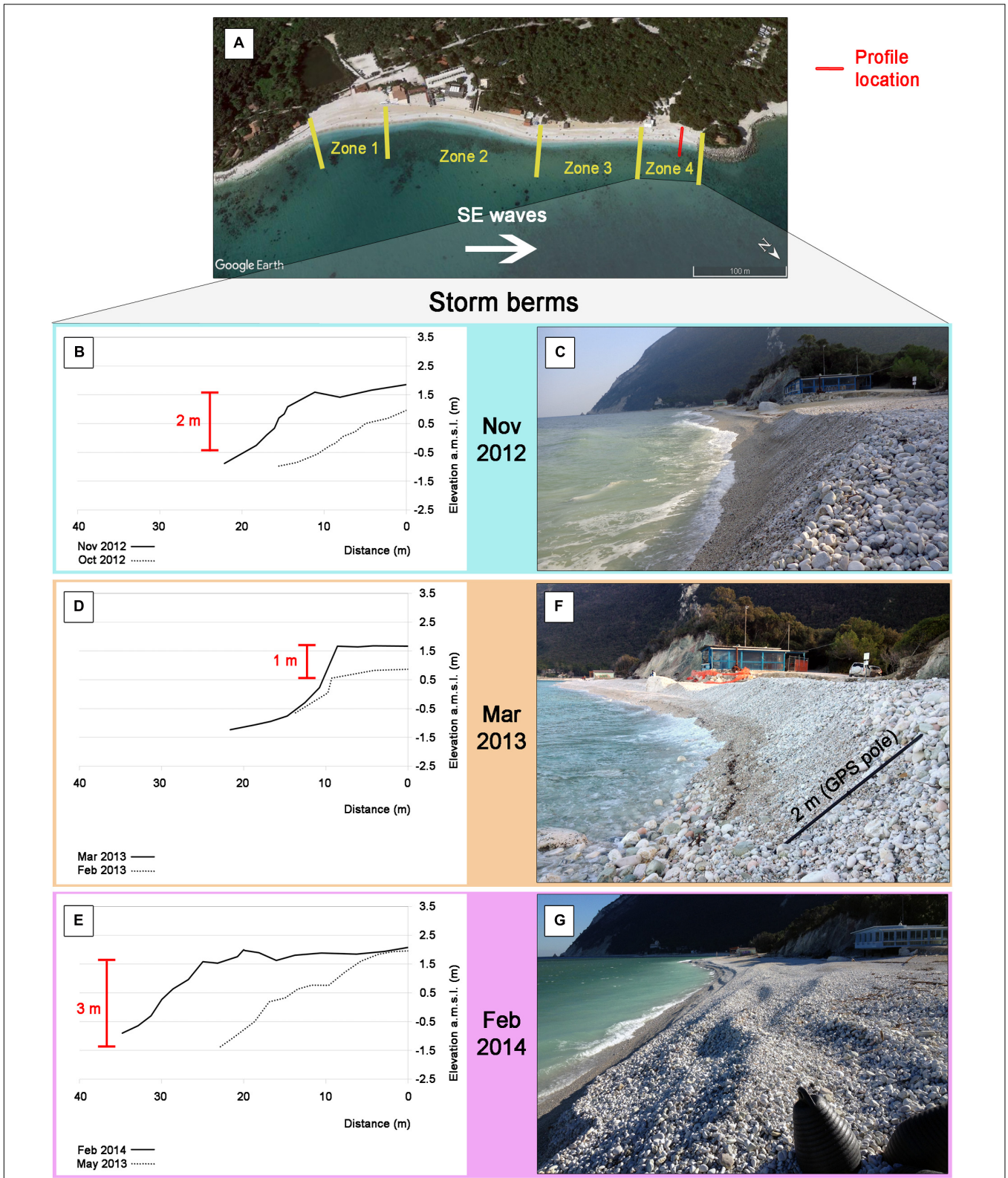

FIGURE 3 | View of the same beach portion of Portonovo (zone 4) after three different storms coming from the SE: **(A)** zone subdivision and focus on zone 4; **(B)** beach topography of November 2012 compared to the previous data available and **(C)** photo of the beach surface of November 2012; **(D)** beach topography of March 2013 compared to the previous data available and **(E)** photo of the beach surface of March 2013; **(F)** beach topography of February 2014 compared to the previous data available and **(G)** photo of the beach surface of February 2014.

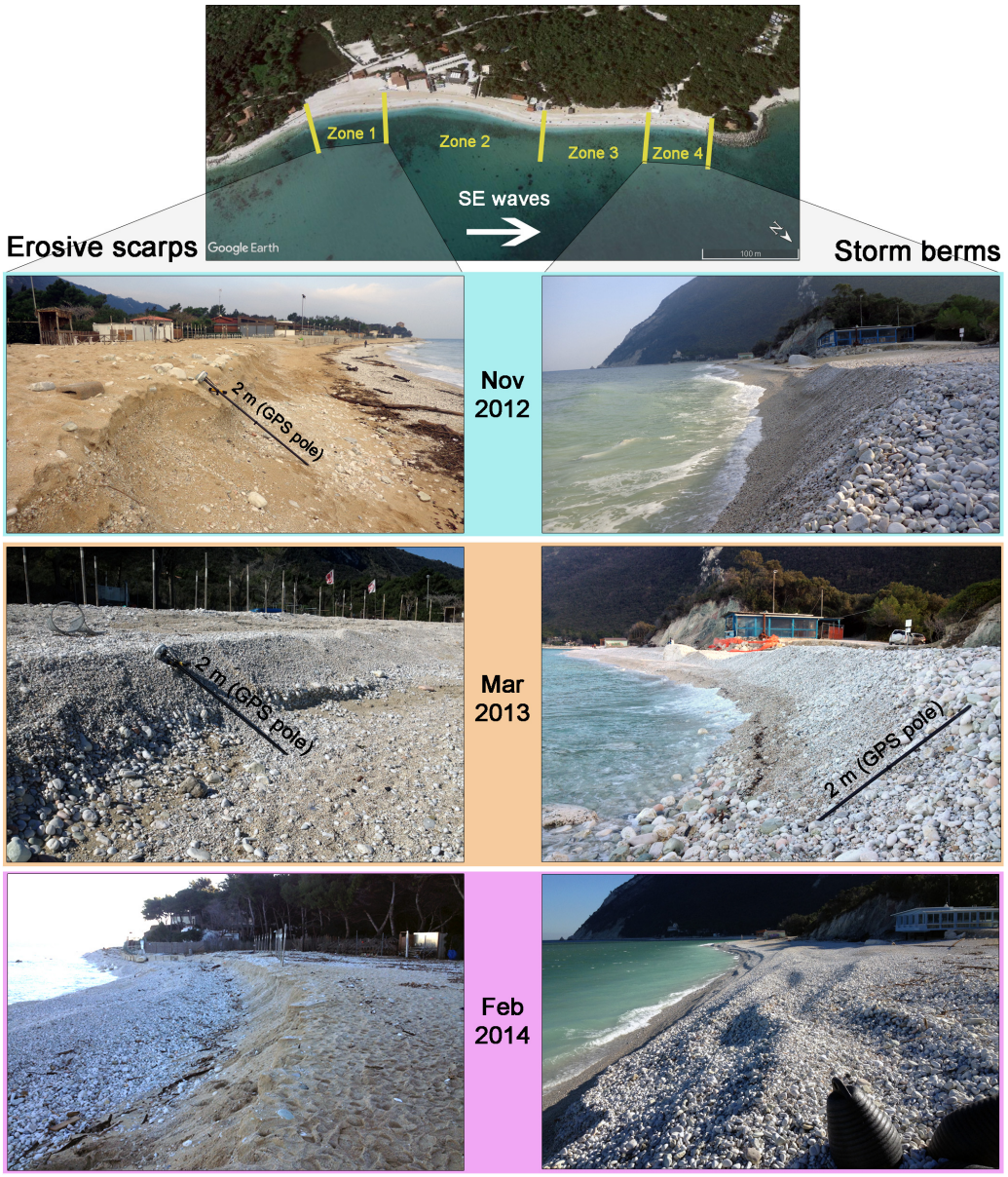

FIGURE 4 | Erosive scarps (on the left) and storm berms (on the right) from the edge zones of Portonovo beach after storm events from SE direction.

downdrift coarsening of sediments in accordance with the storm direction was already experienced by Carr et al. (1970) in Chesil Beach (United Kingdom). In Portonovo, when a severe storm approaches from the SE, the southern part of the beach (zone 1 and 2; **Figure 4**) is affected by erosive scarps of the same vertical extent of the storm berms that form in the northern part (zone 3 and 4; **Figure 4**). In Sirolo, where only a few datasets were available, it is not possible to clearly quantify burial (or erosion) extents, but it is likely that the larger accommodation space prevents the creation of storm berms and erosive scarps of the same size of Portonovo (**Figure 5**). The encouraging aspect of pocket beaches like Sirolo and Portonovo, where the tide is not an important factor, is that beach rotation, due to the bimodal direction of storms (NE and SE, **Figure 6**), represents the main factor responsible for beach recovery (Harley et al., 2014; Grottoli et al., 2017). Burial processes on mixed beaches were already explained by Hayes et al. (1991), highlighting the dangerous concomitance of storm berm deposition, beach rotation and downdrift coarsening of sediments after a storm event. In Portonovo, storm berms are very close to the shoreline, with their seaward steep side often joined to the beachface (**Figures 3C,E,G**): therefore, the burial generated by storm berms has to be taken into serious consideration in the case of an oil spill event since the contaminant is expected to penetrate the beach body from the beachface, which could be rapidly buried if severe storm waves are approaching the beach. As suggested by

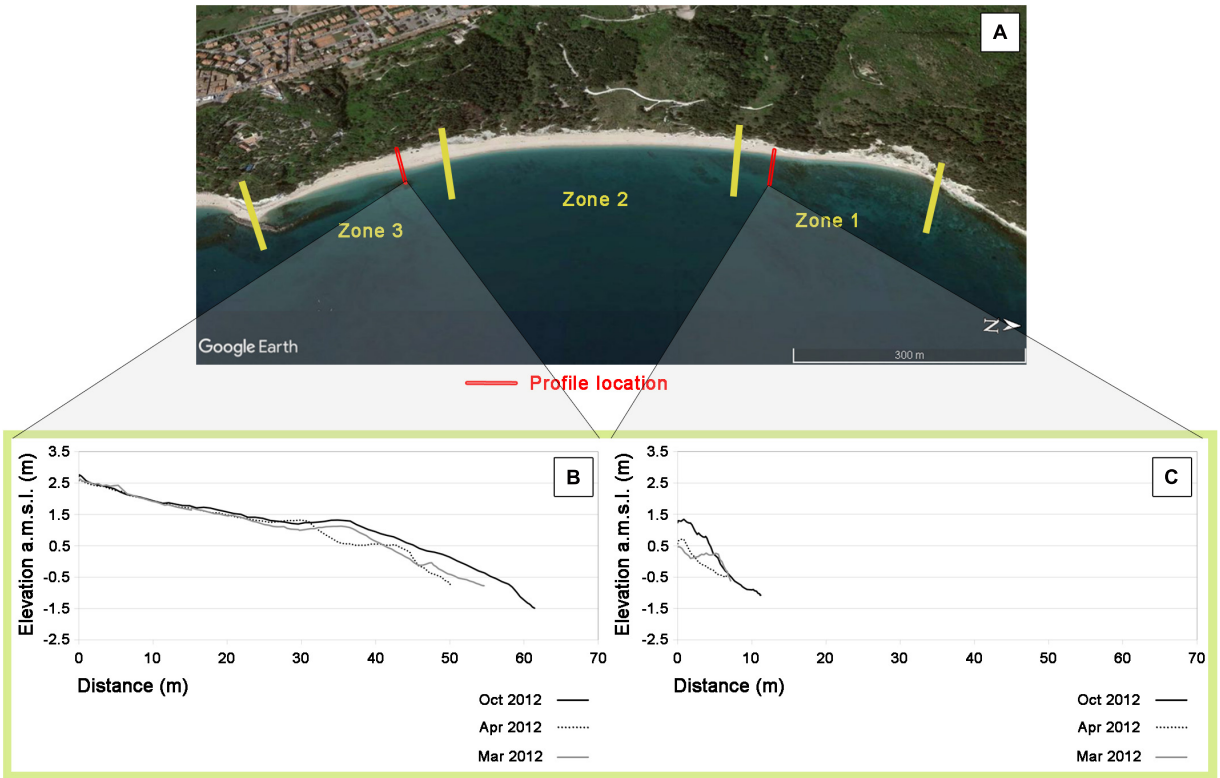

FIGURE 5 | Profile variation at the edge zones of Sirolo beach between March and October 2012: **(A)** zone subdivision and profile location; **(B)** profile variation in zone 3; **(C)** profile variation in zone 1. Profiles have been chosen according to the larger topographic variation visible.

Quick and Dyksterhuis (1994), storm berm formation on highly permeable beaches is mainly due to wave breaking [typically by plunging on this type of beaches, Grottoli et al. (2019)], which produces a net onshore shear stress over the swash and backwash cycle, leading to net onshore transport and profile steepening as experienced in Portonovo (**Figure 3**). Moreover, the hydraulic conductivity, related to the coarse sediment size of the beach, is directly responsible for the steep profile (Mason and Coates, 2001) and should be an aspect that still needs further consideration on mixed sand and gravel beaches. Since in the case of an oil spill event, the oil would primarily reach the intertidal zone, another aspect that has to be taken into consideration is the typical mixing depth of the site. The mixing depth in the intertidal zone of Portonovo was already tested in the field by Grottoli et al. (2015) as 0.25–0.3 m (experienced with ordinary waves, namely Hs of 0.3–0.4 m). In Sirolo, mixing depth was derived using the experimental formulas of Ciavola et al. (1997) and Ferreira et al. (2000), specifically developed for steep and coarse sandy beaches. Those formulas, computed for the intertidal zone of Sirolo, with a typical Hs of 0.5 m, returned mixing depth values of 0.13–0.16 m (**Table 6**).

Hence, in the worst-case scenario, represented by the deposition of oil on the beach immediately before a storm event (or a cluster of storms), the three factors that can increase the maximum depth reachable by the oil are: (i) the maximum burial due to storm berm formation (**Figure 3**); (ii) the typically large mixing depth, and (iii) the expected oil penetration related to the sediment characteristics of the beach at the oil deposition point (according to National Oceanic and Atmospheric Administration [NOAA], 2002). These three factors can be concomitant if the oil is stranded on the beach immediately before a storm (or a cluster of storms) and if summed, they give a maximum potential depth of 3.80–4.30 m in Portonovo and 1.10–1.85 m in Sirolo (**Table 6**).

Comparable burial rates were recorded by González et al. (2009) in sandy macro-tidal beaches of Galicia (Spain): oil was found at depths of 2–3 m 2 years after a big oil spill event. Similar burial depths (1.5 m) were also expected in the sandy meso-tidal beaches of New Zealand (de Lange et al., 2016). Prompt cleaning operations after the oil spill led to a complete cleaning after 1 year from the incident with the help of natural oil degradation (de Lange et al., 2016). Oil was buried under storm berms of 1.2 m in the gravel beach of Prince William Sound (Alaska; Hayes et al., 1991). In coarse grained beaches (ESI 5 and 6) oil could persist within the beach body for years (Gundlach and Hayes, 1978; Hanna, 1995; National Oceanic and Atmospheric Administration [NOAA], 2002); therefore, a better understanding of the internal structure and sediment variability under the beach surface is particularly needed. A valid tool is Ground Penetration Radar (GPR), which has already been used to detect oil layers down to a depth of 0.5 m from the beach surface by Lorenzo et al. (2009) in Galicia (Spain). The same oil depth was documented by Michel and Hayes (1993) 3.5 years

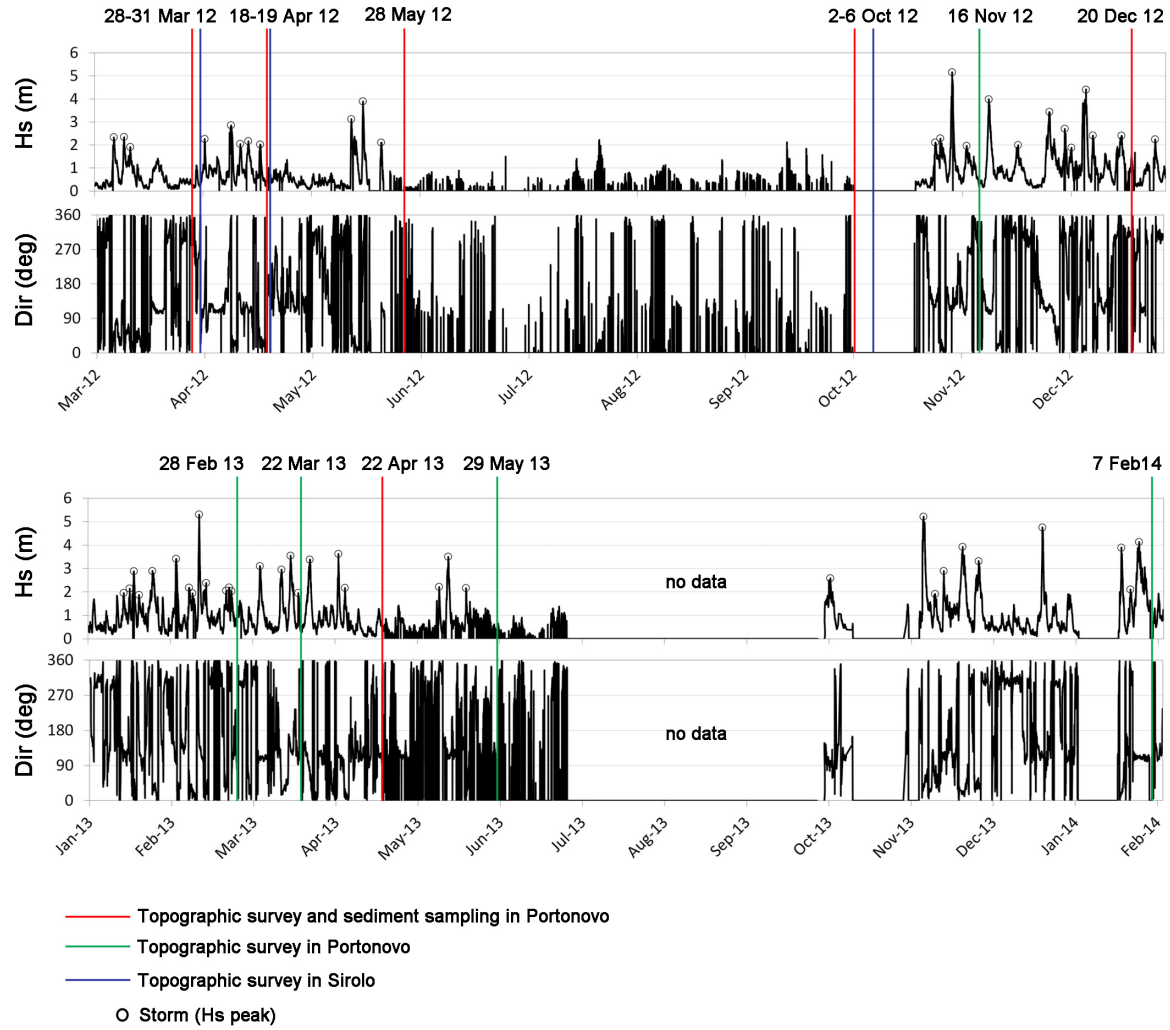

FIGURE 6 | Wave dataset from March 2012 to February 2014. The topographic surveys and sampling are also marked for both beaches.

TABLE 6 | Estimation of the max potential depth that oil can reach in the case of an oil spill event in Portonovo and Sirolo.

	Max burial due to storm berms	Mixing depth	Ascribable ESI ranks (NOAA 2002)				Max potential oil depth
			Oil penetration according to beach sediment (Rank 1)	Oil penetration according to beach sediment (Rank 4)	Oil penetration according to beach sediment (Rank 5)	Oil penetration according to beach sediment (Rank 6)	
Portonovo	3	0.30	–	–	0.50	1	3.80–4.30
Sirolo	0.70	0.15	0	0.25	0.50	1	1.10–1.85

Values are given in meters.

after the Exxon Valdez oil spill of 1989 in some gravel beaches of Prince William Sound (PWS) in Alaska. Another aspect to better investigate is the actual penetration and persistence of oil: Li and Boufadel (2010) proposed a valid model for tidal gravel beaches based on an internal structure made by two layers, with the lower layer characterized by low permeability and therefore being able to entrap oil for years, as happened to the gravel beach of PWS after the Exxon Valdez oil spill (Hayes and Michel, 1999). According to Nixon and Michel (2018), these oil residues are typically located in finer-grained sand and gravel sediments, often under an armor of cobble- or boulder-sized clasts, in areas with limited groundwater flow and porosity. According to Nixon et al. (2013) the oil persistence, nearly 20 years after the Exxon Valdez oil spill on the intermittently exposed gravel beaches, is due to

a complex interaction between small-scale geomorphic features (e.g., armoring) that proved shelter from the local incident wave energy. They documented subsurface oiled layers down to an average burial depth between 13.6 and 18.6 cm.

Mixed sand and gravel beaches in microtidal environments which experience huge variability like Portonovo and Sirolo need more attention since the amount of sediment that can bury the oil is more significant due to the formation of storm berms right behind the narrow intertidal zone. After the Deepwater Horizon spill, which was the largest marine oil spill in United States waters affecting hundreds of kilometers of shorelines (Zengel et al., 2015, 2016), the geomorphic state of the beach was recognized as one of the most important issues during the response operations to the spill (Michel et al., 2013); during the initial heavy oiling many beaches of the Gulf of Mexico were in an erosional state, and this led to oil burial in the following months as the beaches accreted. Michel et al. (2013) documented that the oil was stranded high in the supratidal zone due to high water levels and wave activity generated by storms in 2010 and that the oil stranded in the intertidal zone was buried at a location of more than 1 m due to the effect of the largest storms in the area (i.e., Tropical Storm Lee and Hurricane Isaac, in May 2010 and January 2013). The case of the Deepwater Horizon spill, where the effects of oil persistence were still documented 3 years after the spill (Michel et al., 2014; Zengel et al., 2015, 2016), represents an example where the knowledge of the vertical variation of the beach surface would be crucial in performing the different oil treatment techniques and reducing challenges to its removal. The continued remobilization of oil buried in both intertidal and nearshore zones resulted in the chronic re-oiling of beaches, even though at trace levels, for over 3 years (Michel et al., 2013, 2014). This suggests that beaches showing high dynamicity should be investigated from a geomorphic point of view for a few years consecutively before a representative beach state can be chosen for vulnerability evaluations.

Recommendations on How Incorporate the Dynamic Nature of the Beach Environment in the ESI Assessment

As demonstrated by this paper, impressive vertical variations of the beach surface together with sediment size changes can be experienced on mixed beaches in both limited time and space. This natural process, primarily induced by storms, can largely affect the cleaning operations of an oiled beach and has in the generation of storm berms the most dangerous factor. As already accomplished for the biological aspect of the ESI assessment, where the appendix entitled "Biological resources" lists in detail the monthly occurrence and the period of nesting, eggs, pupping, etc., of each species (National Oceanic and Atmospheric Administration [NOAA], 2007), an extra detailed appendix, entitled "Geomorphic characteristics," could be added in the ESI map. During the "Ground verification" phase within the field measurements undertaken by geologists for the ESI assessment (National Oceanic and Atmospheric Administration [NOAA], 2002), surface sediment samplings and GPS cross-shore measurements should be included. These data should be gathered seasonally or at least twice per year during the period that lasts until the next scheduled ESI update, which is usually 5–7 years later. After this period, it would be possible to understand how the beach responds to storms and what potential depth could be reached by the oil according to the wave climate and the geomorphic features developed (e.g., storm berms) on the site. As shown in **Table 6**, an analog table could be created for each ESI map concerning the expected site-specific values of: (i) the maximum burial due to storm berm formation between one survey to another; (ii) the typical mixing depth of the site; and (iii) the oil penetration according to the sediment characteristics of the beach (according to National Oceanic and Atmospheric Administration [NOAA], 2002). These values, if summed, return the maximum potential depth that could be reached by the oil in the worst-case, namely the occurrence of a storm (or a cluster of storms) in the immediate aftermath of the oil deposition. Due to financial and logistic difficulties which may arise in obtaining these data, at least a ground verification survey should be repeated twice per year (at the beginning and at the end of the storm season) and within a single time span between two ESI updates (usually 5–7 years). Considering the huge shoreline extent that needs to be mapped and in order to have a satisfying spatial resolution, a geomorphic assessment every 500 m should be performed, and a zone subdivision of the shoreline could be conceived. After one single assessment period (5–7 years), a good estimation of the maximum potential burial of oil could be obtained for each zone. The assessment does not need to be repeated unless drastic environmental variations occur, such as construction of protection structures or beach replenishments. This detailed geomorphic assessment could be undertaken only on those beaches that are known to be highly dynamic, and it could largely improve the expectations of the authorities in charge of cleaning operations [e.g., the Shoreline Cleanup Assessment Technique (SCAT) Program; Owens and Teal (1990), Owens and Sergy (2000)] on how deep the oil could be found under the beach surface after a storm period. Unfortunately, this information is often site-specific due to a local combination of factors that may affect the oil fate along the shoreline (Michel et al., 2013); therefore, a geomorphic database for each ESI map could represent a relevant benefit as demonstrated by the GIS database built after the Deepwater Horizon for the Gulf of Mexico (Nixon et al., 2016).

CONCLUSION

Due to their large variety of grain sizes and the high dynamicity of their landforms, the opportunity to better assess the oil spill vulnerability of coastal environments from a geomorphic point of view could only arise from mixed sand and gravel beaches.

Both Portonovo and Sirolo can be classified as ESI 5 (mixed sand and gravel beaches) or 6A (gravel beaches), with Sirolo equally classifiable among the two ESIs for most of the time and Portonovo with a prevalent trend toward ESI 5, thanks to the more exhaustive sediment dataset from previous field measurements. Grain size is the most determinant factor in assessing the oil spill vulnerability according to ESI guidelines when both slope and sediment size are available.

The high geomorphic variability on the two sites is mainly related to storm berms due to the bimodal direction of storms. Storm berms demonstrate that rapid burial processes can occur on both beaches, with a potential maximum burial of 3.80–4.30 m in Portonovo in the northernmost edge of the beach and 1.10–1.85 m in the edges of Sirolo beach. The different burial magnitude of the two sites is mainly ascribable to smaller accommodation space for sediment transport of Portonovo beach because of its landward and cross-shore physical barriers, which increase the vertical accumulation of gravelly sediments in proximity to the shoreline. The maximum potential oil depth, predominantly related to storm berms, is the most alarming factor to be considered in the case of an oil spill event, especially in dynamic microtidal beaches where storm berms are usually very close to the shoreline. A better interpretation of the internal structure of mixed sand and gravel beaches is also needed to understand how sediment variability affects oil penetration and persistence. The National Oceanic and Atmospheric Administration [NOAA] (2002) classification, conceived for oceanic beaches of the United States, could be improved with the addition of a morphodynamics factor that could account for significant short-term and site-specific variations in terms of sediments and geomorphic features. In this sense, a quantification of the vertical variation of the beach surface by means of repeated and consequent field measurements is needed, and this aspect should be included in ESI maps as an appendix as already happens for the biological characteristics.

DATA AVAILABILITY

All datasets generated for this study are included in the manuscript and/or the supplementary files.

AUTHOR CONTRIBUTIONS

PC and EG conceptualized the work. EG conducted the field work, laboratory analyses, and data curation, and wrote the original manuscript. PC reviewed and supervised the manuscript.

ACKNOWLEDGMENTS

A previous version of this research work was presented at the Sixth International Symposium Monitoring of Mediterranean Coastal Areas: Problems and Measurements Techniques, Livorno (Italy), September 28–29, 2016, with the title "Vulnerability Assessment of Two Adriatic Mixed Beaches for Potential Oil Spill Events," by EG, PC, and Michele Molinelli. We are thankful to Michele Molinelli for his help during the data collection in the field and grain size analyses. We are also thankful to Duccio Bertoni, Alessandro Pozzebon, and Giannino Grottoli for their help during the sediment sampling in Portonovo.

REFERENCES

Aps, R., Tõnisson, H., Anfuso, G., Perales, J. A., Orviku, K., and Suursaar, Ü. (2014). Incorporating dynamic factors to the environmental sensitivity index (ESI) shoreline classification-estonian and Spanish examples. *J. Coast. Res.* 70, 235–240. doi: 10.2112/SI70-040.1

Aps, R., Tõnisson, H., Suursaar, Ü., and Orviku, K. (2016). Regional environmental sensitivity index (RESI) classification of estonian shoreline (Baltic Sea). *J. Coast. Res.* 75, 972–976. doi: 10.2112/SI75-195.1

Bello Smith, A., Cerasuolo, G., Perales, J. A., and Anfuso, G. (2011). Environmental sensitivity maps: the northern coast of gibraltar strait example. *J. Coast. Res.* 64, 875–879.

Bencivenga, M., Nardone, G., Ruggiero, F., and Calore, D. (2012). The italian data buoy network (RON). *Proc. Advan. Fluid Mech.* 74, 321–332.

Blott, S. J., and Pye, K. (2001). GRADISTAT: a grain size distribution and statistics package for the analysis of unconsolidated sediments. *Earth Surf. Process. Landf.* 26, 1237–1248. doi: 10.1002/esp.261

Brekke, C., and Solberg, A. H. (2005). Oil spill detection by satellite remote sensing. *Remote Sens. Envir.* 95, 1–13. doi: 10.1016/j.rse.2004.11.015

British Petroleum [BP] (2018). *BP Statistical Review of World Energy*, 67th Edn. London: British Petroleum.

Carr, A. P., Gleason, R., and King, A. (1970). Significance of pebble size and shape in sorting by waves. *Sed. Geol.* 4, 89–101. doi: 10.1016/0037-0738(70)90005-9

Castanedo, S., Juanes, J. A., Medina, R., Puente, A., Fernandez, F., Olabarrieta, M., et al. (2009). Oil spill vulnerability assessment integrating physical, biological and socio-economical aspects: application to the Cantabrian coast (Bay of Biscay, Spain). *J. Env. Man.* 91, 149–159. doi: 10.1016/j.jenvman.2009.07.013

Ciavola, P., Taborda, R., Ferreira, Ó., and Dias, J. A. (1997). Field observations of sand-mixing depths on steep beaches. *Mar. Geol.* 141, 147–156. doi: 10.1016/S0025-3227(97)00054-6

Colantoni, P., Mencucci, D., and Baldelli, G. (2003). "Idrologia e idraulica costiere processi litorali attuali e deposizione dei sedimenti," in *Verso La Gestione Integrata Della Costa Del Monte San Bartolo, Risultati Di Un Progetto Pilota*, ed. R. Coccioni, (Urbania: Quaderni del Centro di Geobiologia, Univ. Urbino), 15–37.

de Lange, W. P., de Groot, N. P. H. M., and Moon, V. G. (2016). Burial and degradation of Rena oil within coastal sediments of the Bay of Plenty. *N. Z. J. Mar. Freshw. Res.* 50, 159–172. doi: 10.1080/00288330.2015.1062401

Fattal, P., Maanan, M., Tillier, I., Rollo, N., Robin, M., and Pottier, P. (2010). Coastal vulnerability to oil spill pollution: the case of Noirmoutier island (France). *J. Coast. Res.* 26, 879–887. doi: 10.2112/08-1159.1

Fernández-Macho, J. (2016). Risk assessment for marine spills along European coastlines. *Mar. Pollut. Bull.* 113, 200–210. doi: 10.1016/j.marpolbul.2016.09.015

Ferreira, Ó., Ciavola, P., Taborda, R., Bairros, M., and Dias, J. A. (2000). Sediment mixing depth determination for steep and gentle foreshores. *J. Coast. Res.* 16, 830–839.

Fingas, M., and Brown, C. E. (2018). A review of oil spill remote sensing. *Sensors* 18: 91. doi: 10.3390/s18010091

Fiscella, B., Giancaspro, A., Nirchio, F., Pavese, P., and Trivero, P. (2000). Oil spill detection using marine SAR images. *Int. J. Remote Sens.* 21, 3561–3566. doi: 10.1080/014311600750037589

Folk, R. L., and Ward, W. C. (1957). Brazos river bar: a study in the significance of grain size parameters. *J. Sed. Petr.* 27, 3–26. doi: 10.1306/74D70646-2B21-11D7-8648000102C1865D

Frazão Santos, C., Carvalho, R., and Andrade, F. (2013). Quantitative assessment of the differential coastal vulnerability associated to oil spills. *J. Coast. Conserv.* 17, 25–36. doi: 10.1007/s11852-012-0215-2

Gambardella, A., Giacinto, G., Migliaccio, M., and Montali, A. (2010). One-class classification for oil spill detection. *Pattern Anal. Appl.* 13, 349–366. doi: 10.1007/s10044-009-0164-z

González, M., Medina, R., Bernabeu, A. M., and Novoa, X. (2009). Influence of beach morphodynamics in the deep burial of fuel in beaches. *J. Coast. Res.* 25, 799–818. doi: 10.2112/08-1033.1

Grottoli, E., Bertoni, D., and Ciavola, P. (2017). Short- and medium-term response to storms on three mediterranean coarse-grained beaches. *Geomorphology* 295, 738–748. doi: 10.1016/j.geomorph.2017.08.007

Grottoli, E., Bertoni, D., Ciavola, P., and Pozzebon, A. (2015). Short term displacements of marked pebbles in the swash zone: focus on particle shape and size. *Mar. Geol.* 367, 143–158. doi: 10.1016/j.margeo.2015.06.006

Grottoli, E., Bertoni, D., Pozzebon, A., and Ciavola, P. (2019). Influence of particle shape on pebble transport in a mixed sand and gravel beach during low energy conditions: implications for nourishment projects. *Ocean Coast. Manag.* 169, 171–181. doi: 10.1016/j.ocecoaman.2018.12.014

Gundlach, E. R., and Hayes, M. O. (1978). Vulnerability of coastal environments to oil spill impacts. *Mar. Tech. Soc. J.* 12, 18–27.

Hanna, R. G. M. (1995). An approach to evaluate the application of the vulnerability index for oil spills in tropical red sea environments. *Spill Sci. Tech. Bull.* 2, 171–186. doi: 10.1016/S1353-2561(96)00016-3

Harley, M. D., Andriolo, U., Armaroli, C., and Ciavola, P. (2014). Shoreline rotation and response to nourishment of a gravel embayed beach using a low-cost video monitoring technique: san michele-sassi neri, central Italy. *J. Coast. Cons.* 18, 551–565. doi: 10.1007/s11852-013-0292-x

Hayes, M. O., and Michel, J. (1999). Factors determining the long-term persistence of Exxon Valdez oil in gravel beaches. *Mar. Pollut. Bull.* 38, 92–101. doi: 10.1016/S0025-326X(99)00099-5

Hayes, M. O., Michel, J., and Noe, D. C. (1991). Factors controlling initial deposition and long-term fate of spilled oil on gravel beaches. *Proc. Int. Oil Spill Conf. Am. Petrol. Inst.* 1, 453–460. doi: 10.7901/2169-3358-1991-1-453

Jennings, R., and Shulmeister, J. (2002). A field based classification scheme for gravel beaches. *Mar. Geol.* 186, 211–228. doi: 10.1016/S0025-3227(02)00314-6

Jensen, J. R., Halls, J. N., and Michel, J. (1998). A systems approach to environmental sensitivity lndex (ESI) mapping for oil spill contingency planning and response. *Photogramm. Eng. Remote Sens.* 64, 1003–1014.

Kirby, M. F., and Law, R. J. (2010). Accidental spills at sea - risk, impact, mitigation and the needfor co-ordinated post-incident monitoring. *Mar. Pollut. Bull.* 60, 797–803. doi: 10.1016/j.marpolbul.2010.03.015

Kirk, R. M. (1980). Mixed sand and gravel beaches: morphology, processes and sediments. *Prog. Phys. Geogr.* 4, 189–210. doi: 10.1177/030913338000400203

Li, H., and Boufadel, M. (2010). Long-term persistence of oil from the Exxon Valdez spill in two-layer beaches. *Nat. Geosci.* 3, 96–99. doi: 10.1038/NGEO749

Lorenzo, H., Rial, F. I., Arias, P., and Armesto, J. (2009). Fighting against coastal oil spill pollution by means of ground-based radar. *J. Coast. Res.* 56, 846–850.

Mason, T., and Coates, T. T. (2001). Sediment transport processes on mixed beaches: a review for shoreline management. *J. Coast. Res.* 17, 645–657.

Michel, J., and Hayes, M. O. (1993). "Persistence and weathering of Exxon Valdez oil in the intertidal zone – 3.5 years later," in *Proceedings of the 1993 International Oil Spill Conference*, (Washington, DC: American Petroleum Insitute), 279–286. doi: 10.7901/2169-3358-1993-1-279

Michel, J., Hayes, M. O., and Brown, P. J. (1978). Application of an oil spill vulnerability index to the shoreline of lower Cook Inlet. *Alaska. Envir. Geol.* 2, 107–117. doi: 10.1007/BF02380473

Michel, J., Nixon, Z., Holton, W., and White, M. (2014). "Three years of shoreline cleanup assessment technique (SCAT) for the deepwater horizon oil spill, Gulf of Mexico, USA," in *Proceedings of the 2014 International Oil Spill Conference* (Washington, DC: American Petroleum Insitute), 279–286. doi: 10.7901/2169-3358-1993-1-279

Michel, J., Owens, E. H., Zengel, S., Graham, A., Nixon, Z., Allard, T., et al. (2013). Extent and degree of shoreline oiling: deepwater horizon oil spill. Gulf of Mexico, USA. *PLoS One* 8:e65087. doi: 10.1371/journal.pone.0065087

Montanari, A., Mainiero, M., Coccioni, R., and Pignocchi, G. (2016). Catastrophic landslide of medieval portonovo (Ancona, Italy). *GSA Bull.* 128, 1660–1678. doi: 10.1130/B31472.1

Nansingh, P., and Jurawan, S. (1999). Environmental sensitivity of a tropical coastline (Trinidad, West Indies) to oil spills. *Spill Sc. Tech. Bull.* 5, 171–172. doi: 10.1016/S1353-2561(98)00052-8

National Oceanic and Atmospheric Administration [NOAA] (2002). *Environmental Sensitivity Index Guidelines, Version 3. NOAA Technical Memorandum Nos OR and R*11. Seattle, WA: NOAA Ocean Service.

National Oceanic and Atmospheric Administration [NOAA] (2007). *Alabama ESIMAP 21: Bon Secour Bay*. Seattle, WA: NOAA Response and Restoration.

Nelson, J. R., and Grubesic, T. H. (2018). Oil spill modeling: risk, spatial vulnerability, and impact assessment. *Prog. Phys. Geogr.* 42, 1–16. doi: 10.1177/0309133317744737

Nixon, Z., and Michel, J. (2018). A Review of distribution and quantity of lingering subsurface oil from the Exxon Valdez Oil Spill. *Deep-Sea Res. Part II* 147, 20–26. doi: 10.1016/j.dsr2.2017.07.009

Nixon, Z., Michel, J., Hayes, M. O., Irvine, G. V., and Short, J. (2013). "Geomorphic factors related to the persistence of subsurface oil from the Exxon Valdez oil spill," in *Proceedings of the Symposium in Applied Coastal Geomorphology to Honor Miles O*, eds T. Kana, J. Michel, and G. Voulgaris, (Hayes: Journal of Coastal Research), 115–127. doi: 10.2112/si_69_9

Nixon, Z., Zengel, S., Baker, M., Steinhoff, M., Fricano, G., Rouhani, S., et al. (2016). Shoreline oiling from the Deepwater Horizon oil spill. *Marine Pollution Bulletin* 107, 170–178. doi: 10.1016/j.marpolbul.2016.04.003

Olita, A., Fazioli, L., Tedesco, C., Simeone, S., Cucco, A., Quattrocchi, G., et al. (2019). Marine and coastal hazard assessment for three coastal oilrigs. *Front. Mar. Sci.* 6:274. doi: 10.3389/fmars.2019.00274

Owens, E. H., and Sergy, G. A. (2000). *The SCAT Manual – A Field Guide to the Documentation and Description of Oiled Shorelines*, 2nd Edn. Edmonton, AB: Environment Canada, 108.

Owens, E. H., and Teal, A. R. (1990). "Shoreline cleanup following the Exxon Valdez oil spill: field data collection within the S.C.*A.T. program*," in *Proceedings of the 13th Arctic and Marine Oil Spill Program Tech*, (Ottawa, ON: Seminar, Environment Canada), 411–421.

Pincinato, F. L., Riedel, P. S., and Milanelli, J. C. C. (2009). Modelling an expert GIS system based on knowledge to evaluate oil spill environmental sensitivity. *Ocean Coast. Manag.* 52, 479–486. doi: 10.1016/j.ocecoaman.2009.08.003

Pourvakhshouri, S. Z., and Mansor, S. (2003). Decision support system in oil spill cases (literature review). *Disaster Prevent. Manag.* 12, 217–221. doi: 10.1108/09653560310480695

Quick, M. C., and Dyksterhuis, P. (1994). "Cross-shore transport for beaches of mixed sand and gravel," in *Proceedings of the International Symposium: Waves-Physical and Numerical Modelling*, (Montreal, QC: Canadian Society of Civil Engineers), 1443–1452.

Regione Marche (2005). Studi, indagini, modelli matematici finalizzati alla redazione del piano di difesa della costa. *Bollet. Uff. Reg. Marche* 21, 4199–4675.

Ribotti, A., Antognarelli, F., Cucco, A., Falcieri, M. C., Fazioli, L., Ferrarin, C., et al. (2019). An operational marine oil spill forecasting tool for the management of emergencies in the italian seas. *J. Mar. Sci. Eng.* 7:1. doi: 10.3390/jmse7010001

Romero, A. F., Abessa, D. M. S., Fontes, R. F. C., and Silva, G. H. (2013). Integrated assessment for establishing an oil environmental vulnerability map: case study for the Santos Basin region. *Brazil Mar. Pollut. Bull.* 74, 156–164. doi: 10.1016/j.marpolbul.2013.07.012

Santos, C. F., and Andrade, F. (2009). Environmental sensitivity of the Portuguese coast in the scope of oil spill events-comparing different assessment approaches. *J. Coast. Res., Spec. Issue* 56, 885–889.

Xu, L., Li, J., and Brenning, A. (2014). A comparative study of different classification techniques for marine oil spill identification using RADARSAT-1 imagery. *Remote Sens. Envir.* 141, 14–23. doi: 10.1016/j.rse.2013.10.012

Zengel, S., Bernik, B. M., Rutherford, N., Nixon, Z., and Michel, J. (2015). Heavily oiled salt marsh following the deepwater horizon oil spill, ecological comparisons of shoreline cleanup treatments and recovery. *PLoS One* 10:e0132324. doi: 10.1371/journal.pone.0132324

Zengel, S., Montague, C. L., Pennings, S. C., Powers, S. P., Steinhoff, M., Fricano, G., et al. (2016). Impacts of the deepwater horizon oil spill on salt marsh periwinkles (*Littoraria irrorata*). *Environ. Sci. Tech.* 50, 643–652. doi: 10.1021/acs.est.5b04371 doi: 10.1021/acs.est.5b04371

Conflict of Interest Statement: The authors declare that the research was conducted in the absence of any commercial or financial relationships that could be construed as a potential conflict of interest.

frontiers in Earth Science

ORIGINAL RESEARCH
published: 13 September 2019
doi: 10.3389/feart.2019.00228

Morphological Evolution of an Intertidal Area Following a Set-Back Scheme: A Case Study From the Perkpolder Basin (Netherlands)

*Riccardo Brunetta[1], João Salvador de Paiva[2] and Paolo Ciavola[1]**

[1] Department of Physics and Earth Sciences, University of Ferrara, Ferrara, Italy, [2] HZ University of Applied Sciences, Vlissingen, Netherlands

OPEN ACCESS

Edited by:
Denise Reed,
The University of New Orleans,
United States

Reviewed by:
Neil Ganju,
USGS Woods Hole Coastal and Marine Science Center, United States
Danika Van Proosdij,
Saint Mary's University, Canada
Harry Frederick Leonard Williams,
University of North Texas,
United States

***Correspondence:**
Paolo Ciavola
cvp@unife.it

Specialty section:
This article was submitted to Geohazards and Georisks, a section of the journal Frontiers in Earth Science

Received: *09 April 2019*
Accepted: *19 August 2019*
Published: *13 September 2019*

Citation:
Brunetta R, de Paiva JS and Ciavola P (2019) Morphological Evolution of an Intertidal Area Following a Set-Back Scheme: A Case Study From the Perkpolder Basin (Netherlands). Front. Earth Sci. 7:228. doi: 10.3389/feart.2019.00228

In the present context of sea-level rise, the reconstruction of previously reclaimed intertidal areas represents an opportunity to build dynamic coastal defences to decrease flooding under storm conditions by the dissipation of wave and surge energy across the vegetated domain. In Europe, this approach started in the late 1990s along the coast of eastern and southern England, but it is becoming common to many European countries around the North Sea margin. The process of salt-marsh restoration normally develops around the opening or removal of flood protection structures and gradual flooding of the hinterland. If the intertidal zone starts to experience vertical accretion, vegetation will colonize the area and a saltmarsh will develop. This paper presents the morphological evolution and sediment distribution in the Perkpolder basin, SW Netherlands (NL), following the conversion of a reclaimed area into a tidal flat, after the opening of an inlet in the flood defence structures in June 2015. The main focus of this study is the description of the evolution of the tidal flat since the opening of the inlet and the identification of spatio-temporal conditions for the evolution of a salt marsh. To reach this objective, several topographic surveys were undertaken, together with sediment surface sampling. Sedimentation rates at fixed sampling stations were assessed during the transition between neap and spring tides over a period of 1 month and 2 weeks. The morphological analysis of the inlet evolution proved that 6–8 months after the opening the inlet reached an equilibrium state. The average accretion rate across the whole study area was about 6–7 cm per year^{-1}. The average deposited sediment was about 100 g per m^{-2} per day. Considering the sedimentation rates in the most elevated regions, 80–110 cm above NAP (Normaal Amsterdams Peil), and assuming that the sedimentation rate will remain constant in time, the conditions for the on-set of salt-marsh formation will not be reached before 8–10 years. Projections indicate that the area located at +50 cm above NAP will not become a mature marsh before 50 years.

Keywords: saltmarsh restoration, artificial tidal flat, building with nature, sedimentation rates, saltmarsh accretion

INTRODUCTION

Tidal flats are intertidal, non-vegetated, soft sediment habitats generally composed of mud and sand (Dyer et al., 2000), often backed by salt marshes that grow at higher elevations within the intertidal fringe. Coastal salt marshes are usually found along low-energy and temperate coastlines (Allen, 1992; Adam, 2011), except for the extensive mangrove forests that are located at tropical latitudes (Odum et al., 1982). Salt marsh plants, mostly herbaceous halophytes, are adapted to tolerate regular saltwater inundation, especially the species that colonize the low-elevated parts (Pratolongo et al., 2019).

Despite the fact that salt marshes were historically considered as a source of insalubrious conditions (humidity, mosquitoes) and as land unsuitable for agriculture (Boavida, 1999), they can offer numerous ecosystem services. Several studies have discussed the benefits derived from these environments to nature and mankind: (i) they support fisheries as they host economically and ecologically important fish species (Boesch and Turner, 1984; MacKenzie and Dionne, 2008; Barbier et al., 2011); (ii) they play a role in the carbon cycle as they are able to shift carbon sequestering from the short-term (10–100 years) to the long-term (1000 years) (Mayor and Hicks, 2009); (iii) they can host leisure activities and have an important role in local cultural aspects (Weis, 2016). The decline of these environments during the last 50 years has caused an important loss of ecosystem services (Millennium Ecosystem Assessment, 2005). Nevertheless, recent assessments on the future of salt marshes are quite controversial. In fact, global-scale predictions suggest that the capacity of marshes to recover against sea-level rise are overestimated (Nardin and Edmonds, 2014; Crosby et al., 2016; Spencer et al., 2016), but local-scale assessments concluded the opposite prediction (Kirwan et al., 2016). The reason behind this discrepancy is that large-scale assessments do not consider the biophysical feedback mechanisms that are included instead in local-scale models (Kirwan et al., 2016). Several local-scale studies demonstrated that coastal wetland loss can be avoided by using nature-based adaptation in coastal management solutions (Schuerch et al., 2018).

One of the most important roles of salt marshes is coastal protection, as they are able to attenuate wave energy and to consequently reduce the flood hazard (Bouma et al., 2014). Many studies demonstrated the effect of vegetation and wetlands on wave impact reduction (Möller et al., 2014; Smolders et al., 2015; Vuik et al., 2016) and storm surge (Stark et al., 2015; Leonardi et al., 2018).

Nature-based solutions are to be preferred to conventional coastal defences because they are effective and have a reduced cost if compared to traditional approaches (Koch et al., 2009; Borsje et al., 2011; Temmerman et al., 2013). In order to support the efficient design of nature-based solutions, a deep understanding of feedback effects between biotic (e.g., vegetation) and non-biotic factors is needed.

Previous studies focussed on established, evolving or deteriorated salt marshes; few works analyzed the processes acting on newly developed salt marshes. Several works defined how hydrological and sedimentological processes influence topographic evolution of the marsh in response to sea level rise, with surface growth following an asymptotic law (Pethick, 1981), and how the hydroperiod spatially and temporally changes sediment accretion and accumulation (Cahoon and Reed, 1995). Furthermore, several studies discussed the adaptation capacity of salt marshes to keep pace with sea level rise (Stevenson et al., 1986; van Wijnen and Bakker, 2001; Schuerch et al., 2013, 2018; Crosby et al., 2016; Kirwan et al., 2016; Spencer et al., 2016). Mathematical models have been implemented to describe sediment transport inside salt marshes and tidal creeks (Kirwan et al., 2010; Green and Hancock, 2012; Reimer et al., 2015), and biological parameters have been introduced to explain how the eco-geomorphological state of marshes influences their contribution to sediment budgets (Stark et al., 2017). In this type of environment, sediment deposition is influenced by a number of factors, such as seasonal conditions (Reef et al., 2018), sediment availability and grain-size distribution (Schuerch et al., 2014), storm frequency and intensity (Schuerch et al., 2012).

Despite our current knowledge of hydrological and sedimentological processes on well-developed salt marshes, there have been few observations and experiments concentrating on the mechanism of salt marsh creation (Gunnell et al., 2013). A better understanding of how a salt marsh develops is necessary to estimate the future distribution of vegetation as well as the time required to observe the transition from tidal flat to marsh environments, natural or artificial.

The capacity of predicting salt marsh development is also important to understand if a "set-back" approach is feasible, i.e., the environment is free to develop without any human intervention, such as building new coastal structures to control the process.

The existence of salt marshes is critically dependent on how fast sediment accumulates with respect to sea level rise (Redfield, 1972; Orson et al., 1985; Schuerch et al., 2012). Using 40 years of study of salt marshes in the Wadden sea (Netherlands), Bakker (2014) evidenced that a natural salt marsh forms when a mud or sand flat rises through vertical accretion until it lies just below the Mean High water Tide level (MHT), so that it is submerged twice a day for several hours and it is dry the rest of the time.

In the current study, this concept will be applied to verify the possibility to predict the future evolution of a young, artificially created, tidal flat at Perkpolder (Zeeland, NL).

The overall aims of the study are: (i) to understand the patterns of morphological variation of the tidal flat; (ii) to describe patterns of sediment accretion across the most elevated parts of the flat; (iii) to predict where and when an optimal elevation will be reached for the establishment of permanent vegetation; (iv) to define the morphological evolution of an artificial inlet that was dredged to establish communication with the estuary.

STUDY SITE

The study area is located in Perkpolder, a previously reclaimed area in the municipality of Hulst, in the province of Zeeland (Netherlands) (**Figure 1**). This site is part of the Scheldt Estuary, characterized by a length of 355 km from source to mouth,

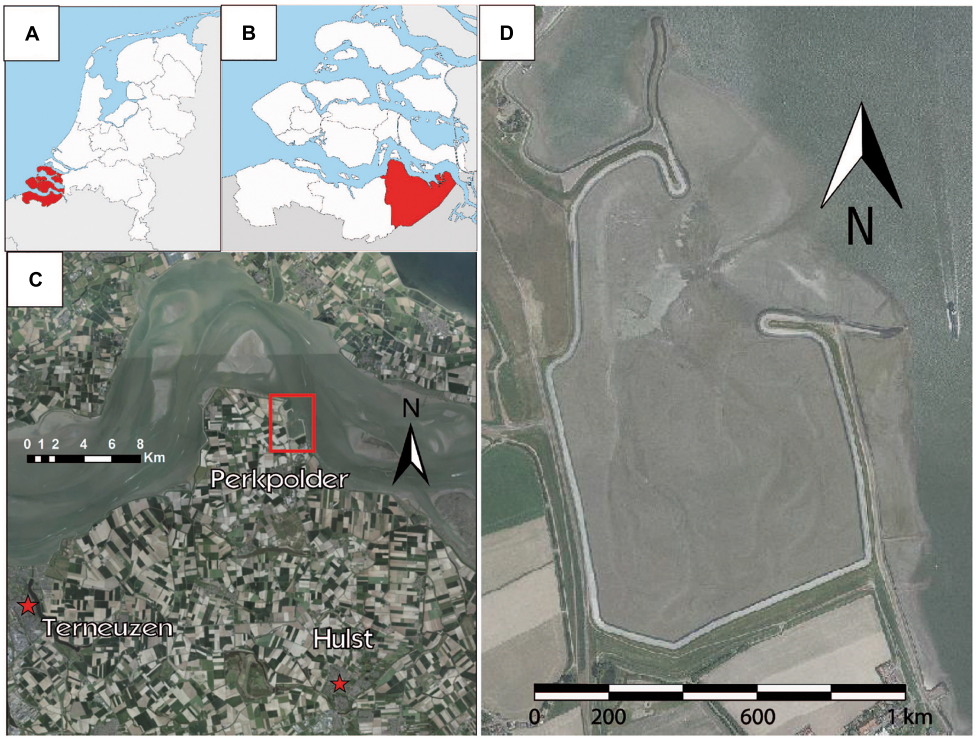

FIGURE 1 | (A) Map of the province of Zeeland and **(B)** the municipality of Hulst. **(C)** Location of the Perkpolder tidal basin within the Scheldt Estuary and **(D)** 1:15000 orthophoto from the Province of Zeeland of the area, captured in June 2017.

with a total catchment area of 21863 km^2. About 10 million people live in the river basin (Meire et al., 2005). According to the geometry of the estuarine channel and its hydraulics, the Scheldt is divided into three different zones: a narrow part dominated by freshwater from Gentbrugge to Rupelmonde, an intermediate zone from Rupelmonde to Hansweert, and a wide and well-mixed part from Hansweert to the mouth (Nihoul et al., 1978). The mud of the Scheldt Estuary has both marine and terrestrial origin; the ratio between these two muds of different sources is highly variable, partially due to the variation in the location of the turbidity maximum (ETM), and partially due to changes in sediment load of the tributaries of the Scheldt (Swart, 1987; Wartel et al., 1993; Brinke, 1994; Chen et al., 2005). The sediment transport rates depend on the seasons and on the tidal cycles. The suspended concentration is usually higher during the flood and during spring tides than during ebb and neap tides. In winter, the suspended concentration and the tidal amplitude are better correlated than during the summer, and the maximum concentration occurs one tide after the highest tide. These seasonal variations are connected to several processes, like changes in freshwater discharge, temperature, land erosion, and, in a less significant way, wave-induced resuspension (Fettweis et al., 1998). The study area falls in the mid-part of the estuary, the most important for sediment transport. The strong tidal currents, combined with the occurrence of flocculation due to the mixing of tidal and riverine water masses, as well as residual currents, increase the residence time of the suspended material, reaching values from hundreds of milligrams per liter to a few grams per liter (Chen et al., 2005). The mean tidal range of the estuary varies from about 3.8 m at Vlissingen (at the mouth) to about 5.2 m at Antwerp (78 km upstream); thus, most of the Western Scheldt is meso-tidal. Current velocities are up to 1–2 m s^{-1} in the main channels, for an average tidal range. The mean Spring tidal range of the study area is about 5 m (Claessens and Belmans, 1984).

The study area is a 75-hectares tidal flat (**Figure 2**), created as a cooperation project between Rijkswaterstaat (Dutch Ministry of Infrastructure and the Environment) and the regional government. This project, started after the closure of the ferry service between Kruiningen (Zuid-Beveland) and Perkpolder (Zeeuws-Vlaanderen) in 2003, was named Plan Perkpolder, and it aims at prompting the socio-economic development of the area by combining the construction of recreational facilities and natural environments. One of the most important objectives of this plan was to recreate a tidally-dominated natural ecosystem (Boersema, 2016). This polder was originally dammed in 1210 and the land was reclaimed for crop growth and for building small villages. Subsequently, the land behind the dike subsided, dropping to an elevation below mean sea level. Due to the proximity of the Schaar van Ossenisse, a deep channel in the Western Scheldt, the coast was susceptible to dyke failure. In 1841, a new dyke of about 1 km was built along the coast, but half of it was quickly lost.

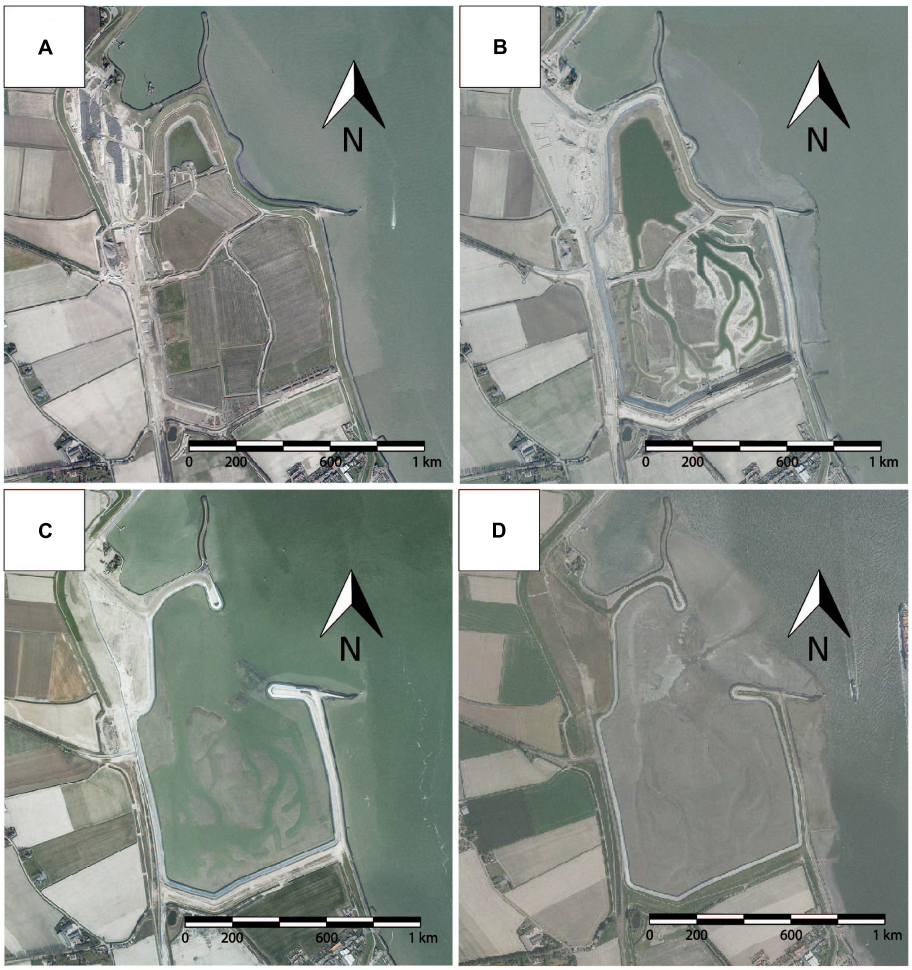

FIGURE 2 | Orthophotos at 1:15000 scale of the Perkpolder basin from the maps of the province of Zeeland; **(A)** before works in March 2014, **(B)** shortly before the opening of the inlet in March 2015, **(C)** in March 2016 and **(D)** in June 2017.

The Perkpolder tidal flat is divided into three zones: the foreshore outside the basin, the pond, and the inner part, where several creeks were dug during the restoration project. There are two main creeks of about 40 m in width; they divide southwards into narrower branches of about 30 m in width, reaching a total length of about 800 m. On 25 June 2015, the dyke was breached (**Figure 2B**) and the salt water of the Western Scheldt started to flow in the basin covering the whole tidal flat. The inlet has a width of about 300 m and its bottom is located at a height of about 0–1 m NAP. The inlet is submerged during high tide only, except for the central part, which is deeper, being at −0.8 m NAP. This deeper permanent channel has a width of about 10 m and allows continuous water exchange between the pond and the open estuary.

Field observations, the basin structure, and the presence of a dyke ring support the idea that the flood and ebb currents were the principal agents causing morphological changes, as wave action is negligible given the small internal fetch and the unlikely penetration across the shallow inlet (**Figures 2C,D**). Field observations after the opening also suggest that benthic macro fauna rapidly started to colonize the area, providing food for bird communities.

METHODOLOGY

Morphological Analysis

The monitoring strategy aimed at identifying the evolution of the area immediately after the opening of the inlet. Following previous authors (Thomas and Ridd, 2004; Nolte et al., 2013), sedimentation patterns are analyzed in a short-time interval, to obtain data from a spring-neap tidal cycle (15 days), as well as over a longer-period (32 days). Additionally, from June 2015 to January 2017, seven multi-beam datasets of the inlet area were obtained from surveys undertaken by Rijkswaterstaat. A cross-section (**Figure 3**) was digitized across the inlet to see its evolution through time, assessing changes in width, depth, and wetted area.

In order to assess the morphological evolution of the tidal flat through time, three Lidar surveys, with a 2 m x 2 m resolution,

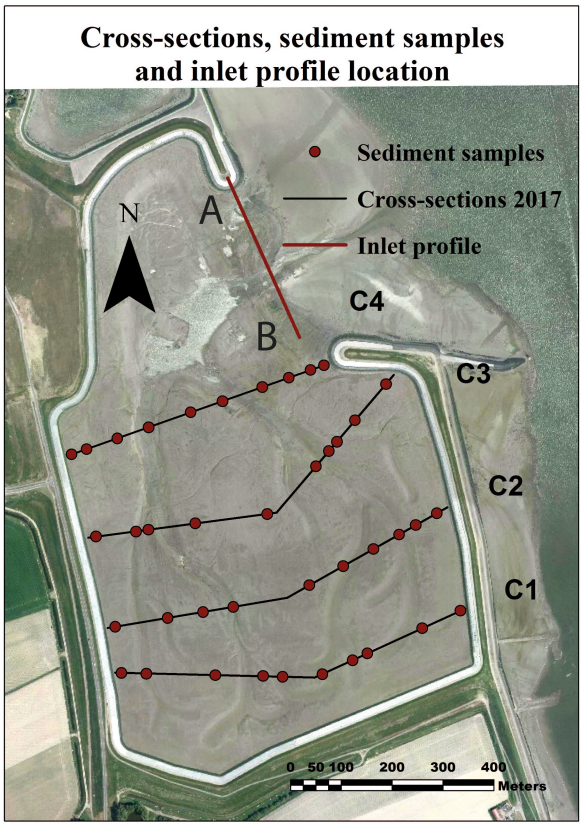

FIGURE 3 | DGPS cross-sections (C1–C4), inlet profile **(A–B)** and location of sediment samples.

were used. The surveys were performed by Rijkswaterstaat. As the unprocessed point clouds were not supplied, a direct evaluation of the vertical accuracy could not be undertaken. Notice that accuracy depends on the Lidar sensor resolution (Wehr and Lohr, 1999), the landscape features of the intertidal environment (Evans et al., 2019) and the presence of vegetation (Hladik and Alber, 2012). In low and high marshes, the vegetation clearly influences the accuracy, causing errors from 0.1 to 0.45 m (Morris et al., 2005; Rosso et al., 2006; Wang et al., 2009; Schmid et al., 2011; Millard et al., 2013), requiring corrections to DTMs. As in Perkpolder, the tidal flat is completely un-vegetated and with no large bed features, it was considered unnecessary to re-process further the DTMs. As shown by Fernandez-Nunez et al. (2017), bare mud in Lidar surveys is represented with very high accuracy (0.04–0.09 m), and the effects of corrections in this kind of environment can be meaningless or even increase the error.

The first survey was undertaken in June 2015, in correspondence with the opening of the inlet; the second survey was undertaken in April 2016, and the third one in February 2017. Two RTK-DGPS fieldwork campaigns were performed on 12–15 June and 6–8 December 2017 (**Figure 3**); the DGPS survey of June was not taken into account for morphological analysis because of its proximity with the Lidar survey of February. Four cross-sections were prepared in advance on ArcGIS software and uploaded on the GPS datalogger to collect the points along selected orientations; during the successive surveys, the points of measurements where repeated with absolute care. The spacing between the surveyed points was about 10 m, except inside the creeks, where the spacing was about 5 m or less; the horizontal and the vertical accuracy was sub-centimetric. The adopted datum is the NAP (Normaal Amsterdam Peil), while the coordinate system is the Amersfoort/RD new. Data was manipulated in the ArcGIS software using "natural neighbor" as an algorithm of interpolation to create the DTMs. To evaluate the rate of sediment accretion and volume gain/loss, the datasets were processed with the Geomorphic Change Detection (GCD) tool of Wheaton et al. (2010). The tool performs an analysis of vertical variations and volume gain and loss, including an evaluation of uncertainty. According to Brasington et al. (2003), the individual errors of DTMs when a DoD (DEM of Difference) is made. They can be propagated as:

$$\delta u_{\mathrm{DoD}} = \sqrt{(\delta z_{\mathrm{new}})^2 + (\delta z_{\mathrm{old}})^2} \quad (1)$$

In equation (1), δu_{DoD} is the propagated error, while δz_{New} and δz_{Old} are the individual errors of each DTM. Because no vertical accuracy was set-up as the unprocessed point clouds were not available, the best option was to consider a range of the individual error in this type of environment (0.04–0.09 m), implying that the error of the new DTMs ranged between 0.06 and 0.12 m. The GCD tool also allows to choose the threshold below which lower variations are considered meaningless: in this case the calculations were made considering thresholds of 0.05, 0.10, 0.15 m, and no threshold at all, as previously done by Duo et al. (2018). Because of different vertical accuracies in the datasets (e.g., Lidar vs. DGPS), the interpretation of DTM changes has higher reliability only when the same types of datasets are compared. This means that the most consistent data intervals are from the first 2 years after the inlet opening (June 2015–February 2017). To study the additional period from February 2017 to December 2017, a comparison between datasets was made (i.e., Lidar vs. DGPS), but the interpretation must be taken with extreme caution.

Particles Size Analysis (PSA)

As the same time as topographic measurements, 40 sediment samples were collected (10 samples distributed in each cross section) to characterize the particle size distribution across the tidal flat. The adopted procedure for Particle Size Analysis (PSA) follows the Italian national standard set by ICRAM (2004). The sediment samples were treated with 120 ml of Hydrogen Peroxide at 16 volumes for several days to remove the organic matter. As the Wentworth scale (Wentworth, 1922) was used to distinguish the sand from mud, the two fractions were separated using a mesh of 63 microns by wet sieving (Widdows et al., 2000). The mud was stored in large pitchers to decant, while the sand was dried at 105°C. Then, all the extraneous material (e.g., whole shells or fragments, etc.) was removed using another sieve of 1 mm and the sand content was quantified. No further analysis on the sand fraction was carried out, considering the small quantity (e.g., a few grams,

less than 30% for most of the samples). After several days, the water in the pitchers was removed and the mud was displaced into smaller beakers and weighed. Part of the mud was then moved into glass petri dishes and dried at 105°C. Finally, a Micromeritics Sedigraph Analyzer was used to discriminate the percentages of silt and clay. The results of the PSA were plotted onto the Shepard's diagram (Shepard, 1954) using the Triplot program (McHone, 1977), and a map of sediment distribution was prepared.

Measurement of Sedimentation Rate Across the Tidal Flat

Sediment deposition was measured using traps built with Perspex Petri dishes with a diameter of 9 cm and a height of 1.5 cm, placed along each cross section at 10 different spots, at the same location of the sediment samples. This kind of sediment trap has been widely used since the 1980s (Reed, 1989; French et al., 1995; Leonard, 1997; Brown, 1998; Culberson et al., 2004; Neumeier and Ciavola, 2004; van Proosdij et al., 2006). This method is highly economical and provides a good spatial resolution of sedimentation (Marion et al., 2009). Despite the fact that this technique is commonly used, there is no settled standard; the structure of the Petri dishes differs from author to author, depending on the purpose of the study, the sediment accretion rate, the occurrence of precipitation, re-suspension, or other considered variables or disturbances. The technique principally varies from using pre-weighted filters for small time periods, to using the petri dish itself as a trap, left in the tidal flat for many days or weeks, like Butzeck et al. (2015) or Temmerman et al. (2003) have done. The choice of this type of Petri dish was based on the seasonal period chosen for our study (winter-summer), the weather conditions normally experienced at the site (for example absence of torrential rainfalls), and the vertical accretion expected on this type of tidal flat from literature studies. All the traps were covered by the tide for the same time period and by all the tides, since neap tides during experimentation were high enough to cover the whole basin. The vertical accretion did not completely bury the traps, with the exception of 2 Petri dishes. These Petri dishes were located in the southern part of the area (cross-section C1) inside the creeks, where the accretion was observed to be the highest even from the analysis of the topographic surveys. Consistent rainfall was absent while traps were operating, so it did not influence the sediment deposition. In order to avoid that near-bed tidal currents displaced traps, the Petri dishes were nailed into the ground using pickets glued in the center of the dish. One spring-neap tidal cycle (15 days) and a long-period tidal cycle (32 days) were measured in two different time intervals (**Figure 4**).

The first measurement campaign employed 40 Petri dishes (10 per cross section) which were deployed from 15 May 2017 to 16 June 2017. A second measurement campaign employed 40 Petri dishes from 13 to 27 June, therefore covering a shorter time interval that represents a spring-neap tidal cycle. Only 57 traps out of 80 deployed were recollected after the two campaigns. The samples were dried and weighed, and the recovered sediment amount was normalized according to the days each Petri dish was left in the tidal flat to obtain values in grams day^{-1}. The normalization was made assuming a constant rate of deposition per day.

Loss on Ignition Analysis

Part of the bed samples was used to determine the LOI content (Loss on Ignition) according to the method of Heiri et al. (2001). The analytic procedure was divided into two phases: (1) each sediment sample was placed in an aluminum cup and then dried for a week in an oven at 80°C to remove water and determine the dry weight; (2) the dried sediment was moved into ceramic cups and weighed. The samples were then burnt at 550°C for 6 h and weighed once again to define the LOI.

RESULTS

Morphological Datasets

Four time intervals of morphological evolution could be considered: (i) from June 2015 to April 2016; (ii) from April 2016 to February 2017; (iii) from February 2017 to December 2017; (iv) the whole period, from June 2015 to December 2017. In **Figure 5** the profiles from Lidar surveys and also from DGPS surveys are shown.

For what concerns the first interval between June 2015 and April 2016 (**Figures 6A,B**), the accretion is centered principally in the areas adjacent to the creeks. Overall, the accretion increases moving southwards on the tidal flat; the highest and the lowest values are located in the western creek, while the lowest parts of the creek show erosion (reaching approx. 115 cm of erosion, 11.5 cm month^{-1}). The accretion is not stable along the creeks, in fact in some areas, in particular in the center of the eastern creek and in the further western creek, the elevation changes are inhomogenous. On the other hand, the upper part of the flat (the southernmost part of the polder) gained a large quantity of sediment (approx. 125 cm of accretion, 12.5 cm month^{-1}).

During the first 10 months after the opening of the inlet, the tidal flat experienced a great sediment gain. If we use the different error thresholds, we observed changes in the order of thousands of cubic meters: (i) with a threshold of 0.05 m the net sediment gain is 19300 $\pm$ 8400 m^3; (ii) with a threshold of 0.10 m the value is about 16900 $\pm$ 10400 m^3; (iii) with a threshold of 0.15 m the net gain is around 13800 $\pm$ 10000 m^3 and (iv) considering no threshold at all the total sediment budget is 20000 m^3. It is clear that even considering the highest threshold, the tidal flat is gaining sediment.

From April 2016 to February 2017, accretion and erosion have a similar trend; both maximum erosion and accretion reach 60 cm in 10 months, 6 cm month^{-1}. The highest values are concentrated in the western creek with the maximum erosion at the beginning of the creek, while the maximum accretion occurs in the central-southern part of the creek. As shown in **Figure 6B**, the rate of accretion seems to become stable in the whole tidal flat, with the exception of the creeks that have the highest rates. This influenced the volume calculations: during this 10 months, the total sediment budget was: (i) with a threshold of 0.05 m, 14000 $\pm$ 8800 m^3; (ii) with a threshold of 0.10 m,

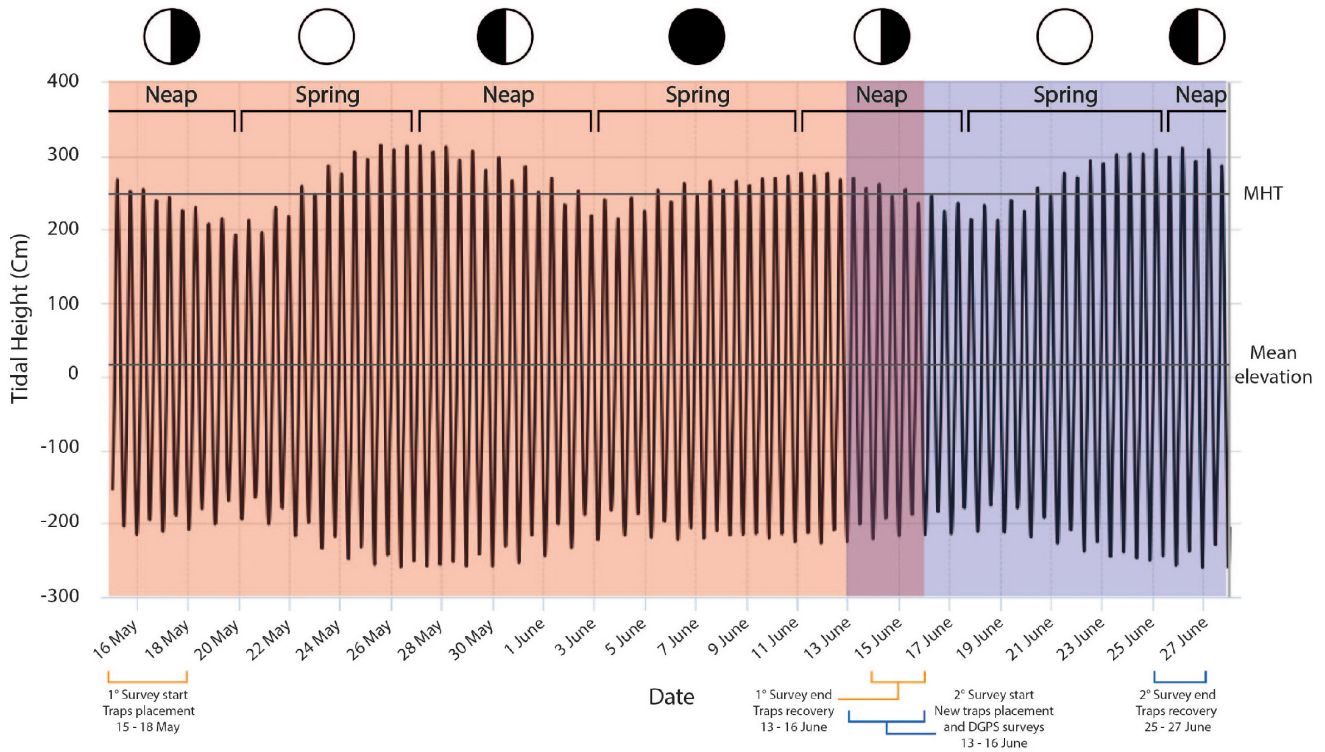

FIGURE 4 | Neap and Spring tides during the experiments. The first experiment is from 15 of May to 16 of June; the second experiment is from 13 to 27 of June. Data from the tidal station of Walsoorden. The "Mean Elevation" horizontal line marks the mean elevation of the tidal flat.

4800 ± 4200 m^3; (i) with a threshold of 0.15 m, 850 ± 1100 m^3 and (iv) with no threshold at all 17000 m^3. However, it is notable that the tidal flat continues to experience sediment accumulation in a homogeneous way, with no evident morphological changes. In the last time interval, between February 2017 and December 2017, the sediment gain estimation is about 16200 m^3.

The net sedimentation rates are: (i) from June 2015 to April 2016, ∼1800 m^3 $month^{-1}$; (ii) from April 2016 to February 2017, ∼1400 m^3 $month^{-1}$; (iii) from June 2017 to December 2017, ∼1600 m^3 $month^{-1}$. Thus, the first two analyzed periods result to have quite similar sedimentation rates, characterized by a reduction of sediment gain as the tidal flat builds up. The last period is characterized by a higher rate of sediment accumulation, but this last calculation derives from the DGPS surveys and the value is probably overestimated. Considering the whole period since the opening of the inlet in June 2015 (**Figure 6C**), the total sediment gain on the whole tidal flat was about ∼30000 m^3 from June 2015 to February 2017, of which over than 16000 m^3 estimated from February to December 2017.

The same logic of error thresholds was employed to find the most reliable sediment accretion rate (**Table 1**). The rate of accretion calculated over the whole study area (i) from June 2015 to April 2016 was 6 ± 2.5 cm $year^{-1}$ (averaged using all thresholds); (ii) from April 2016 to February 2017 was 4.8 ± 3 cm $year^{-1}$ (using only the 0.05 threshold as data variability was smaller); (iii) from February 2017 to December 2017, only an estimation of 5.7 cm $year^{-1}$ can be produced. No quantification of the error can be performed as two heterogeneous datasets (DGPS vs. Lidar) were used.

Surface Sediment Characteristics

The granulometric classes in which the sediment samples fall are sand, silty sand, sandy silt, loam and clayey silt. Overall, the samples that contain a significant amount of sand were found next to the channels; the sand content decreases moving southwards, as showed in **Figure 7A**. In **Figure 7B** the collected samples are classified using Shepard's diagram. Notice that pure silt and clay fractions are generally under-represented.

Sedimentation Rates

No traps were completely buried, except two, implying that the collected sediment was a realistic measure of the total sediment flux. These Petri dishes were located in the southern part (cross-section C1) and inside the creeks, where the accretion measured by topographic surveys was the highest.

The data from the surveys are shown in **Figures 8A,B**, where values of sedimentation rates are presented in grams/m^2 day^{-1}. Due to the strong tidal flow during the first survey, only 18 Petri dishes out of 40 were recovered. Subsequently, because of the reduced density of measurements, it was decided to not interpolate the data.

From 15 May to 17 June 2017 (**Figure 8A**), the amount of sediment trapped ranges between 6.3 g/m^2 day^{-1} to

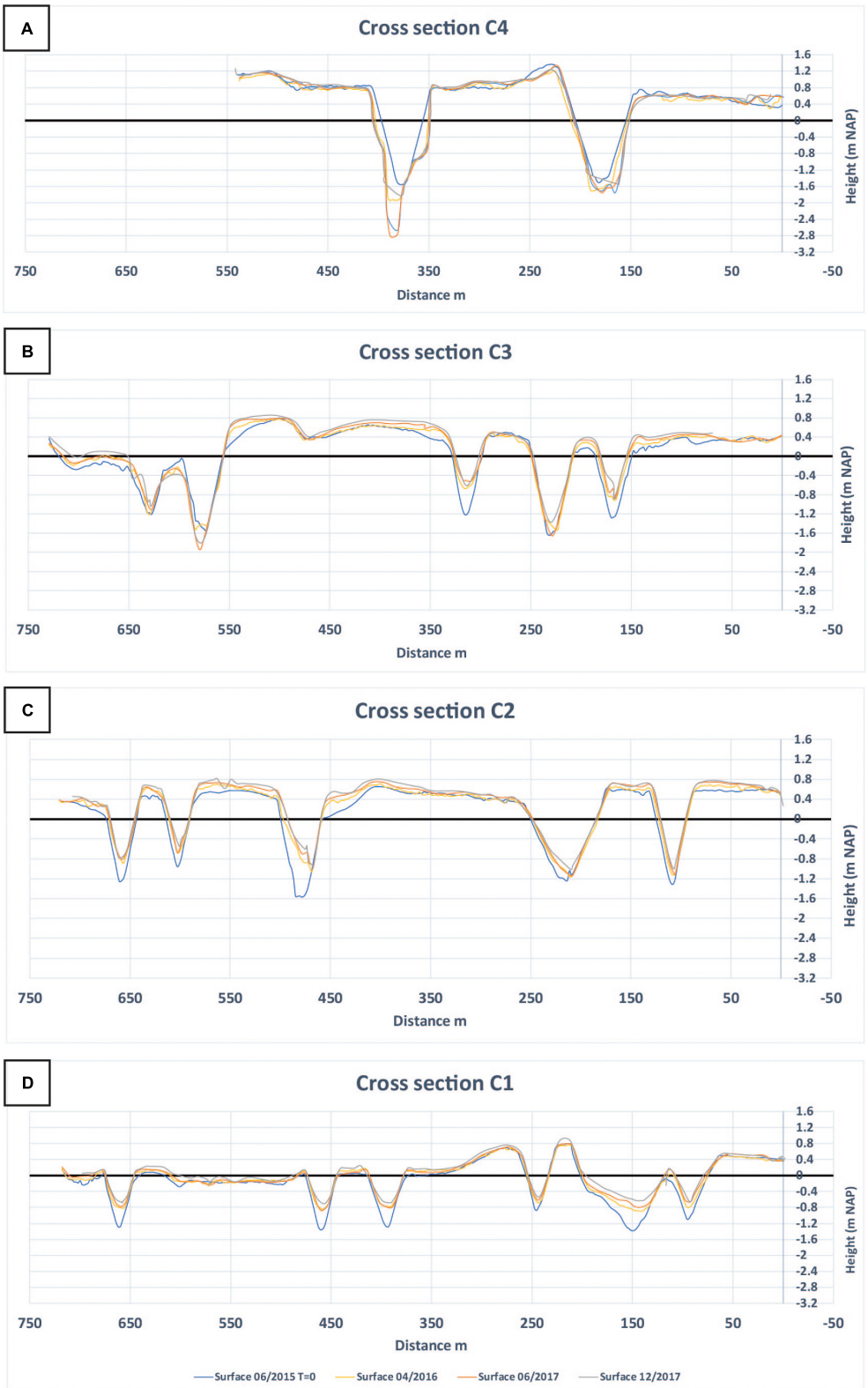

FIGURE 5 | Cross sections from North to South **(A)** C4, **(B)** C3, **(C)** C2, **(D)** C1 extracted from Lidars (2015 and 2016) and from DGPS surveys (June and December 2017). To notice that in the graphs the survey of June 2017 is presented (orange line) to qualitatively assess bed changes but this was not used for volume calculations as it was too close in time with the preceding and subsequent surveys.

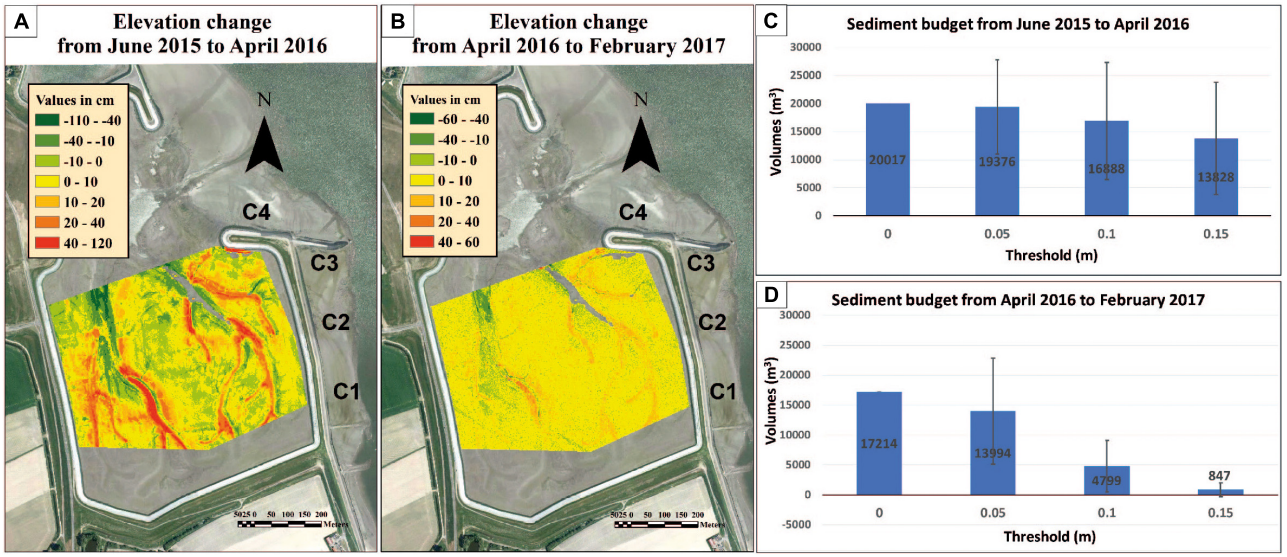

FIGURE 6 | On the left and in the centre **(A,B)** elevation change computed from June 2015 to April 2016 and from April 2016 to February 2017; on the right **(C,D)** sedimentary budget computed for both periods considering errors of 0, 0.05, 0.10 and 0.15 m. See the text for further details on survey methodologies.

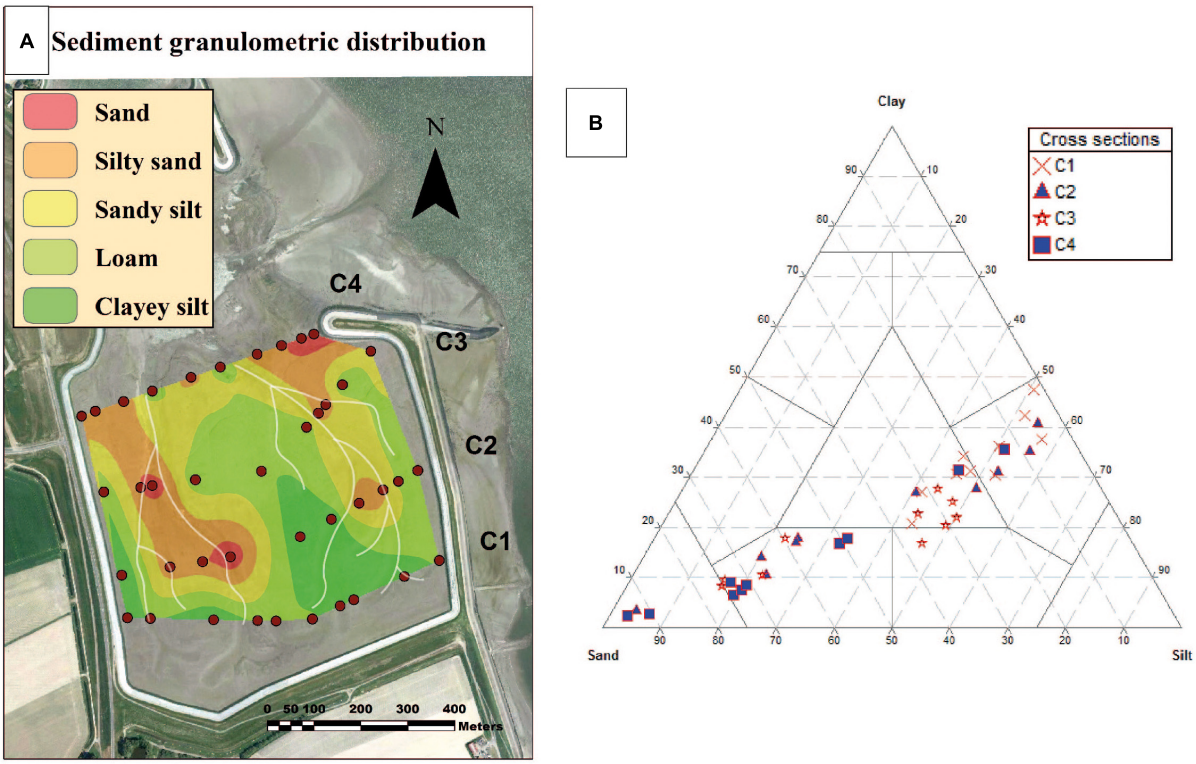

FIGURE 7 | On the left **(A)** sediment granulometric distribution map derived from the analysis of 40 samples collected in Perkpolder. The map was produced using the natural neighbor interpolation. On the right **(B)** Shepard's diagram shows how all samples result from a mixture of end-members of dominant sand and silt fractions.

TABLE 1 | Volume changes and rates of accretion of the study area considering different thresholds for error in the DTM.

DTM Error threshold (m)	Time interval	Volumes (m^3)	Volume Error (m^3)	Rate of accretion (cm $year^{-1}$)	Error (cm $year^{-1}$)
0	June 2015–April 2016	20000	/	6.8	/
0.05	June 2015–April 2016	19300	±8400	6.6	±2.9
0.1	June 2015–April 2016	16900	±10400	5.7	±3.5
0.15	June 2015–April 2016	13800	±10000	4.7	±3.4
0	April 2016–February 2017	17000	/	5.9	/
0.05	April 2016–February 2017	14000	±8800	4.8	±3
0.1	April 2016–February 2017	4800	±4200	1.6	±1.5
0.15	April 2016–February 2017	850	±1100	0.3	±0.4
/	February 2017–December 2017	16200	/	5.7	/

The last row derives from comparison between Lidar and DGPS dataset and errors cannot be estimated due to non-heterogenous datasets.

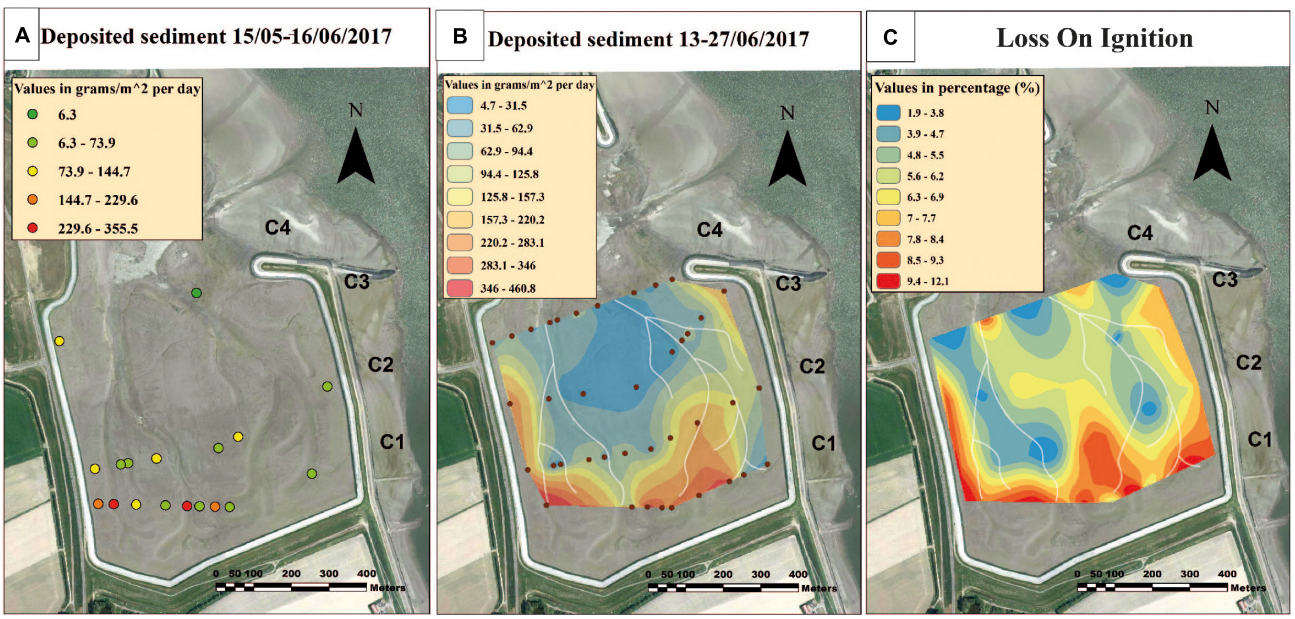

FIGURE 8 | On the left **(A)** sedimentation rates from the 15 May to the 16 June 2017. In the center **(B)** sedimentation rates from 13 June to 27 June 2017. On the right **(C)** Percentage of LOI distribution. All maps were produced using the "natural neighbor" algorithm.

355.5 g/m^2 day^{-1}. The sediment amount increases moving southwards on the tidal flat.

After the second survey, performed after the spring tide of June 2017, 39 petri dishes were collected and analyzed (**Figure 8B**). The amount of deposited sediment per day is in the same range of the first sampling, i.e., between 4.7 g/m^2 and 460.8 g/m^2. The southernmost areas are characterized by larger accumulation, especially next to the creeks and at the border of the tidal flat. The average sediment deposition across the flat is about 111.9 g/m^2 day^{-1} in the first survey and about 117.6 g/m^2 day^{-1} in the second one.

Loss on Ignition

The distribution LOI is presented in **Figure 8C**. Overall, the organic carbon content increases moving southwards across the basin. The greatest amount is distributed around the edges, next to the dyke, and in the central area. Clayey silts contain the highest concentration of organic carbon, reaching values around 8.39–12.07%. The lowest values of 1.85–4.74% are located next to the creeks, associated to sandy sediments.

Inlet Morphology

The Dutch Ministry of Public Works (Rijkswaterstaat) supplied eight multi-beam surveys, with a cell size of 1 m x 1 m, performed between June 2015 and January 2017 (respectively 25 June 2015, 30 July 2015, 17 September 2015, 8 January 2016, 19 April 2016, 20 July 2016, 31 October 2016, 27 January 2017). For each survey, the rate of change of the width, depth, and area of the cross-section of the inlet was calculated.

The width was calculated at the bankfull, choosing as boundaries the points of increasing slope as shown in **Figure 9A**. The depth of the thalweg was measured considering the differences of heights between the

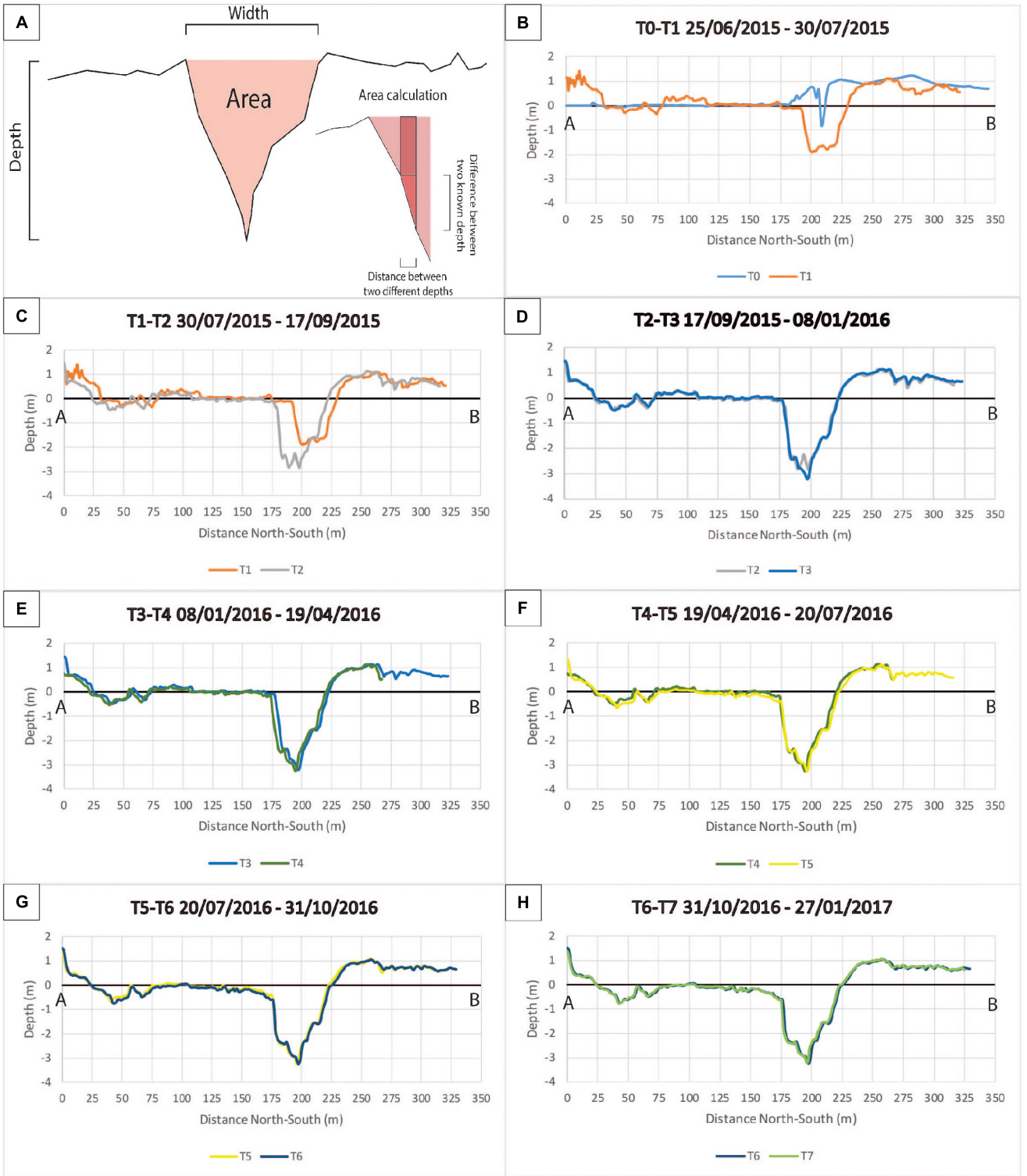

FIGURE 9 | (A) Scheme of the calculated parameters and **(B–H)** profile changes from the opening of the inlet in June 2015 to January 2017.

vertical position between two time intervals. Changes in inlet characteristics were calculated by dividing one observation by the previous one. Therefore no change equals to 1, width or depth reduction is represented by values <1, and width or depth increase by values >1. In **Figures 9B–H** the profile changes from June 2015 to January 2017 are presented.

As shown in **Figure 10**, after 2–4 months the rate of change slowly decreased, and after 6–8 months the inlet became almost stable.

DISCUSSION

Sedimentological Characteristics of the Tidal Flat

From a sedimentological point of view, the conditions found on this reconstructed tidal flat reflect the typical characteristics of back-barrier flats as outlined by Friedrichs (2011); the pattern of the sediment distribution, defined by coarser sediment in the creeks and on lower flats grading to finer sediment on upper flats reflect the hydrodynamic energy level and sediment supply (Mai and Bartholomä, 2000). As the dominant grain size is silt and clay, defining this as a muddy flat, the presence of coarser sediment in the creeks could be exclusively related to higher peak tidal velocities (Grabemann et al., 2004). In turn, the dominance of muddy sediment in the upper flat may depends on the location of the maximum flood line compared to the tidal flat elevation (Gadow, 1970). Because of the high tidal range, the tidal flat of Perkpolder is completely covered by the water and completely dried every day, with the exception of the northern part of the creeks. Consequently, the proximity to the creeks reflects the higher energy of the flow, allowing the transport of the coarser (sand) sediment as bedload, while the other parts of the tidal flat are characterized by fine suspended sediment due to a lower hydrodynamic regime. Furthermore, due to the reduced fetch of the basin enclosed by the dyke, it is conceivable to consider wave action not very significant, therefore the distribution of the grain size can be directly related to the peak tidal flow (Amos, 1995). Another important aspect to consider is the source of the sediment deposited inside the polder. The increasing sediment budget and the quick equilibrium state reached by the inlet strongly support the hypothesis that the sediment derives from outside the basin, also favored by the proximity of the tidal flat to the tide-dominated ETM (Nihoul et al., 1978; Chen et al., 2005). However, it must be taken into account that before the opening of the inlet, the nature of soils used for agriculture was indeed predominantly sandy. As erosion rates resulted to be more pronounced in the Northern part of the tidal flat, the higher percentage of sand in the samples could derive from the reworking by tidal currents of the original agricultural soils. It is also noticeable, as expected, the similarity in the distribution of LOI with the particle size distribution. Low values of LOI coincide with the location of coarser sediment, an indicator of higher tidal currents. The association between fine sediments and high values of organic matter is found in locations with weak hydrodynamic regimes.

Sediment Budget of the Tidal Flat

Overall, the sediment budget of the tidal flat is positive and the speed of accretion, after a very rapid onset immediately after basin opening, seems to have slightly decreased toward the end of the monitored period. During the first period of monitoring, the vertical changes were remarkable, meaning that all error thresholds could be considered as they were smaller than the order of change. Thus, the sediment budget was obtained as the average between the volumes calculated using all thresholds, resulting as $\sim$22000 m^3 $year^{-1}$, that is, $\sim$1800 m^3 $month^{-1}$; the second period also had a positive sediment budget, but Vertical variations are smaller than the first period and most of them were lower than the error threshold of 0.10–0.15 m. Thus, only the threshold of 0.05 m was used. The sediment budget decreased to $\sim$16800 m^3 $year^{-1}$, equivalent to $\sim$1400 m^3 $month^{-1}$. Finally, the volumes derived from the last period can only be considered as a gross estimate of how the tidal flat is developing, considering that two different techniques were compared (DGPS vs. Lidar). In these last 10 months the sediment gain was $\sim$19000 m^3 $year^{-1}$, so 1600 m^3 $month^{-1}$; the sediment budget of the tidal flat is still positive and the orders of volume accretion are comparable.

The accretion occurs in different areas of the tidal flat, but mostly in the creeks and at its edges. It is interesting to note that the sedimentation rate from the traps deployed during the Spring tidal cycle of June and the tidal cycle of May – June is quite the same (111.9 g/m^2 vs. 117.7 g/m^2), adding reliability to the figures.

From a morphodynamics viewpoint, this "artificial" tidal flat presents an unusual behavior compared to natural ones. The most evident difference is in the creeks. Natural creeks of young marshes are typically characterized by a deepening and enlarging phase, caused by the increase in flow resistance on the marsh platform which concentrates the flow in the channel (D'Alpaos et al., 2006). The opposite condition is found in this study area, where the creeks are filling up. This is clearly visible in **Figure 4**, except for the cross section C4 which is located at the beginning of the creeks, where erosion is dominant, caused by high current velocities. On the other hand, the work of D'Alpaos et al. (2006) relates to an environment where vegetation starts to be present, while here there is no evidence of features (e.g., large bedforms, pioneering vegetation, bioconstructions) that could cause spatial changes in flow resistance. One could speculate that while the flow is inside the creek, velocities remain high, favoring the transit of consistent quantities of sediment. As the tide rises and overspills the creek banks, the expansion of the flow decreases its speed and the heaviest particles transported as bedload (e.g., sand) quickly settle inside the creek, while the fines are transported in suspension across the flat and settle in its upper part when slack tide occurs.

At last, on the basis of the inlet morphological analysis, the main channel that connects the tidal flat to the sea has become nearly stable, possibly providing a stable route for sediment input from the open estuary to the tidal flat. From a management viewpoint this is an important aspect, as future designs of similar schemes could benefit from this successful attempt to allow the system to reach an equilibrium with no intervention by man after the initial dredging.

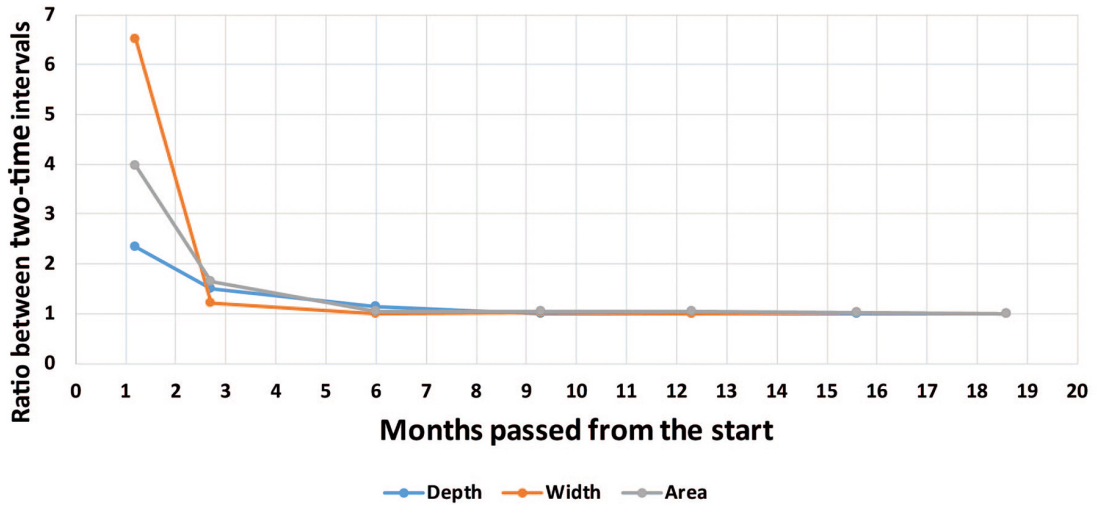

FIGURE 10 | Variation of depth, width and cross-section of the inlet expressed as the ratio between two-time intervals from June 2015 to January 2017.

Salt Marsh Formation

According to Bakker (2014), the conventional limit between salt marsh and tidal flat is defined by the Mean High Tide, obtained by averaging between the Mean High Spring Tide and the Mean High Neap Tide. On the basis of the tidal records of the year 2016 at the Walsoorden tidal station, for this part of the estuary this limit can be identified at about +2.53 m NAP. All the Lidar maps showed that the highest elevation ranged between +0.8 m NAP and +1.10 m NAP, exception for small spots that reached +2.30 m NAP. Thus, the tidal flat has a low elevation and it is still far from becoming appropriate for salt marsh development as the basin is constantly submerged by the tide. If the highest elevation portions are masked after choosing an arbitrary value (e.g., elevation higher than 50 cm above NAP), and a specific accretion map of these areas is created (**Figure 11A**), it becomes evident that the sediment is filling the lower areas, even if accretion values of **Figure 11B** are slighty smaller than the previous in **Figure 11A**. This mechanism of growth is typical of tidal flat and salt marshes and it was described by previous studies (e.g., Leonard, 1997; Allen, 2000; Temmerman et al., 2004).

The most elevated areas are located in the center and at the borders (North-West and North-East principally) (**Figure 11B**). In order to find how many years will be necessary for the tidal flat to reach the Mean High Tide at +2.53 m NAP, the best compromise was to consider the vertical accretion observed in these areas higher than 50 cm NAP. During the first period, from June 2015 to April 2016, the accretion rates of these areas was about 3.2 ± 1.7 cm year^{-1}. During the second period, from April 2016 to February 2017, the average decreased to 2.6 ± 1.5 cm year^{-1}. Furthermore, during the second period, the areas above 50 cm NAP became wider.

If the most elevated areas are taken into account (i.e., located in the northern areas at around 80 - 110 cm NAP), the highest rate of accretion are about 25 cm over 20 months, which means that these limited zones of the tidal flat will become a salt marsh not before a further 8–10 years, assuming that the sedimentation rate will remain constant in time. However, as already mentioned, the accretion of a salt marsh follows an asymptotic growth, consequently, the accretion will decrease in time. Considering now the whole areas above 50 cm NAP with an average of 3 ± 1.6 cm year^{-1} will become a marsh after approximately more than 50 years. The north-west zone could be a good candidate but it is still too exposed to high hydrodynamic conditions and it will probably take longer than the other two areas.

It should also be taken into account that every plant species has a different vertical distribution above the high tide level (Gray, 1992). Gray et al. (1989) compared the vertical distribution of *Spartina anglica* along 107 transects across saltmarshes in 19 estuaries in south and west Britain, producing Eq. 2 that predicts the elevation limits for the existence of *Spartina*:

$$LL = -0.805 + 0.366SR + 0.053F + 0.135Log_eA \quad (2)$$

where LL represents the lower limit of *Spartina* in meters above the NAP, SR is the Spring tidal Range (m), F is the fetch in the direction of the tidal flat transect (km) and Log_eA is the area of the estuary (km^2). Perkpolder has a SR = 5.32 m, F = 3.30 km and the estuary area is 21863 km^2. Therefore, LL equals to 2.67 m. This value is slightly higher than the 2.53 m found by Gray et al. (1989) for British estuaries, meaning that here the condition for *Spartina* establishment could require the tidal flat to reach a higher elevation than the one identified along UK shores. It should be underlined that Gray's equation is based on data collected on natural salt marshes in Britain, developed along open estuaries, while the tidal flat of Perkpolder is enclosed by dykes and has a limited tidal exchange through the inlet, subsequently this approach must be taken with caution and needs validation.

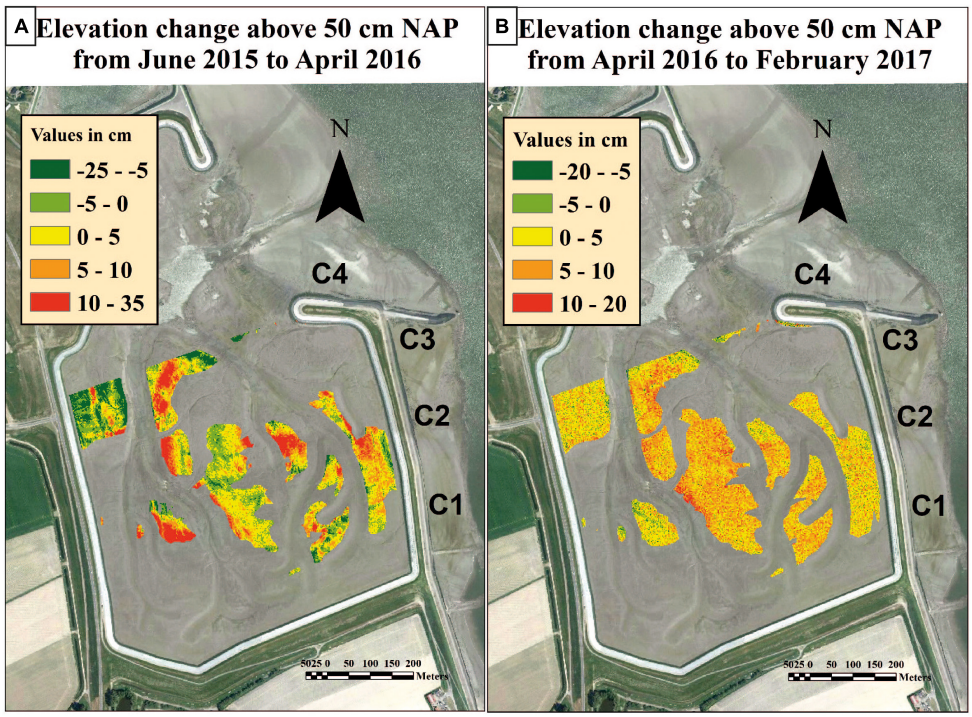

FIGURE 11 | On the left **(A)** elevation changes from June 2015 to April 2016 and on the right **(B)** from April 2016 to February 2017.

TABLE 2 | Average rates of accretion of different study cases from the Western Scheldt (Netherlands) and South England.

Location	Average rates (cm year^{-1})		Months	MHWT (m)
Perkpolder (NL)	6 (Tot)	3.2 (>0.5)	10	Approx. 5
	4.8 (Tot)	2.6 (>0.5)	20	
	5.7* (Tot)		30	
Tollesbury (UK)	3.3		22	Approx. 5
Langenhoe (UK)	6		22	
Molenplaat (NL)	2.4 (Approx. 0)		432	Approx. 5
Lippenbroek (NL)	12.5 (0–0.3)	4.8 (0.3–0.6)	12	1.3
	8.5 (0–0.3)	3.8 (0.3–0.6)	48	
	2.35 (Tot)		108	

*In brackets the elevation above NAP (in meters) used for computing rates is presented. *The total rate after 30 months includes Lidar and DGPS surveys, so should be taken with attention as it might be overestimated for the last period.*

Comparison With Other Case Studies in the North Sea Area

Recent studies of other tidal flats showed how different accretion rates can occur despite similarities in tidal range. Widdows et al. (2004) described another tidal flat of the Westerschelde Estuary, Molenplaat, not so far from Perkpolder (around 6 km North-Westwards). This tidal flat has a sediment accretion of 2.4 cm year^{-1}, that is lower than the Perkpolder one. This could be related to granulometric differences between the two sites. The deposition rate is much lower on the open Molenplaat, with an average of 15 g/m^2 day^{-1} while Perkpolder has a much larger rate, higher than 100 g/m^2 day^{-1}. The Molenplaat tidal flat is characterized by a sand percentage between 61–99%, while the tidal flat of Perkpolder is dominantly silty (as already mentioned, most of the samples have less than 30% of sand; there are only 2 samples composed of more than 90% of sand). The causes of these differences, even if the tidal range and the elevation above mean sea level are the same, could be due to a different regime of tidal currents. Molenplaat is an open tidal flat located in the mid-part of the estuary and the hydrodynamic energy is probably higher than in the Perkpolder basin, that is, instead, enclosed by the dyke ring. According to Nihoul et al. (1978) Molenplaat is located in a characterized by strong hydrodynamics.

A recent paper by Oosterlee et al. (2017) studied another natural restoration project in the salt marsh of Lippenbroek, in the internal part of the Scheldt estuary. A long-term analysis of nine years of monitoring was performed for this 8 ha wetland, demonstrating that the rate of accretion was about 2.35 cm year^{-1}. Even in this case, the sedimentation rates are lower than Perkpolder. The reason behind this difference could be that Lippenbroek is a tidal flat that has developed into a proper salt marsh, and a decrease in sedimentation is expected as high elevations are reached. Many authors (e.g., Pethick, 1981; Marani et al., 2007, 2010; D'Alpaos et al., 2011) showed that the accretion of a salt marsh follows an asymptotic growth that depends on sediment accretion, erosion and biomass, if it is present. Besides, this site is a Controlled Reduced Tide (CRT) marsh, with an artificially controlled tidal range (1.30 m at spring tides instead of the expected 5.40 m). Nevertheless, previous work of Vandenbruwaene et al. (2011) showed that the first year of this

CTR marsh was characterized by an initial average sedimentation rate of about 6 cm year^{-1}, which is comparable with the 6 cm year^{-1} observed during the first ten months of the evolution of Perkpolder. During the following four years, the rates of accretion of Lippenbroek decreased to less than 4 cm year^{-1}; similarly, the rate of accretion of the most elevated areas of Perkpolder after 20 months decreased to 4.8 cm year^{-1}. After nine years, the evolution and the accretion rates of the site of Lippenbroek become very similar to marshes in the UK, despite the different tidal regimes. On this basis, the accretion rates at Perkpolder could be expected to decrease in the future, reaching the values of natural marshes. An important difference is found in the mechanisms of channels formation. Vandenbruwaene et al. (2012) noticed that certain features influences channel formation, like low-elevated zones and areas with compacted polder clay. In the tidal flat of Lippenbroek, channels were easily ditched in low-elevated zones but were hampered by compacted clay. In the tidal flat of Perkpolder, this statement seems to not be applicable. In fact, channels started to develop in the northern areas, even in high elevation zones, but at the same time, they could not evolve in the southern areas, where silt-clay sediment is dominant but not compacted, according to field observations by the authors. Mud here is at times liquid to the point that during field surveys by DGPS the authors were sinking to the waist.

Cousins et al. (2017) installed numerous experimental clay-terraces on engineered sea walls in the marshes of Tollesbury and Langenhoe (Essex, South-Eastern England) from October 2012 to July 2014. After 22 months, the terraces in Langenhoe gained sediment at a rate of 6 cm year^{-1}, while in Tollesbury the rate was 3.3 cm year^{-1}. Compared to the study case of this paper, the sediment accretion rates of the Perkpolder tidal flats are slightly higher than those of the UK sites. Furthermore, the sediment deposition in the UK cases could have been controlled by the presence of vegetation. The Perkpolder basin is instead a young tidal flat, surrounded by dykes and located at around mean sea level NAP where vegetation is not yet able to grow. In **Table 2** the different average rates of accretion of the study cases previously discussed are summarized.

CONCLUSION

The Perkpolder basin is a young artificial tidal flat that is still under development. Since the opening of the inlet on 25 June 2015, the site has been exposed to a semidiurnal tidal regime. Field surveys and sediment sampling proved that the basin is infilling by sand (small amounts), silty sand, sandy silt, loam and clayey silt. Organic Carbon, determined as LOI varies from 1.9% and 12.1%. Between May and June 2017, during a whole Spring to Neap tidal cycle, the deposited sediment ranged from 6.3 g/m^2 day^{-1} to a maximum of 355.5 g/m^2 day^{-1}. During the following tidal cycle up to the Spring tide of the end of June 2017, the sediment quantity varied from 4.7 g/m^2 day^{-1} to 460.8 g/m^2 day^{-1}. The inlet morphology analysis proved that after a quick evolution following the opening, after 6–8 months the inlet stopped its morphodynamics and reached equilibrium conditions. The total sedimentary balance was about 22000 m^3 during the first year of life of the tidal flat (1800 m^3 per month) and 16800 m^3 during the second year (1400 m^3 per month). The average accretion rate of the whole study area was about 6 cm year^{-1}. The most elevated areas, located 50 cm above NAP datum, like the central part of the flat and its borders, gained about 3 cm year^{-1}. Considering the highest regions of the study area, the conditions for initial salt marsh formation will not be established before a further 8–10 years. The portions of the tidal flat that will first become a salt marsh are mainly located in the central area, between the two artificial creeks, and in the Northeastern and Eastern areas. This study provides indication for the ecosystem-based design of innovative coastal defences, giving indications of the time required by the scheme for reaching full efficiency. The establishment of an optimal height for colonization by vegetation can be an important design guideline if a tidal flat is built by dumping of dredged material. Likewise, it provides an indication for optimal conditions if planting should be considered.

DATA AVAILABILITY

The datasets generated for this study are available on request to the corresponding author.

AUTHOR CONTRIBUTIONS

RB and JP carried out the fieldwork and designed the surveys. RB analyzed the data under the supervision of JP and PC. RB and PC wrote the manuscript.

FUNDING

This study did not receive funding with the exception of fieldwork support from HZ University of Applied Sciences to RB.

ACKNOWLEDGMENTS

We would like to express our deepest gratitude to the Centre of Expertise Delta Technology, a consortium between HZ University of Applied Sciences, Royal Netherlands Institute for Sea Research (NIOZ), Wageningen University and Research (WUR), Deltares, and the Dutch Ministry of Infrastructure and Environment (Rijkswaterstaat) for providing us all the data necessaries to reach the purpose of this study. The Orthophotos used for this study are available from the Province of Zeeland: https://zldgwb.zeeland.nl/geoloket/?Viewer=Luchtfotos. Thanks should also go to the numerous students from HZ University of Applied Sciences and Fabio Piazzi who helped during the fieldworks. Many thanks to Michelangelo Brunetta and Cinzia Greco for the ideas exploited to build the sediment traps. Finally, we thank Enrico Duo for the great help in introducing us to the theory of error estimations in DTM analysis. Finally, we are deeply indebted to Dr. Clara Armaroli, who provided constructive scientific criticism to an early version of the manuscript as well as language editing of the text.

REFERENCES

Adam, P. (2011). *Plant Life History Studies in Saltmarsh Ecology*. Cambridge: Cambridge University Press, 309–334.

Allen, J. (2000). Morphodynamics of holocene salt marshes: a review sketch from the Atlantic and Southern North Sea coasts of Europe. *Quat. Sci. Rev.* 19, 1155–1231. doi: 10.1016/S0277-3791(99)00034-7

Allen, J. R. L. (ed.) (1992). *Saltmarshes: Morphodynamics, Conservation and Engineering Significance*. Cambridge: Cambridge University Press.

Amos, C. L. (1995). "Siliciclastic tidal flats," in *Geomorphology and Sedimentology of Estuaries*, ed. G. M. E. Perillo (Amsterdam: Elsevier), 273–306. doi: 10.1016/s0070-4571(05)80030-5

Bakker, J. P. (2014). *Ecology of Salt Marshes: 40 Years of Research in the Wadden Sea*. Leeuwarden: Wadden Academy, 53.

Barbier, E. B., Hacker, S. D., Kennedy, C., Koch, E. W., Stier, A. C., and Silliman, B. R. (2011). The value of estuarine and coastal ecosystem services. *Ecol. Monogr.* 81, 169–193. doi: 10.1890/10-1510.1

Boavida, M. J. (1999). Wetlands: most relevant structural and functional aspects. *Limnetica* 17, 57–63.

Boersema, M. (2016). *Perkpolder Tidal Restoration: One Year After Realisation Draft Progress Report*. Vlissingen: HZ University of Applied Sciences.

Boesch, D. F., and Turner, R. E. (1984). Dependence of fishery species on salt marshes: the role of food and refuge. *Estuaries* 7, 460–468. doi: 10.2307/1351627

Borsje, B. W., van Wesenbeeck, B. K., Dekker, F., Paalvast, P., Bouma, T. J., van Katwijk, M. M., et al. (2011). How ecological engineering can serve in coastal protection. *Ecol. Eng.* 37, 113–122. doi: 10.1016/j.ecoleng.2010.11.027

Bouma, T. J., van Belzen, J., Balke, T., Zhu, Z., Airoldi, L., Blight, A. J., et al. (2014). Identifying knowledge gaps hampering application of intertidal habitats in coastal protection: opportunities & steps to take. *Coast. Eng.* 87, 147–157. doi: 10.1016/j.coastaleng.2013.11.014

Brasington, J., Langham, J., and Rumsby, B. (2003). Methodological sensitivity of morphometric estimates of coarse fluvial sediment transport. *Geomorphology* 53, 299–316. doi: 10.1016/S0169-555X(02)00320-3

Brinke, W. B. M. (1994). The mixing of marine and riverine mud in the Scheldt estuary. ESTUCON. (in Dutch). 14.

Brown, S. L. (1998). Sedimentation on a Humber saltmarsh. *Geol. Soc. Lond. Special Publ.* 139, 69–83. doi: 10.1144/GSL.SP.1998.139.01.06

Butzeck, C., Eschenbach, A., Gröngröft, A., Hansen, K., Nolte, S., and Jensen, K. (2015). Sediment deposition and accretion rates in tidal marshes are highly variable along estuarine salinity and flooding gradients. *Estuaries Coasts* 38, 434–450. doi: 10.1007/s12237-014-9848-8

Cahoon, D. R., and Reed, D. J. (1995). Relationships among Marsh surface topography, hydroperiod, and soil accretion in a deteriorating Louisiana Salt Marsh. *J. Coast. Res.* 11:15.

Chen, M. S., Wartel, S., Eck, B. V., and Maldegem, D. V. (2005). Suspended matter in the Scheldt estuary. *Hydrobiologia* 540, 79–104. doi: 10.1007/s10750-004-7122-y

Claessens, J., and Belmans, H. (1984). Overview of the tidal observations in the Scheldt basin during the decennium 1971–1980. *Tijdschrift der Openbare Werken van Belgie, No.* 3.

Cousins, L. J., Cousins, M. S., Gardiner, T., and Underwood, G. J. C. (2017). Factors influencing the initial establishment of salt marsh vegetation on engineered sea wall terraces in south east England. *Ocean Coast. Manag.* 143, 96–104. doi: 10.1016/j.ocecoaman.2016.11.010

Crosby, S. C., Sax, D. F., Palmer, M. E., Booth, H. S., Deegan, L. A., Bertness, M. D., et al. (2016). Salt marsh persistence is threatened by predicted sea-level rise. *Estuar. Coast. Shelf Sci.* 181, 93–99. doi: 10.1016/j.ecss.2016.08.018

Culberson, S. D., Foin, T. C., and Collins, J. N. (2004). The role of sedimentation in estuarine marsh development within the San Francisco Estuary, CA, USA. *J. Coast. Res.* 20, 970–979. doi: 10.2112/03-0033.1

D'Alpaos, A., Lanzoni, S., Mudd, S. M., and Fagherazzi, S. (2006). Modeling the influence of hydroperiod and vegetation on the cross-sectional formation of tidal channels. *Estuar. Coast. Shelf Sci.* 69, 311–324. doi: 10.1016/j.ecss.2006.05.002.brasin

D'Alpaos, A., Mudd, S. M., and Carniello, L. (2011). Dynamic response of marshes to perturbations in suspended sediment concentrations and rates of relative sea level rise. *J. Geophys. Res.* 116:F04020. doi: 10.1029/2011JF002093

Duo, E., Trembanis, A. C., Dohner, S., Grottoli, E., and Ciavola, P. (2018). Local-scale post-event assessments with GPS and UAV-based quick-response surveys: a pilot case from the Emilia–Romagna (Italy) coast. *Nat. Hazards Earth Syst. Sci.* 18, 2969–2989. doi: 10.5194/nhess-18-2969-2018

Dyer, K. R., Christie, M. C., and Wright, E. W. (2000). The classification of intertidal mudflats. *Cont. Shelf Res.* 20, 1039–1060. doi: 10.1016/S0278-4343(00)00011-X

Evans, B. R., Möller, I., Spencer, T., and Smith, G. (2019). Dynamics of salt marsh margins are related to their three dimensional functional form. *Earth Surf. Process. Landf.* 44, 1816–1827. doi: 10.1002/esp.4614

Fernandez-Nunez, M., Burningham, H., and Ojeda Zujar, J. (2017). Improving accuracy of LiDAR-derived digital terrain models for saltmarsh management. *J. Coast. Conserv.* 21, 209–222. doi: 10.1007/s11852-016-0492-2

Fettweis, M., Sas, M., and Monbaliu, J. (1998). Seasonal, Neap-spring and tidal variation of cohesive sediment concentration in the Scheldt Estuary, Belgium. *Estuar. Coast. Shelf Sci.* 47, 21–36. doi: 10.1006/ecss.1998.0338

French, J. R., Spencer, T., Murray, A. L., and Arnold, N. S. (1995). Geostatistical analysis of sediment deposition in two small tidal wetlands, Norfolk, U.K. *J. Coast. Res.* 11:14.

Friedrichs, C. T. (2011). "Tidal flat morphodynamics," in *Treatise on Estuarine and Coastal Science*, eds E. Wolanski and D. McLusky (Waltham: Academic Press), 137–170. doi: 10.1016/b978-0-12-374711-2.00307-7

Gadow, S. (1970). "Sedimente und chemismus," in *Das Watt, Ablagerungs- und Lebensraum*, ed. H. E. Reineck (Frankfurt: Waldemar Kramer), 23–35.

Grabemann, H.-J., Grabemann, I., and Eppel, D. P. (2004). *Climate Change and Hydrodynamic Impact in the Jade-Weser Area: a Case Study, Coastline Report, 1*. Warnemunde: Geographie Der Department of Drainage and Irrigation, Kuala Meere Und Küste, 9.

Gray, A. J. (1992). "Saltmarsh plant ecology: zonation and succession revisited," in *Saltmarshes: Morphodynamics, Conservation and Engineering Significance*, eds J. R. L. Allen and K. Pye (Cambridge: Cambridge University Press), 63–79.

Gray, A. J., Clarke, R. T., Warman, E. A., and Johnson, P. J. (1989). *Prediction of Marginal Vegetation in a Post-Barrage Environment*. Wareham: Institute of Terrestrial Ecology.

Green, M. O., and Hancock, N. J. (2012). Sediment transport through a tidal creek. *Estuar. Coast. Shelf Sci.* 109, 116–132. doi: 10.1016/j.ecss.2012.05.030

Gunnell, J. R., Rodriguez, A. B., and McKee, B. A. (2013). How a marsh is built from the bottom up. *Geology* 41, 859–862. doi: 10.1130/G34582.1

Heiri, O., Lotter, A. F., and Lemcke, G. (2001). Loss on ignition as a method for estimating organic and carbonate content in sediments: reproducibility and comparability of results. *J. Paleolimnol.* 25, 101–110.

Hladik, C., and Alber, M. (2012). Accuracy assessment and correction of a LIDAR-derived salt marsh digital elevation model. *Remote Sens. Environ.* 121, 224–235. doi: 10.1016/j.rse.2012.01.018

ICRAM (2004). Ministero Dell'ambiente e Della Tutela del Territorio. Servizion Difesa Mare. Metodologie Analitiche di Riferimento. Programma di Monitoraggio per il Controllo Dell'ambiente Marino-Costiero (triennio 2001-2003). Available at: http://www.isprambiente.gov.it/it/pubblicazioni/manuali-e-linee-guida/ (accessed August 29, 2019).

Kirwan, M. L., Guntenspergen, G. R., D'Alpaos, A., Morris, J. T., Mudd, S. M., and Temmerman, S. (2010). Limits on the adaptability of coastal marshes to rising sea level: ecogeomorphic limits to wetland survival. *Geophys. Res. Lett.* 37:L23401. doi: 10.1029/2010GL045489

Kirwan, M. L., Temmerman, S., Skeehan, E. E., Guntenspergen, G. R., and Fagherazzi, S. (2016). Overestimation of marsh vulnerability to sea level rise. *Nat. Clim. Change* 6, 253–260. doi: 10.1038/nclimate2909

Koch, E. W., Barbier, E. B., Silliman, B. R., Reed, D. J., Perillo, G. M., Hacker, S. D., et al. (2009). Non-linearity in ecosystem services: temporal and spatial variability in coastal protection. *Front. Ecol. Environ.* 7:29–37. doi: 10.1890/080126

Leonard, L. A. (1997). Controls of sediment transport and deposition in an incised mainland marsh basin, southeastern North Carolina. *Wetlands* 17, 263–274. doi: 10.1007/BF03161414

Leonardi, N., Carnacina, I., Donatelli, C., Ganju, N. K., Plater, A. J., Schuerch, M., et al. (2018). Dynamic interactions between coastal storms and salt marshes: a review. *Geomorphology* 301, 92–107. doi: 10.1016/j.geomorph.2017.11.001

MacKenzie, R., and Dionne, M. (2008). Habitat heterogeneity: importance of salt marsh pools and high marsh surfaces to fish production in two Gulf of Maine salt marshes. *Mar. Ecol. Prog. Ser.* 368, 217–230. doi: 10.3354/meps07560

Mai, S., and Bartholomä, A. (2000). "The missing mud flats of the Wadden Sea: a reconstruction of sediments and accommodation space lost in the wake of land reclamation," in *Muddy Coast Dynamics and Resource Management*, Vol. 2, eds B. W. Flemming, M. T. Delafontaine, and G. Liebezeit (Amsterdam: Elsevier), 257–272. doi: 10.1016/s1568-2692(00)80021-2

Marani, M., D'Alpaos, A., Lanzoni, S., Carniello, L., and Rinaldo, A. (2007). Biologically-controlled multiple equilibria of tidal landforms and the fate of the Venice lagoon. *Geophys. Res. Lett.* 34:L11402. doi: 10.1029/2007GL030178

Marani, M., D'Alpaos, A., Lanzoni, S., Carniello, L., and Rinaldo, A. (2010). The importance of being coupled: stable states and catastrophic shifts in tidal biomorphodynamics. *J. Geophys. Res.* 115:F04004. doi: 10.1029/2009JF001600

Marion, C., Anthony, E. J., and Trentesaux, A. (2009). Short-term (=2 yrs) estuarine mudflat and saltmarsh sedimentation: high-resolution data from ultrasonic altimetery, rod surface-elevation table, and filter traps. *Estuar. Coast. Shelf Sci.* 83, 475–484. doi: 10.1016/j.ecss.2009.03.039

Mayor, J. R., and Hicks, C. E. (2009). "Potential impacts of elevated CO2 on plant interactions, sustained growth, and carbon cycling in salt marsh ecosystems," in *Human Impacts on Salt Marshes: A Global Perspective*, eds B. R. Silliman, E. D. Grosholz, and M. D. Bertness (Berkeley, CA: University of California Press), 207–228.

McHone, J. G. (1977). Triplot: an APL program for plotting triangular diagrams. *Comput. Geosci.* 3, 633–635. doi: 10.1016/0098-3004(77)90044-9

Meire, P., Ysebaert, T., Damme, S. V., Bergh, E. V., den Maris, T., and Struyf, E. (2005). The Scheldt estuary: a description of a changing ecosystem. *Hydrobiologia* 540, 1–11. doi: 10.1007/s10750-005-0896-8

Millard, K., Redden, A. M., Webster, T., and Stewart, H. (2013). Use of GIS and high resolution LiDAR in salt marsh restoration site suitability assessments in the upper Bay of Fundy. Canada. *Wetlands Ecol. Manag.* 21, 243–262. doi: 10.1007/s11273-013-9303-9

Millennium Ecosystem Assessment (2005). *Ecosystems and Human Well-Being: Synthesis*. Washington, DC: Island Press.

Möller, I., Kudella, M., Rupprecht, F., Spencer, T., Paul, M., van Wesenbeeck, B. K., et al. (2014). Wave attenuation over coastal salt marshes under storm surge conditions. *Nat. Geosci.* 7, 727–731. doi: 10.1038/ngeo2251

Morris, J. T., Porter, D., Neet, M., Noble, P. A., Schmidt, L., Lapine, L. A., et al. (2005). Integrating LIDAR elevation data, multi-spectral imagery and neural network modelling for marsh characterization. *Int. J. Remote Sens.* 26, 5221–5234. doi: 10.1080/01431160500219018

Nardin, W., and Edmonds, D. A. (2014). Optimum vegetation height and density for inorganic sedimentation in deltaic marshes. *Nat. Geosci.* 7, 722–726. doi: 10.1038/ngeo2233

Neumeier, U., and Ciavola, P. (2004). Flow resistance and associated sedimentary processes in a *spartina maritima* salt-marsh. *J. Coast. Res.* 20, 435–447. doi: 10.2112/1551-5036(2004)020[0435:FRAASP]2.0.CO;2

Nihoul, J. C. J., Ronday, F. C., Peters, J. J., and Sterling, A. (1978). "Hydrodynamics of the Scheldt Estuary," in *Hydrodynamics of Estuaries and Fjords*, ed. J. C. J. Nihoul (Amsterdam: Elsevier), 27–53. doi: 10.1016/s0422-9894(08)71270-4

Nolte, S., Koppenaal, E. C., Esselink, P., Dijkema, K. S., Schuerch, M., De Groot, A. V., et al. (2013). Measuring sedimentation in tidal marshes: a review on methods and their applicability in biogeomorphological studies. *J. Coast. Conserv.* 17, 301–325. doi: 10.1007/s11852-013-0238-3

Odum, W. E., McIvor, C. C., and Smith, T. J. (1982). *The Ecology of the Mangroves of South Florida: A Community Profile*. Washington, DC: U.S. Fish and Wildlife Service, 156.

Oosterlee, L., Cox, T. J. S., Vandenbruwaene, W., Maris, T., Temmerman, S., and Meire, P. (2017). Tidal Marsh restoration design affects feedbacks between inundation and elevation change. *Estuaries Coasts* 41, 613–625. doi: 10.1007/s12237-017-0314-2

Orson, R., Panageotou, W., and Leatherman, S. P. (1985). Response of tidal salt Marshes of the U.S. Atlantic and Gulf Coasts to rising sea levels. *J. Coast. Res.* 1, 29–37.

Pethick, J. S. (1981). Long-term accretion rates on tidal salt Marshes. *J. Sediment. Res.* 51, 571–577. doi: 10.1306/212F7CDE-2B24-11D7-8648000102C1865D

Pratolongo, P., Leonardi, N., Kirby, J. R., and Plater, A. (2019). "Temperate coastal wetlands," in *Coastal Wetlands*, eds G. Perillo, E. Wolanski, D. Cahoon, and M. Brinson (Amsterdam: Elsevier), 105–152. doi: 10.1016/b978-0-444-63893-9.00003-4

Redfield, A. C. (1972). Development of a New England Salt Marsh. *Ecol. Monogr.* 42, 201–237. doi: 10.2307/1942263

Reed, D. J. (1989). Patterns of sediment deposition in subsiding coastal salt Marshes, Terrebonne Bay, Louisiana: the role of winter storms. *Estuaries* 12, 222–227. doi: 10.2307/1351901

Reef, R., Schuerch, M., Christie, E. K., Möller, I., and Spencer, T. (2018). The effect of vegetation height and biomass on the sediment budget of a European saltmarsh. *Estuar. Coast. Shelf Sci.* 202, 125–133. doi: 10.1016/j.ecss.2017.12.016

Reimer, J., Schuerch, M., and Slawig, T. (2015). Optimization of model parameters and experimental designs with the optimal experimental design toolbox (v1.0) exemplified by sedimentation in salt marshes. *Geosci. Model Dev.* 8, 791–804. doi: 10.5194/gmd-8-791-2015

Rosso, P. H., Ustin, S. L., and Hastings, A. (2006). Use of lidar to study changes associated with Spartina invasion in San Francisco Bay marshes. *Remote Sens. Environ.* 100, 295–306. doi: 10.1016/j.rse.2005.10.012

Schmid, K. A., Hadley, B. C., and Wijekoon, N. (2011). Vertical accuracy and use of topographic LIDAR data in coastal Marshes. *J. Coast. Res.* 275, 116–132. doi: 10.2112/JCOASTRES-D-10-00188.1

Schuerch, M., Dolch, T., Reise, K., and Vafeidis, A. T. (2014). Unravelling interactions between salt marsh evolution and sedimentary processes in the Wadden Sea (southeastern North Sea). *Prog. Phys. Geogr.* 38, 691–715. doi: 10.1177/0309133314548746

Schuerch, M., Rapaglia, J., Liebetrau, V., Vafeidis, A., and Reise, K. (2012). Salt Marsh accretion and storm tide variation: an example from a Barrier Island in the North Sea. *Estuaries Coasts* 35, 486–500. doi: 10.1007/s12237-011-9461-z

Schuerch, M., Spencer, T., Temmerman, S., Kirwan, M. L., Wolff, C., Lincke, D., et al. (2018). Future response of global coastal wetlands to sea-level rise. *Nature* 561, 231–234. doi: 10.1038/s41586-018-0476-5

Schuerch, M., Vafeidis, A., Slawig, T., and Temmerman, S. (2013). Modeling the influence of changing storm patterns on the ability of a salt marsh to keep pace with sea level rise: salt marsh accretion and storm activity. *J. Geophys. Res. Earth Surf.* 118, 84–96. doi: 10.1029/2012JF002471

Shepard, F. P. (1954). Nomenclature based on sand-silt-clay ratios. *J. Sediment. Res.* 24, 151–158. doi: 10.1306/D4269774-2B26-11D7-8648000102C1865D

Smolders, S., Plancke, Y., Ides, S., Meire, P., and Temmerman, S. (2015). Role of intertidal wetlands for tidal and storm tide attenuation along a confined estuary: a model study. *Nat. Hazards Earth Syst. Sci.* 15, 1659–1675. doi: 10.5194/nhess-15-1659-2015

Spencer, T., Schuerch, M., Nicholls, R. J., Hinkel, J., Lincke, D., Vafeidis, A. T., et al. (2016). Global coastal wetland change under sea-level rise and related stresses: the DIVA wetland change model. *Glob. Planet. Change* 139, 15–30. doi: 10.1016/j.gloplacha.2015.12.018

Stark, J., Meire, P., and Temmerman, S. (2017). Changing tidal hydrodynamics during different stages of eco-geomorphological development of a tidal marsh: a numerical modeling study. *Estuar. Coast. Shelf Sci.* 188, 56–68. doi: 10.1016/j.ecss.2017.02.014

Stark, J., Van Oyen, T., Meire, P., and Temmerman, S. (2015). Observations of tidal and storm surge attenuation in a large tidal marsh: tidal and storm surge attenuation in a Marsh. *Limnol. Oceanogr.* 60, 1371–1381. doi: 10.1002/lno.10104

Stevenson, J. C., Ward, L. G., and Kearney, M. S. (1986). "Vertical accretion in marshes with varying rates of sea level rise," in *Estuarine Variability*, ed. D. Wolf (New York, NY: Academic Press), 241–259. doi: 10.1016/b978-0-12-761890-6.50020-4

Swart, J. P. (1987). *Research on the Ratio Marine/Riverine Mud in the Western Scheldt Estuary. Nota NXL-97.015*. Utrecht: Rijkswaterstaat, 14.

Temmerman, S., Govers, G., Wartel, S., and Meire, P. (2003). Spatial and temporal factors controlling short-term sedimentation in a salt and freshwater tidal marsh, Scheldt estuary, Belgium, SW Netherlands. *Earth Surf. Process. Landf.* 28, 739–755. doi: 10.1002/esp.495

Temmerman, S., Govers, G., Wartel, S., and Meire, P. (2004). Modelling estuarine variations in tidal marsh sedimentation: response to changing sea level and

suspended sediment concentrations. *Mar. Geol.* 212, 1–19. doi: 10.1016/j.margeo.2004.10.021

Temmerman, S., Meire, P., Bouma, T. J., Herman, P. M. J., Ysebaert, T., and De Vriend, H. J. (2013). Ecosystem-based coastal defence in the face of global change. *Nature* 504, 79–83. doi: 10.1038/nature12859

Thomas, S., and Ridd, P. V. (2004). Review of methods to measure short time scale sediment accumulation. *Mar. Geol.* 207, 95–114. doi: 10.1016/j.margeo.2004.03.011

van Proosdij, D., Davidson-Arnott, R. G. D., and Ollerhead, J. (2006). Controls on spatial patterns of sediment deposition across a macro-tidal salt marsh surface over single tidal cycles. *Estuar. Coast. Shelf Sci.* 69, 64–86. doi: 10.1016/j.ecss.2006.04.022

van Wijnen, H. J., and Bakker, J. P. (2001). Long-term surface elevation change in salt Marshes: a prediction of Marsh response to future sea-level rise. *Estuar. Coast. Shelf Sci.* 52, 381–390. doi: 10.1006/ecss.2000.0744

Vandenbruwaene, W., Maris, T., Cox, T. J. S., Cahoon, D. R., Meire, P., and Temmerman, S. (2011). Sedimentation and response to sea-level rise of a restored marsh with reduced tidal exchange: comparison with a natural tidal marsh. *Geomorphology* 130, 115–126. doi: 10.1016/j.geomorph.2011.03.004

Vandenbruwaene, W., Meire, P., and Temmerman, S. (2012). Formation and evolution of a tidal channel network within a constructed tidal marsh. *Geomorphology* 151–152, 114–125. doi: 10.1016/j.geomorph.2012.01.022

Vuik, V., Jonkman, S. N., and van Vuren, S. (2016). Nature-based flood protection: using vegetated foreshores for reducing coastal risk. *E3S Web Conf.* 7:13014. doi: 10.1051/e3sconf/20160713014

Wang, C., Menenti, M., Stoll, M.-P., Feola, A., Belluco, E., and Marani, M. (2009). Separation of ground and low vegetation signatures in LiDAR measurements of salt-marsh environments. *IEEE Trans. Geosci. Remote Sens.* 47, 2014–2023. doi: 10.1109/TGRS.2008.2010490

Wartel, S., Keppens, E., Nielsen, P., Dehairs, F., Van Den Winkel, P., and Cornand, L. (1993). *Determination of the Ratio Marine to Terrestrial Mud in the Belgian Part of the Scheldt Estuary. KBIN and VUB report*. Brussels: Ministerie van de Vlaamse Gemeenschap, 16.

Wehr, A., and Lohr, U. (1999). Airborne laser scanning—an introduction and overview. *ISPRS J. Photogramm. Remote Sens.* 54, 68–82. doi: 10.1016/S0924-2716(99)00011-8

Weis, P. (2016). "Salt Marsh accretion," in *Encyclopedia of Estuaries*, ed. M. J. Kennish (Dordrecht: Springer), 513–515. doi: 10.1007/978-94-017-8801-4_28

Wentworth, C. K. (1922). A scale of grade and class terms for clastic sediments. *J. Geol.* 30, 377–392. doi: 10.1086/622910

Wheaton, J. M., Brasington, J., Darby, S. E., and Sear, D. A. (2010). Accounting for uncertainty in DEMs from repeat topographic surveys: improved sediment budgets. *Earth Surf. Process. Landf.* 35, 136–156. doi: 10.1002/esp.1886

Widdows, J., Blauw, A., Heip, C., Herman, P., Lucas, C., Middelburg, J., et al. (2004). Role of physical and biological processes in sediment dynamics of a tidal flat in Westerschelde Estuary, SW Netherlands. *Mar. Ecol. Prog. Ser.* 274, 41–56. doi: 10.3354/meps274041

Widdows, J., Brinsley, M., Salkeld, P., and Lucas, C. (2000). Influence of biota on spatial and temporal variation in sediment erodability and material flux on a tidal flat (Westerschelde, The Netherlands). *Mar. Ecol. Prog. Ser.* 194, 23–37. doi: 10.3354/meps194023

Conflict of Interest Statement: The authors declare that the research was conducted in the absence of any commercial or financial relationships that could be construed as a potential conflict of interest.

frontiers in Earth Science

PERSPECTIVE
published: 02 October 2019
doi: 10.3389/feart.2019.00260

Coasts in Peril? A Shoreline Health Perspective

J. A. G. Cooper[1,2]* *and Derek W. T. Jackson*[1]

[1] School of Geography and Environmental Science, Ulster University, Coleraine, United Kingdom, [2] Discipline of Geology, School of Agriculture, Earth and Environmental Sciences, University of KwaZulu – Natal, Durban, South Africa

Most assessments of coastal vulnerability are undertaken from the perspective of the risk posed to humans, their property and activities. This anthropocentric view is based on widespread public perception (a) that coastal change is primarily a hazard to property and infrastructure and (b) that sea defenses (whether soft or hard) are required to mitigate and eliminate coastal hazards. From the perspective of coastal ecosystems, such a view is both perverse and damaging. In this paper we present an alternative approach to coastal assessment that centers on the physical integrity of the coast and its associated ecosystems both now and in the near-future. The shoreline health approach represents a new paradigm for coastal management and is intended to provide a much-needed ecosystem perspective. Its premise is to categorize coasts on the degree to which their ability to function morphodynamically has been compromised by human intervention. We present an expert assessment approach involving five categories that range from "Good Health" (with "Health Warning" and "Minor Wounds" sub-divisions), through "Minor Injury," "Major Injury," "On Life Support" to "Deceased." We illustrate the concept using tabulated examples of each category from cliffed, clastic and delta coasts and demonstrate its utility through two applications. This approach has the potential to quantify the degree to which coastal ecosystems have been damaged and to focus attention on the cumulative impact of human activities on coastal ecosystems.

Keywords: coastal morphodynamics, coastal risk, ecosystem – based management, sea – level change, coastal management, South Africa

OPEN ACCESS

Edited by:
Christina Robyn Magill, Macquarie University, Australia

Reviewed by:
Yo Fukutani, Kanto Gakuin University, Japan
Alan S. Trenhaile, University of Windsor, Canada

***Correspondence:**
J. A. G. Cooper
jag.cooper@ulster.ac.uk

Specialty section:
This article was submitted to Geohazards and Georisks, a section of the journal Frontiers in Earth Science

Received: *13 February 2019*
Accepted: *20 September 2019*
Published: *02 October 2019*

Citation:
Cooper JAG and Jackson DWT (2019) Coasts in Peril? A Shoreline Health Perspective. Front. Earth Sci. 7:260. doi: 10.3389/feart.2019.00260

INTRODUCTION

The earth's most diverse and productive ecosystems occur at the coast (Ray, 1988). They deliver a host of ecosystem services (Barbier et al., 2011; Jones et al., 2011) and are intensively inhabited by humans. Coastal human communities are susceptible to a variety of natural hazards (flooding, inundation, erosion, and sedimentation) that are driven by episodic events (storms and tsunami, etc.) and long-term changes in sediment supply, sea level, and climate.

Physical coastal change is consequently viewed from an anthropocentric natural hazard or vulnerability perspective (McGranahan et al., 2007; Meur-Férec et al., 2008; Dawson et al., 2009; Serafim et al., 2019) based on societal concern about risks to infrastructure and property (Bonetti and Woodroffe, 2016; Bonetti et al., 2018). There is a widespread public perception that sea defenses are required to mitigate and eliminate coastal hazards (Cooper and McKenna, 2008; Pilkey and Cooper, 2014), creating a demand for "adaptation" measures that resist coastal change

(Cooper and Pile, 2014). This view is underpinned by regional and global assessments that portray high risk in areas that lack coastal defenses (Vafeidis et al., 2008; Hinkel et al., 2014, 2015).

Shoreline stabilization impacts on ecosystem functioning and causes loss of habitat (Cooper and Pilkey, 2012). Activities such as beach nourishment and dredging have immediate local impacts, while other, and longer term impacts (e.g., sediment reduction) are less readily appreciated. Poor public understanding of the negative impacts of shoreline stabilization and a widespread demand for protection of human interests is supported by widespread application of coastal vulnerability indices (Thieler and Hammar-Klose, 2000; Abuodha and Woodroffe, 2010; McLaughlin and Cooper, 2010; Nguyen et al., 2016).

To encourage a paradigm shift in society's view of physical coastal change, we present a new approach that assesses human risks to the ecosystem, rather than ecosystem risks to human interests. The approach involves a rapid assessment of the physical status of a coast and of its ability to function. Natural functioning implies a coast's ability to respond to changes from external dynamic forcing within the constraints imposed by its internal characteristics in order to retain the system's integrity (resilience) both now and in the near future.

MEASURES OF PHYSICAL SHORELINE HEALTH

Ecosystem Health (Costanza et al., 1992) is a complex concept that involves physical, chemical and biological components that interact with each other in the presence of human activity. The metaphor of ecosystem health is also appropriate to the consideration of the status of physical coastal systems. Like organisms, they respond to external and internal stimuli and their ability to do so can be compromised to varying degrees by human actions. We take the view that from a physical viewpoint, any natural coastal system is at the optimum state and cannot be "improved" to achieve "optimum goals" (Barbier et al., 2008).

Physical coastal systems represent a complex interaction of dynamics (wind, waves, and tides), and materials (sediment and rock) within a particular geological framework. The interaction involves internal constraints, external dynamics and feedbacks at various temporal and spatial scales (Cooper et al., 2018), and is encompassed in the concept of morphodynamics (Woodroffe, 2002). Our approach is to determine the extent of human interventions that alter, or have the potential to alter, the natural system. We assess the health of the coastal system according to the degree to which the system's integrity and functioning has been compromised by past and present human activities (and may be impacted in the future by structures or activities that inhibit its response to sea level rise). This approach is in direct contrast to the view (e.g., Lazarus et al., 2016) of coasts as coupled human-natural systems; we view human intervention as compromising coastal functioning.

The universal view of pollution as negative means that the assessment of coastal water and sediment quality is straight forward (e.g., Cooper et al., 1994). Similarly, biotic measures of ecosystem health can readily be conducted by comparison to reference conditions (e.g., Harrison and Whitfield, 2004). The health of the physical coastal ecosystem, however, depends on its ability to adjust and respond to environmental changes now and in the near-future, and this is routinely overlooked in ecosystem assessments. This distortion is likely a result of the dominance of the competing "hazard paradigm" that focusses on human risks from shoreline processes.

Impacts on physical coastal systems arise from human activities both at the coast and distant from it. They involve the following kinds of intervention:

- Alteration of hydrodynamics (e.g., by coastal structures onshore and offshore).
- Alteration of accommodation space/surrounding geological framework (e.g., by construction of harbors, groins, and seawalls).
- Changes in sediment supply (removal/addition) (e.g., by damming rivers, sand extraction, dredging, and beach replenishment).
- Direct impact on existing coastal systems (e.g., by urbanization, land claim, and construction directly on parts of the existing coastal system). The loss can be total or partial.
- Impacts that constrain the coast's future ability to adjust (to sea-level change and future storms) (e.g., roads, buildings, or other impediments to the landward or alongshore migration of landforms).

By assessing the extent to which these impacts are present, it is possible to diagnose the present and near-future state of the coastal morphodynamic system. This can be done through expert assessment when sufficient knowledge is available for any stretch of coast. Below we present a framework for health assessment and apply it in two contrasting settings.

ASSESSING COASTAL HEALTH STATUS

The coast's ability to function morphodynamically is a measure of its health. This implies an ability to change in response to dynamic forcing (especially storms) and to longer term natural changes in sediment supply and volume. At a time of global sea level rise, the ability of a coast to adjust in the near future is also important (our approximate temporal scale is the next century). We propose a diagnosis of shoreline health using a medical terminology to define a spectrum of categories. These range from a system that is in "Good Health" through to one that is beyond remedial care and is functionally "Deceased." These categories reflect the degree to which human activities modify or constrain the natural operation of coastal processes. The major categories are listed below and a fuller description with examples of each condition is provided in **Table 1** for cliffed, clastic and delta coasts. With knowledge of the physical processes and background conditions for a given coast this approach can be applied by a suitably experienced geomorphologist.

1. **Good Health:** no human impediment to shoreline ecosystem functioning.

TABLE 1 | Shoreline health categories with descriptors for (i) cliffed (soft or hard rock cliffs), (ii) clastic (sand or gravel beaches, barriers, and headand-embayment coasts), and (iii) deltas.

Shoreline health category	Rock coast	Clastic coast (barrier/lagoon, headland-embayment)	Delta coast
General descriptors	**Descriptor/example**	**Descriptor/example**	**Descriptor/example**
1. Good health: There is no human impediment to shoreline ecosystem functioning now or in the near future	A natural rock coast where erosion poses no immediate threat to property or infrastructure and eroded material can move freely according to wave action. It may sustain adjacent sedimentary deposits on the rocky coast.	A natural beach or barrier system with no impediment to cross-shore or longshore sediment movement. No interference in sediment supply and space available for landward migration	A delta coast with no existing major impoundments and no impediments to sediment dispersal at the coast (e.g., Rovuma and Mozambique)
1a. Health warning: Actual or planned human structures or planned activities impede the coast's ability to evolve in the near future. The future impact on the system will depend on human response to perceived threats	Infrastructure in proximity to cliff edge poses threat to future cliff mobility	Problems are imminent. For example, a developed area landward of active coastal system with no plan for relocation in the event of sea-level rise (e.g., Balneario Camboriu, Brazil; Gold Coast, Australia)	Planned near-future activities (e.g., dam construction) poses a future threat (e.g., Rufiji and Tanzania)
1b. Surface wounds/scar tissue. Actual human intervention is evident but is not creating problems or past human activity has caused damage. These activities have since stopped and the system is continuing to operate	Small scale infrastructure does not pose a threat to coastal system. Abandoned infrastructure is decaying and being removed by weathering and erosion (e.g., Roman harbors in Mediterranean (Knidos and Turkey); Decayed sea defenses at Happisburgh, England)	Small scale sediment removal Past damage from human activities but now stopped and system is recovered/recovering (e.g., scars from former dune mining, Sefton Coast, England; erosion of man-made "dune" on Outer Banks, North Carolina)	Farming on delta plain, urban development, salt production, but no substantial impact on delta sedimentary system (e.g., Menderes, Turkey). Former human interventions are abandoned and system begins to recover. e.g., Dredged channels are abandoned and begin to silt-up
2. Minor Injury (coast can recover). Human intervention modifies the morphology or rates of sediment supply such that the system continues to operate but differently from its natural condition	Small scale or discontinuous sea defenses. These cause a local reduction in rates of cliff retreat and associated sediment supply (e.g., Streckelsberg, Germany)	A single structure causes changes in the sedimentary system. For example, a groin or jetty interrupts sediment supply, causing updrift accumulation, and downdrift erosion- (e.g., Ocean City Maryland). The system continues to operate but with a different morphology and rates of change.	Sediment supply is somewhat reduced, some channels are dredged, and some inlets have jetties but much of the delta remains in a natural condition (e.g., Zambezi Delta, Mozambique)
3. Major Injury (potentially fatal)	Extensive sea defenses severely reduce or locally halt cliff retreat, impacting cliff processes and sediment supply (e.g., Antrim Coast Road, Northern Ireland)	Often evolving from minor injury category, whereby additional measures are put in place in respinse to changes associated with initial intervention. This usually involves numerous structures (jetties, groins, and seawalls) and/or beach nourishment as the impacts extend along the shoreline (e.g., Multiple breakwaters, Donnalucata, Sicily; multiple groins, Sussex coast, England).	Sediment supply is severely reduced, urbanization is widespread on delta surface, delta shoreline has been heavily modified (e.g., shrimp farms replace mangroves, dykes, and sea defenses abound (e.g., Red River Delta, Vietnam)
4. On life support (system is maintained only by regular human intervention)	Defenses to halt cliff recession eliminate sediment supply to adjacent areas. These are maintained by artificial beach replenishment (e.g., Barton-on-Sea and High cliffe, England)	A beach which is maintained only by ongoing artificial replenishment (e.g., Benidorm, Spain, Gold Coast, Australia) or a tidal inlet system maintained by dredging of channel and tidal deltas (e.g., most inlets on East coast of United States)	The delta sedimentary system has been severely disrupted. Some parts of the system are maintained by human interventions (e.g., Mississippi, United States)
5. Deceased (system has been eliminated-covered/eroded/degraded)	Cliff has been stabilized, covered by concrete or isolated from wave processes by structures. It no longer operates as a sedimentary system (e.g., Withernsea, Yorkshire)	The sedimentary system has been destroyed. For example, sand has been mined to the extent that a beach has disappeared (e.g., Hallsands, England), or coastal structures obliterate the former system (e.g., Portcawl, Wales), or a seawall has prevented beach migration, causing beach loss (e.g., Nantasket Beach, Boston, Pudicherry, India)	The delta sediment supply is severely reduced, sudsidence continues, the delta surface is heavily developed and flooding and erosion are serious issues (e.g., Chao Phraya, Thailand) or the delta is dessicated and being reworked (e.g., Colorado Delta, Mexico)

(Sub-division: With Health Warning): position of human infrastructure may cause concern in the near future - requires planning for future status.

Sub division (Surface Wounds/Scar Tissue): the surface has been modified – e.g., by agriculture, vegetation alteration, recreational space, and/or there are remains of past damage.

1. **Minor Injury:** despite human interventions, the system continues to operate but in a diminished way (e.g., by small scale, discontinuous coastal defenses).
2. **Major Injury:** alteration of sediment supply (e.g., by dams, mining, dumping), or dynamics (by groins, offshore structures, beach being squeezed against seawall, sediment supply fatally compromised, and cliff stabilized). Such systems are capable of resuscitation - e.g., Durham Coast of England.
3. **On Life Support:** system maintained only by continued human intervention, e.g., beach nourishment.
4. **Deceased:** The natural coastal system has been eliminated (covered, eroded, and degraded).

SPATIAL APPLICATION

To demonstrate the approach, we consider two contrasting shorelines: North of Durban, South Africa (**Figure 1**), and NW Northern Ireland (**Figure 2**).

The jetties at the mouth of Durban Harbor (**Figure 1**) interrupt the longshore sediment transport and alter wave conditions such that the Durban beachfront is sediment-starved. The presence of high-rise beachfront development and associated infrastructure immediately landward of (and in some cases on top of) the beach, impedes future migration of the shoreline. The contemporary beach is sustained only by beach replenishment and groins to retain the placed sand. Several recent erosion incidents have highlighted the area's total reliance on artificial sand placement to sustain the ecosystem. It is thus firmly in the "On Life Support" category.

Northward, at the mouth of the Mgeni River the coastline emerges from a zeta-bay configuration to become a linear sandy coast with occasional outcrops of bedrock. The Mgeni River has been heavily dammed. The most recent dam (completed in 1988) is 32 km upstream of the coast. It has reduced the sediment supply, particularly during fluvial floods (Cooper et al., 1990), and beaches are anticipated to become narrower as a result (Garland and Moleko, 2000). For this reason, a 2.5 km stretch of coast downdrift of the Mgeni has been categorized in the "Minor Injury" category. This was chosen over "Major Injury" because the coastal system will continue to operate, but at a different rate. The extent to which the loss of the Mgeni system affects the overall northward longshore transport (Schoonees, 2000) is not known, but the longshore drift to the north is not wholly reliant on the Mgeni River; beyond the lee of the Durban jetties, longshore drift is augmented by sediment that bypasses the harbor entrance. Northwards, the coast is backed by a healthy forested dune, with a golf course and airstrip to landward. These do not impinge on the dune and do not pose an imminent threat to coastal migration. Consequently, this stretch of coast is classified in "Good Health." Northward, the coastline is developed to varying degrees of intensity from large single-family units to multi-unit high-rises at Umhlanga Rocks. All of this development has impinged on or obliterated coastal dunes, and they pose an immediate impediment to modern and near-future shoreline change as evidenced by coastal erosion and property damage during a succession of storms in 2007–2008 (Smith et al., 2010). This is assigned to category "1a: Health Warning," because the coast's future state depends upon human adaptation actions. A retreat from the coast will enable it to recover its health. Construction of hard defenses will place it in the "Major Injury" category and the implementation of beach nourishment would place it on "Life Support."

North of Umhlanga Rocks, the lagoon, barrier beach and dunes are not affected by human activity in such a way as to impede natural processes (="Good Health"). An increase in discharge from a water treatment works has increased the frequency of barrier breaching on the Mhlanga Lagoon (Cooper, 2014). This constitutes a change in frequency rather than a restriction on natural processes and so is discounted in this classification. Northward the coast reverts to a "1a Health Warning" status in the area of Umdloti where a combination of high and low-rise developments and road infrastructure impede future migration of the shoreline.

In the Northern Ireland case study (**Figure 2**) are examples of some additional categories. In the west, a former salt marsh has been subject to land claim and is fronted by a sea defense that isolates it from the remnant tidal flats. To this extent, the shoreline is regarded as "Deceased." Much of the remaining estuarine shoreline is eroding in response to wind-generated estuarine waves, and yielding sediment to the tidal flats. This stretch is in "Good Health." This area provides a useful example of the direct contradiction between shoreline health and the prevailing "risk-orientated" views. Landowners regularly appeal for help to protect property on this eroding shoreline and it's soft, low-lying nature, with the high and consistent rates of shoreline recession would typically identify it as an area of high risk (Cooper and McLaughlin, 1998). At a local scale, some areas have been subject to periodic small-scale attempts to hold the shoreline, but these have been ineffective and do not interfere with the coastal system. They are, in any case too small to map at this scale and are in fact prohibited by existing nature conservation designations. Mapping at a larger scale would likely place them in the "Surface Wounds" category. Similarly, a small jetty near the apex of Magilligan Point appears to cause only local perturbations, rather than a major impact on the coastal system.

The ocean shoreline as far as Portrush is under a variety of conservation designations and is not affected in any major way by human activities or infrastructure. At Portrush, however, a seawall at the rear of West Strand has isolated the beach from adjacent eroding dunes and has led to a lowering and narrowing of the intertidal beach (Carter, 1991). This is regarded as a "Major Injury" that may prove fatal to the coastal system. On the adjacent rocky coast "Surface Wounds" are evident in the form of small concrete structures built to facilitate boat launching

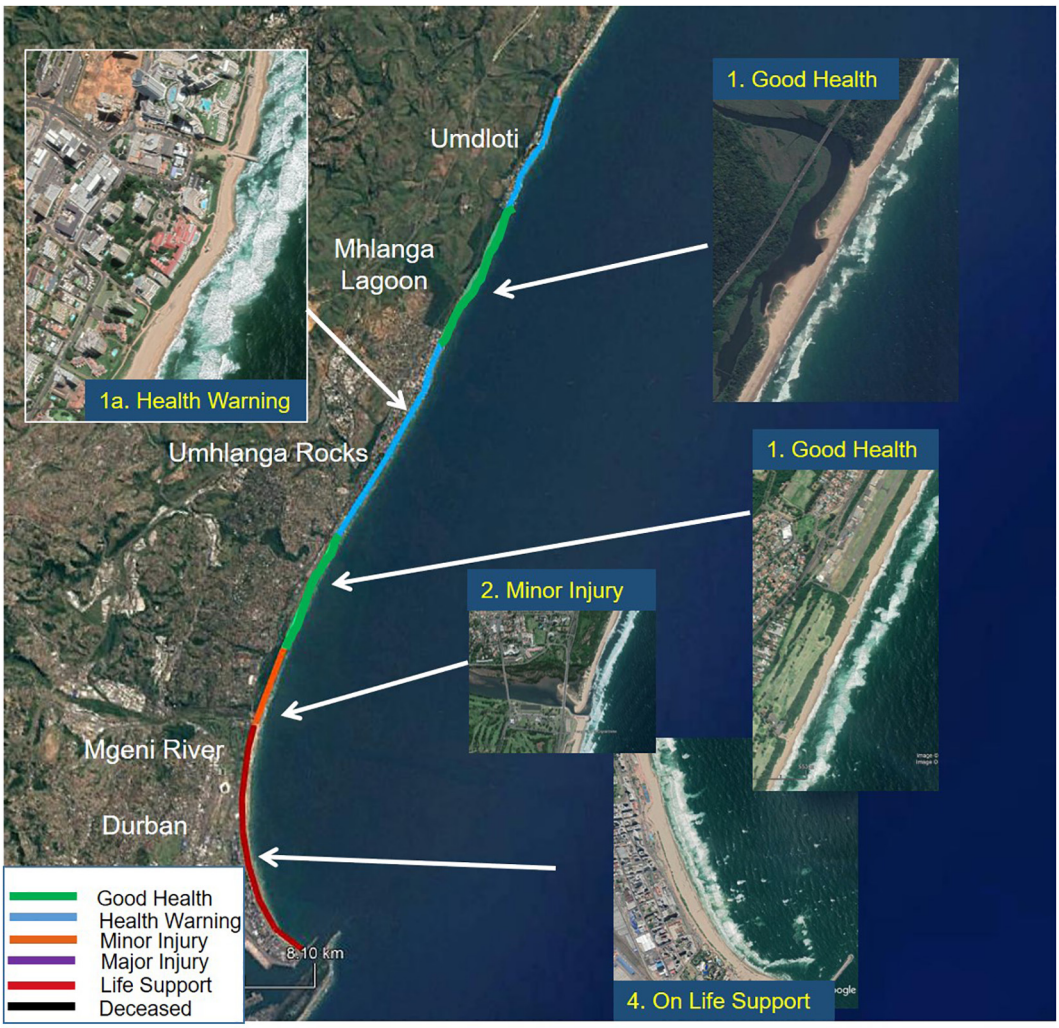

FIGURE 1 | Shoreline Health assessment of a section of the KwaZulu – Natal Coast of South Africa. For description see text. Main image and insets from Google Earth, Map data: SIO, NOAA, U.S. Navy, GEBCO, and AFRIGIS. Data (Insets) 2019 Digitalglobe.

and which may interfere with the movement of material on the shore platform.

Beyond this is an area where the sand dunes are occupied by a golf course. Limited armoring of the base of the dunes has been carried out along a 50 m frontage. Likely shoreline recession under continued sea-level rise, is likely to lead for calls for more armoring, and consequently, this stretch of coast has a Health Warning because of likely future management options that may cause a deterioration in its status. To the east, a stretch of undeveloped rocky coast is under conservation designations and ownership of conservation charities. It is in "Good Health." An exception is the small formerly sandy beach at Portballintrae. As a result of successive human interventions this has been almost entirely eroded, the backing cliffs have been stabilized and armored and the wide sandy beach replaced by a narrow gravel beach on an eroded bedrock surface (Jackson, 2012), placing this coast in the "Deceased" category.

CAN COASTS RECOVER?

For shorelines that have not been fatally damaged, it may be possible to prescribe a remedy such that the shoreline recovers. Like applying a stent in a human heart patient, the health of a shoreline can be greatly improved by removal or repair of damaged parts. A few examples serve to illustrate the principle.

On the west coast of the United States dam construction during the 20th century reduced fluvial sediment supply to the coast, causing erosion in several locations. Recognition of this fact and the desire to reinstate the hydrological regime, led to the deliberate removal of several dams. The Elwha delta in Puget Sound, Washington was studied in detail after removal of a dam in 2011 (Gelfenbaum et al., 2015). An equivalent of 100 years sediment supply was delivered to the coast within 2 years of dam removal. The delta showed significant progradation and development of subtidal and intertidal landforms. Sediment was

FIGURE 2 | Shoreline Health assessment of a section of the north coast of Northern Ireland. For description see text. Main image and insets from Google Earth. Data (Main Image): SIO, NOAA, U.S. Navy, and GEBCO. Data (Insets) 2019 Digitalglobe.

also delivered from the delta to adjacent stretches of coast, restoring the coastal system's morphodynamic function.

On a 12 km stretch of the County Durham Coast in northeast England, 40 million tones of colliery waste was dumped directly on adjacent beaches during the 20th century up to 1993 when mining ceased (Johnson and Frid, 1995). Wave action reworked the leading edge of some of the waste deposits, creating a functioning beach system, albeit composed of large proportions of brick, concrete and ironwork, as well as the coal tailings. However, the beaches were severely degraded: sulfur was being precipitated and the beach interstitial waters were highly acidic (Lawrence et al., 2004). In an initiative to clean up the coast (Durham Heritage Coast) derelict structures were removed, and 1.3 million tones of colliery spoil was removed from beaches. The coast has now been rehabilitated and a natural sedimentary system is being reinstated after a century of damaging intervention.

The practice of "managed realignment" (Esteves, 2014), whereby attempts are made to restore formerly degraded salt marshes by breaching sea defenses and allowing reflooding of agricultural lands is primarily a habitat-creation scheme. Although few such schemes have been adequately monitored, the perception is that such interventions can resuscitate a dying ecosystem, although some assessments point to differences in vegetation structure of reclaimed marshes compared to natural equivalents (Mossman et al., 2012).

These examples illustrate that, as long as the damage is not too great (up to and including the "Major Injury" category), and there is a willingness to do so, shorelines *can* be nursed back to health through remedial action to remove the damaging interventions. In areas that have suffered high levels of degradation, however, recovery may not be possible. In many instances, it is acknowledged that only partial restoration is possible (Simenstad et al., 2006), but the coastal ecosystem continues to exist and operate in a diminished way. On some such severely impacted coasts, attempts have also been made to create artificial habitats, e.g., coastal dunes. These usually require continued intervention and maintenance. Such systems are *not* examples of recovery of deceased coastal systems but are artificial substitutes that replace the former system. They are common

on nourished beach systems (Nordstrom and Mauriello, 2001) and are symptomatic of coasts in the "Life Support" category. On other "Deceased" coastal systems artificial coastal habitats (Nordstrom and Jackson, 2013), are not examples of restoring the health of a system, rather they are substitutes.

DISCUSSION

Preoccupation with the potential impact of coastal hazards on property and infrastructure has distorted approaches to assessing and managing physical coastal systems. This "anthropocentric view" has had a damaging effect by encouraging initiatives that damage the ecosystem. As a prelude to changing this view, an easily understood and easily applied measure of shoreline health is needed that assesses the degree to which physical coastal systems can operate. Our 5-category health assessment represents such an approach. This approach may require further codification, and particularly of boundary definitions between the various classes, but we present the approach as a viable and necessary alternative to coastal vulnerability indices, set firmly within the ecosystem-based management paradigm. Human activities, property and infrastructure are seen as potential impediments to the continued functioning of natural coastal systems, rather than as assets to be protected from natural patterns of coastal change.

Human activities have inflicted damage on coastal systems for centuries or longer and, in many cases, it is difficult to identify these impacts. Human-induced changes in sediment supply, for example, have been widely reported from antiquity to the modern period (e.g., Hein et al., 2014). Some of these impacts continue to the present, while others involved periods of activity that have long ceased (e.g., mining, or past agricultural practices), but which continue to exert an influence on contemporary coastal systems (Oyedotun, 2016). The baseline against which "natural" conditions are assessed will have to be determined in such instances. However, for most of the world's coast, a straightforward assessment of the degree to which human activities compromise physical coastal functioning now and in the near future is quite feasible.

AUTHOR CONTRIBUTIONS

JC wrote the manuscript. DJ contributed in development of the concept, discussion of the content, and review of the draft manuscript.

FUNDING

This work was undertaken in the course of the MarPAMM (Marine Protected Area Management and Monitoring) project. The project is supported by the European Union's INTERREG VA Programme, managed by the Special EU Programmes Body (SEUPB). Match funding was provided by the Department of Agriculture, Environment and Rural Affairs in Northern Ireland and the Department of Housing, Planning and Local Government in Ireland. The views and opinions expressed in this paper do not necessarily reflect those of the European Commission or the Special EU Programmes Body (SEUPB).

REFERENCES

Abuodha, P. A., and Woodroffe, C. D. (2010). Assessing vulnerability to sea-level rise using a coastal sensitivity index: a case study from southeast Australia. *J. Coast. Conserv.* 14, 189–205. doi: 10.1007/s11852-010-0097-0

Barbier, E. B., Hacker, S. D., Kennedy, C., Koch, E. W., Stier, A. C., and Silliman, B. R. (2011). The value of estuarine and coastal ecosystem services. *Ecol. Monogr.* 81, 169–193.

Barbier, E. B., Koch, E. W., Silliman, B. R., Hacker, S. D., Wolanski, E., Primavera, J., et al. (2008). Coastal ecosystem-based management with nonlinear ecological functions and values. *Science* 319, 321–323. doi: 10.1126/science.1150349

Bonetti, J., de Moraes Rudorff, F., Campos, A. V., and Serafim, M. B. (2018). Geoindicator-based assessment of Santa Catarina (Brazil) sandy beaches susceptibility to erosion. *Ocean Coast. Manag.* 156, 198–208. doi: 10.1016/j.ocecoaman.2017.08.009

Bonetti, J., and Woodroffe, C. (2016). "Spatial analysis for coastal vulnerability assessment," in *Geoinformatics for Marine and Coastal Management*, eds D. Bartlett, and L. Celliers, (Boca Raton, FL: CRC Press), 367–395.

Carter, R. W. G. (1991). Near-future sea level impacts on coastal dune landscapes. *Landsc. Ecol.* 6, 29–39. doi: 10.1007/BF00157742

Costanza, R., Norton, B. G., and Haskell, B. D. (1992). *Ecosystem Health: New Goals for Environmental Management*. Washington: Island Press.

Cooper, J. A. G. (2014). "Coastal Lakes," in *Ugu Lwethu – Our Coast. A Profile of Coastal KwaZulu-Natal*, eds B. J. Goble, R. P. van der Elst, and L. K. Oellermann, (Cedara: KwaZulu-Natal Department of Agriculture and Environmental Affairs and the Oceanographic Research Institute), 37–39.

Cooper, J. A. G., Green, A. N., and Loureiro, C. (2018). Geological constraints on mesoscale coastal barrier behaviour. *Glob. Planet. Change* 168, 15–34. doi: 10.1016/j.gloplacha.2018.06.006

Cooper, J. A. G., Mason, T. R., Reddering, J. S. V., and Illenberger, W. K. (1990). Geomorphological effects of catastrophic flooding on a small subtropical estuary. *Earth Surf. Process. Landf.* 15, 25–41. doi: 10.1002/esp.3290150104

Cooper, J. A. G., and McKenna, J. (2008). Working with natural processes: the challenge for coastal protection strategies. *Geogr. J.* 174, 315–331. doi: 10.1111/j.1475-4959.2008.00302.x

Cooper, J. A. G., and McLaughlin, S. (1998). Contemporary multidisciplinary approaches to coastal classification and environmental risk analysis. *J. Coast. Res.* 14, 512–524.

Cooper, J. A. G., and Pile, J. (2014). The adaptation-resistance spectrum: a classification of contemporary adaptation approaches to climate-related coastal change. *Ocean Coast. Manag.* 94, 90–98. doi: 10.1016/j.ocecoaman.2013.09.006

Cooper, J. A. G., and Pilkey, O. H. (eds) (2012). *Pitfalls of Shoreline Stabilization: Selected Case Studies*. Dordrecht: Springer.

Cooper, J. A. G., Ramm, A. E. L., and Harrison, T. D. (1994). The estuarine health index: a new approach to scientific information transfer. *Ocean Shoreline Manag.* 25, 103–141. doi: 10.1016/0964-5691(94)90043-4

Dawson, R. J., Dickson, M. E., Nicholls, R. J., Hall, J. W., Walkden, M. J., Stansby, P. K., et al. (2009). Integrated analysis of risks of coastal flooding and cliff erosion under scenarios of long term change. *Clim. Change* 95, 249–288. doi: 10.1007/s10584-008-9532-8

Durham Heritage Coast, Available at: http://www.turning-the-tide.org.uk/ (accessed September 25, 2019).

Esteves, L. S. (2014). *Managed Realignment: A Viable Long-Term Coastal Management Strategy?* Dordrecht: Springer.

Garland, G., and Moleko, L. (2000). Geomorphological impacts of Inanda Dam on the Mgeni estuary, north of Durban, South Africa. *Bull. Eng. Geol. Environ.* 59, 119–126. doi: 10.1007/s100640000057

Gelfenbaum, G., Stevens, A. W., Miller, I., Warrick, J. A., Ogston, A. S., and Eidam, E. (2015). Large-scale dam removal on the Elwha River, Washington, USA: coastal geomorphic change. *Geomorphology* 246, 649–668. doi: 10.1371/journal.pone.0187742

Harrison, T. D., and Whitfield, A. K. (2004). A multi-metric fish index to assess the environmental condition of estuaries. *J. Fish Biol.* 65, 683–710. doi: 10.1016/j.marpolbul.2008.07.020

Hein, C. J., FitzGerald, D. M., Buynevich, I. V., Van Heteren, S., and Kelley, J. T. (2014). Evolution of paraglacial coasts in response to changes in fluvial sediment supply. *Geol. Soc. Lond. Spec. Publ.* 388:247. doi: 10.1144/sp388.15

Hinkel, J., Jaeger, C., Nicholls, R. J., Lowe, J., Renn, O., and Peijun, S. (2015). Sea-level rise scenarios and coastal risk management. *Nat. Clim. Change* 5, 188–190. doi: 10.1038/nclimate2505

Hinkel, J., Lincke, D., Vafeidis, A. T., Perrette, M., Nicholls, R. J., Tol, R. S., et al. (2014). Coastal flood damage and adaptation costs under 21st century sea-level rise. *Proc. Natl. Acad. Sci. U.S.A.* 111, 3292–3297. doi: 10.1073/pnas.1222469111

Jackson, D. W. (2012). "Portballintrae Bay, Northern Ireland: 116 years of misplaced management," in *Pitfalls of Shoreline Stabilization*, eds J. Cooper, and O. Pilkey, (Dordrecht: Springer), 93–104. doi: 10.1007/978-94-007-4123-2_6

Johnson, L. J., and Frid, C. L. J. (1995). The recovery of benthic communities along the County Durham coast after cessation of colliery spoil dumping. *Mar. Pollut. Bull.* 30, 215–220. doi: 10.1016/0025-326x(94)00145-y

Jones, L., Angus, S., Cooper, A., Doody, P., Everard, M., Garbutt, A., et al. (2011). *Coastal Margin Habitats. in UK National Ecosystem Assessment. Understanding Nature's Value to Society. Technical Report*. Cambridge: UNEP-WCMC.

Lawrence, D. J., Vye, C. L., and Young, B. (2004). *Durham Geodiversity Audit*. Available at: https://www.durham.gov.uk/media/3683/County-Durham-Geodiversity-Audit/pdf/CountyDurhamGeodiversityAudit.pdf?m=635901951858470000 (accessed September 25, 2019).

Lazarus, E. D., Ellis, M. A., Murray, A. B., and Hall, D. M. (2016). An evolving research agenda for human–coastal systems. *Geomorphology* 256, 81–90. doi: 10.1016/j.geomorph.2015.07.043

McGranahan, G., Balk, D., and Anderson, B. (2007). The rising tide: assessing the risks of climate change and human settlements in low elevation coastal zones. *Environ. Urban.* 19, 17–37. doi: 10.1177/0956247807076960

McLaughlin, S., and Cooper, J. A. G. (2010). A multi-scale coastal vulnerability index: a tool for coastal managers? *Environ. Hazards* 9, 233–248. doi: 10.3763/ehaz.2010.0052

Meur-Férec, C., Deboudt, P., and Morel, V. (2008). Coastal risks in France: an integrated method for evaluating vulnerability. *J. Coast. Res.* 24, 178–189. doi: 10.2112/05-0609.1

Mossman, H. L., Davy, A. J., and Grant, A. (2012). Does managed coastal realignment create saltmarshes with 'equivalent biological characteristics' to natural reference sites? *J. Appl. Ecol.* 49, 1446–1456. doi: 10.1111/j.1365-2664.2012.02198.x

Nguyen, T. T., Bonetti, J., Rogers, K., and Woodroffe, C. D. (2016). Indicator-based assessment of climate-change impacts on coasts: a review of concepts, methodological approaches and vulnerability indices. *Ocean Coast. Manag.* 123, 18–43. doi: 10.1016/j.ocecoaman.2015.11.022

Nordstrom, K. F., and Jackson, N. L. (2013). "Foredune restoration in urban settings," in *Restoration of Coastal Dunes. Springer Series on Environmental Management*, eds M. Martínez, J. Gallego-Fernández, and P. Hesp, (Berlin: Springer), 17–31. doi: 10.1007/978-3-642-33445-0_2

Nordstrom, K. F., and Mauriello, M. N. (2001). Restoring and maintaining naturally-functioning landforms and biota on intensively developed barrier islands under a no-retreat alternative. *Shore Beach* 69, 19–28.

Oyedotun, T. D. T. (2016). Historical mining signatures: geochemical and mineralogical evaluation of sediments in three coastal-estuarine systems. *J. Coast. Zone Manag.* 19:432.

Pilkey, O. H., and Cooper, J. A. G. (2014). *The Last Beach*. Durham, NC: Duke University Press.

Ray, G. C. (1988). "Ecological diversity in coastal zones and oceans," in *Biodiversity*, ed. E. O. Wilson, (Washington, DC: National Academy of Sciences/Smithsonian Institution), 36–50.

Schoonees, J. S. (2000). Annual variation in the net longshore sediment transport rate. *Coast. Eng.* 40, 141–160. doi: 10.1016/S0378-3839(00)00009-0

Simenstad, C., Reed, D., and Ford, M. (2006). When is restoration not?: Incorporating landscape-scale processes to restore self-sustaining ecosystems in coastal wetland restoration. *Ecol. Eng.* 26, 27–39. doi: 10.1016/j.ecoleng.2005.09.007

Serafim, M. B., Siegle, E., Corsi, A. C., and Bonetti, J. (2019). Coastal vulnerability to wave impacts using a multi-criteria index: Santa Catarina (Brazil). *J. Environ. Manage.* 230, 21–32. doi: 10.1016/j.jenvman.2018.09.052

Smith, A. M., Mather, A. A., Bundy, S. C., Cooper, J. A. G., Guastella, L. A., Ramsay, P. J., et al. (2010). Contrasting styles of swell-driven coastal erosion: examples from KwaZulu-Natal. South Africa. *Geol. Mag.* 147, 940–953. doi: 10.1017/s0016756810000361

Thieler, E. R., and Hammar-Klose, E. S. (2000). *National Assessment of Coastal Vulnerability to Sea-Level Rise; Preliminary Results for the US Gulf of Mexico Coast. USGS Open File Report No. 2000–2179*. Reston, VA: United States Geological Survey.

Vafeidis, A. T., Nicholls, R. J., McFadden, L., Tol, R. S., Hinkel, J., Spencer, T., et al. (2008). A new global coastal database for impact and vulnerability analysis to sea-level rise. *J. Coast. Res.* 24, 917–924. doi: 10.2112/06-0725.1

Woodroffe, C. D. (2002). *Coasts: Form, Process and Evolution*. Cambridge: Cambridge University Press.

Conflict of Interest: The authors declare that the research was conducted in the absence of any commercial or financial relationships that could be construed as a potential conflict of interest.

Advantages of publishing in Frontiers

OPEN ACCESS
Articles are free to read for greatest visibility and readership

FAST PUBLICATION
Around 90 days from submission to decision

HIGH QUALITY PEER-REVIEW
Rigorous, collaborative, and constructive peer-review

TRANSPARENT PEER-REVIEW
Editors and reviewers acknowledged by name on published articles

Frontiers
Avenue du Tribunal-Fédéral 34
1005 Lausanne | Switzerland

Visit us: www.frontiersin.org
Contact us: info@frontiersin.org | +41 21 510 17 00

REPRODUCIBILITY OF RESEARCH
Support open data and methods to enhance research reproducibility

DIGITAL PUBLISHING
Articles designed for optimal readership across devices

FOLLOW US
@frontiersin

IMPACT METRICS
Advanced article metrics track visibility across digital media

EXTENSIVE PROMOTION
Marketing and promotion of impactful research

LOOP RESEARCH NETWORK
Our network increases your article's readership